

General Disclaimer

One or more of the Following Statements may affect this Document

- This document has been reproduced from the best copy furnished by the organizational source. It is being released in the interest of making available as much information as possible.
- This document may contain data, which exceeds the sheet parameters. It was furnished in this condition by the organizational source and is the best copy available.
- This document may contain tone-on-tone or color graphs, charts and/or pictures, which have been reproduced in black and white.
- This document is paginated as submitted by the original source.
- Portions of this document are not fully legible due to the historical nature of some of the material. However, it is the best reproduction available from the original submission.

NASA CR NO. 72967-1

VOLUME I

EXPERIMENTAL QUIET ENGINE PROGRAM

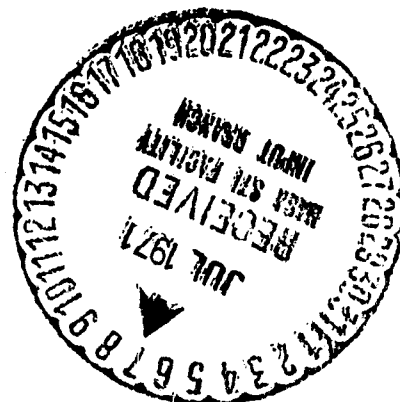
Contract No. NAS3-12430

PHASE I

ENGINE DESIGN REPORT

VOLUME I

March 15, 1970



Prepared for:

National Aeronautics and Space Administration
Lewis Research Center
Cleveland, Ohio, 44135

FACILITY FORM 602

N71-29187	
(ACCESSION NUMBER)	(THRU)
366	63
(PAGES)	(CODE)
CR-72967-1	28
(NASA CR OR TMX OR AD NUMBER)	(CATEGORY)

ADVANCED TECHNOLOGY PROGRAMS DEPARTMENT

GENERAL  ELECTRIC

CINCINNATI, OHIO 45215

VOLUME I

EXPERIMENTAL QUIET ENGINE PROGRAM

Contract No. NAS3-12430

PHASE I ENGINE DESIGN REPORT

VOLUME I, PART I

March 15, 1970

ADVANCED TECHNOLOGY PROGRAMS DEPARTMENT

GENERAL  ELECTRIC

CINCINNATI, OHIO 45215

TABLE OF CONTENTS

<u>Section</u>	<u>VOLUME I</u>	<u>Page</u>
1.0	INTRODUCTION	1
2.0	SUMMARY	3
3.0	AEROACOUSTIC DESIGN	5
3.1	SUMMARY	5
3.2	AEROACOUSTIC DESIGN	5
3.2.1	Basic Fan Design Considerations	5
3.2.2	Blade Row Spacing	7
3.2.3	Vane and Blade Number Selection	7
3.3	UNSUPPRESSED TURBOFAN NOISE PREDICTION	11
3.3.1	Basic Noise Elements	11
3.3.2	Fan Blade Passing Frequency and Harmonic Level Prediction	13
3.3.3	Fan Broadband Noise	14
3.3.4	Multiple Pure Tones (MPT's)	14
3.3.5	Fan and Core Jet Noise	14
3.3.6	Fan Noise Directivity	14
3.3.7	Turbine and Compressor Noise	14
3.3.8	Arc and Maximum Sideline PNL Predictions	16
3.4	SELECTION OF ACOUSTIC TREATMENT	23
3.4.1	Basic Selection Criterion	23
3.4.2	Suppression Bandwidth	23
3.4.3	Maximum Suppression Study	23
3.5	DESIGN OF ACOUSTIC TREATMENT	35
3.5.1	General Considerations	35
3.5.2	Fan Frame Acoustic Treatment	37
3.5.3	Compressor Inlet Acoustic Treatment	42
3.6	DEFINITION OF LOW NOISE FEATURES	43
3.6.1	Outer Case Boundary Layer Bleeding	43
3.6.2	Serrated Rotor	47
3.6.3	Slotted Rotor	49
3.7	TEST PLAN FOR ACOUSTIC SCALE MODEL VEHICLE	50
4.0	FAN AERODYNAMIC DESIGN	61
4.1	SUMMARY	61
4.2	BASIC DESIGN FEATURES	62
4.2.1	Method of Calculation	62
4.2.2	Flowpath	64
4.2.3	Total Pressure Ratio and Loss Coefficient	65
4.3	BLADE PROFILE SELECTION	69
4.3.1	Blade Design	69
4.4	VANE DESIGN	75

TABLE OF CONTENTS (CONTINUED)

<u>Section</u>		<u>Page</u>
5.0	FAN MECHANICAL DESIGN	119
5.1	FAN ROTOR DESIGN	119
5.1.1	Summary	119
5.1.1.1	Fan A Rotor	119
5.1.1.1.1	Material Selection	121
5.1.1.1.2	Blade Design	121
5.1.1.1.3	Disc Design	153
5.1.1.1.4	Coupled Blade-Disc System Vibration Analysis	156
5.1.1.1.5	Other Components	167
5.1.1.2	Fan B Rotor	167
5.1.1.2.1	Blade Design	168
5.1.1.2.2	Disc Design	206
5.1.1.3	Fan C Rotor	214
5.1.1.3.1	Blade Design	214
5.1.1.3.2	Midspan Damper	224
5.1.1.3.3	Disc	230
5.1.1.3.4	Other Rotor Components	235
5.2	FAN STRUCTURES DESIGN	235
5.2.1	Summary	235
5.2.1.1	Fan A Structures	236
5.2.1.1.1	Fan A Frame	236
5.2.1.1.2	Fan A Stator	248
5.2.1.1.3	Acoustic Panels	264
5.2.1.2	Fan B Structures	265
5.2.1.2.1	Fan B Frame	269
5.2.1.2.2	Fan B Stator	269
5.2.1.3	Fan C Structures	282
5.2.1.3.1	Fan C Frame	287
5.2.1.3.2	Fan C Stator	288
5.2.1.4	Engine Design	309
5.2.1.4.1	Fan Module	309
5.2.1.4.2	Engine Mount System	311
5.2.1.4.3	Bypass Ducting, Pylons, and Fan Nozzle	327
6.0	LOW PRESSURE TURBINE AERODYNAMIC DESIGN	329
6.1	SUMMARY	329
6.2	FANS A, B, AND C LOW PRESSURE TURBINE DESIGN REQUIREMENTS	330
6.3	FANS A AND B LOW PRESSURE TURBINE	330
6.4	FAN C LOW PRESSURE TURBINE	334

TABLE OF CONTENTS (CONTINUED)

<u>Section</u>	<u>VOLUME II</u>	<u>Page</u>
7.0	TURBINE AND EXHAUST NOZZLE MECHANICAL DESIGN	337
7.1	LOW PRESSURE TURBINE ROTOR DESIGN	337
7.1.1	Summary	337
7.1.1.1	Fans A and B Turbine	337
7.1.1.1.1	Turbine Rotor	337
7.1.1.1.2	Turbine Cooling	339
7.1.1.1.3	Turbine Rotor Materials	341
7.1.1.1.4	Design Requirements	341
7.1.1.1.5	Design Analysis	349
7.1.1.2	Fan C Turbine	409
7.1.1.2.1	Turbine Rotor	416
7.1.1.2.2	Turbine Cooling	416
7.1.1.2.3	Turbine Rotor Materials	417
7.1.1.2.4	Design Analysis	417
7.2	LOW PRESSURE TURBINE STATOR DESIGN	455
7.2.1	Summary	455
7.2.2	Turbine Stator, Fans A and B	457
7.2.2.1	Turbine Nozzles	457
7.2.2.2	Turbine Casing	466
7.2.2.3	Turbine Shrouds	466
7.2.2.4	Interstage Seals	478
7.2.2.5	Axial Clearances	479
7.2.3	Turbine Stator, Fan C	481
7.2.3.1	Turbine Nozzle, Stage 2	481
7.2.3.2	Turbine Casing	486
7.2.3.3	Turbine Shrouds	486
7.2.3.4	Interstage Seal	492
7.3	LOW PRESSURE TURBINE FRAME AND EXHAUST NOZZLE DESIGN	493
7.3.1	Summary	493
7.3.1.1	Material Selection, Frames and Exhaust Nozzles	493
7.3.1.2	Engine A/B Frame and Nozzle Design	496
7.3.1.2.1	Engine A/B Midframe Design	496
7.3.1.2.2	Engine A/B Rear Frame Design	496
7.3.1.2.3	Engine A/B Exhaust Nozzle Design	496
7.3.1.3	Engine C Turbine Frame and Exhaust Nozzle Design	496
7.3.1.3.1	Engine C Turbine Midframe Design	496
7.3.1.3.2	Engine C Turbine Rear Frame Design	510
7.3.1.3.3	Engine C Exhaust Nozzle Design	510

TABLE OF CONTENTS (CONTINUED)

<u>Section</u>	<u>Page</u>
7.3.1.4 Thermal and Mechanical Stress Analysis - Turbine Frames and Exhaust Nozzles	510
7.3.1.4.1 Analysis, A/B Turbine Midframe	512
7.3.1.4.2 Analysis, A/B Turbine Rear Frame	512
7.3.1.4.3 Analysis, A/B Exhaust Nozzle	528
7.3.1.4.4 Analysis, Engine C Turbine Midframe	528
7.3.1.4.5 Analysis, Engine C Turbine Rear Frame	536
7.3.1.4.6 Analysis, Engine C Exhaust Nozzle	546
8.0 TURBINE THRUST BALANCE AND PARASITIC FLOW ANALYSIS	551
8.1 SUMMARY	551
8.2 METHOD OF ANALYSIS	551
8.3 RESULTS OF ANALYSIS	552
9.0 BEARINGS AND SEALS DESIGN	565
9.1 SUMMARY	565
9.2 FULL SCALE FAN COMPONENT BEARINGS AND SEALS DESIGN	565
9.2.1 Bearing Design	565
9.2.2 Lube and Scavenge System Design	569
9.3 CF6 BEARINGS, SEALS, AND DRIVES DESIGN	569
9.3.1 Bearings and Seals	569
9.3.2 Accessory Drives	574
9.4 CF6 LUBRICATION SYSTEM	575
9.4.1 Lubrication Subsystems	576
9.4.1.1 Lube Supply	577
9.4.1.2 Lube Scavenge	577
9.4.1.3 Sump Air Pressurization	581
9.4.1.4 Vent Air	582
9.5 EXPERIMENTAL QUIET ENGINE BEARINGS AND SEALS DESIGN	583
9.5.1 Sumps and Accessory Drives	583
9.5.2 Bearing and Seal Design	583
9.5.3 Lubrication System	584
10.0 CONTROLS AND ACCESSORIES AND CONFIGURATION DESIGN	585
10.1 SUMMARY	585

TABLE OF CONTENTS (CONCLUDED)

<u>Section</u>	<u>Page</u>
10.1.1 Power Control System	585
10.1.2 Fuel Supply System	586
10.1.3 Electrical System	586
10.1.4 Configuration Design	586
11.0 INSTALLATION AERODYNAMICS AND PERFORMANCE	591
11.1 SUMMARY	591
11.1.1 Inlet Cowl and Diffuser Aerodynamic Design	591
11.1.2 Fan Bypass Duct and Nozzle Aerodynamic Design	591
11.1.3 Core Duct and Nozzle Aerodynamic Design	594
11.1.4 Core Cowl Aerodynamic Design	600
11.1.5 Aircraft Pylon and Lower Pylon Fairing Aerodynamic Design	600
11.1.6 NASA-Lewis Facility Installation Aerodynamic Design	604
12.0 TEST AND INSTRUMENTATION	611
12.1 SUMMARY	611
12.2 FULL SCALE COMPONENT TESTING OF FANS A, B, C, AND X	611
12.2.1 Test Objectives	611
12.2.2 Instrumentation	612
12.2.2.1 Aerodynamic Instrumentation	612
12.2.2.2 Acoustic Instrumentation	615
12.2.2.3 Safety Instrumentation	615
12.3 SCALE MODEL ACOUSTIC TESTING OF CONFIGURATIONS B AND C	616
12.3.1 Test Objectives	616
12.3.2 Acoustic Instrumentation	616
12.3.2.1 Aerodynamic Instrumentation	616
12.3.2.2 Acoustic Instrumentation	618
12.3.2.3 Safety Instrumentation	618
12.4 FULL SCALE ENGINE TESTING	618
12.4.1 Test Objectives	619
12.4.2 Instrumentation	619
12.4.2.1 Aerodynamic Instrumentation	619
12.4.2.2 Acoustic Instrumentation	621
12.4.2.3 Safety Instrumentation	622
13.0 ENGINE CYCLE PERFORMANCE	623
13.1 SUMMARY	623
13.2 ENGINE CYCLE PERFORMANCE	623
14.0 REFERENCES	627

LIST OF ILLUSTRATIONS

VOLUME I

<u>Figure</u>		<u>Page</u>
1	Noise Spectra Comparison Between Low Speed and Low Loading Designs	6
2	Aerodynamically Predicted Blade Row Spacing Effects	8
3	Measured Blade Row Spacing Effects	9
4	Comparison of Fundamental Power Levels (PWL's) for Vane/Blade Ratios of 1.26 and 2.1	10
5	Blade Number Effect on Perceived Noise Levels	12
6	Fan A Spectra - Takeoff, 250-Foot Arc, Aft Maximum	17
7	Fan A Spectra - Approach, 250-Foot Arc, Aft Maximum	18
8	Fan B Spectra - Takeoff, 250-Foot Arc, Aft Maximum	19
9	Fan B Spectra - Approach, 250-Foot Arc, Aft Maximum	20
10	Fan C Spectra - Takeoff, 250-Foot Arc, Aft Maximum	21
11	Fan C Spectra - Approach, 250-Foot Arc, Aft Maximum	22
12	Suppression Bandwidth for 1-Inch MDOF Treatment, Approach Power, Aft Maximum	24
13	Suppression Bandwidth for 1-Inch MDOF Treatment, Take-Off Power, Aft Maximum	25
14	Frame Acoustic Treatment and Compressor Inlet Treatment in Quiet Engine "A"	26
15	Frame Acoustic Treatment and Compressor Inlet Treatment in Quiet Engine "B"	27
16	Frame Acoustic Treatment and Compressor Inlet Treatment in Quiet Engine "C"	28
17	Tuning Study, Fan A, Takeoff	29
18	Tuning Study, Fan A, Approach	30
19	Tuning Study, Fan B, Takeoff	31
20	Suppressed Fan PNdB Versus Peak Suppression Frequency, Fan B, Approach	32

LIST OF ILLUSTRATIONS (CONTINUED)

<u>Figure</u>		<u>Page</u>
21	Tuning Study, Fan C, Takeoff	33
22	Tuning Study, Fan C, Approach	34
23	Three-Degree-of-Freedom Analytical Model	36
24	Resonant Frequencies for 3/4" Thick MDOF Panel with 10% Open Face Plate	38
25	Rectangular Transmission Loss Duct (C68050811)	39
26	Quiet Engine Fan Frame Acoustic Treatment Design	40
27	Acoustic Transmission Loss of the Quiet Engine Fan Frame Treatment	41
28	Acoustic Transmission Loss of the Quiet Engine Compressor Inlet Acoustic Treatment	44
29	Compressor Inlet Acoustic Treatment for Quiet Engines	45
30	Effect of Inlet Boundary Layer Ring, 1/3 Octave Power Level Spectrum	46
31	Boundary Layer Bleed Slot	48
32	Sawtooth Rotor Leading Edge (342297)	52
33	Acoustic Scale Model (CDC 11444)	53
34	Peebles Test Site (CDC 9876)	54
35	Peebles Site 4B - Microphone Field Schematic	55
36	Fan B Acoustic Scale Model, Acoustic Probe Locations	57
37	Quiet Engine Flowpaths	66
38	Radial Variation of Diffusion Factor	67
39	Radial Variation of Turning Angle and Total Pressure	68
40	Radial Variation of Total Pressure Loss Coefficient	70
41	Radial Variation of Incidence Angle	72

LIST OF ILLUSTRATIONS (CONTINUED)

<u>Figure</u>		<u>Page</u>
42	Radial Variation of Deviation Angle and Empirical Deviation Angle Adjustment	73
43	Radial Variation of Percent Throat Margin	74
44	NASA Quiet Engine Fan A Streamline Blade Sections	76
45	NASA Quiet Engine Fan B Streamline Blade Sections	77
46	NASA Quiet Engine Fan C Streamline Blade Sections	78
47	Typical Fan B Tandem Cascade	79
48	Typical Fan B Tandem Cascade Blade Surface Velocity Distribution	80
49	Typical Fan B Tandem Cascade Blade Meanline Angles	82
50	Radial Variation of Inlet Mach Number	83
51	Radial Variation of Static Pressure Rise Coefficient	84
52	NASA Quiet Engine Program Pretest Predicted-Performance Map for Fan A	85
53	NASA Quiet Engine Program Pretest Predicted-Performance Map for Fan B	86
54	NASA Quiet Engine Program Pretest Predicted-Performance Map for Fan C	87
55	Fan A Blade Configuration	120
56	Fan A Aerodynamic Blade Loads (3624 RPM)	122
57	Fan A Final Blade Design - Blade Chord and T_M/c Vs. Average Radius, $N_b = 40$	123
58	Fan A Final Blade Design - Camber and Stagger Vs. Average Radius, $N_b = 40$	124
59	Campbell Diagram, Fan A, Final Blade Design (Ti6Al-4V)	127
60	Fan A Pitch Line at Stall	129

LIST OF ILLUSTRATIONS (CONTINUED)

<u>Figure</u>		<u>Page</u>
61	Aeroelastic Stability Map, Fan A, SLS at Stall	130
62	Fan A Effective Stress Vs Radius, Steady State (Ti6Al-4V @ 3881 RPM)	132
63	Fan A Steady State Effective Stress Vs Radius (Ti6Al-4V @ 3624 RPM)	133
64	Fan A Stage 1 Blade Strain Distribution	134
65	Fan A Stage 2 Blade Strain Distribution	135
66	Fan A Stage 3 Blade Strain Distribution	136
67	Fan A First Flexural Stress/Maximum Stress Vs Percent Blade Height for Ti6Al-4V @ 3881 RPM	139
68	Fan A Second Flexural Stress/Maximum Stress Vs Percent Blade Height for Ti6Al-4V @ 3881 RPM	140
69	Fan A First Torsional Stress/Maximum Stress Vs Percent Blade Height for Ti6Al-4V @ 3881 RPM	141
70	6Al-4V Titanium (C50T88) Blade Dovetail 200°F Stress Range Diagram, Bending Alternating Stress (3 σ Deviation Included), First Flexural, SLS @ 3881 RPM	142
71	6Al-4V Titanium (C50T88) Blade Dovetail 200°F Stress Range Diagram, Bending Alternating Stress (3 σ Deviation Included), 2nd Flexural, SLS @ 3881 RPM	143
72	6Al-4V Titanium (C50T88) Blade Dovetail 200°F Stress Range Diagram, Bending Alternating Stress (3 σ Deviation Included), First Torsional, SLS @ 3881 RPM	144
73	Fan A Blade Dovetail Configuration	145
74	Definitions for Single-Hook Dovetail	146
75	Fan A Tip Shroud Schematic, Top View	150
76	Fan A Detail of Shroud Inclination	151
77	Fan A Disc Stress Distribution	154
78	Fan A Stress Analysis Results	155

LIST OF ILLUSTRATIONS (CONTINUED)

<u>Figure</u>		<u>Page</u>
79	Fan A Disc Dovetail Stress Range Diagram for 4340 Steel (B50T1133)	157
80	Coupled Blade - Disc Model Schematic	159
81	Membrane Analysis - Fan A Disc Rim	160
82	Fan A Blade-Disc Campbell Diagram, 2-Diameter Mode	162
83	Fan A Blade-Disc Campbell Diagram, 3-Diameter Mode	163
84	Fan A Coupled Blade-Disc Modes (2-Diameter, 3624 RPM, Fixed Tangentially)	164
85	Fan A Coupled Blade-Disc Modes (2-Diameter, 3624 RPM, Free Tangentially)	165
86	Goodman Diagram for 7075-T73 Aluminim, Estimated from Data in ALCOA Green Letter No. 206, August 1965	171
87	Quiet Engine Fan B Rotating Beam Fatigue Data for a 7075 Al Forging, Ambient Temperature (Fan Blade Test Forging No. PN 4013103-043)	172
88	Stress Range Diagram for Fan B Ti 6Al-4V Blades at 400°F	176
89	Quiet Engine Fan B Aluminum Airfoil T_m/c Vs Blade Height	177
90	Quiet Engine Fan B Camber Vs Blade Height	178
91	Quiet Engine Fan B Chord Vs Blade Height	179
92	Quiet Engine Fan B Angle of Chord of Blade Vs Blade Height	180
93	Campbell Diagram for the Fan B Aluminum Blade	182
94	Fan B Blade Stability	183
95	Goodman Diagram, Fan B Aluminum Blade	184
96	Fan B Blade Pretwist Distribution	185
97	Quiet Engine Fan B Blade Loads at 3624 RPM	187
98	Quiet Engine Fan B Aluminum Blade Steady State Stress Vs Blade Height (N = 3986 RPM, Concave and Convex Sides)	188

LIST OF ILLUSTRATIONS (CONTINUED)

<u>Figure</u>		<u>Page</u>
99	Quiet Engine Fan B Aluminum Blade Steady State Stress Vs Blade Height (N = 3986 RPM, Leading and Trailing Edges)	189
100	Quiet Engine Fan B Aluminum Blade Vibratory Stress Vs Blade Height in the 1st Flexural Mode (N = 3986 RPM)	190
101	Quiet Engine Fan B Goodman Diagram Showing Location of Critical Stress Points for Aluminum Blades in the 1st Flexural Mode at 3986 RPM	191
102	Blade Dovetail Boundary Loads	192
103	Campbell Diagram for the Fan B Titanium Blade	195
104	Titanium Blade Steady State Stress Vs Blade Height (N = 3986 RPM - 110% Speed)	196
105	Titanium Blade Steady State Stress Vs Blade Height (N = 3986 RPM - 110% Speed)	197
106	Titanium Blade Vibratory Stress Vs Blade Height for the 1st Flexural Mode (N = 3986 RPM)	198
107	Titanium Blade Vibratory Stress Vs Blade Height for the 2nd Flexural Mode (N = 3986 RPM)	199
108	Titanium Blade Vibratory Stress Vs Blade Height for the 1st Torsional Mode (N = 3986 RPM)	200
109	Goodman Diagram for Ti 6Al-4V Titanium Blades, Showing the Location of Critical Stress Points in the First Flexural Mode (N = 3986 RPM - 110% Speed)	201
110	Goodman Diagram for Ti 6Al-4V Titanium Blades, Showing the Location of Critical Stress Points in the Second Flexural Mode (N = 3986 RPM - 110% Speed)	202
111	Goodman Diagram for Ti 6Al-4V Titanium Blades, Showing the Location of Critical Stress Points in the First Torsional Mode (N = 3986 RPM - 110% Speed)	203
112	Disc Dovetail Boundary Loads	205
113	Fan B Goodman Diagram for a 4340 Steel Rotor Disc	209

LIST OF ILLUSTRATIONS (CONTINUED)

<u>Figure</u>		<u>Page</u>
114	Fan B Rotor Disc Elastic Disc Stresses Vs Radius (Titanium Blade, $N = 3986 \text{ RPM}$, $\Delta T = 130^\circ\text{F}$)	210
115	Model, Quiet Engine B Configuration Fan Rotor Boundary Loads (Titanium Blades, 3986 RPM)	211
116	Model, Quiet Engine B Configuration Fan Rotor Stresses (Titanium Blades, 3986 RPM)	212
117	Model, Quiet Engine B Configuration Fan Rotor Deflections (Titanium Blades, 3986 RPM)	213
118	Fan C Airfoil Chord Distribution	215
119	Fan C Airfoil Stagger Variation	216
120	Fan C Airfoil Camber Variation	217
121	Fan C Airfoil Thickness Distribution	218
122	Fan C Airfoil Solidity Variation	219
123	Fan C Leading Edge Steady State Blade Stress	220
124	Fan C Trailing Edge Steady State Blade Stress	221
125	Fan C Concave Side Steady State Blade Stress	222
126	Fan C Convex Side Steady State Blade Stress	223
127	Fan C Allowable Vibratory Stress Ratio, First Flexural Mode	225
128	Fan C Blade Goodman Diagram	226
129	Fan C Blade Campbell Diagram	227
130	Fan C Blade Shroud Thickness Distribution	228
131	Fan C Blade Shroud Effective Steady State Stress Distribution	229
132	Fan C Blade Shroud Radial Deflection Distribution	231
133	Fan C Steady State Disc Stress Distribution	234

LIST OF ILLUSTRATIONS (CONTINUED)

<u>Figure</u>		<u>Page</u>
134	Fan A Full Scale Fan Test Vehicle	237
135	Fan A FSFT Fan Frame Loading	241
136	Fan A Fan Frame Analytical Model	243
137	Fan A Frame Analytical Loading Configurations	244
138	Fan A Frame Maximum Stresses	245
139	Fan A Engine Mount Analytical Model and Results	246
140	Fan A Engine Mount Allowable Alternating Stress	247
141	Campbell Diagram Fan A Bearing Support System	249
142	High Boss Vane	250
143	Fan A Bypass OGV Stress Distribution, Hi C Point, Convex Side	255
144	Fan A Core OGV Stress Distribution, Hi C Point, Convex Side	256
145	Fan A Vane Goodman Diagram	257
146	Campbell Diagram, Fan A Bypass OGV	258
147	Campbell Diagram, Fan A Core OGV	259
148	Fan A Vane Stability Plots	260
149	Campbell Diagram, Fan A Casings	262
150	Typical Strain Gage Map, Bench Test	263
151	Bypass and Core Acoustic Panel Construction	266
152	Fan B FSFT Scale Fan Test Vehicle	267
153	Fan B Frame Maximum Stresses	270
154	Fans B and C Core Stream OGV Mechanics	271
155	Fan B Bypass OGV Stress Distribution, Hi C Point, Convex Side	273

LIST OF ILLUSTRATIONS (CONTINUED)

<u>Figure</u>		<u>Page</u>
156	Fan B Forward Core OGV Stress Distribution, Leading Edge	274
157	Fan B Aft Core OGV Stress Distribution, Trailing Edge	275
158	Goodman Diagram, Fan B Vane	276
159	Campbell Diagram for the Fan B Forward Core OGV	277
160	Campbell Diagram for the Fan B Aft Core OGV	278
161	Campbell Diagram for the Fan B Bypass OGV	279
162	Vane Stability Plot for the Fan B Bypass OGV	280
163	Vane Stability Plots for the Fan B Core OGV's	281
164	Campbell Diagram for the Fan B Casings	283
165	Fan C Full Scale Fan Test (FSFT) Vehicle	285
166	Fan C Frame Analytical Model	295
167	Fan C Frame Analytical Loading Configurations	296
168	Fan C Frame Loading Cases, 12-O'clock Side View	297
169	Fan C Frame Maximum Stresses	298
170	Fan C Bypass OGV Stress Distribution, Trailing Edge	300
171	Fan C Forward Core OGV Stress Distribution, Trailing Edge	301
172	Fan C Aft Core OGV Stress Distribution, Leading Edge	302
173	Goodman Diagram, Fan C Vane	303
174	Campbell Diagram, Fan C Bypass OGV	304
175	Campbell Diagram, Fan C Forward Core OGV	305
176	Campbell Diagram, Fan C Aft Core OGV	306
177	Vane Stability Plots for the Fan C Core OGV's	307
178	Vane Stability Plot for the Fan C Bypass OGV's	308

LIST OF ILLUSTRATIONS (CONTINUED)

<u>Figure</u>		<u>Page</u>
179	Campbell Diagram for the Fan C Casings	310
180	Fan B Engine Installation	313
181	Fan A Engine Configuration	314
182	Fan B Engine Configuration	315
183	Fan C Engine Configuration	316
184	Engine Mounting System, Location of Load Components	317
185	Flight Maneuver Loading Diagram	320
186	Engine Mount System and Facility Mount Adapter	323
187	Fan C - Engine Installation	325
188	Engine Configuration A, Low Pressure Turbine Map	331
189	Engine Configuration B, Low Pressure Turbine Map	332
190	Engine Configuration C, Low Pressure Turbine Map	335
<u>VOLUME II</u>		
191	Low Pressure Turbine for Fans A and B	338
192	Low Pressure Turbine Blade Retainer Design	340
193	Temperature Profiles for the Fans A and B Low Pressure Turbine Blades	345
194	Hot Flowpath for the Fan C Low Pressure Turbine	346
195	Temperature Profiles for the Fan C Low Pressure Turbine Blades	348
196	Blade Nomenclature for the Fans A, B, and C Low Pressure Turbines	350
197	Fans A/B Stage 1 Turbine Blade Steady State Stress	352
198	Fans A/B Stage 2 Turbine Blade Steady State Stress	353
199	Fans A/B Stage 3 Turbine Blade Steady State Stress	354
200	Fans A/B Stage 4 Turbine Blade Steady State Stress	355

LIST OF ILLUSTRATIONS (CONTINUED)

<u>Figure</u>		<u>Page</u>
201	Campbell Diagram for the Fans A/B Stage 1 Turbine Rotor	356
202	Campbell Diagram for the Fans A/B Stage 2 Turbine Rotor	357
203	Campbell Diagram for the Fans A/B Stage 3 Turbine Rotor	358
204	Campbell Diagram for the Fans A/B Stage 4 Turbine Rotor	359
205	Stress Distribution for the Fans A/B Stage 1 Turbine, 444 CPS, 1st Flexural, In-Phase	361
206	Stress Distribution for the Fans A/B Stage 1 Turbine, 1067 CPS, 1st Axial, Out-of-Phase	362
207	Stress Distribution for the Fans A/B Stage 1 Turbine, 4315 CPS, 2nd Flexural, Out-of-Phase	363
208	Stress Distribution for the Fans A/B Stage 1 Turbine, 2041 CPS, 1st Flexural, Out-of-Phase	364
209	Stress Distribution for the Fans A/B Stage 1 Turbine, 2206 CPS, 1st Torsional, Out-of-Phase	365
210	Stress Distribution for the Fans A/B Stage 2 Turbine, 321 CPS, 1st Flexural, In-Phase	366
211	Stress Distribution for the Fans A/B Stage 2 Turbine, 801 CPS, 1st Axial, Out-of-Phase	367
212	Stress Distribution for the Fans A/B Stage 2 Turbine, 1430 CPS, 1st Flexural, Out-of-Phase	368
213	Stress Distribution for the Fans A/B Stage 2 Turbine, 1992 CPS, 1st Torsional, Out-of-Phase	369
214	Stress Distribution for the Fans A/B Stage 3 Turbine, 224 CPS, 1st Flexural, In-Phase	370
215	Stress Distribution for the Fans A/B Stage 3 Turbine, 657 CPS, 1st Axial, Out-of-Phase	371
216	Stress Distribution for the Fans A/B Stage 3 Turbine, 940 CPS, 1st Flexural, Out-of-Phase	372
217	Stress Distribution for the Fans A/B Stage 3 Turbine, 1365 CPS, 1st Torsional, Out-of-Phase	373

LIST OF ILLUSTRATIONS (CONTINUED)

<u>Figure</u>		<u>Page</u>
218	Stress Distribution for the Fans A/B Stage 3 Turbine, 2633 CPS, 2nd Flexural, Out-of-Phase	374
219	Stress Distribution for the Fans A/B Stage 4 Turbine, 168 CPS, 1st Flexural, In-Phase	375
220	Stress Distribution for the Fans A/B Stage 4 Turbine, 521 CPS, 1st Axial, Out-of-Phase	376
221	Stress Distribution for the Fans A/B Stage 4 Turbine, 666 CPS, 1st Flexural, Out-of-Phase	377
222	Stress Distribution for the Fans A/B Stage 4 Turbine, 1207 CPS, 1st Torsional, Out-of-Phase	378
223	Stress Distribution for the Fans A/B Stage 4 Turbine, 1860 CPS, 2nd Flexural, Out-of-Phase	379
224	Blade Dovetail Schematic	380
225	Fans A/B, LP Turbine Rotor, Dovetail Stress Analysis, Stage 1	386
226	Fans A/B, LP Turbine Rotor, Dovetail Stress Analysis, Stage 2	387
227	Fans A/B, LP Turbine Rotor, Dovetail Stress Analysis, Stage 3	388
228	Fans A/B, LP Turbine Rotor, Dovetail Stress Analysis, Stage 4	389
229	Fans A/B, LP Turbine Rotor, Stage 1 Steady State Stress, 3236 RPM	392
230	Fans A/B, LP Turbine Rotor, Stage 1 Steady State Stress, 3830 RPM	393
231	Fans A/B, LP Turbine Rotor, Stage 2 Steady State Stress, 3236 RPM	394
232	Fans A/B, LP Turbine Rotor, Stage 2 Steady State Stress, 3830 RPM	395
233	Fans A/B, LP Turbine Rotor, Stage 3 Steady State Stress, 3236 RPM	396

LIST OF ILLUSTRATIONS (CONTINUED)

<u>Figure</u>		<u>Page</u>
234	Fans A/B, LP Turbine Rotor, Stage 3 Steady State Stress, 3830 RPM	397
235	Fans A/B, LP Turbine Rotor, Stage 4 Steady State Stress, 3236 RPM	398
236	Fans A/B, LP Turbine Rotor, Stage 4 Steady State Stress, 3830 RPM	399
237	Fans A/B, LP Turbine Steady State Disc Temperature	400
238	Fans A and B Turbine Rotor Multishell Analysis, Effective Surface Stress, KSI	406
239	Fans A/B LP Turbine, Stage 1 Campbell Diagram	410
240	Fans A/B LP Turbine, Stage 2 Campbell Diagram	411
241	Fans A/B LP Turbine, Stage 3 Campbell Diagram	412
242	Fans A/B LP Turbine, Stage 4 Campbell Diagram	413
243	Fans A and B LP Turbine Rotor Steady State Temperatures	414
244	Fan C Low Pressure (LP) Turbine	415
245	Fan C LP Turbine Stage 1 Blade, Steady State Stress	420
246	Fan C LP Turbine Stage 2 Blade, Steady State Stress	421
247	Fan C LP Turbine, Stage 1 Campbell Diagram	423
248	Fan C LP Turbine, Stage 2 Campbell Diagram	424
249	Stress Distribution for the Fan C Stage 1 Turbine, 378 CPS, 1st Flexural, In-Phase	428
250	Stress Distribution for the Fan C Stage 1 Turbine, 748 CPS, 1st Axial, In-Phase	429
251	Stress Distribution for the Fan C Stage 1 Turbine, 1601 CPS, 1st Flexural, Out-of-Phase	430
252	Stress Distribution for the Fan C Stage 1 Turbine, 2351 CPS, 1st Torsional, Out-of-Phase	431

LIST OF ILLUSTRATIONS (CONTINUED)

<u>Figure</u>		<u>Page</u>
253	Stress Distribution for the Fan C Stage 1 Turbine, 4241 CPS, 2nd Flexural, Out-of-Phase	432
254	Stress Distribution for the Fan C Stage 2 Turbine, 234 CPS, 1st Flexural, In-Phase	433
255	Stress Distribution for the Fan C Stage 2 Turbine, 642 CPS, 1st Axial, In-Phase	434
256	Stress Distribution for the Fan C Stage 2 Turbine, 868 CPS, 1st Flexural, Out-of-Phase	435
257	Stress Distribution for the Fan C Stage 2 Turbine, 1645 CPS, 1st Torsional, Out-of-Phase	436
258	Stress Distribution for the Fan C Stage 2 Turbine, 2392 CPS, 2nd Flexural, Out-of-Phase	437
259	Fan C, LP Turbine Rotor, Dovetail Stress Analysis, Stage 1	438
260	Fan C, LP Turbine Rotor, Dovetail Stress Analysis, Stage 2	439
261	Fan C, LP Turbine Rotor, Stage 1 Steady State Stress, 4604 RPM	443
262	Fan C, LP Turbine Rotor, Stage 2 Steady State Stress, 4604 RPM	444
263	Fan C, LP Turbine Rotor, Stage 1 Steady State Stress, 5440 RPM (Overspeed)	445
264	Fan C, LP Turbine Rotor, Stage 2 Steady State Stress, 5440 RPM (Overspeed)	446
265	Fan C LP Turbine Steady State Disc Temperature	447
266	Fan C LP Turbine Rotor Multishell Analysis, Effective Surface Stress, KSI (4605 RPM)	451
267	Fan C Interstage Seal Campbell Diagram	453
268	Fan C Pressure Balance Seal Campbell Diagram	454

LIST OF ILLUSTRATIONS (CONTINUED)

<u>Figure</u>		<u>Page</u>
269	Fan C LP Turbine Rotor Steady State Temperatures	456
270	Radial Temperature Profile Entering the Fan A and B LP Turbine Nozzles	458
271	Cast Material Properties, Rene' 80 (C50TF28), 3 Standard Deviations	460
272	Fans A and B LP Turbine Stator Details	461
273	Fans A and B Stage 1 Vane, Gas Load Stresses	462
274	Fans A and B Stage 2 Vane, Gas Load Stresses	463
275	Fans A and B Stage 3 Vane, Gas Load Stresses	464
276	Fans A and B Stage 4 Vane, Gas Load Stresses	465
277	Campbell Diagram for the Fans A/B Stage 1 Vane, In-Phase Modes	467
278	Campbell Diagram for the Fans A/B Stage 1 Vane, Out-of-Phase Modes	468
279	Campbell Diagram for the Fans A/B Stage 2 Vane, In-Phase Modes	469
280	Campbell Diagram for the Fans A/B Stage 2 Vane, Out-of-Phase Modes	470
281	Campbell Diagram for the Fans A/B Stage 3 Vane, In-Phase Modes	471
282	Campbell Diagram for the Fans A/B Stage 3 Vane, Out-of-Phase Modes	472
283	Campbell Diagram for the Fans A/B Stage 4 Vane, In-Phase Modes	473
284	Campbell Diagram for the Fans A/B Stage 4 Vane, Out-of-Phase Modes	474
285	LP Turbine Casing Temperatures for Fans A and B	475
286	LP Turbine Casing Stresses for Fans A and B	476

LIST OF ILLUSTRATIONS (CONTINUED)

<u>Figure</u>		<u>Page</u>
287	Forced Inconel 718 Material Properties	477
288	Vibration Analysis of Static Interstage Seals for LP Turbine Stages 1 through 4, Fans A and B	480
289	Flowpath, Fan C Low Pressure Turbine	482
290	Radial Temperature Profile for the Fan C Low Pressure Turbine Stage 2 Vane, Inlet Temperature	483
291	Tangential Load Stop for the Fan C LP Turbine Stage 2 Vane	484
292	Fan C Stage 2 Vane, Gas Load Stresses	485
293	Campbell Diagram for the Fan C Stage 2 Vane, In-Phase Modes	487
294	Campbell Diagram for the Fan C Stage 2 Vane, Out-of-Phase Modes	488
295	Turbine Casing Metal Temperatures for the Fan C Low Pressure Turbine	489
296	Turbine Casing Maximum Stresses for the Fan C Low Pressure Turbine	490
297	Tangential Load Stop for the Fan C LP Turbine Stage 1 Shroud	491
298	Vibration Analysis of the Stage 2 Seal for the Fan C LP Turbine	494
299	Engine A and B Low Pressure Turbine Frame Assembly	498
300	Engine A and B Exhaust Nozzle Assembly	501
301	Engine A and B Turbine Midframe Isometric	503
302	Engine A and B Turbine Midframe Bolt Connection of Frame Struts	504
303	Turbine Rear Frame Assembly	505
304	Engine C Low Pressure Turbine Frame and Exhaust Nozzle Assembly	507

LIST OF ILLUSTRATIONS (CONTINUED)

<u>Figure</u>		<u>Page</u>
305	Fan C Turbine Midframe Strut Casting (311788)	509
306	Turbine Midframe Maximum Mount Loads	513
307	Bearing Cone Stresses	514
308	Flight Maneuver Loading Diagram	517
309	Engine A/B Turbine Axial Loads, Pounds	519
310	Maximum Stresses Engine A/B Turbine Midframe	520
311	Strut Maximum Stresses, Turbine Midframe	521
312	Turbine Midframe Mount Stress Summary	522
313	Inconel 718 Sheet Material Properties, 3 σ Deviation	523
314	Inconel 718 Cast Material Properties, 3 σ Deviation	524
315	Rene' 41 Cast Material Properties, 3 σ Deviation	525
316	Engine A Integrated Profile of Peaks	526
317	Engine B Integrated Profile of Peaks	527
318	Engine A/B Turbine Rear Frame Maximum Str. s	529
319	Turbine Rear Frame Maximum Strut Stresses	530
320	Frame Temperatures, Engine A/B	532
321	Inconel 718 Cast Material Properties, 3 σ Deviation	533
322	Engine A/B Exhaust Nozzle Shell Stability	534
323	Hastelloy X Yield and Rupture Stresses with 3 σ Deviation	535
324	Engine C Frame Temperatures	538
325	Engine C Turbine Midframe Outer and Inner Ring Stresses	539
326	Cast Rene' 41 Material Properties, 3 σ Deviation (Engine C Turbine Midframe Maximum Stresses)	540

LIST OF ILLUSTRATIONS (CONTINUED)

<u>Figure</u>		<u>Page</u>
327	A-286 Forged Material Properties, 3 σ Deviation	541
328	Inconel 718 Material Properties, 3 σ Deviation (Engine C Turbine Midframe Maximum Stresses)	542
329	Engine C Turbine Axial Loads, Pounds	543
330	Engine C LP Turbine Stage 1 Vane Natural Frequencies	544
331	Engine C Integrated Profile of Peaks	545
332	Engine C Turbine Rear Frame Maximum Stresses	547
333	Inconel 718 Cast Material Properties, 3 σ Deviation (Engine C Turbine Rear Frame Maximum Stress)	548
334	Engine C Exhaust Nozzle Shell Stability	549
335	Engine Forward Cavity Pressures and Flows, Fans A/B	555
336	Engine Forward Cavity Pressures and Flows, Fan C	556
337	Engine Mid-Cavity Pressures and Flows, Fan A	557
338	Engine Mid-Cavity Pressures and Flows, Fan B	558
339	Engine Mid-Cavity Pressures and Flows, Fan C	559
340	Engine Aft Cavity Pressures and Flows, Fan A	560
341	Engine Aft Cavity Pressures and Flows, Fan B	561
342	Engine Aft Cavity Pressures and Flows, Fan C	563
343	Full Scale Fan Component and Test Facility Assembly	567
344	CF6 B Sump	571
345	CF6 Bearing Arrangements	573
346	Lube System Schematic	579
347	Left Side, CF6 Engine	587
348	Right Side, CF6 Engine	587
349	Schematic of the Thick-Lip Inlet for Engine B	592

LIST OF ILLUSTRATIONS (CONCLUDED)

<u>Figure</u>		<u>Page</u>
350	Fan B Inlet Diffuser and Equivalent Conical Diffusion Angle With and Without the 13-Inch Cylindrical Section	593
351	Schematic of the Experimental Quiet Engine Installation	595
352	Fan Duct and Nozzle Mach Number Distribution for Distribution for Engines A, B, and C at Cruise Conditions	596
353	Fan Duct and Nozzle Mach Number Distribution for Engines A, B, and C at Take-off Conditions ($M_0 = 0$)	597
354	Flow Area Distributions for Engines A, B, and C Fan Duct and Nozzle	598
355	Core Duct and Nozzle Mach Number Distribution for Engines A, B, and C at Cruise Conditions	601
356	Core Duct and Nozzle Mach Number Distribution for Engines A, B, and C at Take-Off Conditions ($M_0 = 0$)	602
357	Flow Area Distributions for Engines A, B, and C Core Duct and Nozzle	603
358	Schematic of the NASA-Lewis Installations Bypass Ducts, Indicating Common Parts and the Proposed Locations of Splitters Used to Increase the Amount of Duct Acoustic Treatment	605
359	Bypass Duct Flow Area Distribution of the NASA-Lewis Installation for Fans A and B	606
360	Bypass Duct Flow Area Distribution of the NASA-Lewis Installation for Fan C	607
361	Core Duct Flow Area Distribution of the NASA-Lewis Installation for Fans A, B, and C	608
362	Bypass Duct Mach Number Distribution for the NASA-Lewis Installations	609
363	Full Scale Fan Instrumentation Schematic	613
364	Instrumentation Planes, Acoustic Scale Model Vehicles	617
365	Typical Station Designations for Aerodynamic Instrumentation	620

LIST OF TABLES

<u>Table</u>	<u>VOLUME I</u>	<u>Page</u>
I.	Vane/Blade Selection for Quiet Engine Program Fans	11
II.	Jet Parameters	15
III.	Quiet Engine Program Noise Prediction with 4 Suppressed Engines	15
IV.	Quiet Engine Program Noise Prediction with 4 Unsuppressed Engines	16
V.	Maximum Suppression Frequency	35
VI.	Core Compressor Transmission Loss Test Panels	42
VII.	Test Plan for Acoustic Scale Model Fan B	59
VIII.	Test Plan for Acoustic Scale Model Fan C	60
IX.	Over-All Characteristics for Fans A, B, and C at the Aerodynamic Design Point	63
X.	NASA Quiet Engine Blade and Vane Geometry	89
XI.	Fan A Materials and Allowable Vs Actual Stress Levels	121
XII.	Fan A Blade Design Features	125
XIII.	Fan A Airfoil Tip Torsional End Effects	137
XIV.	Dovetail Stress Results, First Flexural Mode	147
XV.	Dovetail Stress Results, Second Flexural Mode	148
XVI.	Dovetail Stress Results, First Torsional Mode	149
XVII.	Fan B Blade Material Comparison	169
XVIII.	Tensile Properties for 7075-T73 Aluminum and 6Al-4V Titanium	170
XIX.	Aluminum Material Properties from ALCOA Green Letter No. 206, August 1965	173
XX.	Tensile Properties of 7075 Aluminum Taken from Fan B Specimen Blade Forging No. 4013103-043 at Room Temperature	173

LIST OF TABLES (CONTINUED)

<u>Table</u>		<u>Page</u>
XXI.	Material Properties, Fan B Ti 6Al-4V Forging, Allowable Stress at 10^7 Cycles, 50-60KS1	175
XXII.	Fan B Blade Tip Deflections for Blade Only at 3986 RPM	186
XXIII.	Aluminum Blade Dovetail Stresses	194
XXIV.	Titanium Blade Dovetail Stresses	204
XXV.	Material Properties of AISI 4340 at Room Temperature	206
XXVI.	Fan B Disc Rim Loads	208
XXVII.	Dovetail Stresses for the Fan C Blade	232
XXVIII.	Dovetail Stresses for the Fan C Disc	233
XXIX.	Fan C Disc Stress Summary	230
XXX.	Fan A Frame Strut Service Identification	239
XXXI.	Material Selection for the Fan A Structural Components	240
XXXII.	Deflection Coefficients - Lynn Installation	242
XXXIII.	Fan A Airfoil Pitchline Data	251
XXXIV.	Material Selection, Fan Stator Components	250
XXXV.	Fan A Vane Clearances	254
XXXVI.	Fan B Airfoil Pitchline Data	269
XXXVII.	Fan B Vane Clearances	272
XXXIX.	Fan C Frame Deflection Coefficients, Overturning Moment Data	290
XL.	Fan C Frame Deflection Coefficients, Radial Shear Loads	291
XLI.	Fan C Frame Deflection Coefficients, Radial Shear Loads	292
XLII.	Fan C Frame Deflection Coefficients, Overturning Moment Data	293
XLIII.	Fan C Frame Deflection Coefficients, Radial Shear Loads	294
XLIV.	Fan C Airfoil Pitchline Data	299

LIST OF TABLES (CONTINUED)

<u>Section</u>	<u>Page</u>
XLV. Fan C Vane Clearances	309
XLVI. Maximum Test Cell Loads, Engine Mounts	319
XLVII. Maximum Flight Loads, Engine Mounts	319
XLVIII. Flight Conditions for Maximum Flight Loads	319
XLIX. Mount System Material Summary	322
L. Design Data, Fans A and B, Maximum-Power Operating Conditions	333
LI. Design data, Fan C, Maximum-Power Operating Conditions	336

VOLUME II

LII. Rotor Material List	342
LIII. LP Turbine Rotor Blade Summary, Fans A and B	344
LIV. Fan C LP Turbine Rotor Blade Summary	347
LV. Fan A and B LP Turbine Rotor Stage 1 Blade Dovetail Stress Analysis (3500 RPM)	381
LVI. Fan A and B LP Turbine Rotor Stage 2 Blade Dovetail Stress Analysis (3500 RPM)	382
LVII. Fan A and B LP Turbine Rotor Stage 3 Blade Dovetail Stress Analysis (3500 RPM)	383
LVIII. Fan A and B LP Turbine Rotor Stage 4 Blade Dovetail Stress Analysis (3500 RPM)	384
LIX. Fan A and B LP Turbine Rotor Stage 1 Disc Dovetail Stress Analysis (3500 RPM)	402
LX. Fan A and B LP Turbine Rotor Stage 2 Disc Dovetail Stress Analysis (3500 RPM)	403
LXI. Fan A and B LP Turbine Rotor Stage 3 Disc Dovetail Stress Analysis (3500 RPM)	404
LXII. Fan A and B LP Turbine Rotor Stage 4 Disc Dovetail Stress Analysis (3500 RPM)	405

LIST OF TABLES (CONTINUED)

<u>Section</u>	<u>Page</u>
LXIII. LP Turbine Shaft and Bolt Stress Summary, SLS - Standard Day	408
LXIV. Fan C Rotor Material List	418
LXV. Fan C LP Turbine Rotor Stage 1 Blade Dovetail Stress Analysis (4605 RPM)	426
LXVI. Fan C LP Turbine Rotor Stage 2 Blade Dovetail Stress Analysis (4605 RPM)	427
LXVII. Fan C LP Turbine Rotor Stage 1 Disc Dovetail Stress Analysis (4605 RPM)	448
LXVIII. Fan C LP Turbine Rotor Stage 2 Disc Dovetail Stress Analysis (4605 RPM)	449
LXIX. Turbine Nozzle Inlet Temperatures and Pressures	457
LXX. Fans A and B Gas-Load Stresses	459
LXXI. Seal Pressures and Temperatures, Fans A and B	478
LXXII. Fans A and B LP Turbine Stator Critical Axial Clearances	479
LXXIII. Fan C Shroud Nominal Radial Clearances	492
LXXIV. Material Selection for Turbine Frames and Exhaust Nozzles	495
LXXV. Frame Spring Constants	511
LXXVI. Maximum Maneuver Load Combinations	515
LXXVII. Fan A/B Turbine Midframe Unit Loads	516
LXXVIII. Unit Bearing Loads for Maneuver Case	518
LXXIX. Frame Temperatures, °F	531
XXC. Fan C Turbine Midframe Unit Loads	531
XIXC. Flow Network Boundary Conditions	553
XVIIIIC. Bearing Thrust Loads	554

LIST OF TABLES (CONCLUDED)

<u>Section</u>	<u>Page</u>
XVIIC. Full Scale Fans A, B, and C Roller Bearing Data	568
XVIC. Experimental Quiet Engine Installation Exhaust Losses	599
XVC. NASA-Lewis Facility Installation Duct Losses	610
XIVC. Predicted Cycle Performance Data	624

1.0 INTRODUCTION

This design report is for work performed by the General Electric Company for the NASA-Lewis Research Center on the Experimental Quiet Engine Program (Contract NAS3-12430).

This design report is for the design effort of Phase I and covers the basic acoustic, aerodynamic, and mechanical design information used to formulate experimental engine designs to be fabricated and acoustically tested in the latter part of the over-all program.

The major objectives of the over-all Experimental Quiet Engine Program are:

- Demonstration of the technology and the design innovations which will reduce the production and radiation of noise in turbofan engines
- Determination of the noise levels produced by engines which are designed for low noise output and confirmation that predicted noise reductions can be achieved
- Acquisition of experimental acoustic and aerodynamic data for high bypass turbofan engines, which are designed for low noise output, to give a basis for correlation of acoustic theory and experiment, and to give a better understanding of the noise production mechanisms in fans, compressors, turbines, and exhaust jets

To provide Quiet Engine designs that will potentially achieve these objectives, emphasis was placed on the acoustic aspects of the designs. Low noise features were incorporated as part of the designs. In addition, to approximate flight-type designs as near as possible insofar as noise is concerned, typical flight-type flowpaths were employed in the designs; and, flowpath obstructions (such as transfer gearbox shafting that might be noise sources) were incorporated into the design. In addition, typical bypass engine performance was a design constraint. In the interest of minimizing the procurement cycle and shortening the program schedule, some areas of the structural design employ substitute materials for materials that would be more apropos to flight designs and, therefore, lighter in weight. For these areas, flight-type designs were developed and then alternate materials and processes substituted, such that practical design features would be maintained.

2.0 SUMMARY

The results of the design effort detailed in this report encompass the design of three full-scale fans, each containing low noise design features. Taken together, the three fan designs span a range of the speed and aerodynamic loading. The effects of these parameters (as they relate to blade passing frequency and broadband noise) may also be evaluated as well as such parameters as blade number, blade vane ratio, and casing treatment.

In addition, these fans (coupled with the TF39/CF6 core, along with low pressure fan turbines) make up three bypass fan engine designs. The design of these engines is also a part of this report.

The aeroacoustic design section presents in detail the relative merits of low-loading versus low-speed fan designs. The number of blades and the rotational speed of the fan determine the blade passing frequency and its harmonics. Also, the selection of the blade-vane ratio is shown to have an appreciable effect on the pure tone noise levels. It is shown that an engine with a moderate amount of acoustic treatment in the fan and core engine flow-paths will result in perceived-noise levels considerably reduced in magnitude. Perceived-noise-level predictions are presented for the Experimental Quiet Engines with and without the acoustic suppression treatment.

Based upon preliminary engine cycle analysis, the three fan designs were selected having bypass pressure ratios of 1.5 for Fans A and B and 1.6 for Fan C. The two low-speed fans (A and B) were designed at a corrected tip speed of 1160 ft/sec while the low-aerodynamic loading Fan C was designed at a corrected tip speed of 1550 ft/sec. The specified corrected weight flow is 41.3 lb/sec - sq ft annulus area for all three fans. The corrected fan flow for Fans A and B is 950 lb/sec, which yields a tip diameter of 73.354 inches. A corrected flow of 915 lbs/sec for Fan C results in a tip diameter of 68.3 inches.

The mechanical design portions delineate the materials selected for the fan designs and low pressure turbines along with the methods of stress and vibration analysis. The materials chosen are proven state-of-the-art alloys. The individual components which make up the rotating and static structure assemblies are analyzed by proven analytical methods for vibration and stress for all conditions within the design operating ranges. These analyses show that many of the components are designed to operate at conservative values when compared to allowable working limits.

The fans were designed for maximum interchangeability of components between the full scale fan test facility at General Electric Lynn, the NASA-Lewis Acoustics Facility, and the full scale experimental engine.

Two low pressure turbine designs are required to match the fan requirements of different rotor rpm. The rotor speeds of Fans A and B are essentially the same as the CF6 engine, resulting in a good match with the CF6 low pressure turbine. Therefore, the first four stages of the five-stage CF6 low pressure turbine are used to drive Fans A and B. A high-loading low pressure turbine design (matching the high pressure turbine diameter, and with a consequently simplified turbine midframe) was selected for Fan C. The low pressure turbines for all fans are designed to operate at conservative conditions of temperature and pressure levels when compared to allowable or proven operating levels.

In the design of bearings and seals for the full scale fan components and experimental engines, extensive use was made of existing CF6/TF39 hardware. The sumps for the full scale fan test vehicles are almost identical. Thrust loading capability is provided when the fan vehicles are used with either the General Electric, Lynn or NASA-Lewis Test Facility. Engines A, B, and C use the same bearing and seals arrangement as the CF6. Since the Engine C low pressure turbine is cantilevered, bearing Number 7 and the D sump have been eliminated. A new sump and pressurizing system is designed for Engines A and B. This system will utilize a proven system from the LM2500 engine.

The controls and accessories used for control of the engine are essentially identical to those used on the CF6. The accessory gearbox is identical, however, the gearbox is moved radially inward to be compatible with the new fan designs. Engines A, B, and C have redesigned gearbox/pylon tubing arrangements and ignition and oil tank mounting provisions. The decrease in Fan C low pressure turbine diameter resulted in redesign of the external piping and bracketry in the turbine area.

The installation aerodynamics section delineates the inlet and exhaust designs selected for component and engine testing. Most of the testing will be accomplished with a standard bellmouth inlet; however, two flight-type inlets (a thick lip and a thin lip) will be designed and evaluated during engine testing. The inlet and exhaust systems are designed to be representative of typical aircraft applications.

The test and instrumentation planning required for acquisition of acoustic and aerodynamic data are presented for the full scale fan components, scale model vehicles, and full scale engine tests. The over-all test objectives for each area of test, as well as the instrumentation requirements, are specified. Also, the safety instrumentation required for adequate protection of the test vehicles is detailed.

An abbreviated engine cycle performance tabulation is included to provide over-all Engine A, B, and C performance data. These data are based on the predicted fan turbine maps, predicted components performance, and predicted installation losses.

3.0 AEROACOUSTIC DESIGN

3.1 SUMMARY

This section presents the aeroacoustic design of the experimental quiet engine configurations A, B, and C. The relative merits of low loading versus low speed fan designs are briefly discussed. The selection of acoustic treatment for Fans A, B, and C, as well as the compressor inlet treatment, is described. Perceived-noise-level predictions are presented for engine configurations A, B, and C with and without suppression treatment. The results indicate that all three engine noise levels are expected to be within 2 PNdB. Finally, the test plan for a fan component program on a half scale model vehicle is briefly described.

3.2 AEROACOUSTIC DESIGN

3.2.1 Basic Fan Design Considerations

Extensive analytic studies have shown that, by reducing the fan aerodynamic loading, a significant reduction in blade passing frequency noise can be obtained. The lower loading can be achieved by lowering fan pressure ratio and increasing fan size in order to maintain thrust, or by increasing fan tip speed while holding the pressure ratio and size constant.

The former method is restricted by installation limitations as well as installed performance requirements. The latter tenet, however, has several advantages. The higher-tip-speed fan reduces the fan tip diameter and the number of low pressure turbine stages required for a given thrust. Thus, installed performance is increased, and engine weight, cost, and complexity are decreased.

The increased tip speed does increase broadband noise generation and will produce the supersonic phenomenon of multiple pure tones (MPT's). The MPT's are known to occur only when the fan rotor tip relative Mach number exceeds unity. MPT frequencies are characteristically well below the blade passing frequency and at multiples of the shaft revolutions of the fan rotor. These tones may be controlled by keeping their frequency low (i.e., in the low annoyance frequency range). This is best achieved by keeping blade number and/or fan rotor rpm as low as possible.

Thus, by judicious selection of fan pressure ratio, fan size, and tip speed, a viable low noise fan design can be obtained (see Figure 1).

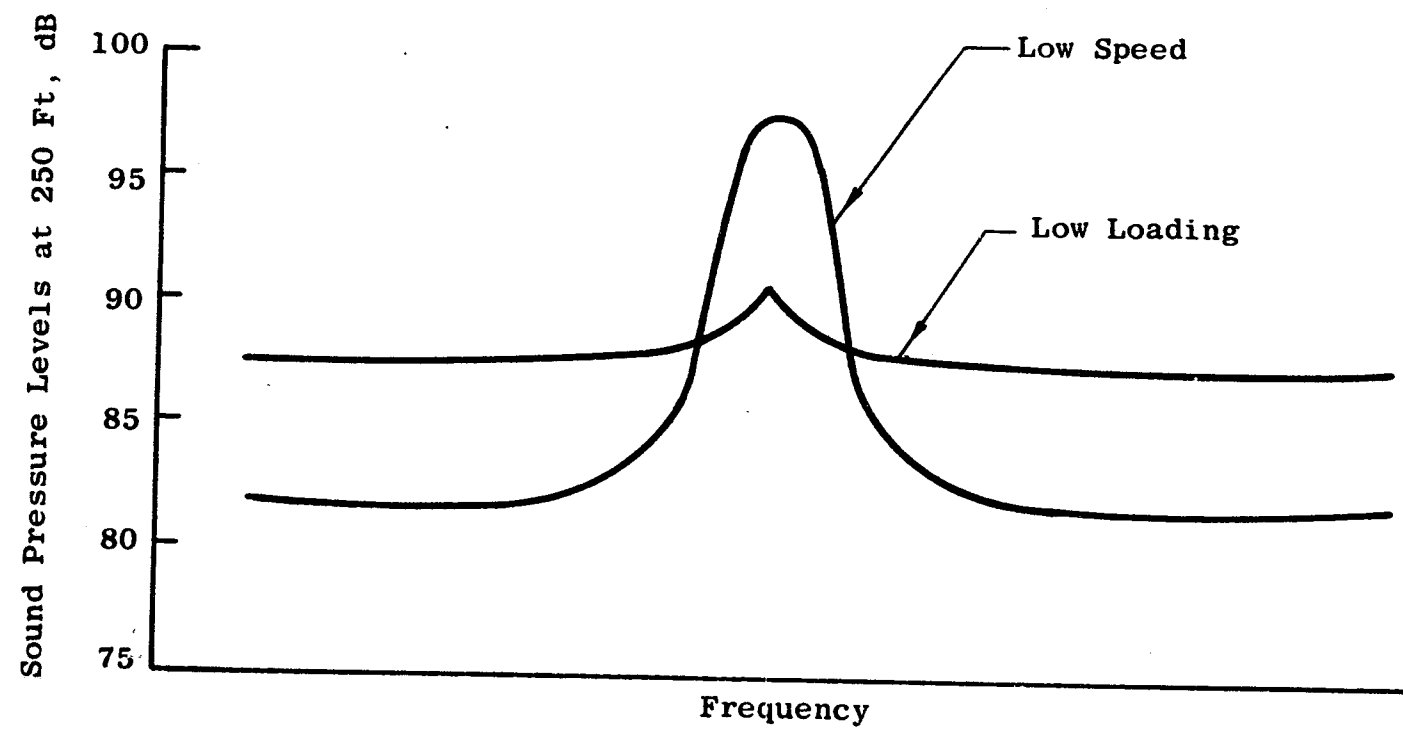


Figure 1. Noise Spectra Comparison Between Low Speed and Low Loading Designs

In order to verify the low loading concept, two basic fan designs were selected for the Experimental Quiet Engine Program: one at a design tip speed of 1160 ft/sec and another at 1550 ft/sec, with each engine developing 4,900 pounds of thrust at the design point.

3.2.2 Blade Row Spacing

Both analytic and experimental studies have shown the advantages of wide rotor/OGV spacing in producing low noise fans. Figure 2 is an analytic study and Figure 3 shows some recently acquired test data. Both curves show that there is considerable gain in going to 2.0-chord spacing with a diminishing gain beyond 2.0 chords.

Due to the small gain obtained in going beyond two-chord spacing and the mechanical problems resulting from such wide spacing, all three fans have their rotor/stator spacing set at two rotor true chords.

3.2.3 Vane and Blade Number Selection

The selection of the number of blades and vanes is intimately connected with both noise generation and its psychoacoustic effects. The number of blades and the rotational speed of the fan determine the blade passing frequency and its harmonics.

$$f_n = \frac{nBN}{60} \text{ Hz}$$

where: n = harmonic number ($n = 1$ is the fundamental)
 N = fan rotational speed, rpm
 B = number of blades

Therefore, one of the design considerations must be to place the pure tones in frequency bands where annoyance levels are low.

The ratio of the number of blades and vanes has been shown to have an appreciable effect on the pure tone noise levels. In general, a vane/blade ratio in excess of two produces a reasonable low noise design. Higher vane/blade ratios can result in still lower noise. However, there is a diminishing return, and serious aeromechanical design problems must be contended with when excessively high vane numbers are employed.

Figure 4 shows the results of a recent test in which this phenomenon was demonstrated. Also noted on Figure 4 are the pertinent positions of the three Experimental Quiet Engine Program Fans. These positions are at points of corresponding tip Mach number.

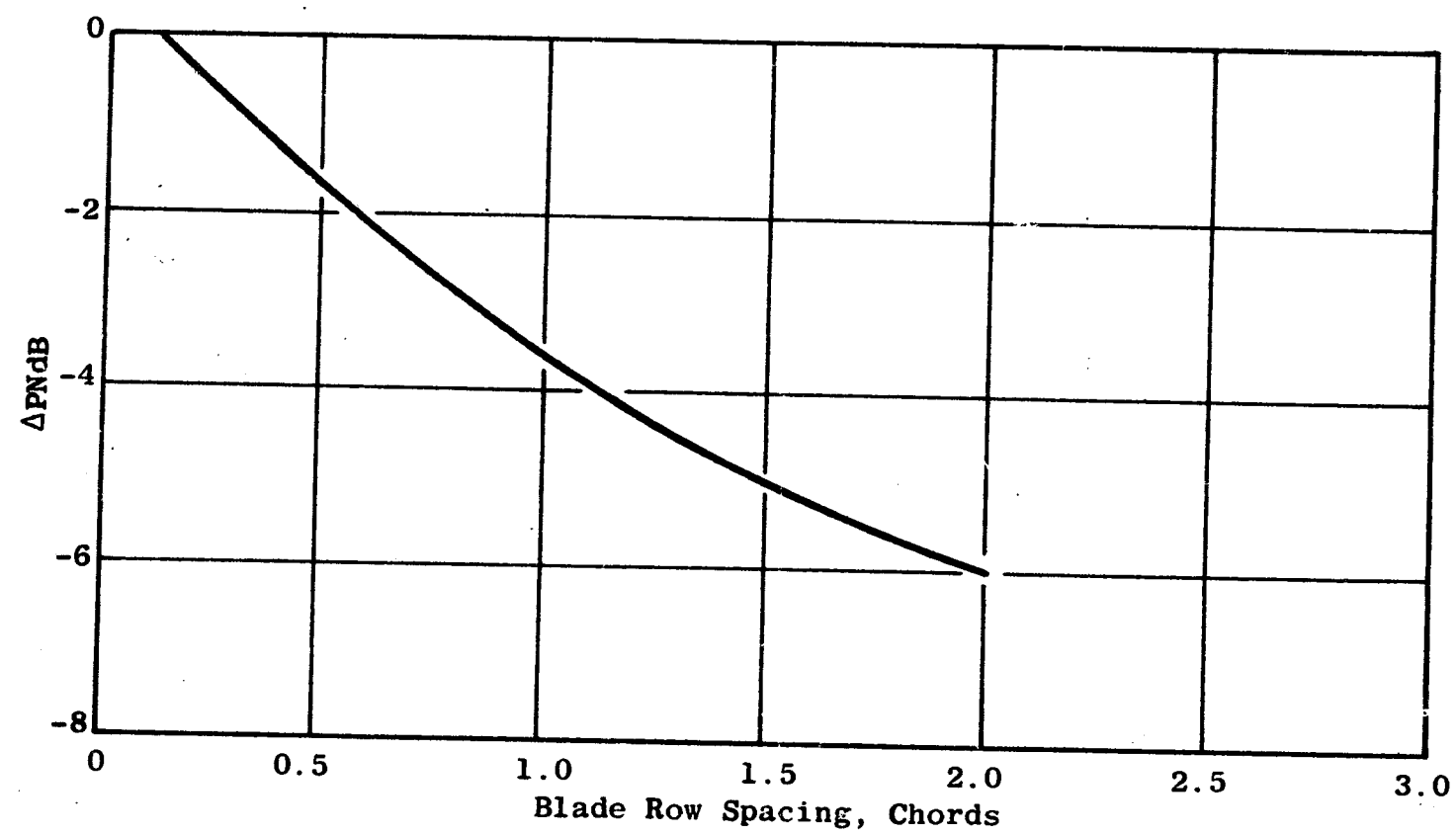


Figure 2. Analytically Predicted Blade Row Spacing Effects

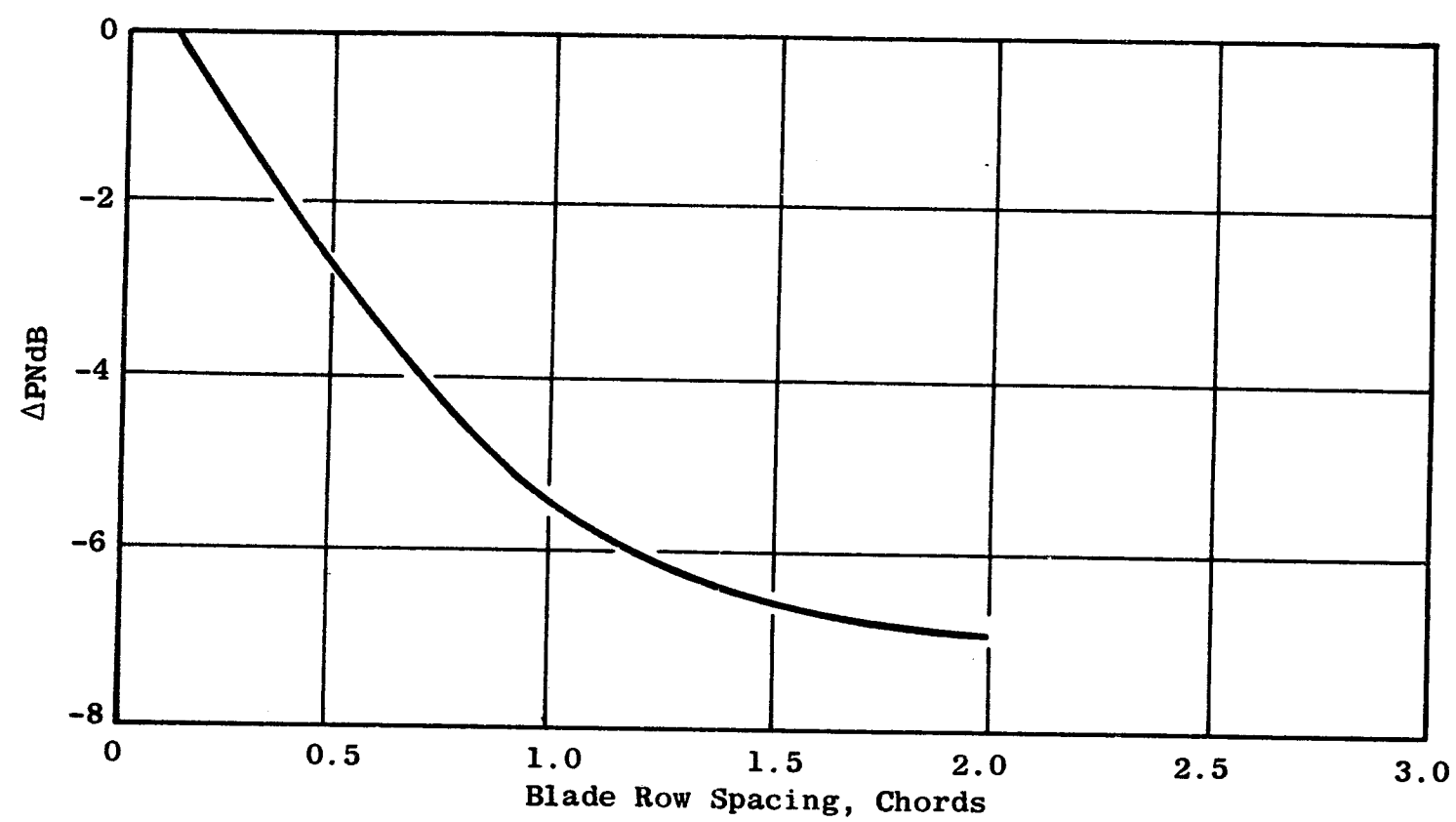


Figure 3. Measured Blade Row Spacing Effects

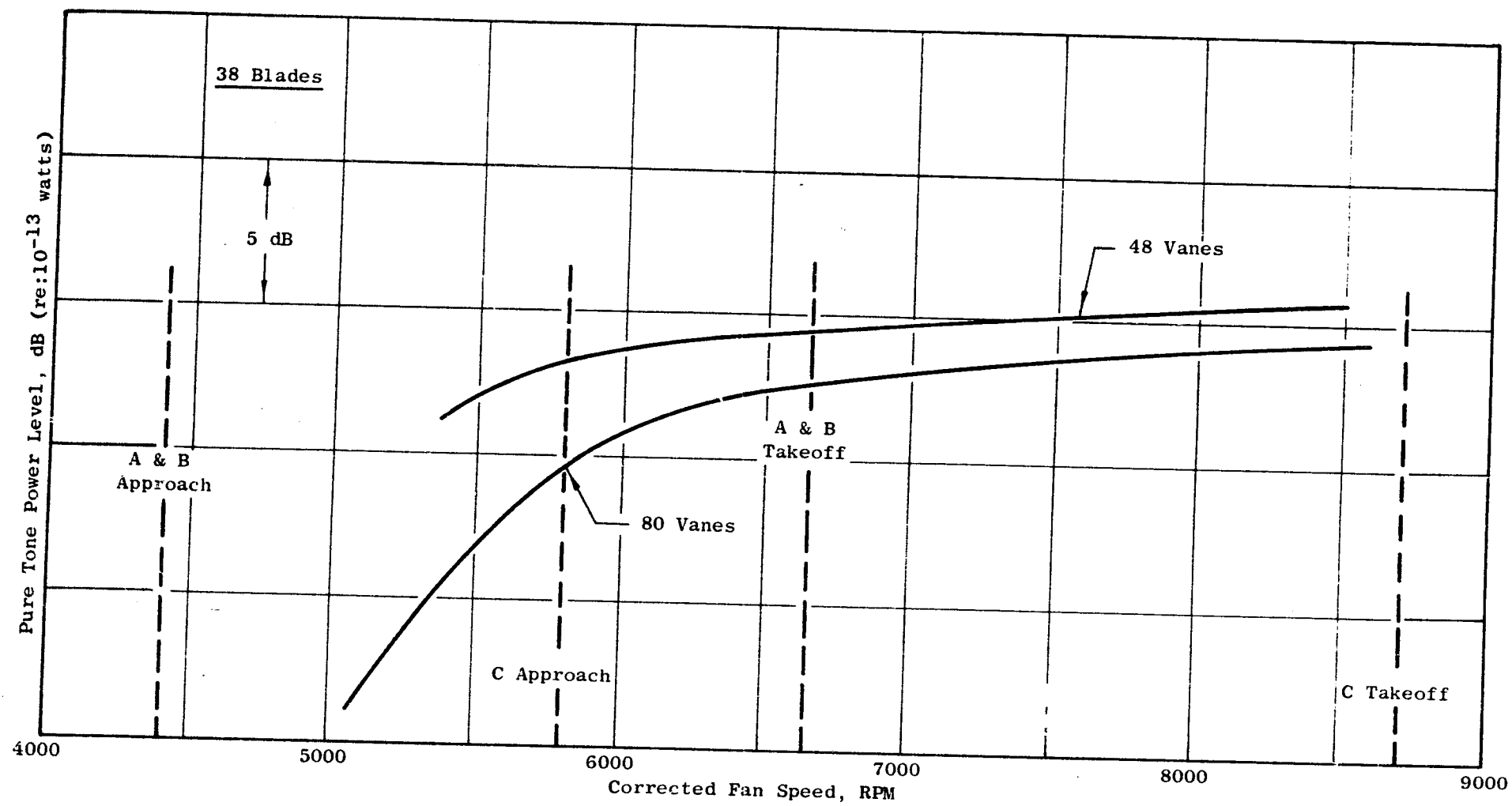


Figure 4. Comparison of Fundamental Power Levels (PWL's) for Vane/Blade Ratios of 1.26 and 2.1

Employing both the noise generation and psychoacoustic phenomena, studies were made to determine vane and blade numbers which would produce low noise fan configurations. A typical result is shown in Figure 5 for Fan C at take-off conditions.

Table I shows the results of these studies for the three fans. The low-tip-speed fans (A and B) will demonstrate the effects of the tradeoff between a low frequency, moderate pure tone noise level fan (Fan B) and a higher frequency, lower level, pure noise generating fan (Fan A) at the same aerodynamic loading. Fan C will provide information on the low loading concept with a blade passing frequency in the same range as Fan A.

Table I. Vane/Blade Selection for Quiet Engine Program Fans

<u>Fan</u>	<u>Number of Blades</u>	<u>Number of Vanes</u>
A	40	90
B	26	60
C	26	60

3.3 UNSUPPRESSED TURBOFAN NOISE PREDICTION

3.3.1 Basic Noise Elements

There are six basic elements which must be evaluated in order to make a maximum sideline noise prediction for a turbofan engine:

- Fan blade passing frequency and harmonic levels
- Fan broadband noise
- Multiple pure tones (if present)
- Fan core jet noise
- Fan noise directivity
- Turbine and compressor contributions (if present)

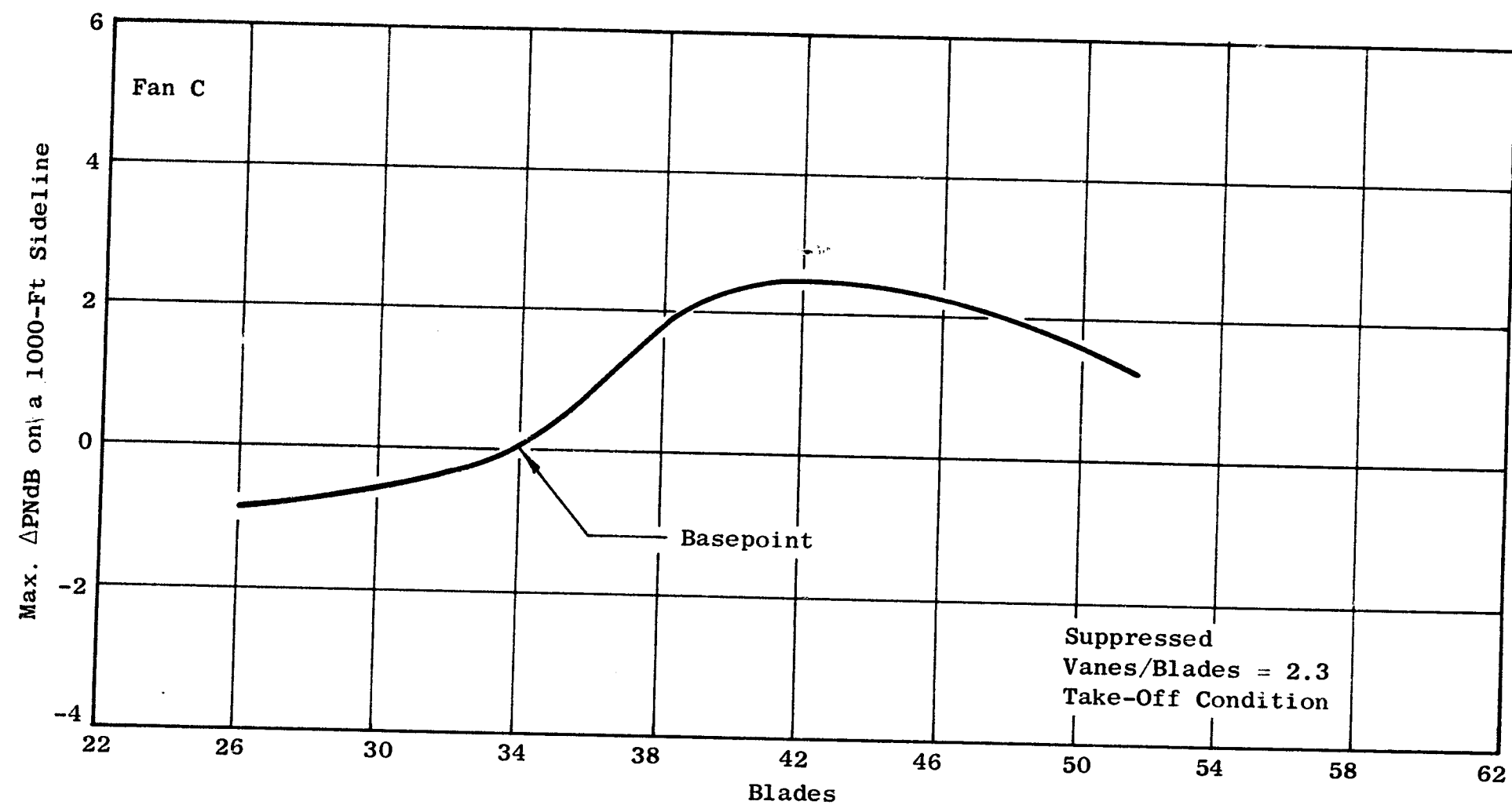


Figure 5. Blade Number Effect on Perceived Noise Levels

3.3.2 Fan Blade Passing Frequency and Harmonic Level Prediction

The generated pure tone levels were predicted analytically, with a mathematical model requiring knowledge of the fan geometry and the velocity triangles. The analysis is programmed on a GE635 computer and provides a prediction of the pure tone power levels generated at the inlet and exhaust of the fan duct.

The general assumptions of the analysis are:

- Spinning mode generation
- Dipole source
- Single airfoil wake shape
- Aerodynamic losses based on NASA low speed cascade data and General Electric data

The pure tone noise sources considered are:

- Rotor-alone noise
- Viscous wake interaction noise
- Potential field interaction noise
- Wake vortex interaction noise

The key parameters entering the analysis are:

- Duct geometry
- Number of blades
- Number of vanes
- Stage velocity diagrams at three radial stations
- Blade row axial spacing at three radial stations
- Blade/vane geometry (inlet/outlet angles) at three radial stations
- Blade/vane solidities at three radial stations

The details of the analysis are described in References 1 and 2.

3.3.3 Fan Broadband Noise

The fan broadband noise is determined from a semiempirical correlation of broadband noise data obtained from several General Electric turbofans. This correlation is based, chiefly, on rotor tip relative Mach number and fan size.

3.3.4 Multiple Pure Tones (MPT's)

Multiple pure tones are factored into the engine spectrum when the fan tip relative Mach number exceeds 1.2. Thus, MPT's have been included only for Fan C at the take-off power setting. MPT levels have been taken from data accumulated on the CF6 engine with frequency and size corrections being applied to obtain the proper spectral shape.

3.3.5 Fan and Core Jet Noise

The jet noise associated with the core and fan jets was determined using a modified SAE method. The velocities used for each jet are shown in Table II. The approach jet noise contributions in all three fans were found to be small in comparison with the fan noise. At take-off power, some jet noise addition is present; however, at most it amounts to 2.0 PNdB in the suppressed fan (see Table III).

3.3.6 Fan Noise Directivity

The peak sideline noise angle was determined by examining existing turbofan noise data at rotor tip Mach numbers corresponding to approach and take-off power settings for each fan. In general, the peak noise angle is at 110° referenced to the engine inlet centerline. On the low tip speed fans, A and B, these data indicate a front end peak at approach power which is nearly equal to the aft peak. Nevertheless, the aft peak is still dominating.

3.3.7 Turbine and Compressor Noise

Efforts have been made to eliminate any core turbomachinery noise sources by employing compressor inlet treatment and turbine exhaust suppression. It is felt that these steps will prevent the compressor and turbine noise from making a significant contribution to the over-all engine noise. No turbomachinery noise has, therefore, been added to the predicted peak sideline spectra.

Table II. Jet Parameters

Parameter	Fan A		Fan B		Fan C	
	App	T/O	App	T/O	App	T/O
Core Jet Velocity (ft/sec)	584	1171	579	1161	512	1025
Core Jet Flow (lb/sec)	75	133	76	136	84	143
Fan Jet Velocity (ft/sec)	555	829	556	830	580	881
Fan Jet Flow (lb/sec)	487	727	487	723	458	590

Table III. Quiet Engine Program Noise Prediction with 4 Suppressed Engines

Configuration	Total	Fan
<u>Approach Condition (375 Ft Altitude)</u>		
A	100.6	100.6
B	100.7	100.7
C	102.7	102.7
<u>Take-Off Condition (1000 Ft Altitude)</u>		
A	100.8	99.3
B	99.1	97.1
C	99.9	99.4

3.3.8 Arc and Maximum Sideline PNL Predictions

Figures 6 through 11 show the resulting spectra for each fan for take-off and approach power settings at 250 feet from the engine in flight; that is, the data are based on jet noise for a flight Mach number of 0.25.

Using SAE recommended air attenuation and spherical divergence, these spectra were extrapolated to their respective sideline distance: 375 feet for approach and 1000 feet for takeoff. The resulting data are shown in Table IV.

Table IV. Quiet Engine Program Noise Prediction With 4 Unsuppressed Engines
(No Acoustic Treatment)

<u>Configuration</u>	<u>Total</u>	<u>Fan</u>
<u>Approach Condition (375 Ft Altitude)</u>		
A	106.3	106.3
B	106.3	106.3
C	108.6	108.6
<u>Take-Off Condition (1000 Ft Altitude)</u>		
A	106.3	105.7
B	104.4	103.7
C	105.8	105.6

Each spectrum clearly shows the low frequency jet noise and the fan blade passing frequency. In addition, Figure 10 (for the Fan C takeoff) shows a peak (unsuppressed) at 800 Hz. This peak is due to the MPT's.

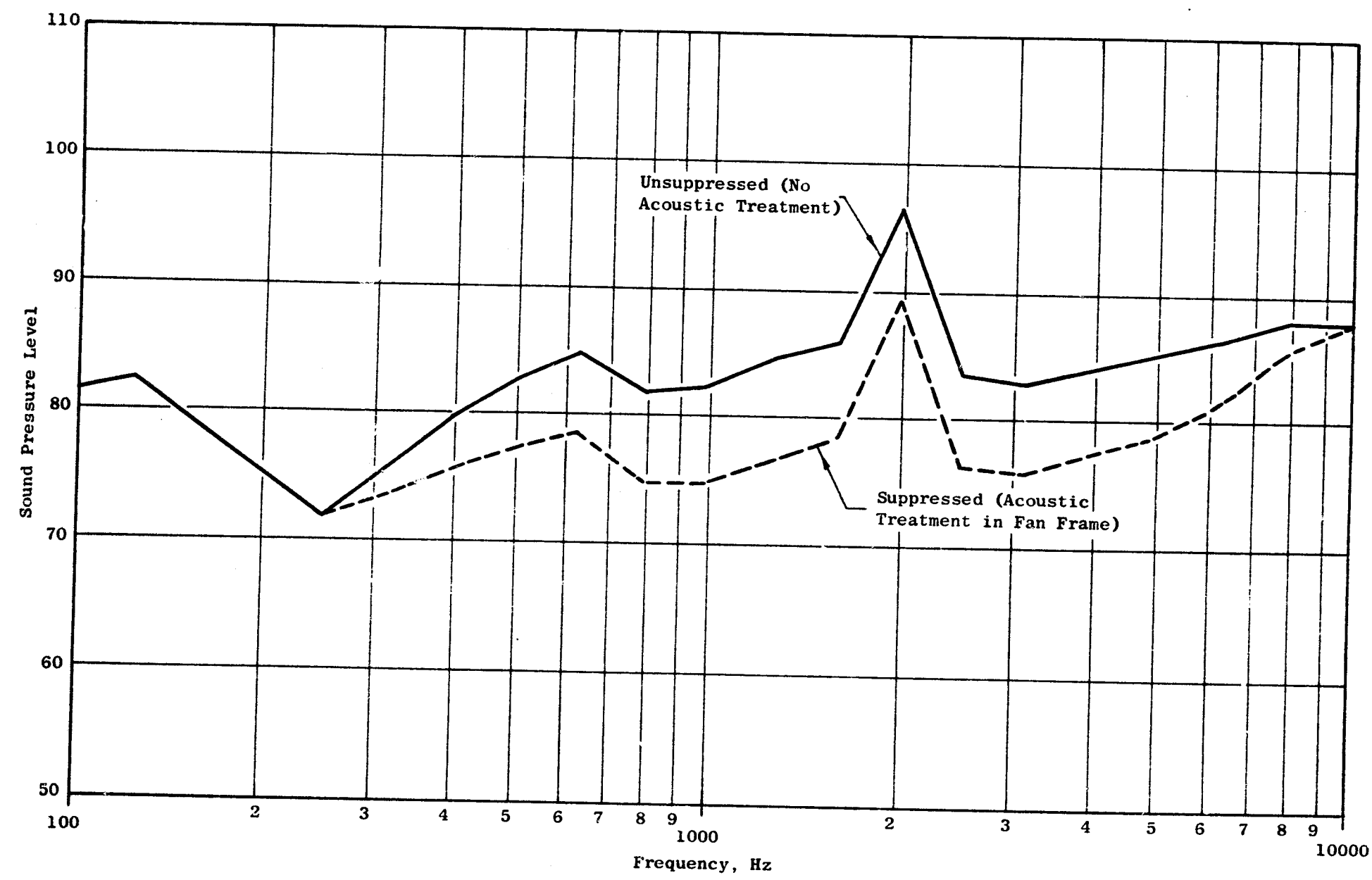


Figure 6. Fan A Spectra - Takeoff, 250-Foot Arc, Aft Maximum

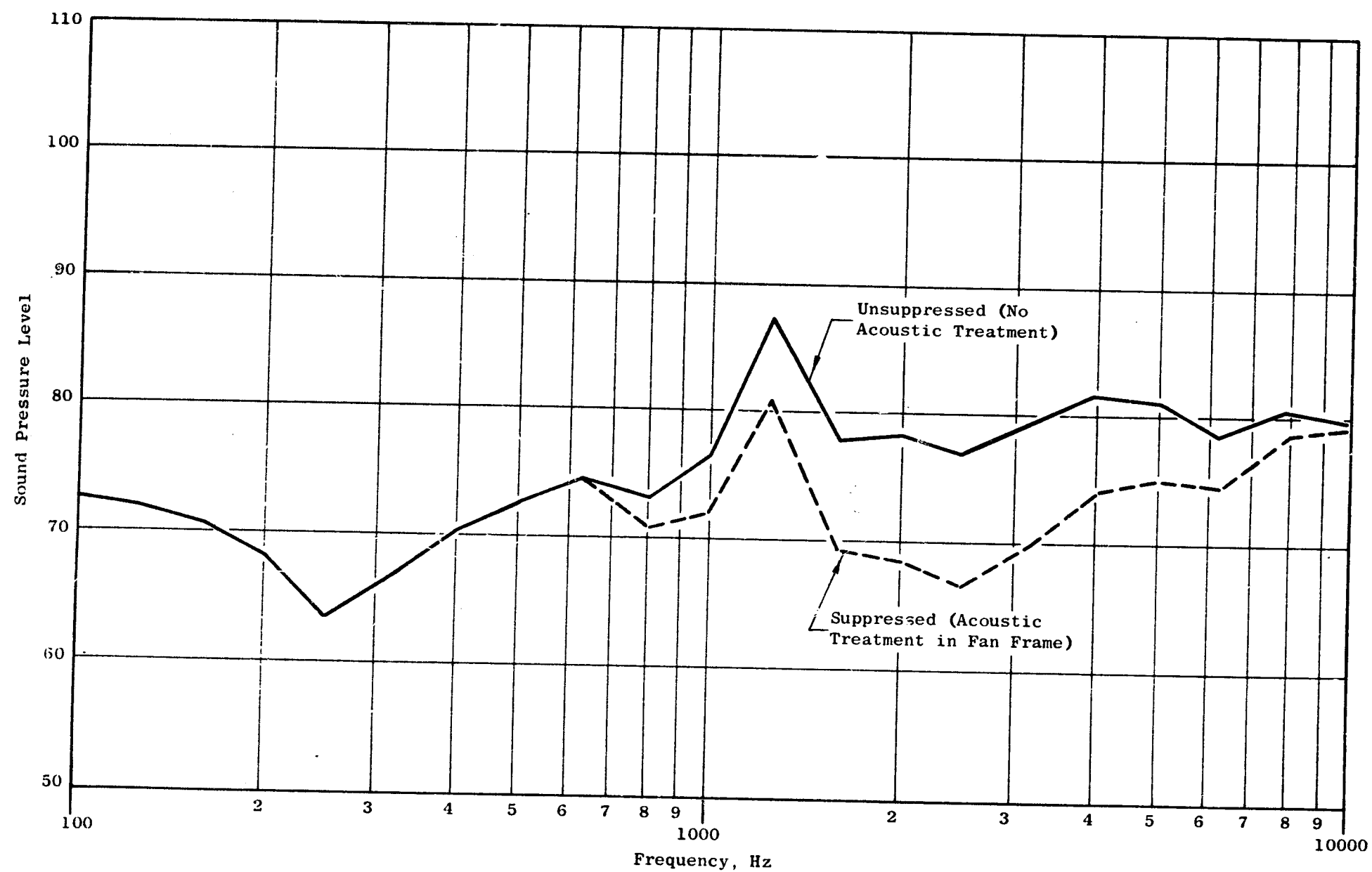


Figure 7. Fan A Spectra - Approach, 250-Foot Arc, Aft Maximum

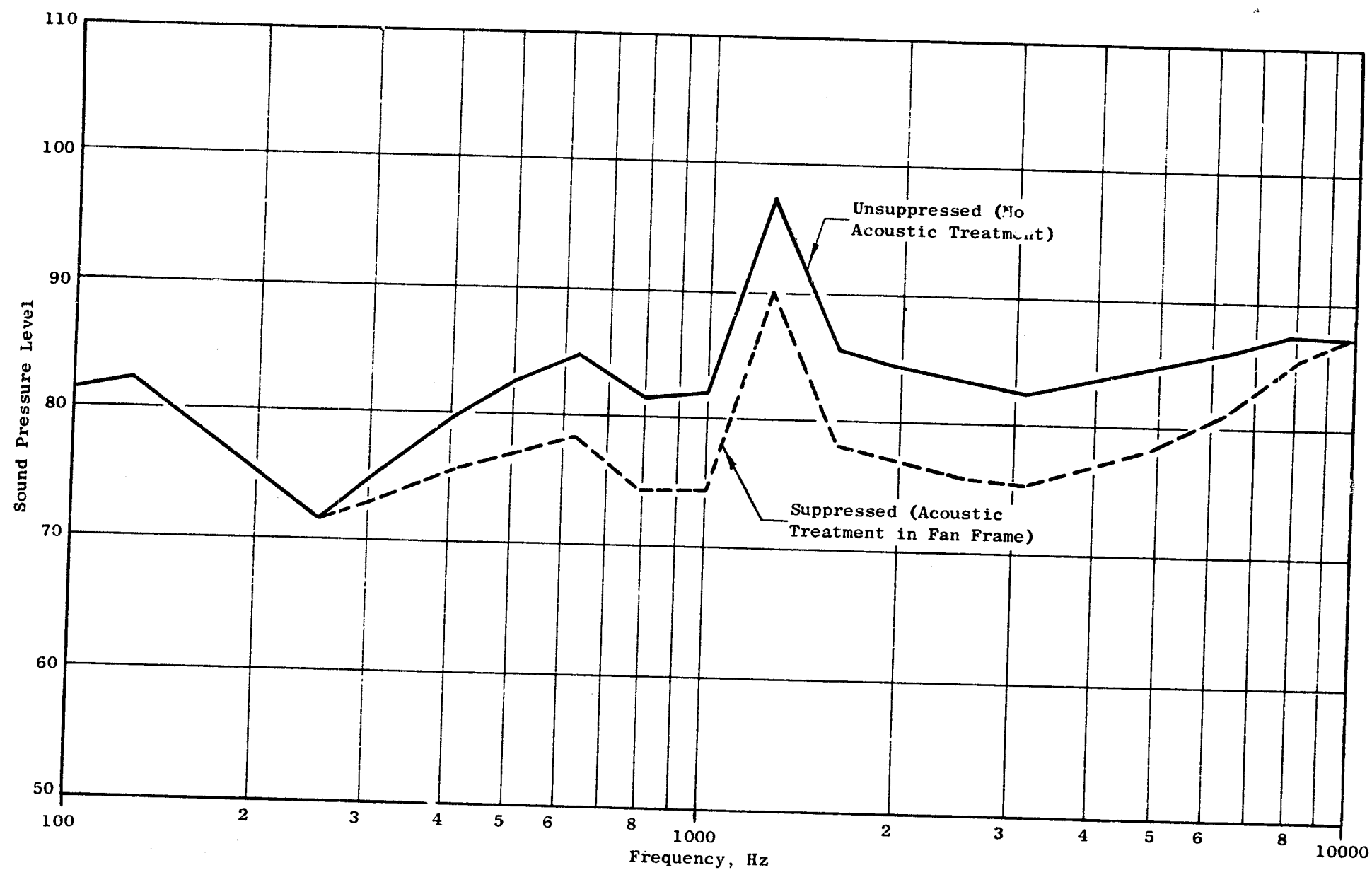


Figure 8. Fan B Spectra - Takeoff, 250-Foot Arc, Aft Maximum

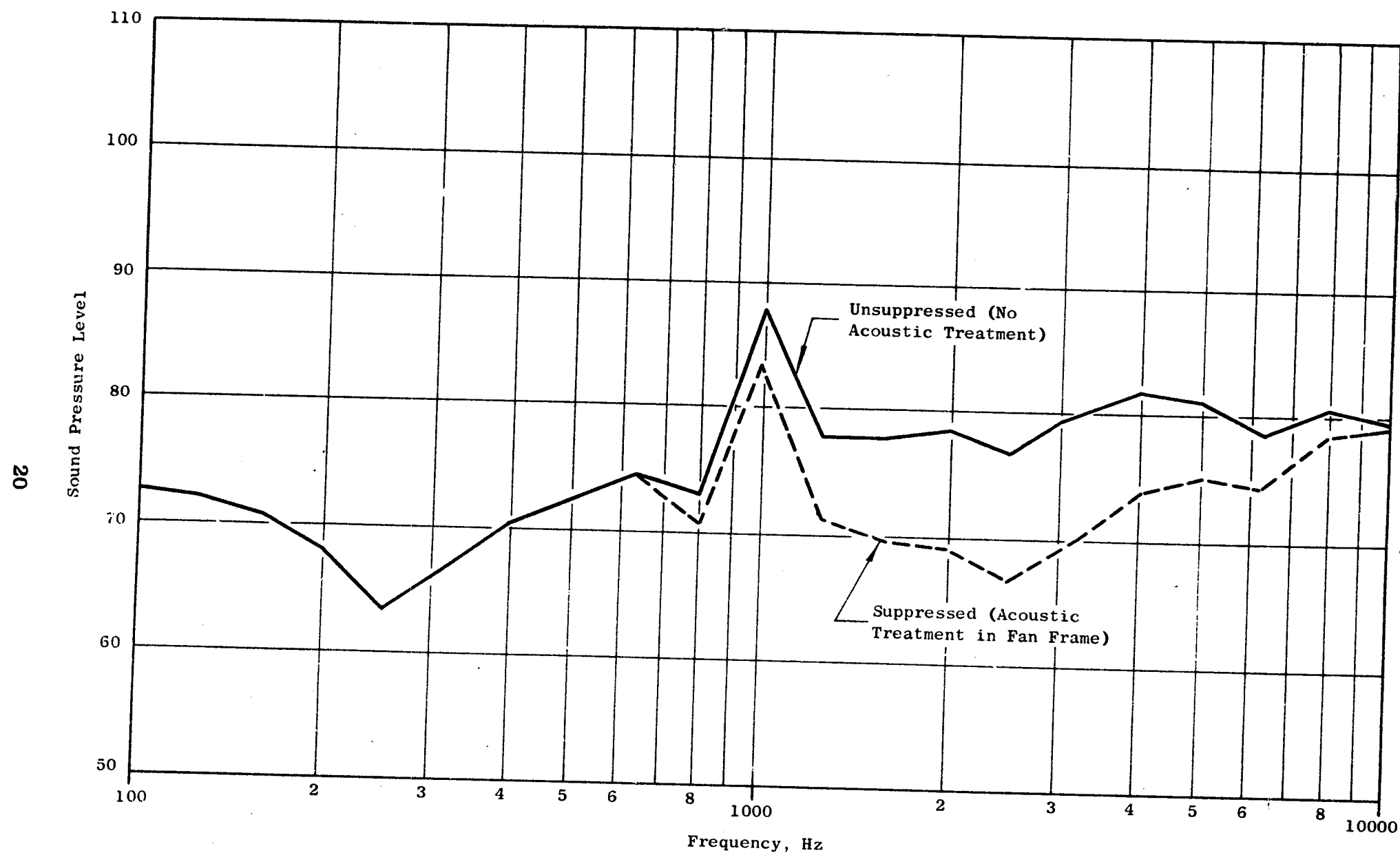


Figure 9. Fan B Spectra - Approach, 250-Foot Arc, Aft Maximum

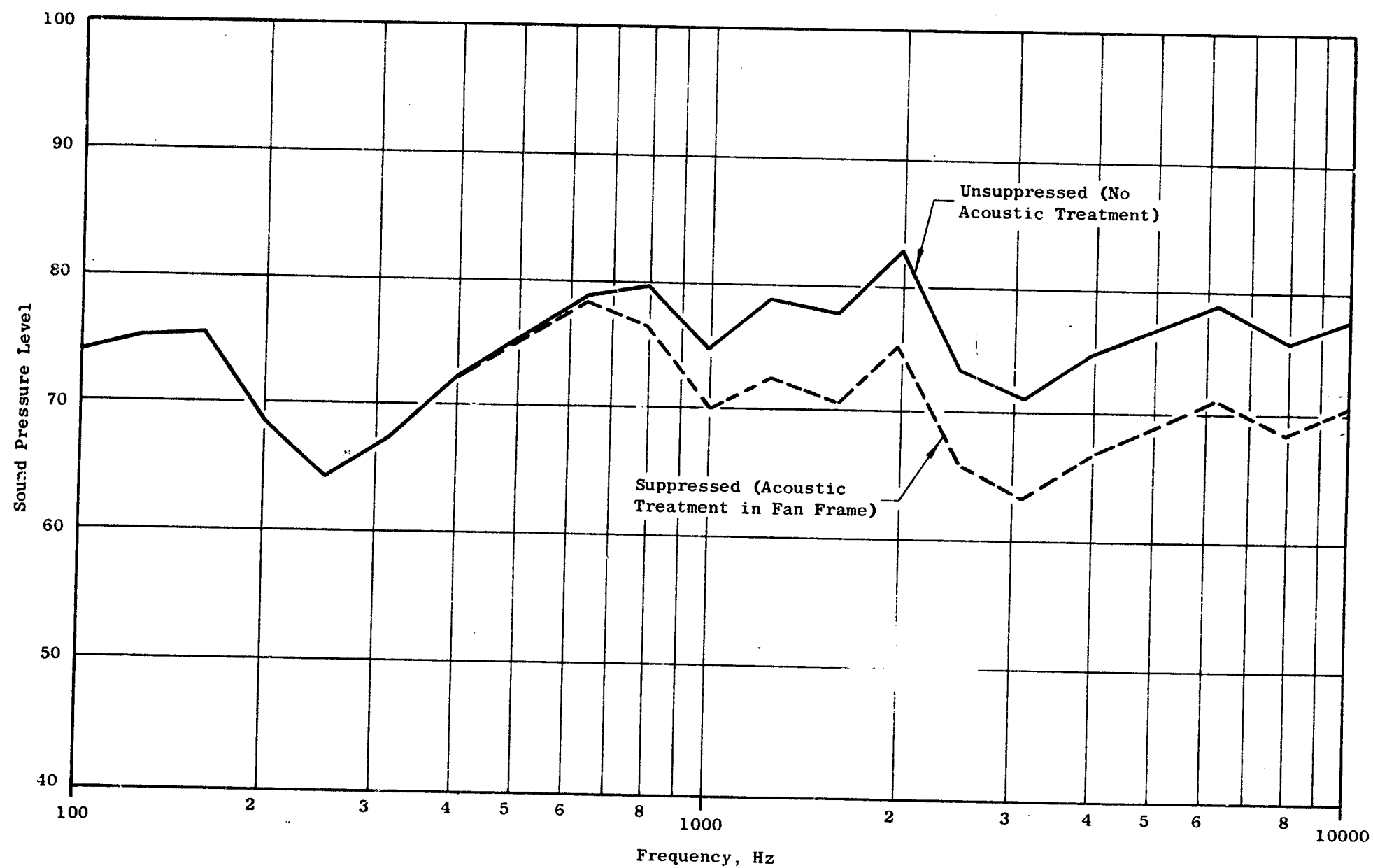


Figure 10. Fan C Spectra - Takeoff, 250-Foot Arc, Aft Maximum

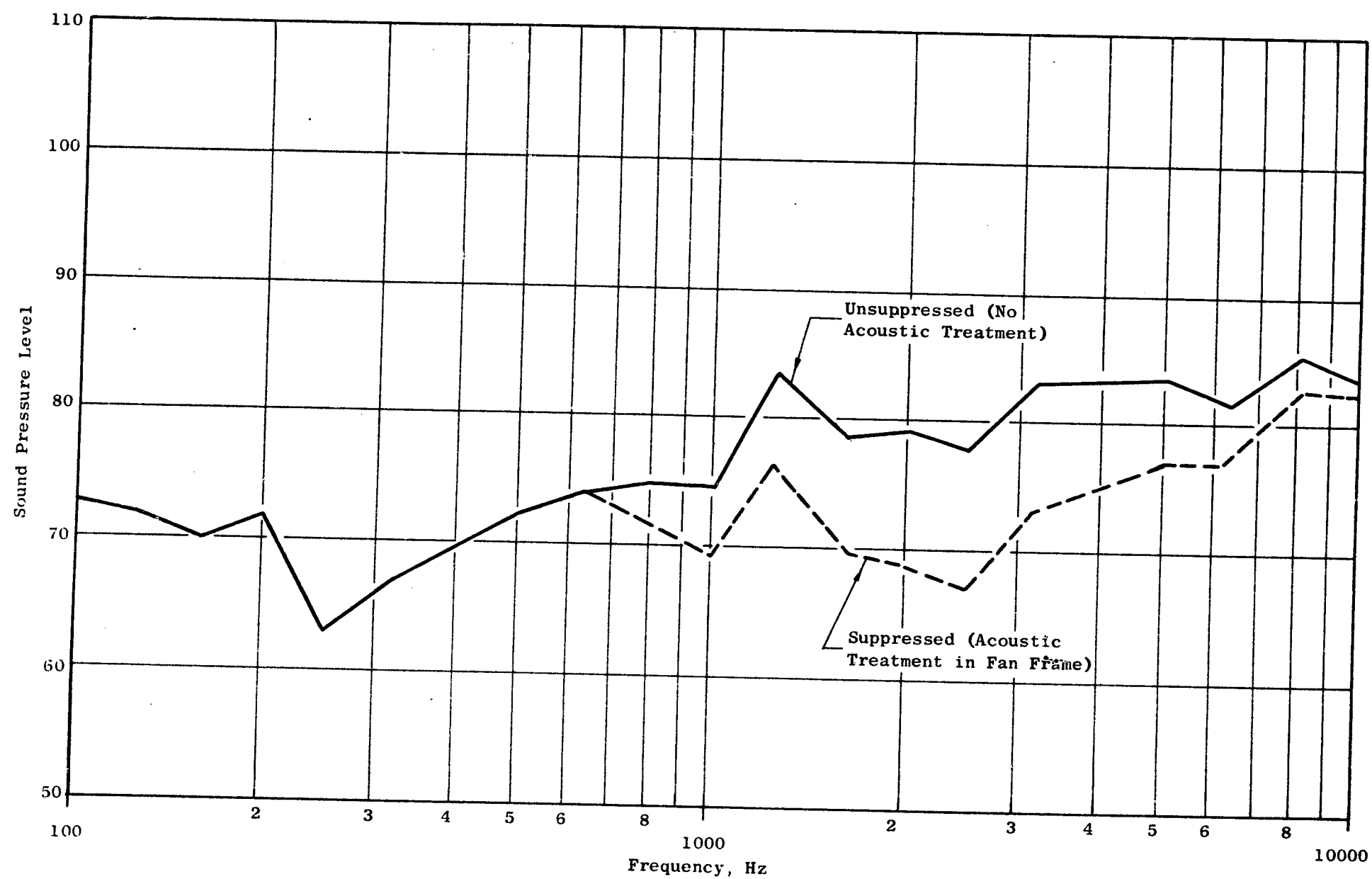


Figure 11. Fan C Spectra - Approach, 250-Foot Arc, Aft Maximum

3.4 SELECTION OF ACOUSTIC TREATMENT

3.4.1 Basic Selection Criterion

The acoustic treatment selection was based primarily on the criterion that the frequency at which the peak absorption occurs should be such that the net PNL reduction is a maximum. The peak absorption frequency can be adjusted by judicious selection of the acoustic material (see Section 3.5).

3.4.2 Suppression Bandwidth

As a first step in the selection of a treatment, a bandwidth must be established. The bandwidth is defined as the level of suppression for each 1/3 octave band from 0-10 KHz. Figures 12 and 13 show the bandwidths established for the Experimental Quiet Engines. These curves are based on the geometry of the treatment as it pertains to its placement in the engine and the design of the treatment itself. The geometrical placement of the treatment largely determines the level of peak suppression, while the physical characteristics of the treatment determines the bandwidth. For the Experimental Quiet Engines, the treatment for each engine has been placed according to Figures 14 through 16. All of these panels are of a multiple-degree-of-freedom (MDOF) type. This kind of design leads to relatively wide bandwidths; that is, the range of frequencies over which there is significant suppression is quite large.

It can be seen that the shapes of the curves in Figures 12 and 13 are different, even though both result from the same treatment configuration. This is a result of the increase in Mach number of the flow over the treatment. The higher Mach numbers tend to decrease the peak suppression, extend the bandwidth, and decrease the frequency of the peak suppression. The effect that these changes have on the maximum PNL suppression, however, is dependent on the unsuppressed spectrum on which they are imposed.

3.4.3 Maximum Suppression Study

In order to determine the optimum placement of the peak suppression frequency, a study was undertaken on each of the three fans for both approach and takeoff. This study consisted of moving the peak suppression frequency across the predicted spectra obtained in Section 3.3 and calculating the resulting reduction in peak PNL. The results of this study are shown in Figures 17 through 22. Table V is a summary of the frequencies of maximum suppression for each fan and operating condition.

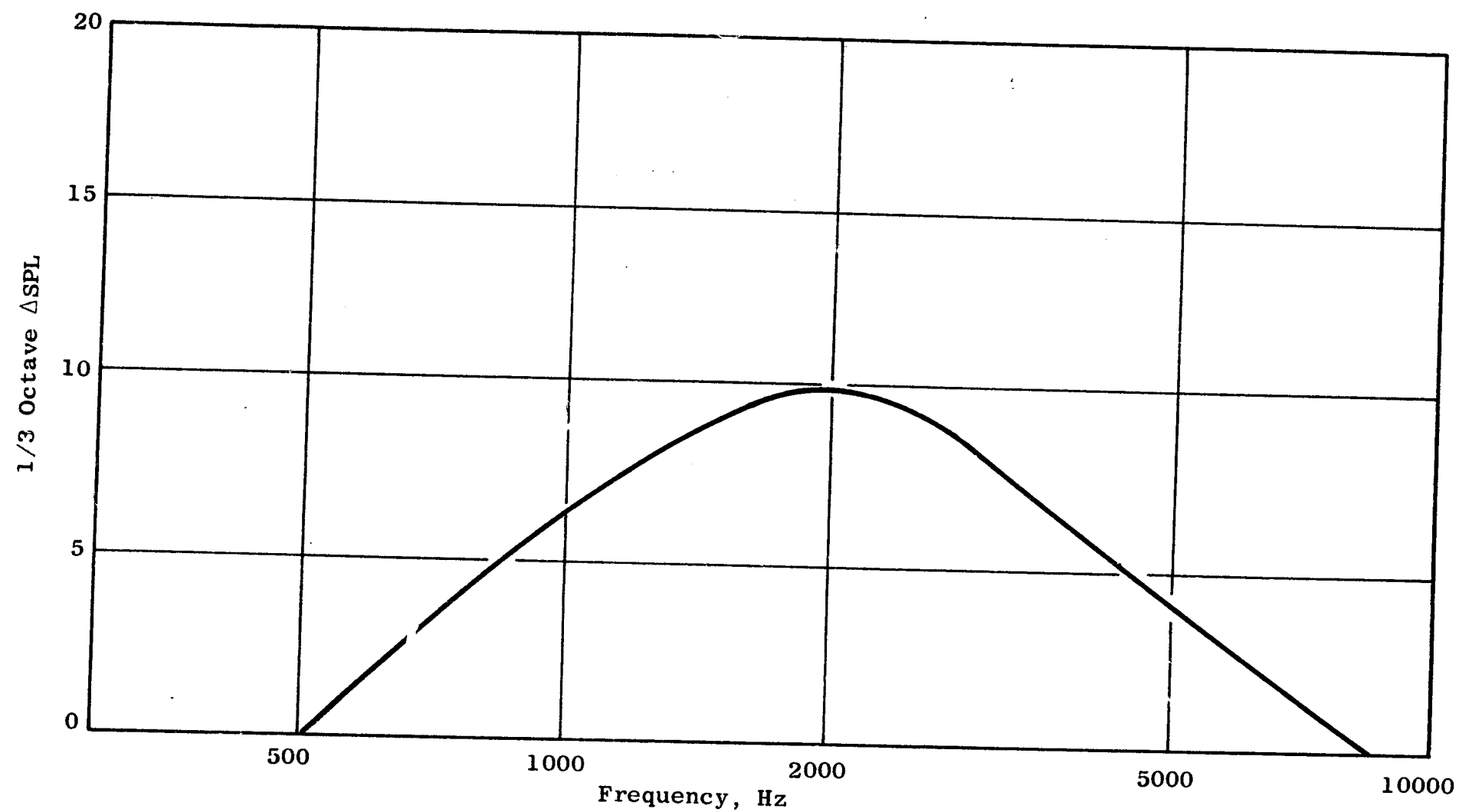


Figure 12. Suppression Bandwidth for 1-Inch MDOF Treatment, Approach Power, Aft Maximum

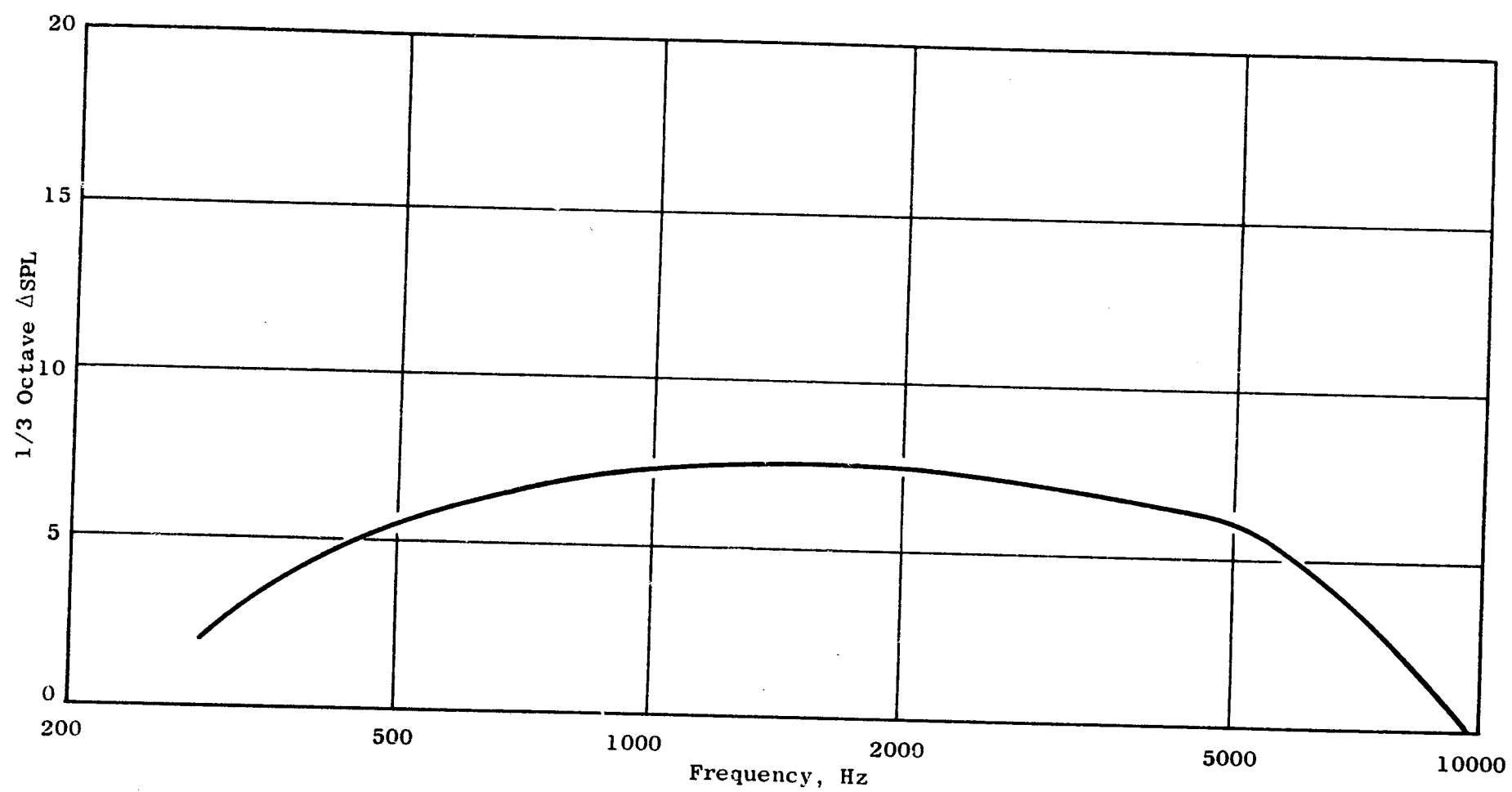


Figure 13. Suppression Bandwidth for 1-Inch MDOF Treatment, Take-Off Power, Aft Maximum

Frame Acoustic Treatment 115 Square Feet
Compressor Inlet Treatment 34 Square Feet

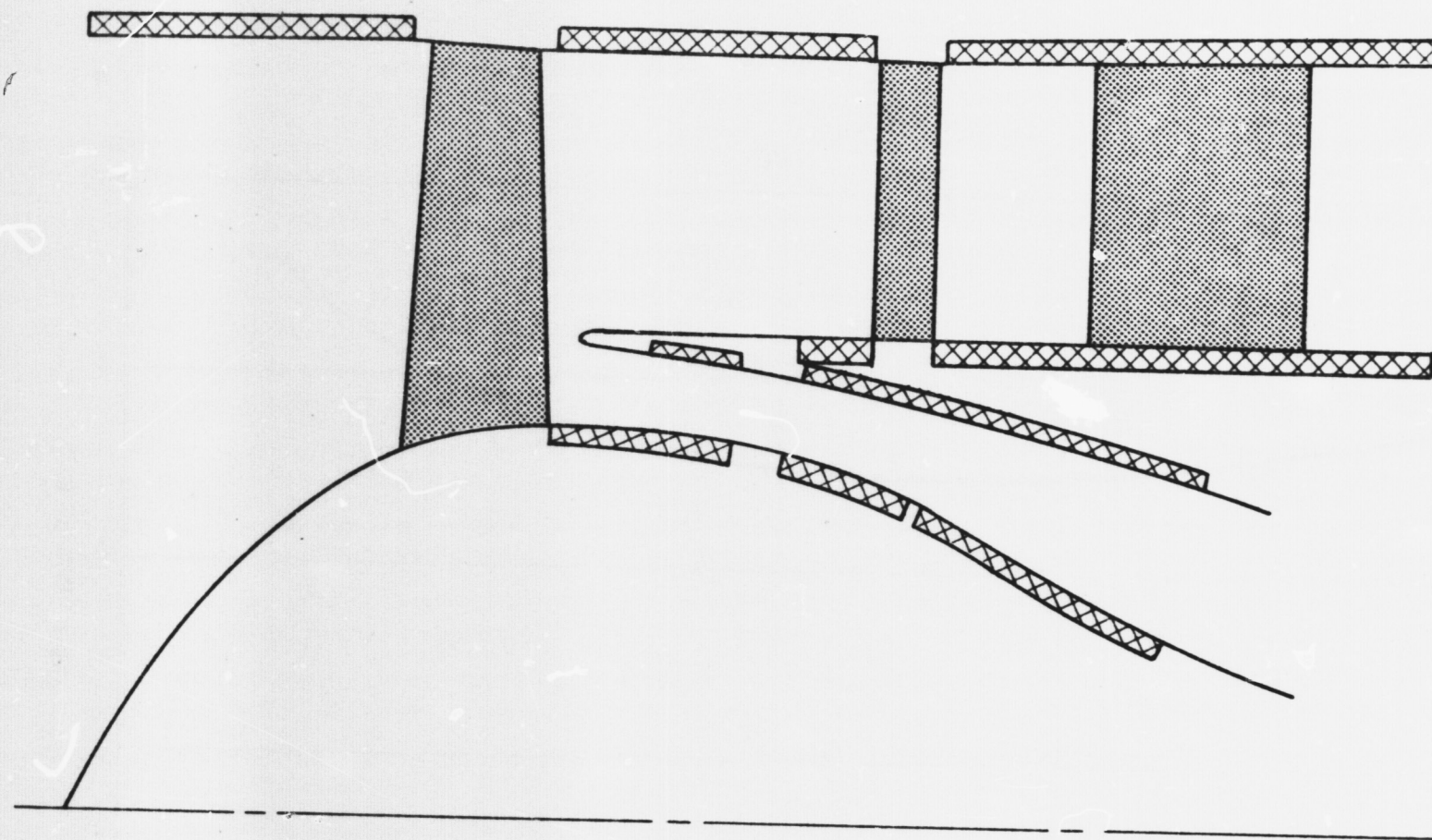


Figure 14. Frame Acoustic Treatment and Compressor Inlet Treatment in Quiet Engine "A"

Frame Acoustic Treatment

114 Square Feet

Compressor Inlet Treatment

30 Square Feet

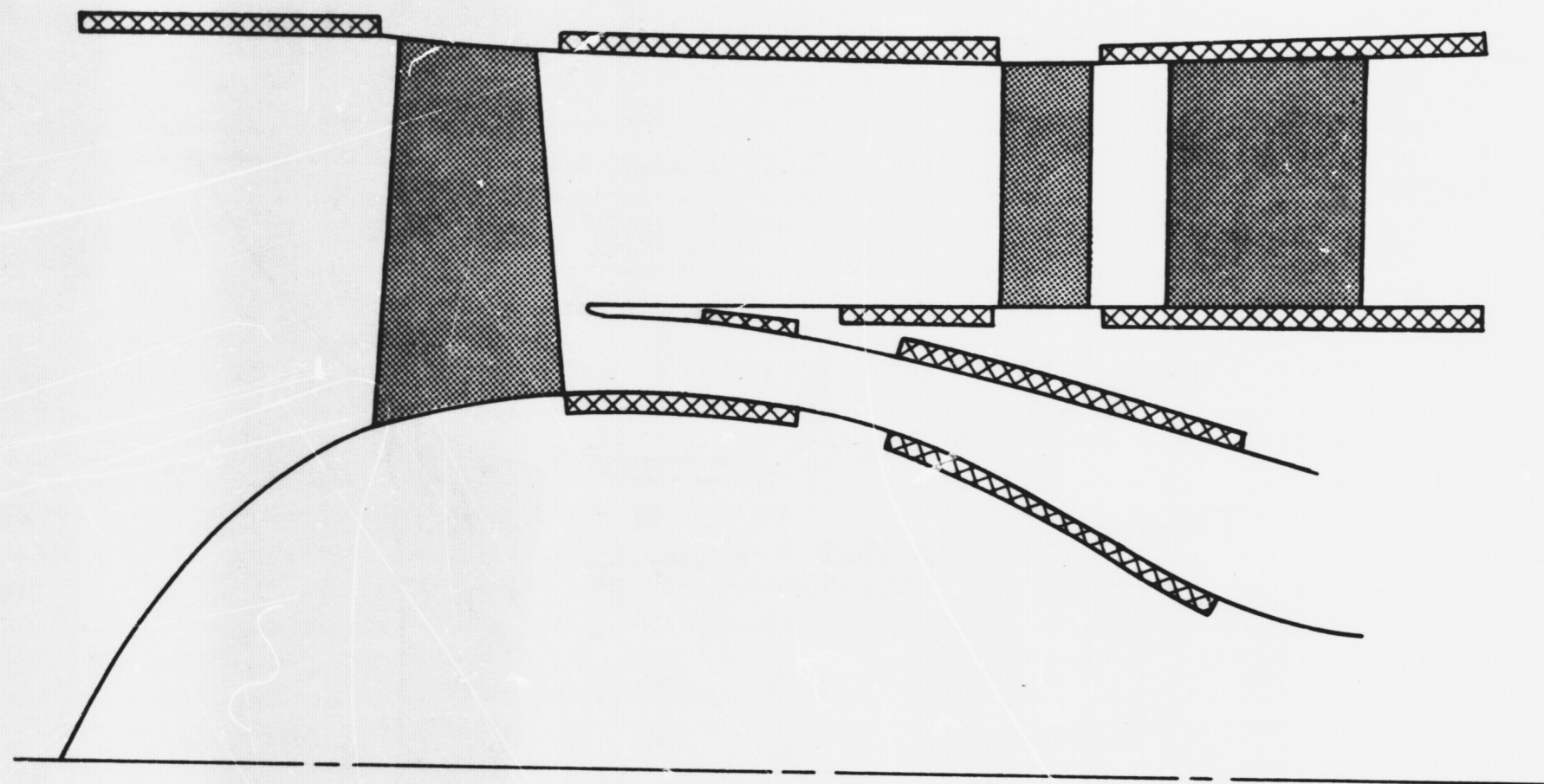


Figure 15. Frame Acoustic Treatment and Compressor Inlet Treatment in Quiet Engine "B"

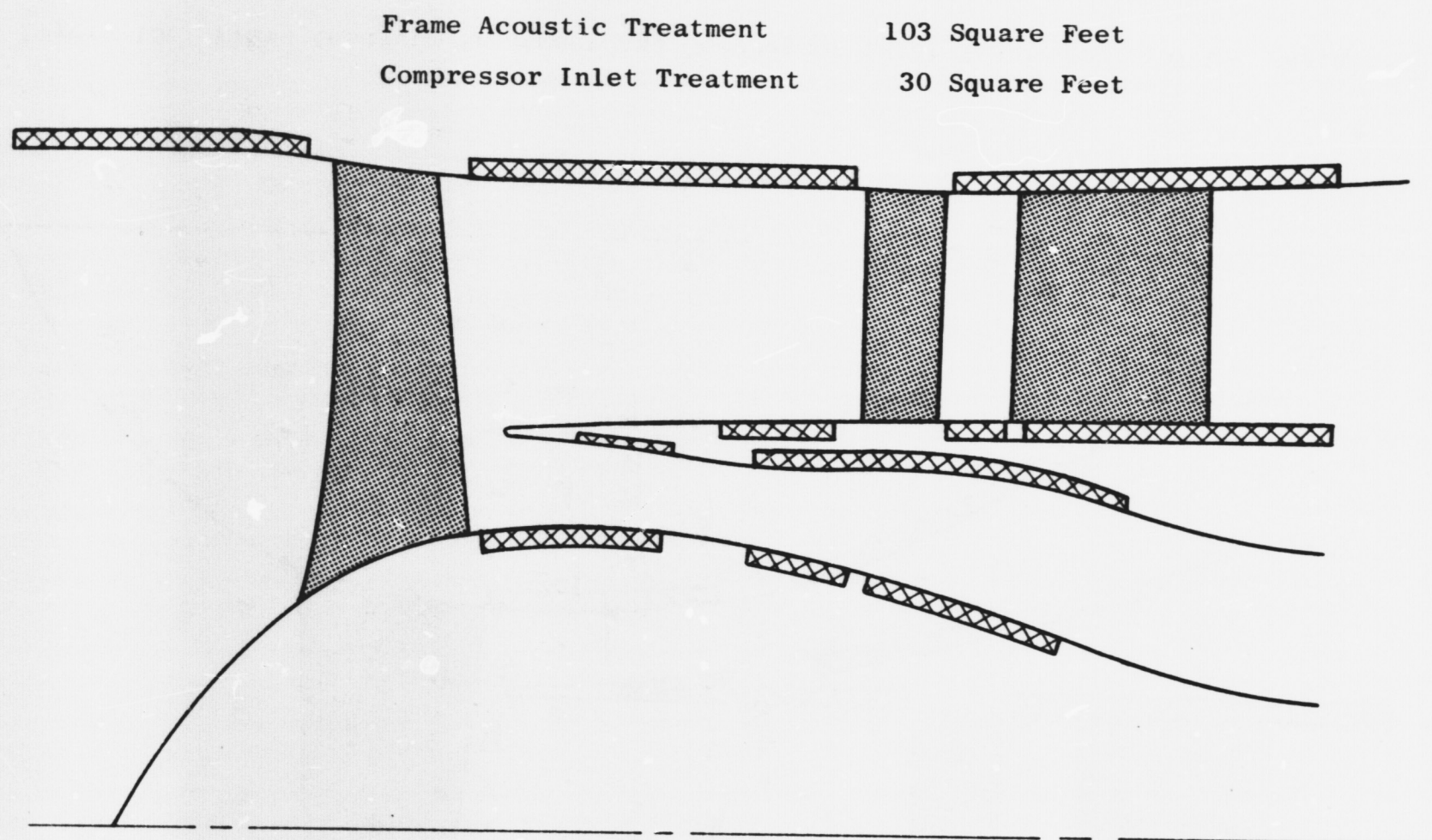


Figure 16. Frame Acoustic Treatment and Compressor Inlet Treatment in Quiet Engine "C"

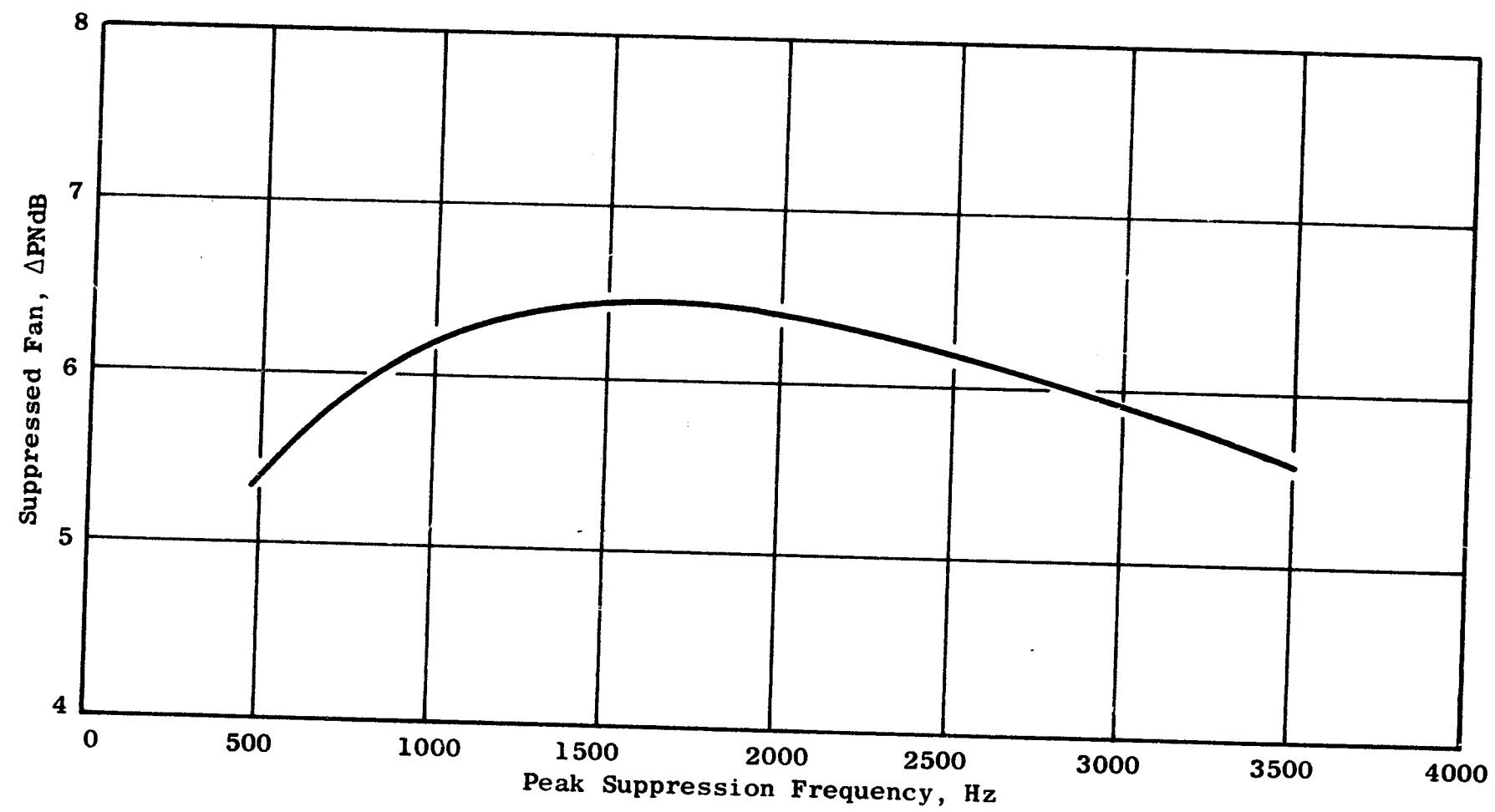


Figure 17. Tuning Study, Fan A, Takeoff

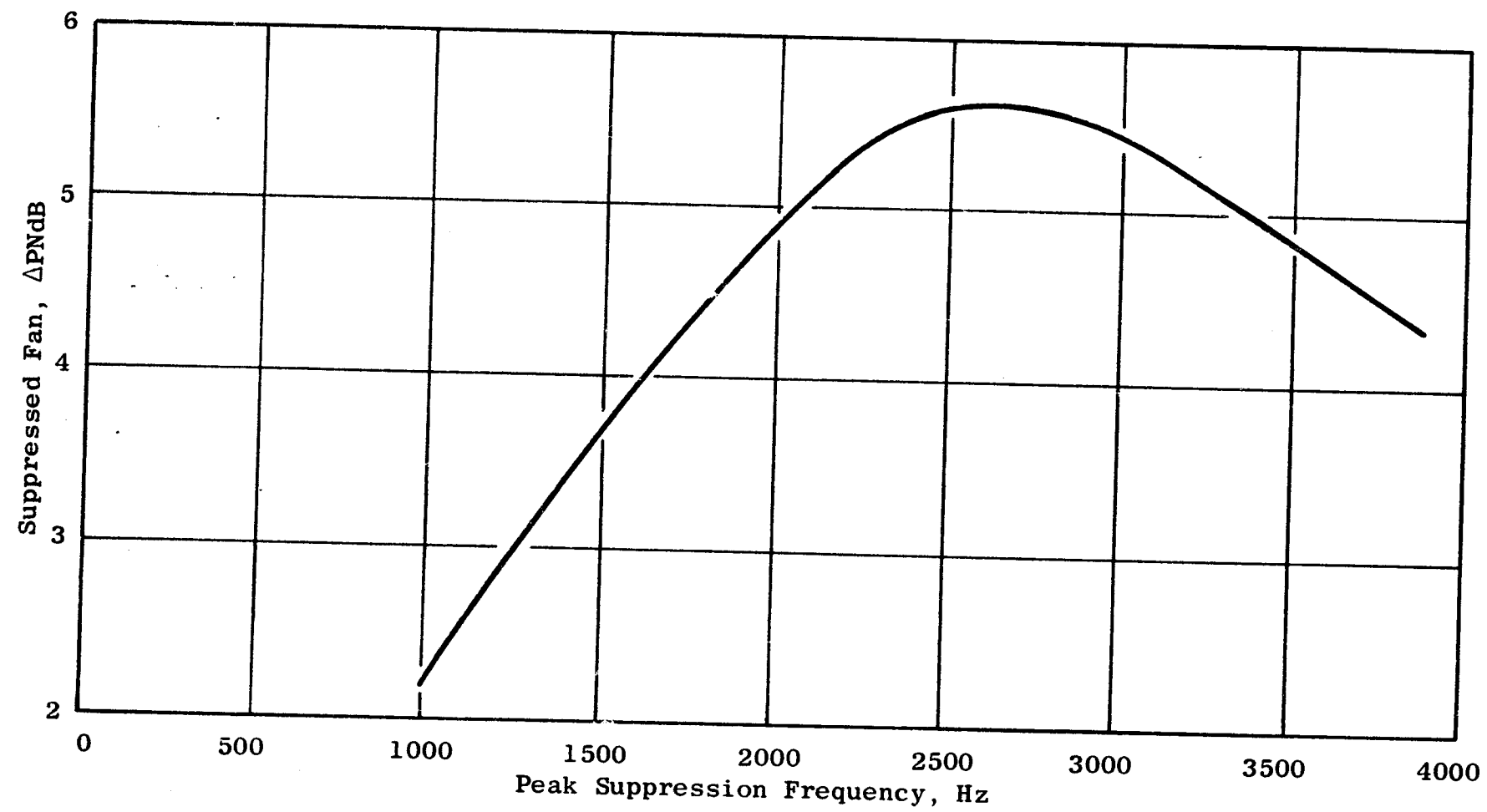


Figure 18. Tuning Study, Fan A, Approach

1.1

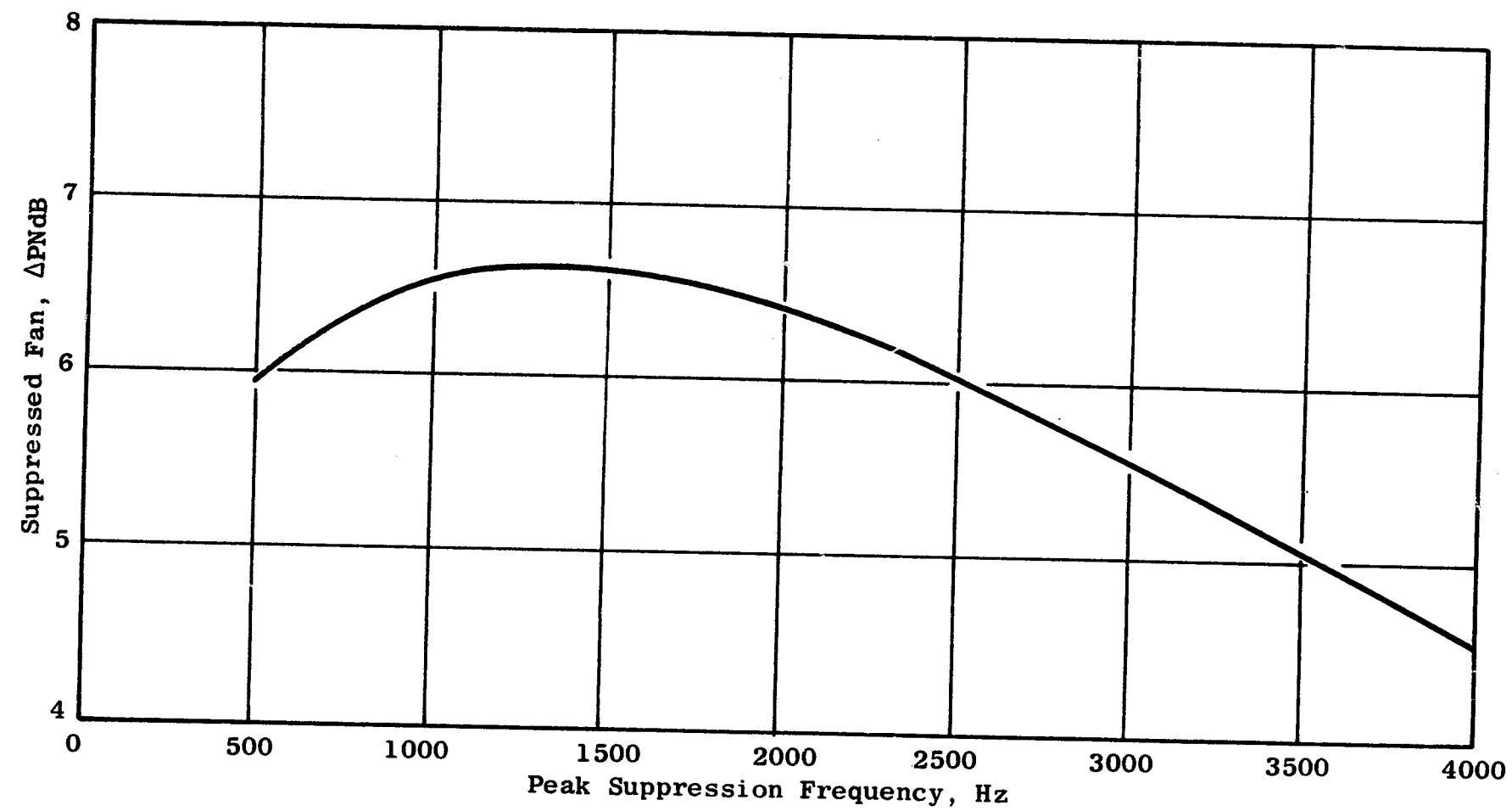


Figure 19. Tuning Study, Fan B, Takeoff

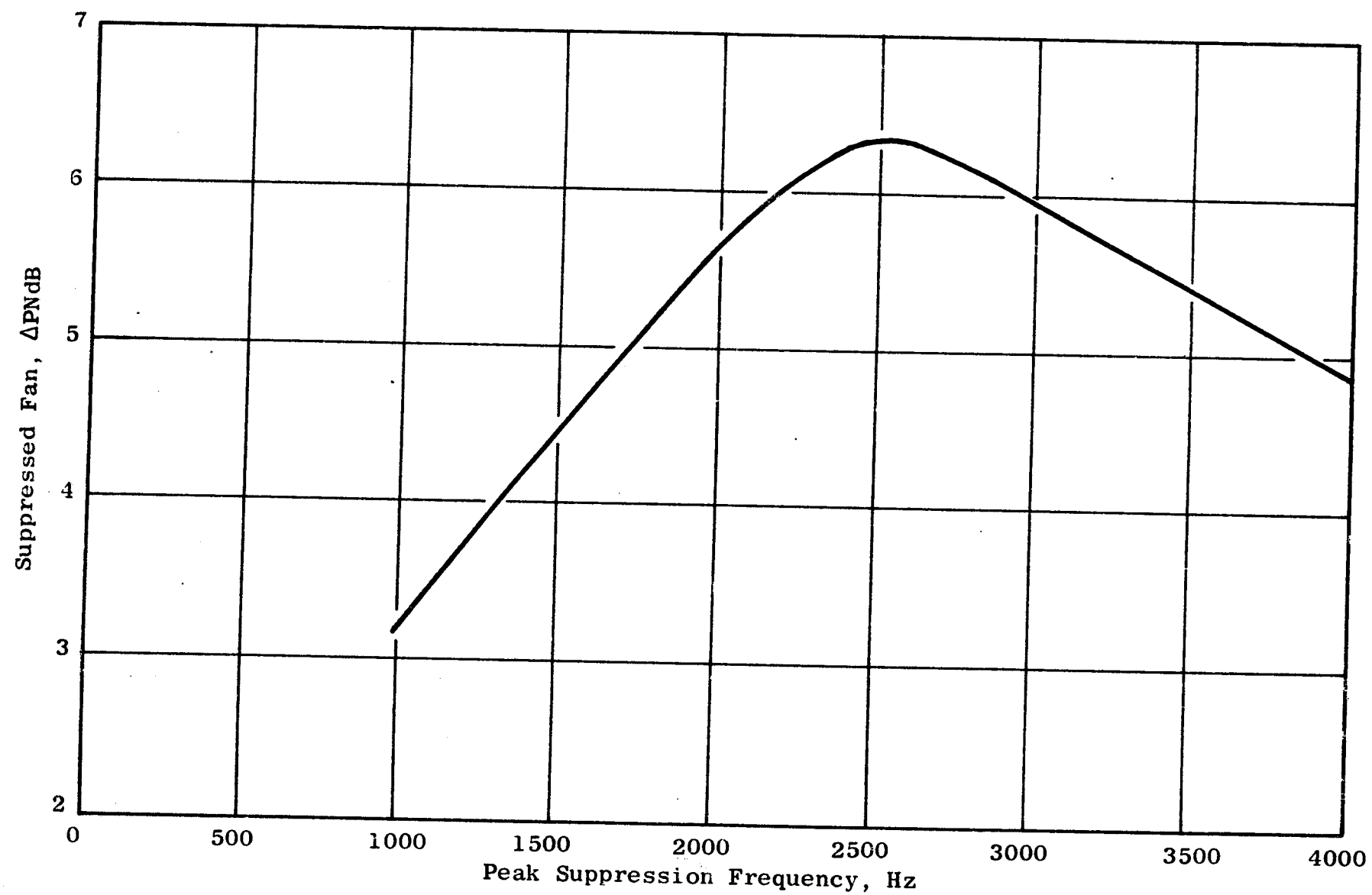


Figure 20. Suppressed Fan PNdB Versus Peak Suppression Frequency, Fan B, Approach

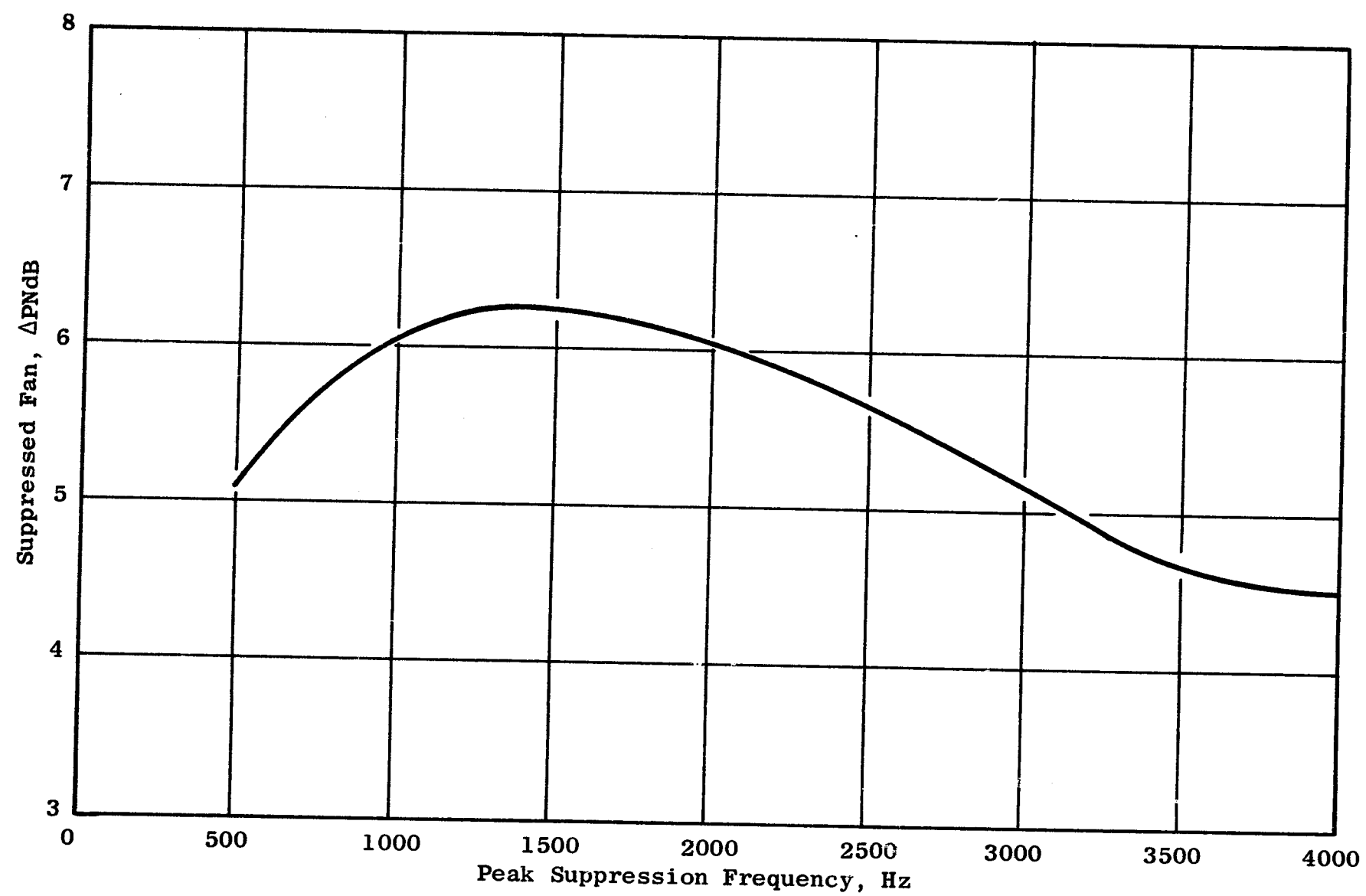


Figure 21. Tuning Study, Fan C, Takeoff

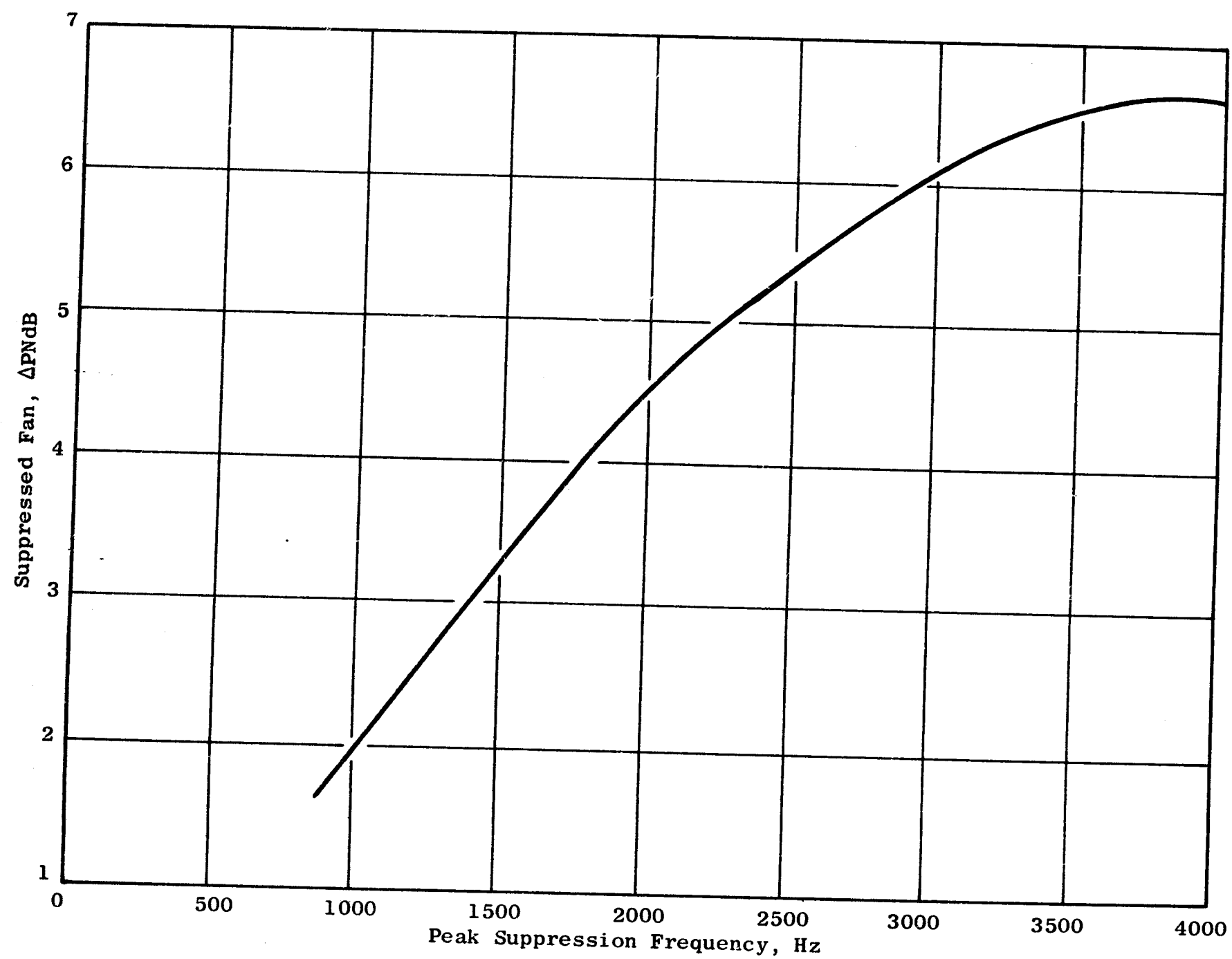


Figure 22. Tuning Study, Fan C, Approach

Table V. Maximum Suppression Frequency

(At which treatment under flow conditions should be tuned)

<u>Fan</u>	<u>Approach</u>	<u>Takeoff</u>
A	2650	1700
B	2500	1300
C	3900	1500

It must be noted that the peak suppression frequency for any given material differs for approach and takeoff. Thus, the results in Table V do not imply that a significant noise reduction at approach and takeoff cannot be obtained with one treatment configuration.

As a result of this study, one acoustic treatment design was obtained for all three fans. The resulting suppressed bandwidths were applied to the spectra shown in Figures 6 through 11. Table III is a summary of the 4-engine suppressed maximum sideline noise levels.

It can be seen that Fans A and B are nearly the same at approach; however, Fan B is the quietest of the three fans at take-off conditions. Fan C follows the other two fans closely within 2 PNdB.

3.5 DESIGN OF ACOUSTIC TREATMENT

3.5.1 General Considerations

Acoustic treatment has been designed for placement in the Experimental Quiet Engine fan flow passages and in the inlet of the core engine compressor passage. In each case, it was desired to have a broadband absorption characteristic (at both approach and take-off power settings) centered at different peak frequencies. The multiple-degree-of-freedom (MDOF) acoustic resonator panel design was selected as the best acoustic treatment for these applications. Figure 23 shows the MDOF analytical model beside one of the many possible physical configurations. When a perforated or porous plate is placed over a cavity whose dimensions are small compared to the wave lengths of interest, the acoustic system is analagous to a series mass-spring element. A single Helmholtz resonance occurs depending on the mass and spring constant, and energy is removed by the viscous

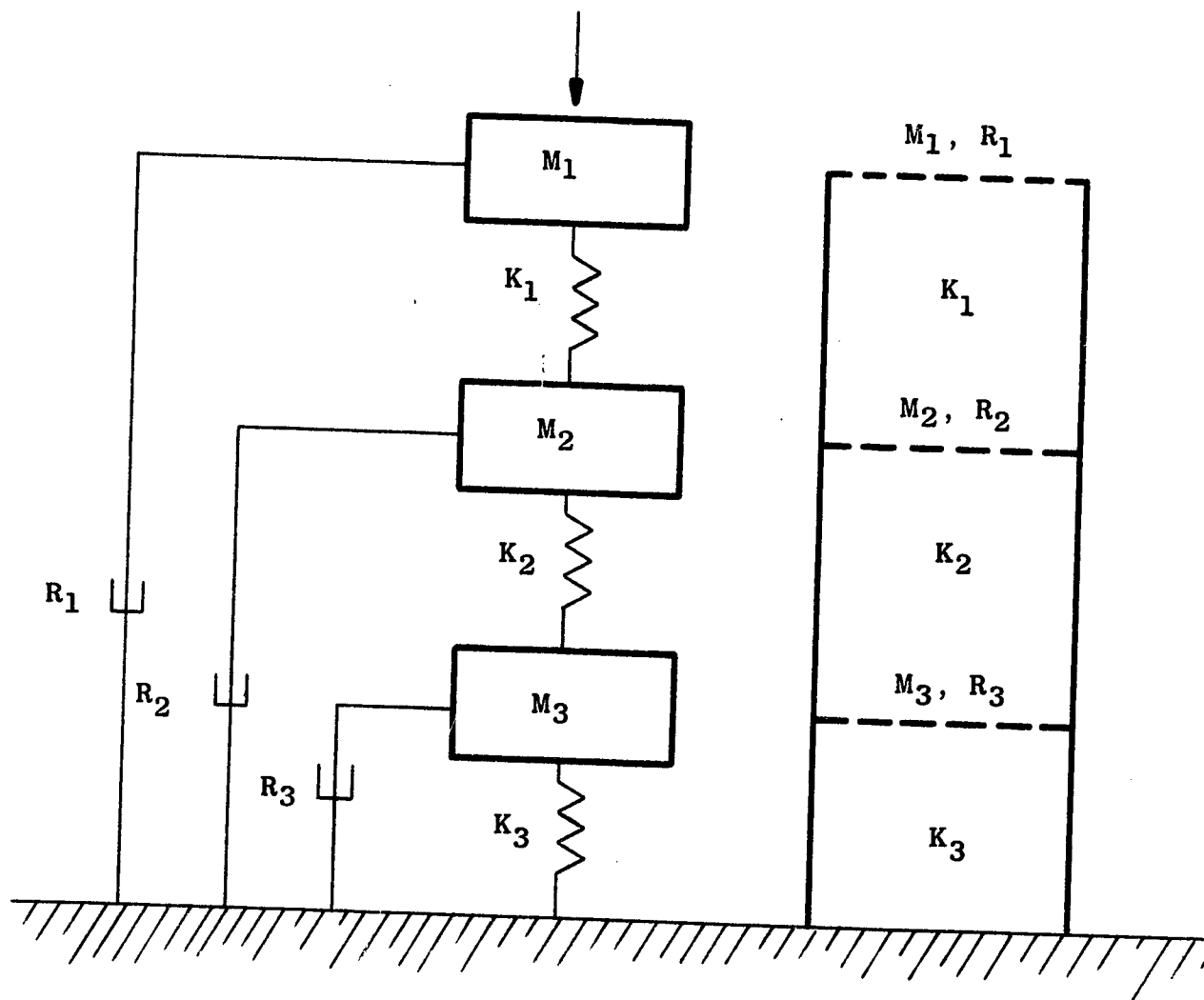


Figure 23. Three-Degree-of-Freedom Analytical Model

resistance to the motion of the gas in the perforated plate. When more than one of these mass-spring systems are connected in series, a multiple-degree-of-freedom resonator is obtained where the number of Helmholtz resonances is determined by the number of mass-spring elements or degrees-of-freedom. The acoustic impedance of these MDOF panels can be accurately calculated, and this analysis shows that the impedance components can be maintained close to the desired values over a wide range of input frequencies. The resonant frequencies and, therefore, the range of "effective acoustic response" can be determined by proper selection of the volume and porosity values of each cavity and perforated plate element. Figure 24 is a typical plot of the three resonances obtainable with a three-degree-of-freedom panel by varying the open area of each perforated element.

After designing each panel for the desired resonant frequencies (depending on the specific application), the panels are evaluated in an environment which duplicates as closely as possible the engine environment. The Acoustic Transmission Loss Duct, shown in Figure 25, enables the evaluation of the acoustic panels under the influences of a steady parallel flow of air and acoustic pressures which are representative of those found in the engine. Height between the treated walls can vary from 5 to 17.5 inches. The sound pressure level distribution upstream and downstream of the panel is measured with various steady flow Mach numbers over a frequency range of interest. The acoustic source is a Hartmann Generator which produces periodic tones with duct SPL's of 140-150 dB from 1 KHz to 6 KHz. The change in the integrated SPL before and after passage over two treated walls is a measure of the transmission loss at each frequency. These transmission loss tests are used to optimize the face plate porosity for maximum acoustic absorption in the duct.

3.5.2 Fan Frame Acoustic Treatment

The result of the tuning study described in Section 3.4 indicated that a panel with a peak absorption around 2.5-3.0 KHz would provide the minimum PNdB values for all three Experimental Quiet Engine configurations. Since the transmission loss peak frequency is a function of both the panel acoustic impedance and the duct geometry, these panels were evaluated in a duct with 12 inches between the treated walls, which is typical of the Experimental Quiet Engines' fan discharge duct heights. The panel shown in Figure 26 was designed for this frequency range, and the measured transmission loss curve is shown in Figure 27 at a flow Mach number of 0.4. This acoustic absorption characteristic provides the best tuning for all three Experimental Quiet Engine fan frame installations. The measured transmission loss of this panel is equivalent to that obtained with a broadband absorber such as open-cell polyurethane.

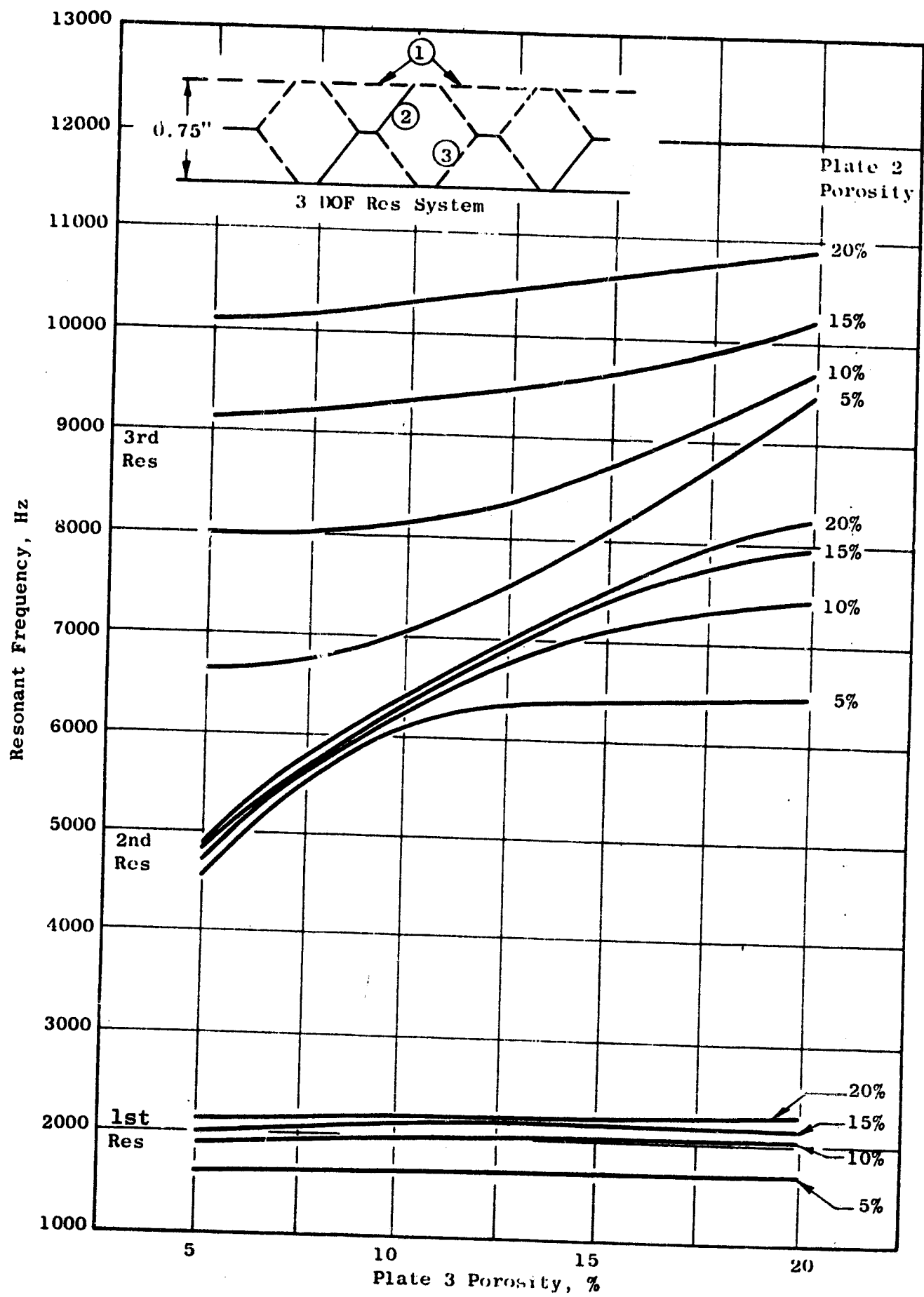


Figure 24. Resonant Frequencies for 3/4" Thick MDOF Panel with 10% Open Face Plate

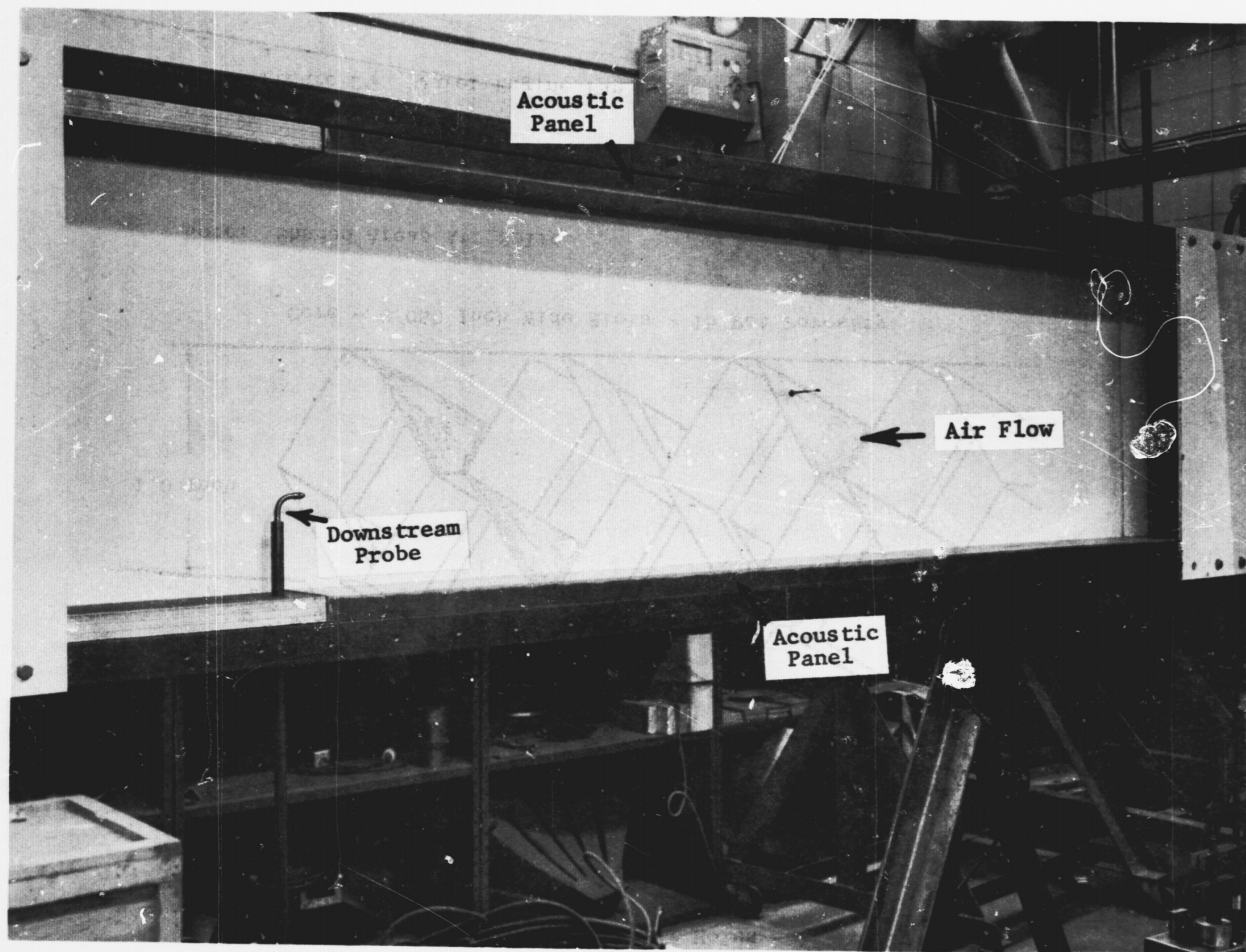
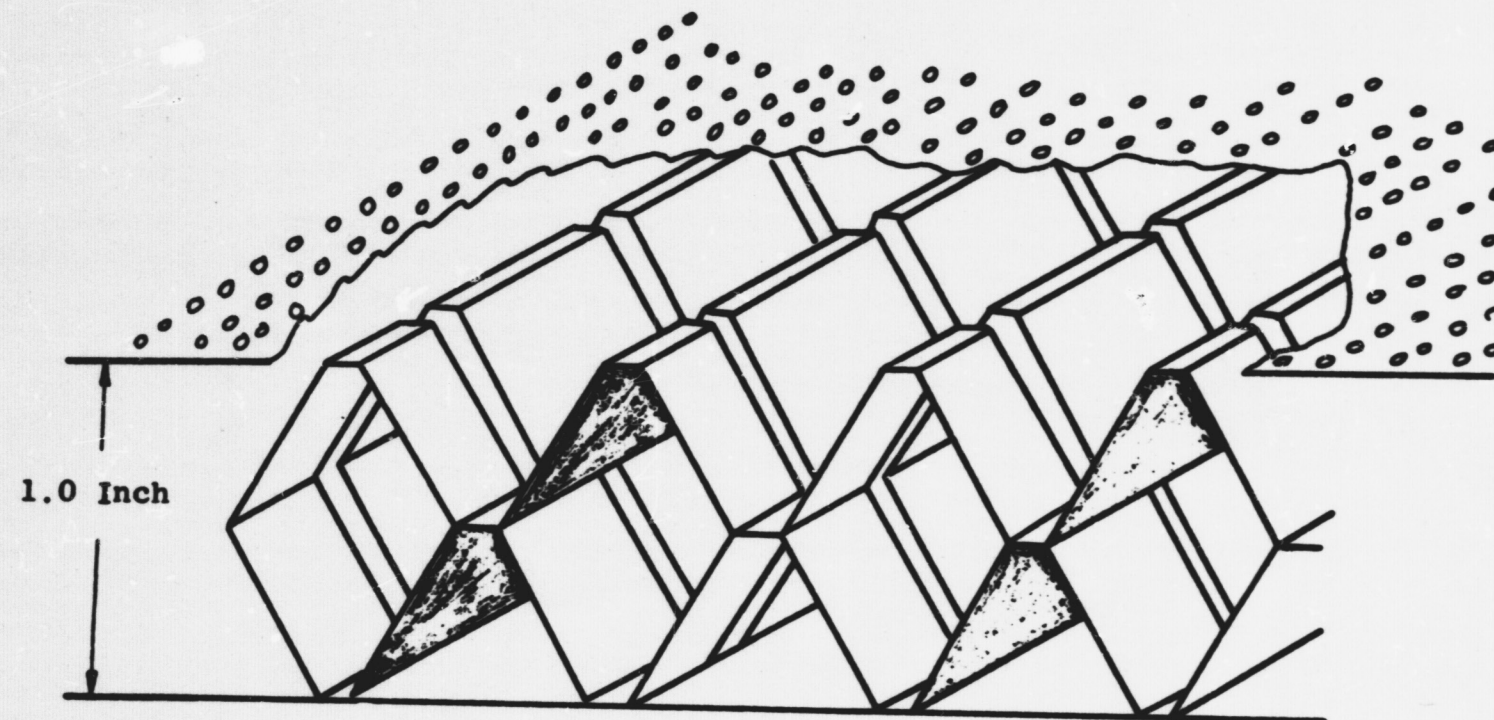


Figure 25. Rectangular Transmission Loss Duct (C68050811)

Face Plate - 1/16 Inch Diameter Holes - 10 Pct Porosity



Core - 0.050 Inch Wide Slots - 15 Pct Porosity

Note: Shaded Areas Are Solid

Figure 26. Quiet Engine Fan Frame Acoustic Treatment Design

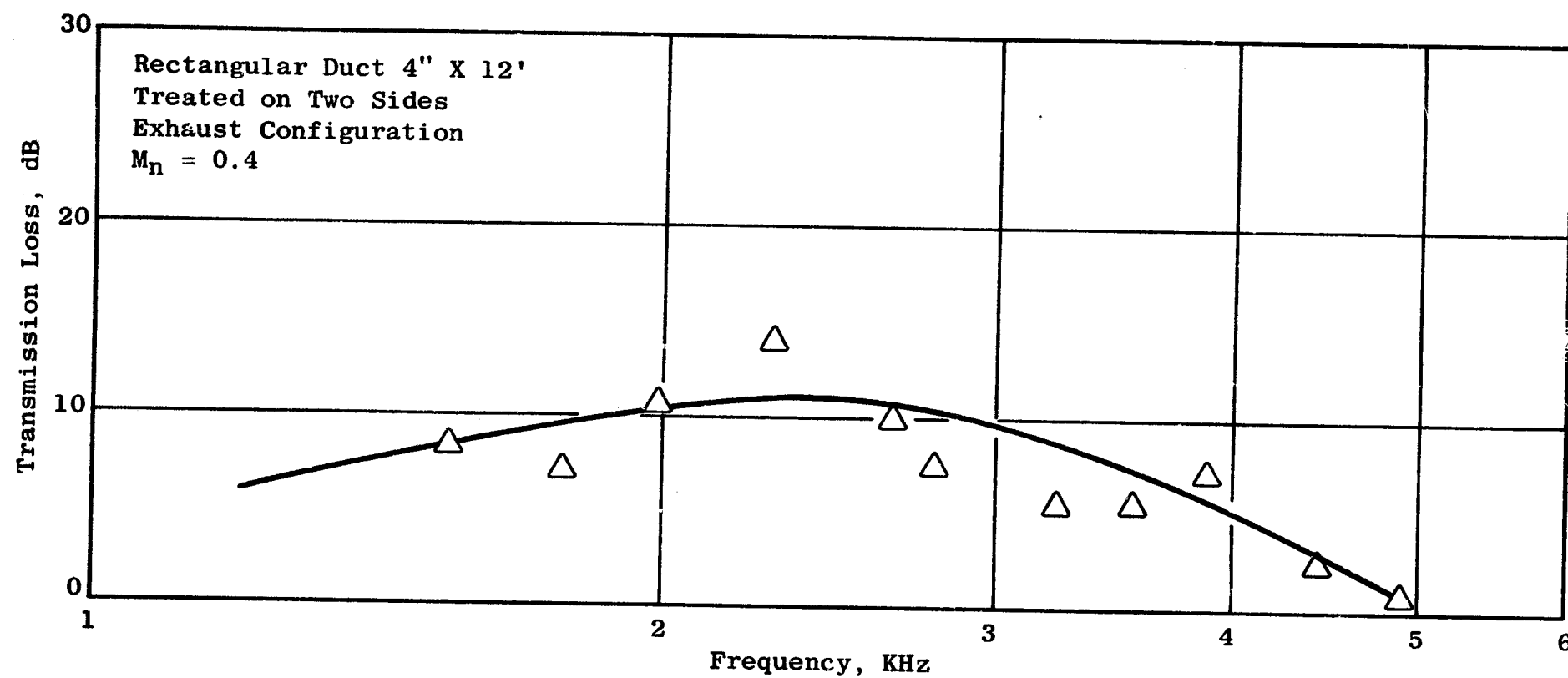


Figure 27. Acoustic Transmission Loss of the Quiet Engine Fan Frame Treatment

3.5.3 Compressor Inlet Acoustic Treatment

The core engine compressor inlet treatment is required to peak in the 3 KHz to 4 KHz frequency range for peak compressor blade passing and compressor broadband noise reduction. Since higher resonant frequencies can be obtained with decreased volumes, this panel thickness was set at 3/4-inch thickness, and four panels were designed. A listing of the test panel configurations is shown in Table VI. Each of these panels was evaluated in the transmission loss facility in order to determine the most effective TL characteristic.

Table VI. Core Compressor Transmission Loss Test Panels

CORE				
Panel	Depth (Inch)	Porosity (%)	Slot Width (Inch)	Slot Spacing (Inch)
1a	3/4	5	0.0625	1.25
1b	3/4	5	0.0625	1.25
II	3/4	7.7	0.0625	0.81
III	3/4	15.5	0.0625	0.405
FACE PLATE				
Porosity (%)	Hole Dia. (Inch)	Thick- ness (Inch)	Resonant Frequency (Hz)	
9	1/16	0.032	1300-3000-5700	
13	3/32	0.032	1400-3900-5900	
15	1/16	0.032	1730-4700-7230	
6	1/16	0.032	1680-5980-7900	

Since all four panels were close to the optimum configuration (set by resonant frequencies and face sheet porosity), very small differences were expected. The final test results at a Mach number equal to 0.4 shows them to be nearly equal in response over the entire frequency range. Figure 28 shows the measured transmission loss curve for the selected panel. The selected panel shown in Figure 29 was slightly better at high frequencies and consequently was specified for the engine installation.

3.6 DEFINITION OF LOW NOISE FEATURES

A large part of the noise from a fan is generated toward the outer portion of the blade (both broadband noise and pure tone noise). This program places emphasis on the reduction of tip-generated noise and, in particular, on the reduction of broadband noise generated at the outer portion of the fan blade. The various methods of reducing this noise will be evaluated on the 36-inch acoustic scale model.

The planned modifications have been selected based on consideration of not only acoustic potential but also their possible application in a realistic engine. Conditions simultaneously considered are:

- 1) Noise reduction potential
- 2) Aerodynamic performance effects
- 3) Mechanical reliability

3.6.1 Outer Case Boundary Layer Bleeding

Work is in progress at General Electric, under NASA sponsorship (NAS 3-7618), to investigate the aerodynamic effects of bleeding or blowing the boundary layer off the outer case of a single-stage 1120-ft/sec fan. Also, some tests were made on the development vehicle (36-inch OD) at the Peebles Proving Ground to determine if the tip boundary layer thickness had any influence on the noise generated. A 0.35-inch deep ring was installed eighteen inches in front of the rotor, creating a thick boundary layer, and measurements were taken on a 250-foot arc in the far field. The results at all speeds indicate, without any doubt, that a thicker-tip boundary layer in front of the blade will increase the broadband noise. Some results are shown on Figure 30; they indicate that the broadband noise increased about 10 dB when the boundary layer thickness was increased. A decrease in tip boundary layer thickness (obtained by bleeding the casing) can, therefore, be expected to reduce the broadband noise.

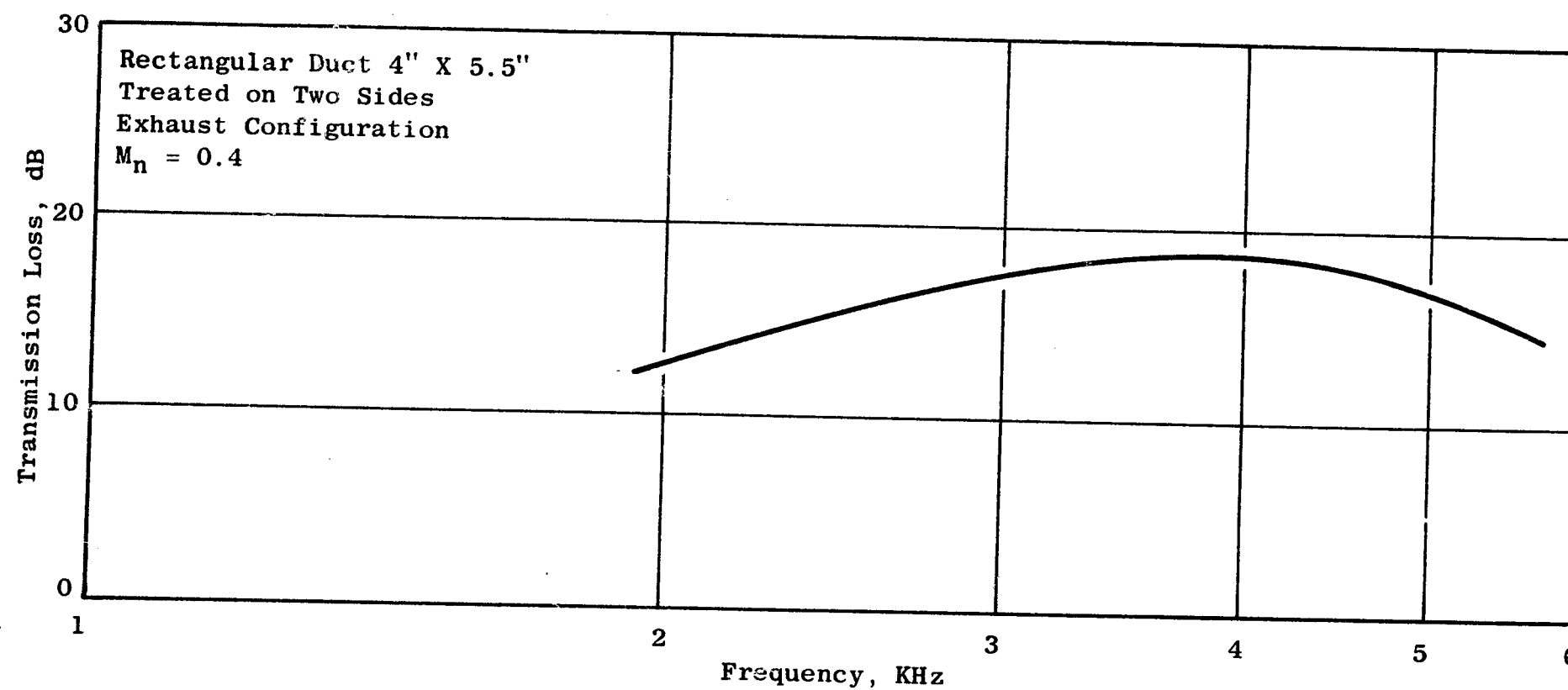
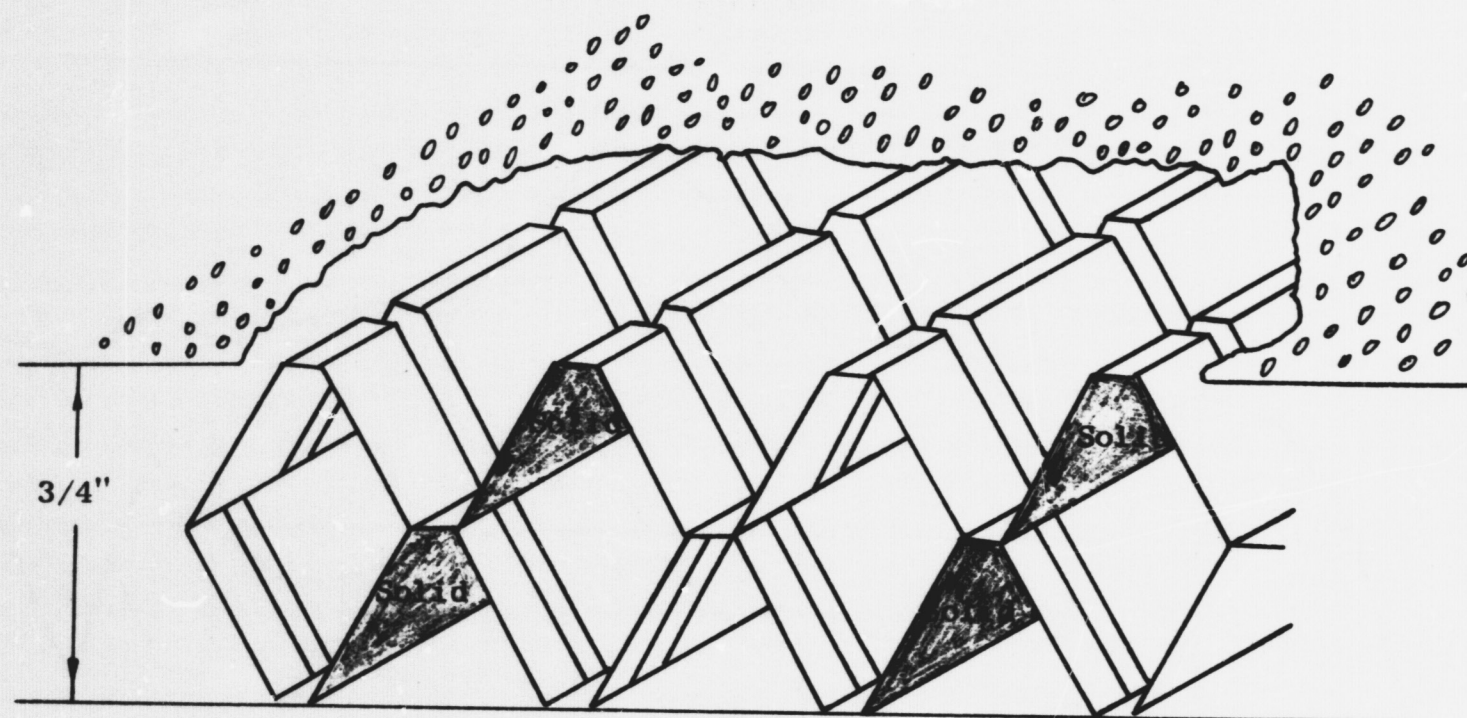


Figure 28. Acoustic Transmission Loss of the Quiet Engine Compressor Inlet Acoustic Treatment

Face Plate - 1/16" Diameter Holes
6% Porosity



Core - 15.5% Porosity
Slots - 0.0625" X 0.370"

Figure 29. Compressor Inlet Acoustic Treatment for Quiet Engines

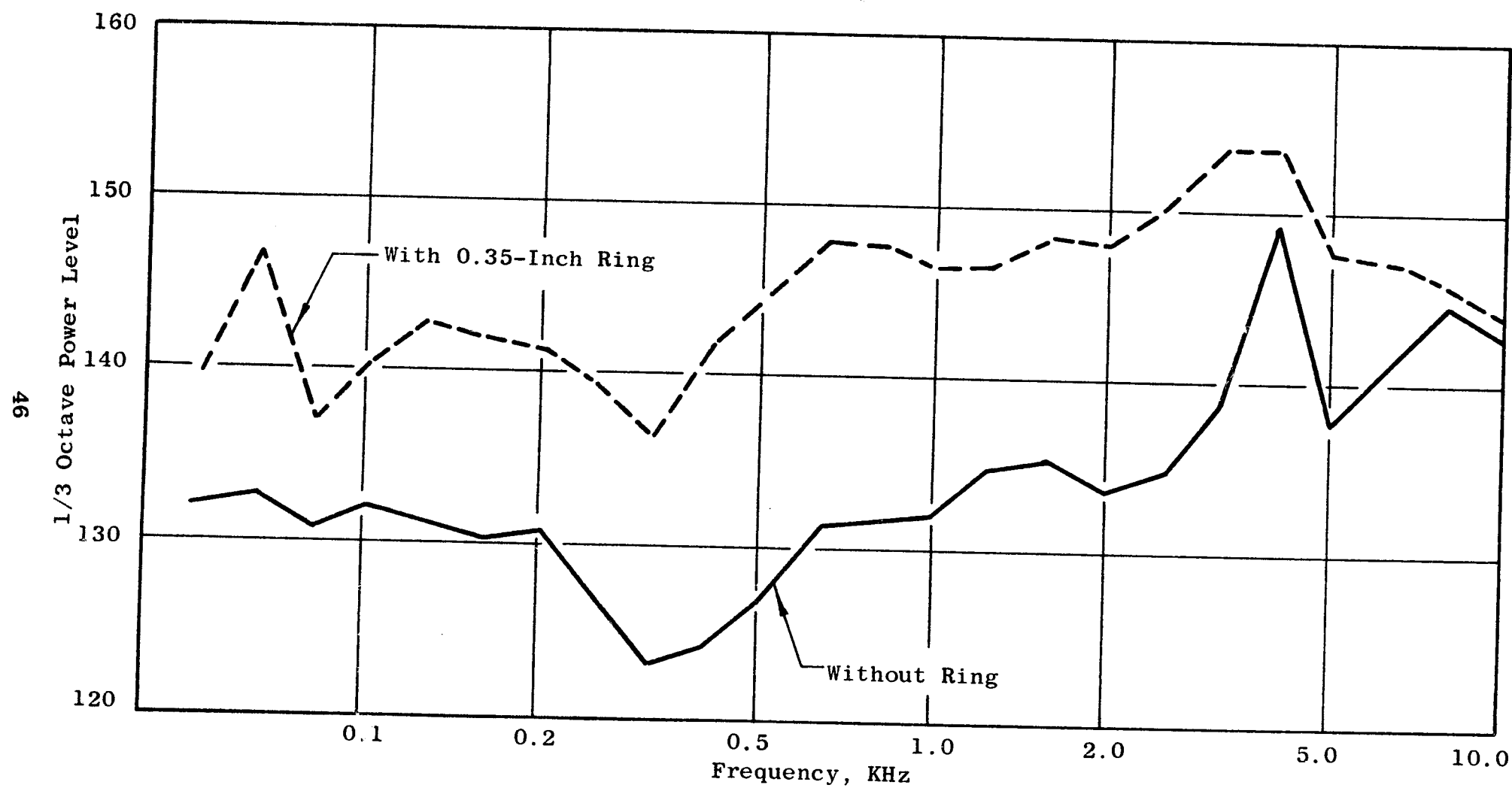


Figure 30. Effect of Inlet Boundary Layer Ring, 1/3 Octave Power Level Spectrum

Tip boundary layer bleed can also be expected to have an aerodynamic benefit. The selection of relatively low tip speeds to favor acoustic requirements necessarily leads to a correspondingly high aerodynamic loading. The aerodynamic strengthening of the blade tip region, by either bleeding off the casing boundary layer or by energizing the low energy air in the blade-end region (by injecting high pressure air into the tip boundary layer), is likely to have a beneficial effect on stall margin and distortion tolerance as well as on tip-generated noise.

Therefore, a bleed configuration was designed (see Figure 31). The system has a bleed flow capacity of 4 percent of the fan airflow. It is expected, however, that 1 percent bleed will suffice. The bleed configuration will be investigated aeroacoustically on the acoustic scale model vehicle described in Section 3.7.

3.6.2 Serrated Rotor

The concept of serrating the rotor leading edges to reduce rotor noise has been investigated at General Electric and found to be acoustically promising. A TF39 outer panel configuration incorporating a sawtooth leading edge was tested on a forty-two-inch ring in an indoor facility, and detailed noise measurements were taken. This configuration consisted of symmetrical sixty-degree wedges with a pitch of approximately four percent of the rotor chord. These "teeth" were located on the leading edge of the rotor along approximately the outermost eighty-five percent of the span. The acoustic results of the tests indicate that a reduction of about four to five db SPL on the fundamental tone was obtained with a sawtooth leading edge. This reduction seems to be due to a thinner wake, which results from a more favorable boundary layer profile on the blade. Some recently conducted (but not yet fully reported) wind tunnel tests on combed blades indicate, however, that the combed configuration modified the pressure distribution along the airfoil and reduced the pressure peak located at the leading edge. In addition, the test results indicated a relatively flat lift coefficient distribution versus angle of attack. It can, therefore, be expected that the broadband noise, which is largely dependent on dC_L/D will also be reduced. Wind tunnel tests are currently in progress at General Electric. A series of leading edge configurations (see, for example, Figure 32) are being aeroacoustically evaluated under different flow conditions. Detailed acoustic and unsteady aerodynamic data are being taken and analyzed. The best "low noise configuration" will be selected at the end of this series of tests. The blade geometry that will be used to evaluate the blade serrations will be carefully selected to guard against introduction of dangerous stress concentrations in either steady state or vibratory loadings. The blading edge contours will also be selected to favor aerodynamic operation at the angle of attack encountered along the operating line. Care will be exercised to insure that

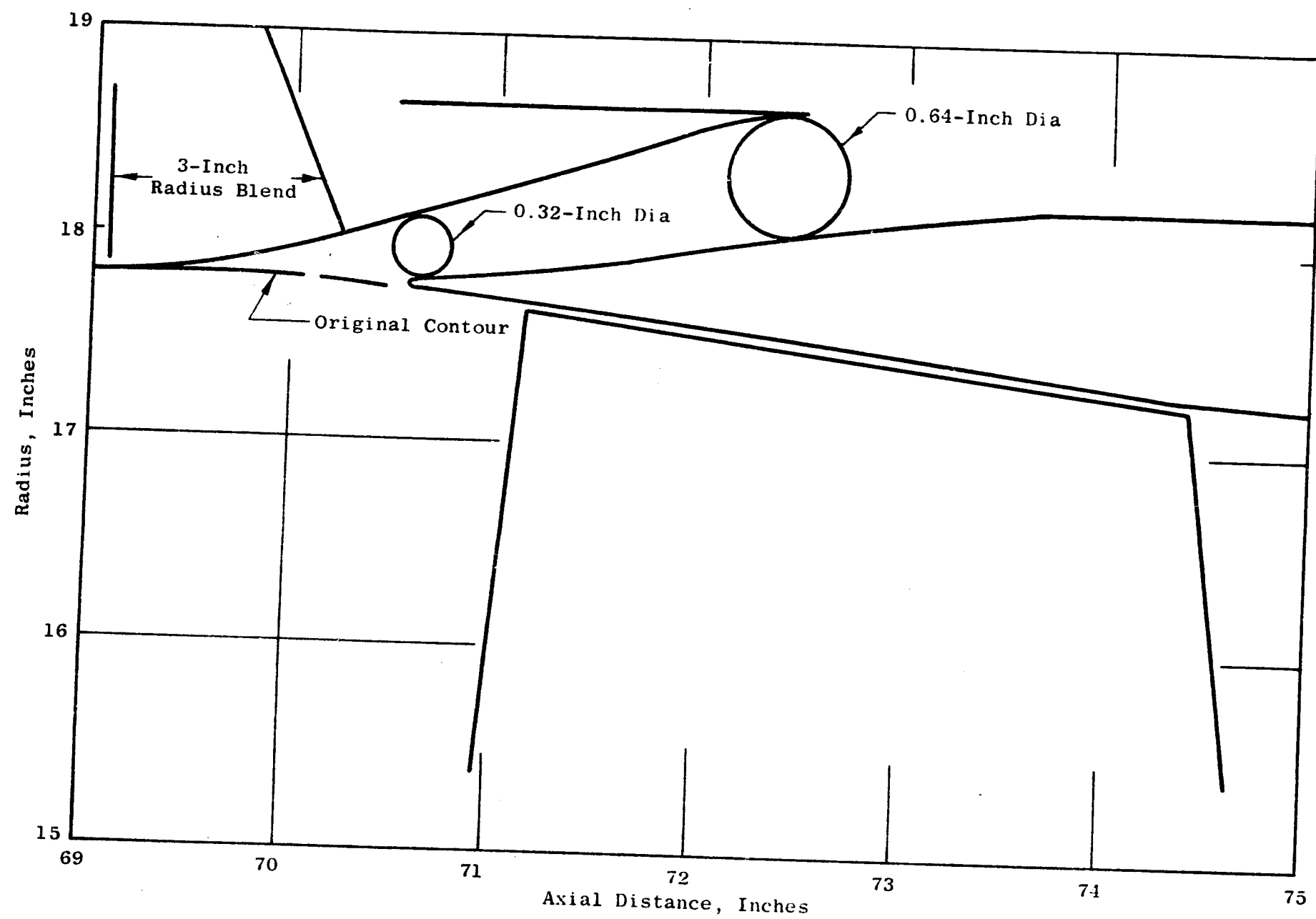


Figure 31. Boundary Layer Bleed Slot

neither mechanical nor aerodynamic performance is inadvertently or unnecessarily compromised when exploring the effects of serrated leading edges.

Acoustic, aeromechanical, and aerodynamic performance data will be obtained in the scale model test program to permit full consideration of the potential (both acoustically and as an engine system) prior to selection of the final fan design.

3.6.3 Slotted Rotor

The major source of blade passing frequency tones in an IGV-less fan is the rotor wake interaction with the downstream stators. The larger part of broadband noise is associated with the vorticity in the rotor blade wakes. Any reduction in the wake size will, therefore, help reduce both the pure tones and the broadband noise.

Extensive work on slotted blades that has been done under NASA sponsorship indicates that an appreciable reduction in the wake size can be expected if the slot is properly located. An adequately slotted rotor is, therefore, expected to have a smaller wake and subsequently result in quieter operation.

The aerodynamic factors involved in the slots near the blade tip are:

- Higher maximum loading capability
- Possible improvement in performance at cruise

The better performance at high incidence angle should help reduce blade wakes and the associated noise at the approach power settings. Increased stall margin and improved distortion tolerance should be obtained at all speeds, since fan stall will originate near the blade tip.

The slot does not normally reduce the minimum loss coefficient of good subsonic airfoils, but (in the case of the proposed fans) the blades operate at supersonic Mach numbers near the tip with relatively high aerodynamic loading. This loading requires a significant amount of subsonic diffusion after a shock which is likely to be strong enough to separate the boundary layer. Proper location of the slot relative to the shock impingement point under these circumstances may help reattach the flow and lead to a more efficient subsonic diffusion at cruise, instead of the subsonic diffusion being obtained as a relatively inefficient dump diffuser when separation exists. This may also reduce broadband noise generation at take-off thrust.

An aeroacoustic evaluation of a series of slotted airfoil designs is currently planned for the transonic tunnel. A selection of the best "low noise" slot will, hopefully, result from these tests. Mechanical analysis of the blade with slots will be carried out to insure that stress distributions are totally satisfactory and that all portions of the blade retain the desired vibratory characteristics.

The slotted rotor blade will be initially designed to influence the flow in the vicinity of the blade tip. Further variations, such as extending the slot along the span to influence the free-stream portion of the flow, could be explored in later configurations if promising acoustic and/or aerodynamic results are obtained in the initial test. The slotted rotor will be evaluated on the acoustic scale model vehicle described in Section 3.7.

3.7 TEST PLAN FOR ACOUSTIC SCALE MODEL VEHICLE

The development test objectives for the acoustic scale model fan are:

- Evaluate the acoustic characteristics of selected fans without the presence of any extraneous sources
- Evaluate the acoustic characteristics of twelve different fan acoustic configurations as a result of incorporating noise reduction features
- Evaluate the effects of the acoustic modifications on the aerodynamic performance of each configuration
- Confirm the mechanical integrity of each acoustic configuration

The approach utilizes a scale model evaluation of the noise reduction features, and the demonstration of the fan selected utilizes the most desirable features on full scale fan components and engine tests. Primary interest will be in the amount of noise reduction achieved on each configuration. The results will provide the earliest possible guidance based upon directly applicable experimental data on the features that should be incorporated in either or both of the full size fan designs.

It has been the experience of General Electric that scale-model acoustic tests are an accurate, effective means by which a great deal of knowledge relative to the acoustic characteristics of a fan can be readily determined without the high cost and changeover time associated with full scale hardware.

In order to systematically evaluate the effects of each of the fan tip noise reduction features described earlier, it will be necessary to conduct a carefully planned and properly executed series of experiments in which the aerodynamic and acoustic characteristics of each of those design features is measured in detail and evaluated for possible use on the full scale engine. Predictions of expected results will be correlated with early experimental investigation of the proposed fan noise reduction features by means of component testing on an acoustic model fan (see Figure 33). The scaled fan will be 36 inches in diameter and will be driven by an LM1500 engine. The tests will be conducted at the Peebles Test Site (see Figure 34) and will help determine at an early date in the program the noise levels generated by the fan. Primary interest will be in the amount of noise reduction achieved by each noise feature and in the evaluation of low-speed versus low-loading designs.

The acoustic scale model fan component utilizes hardware from the CF6 scale model fan component which was recently tested at Peebles. Acoustic measurements will be taken in the far field with microphones spaced 10 degrees apart along a 150-foot radius (see Figure 35). Under selected conditions, acoustic probe measurements will be taken at different axial positions within the fan (see Figure 36) and at the fan nozzle exit.

Tables VII and VIII describe the test plans for scale model Fans B and C, respectively.

- As can be seen, most configurations will be investigated with/without the effects of treatment in the fan frame.
- Acoustic data will be taken along three operating lines on the baseline configurations.
- Aerodynamic data will be taken; the aerodynamic probes will be pulled out; and, only then, will the acoustic far field data be taken (to eliminate any probe interference noise).
- The acoustic probe data will be taken only after the far field data acquisition is completed (again to avoid probe interference noise).

The acoustic data collected in both the near field (probe) and the far field will be analyzed in one-third octave bands (with selected narrow bands when needed) and reduced to standard atmosphere and humidity to provide a meaningful comparison between configurations. Projections to the full scale fan size will be made on each configuration tested.

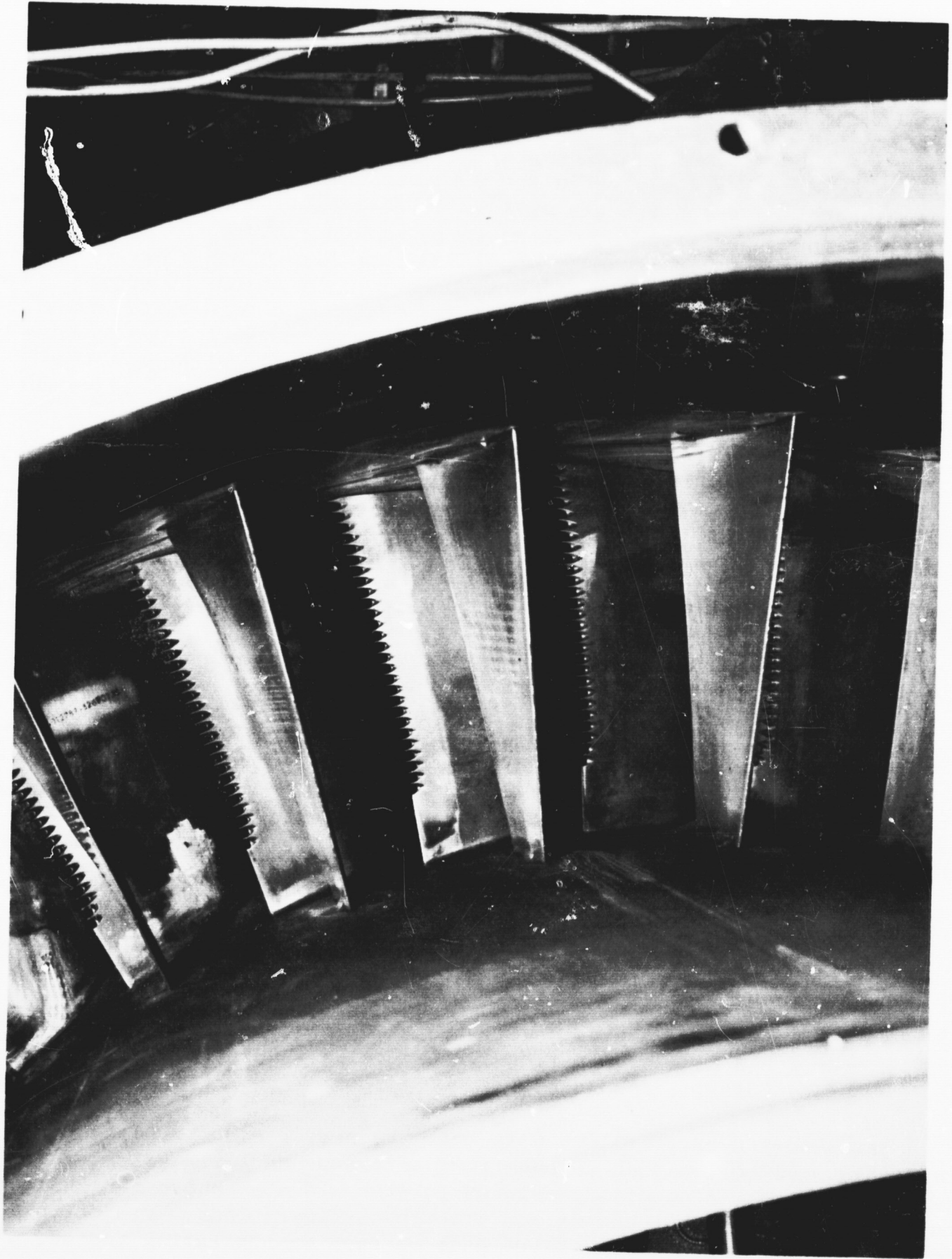


Figure 32. Sawtooth Rotor Leading Edge (342297)

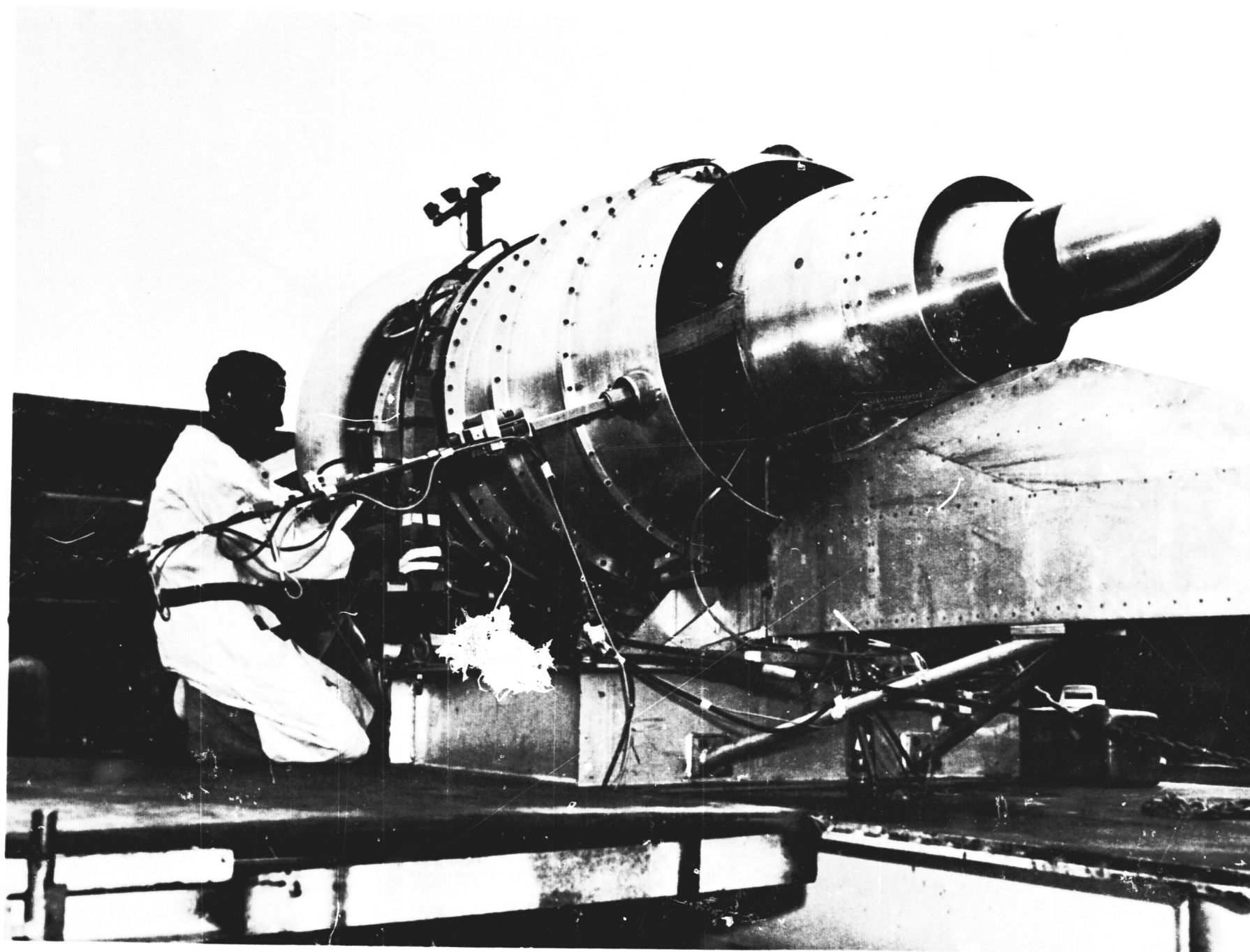


Figure 33. Acoustic Scale Model (CDC 11444)

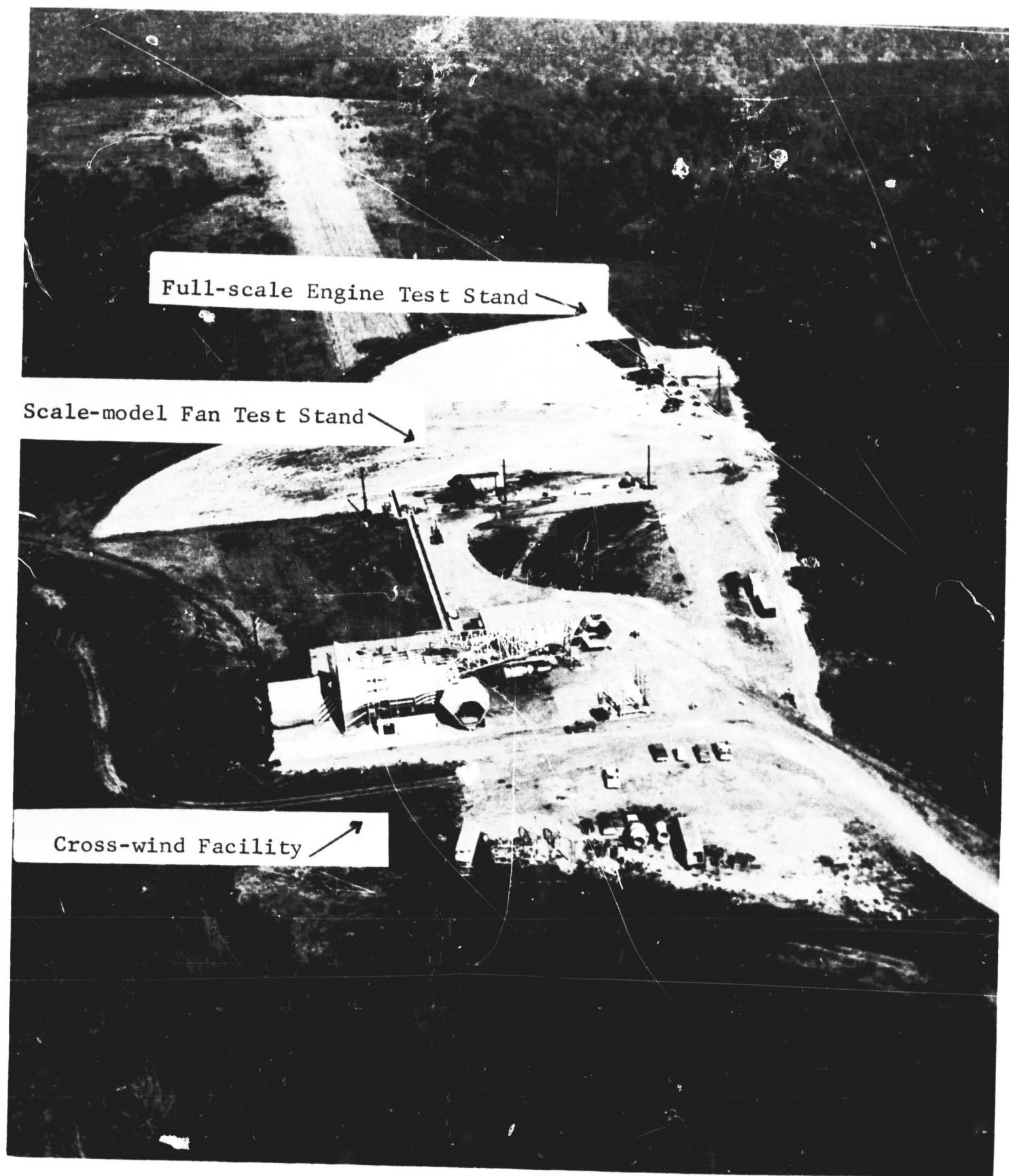


Figure 34. Peebles Test Site (CDC 9876)

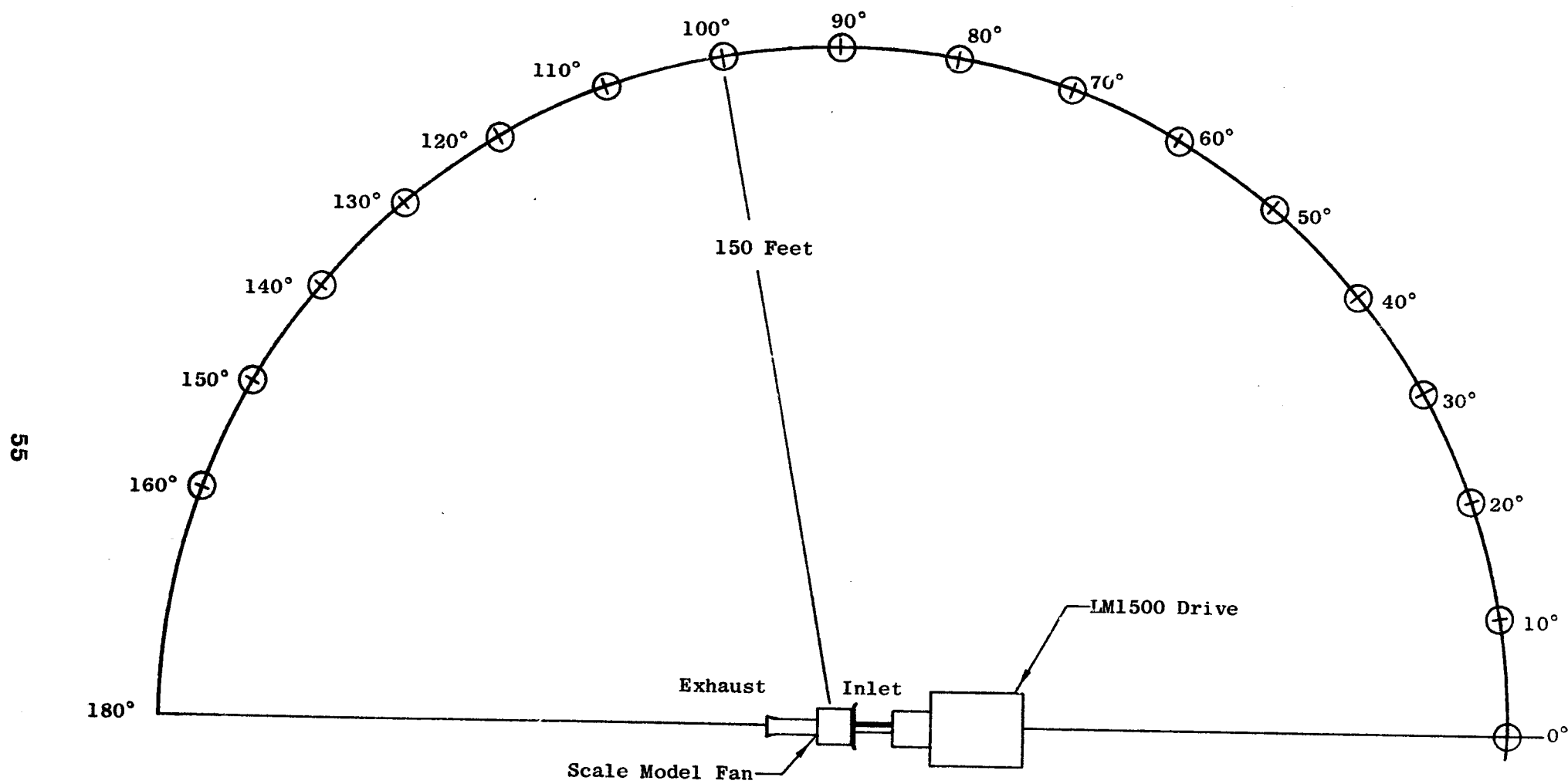
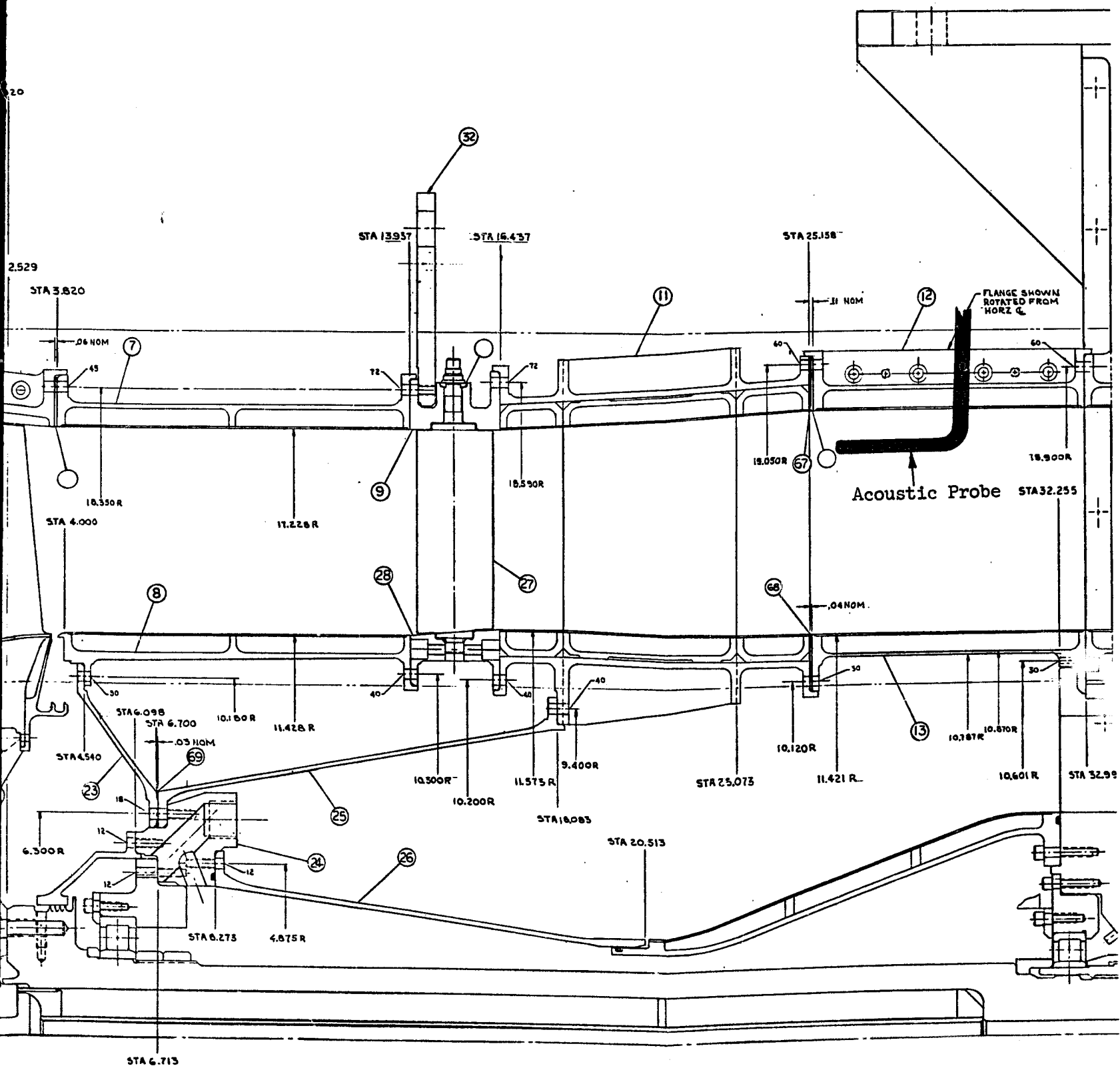


Figure 35. Peebles Site 4B - Microphone Field Schematic



PRECEDING PAGE BLANK NOT FILMED

Scale Model, Acoustic Probe Locations

FOLDOUT FRAME
Page 57

Table VII. Test Plan for Acoustic Scale Model Fan B

Config- uration	Fan Type	Tip Feature	Treatment Location	Aero Data	Probe Data	No. of Oper Lines	Remarks
SM 1	B	None	Covered	Yes	Std Oper Line Only	3	First aero and no acoustic - then take aero probes out and take acoustic data
SM 2	B	None	Frame	No	Std Oper Line Only	3	---
SM 3	B	Tip Bleed	Covered	Yes	Yes	1	First aero and no acoustic - then take aero probes out and take acoustic data
SM 4	B	Tip Bleed	Frame	No	Yes	1	---
SM 5	B	Serrated	Covered	Yes	Yes	1	First aero and no acoustic - then take aero probes out and take acoustic data
SM 6	B	Serrated	Frame	No	Yes	1	---
SM 7	B	Slotted	Covered	Yes	Yes	1	First aero and no acoustic - then take aero probes out and take acoustic data
SM 8	B	Slotted	Frame	No	Yes	1	---

PRECEDING PAGE BLANK NOT FILMED

Table VIII. Test Plan for Acoustic Scale Model Fan C

Config- uration	Fan Type	Tip Feature	Treatment Location	Aero Data	Probe Data	No. of Oper Lines	Remarks
SM 9	C	None	Covered	Yes	Std Oper Line Only	3	First aero and no acoustic - then take aero probes out and take acoustic data
SM 10	C	None	Frame	No	Std Oper Line Only	3	---
SM 11	C	Mod 1	Frame	Yes	Yes	1	First aero and no acoustic - then take aero probes out and take acoustic data
SM 12	C	Mod 2	Frame	Yes	Yes	1	First aero and no acoustic - then take aero probes out and take acoustic data

4.0 FAN AERODYNAMIC DESIGN

4.1 SUMMARY

This section presents the aerodynamic design of Experimental Quiet Engine Fans A, B, and C.

Two low-speed and one low-aerodynamic-loading axial-flow front fans were designed to provide vehicles for the experimental evaluation of methods and techniques to achieve reduced engine noise levels. The two low-speed fans, designated Fan A and Fan B, were designed at a corrected tip speed of 1160 ft/sec and a bypass pressure ratio of 1.50. Tip diffusion factors of 0.35 and 0.375 result, for Fan A and B respectively, for the assumed loss coefficients. The low-aerodynamic-loading fan, designated Fan C, was designed at a corrected tip speed of 1550 ft/sec and a bypass pressure ratio of 1.60. A tip diffusion factor of 0.324 results for Fan C for the assumed loss coefficient. The inlet hub-tip radius ratio is 0.465 for Fans A and B and 0.360 for Fan C. The specific corrected weight flow is 41.3 lb/sec-sq ft annulus area for all three fans. The corrected fan flow for Fans A and B is 950 lb/sec, which yields a tip diameter of 73.354 inches. A corrected fan flow of 915 lb/sec for Fan C results in a tip diameter of 68.30 inches.

The axial spacing between blades and vanes was selected for the acoustic consideration of minimizing noise generation. The axial distance between the rotor and outer OGV, expressed in number of rotor chords, is a minimum of 2.0 for each of the three fans. The axial distance between the rotor and inner OGV, expressed in number of rotor chords, is a minimum of 1.25 for each of the three fans. No inlet guide vanes (IGV's) were incorporated in the configuration selection. Fan A rotor utilizes a medium-aspect-ratio, tip-shrouded blade. Fan B rotor utilizes a moderately-low-aspect-ratio, unshrouded blade. Fan C rotor utilizes a moderate-aspect-ratio blade with a part-span shroud. The shrouding on Fans A and C is needed to assure operation without encountering self-excited vibration.

Two scale fans which model the bypass portions of Fan B and Fan C were also designed. These scale model fans are designed to enable evaluation of the acoustic characteristics and aerodynamic performance as a result of incorporating various noise reduction features. Scale Fan B models the outer 84.5 percent of the full scale Fan B flow and scale Fan C models the outer 78.1 percent of the full scale Fan C flow. The tip diameter and inlet hub-tip radius ratio is 35.500 and 0.579, and 35.986 and 0.569 for model Fans B and C, respectively. The design conditions for the scale fans are at the same corrected tip speed, corrected specific weight flow, and pressure ratio as the full scale fans. A design corrected weight flow of 188.0 lb/sec and 198.4 lb/sec result for model Fans B and C, respectively.

4.2 BASIC DESIGN FEATURES

For the two low-speed and one low-aerodynamic-loading high bypass ratio axial-flow front fans, since the realization of good performance at the altitude cruise condition is a prime requirement for high bypass ratio subsonic cruise engines, the aerodynamic design point is selected as the altitude cruise condition of 0.82 flight Mach number at 35,000 ft. At this condition the over-all characteristics for the two low-speed fans, designated as Fan A and Fan B, and the low-aerodynamic-loading fan, designated as Fan C, are shown in Table IX.

Observations of past trends indicate that as tip speed increases, at constant aerodynamic loading, fan broadband noise increases. Also, at constant tip speed, a reduction in aerodynamic loading is observed to decrease fan pure tone noise. For a given cycle requirement, the minimum noise configuration requires consideration of the weighted sum of the two types of noise.

The low-design-point corrected tip speed of Fans A and B, 1160 ft/sec (≈ 1050 ft/sec at a take-off thrust of 22,000 lbs), was selected to investigate the low noise potential of low-tip-speed fans. The aerodynamic loading and stall margin considerations of the low-speed fans, for reasonable aspect ratios and solidities, limited the pressure ratio of the bypass portion to 1.50 at the design point. The desirability of good core engine supercharging restricted the inlet hub-tip radius ratio to 0.465.

The higher-design-point corrected speed of Fan C, 1550 ft/sec (≈ 1400 ft/sec at a take-off thrust of 22,000 lbs), was selected to investigate the low noise potential of low-aerodynamic-loading fans. The elevation of the bypass stream total pressure ratio to 1.60, which is desirable to minimize fan size for a given engine thrust, was possible with the increased blade speed and still realized a significant reduction to the aerodynamic loading from the level of Fans A and B. The reduction of inlet hub-tip radius ratio to 0.36, which is desirable to minimize fan diameter and transition duct losses, was made possible by the increased tip speed while maintaining hub supercharging.

The axial spacings and blade/vane ratios were selected to minimize noise generation. The remaining items were selected as being typical of current state-of-the-art fan design.

4.2.1 Method of Calculation

The over-all calculation procedure used in this design to select the flowpath and determine the vector diagrams, is the Compressor Axisymmetric Flow Determination (CAFD) program which is outlined in Reference 3. In

Table IX. Over-All Characteristics for Fans A, B, and C at the Aerodynamic Design Point

Characteristic	Fan A	Fan B	Fan C
Corrected rotor tip speed, ft/sec	1160	1160	1550
Inlet hub/tip radius ratio	0.465	0.465	0.360
Rotor inlet tip diameter, inches	73.354	73.354	68.300
Corrected airflow, lb/sec	950	950	915
Inlet corrected specific flow, lb/sec-sq/ft annulus area	41.3	41.3	41.3
Number of rotor chords axially separating rotor and outer OGV	2.0	2.0	2.0
Number of rotor chords axially separating rotor and inner OGV	1.25	1.25	1.25
Bypass portion total pressure ratio	1.50	1.50	1.60
Hub portion total pressure ratio	1.32	1.43	1.49
Bypass ratio: Design Latest cycle match	5.6 5.5	5.4 5.3	5.0 4.9
Rotor aspect ratio	2.32	1.71	2.09
Rotor solidity: OD ID	1.45 2.50	1.30 2.16	1.40 2.45
Objective bypass adiabatic efficiency	0.865	0.870	0.842
Number of Rotor Blades	40	26	26
Number of outer OGV's	90	60	60
Number of inner OGV's	90	60	60

addition to calculation stations at the blade edges and in the spaces between blades, calculation stations interior to the rotor blade were included to improve the over-all accuracy of the solution by including in fair detail the effects of blade thickness blockage and energy addition on the streamline slopes and curvatures.

The energy addition was distributed along axisymmetric stream surfaces in the axial space of the blade according to the first quarter cycle of a sine wave. This selection provides a reasonably good representation of work input distribution; furthermore, it is not a critical selection, since the axial distribution does not have an important influence on the radial positioning of the streamlines.

In application of the CAFD procedure to this design, no attempt was made to calculate the localized velocity variations that occur deep in the wall boundary layer. Instead, an effective area coefficient that accounts for the displacement thickness of the wall boundary layer and the wakes from upstream blade rows was used. Values of effective area coefficient were selected from past experience. A constant value for the effective area coefficient was used in the axial space between blade rows. An effective area coefficient of 0.98 was used forward of the rotor and 0.96 was used at stations between the rotor and the inner and outer outlet guide vanes. Modifications to the effective area coefficient were employed at the internal blade row stations to reflect the flow area reduction due to the tangential thickness of the blade. For Fan C, the blockage of the part-span shroud was spread uniformly across the entire annulus. Modifications to the edge values of the axial derivative of total effective area coefficient and the axial derivative of angular momentum, that are used in the radial equilibrium equation, were made to minimize abnormal influences of large changes from point-to-point in the calculation grid.

4.2.2 Flowpath

The fan does not employ inlet guide vanes ahead of the rotor. Immediately downstream of the rotor, a flow splitter is located which separates the bypass-portion flow from the hub-portion flow. This splitter requires a split outlet guide vane system but permits independent area control of the two streams. An axial spacing of 2.0 rotor chords and 1.25 rotor chords separate the outer outlet guide vane and inner outlet guide vane, respectively, from the rotor. Aft of the outer outlet guide vanes, the bypass flow is ducted through the frame struts to a nozzle. The hub portion of the flow is ducted into the core compressor. The detailed flowpath selection was based on the axisymmetric flow calculations from CAFD. The flowpaths were intended to provide an optimum balance between blade loading, axial velocity level, and axial velocity distribution, as weighted with the physical constraints imposed by the use of an existing fan frame and the axial space requirement between blade rows for minimizing noise generation. The flowpaths which resulted for Fans A, B, and C are

shown in Figure 37. As is shown in this figure by the dotted line, the modeling by scale Fans B and C is restricted to the bypass portion of Fans B and C. The scale model Fan B models the entire bypass portion of Fan B. The ducting of scale model Fans B and C, aft of the outlet guide vanes, was made identical for ease of interchangeability of the two types of fans. Accordingly, that portion of the Fan C bypass flow which is modeled by the scale model Fan C was determined.

It will be observed from the Fan B flowpath, that the scale model Fan B (in the region of the rotor hub ID) has a somewhat different shape than that of the splitter stagnation streamline. Had the stagnation streamline been assumed, the D-factors shown in Figure 38 at a stream function of 0.845 would exist at the rotor hub. A value of 0.55 for a rotor hub adjacent to a wall is clearly excessive. The flowpath selected in the scale model fan rotor hub region increases the annulus convergence across the blade row and introduces curvature of the proper sign which tend to alleviate the abnormal loadings. An aggravating effect on the hub loading in the scale model fan designs, is the increased level of loss coefficient, relative to that employed at the same streamline in the full scale fan designs. Because of the end-wall-blade boundary layer interaction, additional work input is required to achieve the desired total pressure ratio. This additional work input results in an increase in the blade loading.

4.2.3 Total Pressure Ratio and Loss Coefficient

A high hub pressure ratio is generally desirable for supercharging the core engine. However, efficiency and distortion attenuation through the fans are also important which tend toward moderate hub pressure ratio. During preliminary design studies of Fans A and B, the radial distribution of fan discharge total-pressure ratio was varied from a radially-constant distribution to one in which the hub pressure ratio was substantially less than average. For each distribution, the average bypass stream pressure ratio was held at 1.50. The selected shape for Fan A and Fan B exit total pressure profiles are shown in Figure 39. A constant radial total pressure profile was selected for the bypass portion of Fan B. The hub portion total-pressure profile was reduced moderately to prevent excessive rotor loadings and to reduce inner outlet guide vane inlet Mach number and loading. The average hub pressure ratio of Fan A was reduced still further so that the effect of hub loading on efficiency, distortion resistance, and noise could be determined. In order to prevent excessive radial total pressure gradients in Fan A, it was necessary to lower the total pressure at the splitter streamline from that used for Fan B. The average bypass total-pressure ratio requirement forced higher pressure ratios at streamlines removed from the splitter. The total-pressure ratio at the tip of Fan A was blended into the value used for Fan B to prevent the occurrence of high rotor tip loadings.

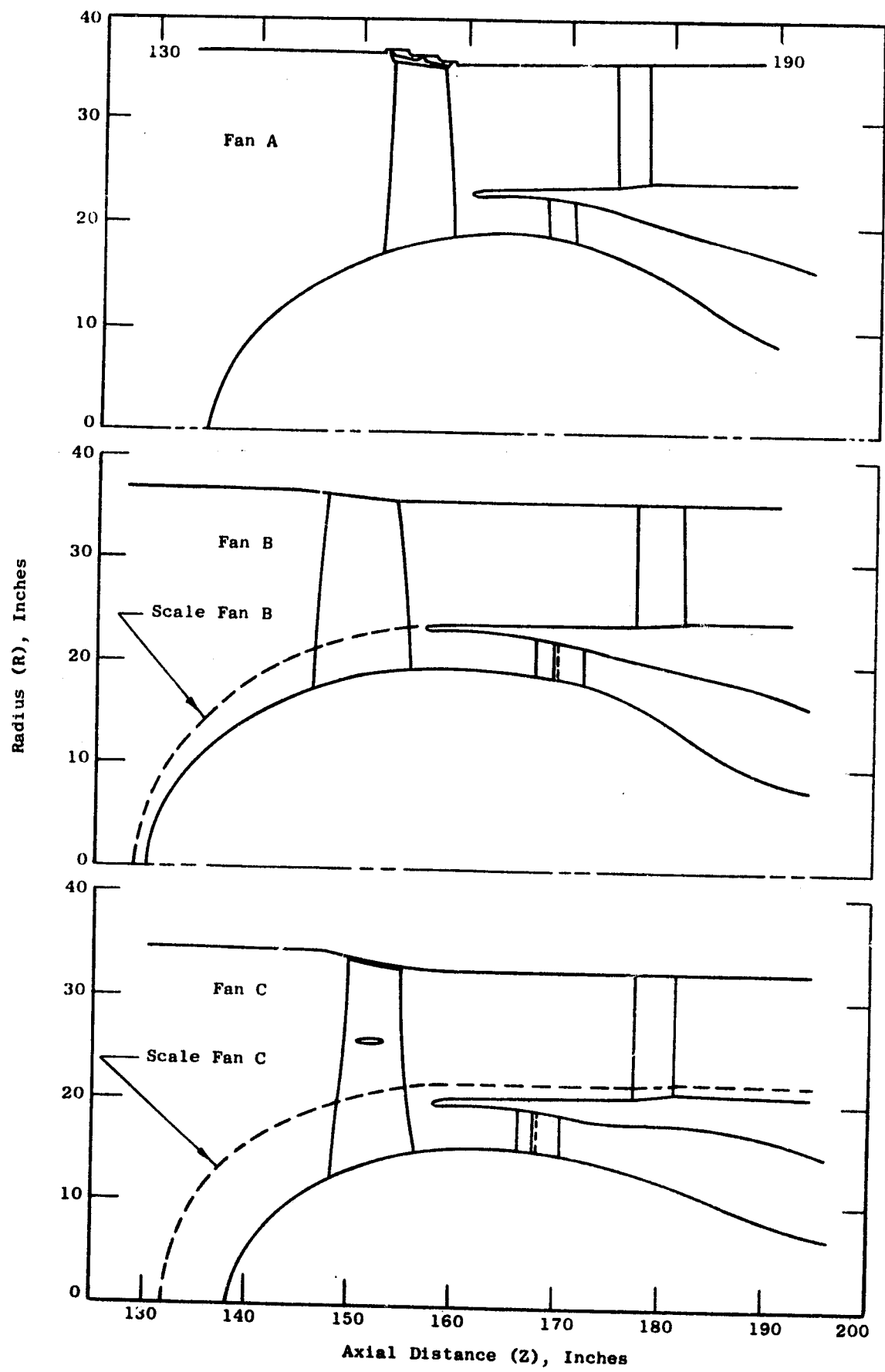


Figure 37. Quiet Engine Flowpaths

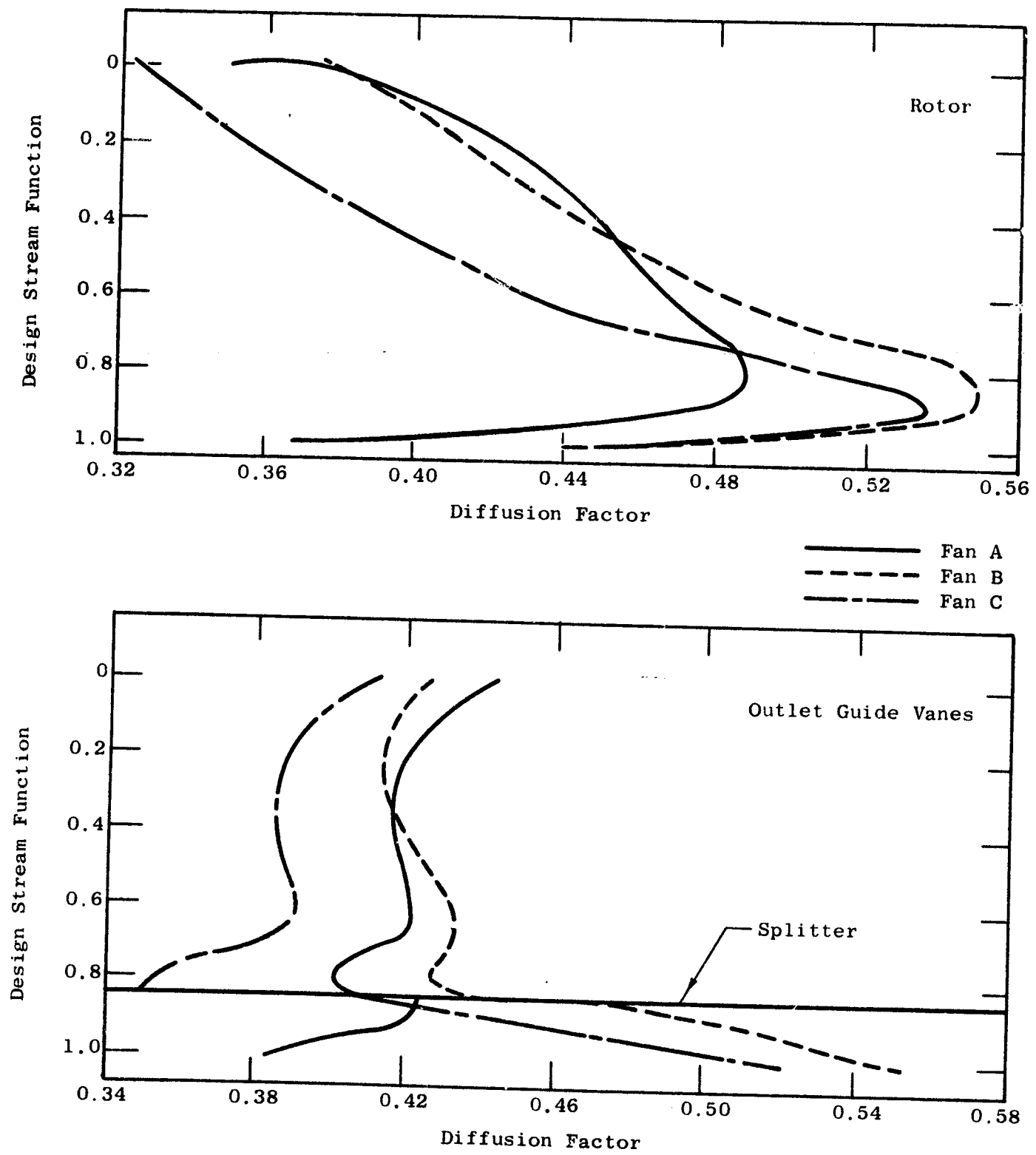


Figure 38. Radial Variation of Diffusion Factor

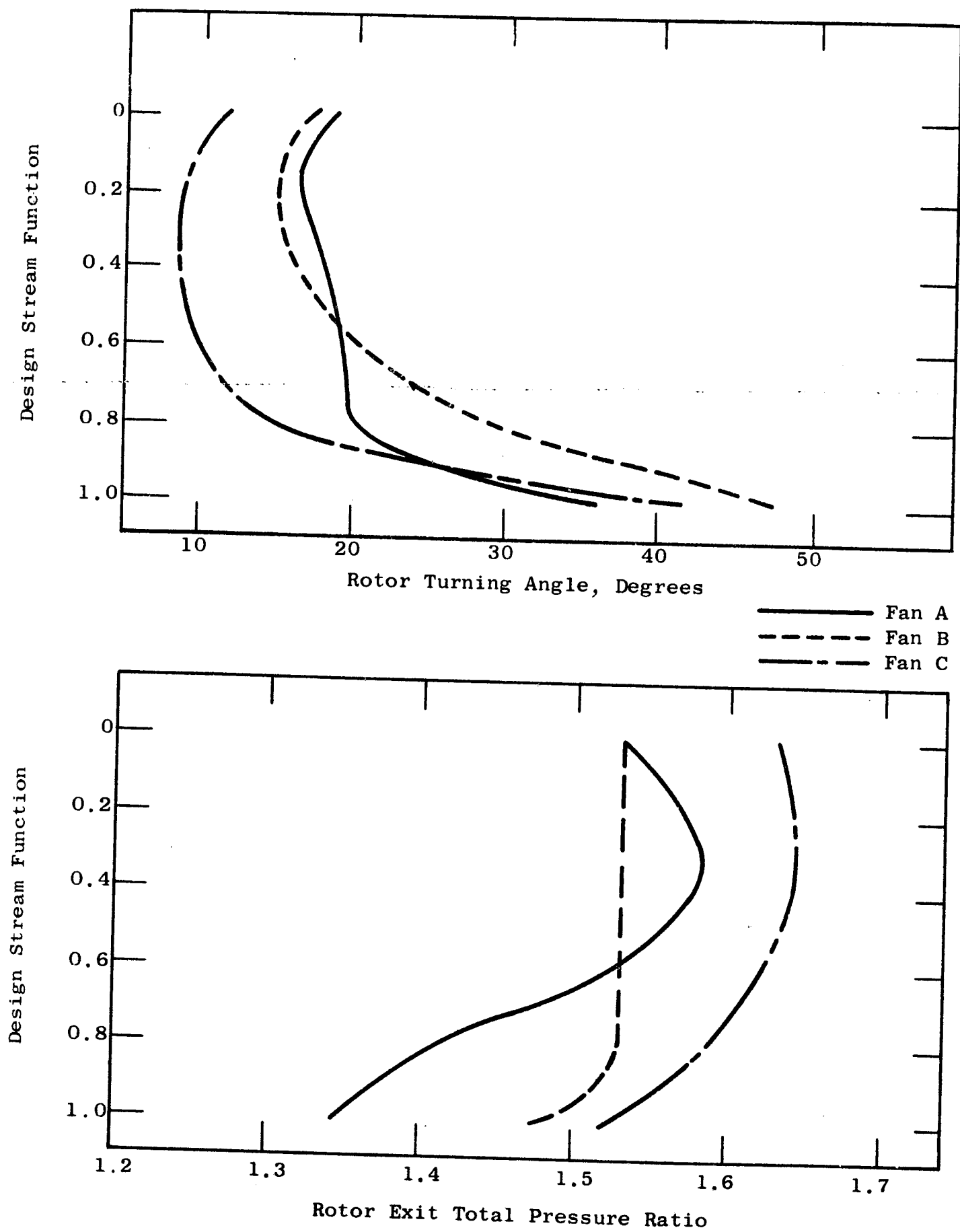


Figure 39. Radial Variation of Turning Angle and Total Pressure

Cycle and engine optimization studies were used to select a bypass total pressure ratio of 1.60 at discharge from the outer outlet guide vane for Fan C. Because of the increased blade speed of Fan C, the loading remained significantly less than that of Fan B (see Figure 38). The total pressure ratio at the hub of Fan C was selected to provide maximum supercharging to the core engine, consistent with established rotor loading level limits, and to limit outlet guide vane problems.

The level of efficiency (total pressure loss coefficient) for the rotor was selected consistent with the projected value for the fan overall efficiency. The radial distribution of rotor efficiency (total pressure loss coefficient as shown in Figure 40) was selected on the basis of past experience and correlation of experimental test results. The total pressure loss coefficients for the outlet guide vanes, also shown in Figure 40, were generally selected to be consistent with the NASA total pressure loss parameter, D-factor correlation.

4.3 BLADE PROFILE SELECTION

With no inlet guide vanes ahead of the rotor, tip relative Mach numbers are supersonic at the altitude-cruise design condition; the rotor tip relative Mach number is 1.20 for Fans A and B and 1.52 for Fan C. The profile shapes employed in the rotor design vary with blade height. In the tip region, where the relative Mach number is supersonic, the profiles were specifically tailored to minimize the Mach number effect on the suction surface, to prevent excessive shock losses and to minimize diffusion losses. In the hub region, where the relative Mach number is subsonic, profiles similar to a double circular arc were used.

The bypass duct outlet guide vanes for all fans and the core duct outlet guide vanes for Fan A operate at moderate conditions of inlet Mach number and diffusion factor. The profile selected for these vane rows was a modified NASA 65 series thickness distribution on a circular arc meanline. The core duct outlet guide vanes for Fan B and Fan C operate in a relatively high inlet-Mach-number environment, when considering the turning requirement and diffusion factor level. Accordingly, a tandem vane row was selected. The profiles were specifically shaped to minimize suction surface Mach numbers and, therefore, prevent shock losses and minimize diffusion losses.

4.3.1 Blade Design

The design of the rotor blade elements was performed along axisymmetric stream surfaces using the projection recommended in Reference 4. This

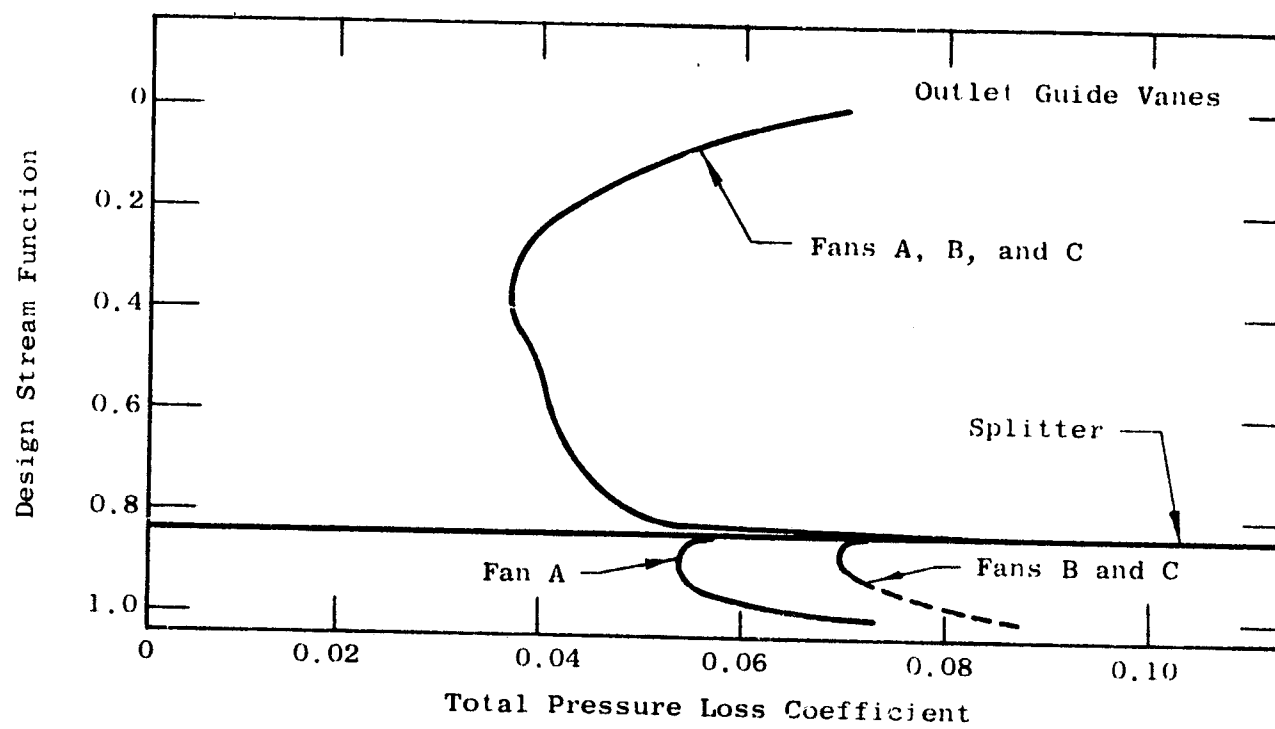
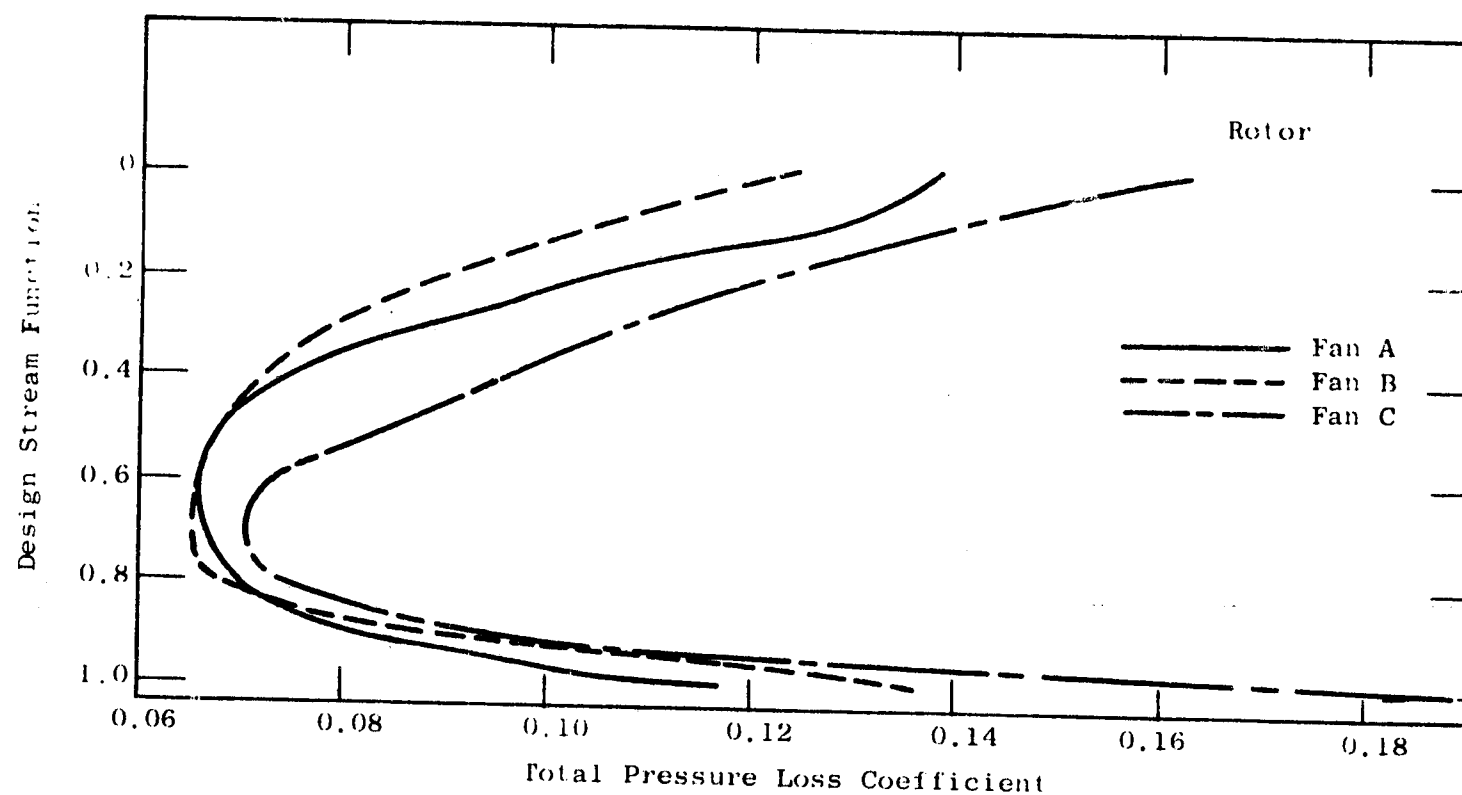


Figure 40. Radial Variation of Total Pressure Loss Coefficient

projection cuts the blades along axisymmetric surfaces but views the cut sections along the blade axis (for these fan designs, the blade axis is a radial line). The incidence and deviation angles are defined in this projection (identified as the cascade projection), and resulting blade angles are termed cascade angles.

The detailed blade layout procedure, employed in the design of the Quiet Engine fans generally parallels the procedures suggested in Reference 5. For supersonic relative Mach numbers, the maximum flow is established by the blade inlet region (i.e., that section of the suction surface upstream of the Mach wave which intersects the leading edge of the following blade, provided, of course, that the throat or minimum area does not restrict the flow). For a two-dimensional cascade of blades which have no camber or leading edge thickness, the flow would align itself with the suction surface. For an actual fan, the annulus convergence, the change in radius of a streamline passing through the blade, and the finite leading-edge thickness have to be taken into account. The flow field which would exist if there were no disturbances or blade forces was calculated and a free-flow streamline determined. The average angle of the suction surface in the inlet region was off-set from this free-flow streamline by a small amount, to account for the effects of leading edge thickness, bow wave losses, and blade boundary layer buildup. With the average angle of the suction surface in the inlet region determined in this manner, relatively little freedom remains for incidence angle selection. The resulting incidence angle values for these fans are shown in Figure 41.

The trailing-edge angle was established by the deviation angle which was obtained from Carter's Rule. The deviation angle was calculated from the camber of an equivalent two-dimensional cascade with an additive empirical adjustment, X . This adjustment is derived from experience with aerodynamic design and performance synthesis for this general type of rotor. The adjustment is shown in Figure 42 along with the calculated deviation angles.

The minimum passage area or throat must be sufficiently large to pass the flow including allowances for boundary layer and losses which occur ahead of the throat. For the supersonic-flow region, Reference 6 suggests the use of the smallest throat area consistent with permitting the design flow to pass. The percent throat margin, the percentage by which the ratio of the effective throat-area-to-capture-area exceeds the critical area ratio, is shown in Figure 43 for each design. The values employed for these designs are consistent with past experience. The bump in the margin curve for Fan C is an extra allowance for the part-span shroud, as it is not directly accounted for in the design procedure.

The meanline shape, which ties the blade profile together, is a balance between the deviation angle requirements, the average angle of the suction surface in the inlet region, the throat area, and the

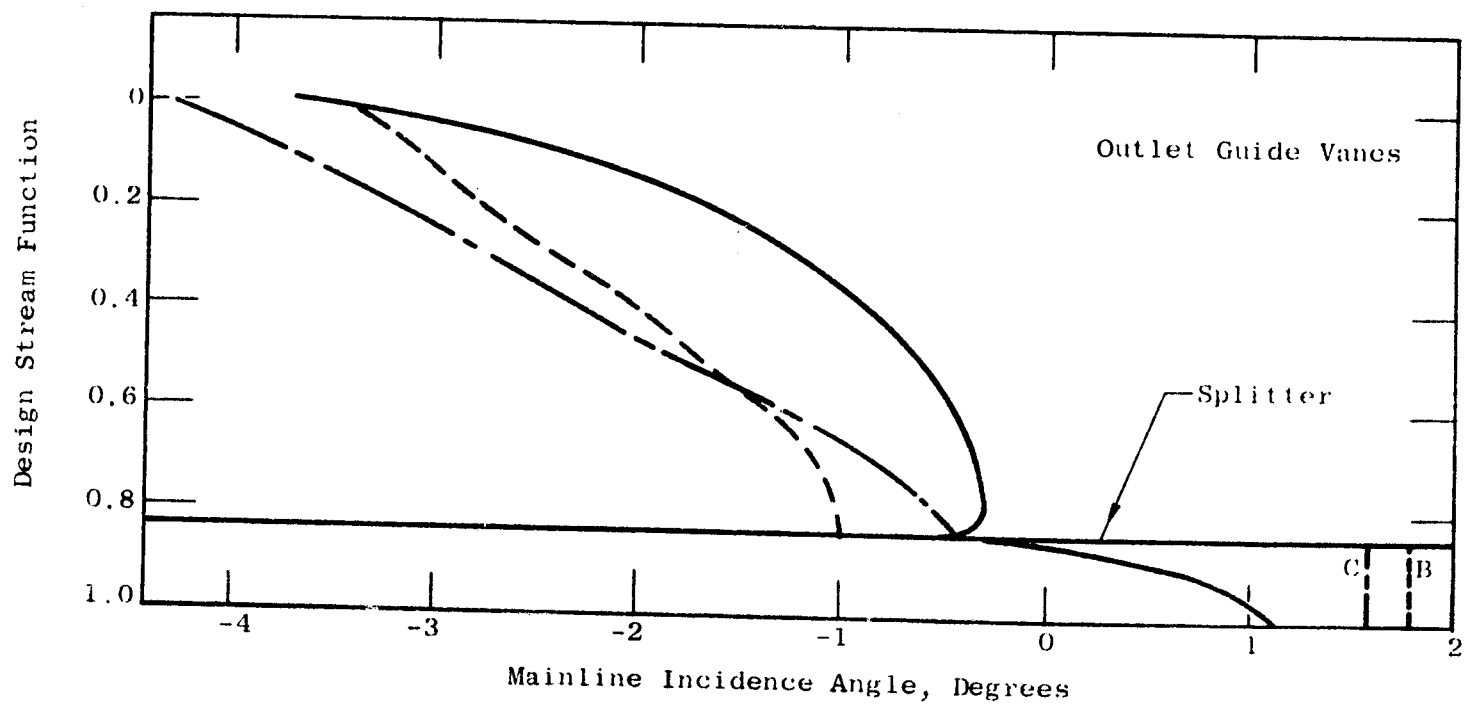
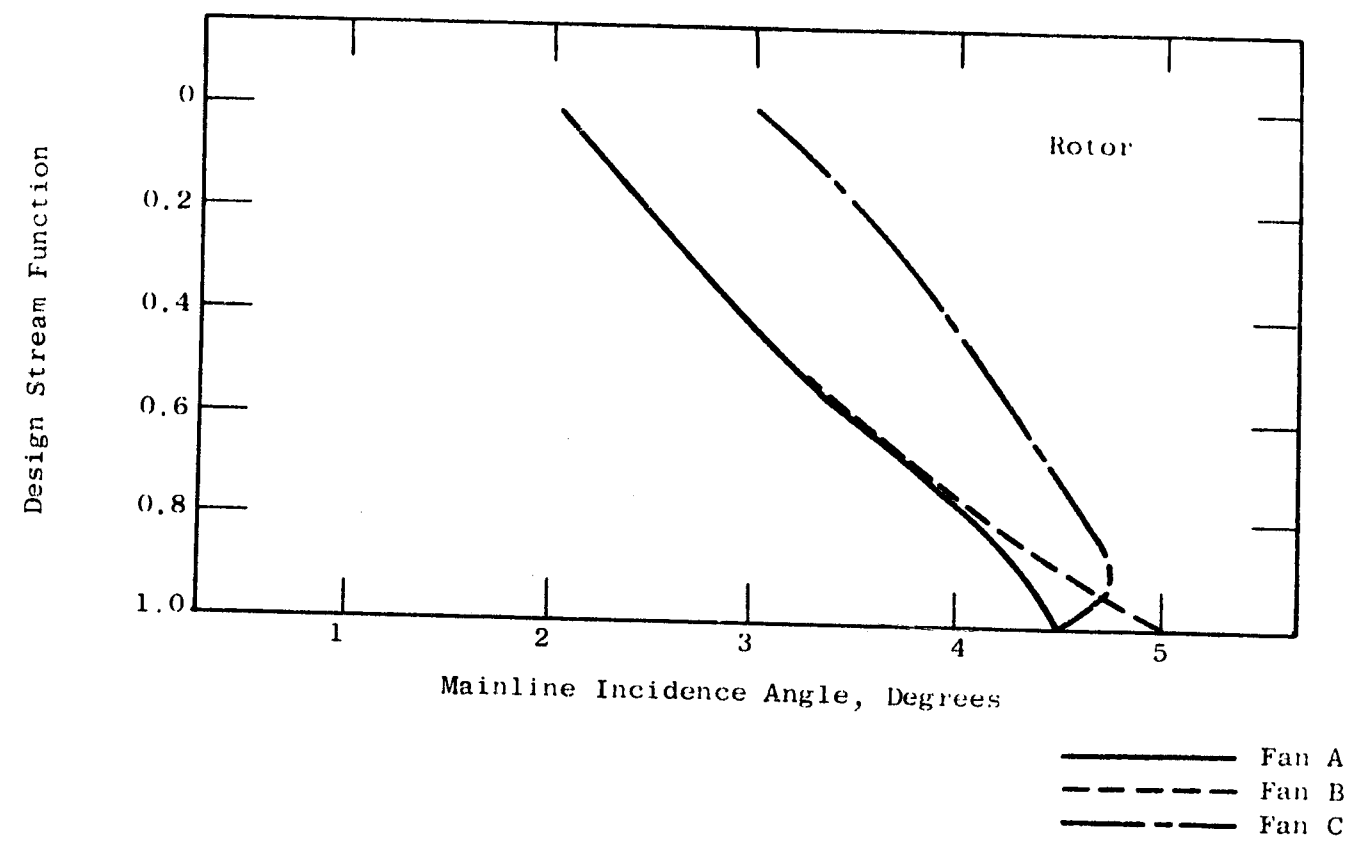


Figure 41. Radial Variation of Incidence Angle

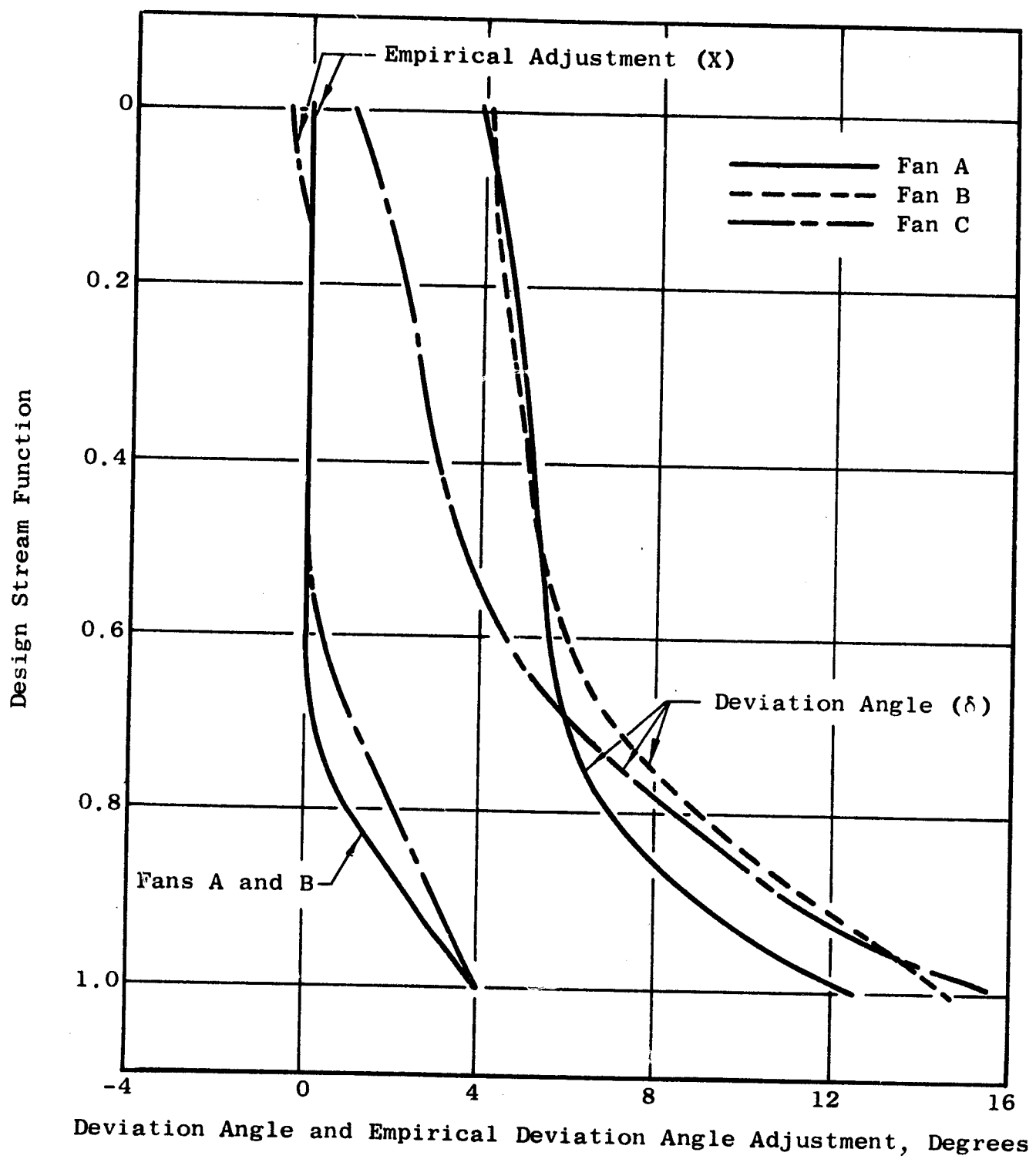


Figure 42. Radial Variation of Deviation Angle and Empirical Deviation Angle Adjustment

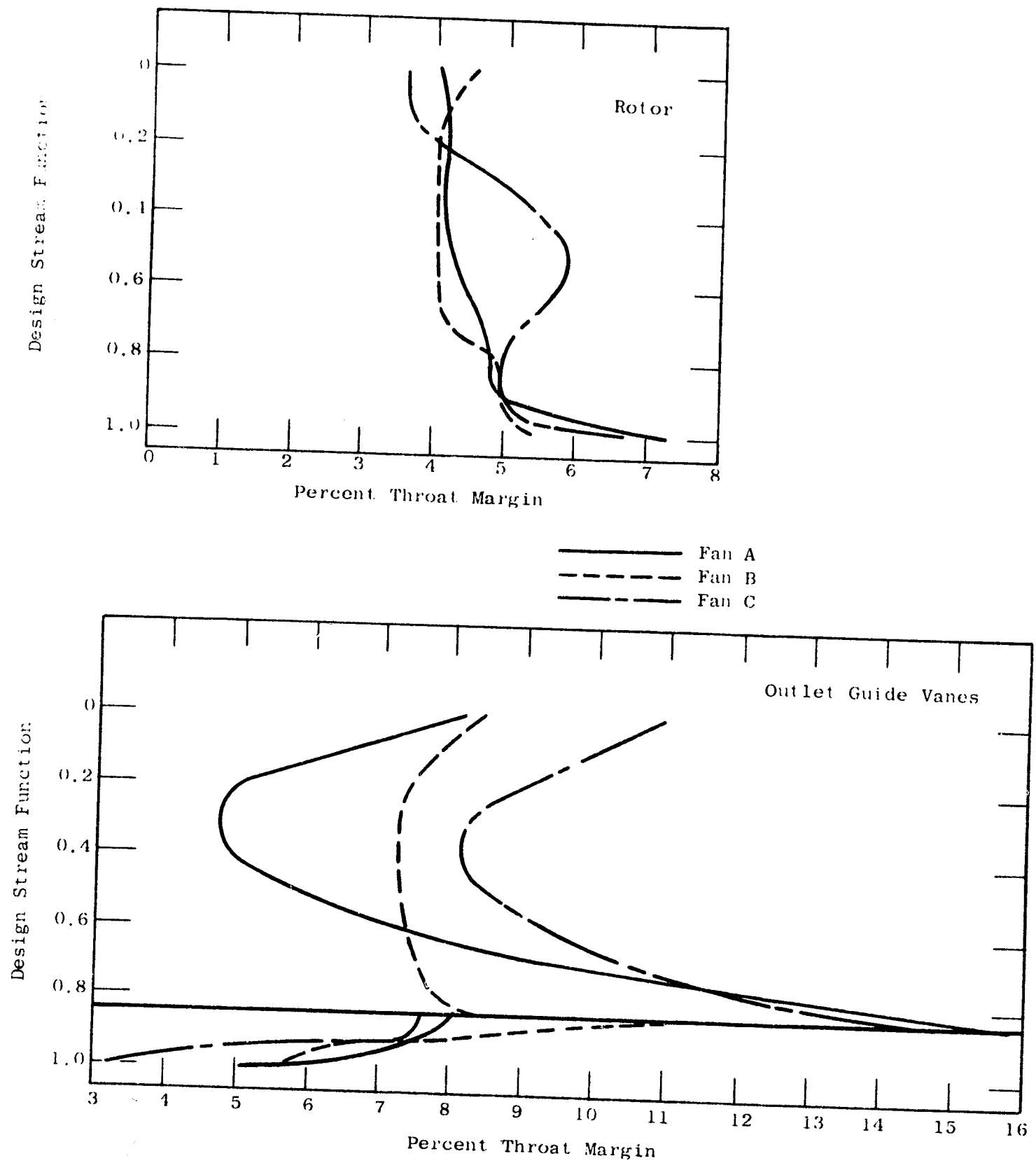


Figure 43. Radial Variation of Percent Throat Margin

desire to balance the accelerating curvatures on the suction surface to minimize the sum of the shock losses and diffusion losses. Figures 44 through 46 show scale layouts of three sections for each of the Fan A, Fan B, and Fan C blades which satisfy these design requirements.

4.4 VANE DESIGN

The bypass duct outlet guide vanes for all fans and the core duct outlet guide vanes for Fan A employ a modified NASA 65-series thickness distribution on a circular-arc meanline. The incidence angle for these vane rows was obtained from a correlation of the NASA low-speed cascade data. The deviation angle was obtained from Carter's Rule, as was described for the rotor blade, but no empirical adjustment was made. Upon completion of the incidence and deviation angle selections, a check was performed to insure that the vanes had sufficient throat area to pass the design flow. In the pitch region of the Fan A outer outlet guide vanes, the throat area was marginally small. Accordingly, in this region, the incidence angle was increased one degree to obtain additional margin. Mechanical analysis of the proposed Fan A core duct outlet guide vane revealed a natural frequency that coincided with blade passing frequency in the high-speed operating region. The thickness increase needed to avoid the resonance problem required an increase in the selected incidence angle. The final values of incidence angle are shown in Figure 41. Figure 43 shows the resulting percent throat margin.

The core duct outlet guide vanes for Fans B and C were selected as two-row tandem cascade configurations. Because of the increased inlet Mach number, aerodynamic loading, and turning angle levels of these vane rows, a specially designed profile was selected for the purpose of preventing any shock losses and minimizing the diffusion losses.

The tandem vanes employed herein consist of two distinct cascades with a relative orientation such that the trailing edge pressure surface of the forward vane and the leading edge suction surface of the aft vane form a smoothly converging passage. A layout of a typical section for the Fan B tandem inner outlet guide vane is shown in Figure 47. The chord length of the forward portion was selected as 40 percent of the chord length of the combined tandem vane. This selection was in part based on the reasoning presented in Reference 7, that a midchord slot location would probably be behind the separation point near the wall and for that reason would not be effective. Also, the over-all loading and camberline shape of the selected tandem cascade are such that the magnitude of surface loading is reduced and its peak level is moved aft relative to that of Reference 7. The calculated velocity distribution around the tandem cascade section depicted in Figure 47 is shown in Figure 48. The inlet Mach number of 0.63, for which the flux plot was run, is below the 0.8 level of inlet Mach for which the cascade is designed, because of prohibitive

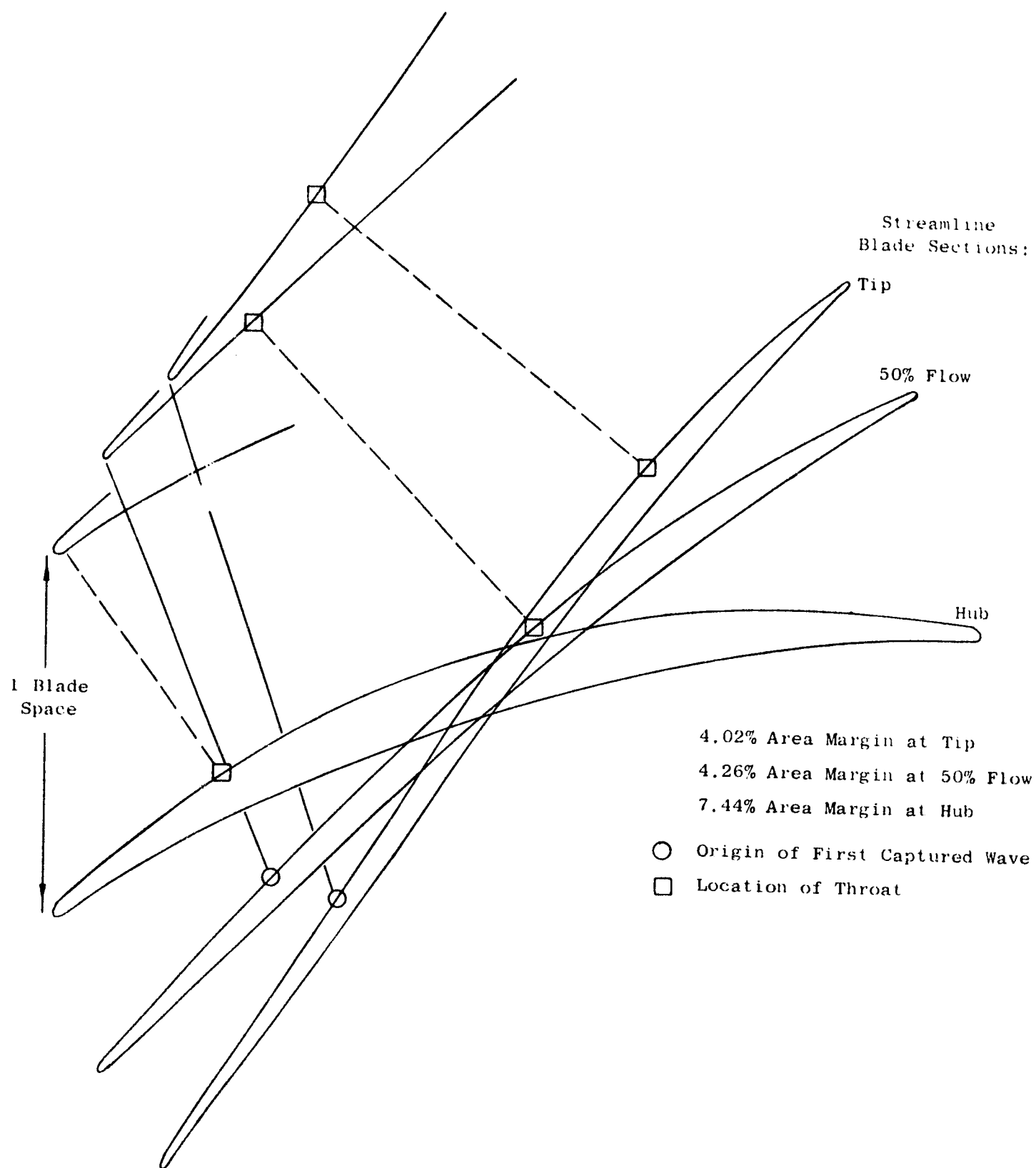


Figure 44. NASA Quiet Engine Fan A Streamline Blade Sections

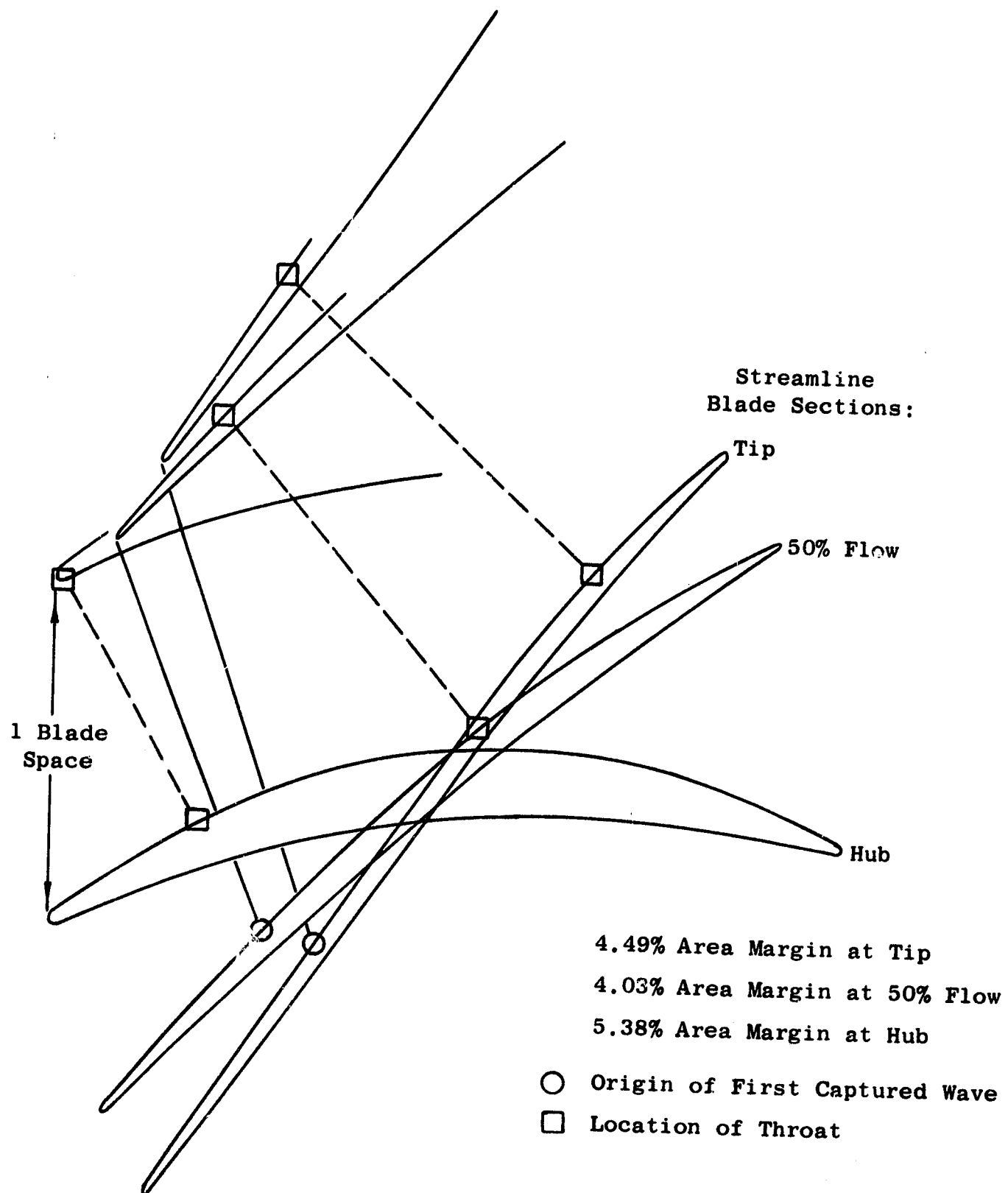


Figure 45. NASA Quiet Engine Fan B Streamline Blade Sections

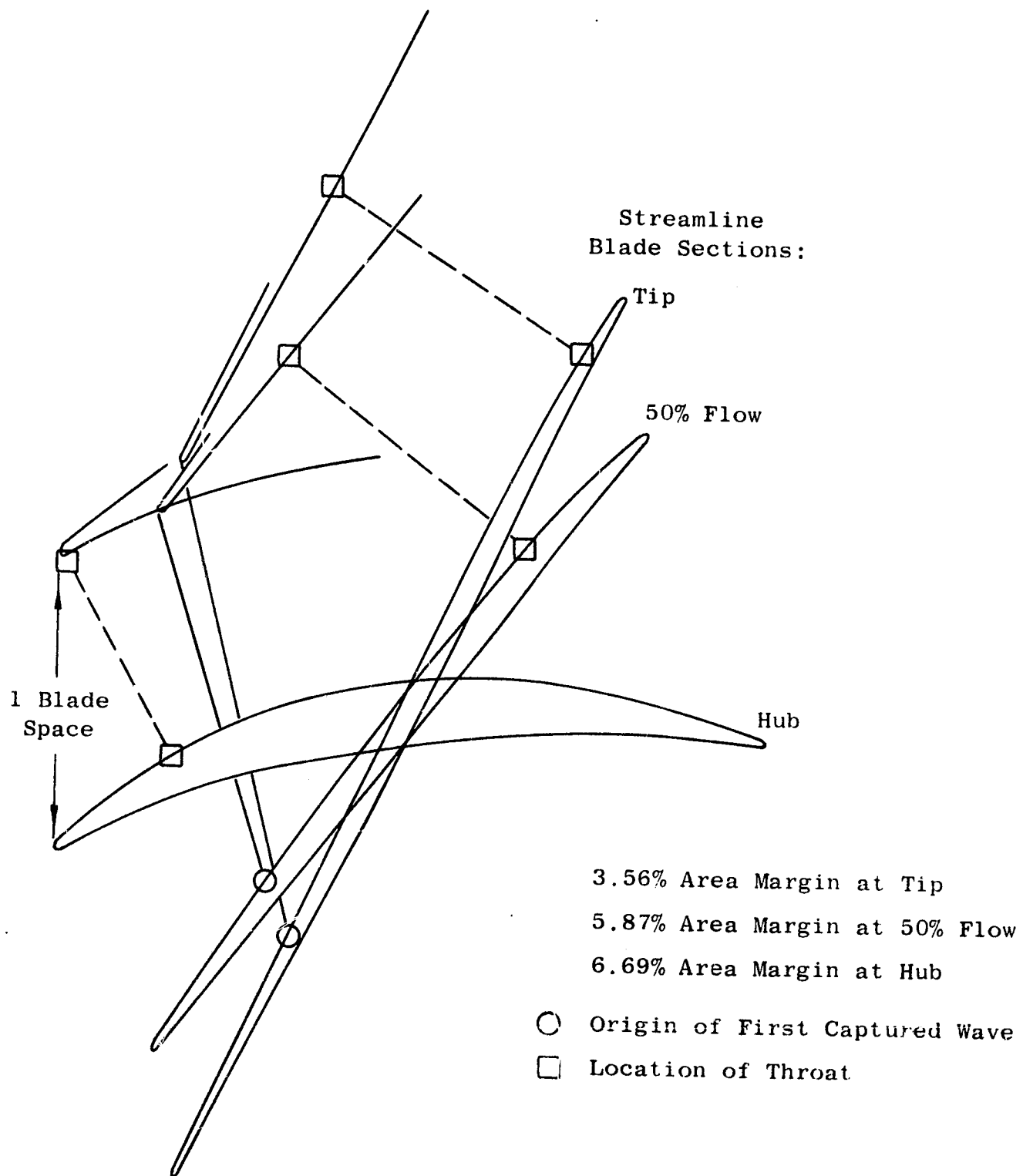


Figure 46. NASA Quiet Engine Fan C Streamline Blade Sections

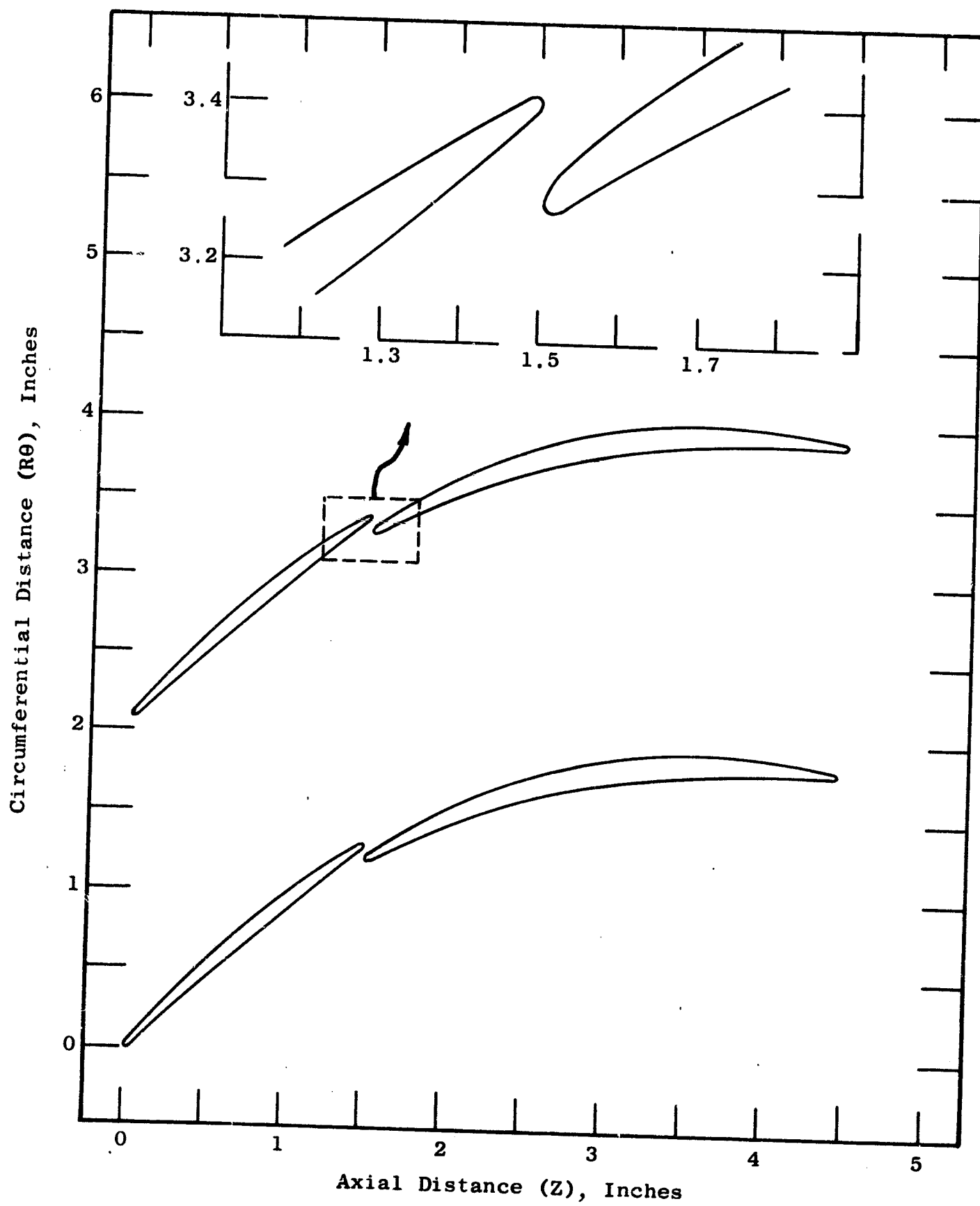


Figure 47. Typical Fan B Tandem Cascade

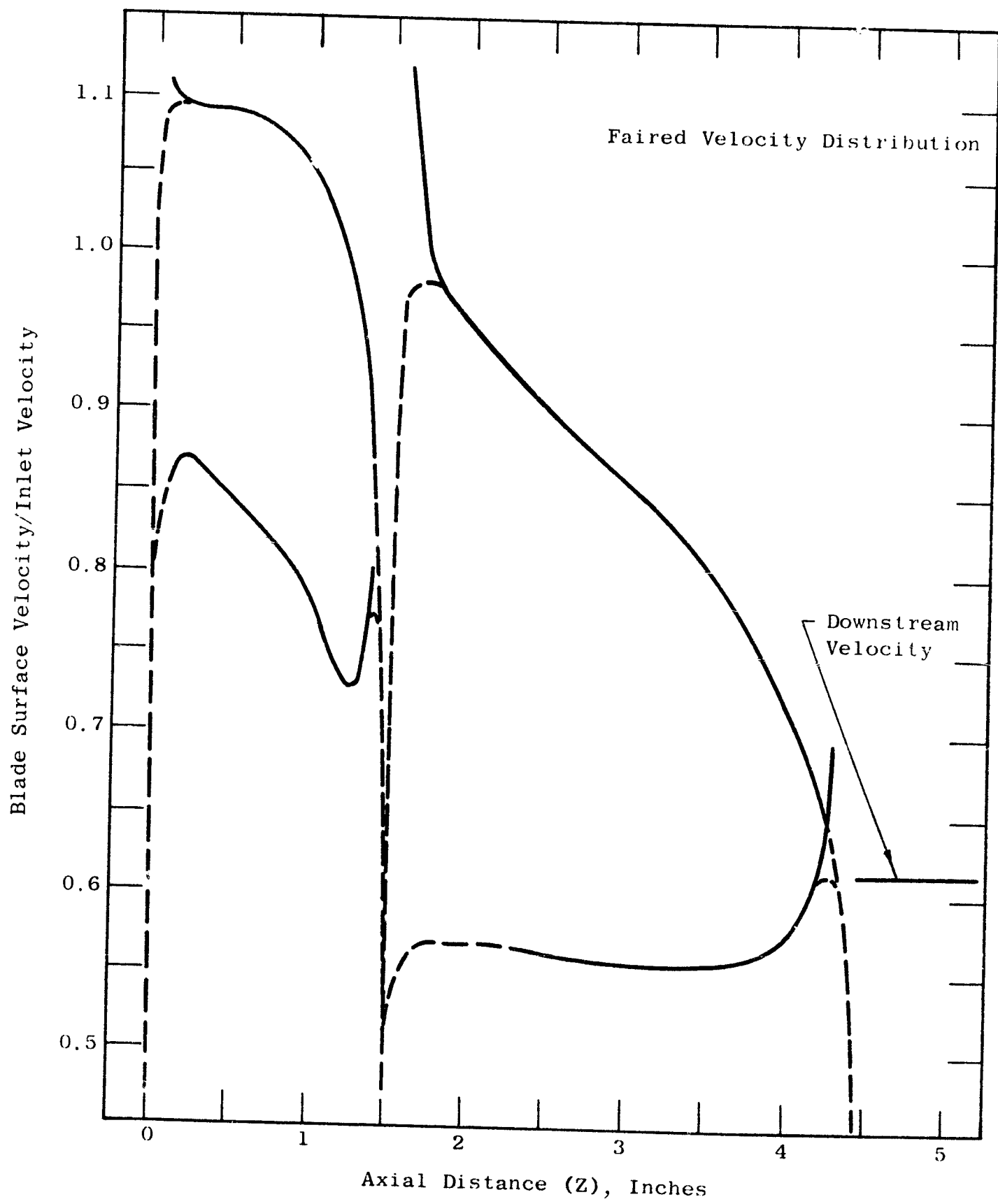


Figure 48. Typical Fan B Tandem Cascade Blade Surface Velocity Distribution

computational time and convergence problems with the computer program. The flow detail around the blade edges and in the slot region are not highly accurate because of the relatively course mesh spacing used in the analysis.

Figure 49 is a plot of the meanline angle distribution for the tandem cascade section. On this type of plot, a circular arc meanline appears as a line that is slightly concaved upward. The meanlines plotted show a near circular arc camberline (actually the forward vane is a slightly hooked trailing edge meanline) for both the forward and aft portions of the cascade, thus bearing close resemblance to a multiple-circular-arc type section.

In the design of the slot, no axial overlap between the forward and aft vane sections was permitted because of the mechanical simplicity it afforded. The circumferential displacement between the aft vane leading edge and the forward vane trailing edge was selected at 8 percent of the vane pitch. The displacement thickness of the boundary layer on the pressure side forward of the vane was estimated to be 0.01 inch, hence, the circumferential displacement of 0.14 inch (8 percent pitch) is considered large. A continuous acceleration was designed into the slot, but the area convergence was not made excessively large so as to avoid an unfavorable location of the leading edge stagnation point on the aft airfoil.

The incidence angle for the forward portion of the tandem cascade was based on the correlation of NASA low-speed cascade, the selected values are shown in Figure 41. This selection was subject to a check of throat margin which, from Figure 43, was assessed as being sufficient. The deviation angle of the aft portion of the tandem cascade was calculated from Carter's Rule. The sum of the chords of the forward and aft portions was used for the solidity in the computation. The cascade-projection camber of each forward vane portion was maintained constant radially, as was the difference between the trailing edge angle of the forward portion and the leading edge angle of the aft portion. The vane sections were stacked on the trailing and leading edges of the forward and aft sections, respectively, so that a constant slot width could be maintained in the radial direction. The mechanical design of the vanes was such that the stagger of both tandem cascade vanes could be independently adjusted as well as the circumferential positioning of the two vanes.

Some other pertinent design data which summarize the CAFD calculations and compare the different fan designs are shown in Figures 50 and 51. A pretest predicted-performance map for the three Fans A, B, and C are included in Figures 52 through 54. These maps present the estimated performance of the bypass portion of the fan versus the fan total flow. Currently, the cycle computations are based on a core duct map which is a scaled representation of the bypass map. Ultimately, a detailed performance map of the core duct performance will be generated from the test phase of the program.

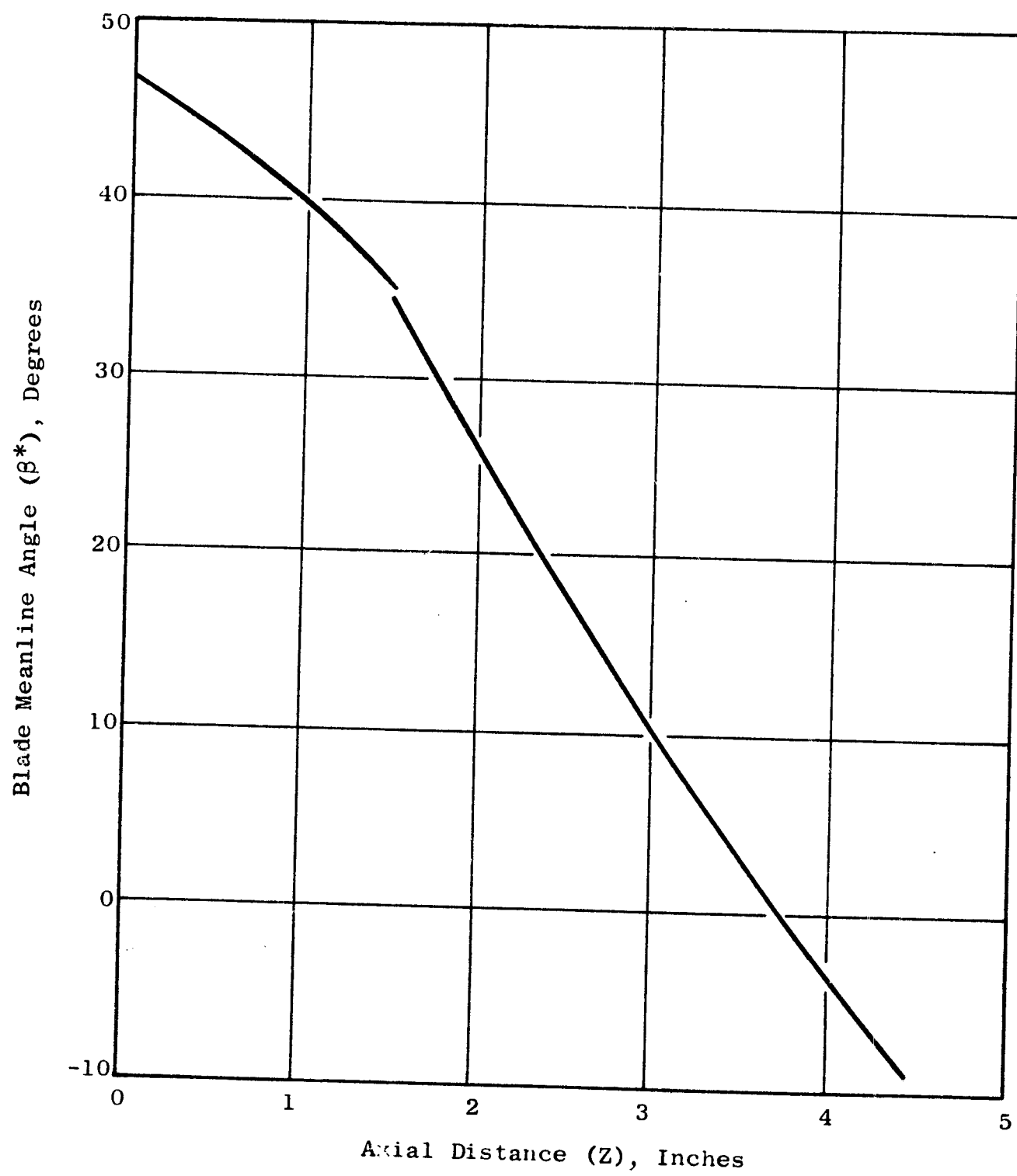


Figure 49. Typical Fan B Tandem Cascade Blade Meanline Angles

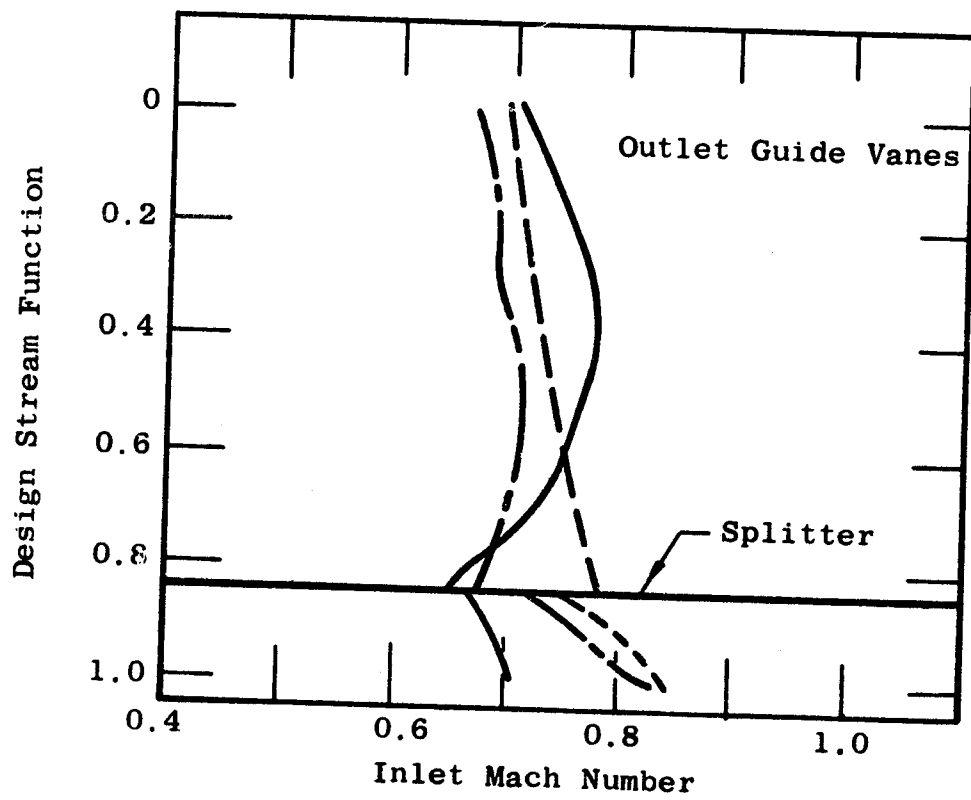
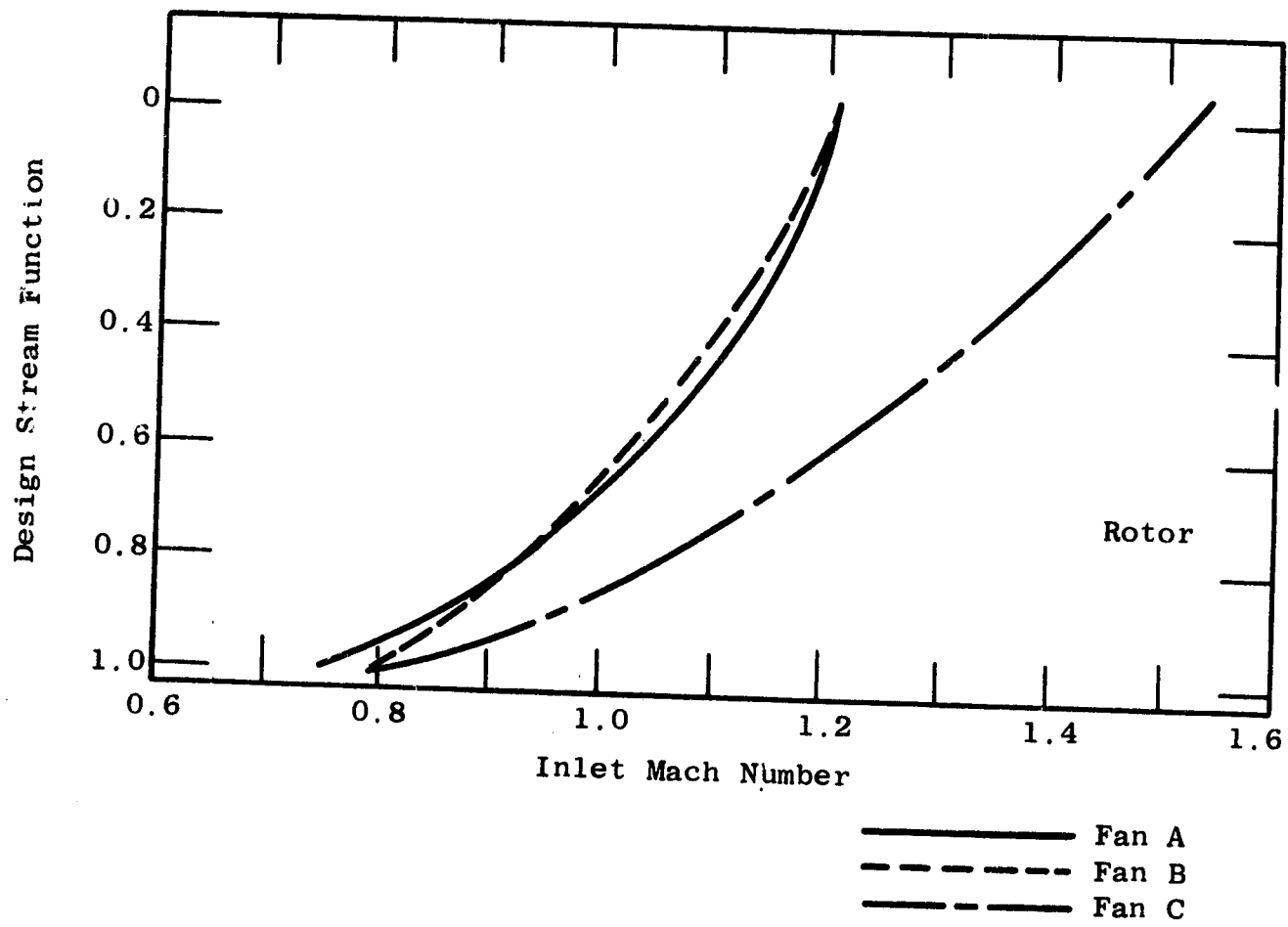


Figure 50. Radial Variation of Inlet Mach Number

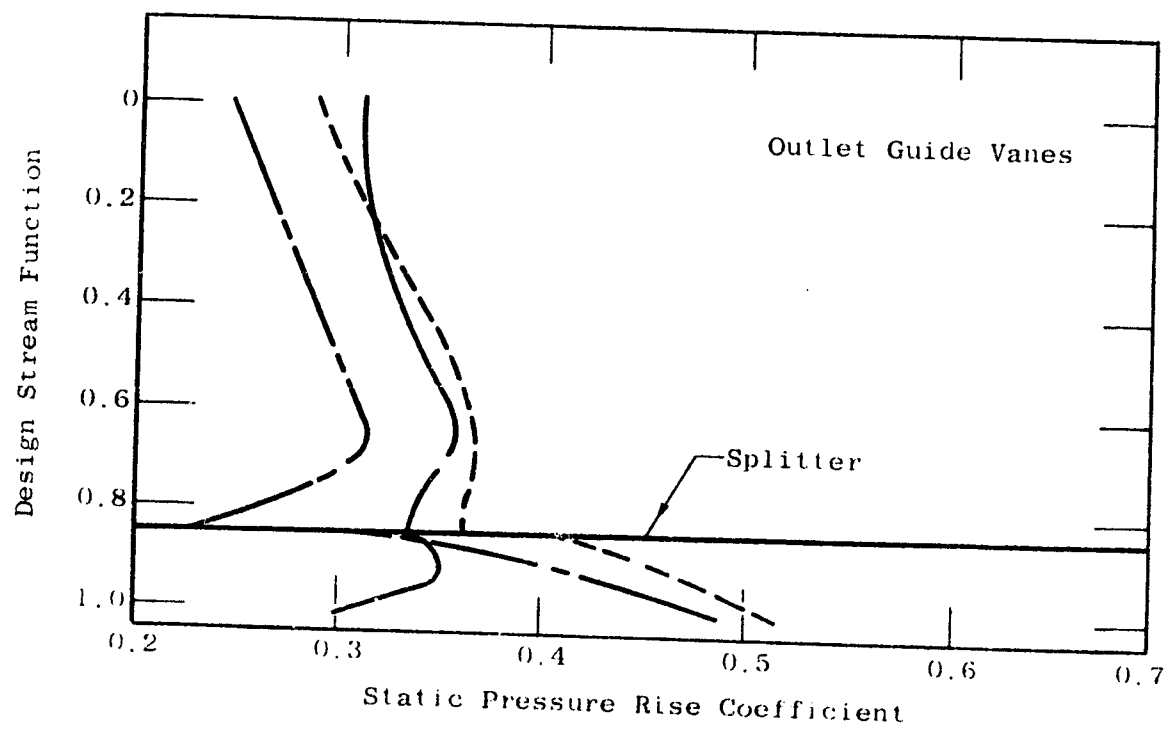
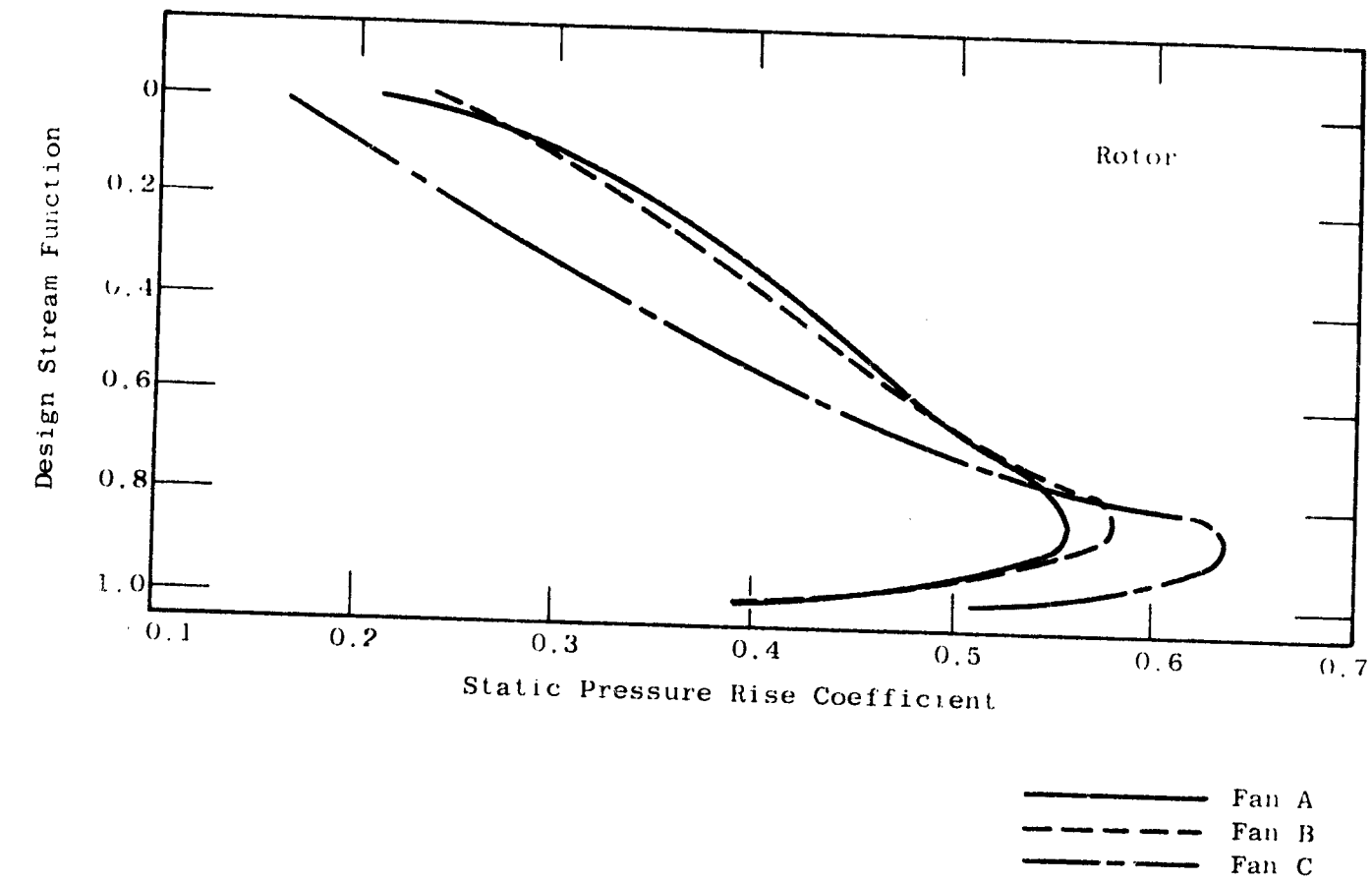


Figure 51. Radial Variation of Static Pressure Rise Coefficient

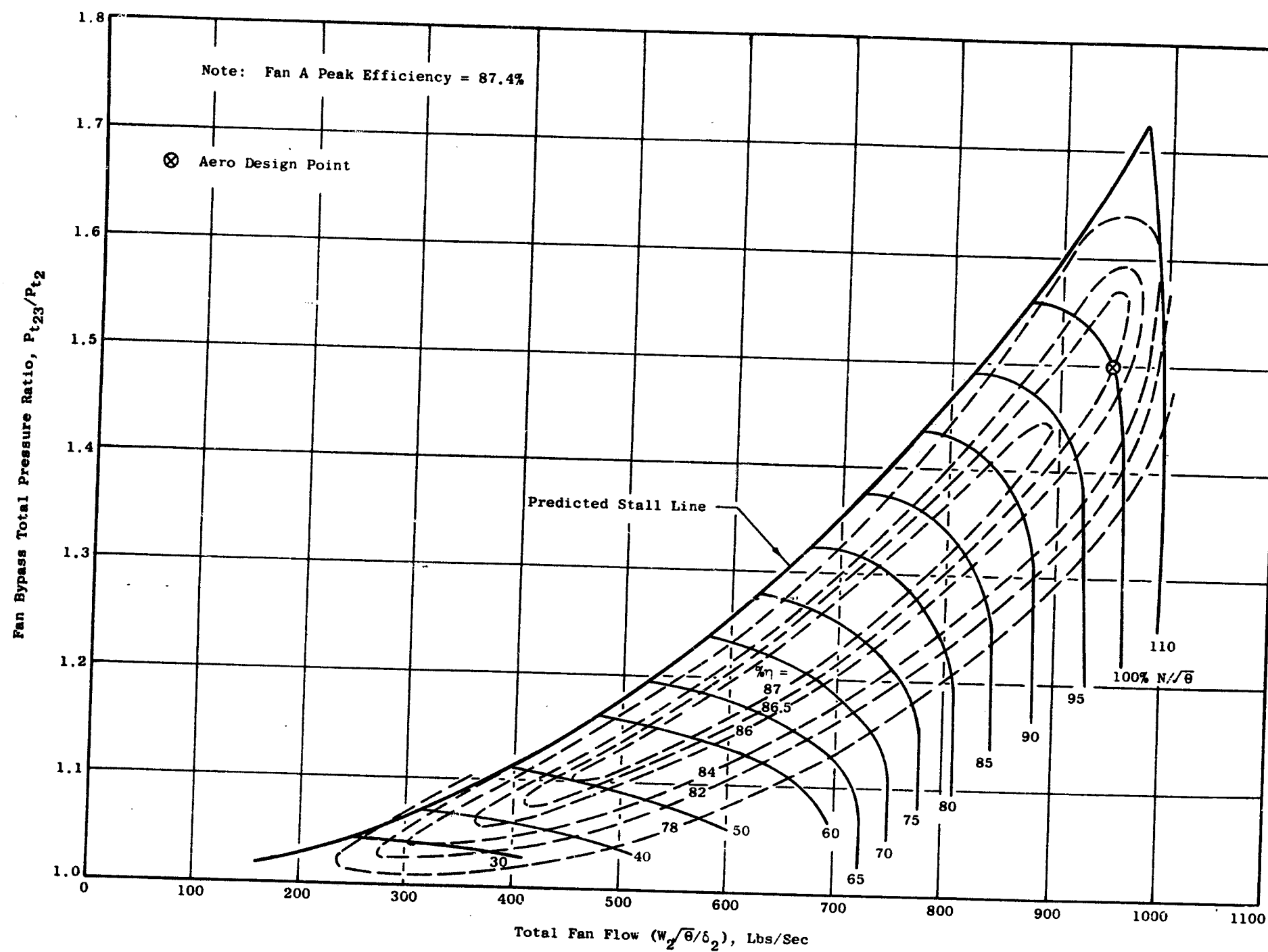


Figure 52. NASA Quiet Engine Program Pretest Predicted-Performance Map for Fan A

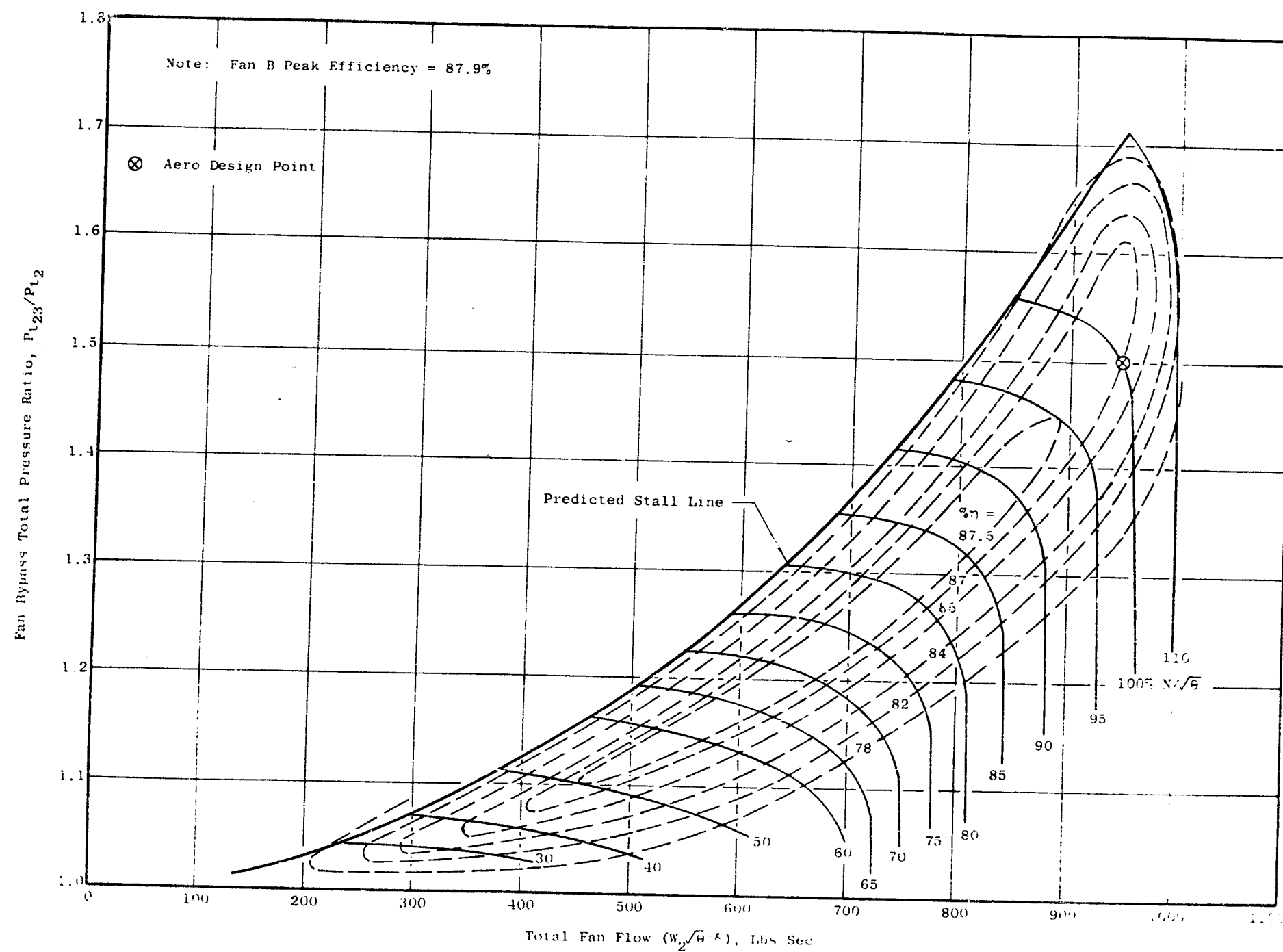


Figure 53. NASA Quiet Engine Program Pretest Predicted-Performance Map for Fan B

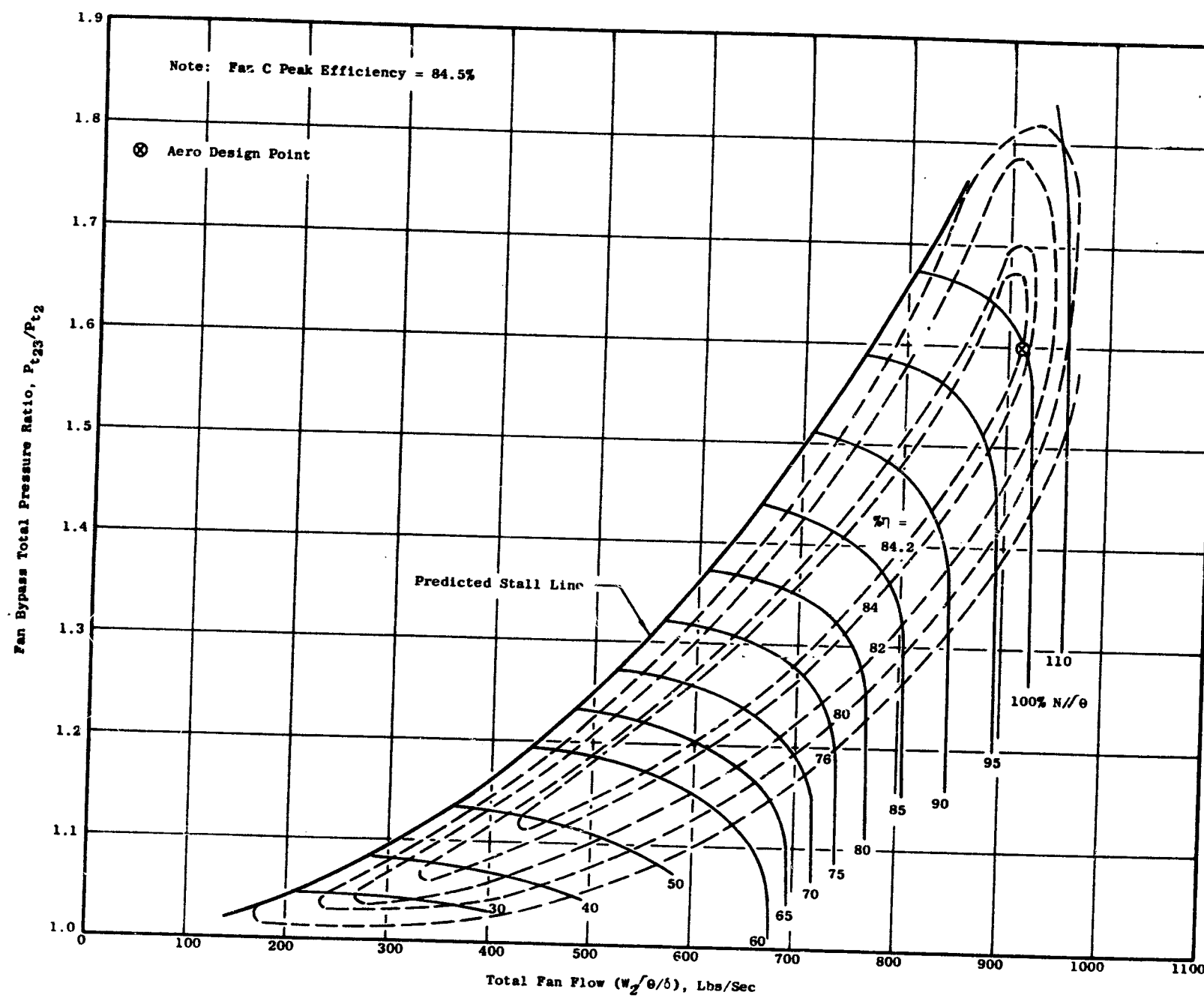


Figure 54. NASA Quiet Engine Program Pretest Predicted-Performance Map for Fan C

A detailed tabulation of the vector diagrams and other pertinent design information at the leading and trailing edge calculation stations is contained in Table X; also included is a tabulation of the geometry for each blade row.

A potential problem with core duct and/or rotor hub performance may be encountered during off-design operation, such as during a throttle chop. The relative differences in the inertia of the low and high pressure spools reduces the flow requirements of the core engine relative to the pumping capacity of the fan, and migration to a high bypass ratio results. This throttling of the hub portion of the fan may itself create a problem or it may stall the inner outlet guide vane. Stall of the inner outlet guide vane does not pose a serious problem in itself, provided it does not propagate into the fan or core compressor.

Table X. NASA Quiet Engine Blade and Vane Geometry

<u>Nomenclature</u>		
C	absolute air velocity	ft/sec
c	blade chord	inches
D	diffusion factor	---
F _a	axial force per unit height	lb/inch
F _t	tangential force per unit height	lb/inch
i	incidence angle	degree
M	Mach number	---
N _b	number of blades/vanes	---
P	pressure	lb/in. ²
q*	P _T -P _S	lb/in. ²
R	radius	inches
T	Temperature	°Rankine
t _e	blade edge thickness	inch
t _m	blade maximum thickness	inch
U	wheel speed	ft/sec
W	relative air velocity	ft/sec
X	empirical deviation angle adjustment	degree
β	relative flow angle with respect to axial	degree
λ	effective area coefficient	---
δ	deviation angle	degree
η _{ad}	adiabatic efficiency	---
ρ	density	lb/ft ³
α	absolute flow angle with respect to axial	degrees
ψ	stream function, % flow contained between a particular point and the outside diameter (OD)	---
\bar{w}	total pressure loss coefficient	---

<u>Subscripts</u>	
i	inlet
S	static
t	total
u	tangential direction
z	axial location

Table X. NASA Quiet Engine Blade and Vane Geometry (Continued)

Fan A - Rotor 1

Inlet

R_i	36.68	35.13	33.59	32.01	30.38	28.66	25.86	22.64	20.67	19.57	18.38	17.06
% Imm	0.0	7.9	15.7	23.8	32.1	40.9	55.2	71.6	81.6	87.2	93.3	100.0
P_t/P_{t_i}	1.0000	1.0000	1.9000	1.0000	1.0000	1.0000	1.0000	1.0000	1.0000	1.0000	1.0000	1.0000
P_s/P_{t_i}	0.8185	0.7887	0.7678	0.7555	0.7479	0.7445	0.7468	0.7558	0.7674	0.7777	0.7901	0.8073
T_t/T_{t_i}	1.0000	1.0000	1.0000	1.0000	1.0000	1.0000	1.0000	1.0000	1.0000	1.0000	1.0000	1.0000
ρ_s/ρ_{t_i}	0.8667	0.8440	0.8280	0.8185	0.8127	0.8100	0.8118	0.8187	0.8277	0.8356	0.8451	0.8582
η_{ad}												
U	1160.0	1111.1	1062.4	1012.6	960.9	906.5	817.7	716.0	653.6	619.0	581.3	539.6
W_u	1160.0	1111.1	1062.4	1012.6	960.9	906.5	817.7	716.0	653.6	619.0	581.3	539.6
C_z	585.5	637.2	672.8	692.6	703.4	706.3	696.8	672.9	645.9	624.0	598.6	565.7
C	588.7	639.3	673.1	692.7	704.5	709.8	706.2	692.2	673.8	657.2	636.9	608.1
W	1300.8	1281.9	1257.6	1226.8	1191.5	1151.3	1080.5	995.9	938.7	902.8	862.3	812.9
α	0.	0.	0.	0.	0.	0.	0.	0.	0.	0.	0.	0.
M_{rel}	1.199	1.188	1.170	1.144	1.112	1.076	1.009	0.928	0.873	0.838	0.799	0.751
M_{abs}	0.543	0.592	0.626	0.646	0.658	0.663	0.660	0.645	0.627	0.610	0.590	0.562
β_1	63.26	60.17	57.66	55.63	53.79	52.08	49.57	46.78	45.34	44.77	44.16	43.64
λ	0.980	0.980	0.980	0.980	0.980	0.980	0.980	0.980	0.980	0.980	0.980	0.980
P_{si}	0.	0.1000	0.2000	0.3000	0.4000	0.5000	0.65000	0.8000	0.8800	0.9200	0.9600	1.0000

Blade

\bar{R}	36.138	34.770	33.376	31.944	30.451	28.873	26.272	23.235	21.336	20.305	19.204	18.020
\bar{w}	0.138	0.128	0.104	0.088	0.074	0.068	0.066	0.069	0.077	0.085	0.098	0.117
D	0.350	0.403	0.422	0.437	0.447	0.457	0.472	0.488	0.483	0.459	0.425	0.368
$\Delta P_s/q^*$	0.215	0.298	0.349	0.389	0.424	0.456	0.498	0.554	0.554	0.523	0.476	0.390
$N_b F_a$	1137	1110	1075	1019	944	851	688	512	427	383	337	286
$N_b F_t$	998	1015	1024	1019	987	938	823	662	599	577	560	544

* See Nomenclature

Table X. NASA Quiet Engine Blade and Vane Geometry (Continued)

Fan A - Rotor 1

Discharge

R_{disc}	35.600	34.410	33.163	31.872	30.521	29.085	26.688	23.830	22.006	21.036	20.028	18.980
% Imm	0.0	7.2	14.7	22.4	30.6	39.2	53.6	70.8	81.8	87.6	93.7	100.0
P_t/P_{t_i}	1.5297	1.5530	1.5730	1.5820	1.5750	1.5550	1.5000	1.4200	1.3830	1.3680	1.3560	1.3440
P_s/P_{t_i}	1.0692	1.1141	1.1243	1.1243	1.1186	1.1085	1.0865	1.0679	1.0408	1.0155	0.9867	0.9500
T_t/T_{t_i}	1.1577	1.1600	1.1585	1.1566	1.1518	1.1460	1.1329	1.1145	1.1065	1.1034	1.1012	1.0993
ρ_s/ρ_{t_i}	1.0230	1.0560	1.0682	1.0718	1.0709	1.0655	1.0517	1.0394	1.0203	1.0022	0.9812	0.9542
η_{ad}	0.819	0.837	0.872	0.894	0.913	0.921	0.924	0.920	0.912	0.902	0.898	0.888
U	1125.9	1088.3	1048.9	1008.0	965.3	919.9	844.1	753.7	696.0	665.3	633.4	600.3
W_u	689.4	630.0	577.9	524.0	475.5	425.4	353.6	280.1	219.4	181.2	135.4	84.8
C_z	715.0	666.2	662.1	660.1	654.7	643.0	615.2	558.4	555.2	569.4	587.5	614.4
C	837.8	809.0	812.7	818.6	817.7	811.4	788.3	736.9	733.5	749.1	772.0	804.1
W	993.3	917.3	879.1	842.9	809.1	771.2	711.3	630.2	599.1	599.7	605.2	622.9
α	31.41	34.52	35.42	36.25	36.81	37.56	38.57	40.30	40.65	40.37	40.29	40.00
M_{rel}	0.870	0.800	0.768	0.737	0.709	0.677	0.627	0.557	0.531	0.534	0.541	0.559
M_{abs}	0.734	0.706	0.710	0.716	0.717	0.713	0.695	0.651	0.650	0.667	0.690	0.722
β_2	43.96	43.40	41.12	38.45	35.99	33.49	29.89	26.64	21.57	17.66	12.98	7.85
λ	0.9600	0.9600	0.9600	0.9600	0.9600	0.9600	0.9600	0.9600	0.9600	0.9600	0.9600	0.9600

Table X. NASA Quiet Engine Blade and Vane Geometry (Continued)

Blade Type Arbitrary Airfoil

Blade Row Fan Rotor - Fan A

Aspect Ratio 2.32

\bar{R}	36.070	34.720	33.320	31.860	30.310	28.680	26.050	23.050	21.220	20.240	19.200	18.100
-----------	--------	--------	--------	--------	--------	--------	--------	--------	--------	--------	--------	--------

Cylindrical Sections

Camber	16.05	15.37	16.62	18.01	19.49	20.93	22.24	26.15	33.25	38.47	44.81	52.34
Stagger	53.08	50.77	47.88	45.23	42.75	40.32	36.52	30.99	26.31	23.52	20.45	16.77
Chord	8.222	8.138	8.047	7.959	7.858	7.763	7.601	7.417	7.308	7.239	7.175	7.107
tm/c	0.0279	0.0285	0.0293	0.0302	0.0315	0.0332	0.0374	0.0445	0.0510	0.0550	0.0595	0.0645
te/c	0.0050	0.0053	0.0057	0.0059	0.0064	0.0069	0.0077	0.0088	0.0097	0.0108	0.0109	0.0121
Solidity	1.451	1.492	1.537	1.590	1.650	1.723	1.878	2.049	2.193	2.277	2.379	2.500

ζ - Plane

i	2.02	2.25	2.47	2.71	2.96	3.22	3.64	4.09	4.31	4.37	4.43	4.50
δ	3.86	4.29	4.58	4.89	5.11	5.34	5.72	6.92	8.59	9.61	10.81	12.39
ζ_1												
ζ_2												
Camber												
Stagger												
X	0.	0.	0.	0.	0.	0.	0.	1.00	2.14	2.73	3.34	4.00

Table X. NASA Quiet Engine Blade and Vane Geometry (Continued)

Fan A - Bypass OGV

Inlet

R _i	35.600	34.419	33.228	32.015	30.760	29.433	27.232	24.607	23.614			
% Imm	0.0	9.9	19.8	29.9	40.4	51.5	89.8	91.7	100.0			
P _t /P _{t_i}	1.5297	1.5530	1.5730	1.5820	1.5750	1.5550	1.5000	1.4200	1.3975			
P _s /P _{t_i}	1.0971	1.0884	1.0783	1.0688	1.0607	1.0545	1.0494	1.0541	1.0523			
T _t /T _{t_i}	1.1577	1.1600	1.1585	1.1566	1.1518	1.1460	1.1329	1.1145	1.1096			
ρ _s /ρ _{t_i}	1.0420	1.0385	1.0368	1.0337	1.0311	1.0282	1.0259	1.0298	1.0284			
η _{ad}												
U												
C _u	436.5	458.1	470.0	481.9	486.1	488.6	480.7	458.6	457.4			
C _z	680.6	698.9	719.3	729.2	728.0	714.5	672.8	595.8	573.7			
C	808.6	835.6	859.3	874.1	875.6	866.1	827.7	752.9	733.8			
W												
α	32.68	33.25	33.16	33.46	33.73	34.37	35.55	37.59	38.57			
M _{rel}												
M _{abs}	0.706	0.731	0.755	0.770	0.773	0.766	0.733	0.667	0.650			
β ₁												
λ	0.9600	0.9600	0.9600	0.9600	0.9600	0.9600	0.9600	0.9600	0.9600			
P _{si}	0.	0.1000	0.2000	0.3000	0.4000	0.5000	0.65000	0.8000	0.8485			

Blade

\bar{R}	35.600	34.420	33.239	32.042	30.805	29.497	27.323	24.733	23.764			
\bar{w}	0.0700	0.0520	0.0424	0.0377	0.0369	0.0397	0.0424	0.0492	0.0800			
D	0.442	0.428	0.419	0.416	0.416	0.419	0.421	0.400	0.412			
ΔP _s /q*	0.309	0.308	0.312	0.319	0.329	0.339	0.357	0.337	0.333			
N _b F _a	305	348	366	377	371	356	317	256	226			
N _b F _t	1142	1201	1228	1230	1187	1116	951	736	674			

Table X. NASA Quiet Engine Blade and Vane Geometry (Continued)

Fan A - Bypass OGV

	Discharge												
R _{disc}	35.600	34.420	33.250	32.069	30.850	29.562	27.415	24.859	23.914				
% Imm	0.0	10.1	20.1	30.2	40.6	51.7	70.0	91.9	100.0				
P _t /P _{t_i}	1.4994	1.5288	1.5520	1.5626	1.5560	1.5351	1.4809	1.4020	1.3699				
P _s /P _{t_i}	1.2308	1.2315	1.2327	1.2325	1.2299	1.2244	1.2101	1.1773	1.1672				
T _t /T _{t_i}	1.1577	1.1600	1.1585	1.1566	1.1518	1.1460	1.1329	1.1145	1.1096				
ρ _s /ρ _{t_i}	1.1248	1.1293	1.1364	1.1404	1.1420	1.1397	1.1316	1.1104	1.1011				
η _{ad}	0.778	0.806	0.844	0.869	0.887	0.893	0.894	0.885	0.858				
U													
C _u	0.	0.	0.	0.	0.	0.	0.	0.	0.				
C _z	629.1	658.2	678.2	687.4	682.8	668.0	628.3	580.2	556.1				
C	629.1	658.2	678.2	687.5	683.1	668.5	629.2	581.5	556.1				
W													
α	0.	0.	0.	0.	0.	0.	0.	0.	0.				
M	0.539	0.565	0.583	0.592	0.590	0.578	0.545	0.506	0.484				
M _{abs}													
β ₂													
λ	0.9500	0.9500	0.9500	0.9500	0.9500	0.9500	0.9500	0.9500	0.9500				

Table X. NASA Quiet Engine Blade and Vane Geometry (Continued)

Blade Type 65-Series Airfoil

Blade Row Bypass OGV - Fan A

Aspect Ratio 3.881

\bar{R}	35.600	34.120	32.639	31.159	29.679	28.198	26.718	25.238	23.757			
-----------	--------	--------	--------	--------	--------	--------	--------	--------	--------	--	--	--

Cylindrical Sections

Camber	46.032	44.422	43.363	43.053	43.240	43.826	44.514	45.625	47.701			
Stagger	13.360	13.104	12.987	13.075	13.292	13.650	14.004	14.491	15.480			
Chord	3.0500	3.0500	3.0500	3.0500	3.0500	3.0500	3.0500	3.0500	3.0500			
tm/c	0.0700	0.0671	0.0637	0.0604	0.0569	0.0536	0.0479	0.0419	0.0400			
te/c	.01	.01	.01	.01	.01	.01	.01	.01	.01			
Solidity	1.2272	1.2804	1.3385	1.4021	1.4720	1.5493	1.6352	1.17311	1.8389			

ζ - Plane

i	-3.70	-2.30	-1.60	-1.20	-0.85	-0.60	-0.40	-0.30	-1.00			
δ	9.66	9.22	8.81	8.59	8.37	8.25	8.13	8.13	8.37			
ζ_1												
ζ_2												
Camber												
Stagger												
X												

Table X. NASA Quiet Engine Blade and Vane Geometry (Continued)

Fan A - Inner OGV

Inlet

96

R_i	22.415	21.689	20.735	19.729	18.650							
% Imm	0.0	19.3	44.6	71.3	100.0							
P_t/P_{t_i}	1.3975	1.3830	1.3680	1.3560	1.3440							
P_s/P_{t_i}	1.0358	0.0176	0.9954	0.9764	0.9650							
T_t/T_{t_i}	1.1096	1.1065	1.1034	1.1012	1.0993							
ρ_s/ρ_{t_i}												
η_{ad}												
U												
C_u	481.9	483.5	491.2	505.6	524.7							
C_z	573.8	582.8	592.3	595.4	582.7							
C	753.1	760.7	772.8	784.0	786.6							
W												
α	40.03	39.68	39.67	40.34	42.00							
M_{rel}												
M_{abs}	0.668	0.677	0.690	0.701	0.705							
β_1												
λ	0.9600	0.9600	0.9600	0.9600	0.9600							
P_{si}	0.8485	0.8800	0.9200	0.9600	1.0000							

Blade

\bar{R}	22.20	21.49	20.54	19.56	18.52							
\bar{W}	0.0589	0.0539	0.0546	0.0577	0.0730							
D	0.423	0.423	0.418	0.398	0.383							
$\Delta P_s/q^*$	0.333	0.348	0.351	0.328	0.298							
$N_b F_a$	238	231	226	223	228							
$N_b F_t$	675	654	635	625	608							

Table X. NASA Quiet Engine Blade and Vane Geometry (Continued)

Fan A - Inner OGV						Discharge							
R _{disc}	21.990	21.284	20.351	19.380	18.380								
% Imm	0.0	19.6	45.4	72.3	100.0								
P _t /P _{t_i}	1.3762	1.3633	1.3476	1.3341	1.3163								
P _s /P _{t_i}	1.1561	1.1447	1.1262	1.1008	1.0777								
T _t /T _{t_i}	1.1096	1.1065	1.1034	1.1012	1.0993								
ρ _s /ρ _{t_i}													
η _{ad}	.871	.870	.861	.848	.823								
U													
Cu	0.	0.	0.	0.	0.								
C _z	567.3	567.2	575.0	595.0	613.3								
C	579.5	579.6	586.4	605.7	616.8								
W													
α	0.	0.	0.	0.	0.								
M	0.505	0.506	0.513	0.531	0.542								
M _{abs}													
β ₂													
λ	0.9500	0.9500	0.9500	0.9500	0.9500								

Table X. NASA Quiet Engine Blade and Vane Geometry (Continued)

Blade Type 65 Series Airfoil

Blade Row Inner OGV - Fan A

Aspect Ratio 1.418

\bar{R}	22.203	21.487	20.543	19.555	18.515							
-----------	--------	--------	--------	--------	--------	--	--	--	--	--	--	--

Cylindrical Sections

Camber	48.79	47.88	47.46	48.22	49.79							
Stagger	15.29	15.05	15.09	15.38	16.25							
Chord	2.6000	2.6000	2.6000	2.6000	2.6000							
tm/c	.09	.085	.08	.075	.072							
te/c	0.01	0.01	0.01	0.01	0.01							
Solidity	1.677	1.749	1.829	1.915	2.011							

ζ - Plane

i	.1	.6	1.0	1.25	1.35							
δ	8.9	8.5	8.2	8.1	8.2							
ζ_1												
ζ_2												
Camber												
Stagger												
X												

Table X. NASA Quiet Engine Blade and Vane Geometry (Continued)

Fan B - Rotor 1

Inlet

R _i	35.68	35.14	33.58	31.98	30.31	28.56	25.72	22.50	20.53	19.46	18.31	17.06
% Imm	0.0	7.9	15.8	24.0	32.5	41.4	55.8	72.3	82.3	87.8	93.6	100.0
P _t /P _{t_i}	1.0000	1.0000	1.0000	1.0000	1.0000	1.0000	1.0000	1.0000	1.0000	1.0000	1.0000	1.0000
P _s /P _{t_i}	0.8169	0.7911	0.7781	0.7685	0.7612	0.7543	0.7481	0.7536	0.7575	0.7594	0.7629	0.7676
T _t /T _{t_i}	1.0000	1.0000	1.0000	1.0000	1.0000	1.0000	1.0000	1.0000	1.0000	1.0000	1.0000	1.0000
ρ _s /ρ _{t_i}	0.8655	0.8459	0.8359	0.8286	0.8229	0.8176	0.8128	0.8170	0.8200	0.8215	0.8242	0.8279
η _{ad}												
U	1160.0	1111.3	1062.1	1011.4	958.6	903.2	813.6	711.6	649.4	615.5	579.1	539.6
W _u	1160.0	1111.3	1062.1	1011.4	958.6	903.2	813.6	711.6	649.4	615.5	579.1	539.6
C _z	587.3	634.5	656.6	671.8	682.6	691.5	695.4	677.7	664.4	656.4	644.6	627.7
C	591.5	635.3	656.6	672.0	683.7	694.5	704.2	695.7	689.6	686.5	681.0	673.5
W	1302.1	1280.1	1248.7	1214.3	1177.5	1139.4	1076.0	995.2	947.2	922.0	893.9	863.0
α	0.	0.	0.	0.	0.	0.	0.	0	0.	0.	0.	0.
M _{rel}	1.200	1.186	1.159	1.129	1.097	1.062	1.005	0.928	0.883	0.859	0.832	0.803
M _{abs}	0.545	0.588	0.610	0.625	0.637	0.648	0.657	0.649	0.643	0.640	0.634	0.626
β ₁	63.15	60.28	58.28	56.41	54.55	52.56	49.48	46.40	44.35	43.16	41.94	40.68
λ	0.9800	0.9800	0.9800	0.9800	0.9800	0.9800	0.9800	0.9800	0.9800	0.9800	0.9800	0.9800
P _{si}	0	0.1	0.2	0.3	0.4	0.5	0.65	0.8	0.88	0.92	0.96	1.0

Blade

\bar{R}	36.14	34.77	33.36	31.90	30.37	28.76	26.13	23.14	21.29	20.30	19.24	18.11
\bar{w}	0.123	0.105	0.090	0.079	0.072	0.068	0.066	0.067	0.081	0.100	0.120	0.136
D	0.376	0.396	0.411	0.426	0.443	0.463	0.495	0.547	0.549	0.530	0.501	0.440
ΔP _s /q*	0.243	0.295	0.336	0.373	0.410	0.447	0.503	0.578	0.572	0.532	0.478	0.389
N _b F _a	1158	1094	1033	968	899	824	702	563	465	401	339	282
N _b F _t	964	948	929	913	901	889	870	824	803	797	784	758

Table X. NASA Quiet Engine Blade and Vane Geometry (Continued)

Fan B - Rotor 1

	Discharge											
R _{disc}	35.600	34.399	33.138	31.815	30.423	28.950	36.543	23.781	22.050	21.134	20.170	19.160
% Imm	0.0	7.3	15.0	23.0	31.5	40.4	55.1	71.9	82.4	88.0	93.9	100.0
P _t /P _{t_i}	1.5297	1.5297	1.5297	1.5297	1.5297	1.5297	1.5297	1.5297	1.5200	1.5100	1.4980	1.4750
P _s /P _{t_i}	1.1000	1.1134	1.1179	1.1171	1.1124	1.1050	1.0878	1.0778	1.0435	1.0093	0.9726	0.9258
T _t /T _{t_i}	1.1545	1.1500	1.1464	1.1437	1.1417	1.1404	1.1392	1.1383	1.1373	1.1371	1.1363	1.1323
ρ _s /ρ _{t_i}	1.0469	1.0601	1.0666	1.0685	1.0672	1.0633	1.0525	1.0465	1.0216	0.9959	0.9684	0.9339
η _{ad}	0.836	0.861	0.882	0.899	0.911	0.920	0.928	0.934	0.926	0.911	0.898	0.888
U	1125.9	1088.0	1048.1	1006.2	962.2	915.6	839.5	752.1	697.4	668.4	637.9	606.0
W _u	698.48	658.29	612.95	561.37	503.23	437.87	322.69	179.32	83.91	29.25	27.99	74.24
C _z	681.3	661.0	650.2	643.7	639.0	634.3	625.1	585.9	587.5	600.8	614.3	644.5
C	804.3	788.6	782.5	782.5	786.8	794.1	811.8	821.8	849.9	877.8	906.7	937.9
W	975.8	933.0	893.7	854.1	813.4	770.8	704.3	616.0	594.1	602.4	616.0	650.0
α	32.11	33.03	33.79	34.65	35.69	36.99	39.58	44.36	46.24	46.77	47.31	46.54
M _{rel}	0.853	0.815	0.782	0.748	0.714	0.677	0.621	0.544	0.527	0.536	0.551	0.585
M _{abs}	0.703	0.689	0.685	0.685	0.690	0.698	0.715	0.725	0.753	0.781	0.810	0.844
β ₂	45.71	44.88	43.31	41.09	38.22	34.62	27.30	17.02	8.13	2.79	-2.61	-6.57
λ	0.9600	0.9600	0.9600	0.9600	0.9600	0.9600	0.9600	0.9600	0.9600	0.9600	0.9600	0.9600

Table X. NASA Quiet Engine Blade and Vane Geometry (Continued)

Blade Type Arbitrary Airfoil

Blade Row Fan Rotor 1 - Fan B

Aspect Ratio 1.71

\bar{R}	36.07	34.72	33.32	31.86	30.31	28.68	26.05	23.05	21.22	20.24	19.20	18.10
-----------	-------	-------	-------	-------	-------	-------	-------	-------	-------	-------	-------	-------

Cylindrical Sections

Camber	13.84	13.85	14.04	15.41	17.48	20.23	27.66	41.84	52.87	58.91	63.72	66.72
Stagger	53.42	51.49	49.44	47.07	44.26	40.99	34.85	25.44	18.17	14.09	10.03	6.18
Chord	11.296	11.153	11.007	10.854	10.696	10.530	10.260	9.955	9.770	9.674	9.569	9.453
tm/c	0.0219	0.0232	0.0247	0.0271	0.0304	0.0362	0.0541	0.0749	0.0831	0.0861	0.883	0.900
te/c	0.0050	0.0053	0.0057	0.0060	0.0064	0.0068	0.0075	0.0091	0.0102	0.0108	0.0113	0.0120
Solidity	1.296	1.329	1.367	1.410	1.460	1.519	1.630	1.787	1.905	1.978	2.062	2.161

ζ - Plane

i	2.03	2.25	2.48	2.72	2.97	3.23	3.66	4.16	4.46	4.63	4.80	4.99
δ	4.07	4.23	4.44	4.72	5.06	5.52	6.42	8.97	11.09	12.27	13.48	14.60
ζ_1												
ζ_2												
Camber												
Stagger												
X	0.00	0.	0.	0.	0.	0.	0.	0.96	2.08	2.69	3.33	4.00

Table X. NASA Quiet Engine Blade and Vane Geometry (Continued)

Fan B - Bypass OGV

Inlet

R _i	35.60	34.40	33.17	31.90	30.57	29.18	26.94	24.44	23.61			
% Imm												
P _t /P _{t_i}	1.5297	1.5297	1.5297	1.5297	1.5297	1.5297	1.5297	1.5297	1.5242			
P _s /P _{t_i}	1.1096	1.1021	1.0941	1.0854	1.0758	0.0652	1.0472	1.0274	1.0193			
T _t /T _{t_i}	1.1545	1.1500	1.1464	1.1437	1.1417	1.1404	1.1392	1.1383	1.1377			
ρ _s /ρ _{t_i}	1.0535	1.0525	1.0503	1.0468	1.0419	1.0358	1.0243	1.0113	1.0051			
η _{ad}												
U												
C _u	427.5	429.6	434.7	443.7	456.7	473.9	509.1	557.4	574.6			
C _z	669.3	675.5	680.8	684.7	687.2	688.2	685.0	671.5	663.2			
C	794.1	800.5	807.7	815.9	825.1	835.6	853.6	873.2	877.5			
W												
α	32.57	32.46	32.56	32.95	33.61	34.55	36.62	39.70	40.91			
M _{rel}												
M _{abs}	0.693	0.701	0.709	0.718	0.727	0.738	0.756	0.776	0.780			
β ₁												
λ	0.960	0.960	0.960	0.960	0.960	0.960	0.960	0.960	0.960			
P _{si}	0	0.1	0.2	0.3	0.4	0.5	0.65	0.8	0.845			

Blade

\bar{R}	35.60	34.40	33.18	31.91	30.59	29.21	26.99	24.56	23.76			
\bar{x}	0.0700	0.0520	0.0424	0.0377	0.0369	0.0397	0.0424	0.0492	0.0800			
D	0.425	0.416	0.413	0.414	0.418	0.425	0.433	0.427	0.445			
ΔP _s /q*	0.287	0.299	0.313	0.326	0.340	0.353	0.369	0.361	0.362			
N _b F _a	293	306	312	319	326	333	355	383	367			
N _b F _t	1117	1098	1078	1062	1048	1035	1019	1004	977			

Table X. NASA Quiet Engine Blade and Vane Geometry (Continued)

Fan B - Bypass OGV					Discharge							
R_{disc}	35.6000	34.4037	33.1785	31.9140	30.6009	29.2287	27.0398	24.6715	23.9140			
% Imm												
P_t/P_{t_i}	1.5003	1.5074	1.5112	1.5129	1.5129	1.5112	1.5092	1.5050	1.4838			
P_s/P_{t_i}	1.2300	1.2301	1.2303	1.2303	1.2300	1.2292	1.2252	2086	1.2022			
T_t/T_{t_i}	1.1545	1.1500	1.1464	1.1437	1.1417	1.1404	1.1392	1.1383	1.1377			
ρ_s/ρ_{t_i}	1.1277	1.1336	1.1382	1.1412	1.1430	1.1434	1.1415	1.1304	1.1222			
η_{ad}	0.796	0.829	0.856	0.874	0.886	0.892	0.896	0.896	0.867			
U												
C_u	0.	0.	0.	0.	0.	0.	0.	0.	0.			
C_z	630	636	639	639	639	638	641	656	643			
C	630	636	639	639	639	639	641	656	643			
W												
α	0.	0.	0.	0.	0.	0.	0.	0.	0.			
M	0.540	0.547	0.550	0.552	0.552	0.551	0.554	0.569	0.557			
M_{abs}												
β_2												
λ	0.9500	0.9500	0.9500	0.9500	0.9500	0.9500	0.9500	0.9500	0.9500			

Table X. NASA Quiet Engine Blade and Vane Geometry (Continued)

Blade Type 65 Series Airfoil

Blade Row Bypass OGV - Fan B

Aspect Ratio 2.58

\bar{R}	35.6000	34.4036	33.1756	31.9069	30.5879	29.2073	26.9930	24.5559	23.7640	23.7567		
-----------	---------	---------	---------	---------	---------	---------	---------	---------	---------	---------	--	--

Cylindrical Sections

Camber	45.60	44.80	44.25	44.08	44.25	44.78	46.47	49.61	50.62	50.63		
Stagger	13.26	13.19	13.19	13.30	13.51	13.84	14.62	15.87	16.39	16.40		
Chord	4.59	4.59	4.59	4.59	4.59	4.59	4.59	4.59	4.59	4.59		
t_m/C	0.0700	0.0670	0.0639	0.0606	0.0573	0.0538	0.0482	0.0420	0.0400	0.400		
t_e/C	0.0100	0.0100	0.0100	0.0100	0.0100	0.0100	0.0100	0.0100	0.0100	0.0100		
Solidity	1.231	1.274	1.321	1.374	1.433	1.500	1.624	1.785	1.844			

ζ - Plane

i	-3.5	-3.1	-2.8	-2.4	-2.0	-1.7	-1.2	-1.0	-1.0			
ζ	9.5	9.2	8.9	8.7	8.6	8.5	8.5	8.8	8.9			
ζ_1												
ζ_2												
Camber												
Stagger												
X												

Table X. NASA Quiet Engine Blade and Vane Geometry (Continued)

Fan B - Inner OGV

Inlet

105

R_i	22.2820	21.4931	20.5553	19.5551	18.4750							
% Imm	0.0	20.7	45.4	71.6	100.0							
P_t/P_{t_i}	1.5242	1.5200	1.5100	1.4980	1.4750							
P_s/P_{t_i}	1.0492	1.0180	0.9870	0.9566	0.9264							
T_t/T_{t_i}	1.1377	1.1373	1.1371	1.1363	1.1323							
ρ_s/ρ_{t_i}												
η_{ad}												
U												
C_u	609	629	657	687	705							
C_z	581	603	609	611	610							
C	847	876	900	923	937							
W												
α	46.33	46.24	47.16	48.36	49.16							
M_{rel}												
M_{abs}	0.750	0.779	0.804	0.827	0.843							
β_1												
λ	0.9600	0.9600	0.9600	0.9600	0.9600							
P_{si}	0.8450	0.8800	0.9200	0.9600	1.0000							

Blade

\bar{R}	21.84	21.08	20.16	19.19	18.14							
\bar{w}	0.0725	0.0695	0.0714	0.0775	0.0860							
D	0.474	0.494	0.516	0.530	0.549							
$\Delta P_s/q^*$	0.402	0.440	0.472	0.490	0.515							
$N_b F_a$	395	404	418	426	423							
$N_b F_t$	895	895	881	860	813							

Table X. NASA Quiet Engine Blade and Vane Geometry (Continued)

Fan B - Inner OGV

Discharge

R_{disc}	21.4020	20.6602	19.7682	18.8181	17.8000							
% Imm	0.0	20.6	45.4	71.7	100.0							
P_t/P_{t_i}	1.4898	1.4851	1.4727	1.4561	1.4278							
P_s/P_{t_i}	1.2401	1.2386	1.2336	1.2219	1.2090							
T_t/T_{t_i}	1.1377	1.1373	1.1371	1.1363	1.1323							
ρ_s/ρ_{t_i}												
η_{ad}	.876	.871	.853	.831	.810							
U												
C_u	0.	0.	0.	0.	0.							
C_z	588	585	578	575	566							
C	602	598	591	588	572							
W												
α	0.	0.	0.	0.	0.							
M	0.519	0.516	0.509	0.507	0.493							
M_{abs}												
β_2												
λ	0.9500	0.9500	0.9500	0.9500	0.9500							

Table X. NASA Quiet Engine Blade and Vane Geometry (Continued)

Blade Type Forward Blade - Arbitrary Airfoil

Blade Row Tandem Inner OGV - Fan B

Aspect Ratio 1.89 (Tandem Vane Aspect Ratio 0.77)

\bar{R}	17.600	17.800	18.245	18.475	19.300	19.800	20.280	21.400	21.978	22.282	22.400	
-----------	--------	--------	--------	--------	--------	--------	--------	--------	--------	--------	--------	--

Cylindrical Sections

Camber	11.20	11.22	11.26	11.32	11.59	11.67	11.67	11.32	10.92	10.73	10.68	
Stagger	43.01	42.99	42.97	42.95	42.43	41.87	41.27	40.17	40.05	40.18	40.24	
Chord	2.000	2.000	2.000	2.000	2.001	2.002	2.001	2.000	2.000	2.000	1.999	
t_m/c	0.050	0.050	0.050	0.050	0.050	0.050	0.050	0.050	0.050	0.050	0.050	
t_e/c	0.01	0.01	0.01	0.01	0.01	0.01	0.01	0.01	0.01	0.01	0.01	
Solidity	1.085	1.073	1.047	1.034	0.990	0.965	0.942	0.893	0.869	0.857	0.852	

ζ - Plane

i	1.8	1.8	1.8	1.8	1.8	1.8	1.8	1.8	1.8	1.8	1.8	
δ												
ζ_1												
ζ_2												
Camber												
Stagger												
x												

Table X. NASA Quiet Engine Blade and Vane Geometry (Continued)

Blade Type Aft Blade - Arbitrary Airfoil

Blade Row Tandem Inner OGV - Fan B

Aspect Ratio 1.22

\bar{R}	17.600	17.800	18.245	18.475	19.300	19.800	20.280	21.400	21.978	22.282	22.400	
-----------	--------	--------	--------	--------	--------	--------	--------	--------	--------	--------	--------	--

Cylindrical Sections

Camber	44.280	44.374	44.524	44.522	43.851	43.142	42.411	41.258	41.334	41.530	41.606	
Stagger	13.335	13.242	13.039	12.919	12.371	12.025	11.740	11.502	11.733	11.903	11.968	
Chord	3.0009	3.0007	3.0003	3.000	2.9990	2.9985	2.9981	2.9978	2.9981	2.9984	2.9984	
tm/c	0.05	0.05	0.05	0.05	0.05	0.05	0.05	0.05	0.05	0.05	0.05	
te/c	0.01	0.01	0.01	0.01	0.01	0.01	0.01	0.01	0.01	0.01	0.01	
Solidity	1.6282	1.6098	1.5703	1.5506	1.4839	1.4461	1.4117	1.3377	1.3027	1.2840	1.2783	

ζ - Plane

i												
δ		8.4			8.54		8.49	8.47	8.54			
ζ_1												
ζ_2												
Camber												
Stagger												
X												

Table X. NASA Quiet Engine Blade and Vane Geometry (Continued)

Fan C - Rotor

Inlet

Ri	34.150	32.508	30.860	29.169	27.405	25.543	22.487	18.925	16.678	15.402	13.966	12.290
% Imm	0.0	7.5	15.0	22.8	30.9	39.4	53.4	69.6	79.9	85.8	92.3	100.0
Pt/P _{ti}	1.0000	1.0000	1.0000	1.0000	1.0000	1.0000	1.0000	1.0000	1.0000	1.0000	1.0000	1.0000
P _s /P _{ti}	0.8295	0.8017	0.7829	0.7688	0.7577	0.7487	0.7400	0.7369	0.7393	0.7455	0.7573	0.7764
Tt/T _{ti}	1.0000	1.0000	1.0000	1.0000	1.0000	1.0000	1.0000	1.0000	1.0000	1.0000	1.0000	1.0000
ρ _s /ρ _{ti}	0.8750	0.8540	0.8396	0.8288	0.8202	0.8132	0.8065	0.8041	0.8059	0.8108	0.8199	0.8346
η _{ad}												
U	1549.7	1475.2	1400.4	1323.6	1243.6	1159.1	1020.5	858.8	756.8	698.9	633.8	557.7
W _u	1549.7	1475.2	1400.4	1323.6	1243.6	1159.1	1020.5	858.8	756.8	698.9	633.8	557.7
C _z	564.4	615.7	648.5	671.5	688.5	701.0	709.3	702.5	685.9	666.0	635.6	592.7
C	569.3	617.6	648.8	671.6	689.2	703.3	716.8	721.5	717.9	708.2	689.8	659.4
W	1650.9	1599.3	1543.4	1484.2	1421.8	1355.8	1247.0	1121.7	1043.1	995.0	936.7	863.6
α	0.	0.	0.	0.	0.	0.	0.	0.	0.	0.	0.	0.
M _{rel}	1.519	1.478	1.432	1.380	1.325	1.266	1.166	1.049	0.976	0.929	0.873	0.802
M _{abs}	0.524	0.571	0.602	0.625	0.642	0.657	0.670	0.675	0.671	0.662	0.643	0.612
β ₁	69.99	67.35	65.15	63.10	61.03	58.84	55.20	50.72	47.81	46.38	44.92	43.26
λ	0.9800	0.9800	0.9800	0.9800	0.9800	0.9800	0.9800	0.9800	0.9800	0.9800	0.9800	0.9800
P _{si}	0.	0.1000	0.2000	0.3000	0.4000	0.5000	0.6500	0.8000	0.8000	0.9200	0.9600	1.000

Blade

\bar{R}	33.436	31.994	30.526	29.003	27.406	25.714	22.925	19.655	17.563	16.407	15.138	13.700
\bar{W}	0.162	0.138	0.122	0.107	0.095	0.085	0.071	0.073	0.088	0.102	0.128	0.185
D	0.324	0.337	0.353	0.370	0.388	0.408	0.442	0.511	0.536	0.521	0.498	0.454
ΔP _s /q*	0.166	0.207	0.245	0.290	0.335	0.384	0.467	0.594	0.634	0.620	0.590	0.509
N _b F _a	1377	1314	1243	1165	1076	977	811	625	510	445	372	284
N _b F _t	852	835	821	804	783	759	709	643	616	605	588	573

Table X. NASA Quiet Engine Blade and Vane Geometry (Continued)

Fan C - Rotor					Discharge							
R _{disc}	32.710	31.479	30.191	28.837	27.407	25.885	23.363	20.385	18.448	17.413	16.310	15.110
% Imm	0.0	7.0	14.3	22.0	30.1	38.8	53.1	70.0	81.0	86.9	93.2	100.0
P _t /P _{t_i}	1.6283	1.6351	1.6399	1.6419	1.6392	1.6317	1.6106	1.5841	1.5623	1.5494	1.5344	1.5201
P _s /P _{t_i}	1.2106	1.2268	1.2342	1.2356	1.2309	1.2210	1.1967	1.1775	1.1329	1.0904	1.0447	0.9846
T _t /T _{t_i}	1.1959	1.1880	1.1828	1.1778	1.1728	1.1678	1.1589	1.1519	1.1485	1.1467	1.1456	1.1467
ρ _s /ρ _{t_i}	1.1018	1.1210	1.1318	1.1379	1.1391	1.1359	1.1241	1.1126	1.0813	1.0513	1.0178	0.9720
η _{ad}	0.7630	0.8024	0.8304	0.8562	0.8778	0.8951	0.9182	0.9244	0.9157	0.9082	0.8939	0.8662
U	1484.3	1428.5	1370.0	1308.6	1243.7	1174.6	1060.2	925.0	837.1	790.2	740.2	685.7
W _u	1073.1	1018.4	954.3	885.2	810.8	729.6	593.2	413.2	284.5	211.5	127.2	18.8
C _z	660.0	643.9	633.7	627.2	622.1	616.6	606.1	560.9	566.3	587.3	602.3	618.6
C	778.0	763.9	758.2	756.8	757.9	760.7	766.6	763.8	792.5	826.1	861.8	913.3
W	1260.0	1205.2	1145.7	1085.0	1022.0	955.4	849.4	701.5	635.2	626.4	619.0	624.3
α	31.93	32.49	33.27	34.02	34.83	35.82	37.62	42.38	44.30	44.58	45.50	47.15
M _{rel}	1.077	1.032	0.983	0.933	0.881	0.825	0.737	0.611	0.556	0.551	0.547	0.556
M _{abs}	0.665	0.654	0.650	0.651	0.653	0.657	0.666	0.665	0.693	0.727	0.762	0.813
β ₂	58.406	57.695	56.412	54.680	52.503	49.798	44.384	36.376	26.672	19.804	11.928	1.740
λ	0.9600	0.9600	0.9600	0.9600	0.9600	0.9600	0.9600	0.9600	0.9600	0.9600	0.9600	0.9600

Table X. NASA Quiet Engine Blade and Vane Geometry (Continued)

Blade Type Arbitrary Airfoil

Blade Row Fan Rotor - Fan C

Aspect Ratio 2.09

\bar{R}	33.400	32.000	30.500	29.000	27.400	25.700	23.000	19.700	17.600	16.400	15.100	13.700
-----------	--------	--------	--------	--------	--------	--------	--------	--------	--------	--------	--------	--------

Cylindrical Sections

Camber	2.25	2.58	3.28	3.94	4.87	6.66	12.20	24.61	37.38	47.51	61.83	79.95
Stagger	63.80	61.70	59.55	57.29	54.81	52.09	46.92	37.02	27.90	21.71	14.31	6.77
Chord	11.301	10.800	10.310	9.860	9.440	9.060	8.600	8.271	8.160	8.130	8.112	8.099
tm/c	0.0250	0.0270	0.0293	0.0318	0.0357	0.0388	0.0405	0.0444	0.0522	0.0603	0.0726	0.0900
te/c	.005	.0053	.0057	.0061	.0066	.0071	.0080	.0092	.010	.0106	.0112	.0120
Solidity	1.400	1.397	1.399	1.407	1.426	1.459	1.547	1.737	1.919	2.051	2.223	2.446

ζ - Plane

i	4.00	3.28	3.52	3.74	3.94	4.13	4.40	4.65	4.75	4.75	4.65	4.50
δ	0.97	1.60	2.19	2.55	2.98	3.58	5.24	8.47	10.53	11.81	13.45	15.51
ζ_1												
ζ_2												
Camber												
Stagger												
X	-0.50	-0.20	0	0	0	0.06	0.60	2.00	2.80	3.20	3.60	4.00

Table X. NASA Quiet Engine Blade and Vane Geometry (Continued)

Fan C - Bypass OGV

Inlet

R_i	32.700	31.491	30.256	28.983	27.657	26.258	23.964	21.283	20.600			
% Imm	0.0	10.0	20.2	30.7	41.7	53.2	72.2	94.4	100.0			
P_t/P_{t_i}	1.6283	1.6351	1.6399	1.6419	1.6392	1.6317	1.6106	1.5841	1.5751			
P_s/P_{t_i}	1.2108	1.2030	1.1947	1.1863	1.1776	1.1687	1.1555	1.1588	1.1615			
T_t/T_{t_i}	1.1959	1.1880	1.1828	1.1778	1.1728	1.1678	1.1589	1.1519	1.1505			
ρ_s/ρ_{t_i}												
η_{ad}												
U												
C_u	411.4	410.0	414.9	421.2	429.0	438.7	455.3	490.2	501.7			
C_z	660.0	673.5	682.4	688.2	689.1	685.0	667.8	610.1	587.3			
C	777.8	788.5	798.6	806.9	811.8	813.6	808.6	783.2	773.1			
W												
α	31.93	31.33	31.30	31.47	31.90	32.64	34.29	38.78	40.51			
M_{rel}												
M_{abs}	0.665	0.677	0.688	0.686	0.704	0.707	0.705	0.683	0.674			
β_1												
λ	0.9600	0.9600	0.9600	0.9600	0.9600	0.9600	0.9600	0.9600	0.9600			
P_{si}	0.	0.1000	0.2000	0.3000	0.4000	0.5000	0.6500	0.8000	0.8330			

Blade

\bar{R}	32.700	31.497	30.271	29.009	27.694	26.309	24.042	21.441	20.800			
\bar{U}	0.0700	0.0520	0.0424	0.0377	0.0369	0.0397	0.0424	0.0492	0.0800			
D	0.4100	0.395	0.388	0.385	0.385	0.387	0.389	0.353	0.350			
$\Delta P_s/q^*$	0.246	0.256	0.266	0.276	0.287	0.298	0.312	0.256	0.226			
$N_b F_a$	256	262	268	270	270	267	262	270	257			
$N_b F_t$	1025	1008	995	976	949	913	843	771	743			

Table X. NASA Quiet Engine Blade and Vane Geometry (Continued)

Fan C - Bypass OGV

Discharge

R_{disc}	32.700	31.503	30.286	29.034	27.732	26.360	24.121	21.600	21.000			
% Imm	0.0	10.2	20.6	31.3	42.5	54.2	73.3	94.9	100.0			
P_t/P_{t_i}	1.5991	1.6127	1.6210	1.6248	1.6222	1.6134	1.5913	1.5632	1.5420			
P_s/P_{t_i}	1.3135	1.3134	1.3130	1.3119	1.3100	1.3067	1.2977	1.2675	1.2549			
T_t/T_{t_i}	1.1959	1.1880	1.1828	1.1778	1.1728	1.1678	1.1589	1.1519	1.1505			
ρ_s/ρ_{t_i}												
η_{ad}	.733	.778	.810	.837	.858	.873	.893	.896	.875			
U												
C_u	0.	0.	0.	0.	0.	0.	0.	0.	0.			
C_z	638.3	649.4	656.3	659.6	658.0	652.1	639.1	644.6	639.4			
C	638.3	649.4	656.3	659.6	658.1	652.3	639.5	646.1	640.3			
W												
α	0.	0.	0.	0.	0	0.	0.	0.	0.			
M	0.538	0.550	0.557	0.561		0.557	0.548	0.556	0.551			
M_{abs}												
β_2												
λ	0.9500	0.9500	0.9500	0.9500	0.9500	0.9500	0.9500	0.9500	0.9500			

Table X. NASA Quiet Engine Blade and Vane Geometry (Continued)

Blade Type 56 Series

Blade Row Bypass OGV - Fan C

Aspect Ratio 3.03

\bar{R}	32.700	31.497	30.271	29.009	27.694	26.309	24.042	21.441	20.800			
-----------	--------	--------	--------	--------	--------	--------	--------	--------	--------	--	--	--

Cylindrical Sections

Camber	46.26	44.48	43.58	42.94	42.75	42.82	43.50	48.09	49.78			
Stagger	13.10	12.80	12.72	12.72	12.84	13.05	13.55	15.09	15.74			
Chord	3.921	3.922	3.921	3.922	3.924	3.923	3.925	3.923	3.921			
t_m/c	0.0700	0.0670	0.0639	0.0607	0.0574	0.0539	0.0482	0.0416	0.0400			
t_e/c	0.0100	0.0100	0.0100	0.0100	0.0100	0.0100	0.0100	0.0100	0.0100			
Solidity	1.1450	1.1890	1.2370	1.2910	1.3530	1.4240	1.5590	1.7470	1.8000			

ζ - Plane

i	-4.30	-3.70	-3.20	-2.70	-2.30	-1.80	-1.00	-0.50	-0.40			
δ	10.03	9.44	9.06	8.74	8.50	8.31	8.08	8.52	8.77			
ζ_1												
ζ_2												
Camber												
Stagger												
X												

Table X. NASA Quiet Engine Blade and Vane Geometry (Continued)

Fan C - Inner OGV

Inlet

115

R _i	19.320	18.236	17.259	16.209	15.050							
% Imm	0.0	25.4	48.3	72.9	100.0							
P _t /P _{t_i}	1.5751	1.5623	1.5494	1.5344	1.5201							
P _s /P _{t_i}	1.1170	1.0805	1.0466	1.0106	0.9694							
T _t /T _{t_i}	1.1505	1.1485	1.1467	1.1456	1.1467							
ρ _s /ρ _{t_i}												
η _{ad}												
U												
C _u	535.0	559.1	583.8	616.8	669.5							
C _z	615.7	632.0	643.0	647.9	641.5							
C	818.9	846.0	870.5	896.1	928.4							
W												
α	40.99	41.5	42.24	43.59	46.23							
M _{rel}												
M _{abs}	0.718	0.745	0.770	0.796	0.828							
β ₁												
λ	0.9600	0.9600	0.9600	0.9600	0.9600							
P _{si}	0.8330	0.8800	0.9200	0.9600	1.000							

Blade

\bar{R}	19.060	18.005	17.043	16.002	14.855							
\bar{W}	0.0725	0.0695	0.0714	0.0775	0.0860							
D	0.403	0.439	0.467	0.495	0.520							
ΔP _s /q*	0.309	0.374	0.420	0.457	0.487							
N _b F _a	272	278	284	291	308							
N _b F _t	746	727	707	685	667							

Table X. NASA Quiet Engine Blade and Vane Geometry (Continued)

Fan C - Inner OGV

Discharge

R_{disc}	18.800	17.773	16.856	15.795	14.660							
% Imm	0.0	24.8	47.7	72.6	100.0							
P_t/P_{t_i}	1.5419	1.5288	1.5135	1.4938	1.4728							
P_s/P_{t_i}	1.2586	1.2608	1.2576	1.2502	1.2376							
T_t/T_{t_i}	1.1505	1.1485	1.1467	1.1456	1.1467							
ρ_s/ρ_{t_i}												
η_{ad}	.875	.869	.857	.835	.797							
U												
C_u	0.	0.	0.	0.	0.							
C_z	632.1	615.2	602.8	590.3	581.3							
C	635.71	619.31	606.97	595.09	588.68							
W												
α	0.	0.	0.	0.	0.							
M	0.546	0.532	0.521	0.511	0.505							
M_{abs}												
β_2	0.9500	0.9500	0.9500	0.9500	0.9500							
λ												

Table X. NASA Quiet Engine Blade and Vane Geometry (Continued)

Blade Type Fwd Vane-Arbitrary Airfoil

Blade Row Inner OGV Tandem - Fan C

Aspect Ratio 2.67 - Tandem Aspect Ratio: 1.10

\bar{R}	14.500	14.789	14.917	14.980	16.000	17.000	18.000	18.972	19.143	19.230	19.450	
-----------	--------	--------	--------	--------	--------	--------	--------	--------	--------	--------	--------	--

Cylindrical Sections

Camber	11.654	11.659	11.661	11.660	11.496	11.316	11.174	11.124	11.129	11.132	11.143	
Stagger	41.775	40.922	40.543	40.358	37.913	36.436	35.590	35.105	35.025	34.999	34.910	
Chord	1.6	1.6	1.6	1.6	1.6	1.6	1.6	1.6	1.6	1.6	1.6	
tm/C	.072	.072	.072	.072	.072	.072	.072	.072	.072	.072	.072	
te/C	.01	.01	.01	.01	.01	.01	.01	.01	.01	.01	.01	
Solidity	1.054	1.033	1.024	1.020	.955	.900	.849	.805	.798	.795	.786	

ζ - Plane

i	1.6	1.6	1.6	1.6	1.6	1.6	1.6	1.6	1.6	1.6	1.6	
δ												
ζ_1												
ζ_2												
Camber												
Stagger												
X												

Table X. NASA Quiet Engine Blade and Vane Geometry (Concluded)

Blade Type Aft Vane-Arbitrary Airfoil

Blade Row Inner OGV Tandem

Aspect Ratio 1.74

\bar{R}	14.500	14.789	14.917	14.980	16.000	17.000	18.000	18.972	19.143	19.230	19.450	
-----------	--------	--------	--------	--------	--------	--------	--------	--------	--------	--------	--------	--

Cylindrical Sections

Camber	42.877	41.910	41.487	41.282	38.687	37.226	36.500	36.178	36.133	36.110	36.052	
Stagger	12.589	12.173	11.991	11.905	10.792	10.103	9.651	9.306	9.245	9.214	9.136	
Chord	2.4	2.4	2.4	2.4	2.4	2.4	2.4	2.4	2.4	2.4	2.4	
tm/c	0.05	0.05	0.05	0.05	0.05	0.05	0.05	0.05	0.05	0.05	0.05	
te/c	0.01	0.01	0.01	0.01	0.01	0.01	0.01	0.01	0.01	0.01	0.01	
Solidity	1.581	1.550	1.536	1.530	1.432	1.348	1.273	1.208	1.197	1.192	1.178	

ζ - Plane

i												
δ	8.21				7.99	7.98	8.07		8.22			
ζ_1												
ζ_2												
Camber												
Stagger												
X												

5.0 FAN MECHANICAL DESIGN

5.1 FAN ROTOR DESIGN

5.1.1 Summary

This section presents the methods and procedures used in the aeromechanical design of the three full scale fan rotors, A, B, and C.

The basic aerodynamic acoustic design features of the three fans are as follows:

- Fan A - Low tip speed, high aspect ratio, 40 blades with a tip shroud
- Fan B - Low tip speed, low aspect ratio, 26 cantilevered blades
- Fan C - High tip speed, high aspect ratio, 26 blades with a mid-span shroud

The mechanical features for the three fan rotor designs have been successfully demonstrated on various turbofan engines. The materials chosen for the fan rotor components are state-of-the-art alloys. These materials provide a strong, reliable structure synonymous with commercial engine design philosophy.

The fans were designed for maximum interchangeability of components between the full scale fan test facility at General Electric, Lynn, the NASA-Lewis Facility, and the full scale experimental engine. Also, to facilitate maintenance, the fan blades are individually replaceable from the front with accessibility to instrumentation in the rotating spinner.

5.1.1.1 Fan A Rotor

The mechanical features and material selections for the Fan A rotor design have been successfully demonstrated on various turbofan engines in the past four years. The active fan rotor will be removable while the vehicle is in the test cell. In addition, individual blades may be removed and replaced. The proposed shroud location, at the blade tip (Figure 55) has been demonstrated under simulated flight conditions on other turbofans and proven to provide maximum efficiency while maintaining mechanical and aerodynamic stability.

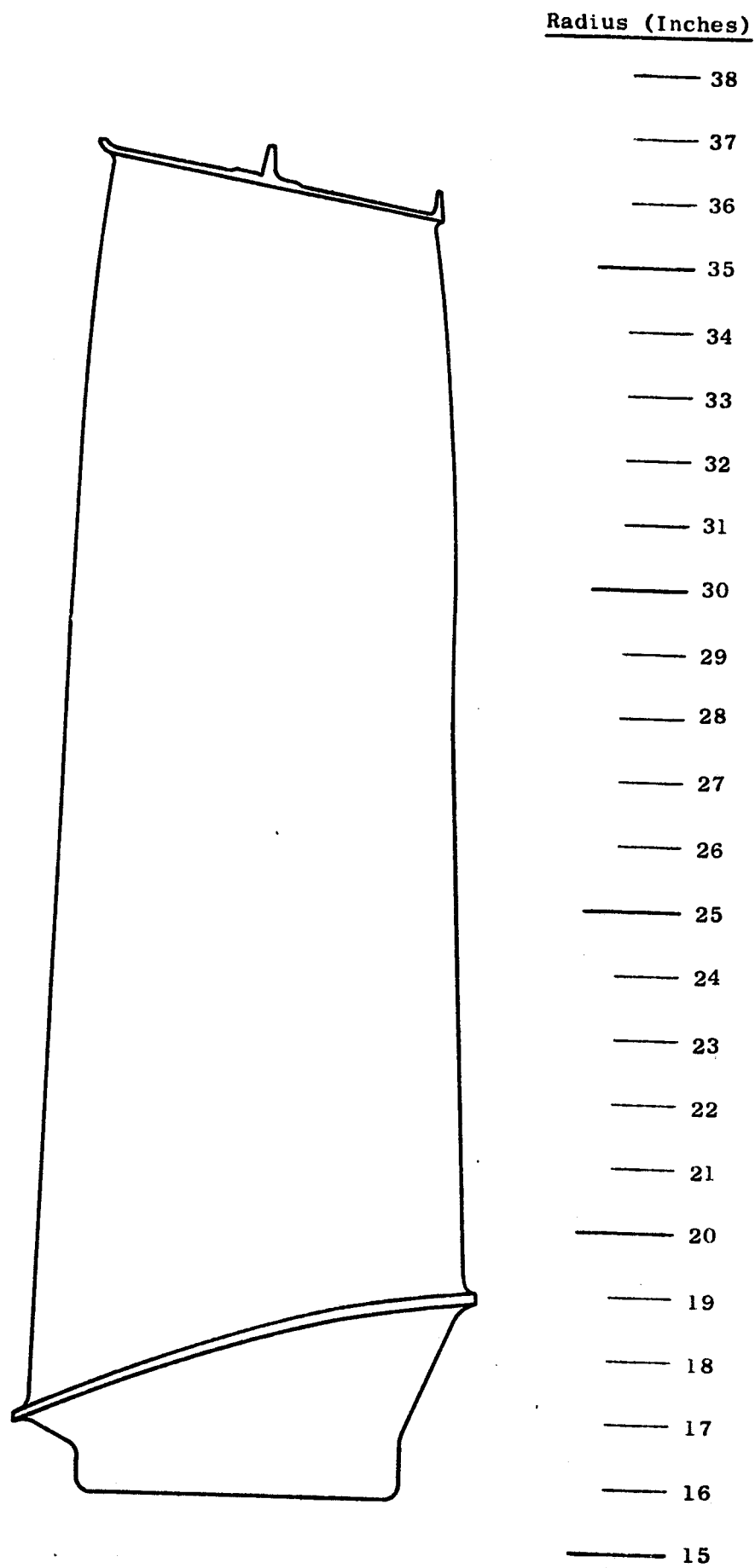


Figure 55. Fan A Blade Configuration

5.1.1.1.1 Material Selection

The materials for use in the Fan A rotor were selected for their availability, low cost, and reliability. Table XI lists the materials, allowable operating stress level, and the actual stress level at a physical speed of 3881 rpm.

Table XI. Fan A Materials and Allowable Vs Actual Stress Levels

Component	Material	Allowable Stress	Actual Stress*
Spinner, Nose	17-4 PH	114,000	17,194
Spinner, Cone	17-4 PH	112,000	55,360
Seal, Air	17-4 PH	110,000	42,400
Cone Transmitter	17-4 PH	112,000	76,992
Spacer, Radial	7075 Al	32,200	-1,437
Disc, Rotor	4340	123,000	85,300
Airfoils	Ti 6-4	90,000	69,500

* Maximum surface effective stress.

Design values were set by minimum property values determined from average properties less three standard material deviations.

The Fan A rotor has been designed to withstand a physical overspeed for two reasons. First, as a factor of safety, and second, it allows simulation of the aerodynamic design point under sea level conditions (i.e., corrected speeds are equal).

The gas loadings and temperatures imputed to the blade and system stress programs are considered to be proportional to the rotor speed squared. Primary aerodynamic loading information is shown in Figure 56.

5.1.1.1.2 Blade Design

A summary of the important design features of the Fan A blade design is shown on Figures 57 and 58 and in Table XII.

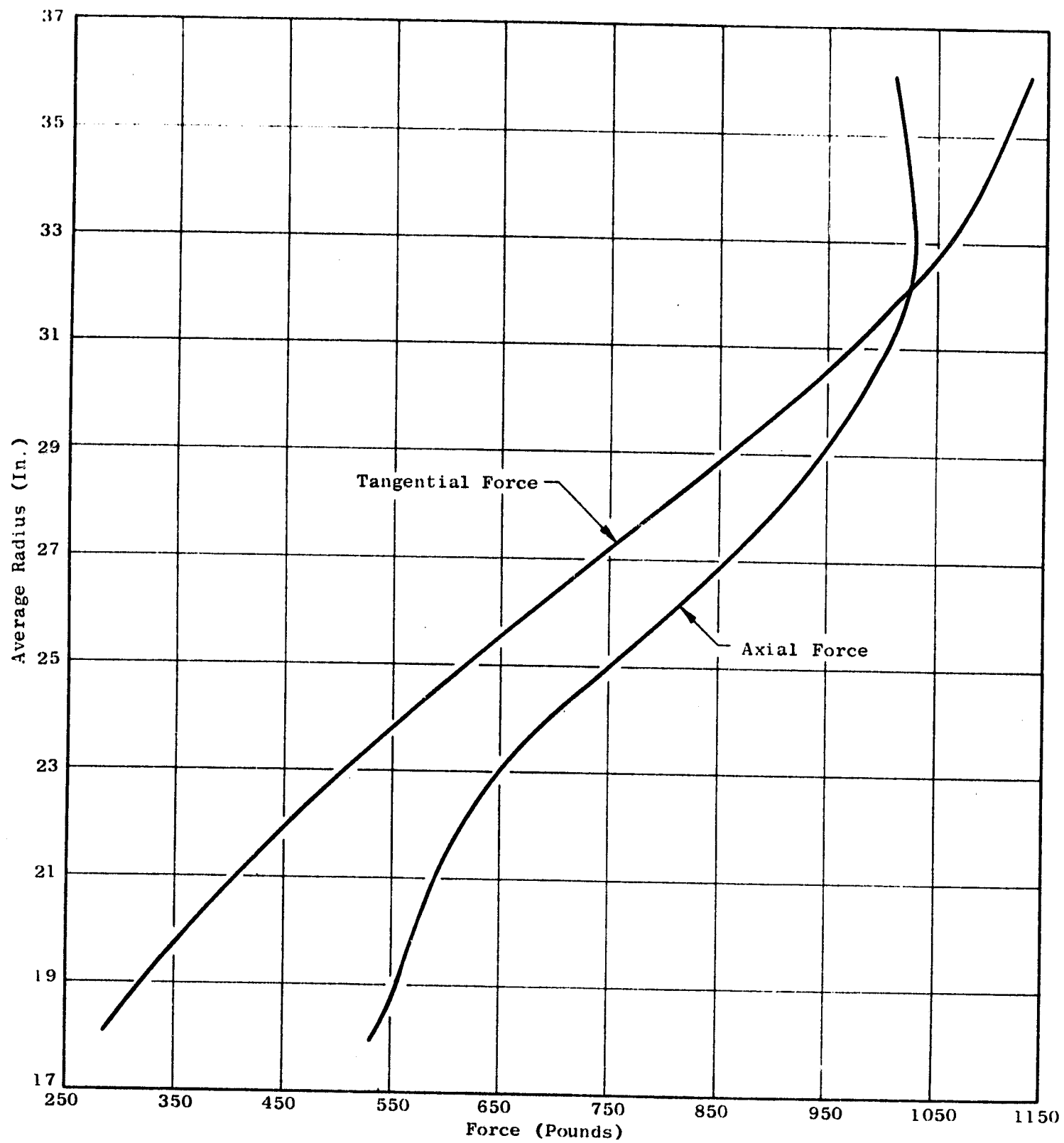


Figure 56. Fan A Aerodynamic Blade Loads (3624 RPM)

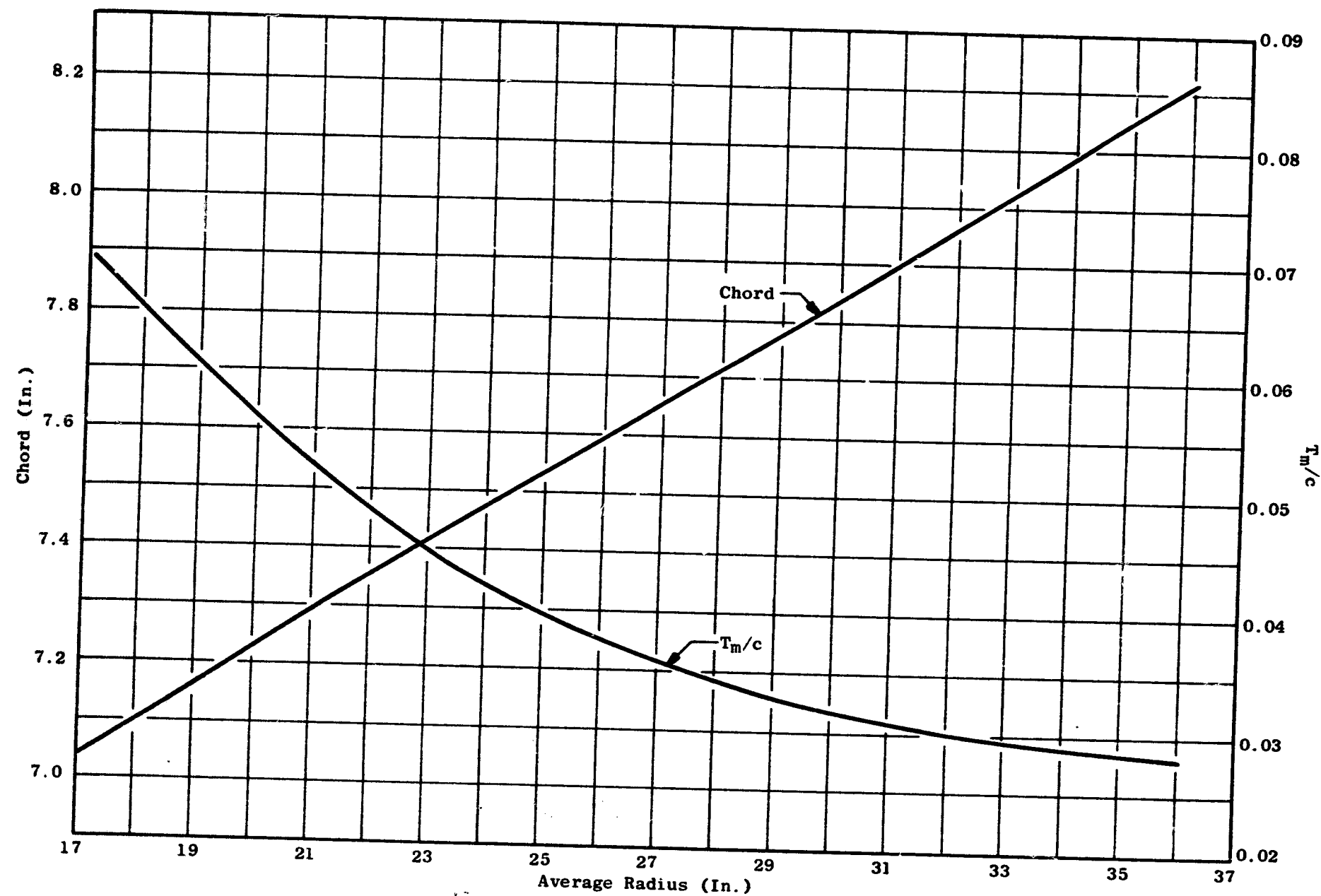


Figure 57. Fan A Final Blade Design - Blade Chord and T_m/c Vs Average Radius, $N_b = 40$

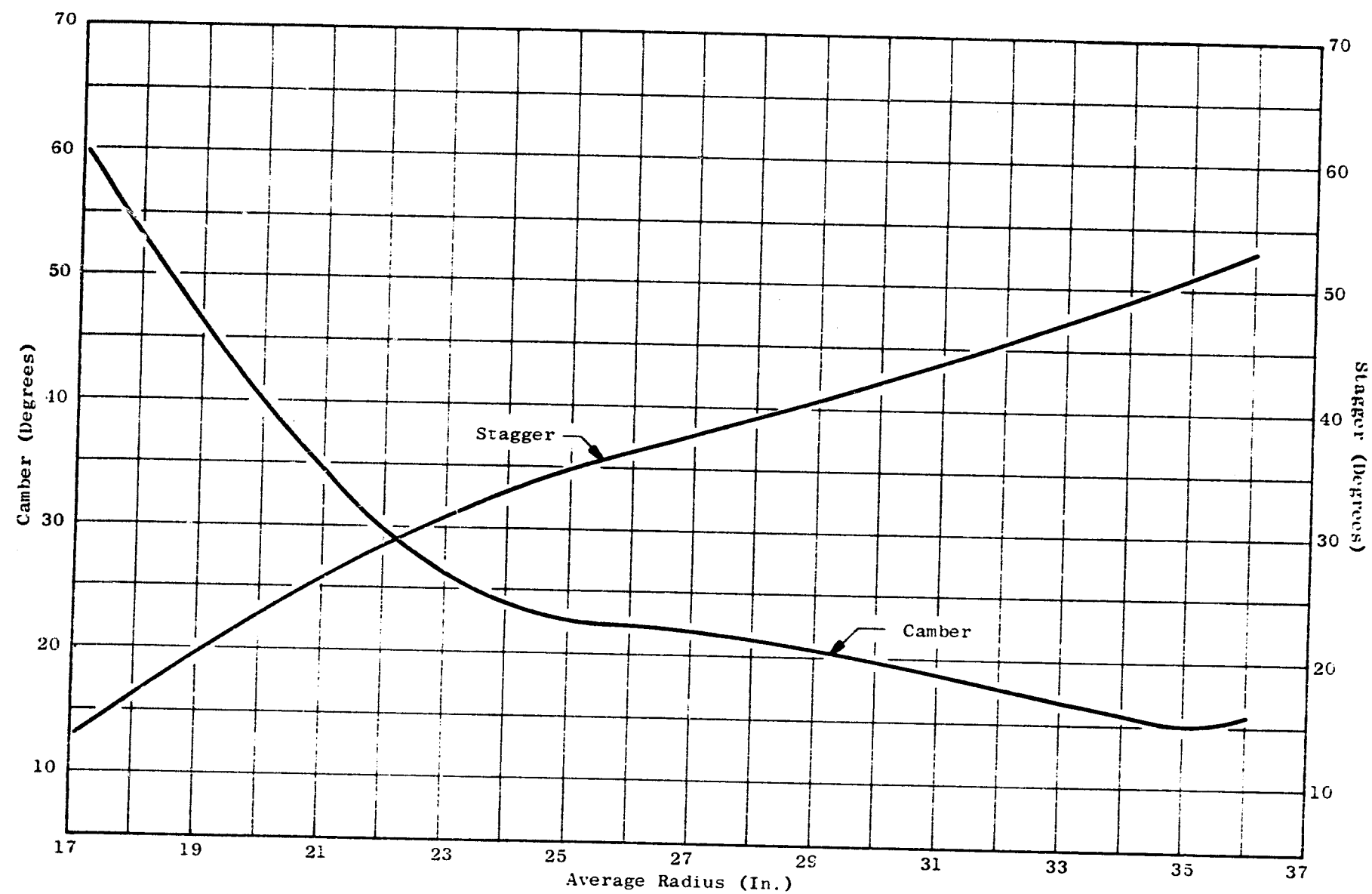


Figure 58. Fan A Final Blade Design - Camber and Stagger Vs Average Radius, $N_b = 40$

Table XII. Fan A Blade Design Features

Tip Radius (LE)	36.6800
Hub Radius (LE)	17.0600
Aspect Ratio	2.4
Number of Blades	40
Chord - Hub	7.0417
Chord - Pitch	7.7629
Chord - Tip	8.2522
t_m/c - Hub	0.0694
t_m/c - Tip	0.0279
Camber - Hub	59.8°
Camber - Tip	16.7°
Stagger - Hub	13.1°
Stagger - Tip	53.8°
Dovetail	Single Tang
Shroud	Tip

• Vibration

Because vibration is the principal factor causing blade failure, Fan A blade design was examined for conditions within the engine operating range where the blade would be resonant with known sources of excitation. The following sources of excitation were examined for coincidence with the blade natural frequency within the fan operating range:

- 2/rev inlet distortion
- Rotating stall
- Stator blade or strut passing frequency (not as likely in a design such as this, due to the large spacing between the rotor blade and the fan struts and stators)

- 3/rev or 4/rev. Possible source of excitation, especially the former, for there are three inlet valves in one of the Lynn, Massachusetts aerodynamic test cells.

To evaluate these possibilities, a stress and vibration analysis was performed using the Advanced Mechanics Twisted Blade Program. This program, within the framework of twisted bar theory and St. Venant Torsional theory, computes the following quantities at each of the spanwise stations inputed:

- Displacement (axial, tangential, and twist)
- Bending and twisting moments and shear
- Stresses (bending, twisting, centrifugal, spanwise resultants, principal, and effective)

The program will also search a specified frequency range, finding all resonances to within a specified tolerance, and compute an entire case (stresses and deflections) at each resonance as if the blade were being forced at this specific frequency. The data obtained from this analysis were then plotted on a Campbell diagram to determine if any of the previously mentioned excitation resonances exist.

This program was run at four different speeds: zero, 1812, 3624, and 3881 rotor rpm. The root of the airfoil was considered to extend below the platforms and encompassed the blade shank and part of the dovetail. At this extremity, boundary conditions were specified such that the blade was built into a rigid foundation: $U = V = \phi = \theta_x = \theta_y = 0$. At the airfoil tip, a dummy section was added which had the approximate mass of the tip shroud. The boundary conditions specified restrained the blade tangentially and torsionally ($U = \phi = M_x = M_y = V_y = 0$).

Where:

U	=	Generalized Load
V	=	Shear
M	=	Moment
θ	=	Root Rotation
ϕ	=	Tip Rotation
Sub x	=	Axial Direction
Sub y	=	Tangential Direction

The resultant Campbell diagram proves this design to be high-flex in nature with the first flexural mode exhibiting a 3.7 percent margin over 4/rev at 3624 rpm. This is the only close excitation in the fan operating region, and, while it may seem unusually close to 4/rev, this excitation is not nearly as strong or as common as the 2/rev. In all actuality, the vibration picture described in the Campbell diagram (Figure 59) does not exist except under special circumstances.

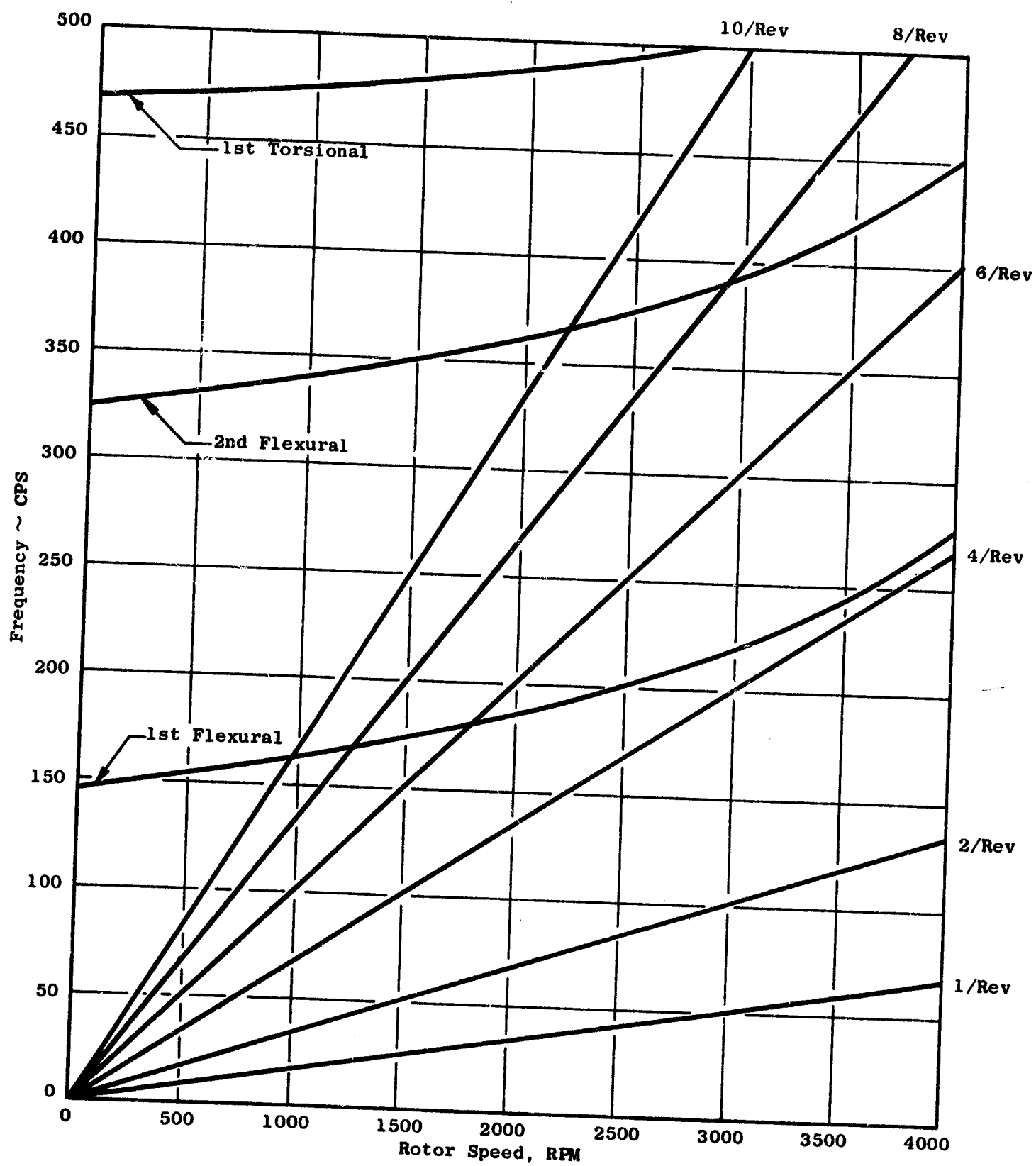


Figure 59. Campbell Diagram, Fan A, Final Blade Design (Ti6Al-4V)

The assumption, that the root of the airfoil is built upon a rigid foundation, is inaccurate. In reality, the blade is attached to an elastic foundation -- that of the rotor disc. The vibration analysis for this situation is described in detail with that of the disc mechanical design. Let it suffice to say that this mode (first flexural), which appears close to 4/rev, drops to where it is between 2/rev and 4/rev with generous margins over and under both.

The one specific case, where an airfoil will act as if it were built on a rigid foundation, occurs when the excitation source is a rotating stall. At this time, a condition exists where stall occurs in a number of local regions in the flow passage while the remaining regions are clear. These regions tend to rotate in the direction of engine rotation at about half engine speed. When, for example, five stall regions occur, each blade will be excited approximately five times in two revolutions or at about 2-1/2/rev. The important consideration is that each blade is being acted upon separately and, therefore, is restrained by its neighbor, resulting in a condition closely resembling a rigid foundation. Thus, for rotating stalls, the Campbell diagram presented in Figure 59 represents a true picture of blade resonant frequency. Excitations of 1/2/rev through 3-1/2/rev, equivalent to one to seven stall regions, are found not to be coincident with any of the blade's natural frequencies within the operating region of the fan.

In addition to the type of forced mechanical vibrations just covered, fan blades are also susceptible to other aeromechanical vibrations such as twist cycle response (stall flutter) and separated-flow vibration.

The limit cycle vibration is a violent form of self-excitation, sometimes occurring without any detectable warning. It has been found to be a function of air density and angle of attack. The best guide to blade stability against this self-excited vibration is the reduced velocity parameter, defined as follows:

$$V_R = \frac{w}{bf_t}, \text{ where:}$$

- b = blade chord, 1/2 span (ft)
- w = inlet relative velocity (ft/sec)
- f_t = first torsional frequency (rad/sec)
- V_R = reduced velocity parameter

Experience has shown that, if the reduced velocity parameter (determined for a speed, at stall) is less than an empirical number, a normal stalling of the airfoil will occur before any unstable limit cycle response can be obtained.

Figure 60 plots stall inlet relative velocity at midspan versus percent speed. This and the blade Campbell diagram can be combined to form a curve of the reduced velocity parameter versus engine speed or incidence angle at stall. This aeromechanical vibration stability criteria is depicted in Figure 61.

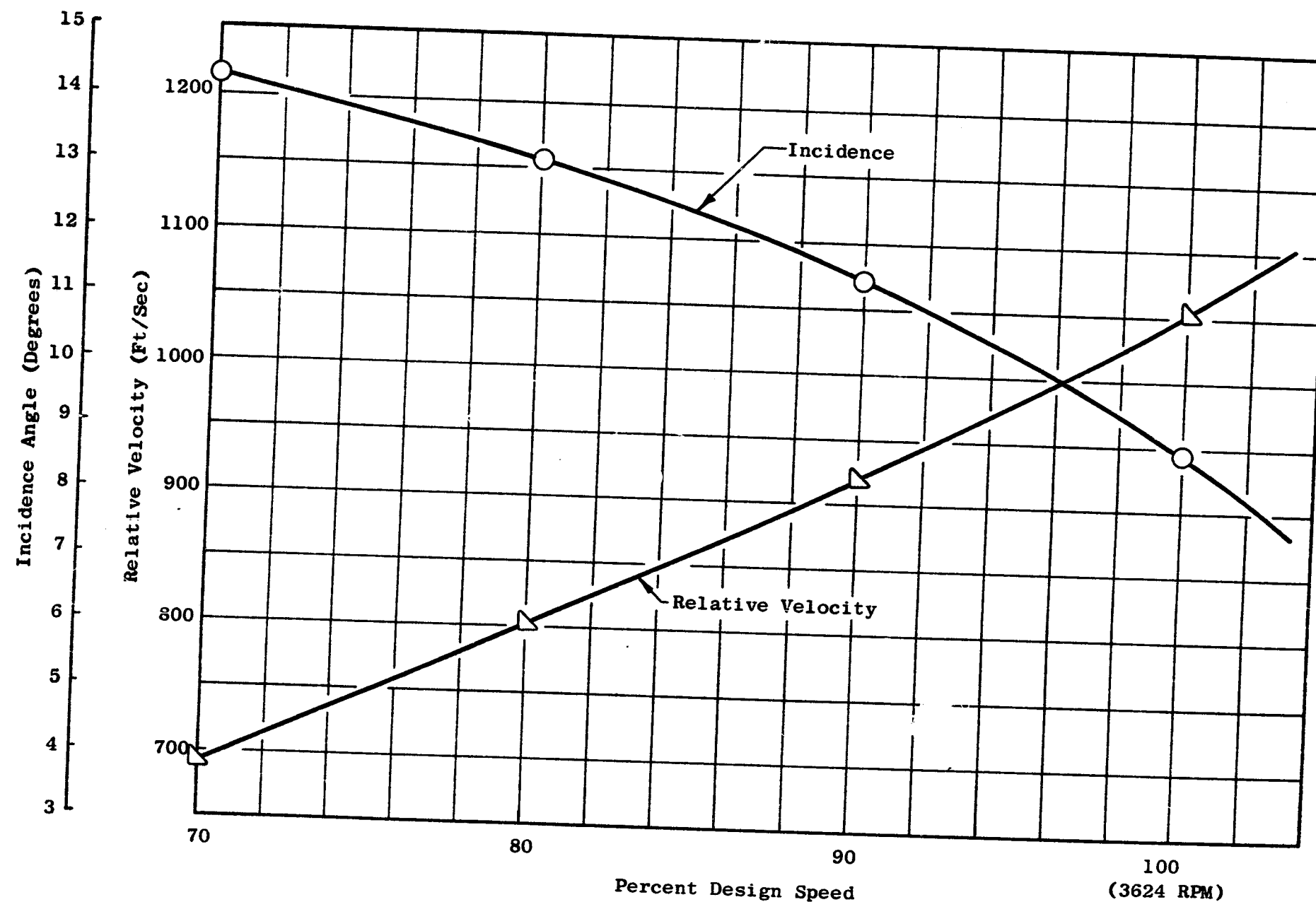


Figure 60. Fan A Pitch Line at Stall

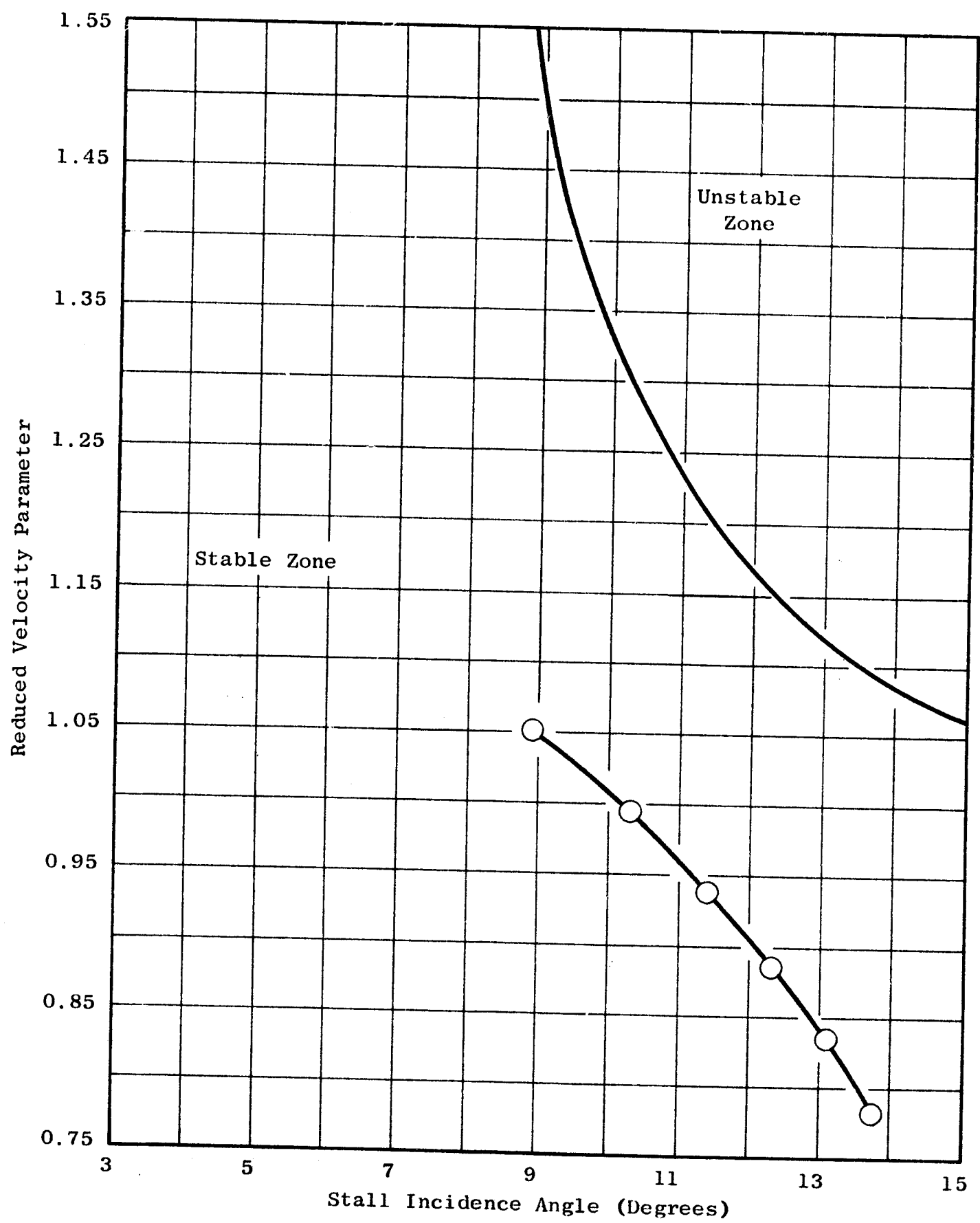


Figure 61. Aeroelastic Stability Map, Fan A , SLS at Stall

• Airfoil Stress

The Twisted Blade program provides stress information as well as vibration resonances. Both steady state blading stress (including centrifugal, bending, shear, and induced bending) and vibratory stress distributions are available through this analysis.

The steady state effective stress distributions at 3881 and 3624 rpm are plotted in Figures 62 and 63, respectively. In both cases, the maximum stress areas would appear to be in the root and tip leading and trailing edges. At both locations, root and tip, a great percentage of the airfoil stress is composed of end effect stresses. These are the induced tensile stresses at a built-in boundary resulting from a torsional moment (M_z). These end effect stresses at the airfoil tip, just under the shroud, became of such concern that the magnitude of the empirical constants K ($\sigma_{ee} = KM_z t_m / t_{sv}$) would determine whether the maximum stress location was at the airfoil root or tip:

Where,

σ_{ee}	=	End Effect Stress
M_z	=	Torsional Moment
t_m	=	Maximum Thickness
t_{sv}	=	Torsional Stiffness
K	=	Empirical Constant

Since a model of the A blade was not available for bench testing, previous testing on three similar fan blades had to be applied to this particular case. These three blades had undergone strain distribution bench testing. The results of a portion of this work, for an imputed torsional moment (M_z), is reviewed in Figures 64 through 66. Table XIII describes the individual blade constants and calculated tip K factors. Using a factor of +0.48, -0.96 for the tip leading edge and +0.95, -1.15 for the tip trailing edge appeared to give edge stresses similar to that being observed on the A blade. Applying these values to the Fan A blade results in a tip trailing edge stress of 69,500 psi at 3881 rpm. This location proved to be the maximum stress point at this overspeed condition only. At lower physical speeds, the root trailing edge became the governing location. This can be seen in comparing Figures 62 and 63, where the static stress spanwise distributions are plotted. Normally, some airfoil tilt would have been introduced to oppose the gas bending moments with centrifugal restoring moments, but this has not proven as successful in shrouded-blade designs.

• Blade Attachment

For the operating condition where the combination of temperature, rpm,

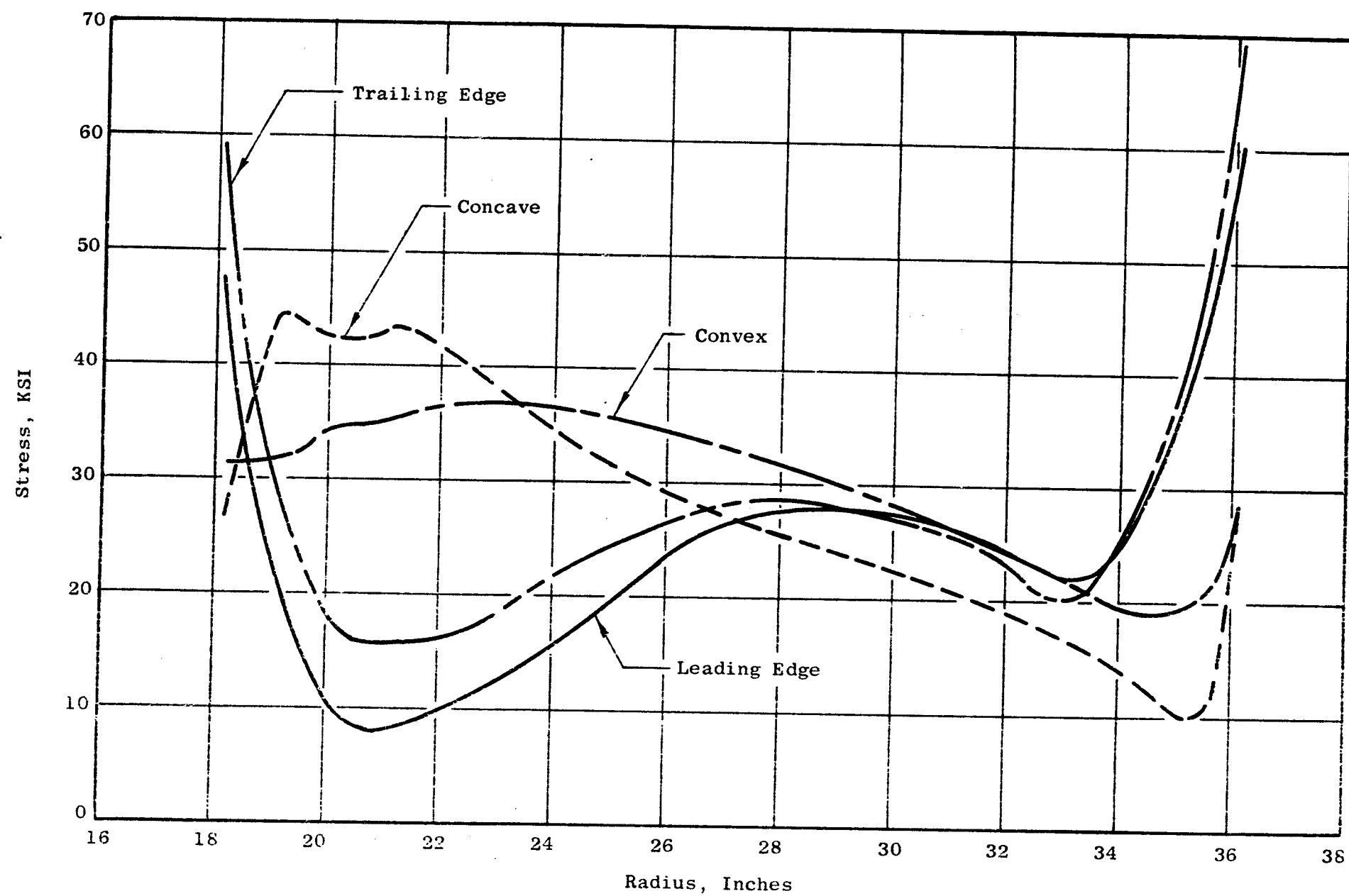


Figure 62. Fan A Effective Stress Vs Radius, Steady State (Ti6Al-4V @ 3881 RPM)

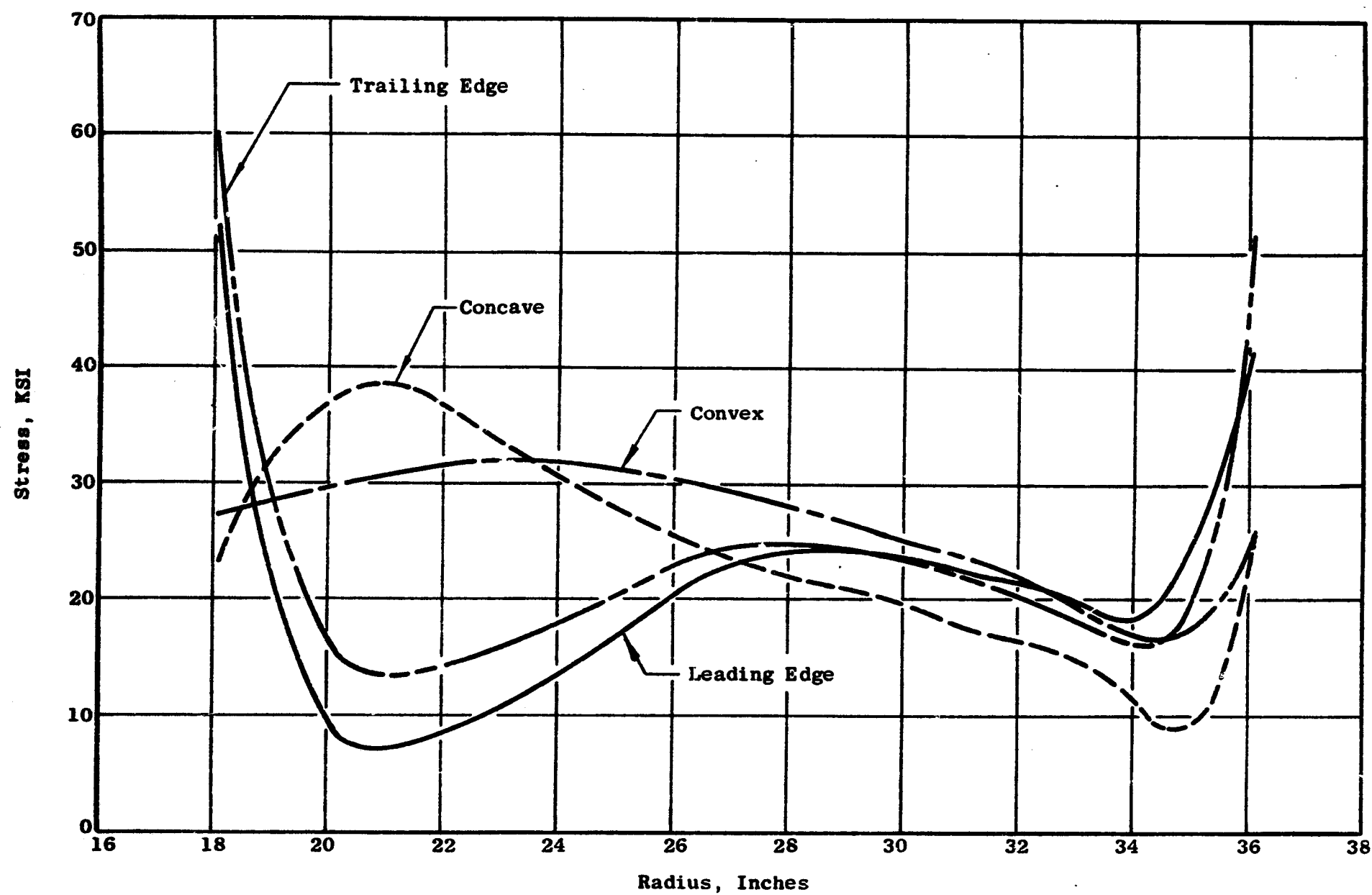


Figure 63. Fan A Steady State Effective Stress Vs Radius (Ti6Al-4V at 3624 RPM)

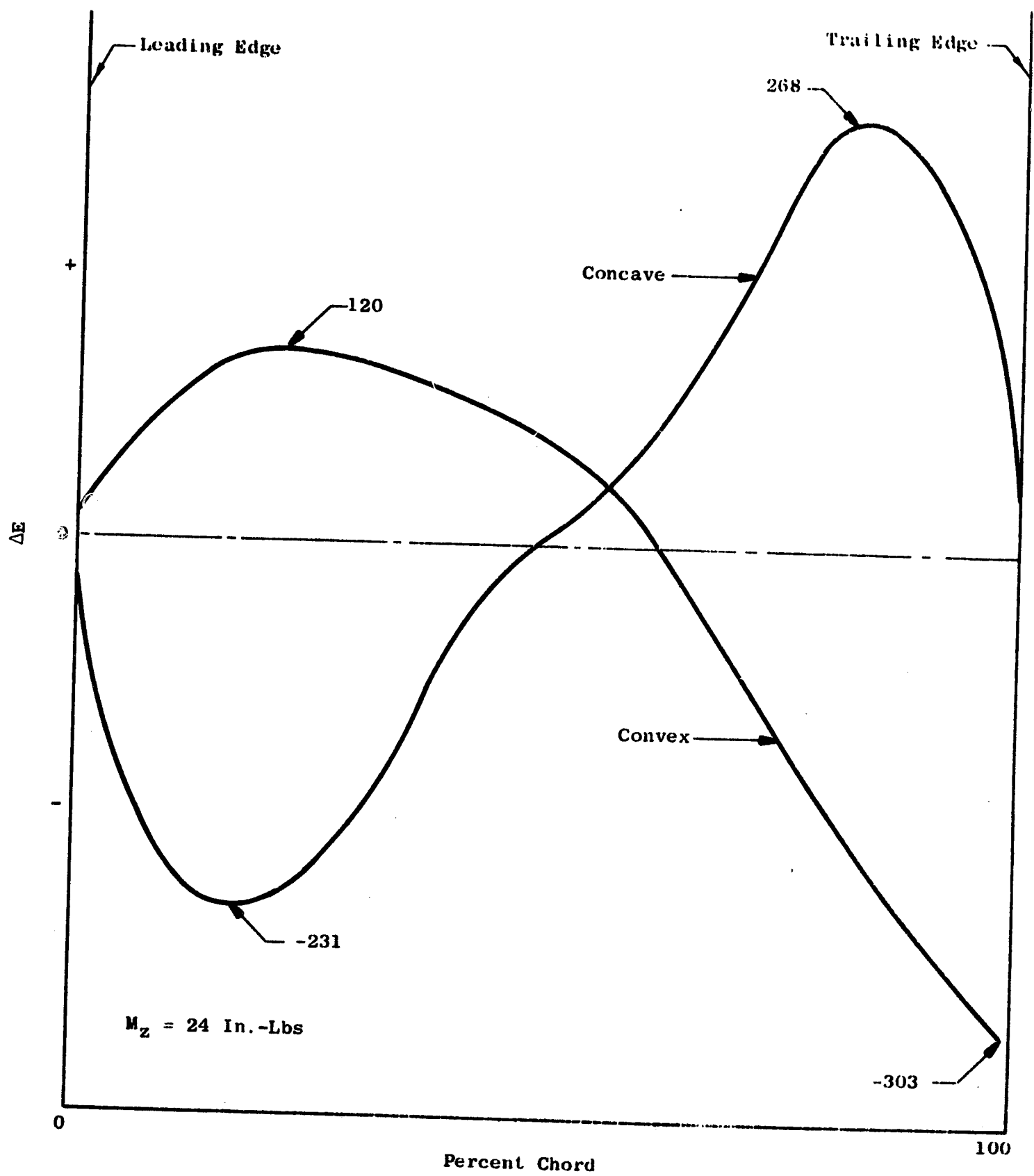


Figure 64. Development Stage 1 Blade Strain Distribution

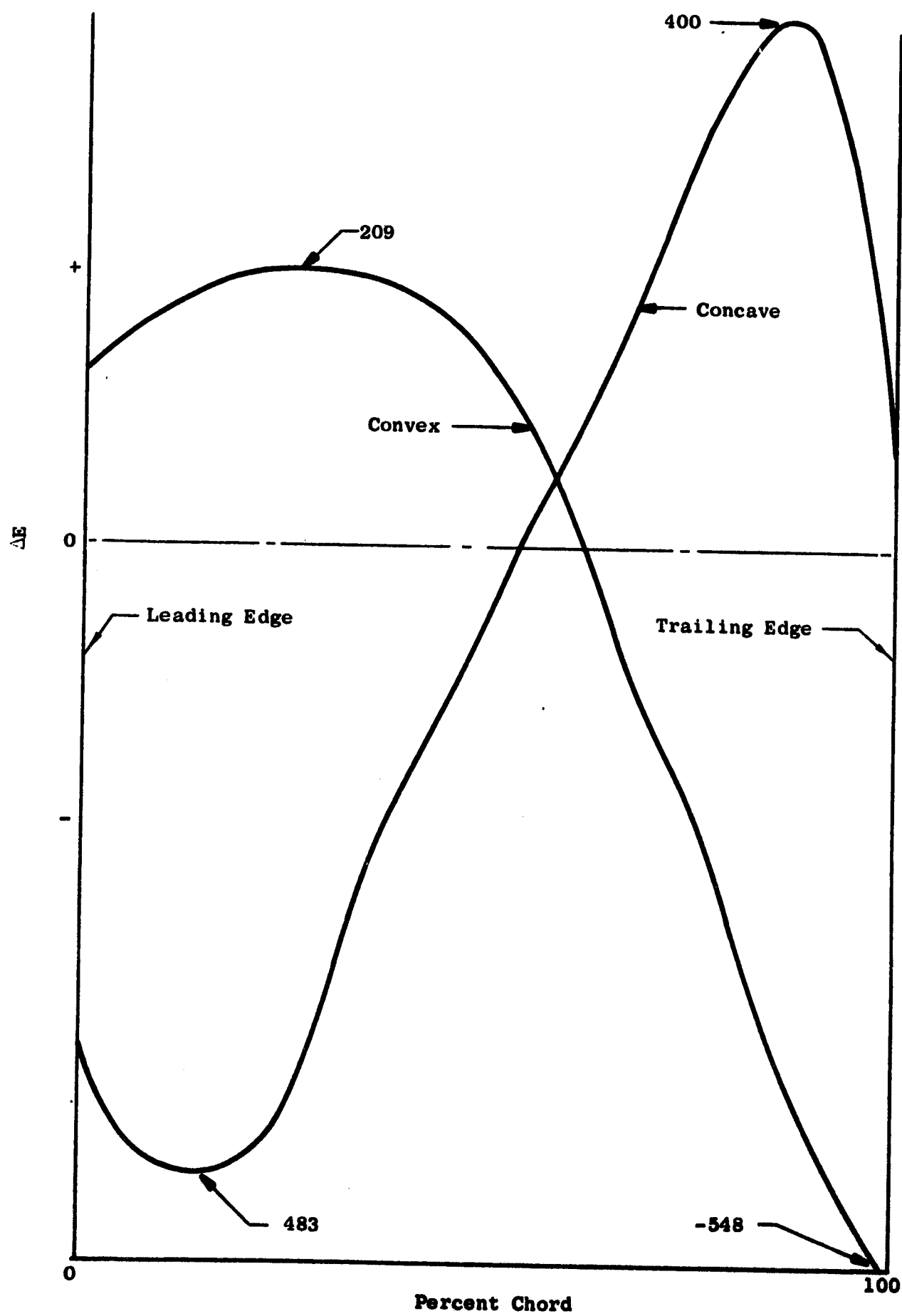


Figure 65. Development Stage 2 Blade Strain Distribution

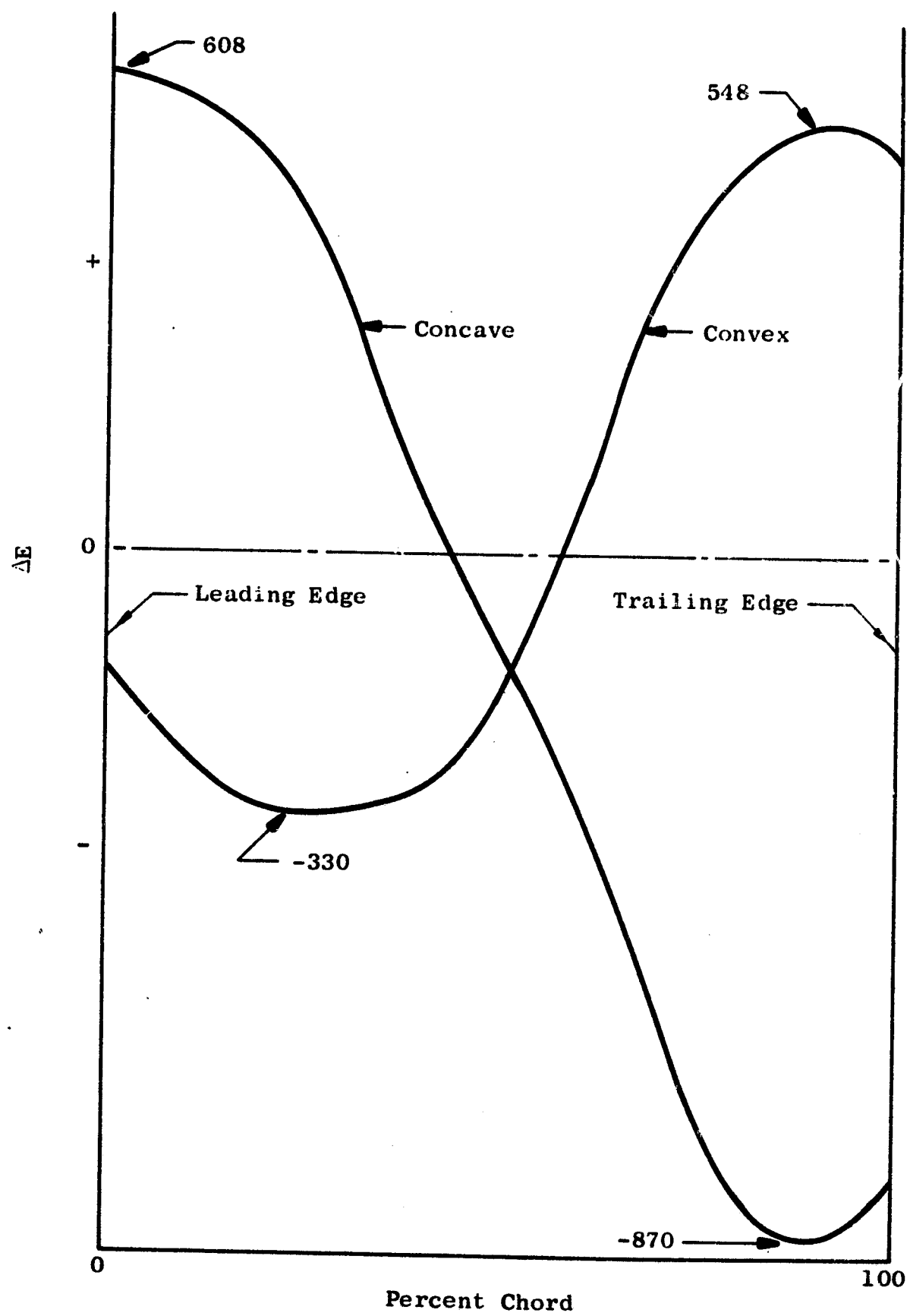


Figure 66. Development Stage 3 Blade Strain Distribution

Table XIII. Development Airfoil Tip Torsional End Effects

Stage	ΔE		$E\Delta E$		t_{sv}/t_m^*	K	
	LE	TE	LE	TE		LE	TE
1	120	268	2106	4703	47.19	0.4138	0.924
	-231	-303	-4054	-5318		-0.7966	-1.045
2	209	400	3668	7020	31.63	0.4834	0.925
	-483	-548	-8477	-9617		-1.117	-1.267
3	-330	-870	-5792	-15269	16.91	0.408	1.075
	608	548	10670	9617		-0.7517	-0.6775

$$\sigma_{ee} = \frac{KM_z t_m}{t_{sv}}$$

$$\therefore K = \frac{\sigma_{ee}}{M_z} \left(\frac{t_{sv}}{t_m} \right)$$

K	
LE	TE
0.48	0.95
-0.96	-1.15

$$^* (t_{sv}/t_m) \times 10^4$$

and gas loads were most severe, vibratory loads were determined which would place the airfoil stresses on the limit line of the modified Goodman diagram. The Twisted Blade Program is used to provide vibratory stress distributions (Figures 67, 68, and 69) for the first three fundamental vibration modes. This information, in conjunction with the static stress distribution, determines the maximum allowable vibratory loading on the blade and disc dovetails. The actual dovetail analysis was then performed using a method developed by H.J. Macke. The results are presented for the blade dovetail on Figures 70, 71, and 72, for the first flexural, second flexural, and first torsional vibration modes, respectively. It can be seen that, in all the cases, a minimum 10 percent margin exists between the blade airfoil and its attachment.

The final configuration of the A fan blade dovetail is shown in Figure 73. The perspective and definition of the loading for the dovetail analysis performed is described in Figure 74. The actual computer output is presented as Tables XIV, XV, and XVI.

The contact surfaces will have a copper/nickel/indium coating applied as an antifretting medium. This coating, along with the relatively low contact stresses, combines to eliminate dovetail fretting, and, at the same time, redistributes high local peak stresses. The dovetail surface is shot-peened and grit-blasted, prior to the coating application in the form of a plasma spray.

● Airfoil Tip Shroud

Rotor tip shrouds have the desirable effects of increasing blade frequencies and reducing the amount of blade untwist. What untwist does occur has been taken in account, by pretwisting those sections so they untwist into their nominal positions.

Figures 75 and 76 represent the current design of two seal teeth and 23-degree interlocks. The leading edge has been turned up to provide a rounded corner to the incoming airflow. The tip flowpath coordinates (hot) have been modified to include a shroud inclination of one degree from the trailing edge. This will insure a clean aerodynamic capture under all operating conditions.

While the design concept is very similar to that of other fan shrouds, structural complications did arise. These problems were created by the combination of large tip radius and a small number of blades. With only forty blades and a tip diameter at the stacking axis of 12.2574 inches, the shroud will overhang the supporting airfoil as much as two inches. The result is a structure which becomes limiting in deflection rather than stress level.

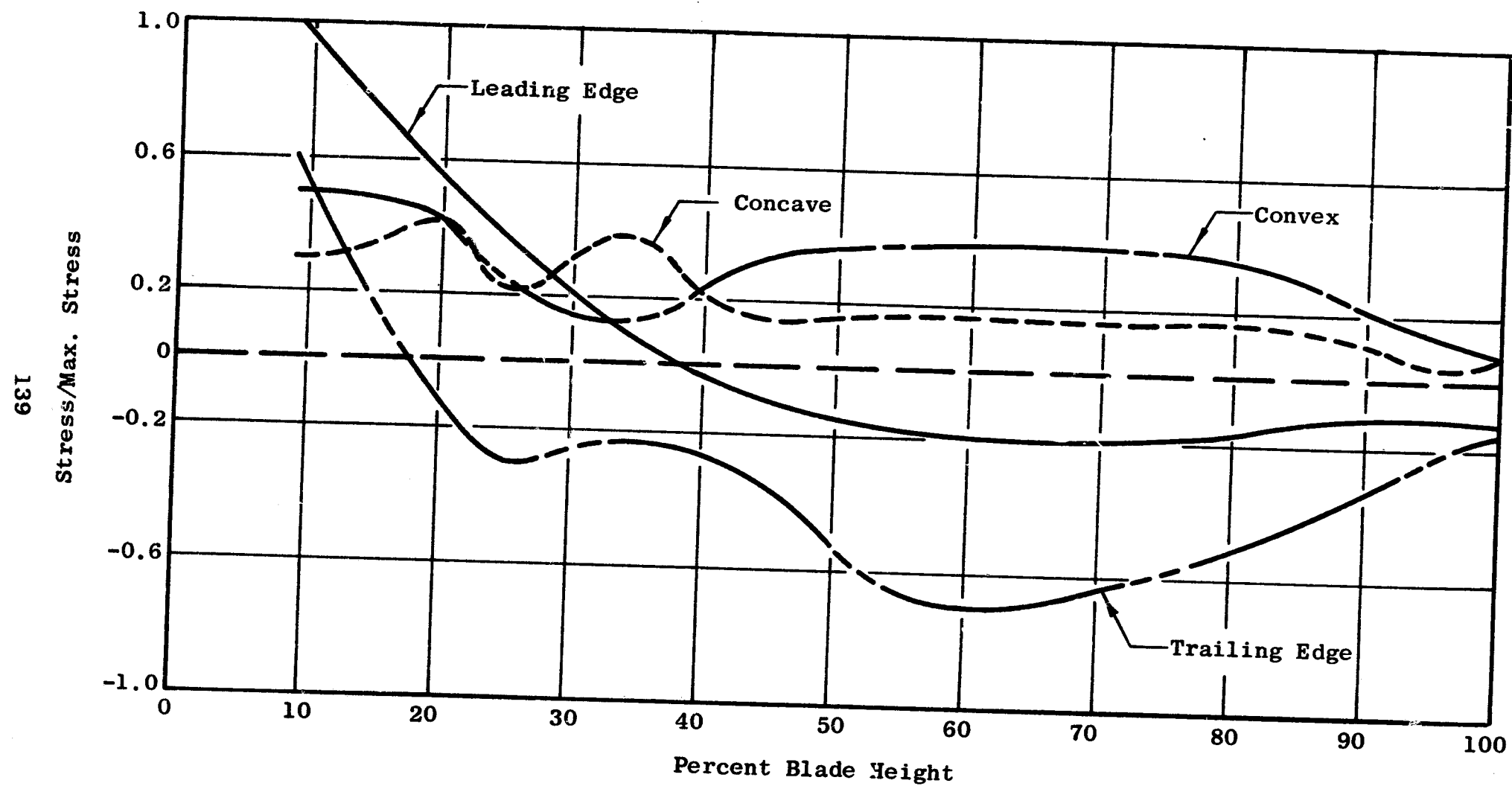


Figure 67. Fan A First Flexural Stress/Maximum Stress Vs Percent Blade Height for Ti6Al-4V @ 3881 RPM

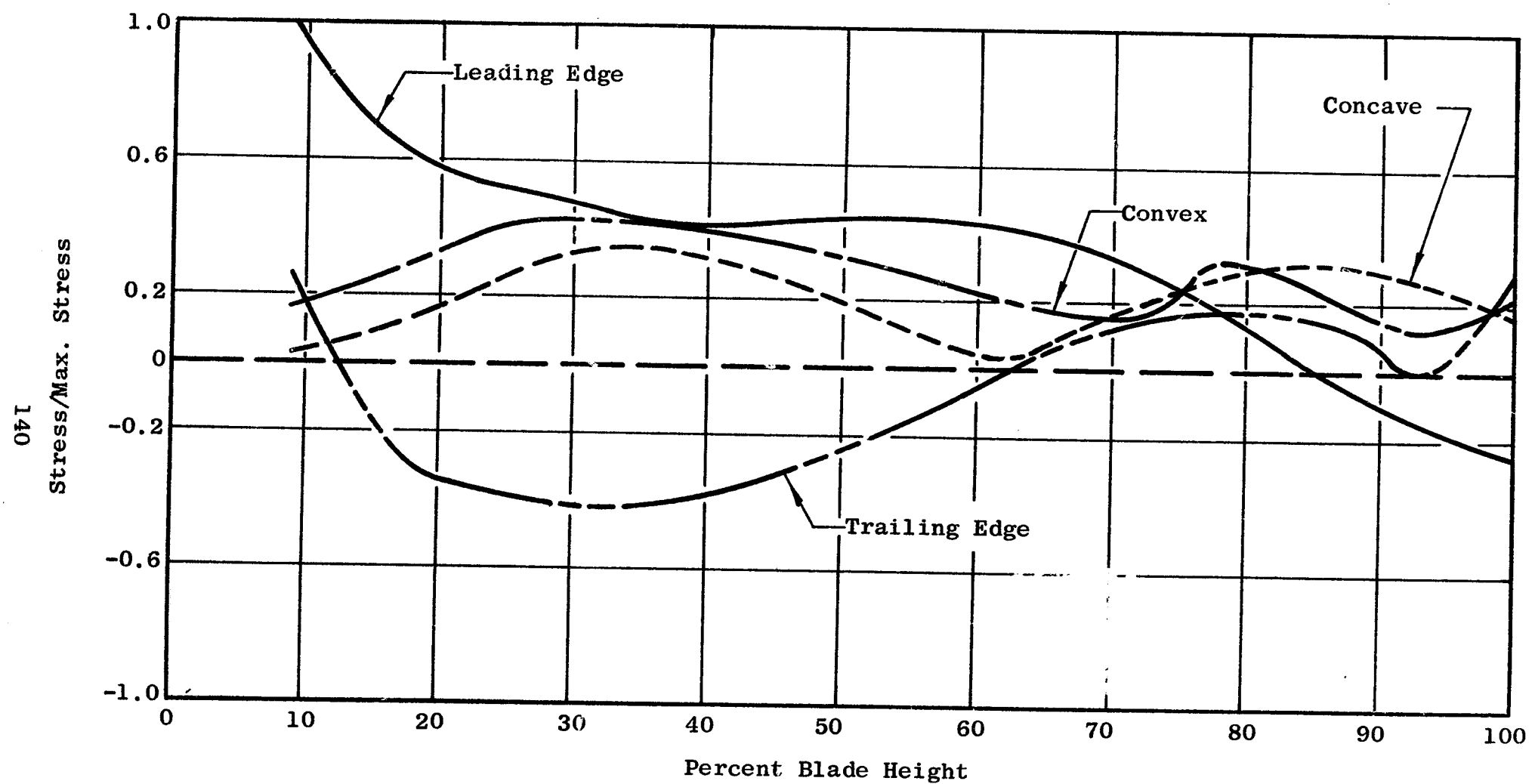


Figure 68. Fan A Second Flexural Stress/Maximum Stress Vs Percent Blade Height for Ti6Al-4V @ 3881 RPM

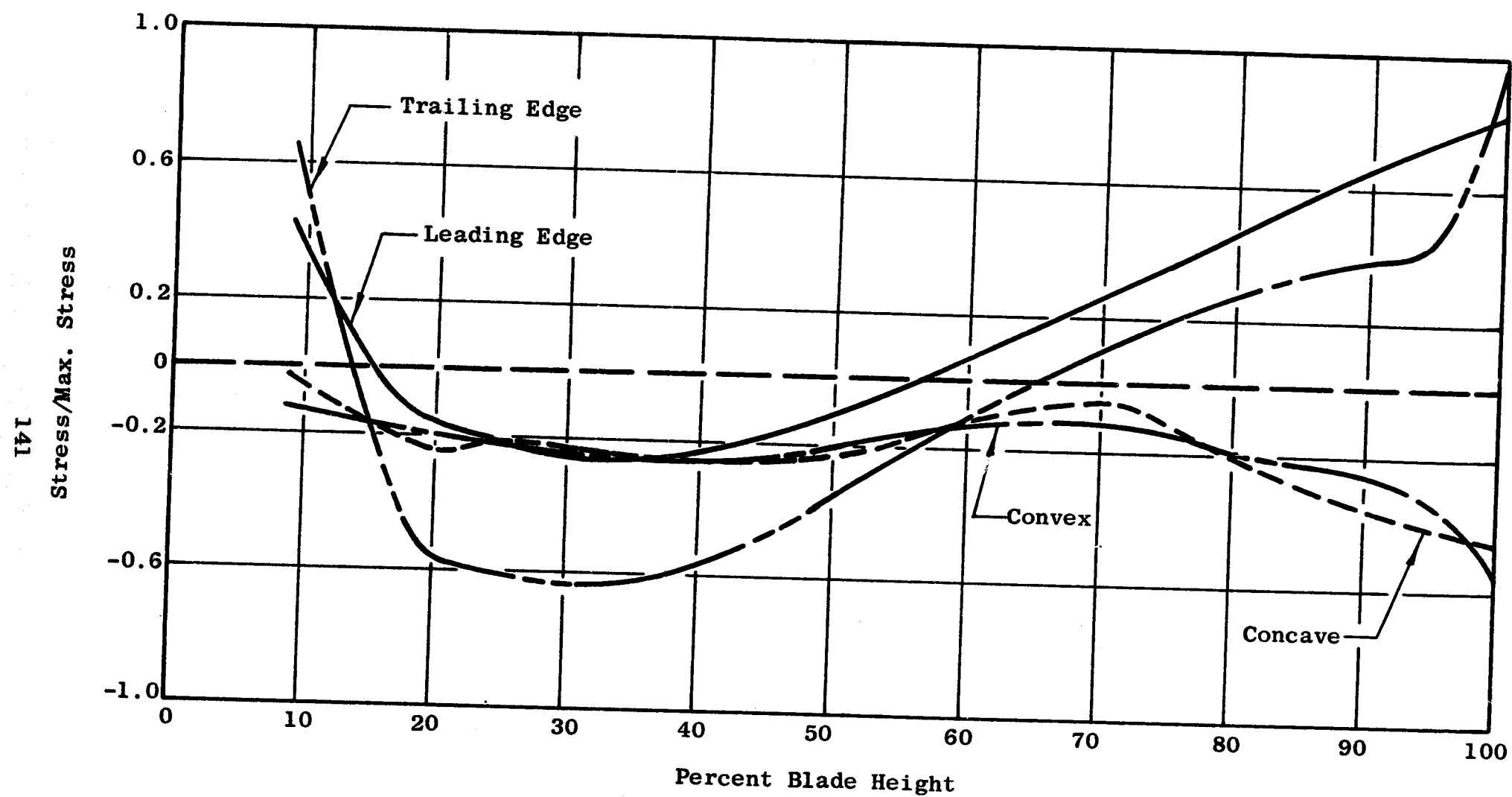


Figure 69. Fan A First Torsional Stress/Maximum Stress Vs Percent Blade Height for Ti6Al-4V @ 3881 RPM

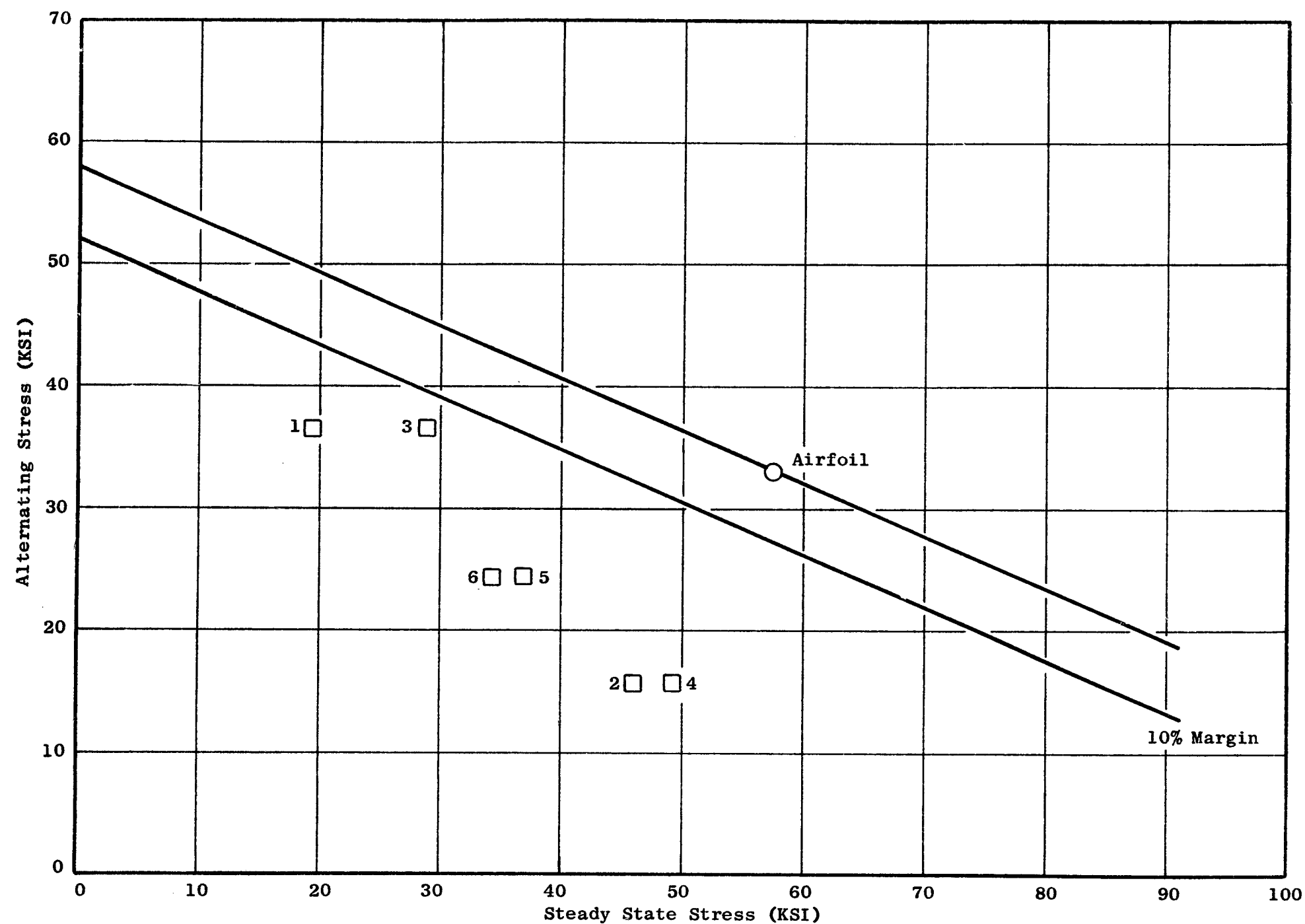


Figure 70. 6Al-4V Titanium (C50T88) Blade Dovetail 200°F Stress Range Diagram, Bending Alternating Stress (3 σ Deviation Included), First Flexural SLS @ 3881 RPM

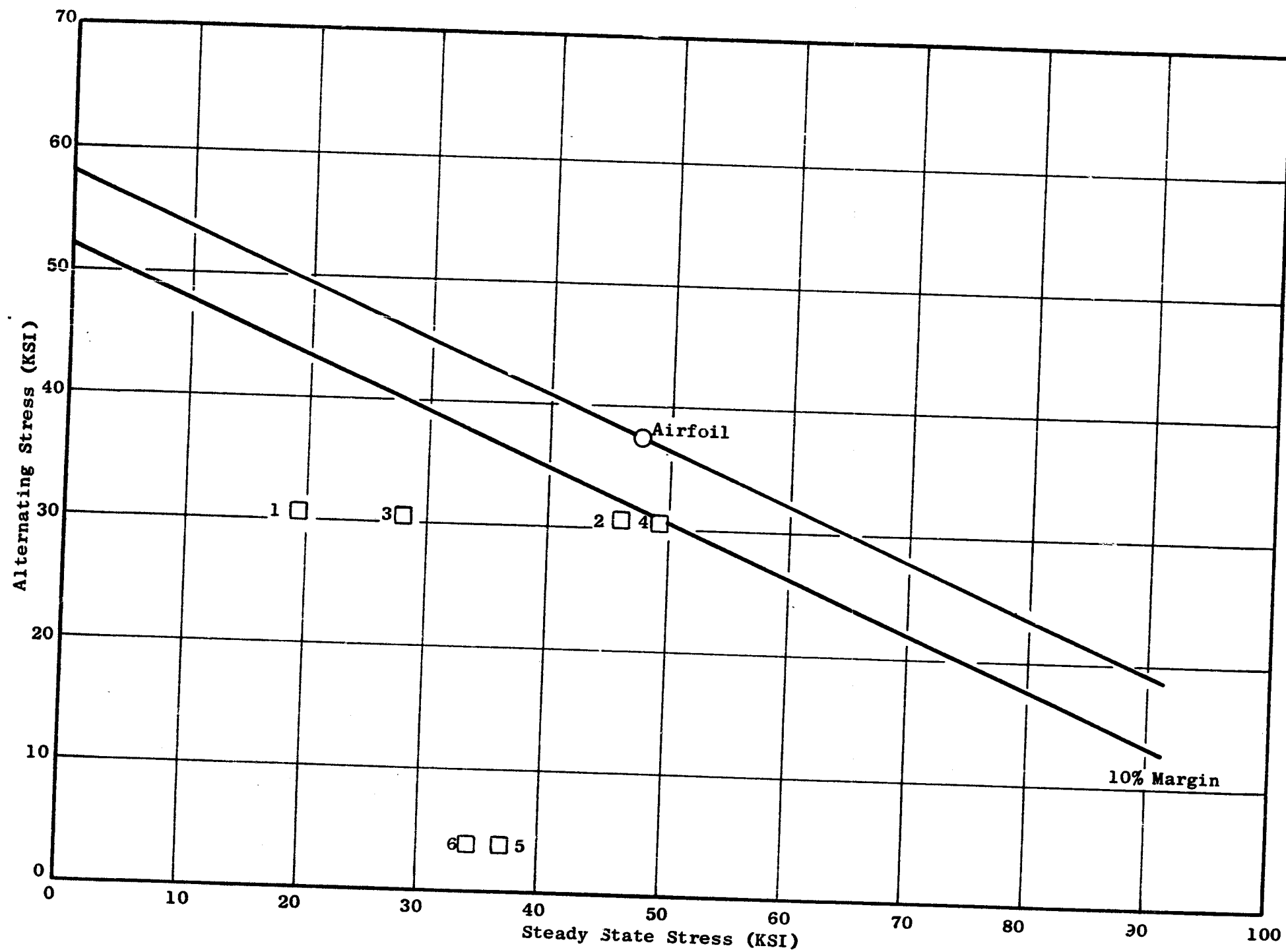


Figure 71. 6Al-4V Titanium (C50T88) Blade Dovetail 200°F Stress Range Diagram, Bending Alternating Stress (3σ Deviation Included), 2nd Flexural, SLS @ 3881 RPM

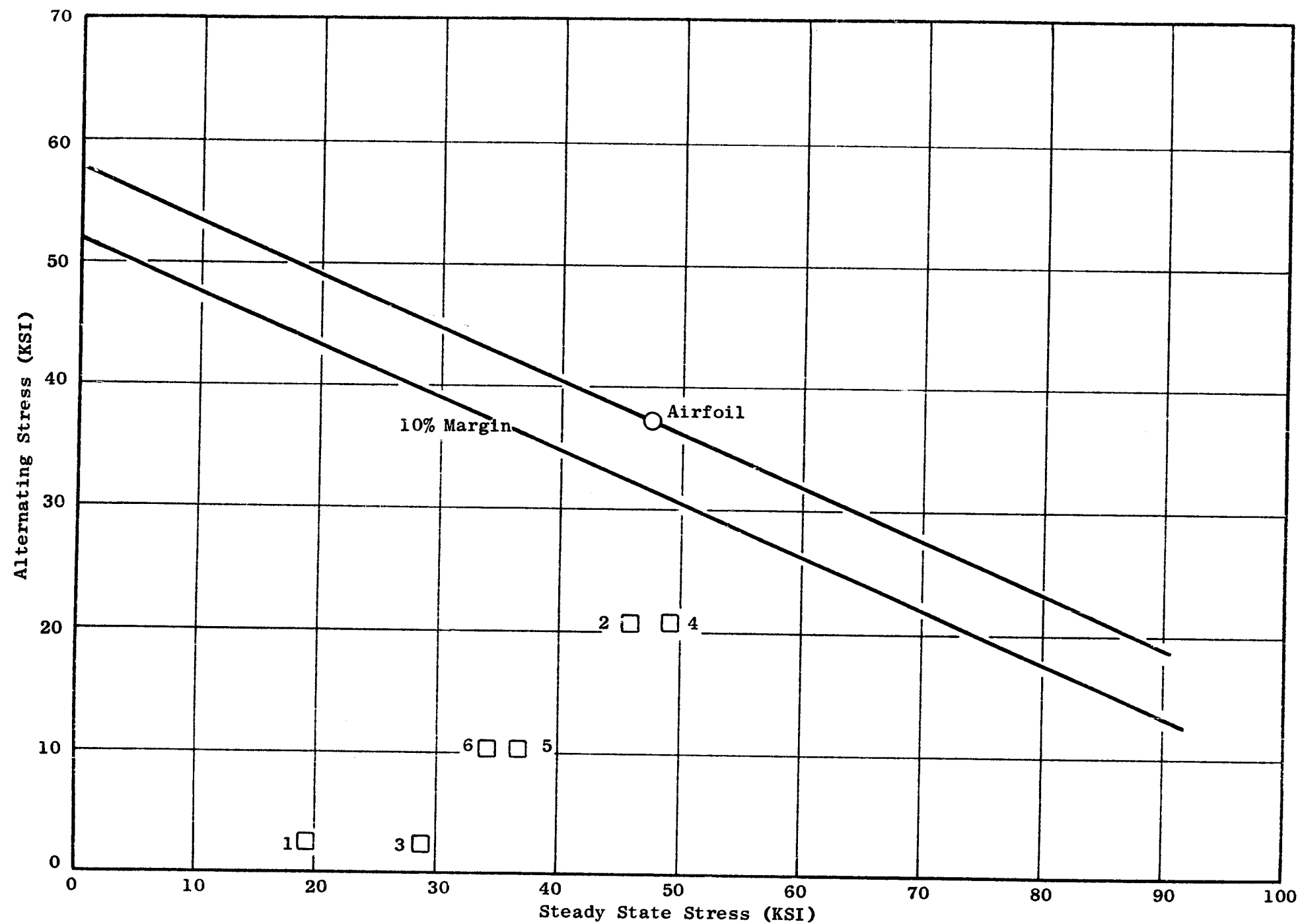


Figure 72. 6Al-4V Titanium (C50T88) Blade Dovetail 200°F Stress Range Diagram, Bending Alternating Stress (30 Deviation Included), First Torsional, SLS @ 3881 RPM

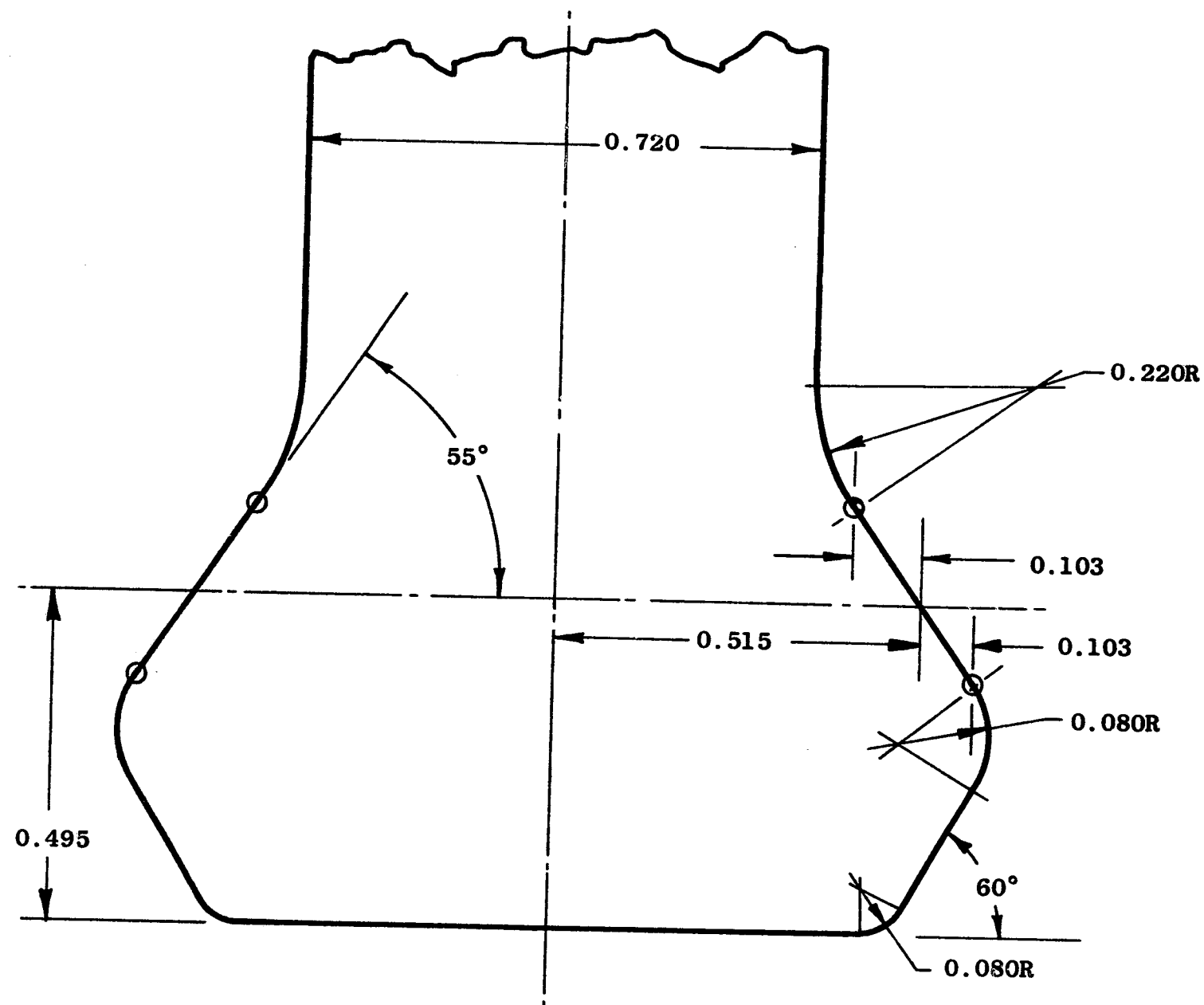
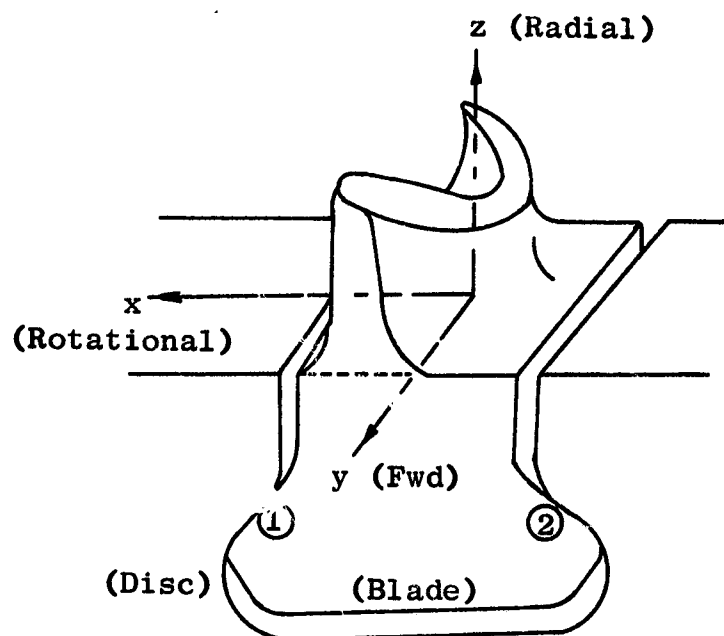
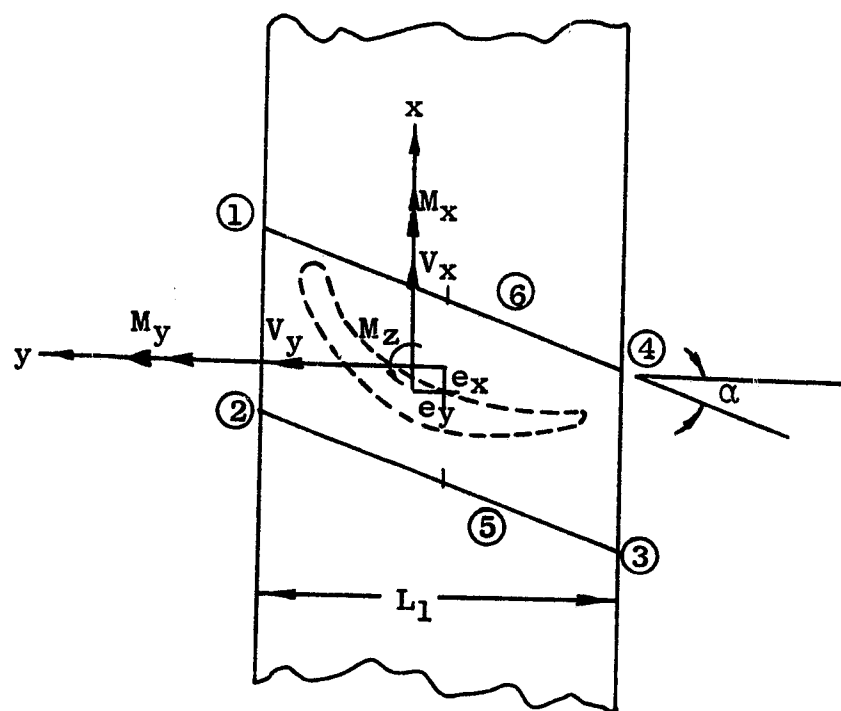


Figure 73. Fan A Blade Dovetail Configuration



(a) Perspective



(b) Loads and Locations

Defined Variables

M_x
 M_y
 M_z
 V_x
 V_y
 e_x
 e_y
 α
 L_1

$F_z = F_c$ (Out of Paper)

Figure 74. Definitions for Single-Hook Dovetail

Table XIV. Dovetail Stress Results (First Flex Mode)

<u>Loc</u>	<u>Total Stress</u>	<u>Neck Stress</u>	<u>Tang Stress</u>	<u>Crush Stress</u>	<u>Load S/V (*-Extreme)</u>
1 (S)	19327.9	7679.26	12599.	18611.6	6056.47
(V)	36538.4	28950.2	10412.3	10086.8	3282.39
2 (S)	45958.	29138.5	20085.4	29670.9	9655.32
(V)	-15769.4	-14153.3	1119.26	1084.28	352.84
3 (S)	27805.2	13763.5	15690.4	23178.5	7542.59
(V)	-36538.4	-28950.2	-10412.3	-10086.8	-3282.39
4 (S)	49150.3	30154.5	22416.1	33113.9	10775.7
(V)	15769.4	14153.3	-1119.26	-1084.28	-352.84
5 (S)	36963.3	21451.	17887.9	26424.7	8598.95
(V)	24459.5	-21551.7	-4646.49	-4501.28	-1464.78
6 (S)	34318.3	18916.9	17507.5	25862.8	8416.09
(V)	24459.5	21551.7	4646.49	4501.28	1464.78

Table XV. Dovetail Stress Results, Second Flexural Mode

LOC	TOTAL STRESS	NECK STRESS	TANG STRESS	CRUSH STRESS	LOAD S/V (*-EXTREME)
1 (S)	19327.9	7679.26	12599.	18611.6	6056.47
(V)	30639.9	18166.1	14557.3	14102.4	4589.1
2 (S)	45958.	29138.5	20085.4	29670.9	9655.32
(V)	30568.1	17951.9	14681.1	14222.3	4628.11
3 (S)	27805.2	13763.5	15690.4	23178.5	7542.59
(V)	-30639.9	-18166.1	-14557.3	-14102.4	-4589.1
4 (S)	40150.3	30154.5	22416.1	33113.9	10775.7
(V)	-30568.1	-17951.9	-14681.1	-14222.3	-4628.11
5 (S)	36865.1	21451.	17887.9	26424.7	8598.95
(V)	3949.21	-107.092	61.8762	59.9424	19.5061
6 (S)	34212.6	18916.9	17507.5	25862.8	8416.09
(V)	3949.21	107.092	-61.8762	-59.9424	-19.5061

Table XVI. Dovetail Stress Results, First Torsional Mode

LOC	TOTAL STRESS	NECK STRESS	TANG STRESS	CRUSH STRESS	LOAD S/V (*-EXTREME)
1 (S)	19327.9	7679.26	12599.	18611.6	6056.47
(V)	-2518.98	1405.38	-3726.25	-3609.79	-1174.67
2 (S)	45958.	29138.5	20085.4	29670.9	9655.32
(V)	-20594.5	-14930.6	-7229.47	-7003.53	-2279.04
3 (S)	27805.2	13763.5	15690.4	23178.5	7542.59
(V)	2518.98	-1405.38	3726.25	3609.79	1174.67
4 (S)	49150.3	30154.5	22416.1	33113.9	10775.7
(V)	20594.5	14930.6	7229.47	7003.53	2279.04
5 (S)	36881.7	21451.	17887.9	26424.7	8598.95
(V)	10380.	-8168.01	-1751.61	-1696.87	-552.183
6 (S)	34230.5	18916.9	17507.5	25862.8	8416.09
(V)	10380.	8168.01	1751.61	1696.87	552.183

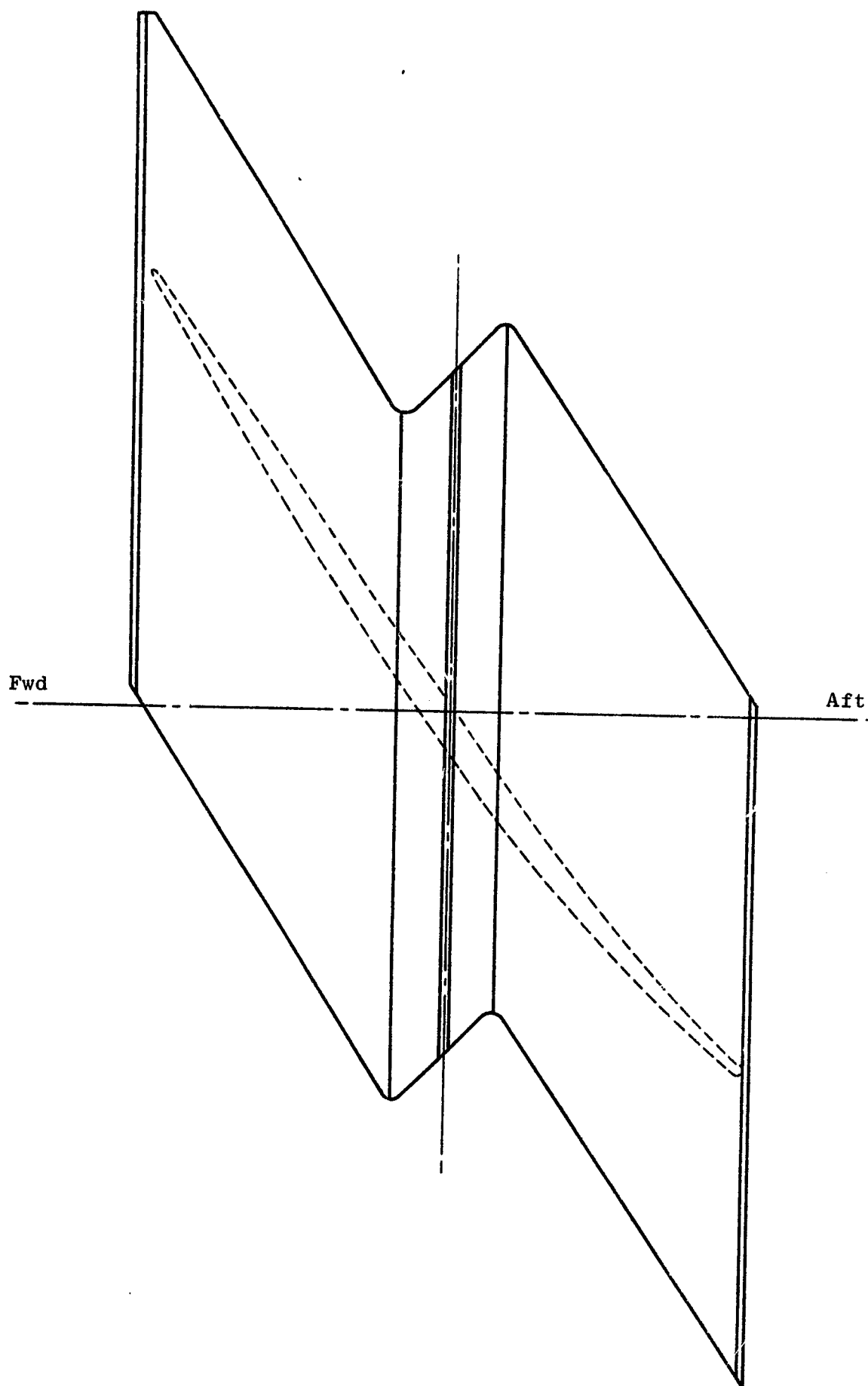


Figure 75. Fan A Tip Shroud Schematic, Top View

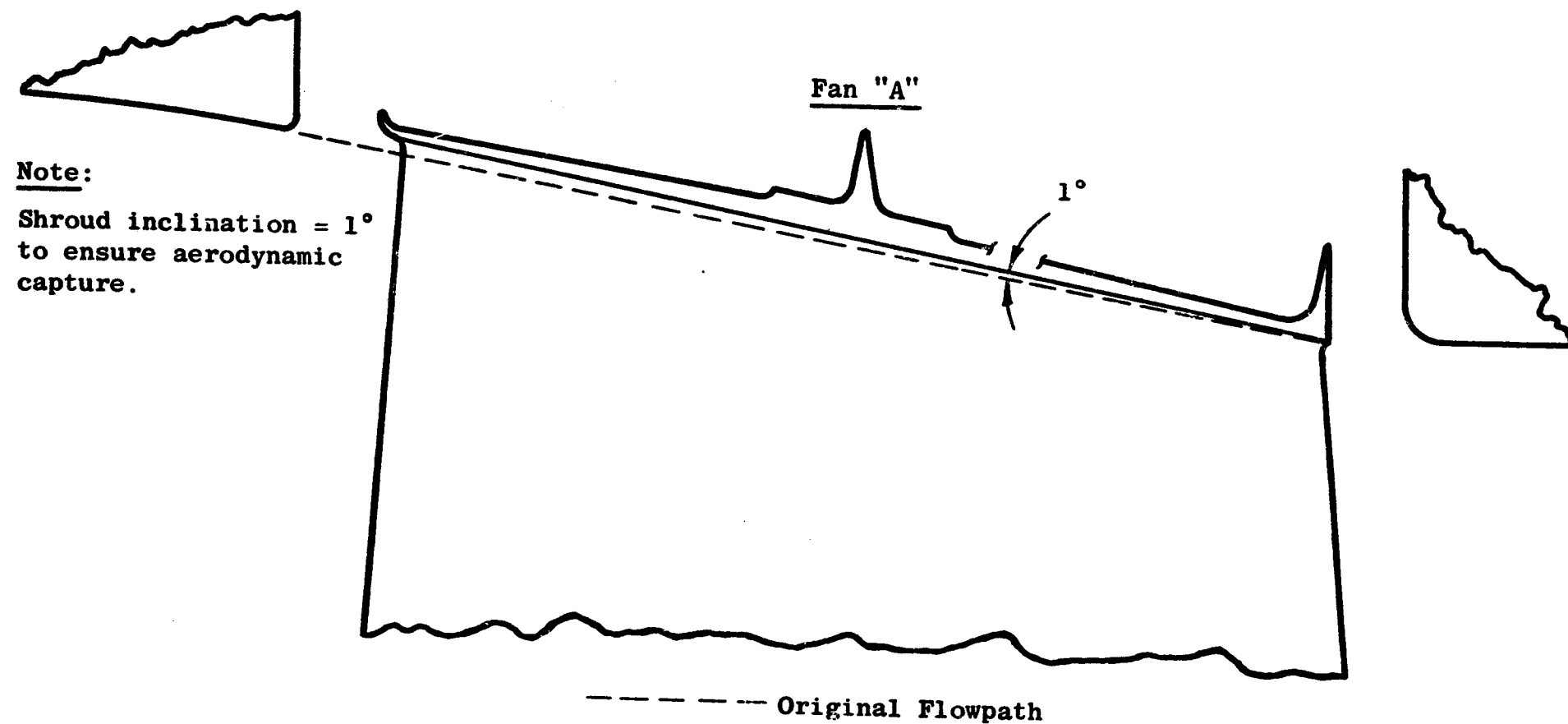


Figure 76. Fan A Detail of Shroud Inclination

An analysis was performed using the plate and beam capability of the MASS Program. This program allows for a model of the system to be constructed out of rectangular and triangular plates in combination with straight and curved beams. The greatest limitation found, was that the beam and plate elements have to be of constant section. Thus, tapering of both plates and beams is reduced to the input of step functions.

Two methods of shroud construction were analyzed. The first was a shroud of constant thickness tangentially but tapered axially which would allow the shroud to be turned on a VTL or similar machine. The deflections are about the airfoil Least Moment of Inertia (LMI) axis, and this machining approach did not result in a steep enough taper in the plates to hold deflections to an acceptable limit. The front right corners of both the forward curl and interlock were shown to have deflected 0.277 inch.

In addition to the already present ribs comprising the middle seal tooth and aft seal tooth, a secondary circumferential rib was added to each shroud panel. These ribs were tapered sufficiently to where they should easily support their own mass with minimal deflection. MASS analysis, however, showed that deflections increased to 0.316 inch at the front right corner. Close inspection of the external forces on the rib joints showed that, contrary to what was expected, the plates were carrying the ribs. Further stiffening of these ribs proved to be of no avail. The rib effective torsional stiffness was not enough to prevent the deflection and rotation due to the 33-degree offset between the rib and the shroud LMI axis.

The second shroud model utilized small rectangular plates parallel to the axis of deflection and a taper ratio of 5. This results in a maximum plate thickness adjacent to the airfoil of 0.150 inch and, along the edge, a thickness of 0.030 inch. The radial deflections for this shroud model are less than 0.090 inch which is acceptable. These deflections will be compensated for in the machining of the shroud so that the design flowpath will be achieved at the operational speed.

Another important cold dimension will be the distance across the shroud interlock. It will be seen later that the locking-up of the shroud is extremely important to the vibration characteristics of this blade. Therefore, dimensions are being specified which will result in a slight shroud interference and zero speed locking.

5.1.1.1.3 Disc Design

The disc design utilized in the Fan A rotor has been analyzed for both steady state and vibratory loading. For reliability and durability, no bolt holes pass through the disc web, reducing the problems of fretting and low cycle fatigue. Where bolt holes are necessary, they have been located in areas where the biaxial stress fields can be determined, i.e., rim flanges. In addition, scalloping has eliminated the hoop stress at the edge of the holes, decreasing further the maximum effective stress and increasing the low cycle fatigue life of the disc.

The disc dovetail has been elongated radially to allow for the replacement of individual blades; or, the entire stage may be removed by direct access to the fan shaft bolts.

This disc has been designed to withstand a continuous 15-percent overspeed without failure.

- Steady State Stresses

To analyze the steady state stress environment of this rotor disc, two analytical tools were employed.

First, the disc was analyzed for radial rim loading and thermal stress only. This provides a quick check into the disc elastic stresses unencumbered with bending. A plot of radial, tangential, and effective disc stresses is presented in Figure 77.

Afterward, the disc was analyzed in conjunction with the rest of the fan system. The General Electric SNAP program, which analyzes shells of revolution, was used. This program allows for centrifugal loading, pressure, axial loads, and temperature gradients. The entire system comprised of the disc, shaft, spinner, seal, and retainers was modeled into this program. Figure 78 illustrates a schematic of the Fan A rotor with the balloons containing the maximum surface effective stress for that individual component.

Of primary importance, aside from stress level, is deflection. The disc has been constructed so that, when acted upon by all external forces, the rim rotation is a minimum.

The information on radial, axial, and rotational deflection was taken into account when the cold dimensions of the disc-blade system were determined. Thus, at speed, the "hot" aerodynamic flowpath can be realized.

- Disc Dovetails

The disc dovetails were analyzed using the Macke dovetail program applied

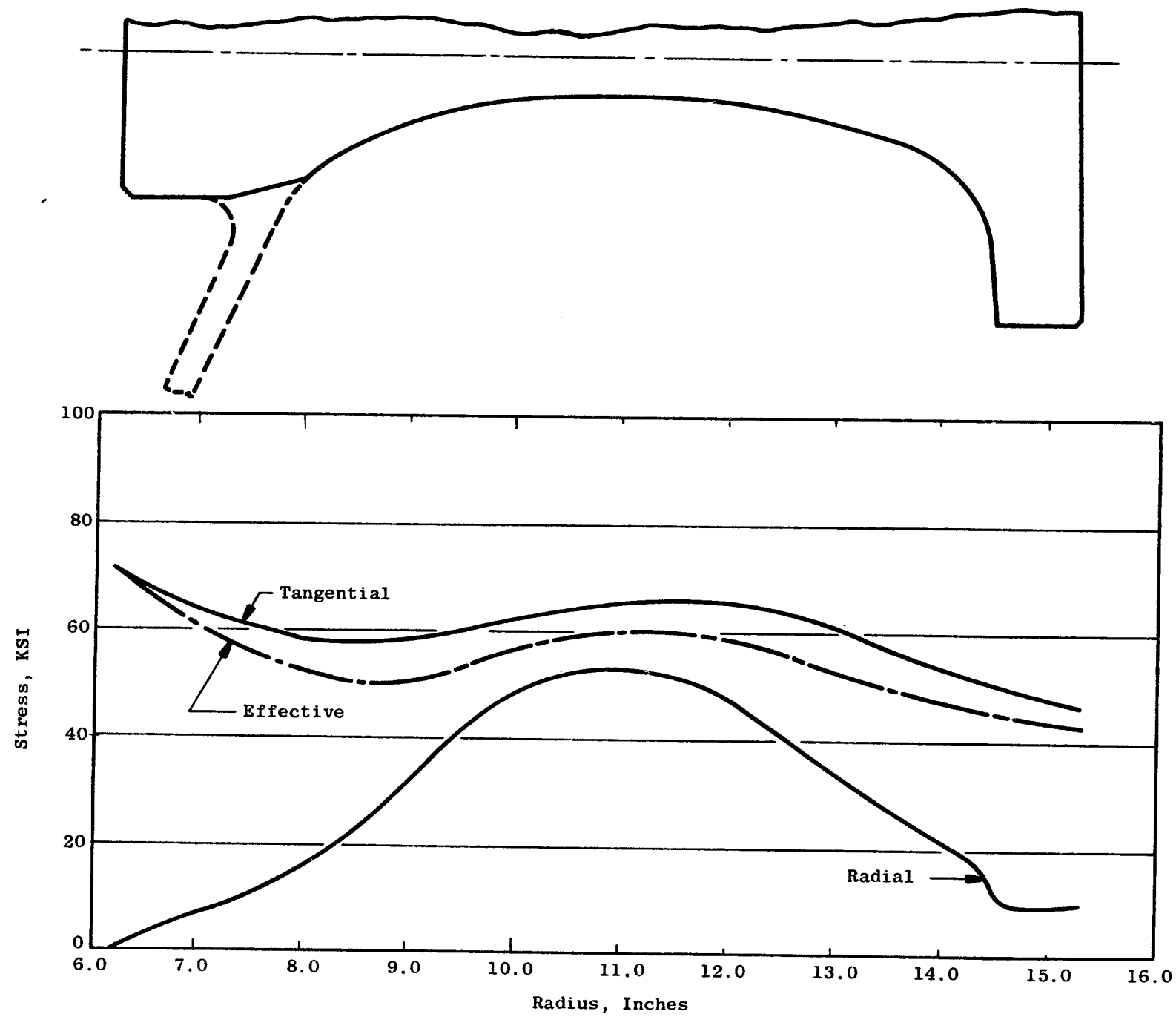


Figure 77. Fan A Disc Stress Distribution

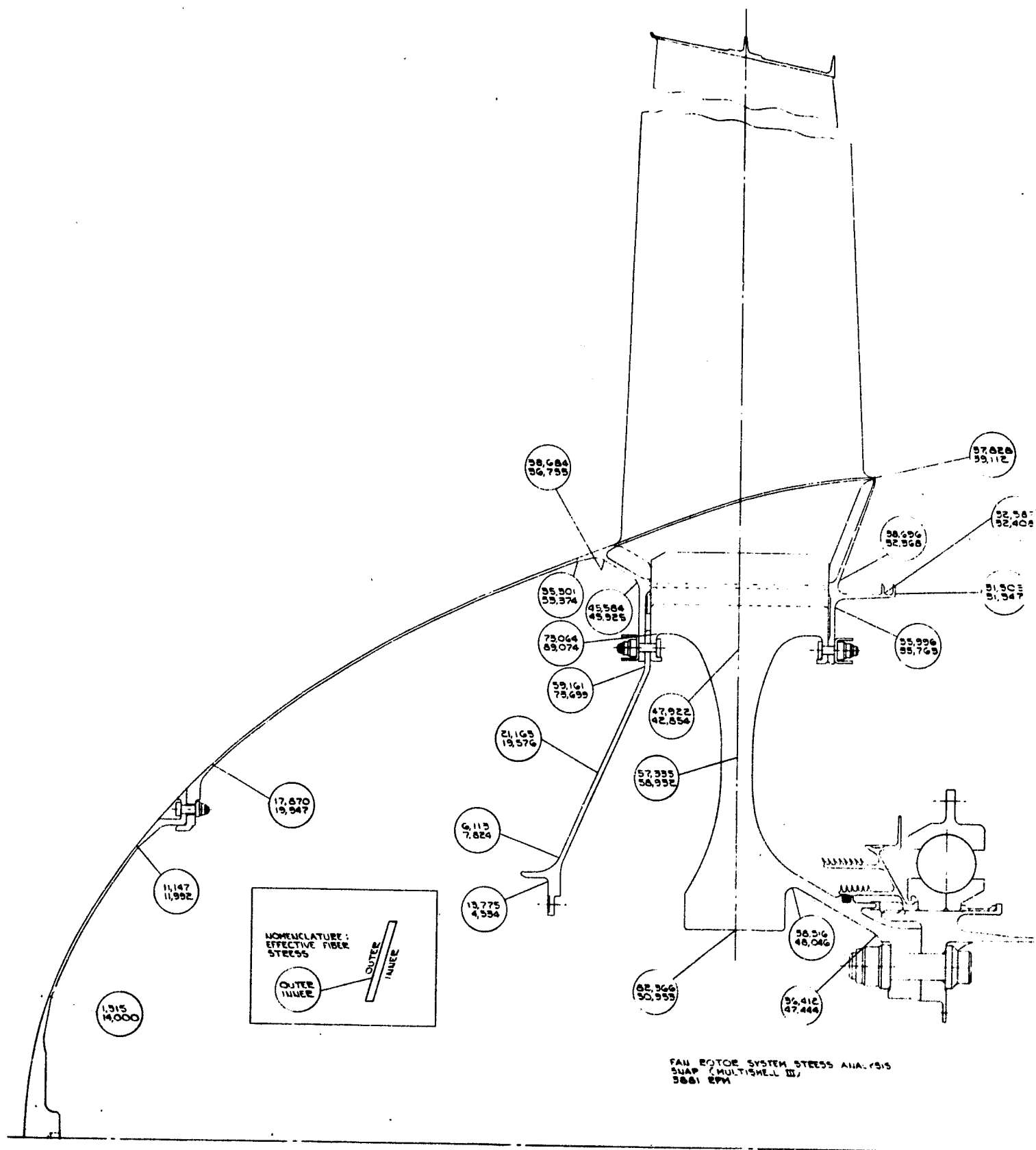


Figure 78. Fan A Stress Analysis Results

to a disc. The steady state and vibratory loads are identical to that of the blade. Figure 79 shows the Goodman diagram for the Fan A disc. As it should be, the disc dovetail is as strong, if not stronger, than the blade attachment.

- Burst

An experimental/analytical procedure has been developed to predict the bursting speed (N_T) of rotor discs.

Calculation of this speed, N_T , is obtained from the expression:

$$N_T = S (N_P - N_E) + N_E, \text{ where,}$$

N_E = Speed at which the average tangential stress equals the smooth-bar ultimate tensile strength

S = Empirical factor based upon the material's notch strength ratio

The following values were obtained for the Fan A rotor disc:

$$S = 0.32$$

$$N_P = 6105 \text{ rpm}$$

$$N_E = 5355 \text{ rpm}$$

$$\therefore N_T = 5374 \text{ rpm}$$

5.1.1.1.4 Coupled Blade-Disc System Vibration Analysis

An analysis was undertaken to investigate the possibility of a 2- and 3-nodal diameter system resonance in the Fan A low pressure compressor. As part of this analysis, the effectiveness of varying the rim torsional stiffness was investigated as a means of tuning the 2-diameter resonances.

This analysis, while somewhat routine in execution, is not particularly straight forward due to the limited amount of experimental correlation available at this time to guide engineering assumptions for this complicated system. Uncertainties exist as to:

- a) Sensitivity to assumptions made to determine disc rim stiffness

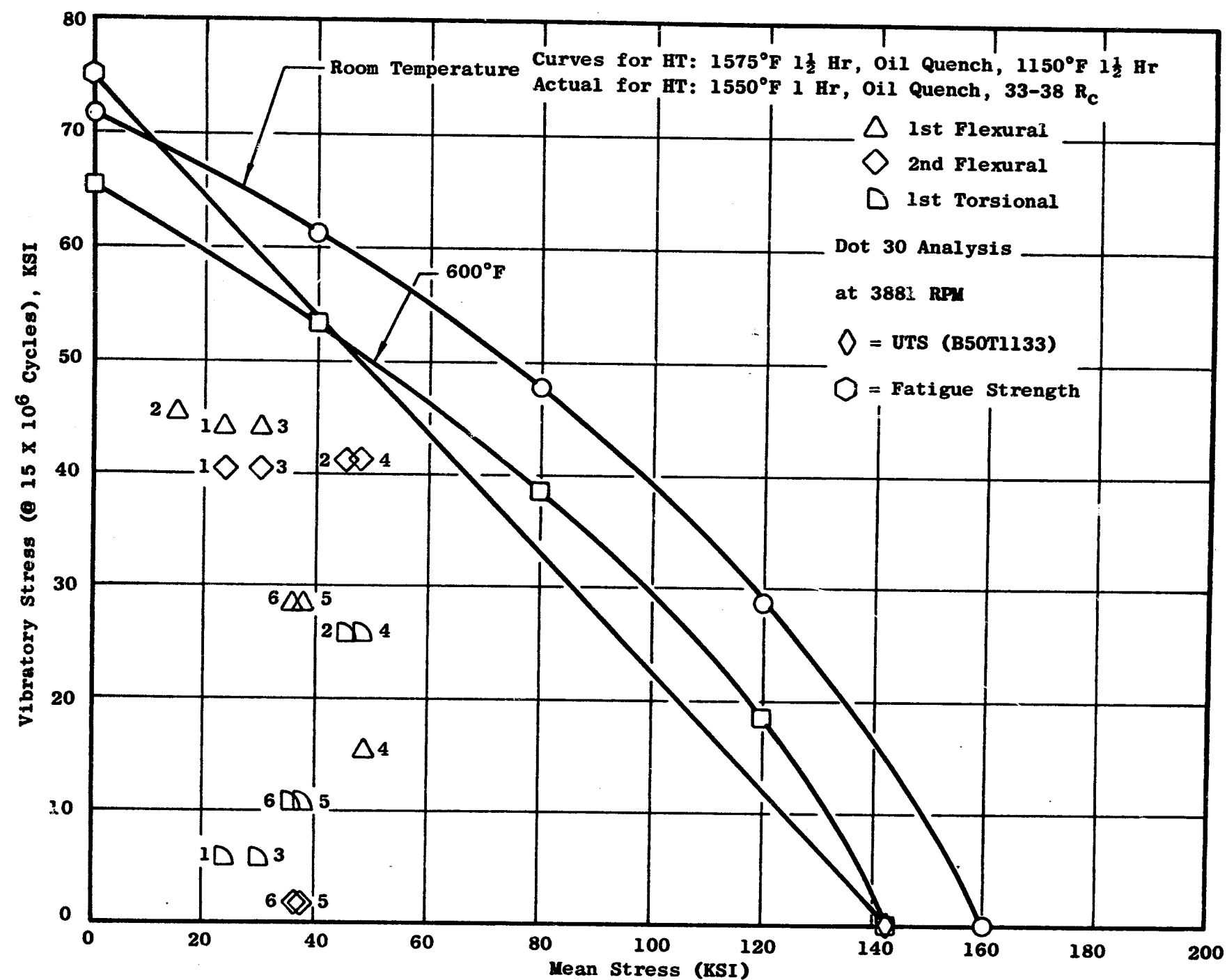


Figure 79. Fan A Disc Dovetail Stress Range Diagram for 4340 Steel (B50T1133)

- b) The degree of tip shroud slipping and/or damping
- c) The ability to treat properly the shaft structure of this overhung disc

A schematic of the disc and spacer structure is shown in Figure 80. For the purposes of stiffness calculation, the spacer was idealized as a cone with a constant thickness equal to the minimum permissible thickness on the detail drawing. The Sandwich Shell Program was run to compute the influence coefficients at the disc-shaft interface with the shaft's other end fixed against any deflection. This was done at both 2-nodal and 3-nodal diameters. All runs were made at zero rpm and zero frequency. The influence coefficient matrix which resulted had to be made symmetric by averaging the cross terms before proceeding.

The three-by-three coefficient matrix representing the forces for unit axial, radial, and rotational displacements was converted to a two-by-two reaction matrix on the disc. To enter this into the blade-disc program, 3 points were chosen along the span of the disc separated by a distance, a , as shown in Figure 80. Attached to these points are translational spring constants, K_1 and K , and a moment spring, Λ , calculated from the disc reaction matrix.

The method of treating the disc is essentially identical with the method used many times previously. In order to get a good steady stress distribution the disc input was continued all the way through the wide flareout to the inner bore. The thin plate theory of the disc-blade program, of course, does not apply in this region; however, the bending displacements are so small in this region that even gross errors will not affect the answers.

The stiffness of the rim was calculated assuming that the rim has the same stiffness as a solid ring whose cross section extends up to the bottom of the dovetail pressure face and as dead load from there radially outward. The moment of inertia of this ring was calculated using a GE time-sharing computer program. The rim torsional stiffness was calculated using two different methods. First, from "Formulas For Stress and Strain" by Roark, a torsion stiffness for a tee section representing the disc rim was calculated. This value, 16.7, was compared to that found using the program Flux Plot. The latter uses a membrane analogy to determine the torsional stiffness. Figure 81 represents the disc rim with contour lines depicting the membrane deflection. The volume bounded by this deflected membrane is one-half the section's torsional stiffness. This value proved to be 11.576, or about 67 percent smaller than that calculated by hand. The program was run using both values to determine the sensitivity to rim torsional stiffness.

The blade section properties were taken from the Twisted Blade Program

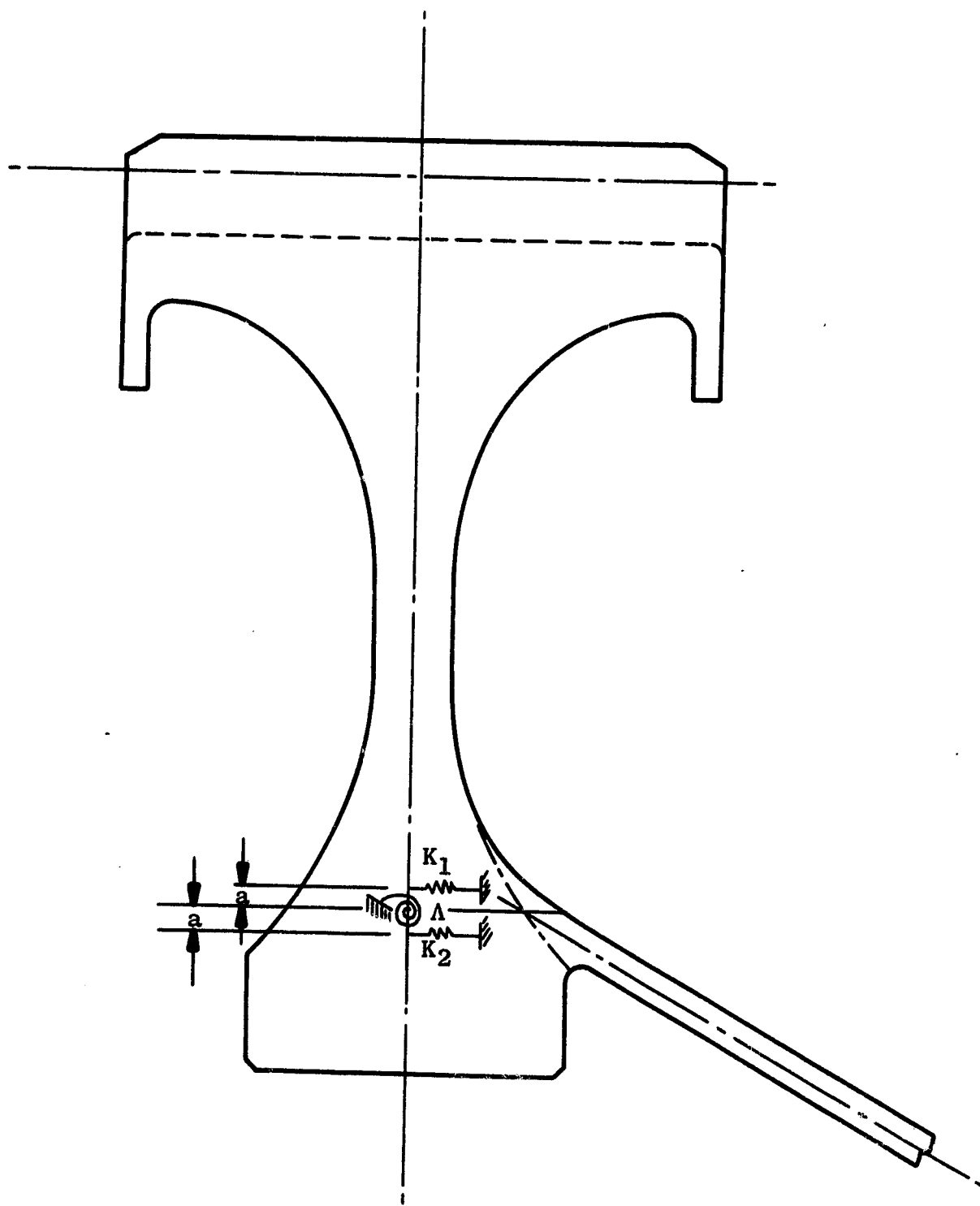


Figure 80. Coupled Blade-Disc Model Schematic

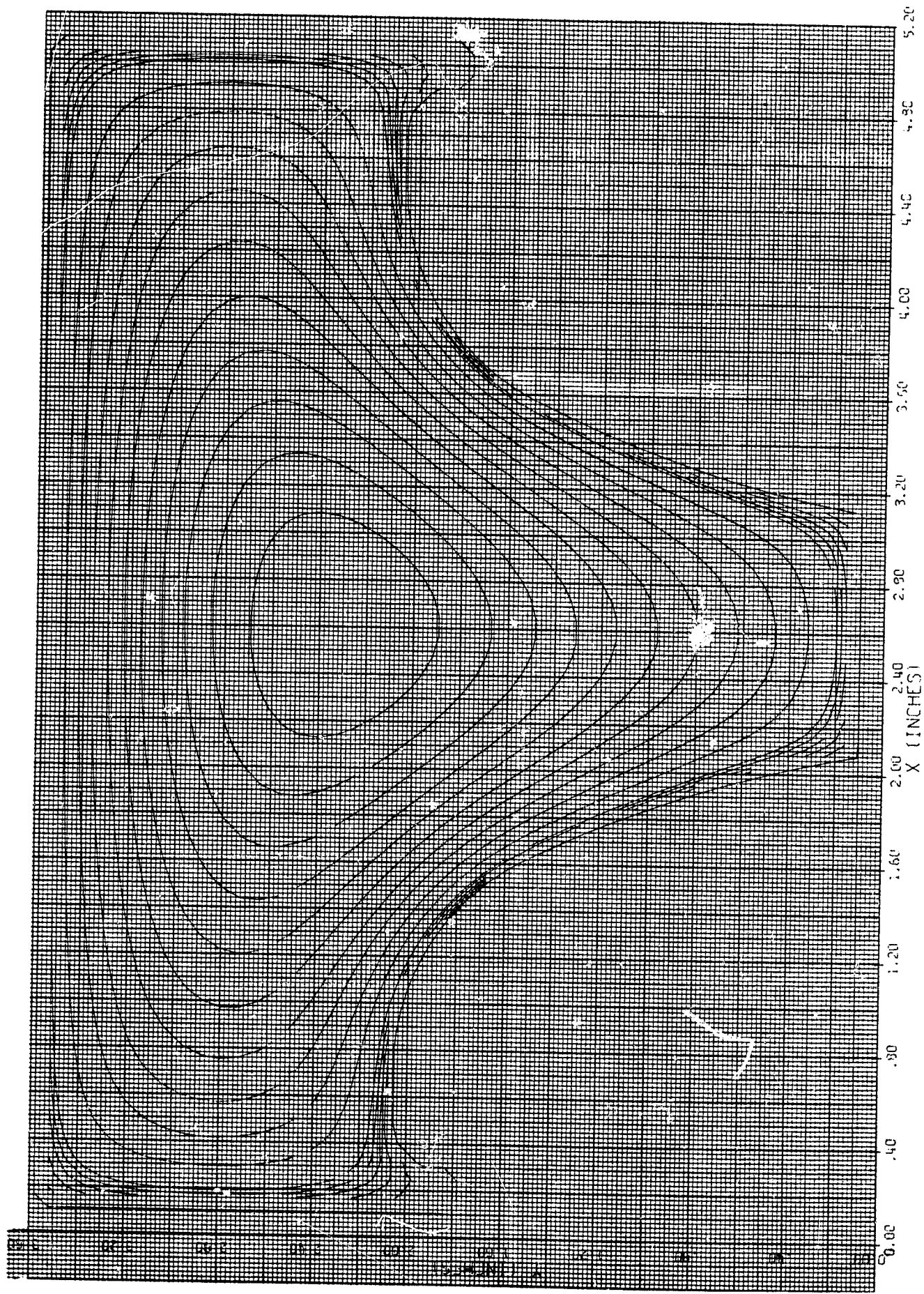


Figure 81. Membrane Analysis - Fan A Disc Rim

previously run to supply individual blade natural frequencies. Two sets of tip boundary conditions were used:

$$\text{Tip fixed tangentially } u = \phi_x = \phi = M_x = V_y = 0$$

$$\text{Tip free tangentially } \phi = M_x = M_y = V_x = V_y = 0$$

The first condition would hold up to the onset of slipping between shrouds; the second, after slipping becomes great.

Campbell diagrams (Figures 82 and 83) show the 2-diameter and 3-diameter responses of the system. The distinguishing characteristics of these modes are summarized below:

(All frequency values are at a speed of 3624 rpm.)

1. Tip Fixed Tangentially

A) 2 Diameters (Figure 84)

First mode (158 cps) is essentially first flexural of the blades with the disc having a strong axial mode evident in d_v/d_z being nearly constant and $V_{\max.} \approx 10 u_{\max.}$ while being in phase.

Second mode (299 cps) is second flexural of the blades with U and V being out of phase and some wheel motion.

Third mode (665 cps)

B) 3 Diameters

First mode (218 cps) is essentially the first flexural of the blade with a strong disc axial mode in evidence.

Second mode (345 cps) is the second flexural of the blades with very little wheel motion.

Third mode (508 cps) shows very little wheel motion and a mode shape closely resembling that of first torsion.

2. Tip Free Tangentially

A) 2 Diameters (Figure 85)

First mode (86 cps) is the first flexural mode of the blade with little disc motion. Both U and V are in phase with $U_{\max.} \approx 3 V_{\max.}$

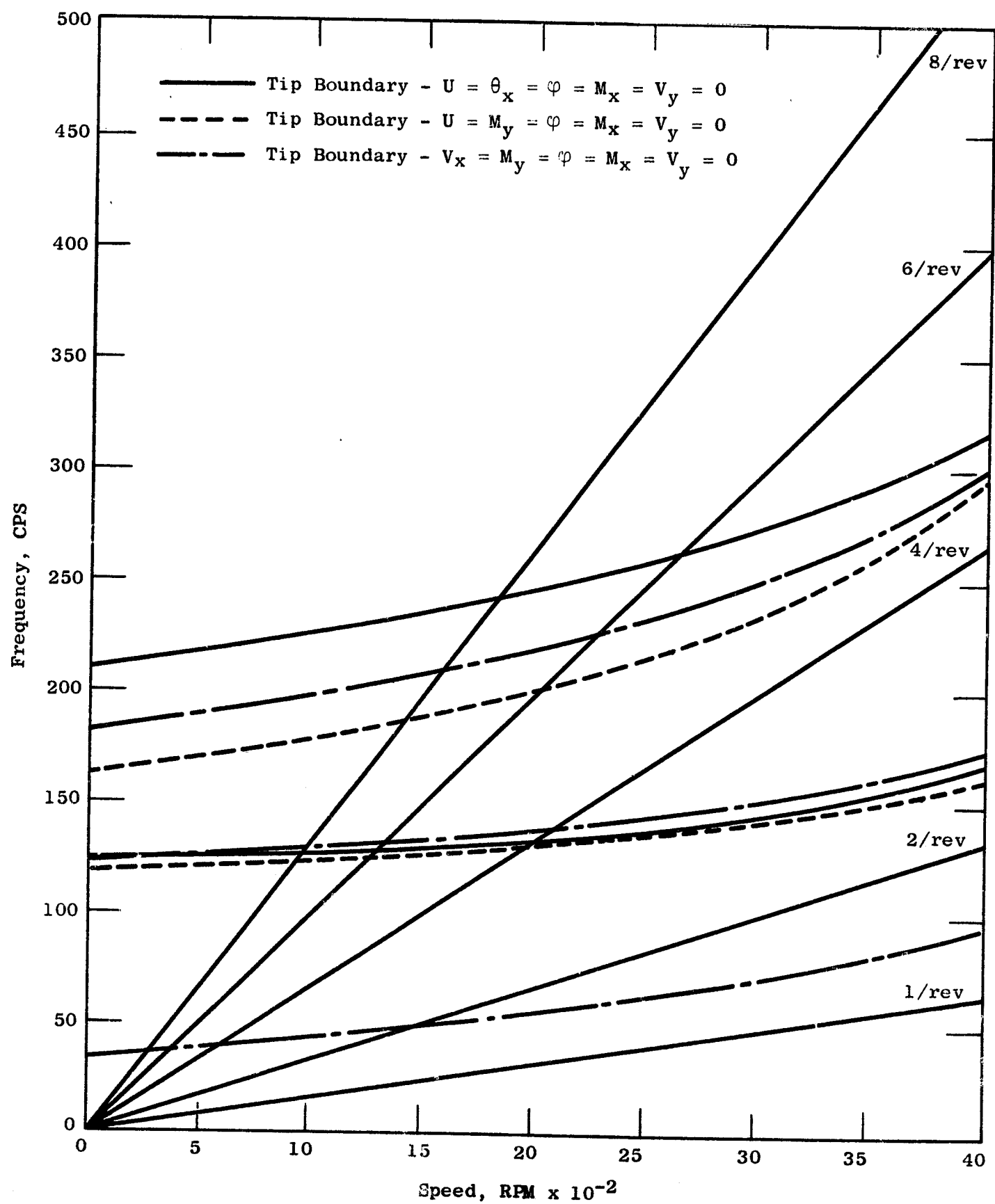


Figure 82. Fan A Blade-Disc Campbell Diagram, 2-Diameter Mode

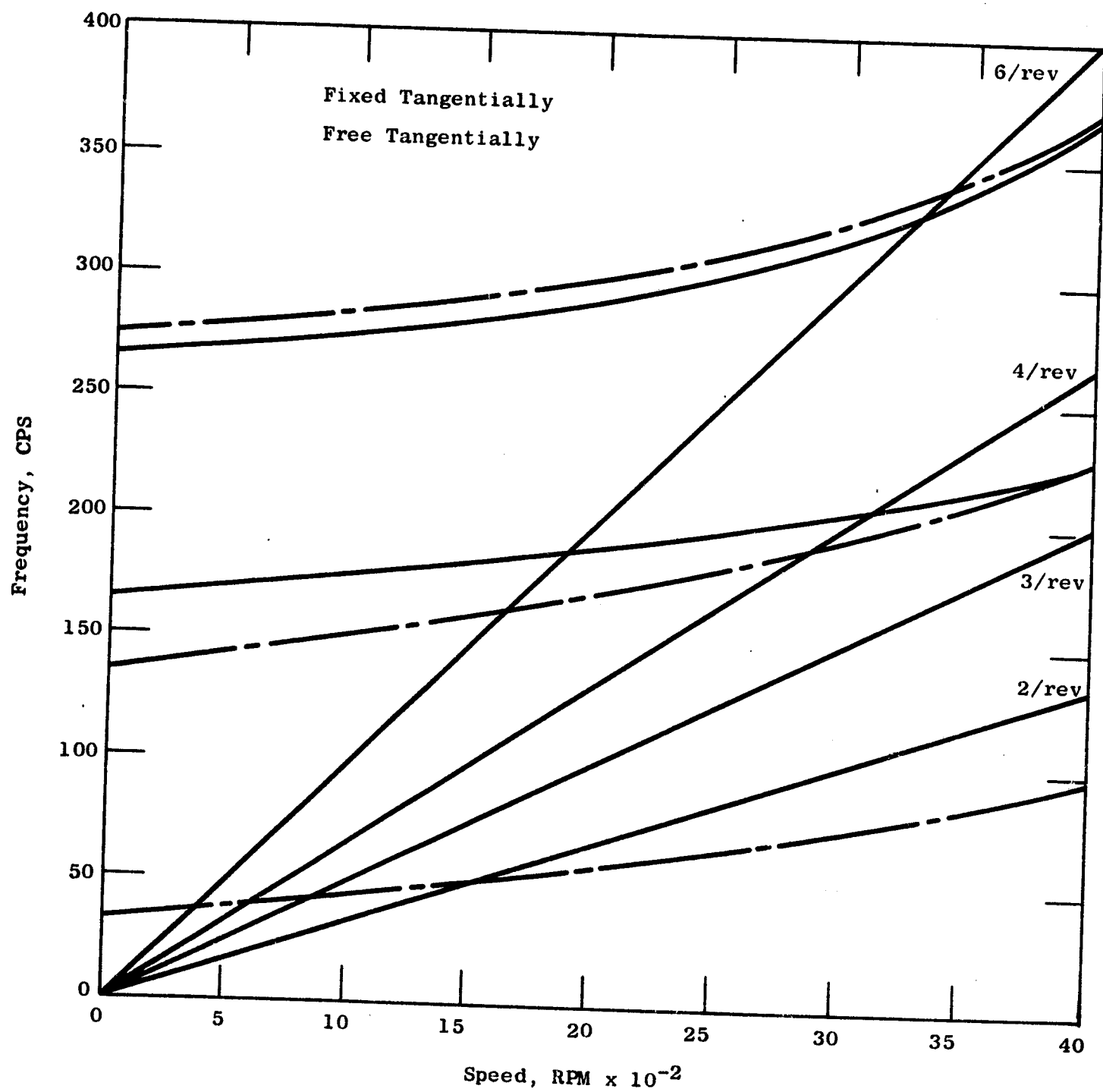


Figure 83. Fan A Blade-Disc Campbell Diagram, 3-Diameter Mode

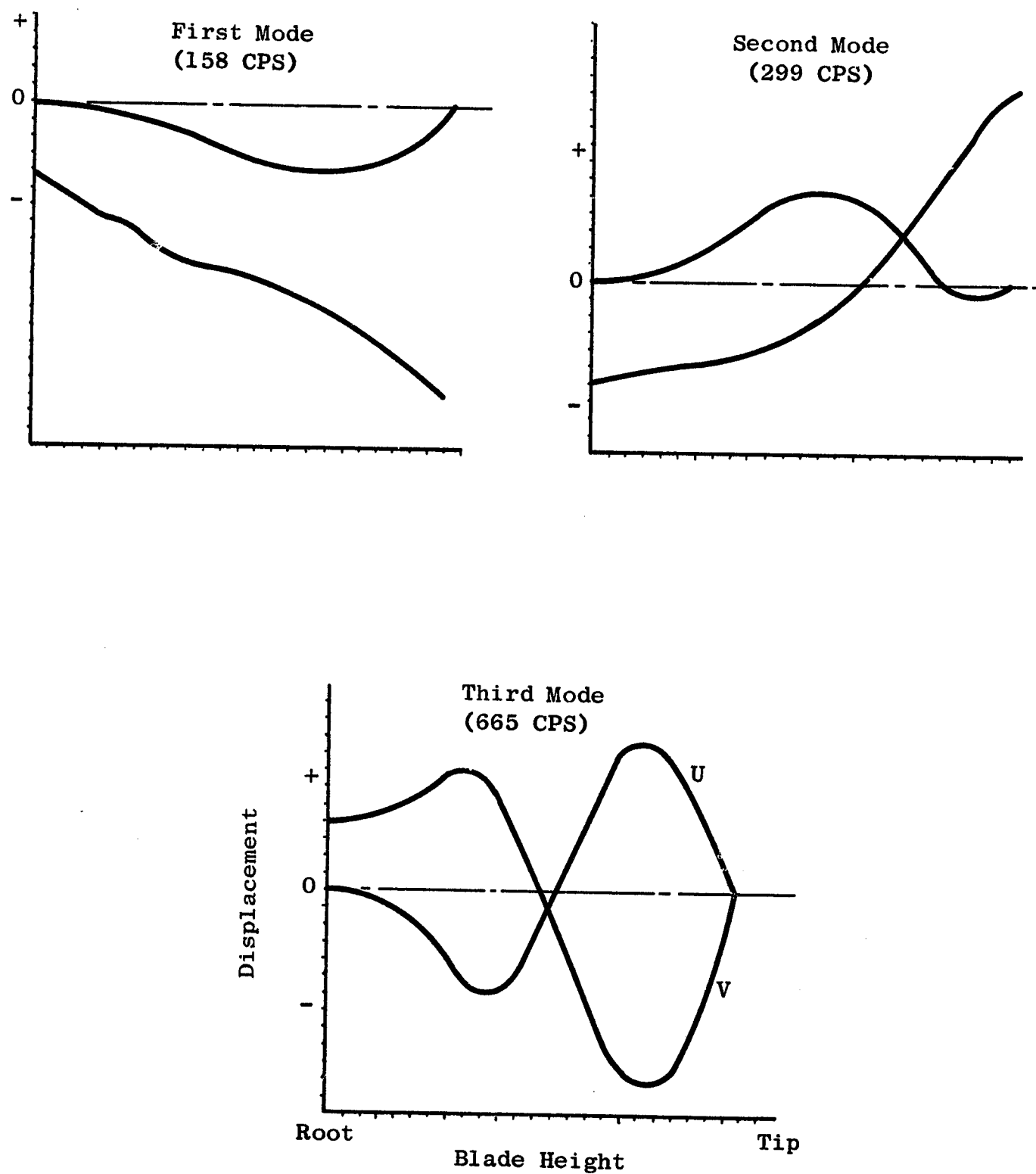
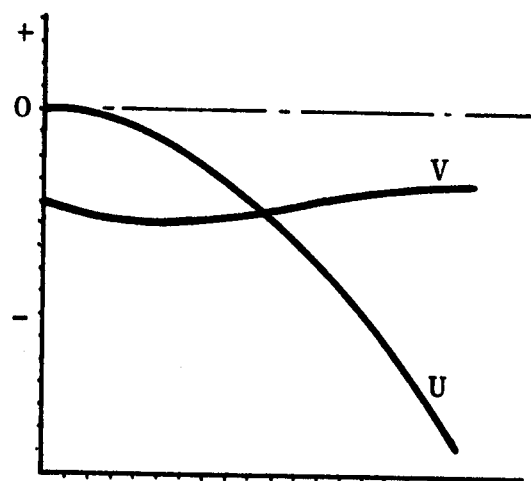
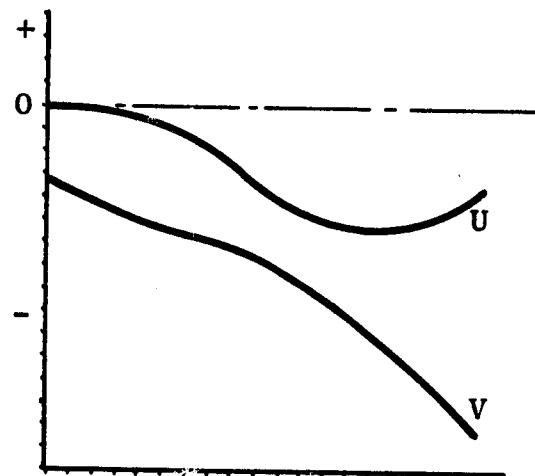


Figure 84. Fan A Coupled Blade-Disc Modes (2-Diameter, 3624 RPM, Fixed Tangentially)



First Mode
(86 CPS)



Second Mode
(161 CPS)

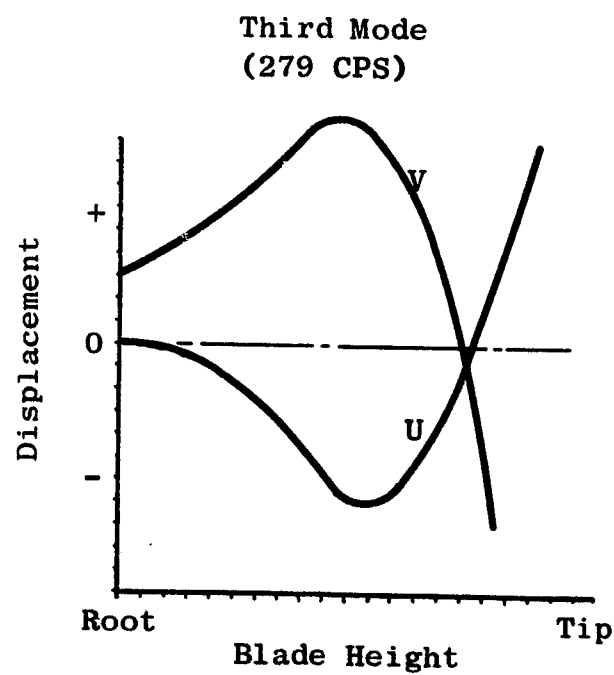


Figure 85. Fan A Coupled Blade-Disc Modes (2-Diameter, 3624 RPM, Free Tangentially)

Second mode (161 cps) is essentially the first axial mode of the disc. U and V are in phase with $V_{\max.} \approx 2.5 U_{\max.}$ and dv/dz is nearly constant.

Third mode (279 cps) is definitely the second flexural of the blades. U and V are out of phase and approximately equal in magnitude.

B) 3 Diameters

First mode (87 cps) is the same as that with 2 Diameters.

Second mode (214 cps) is primarily a disc mode with some blade first flex in evidence. U and V are in phase and $V_{\max.} \approx 2.5 U_{\max.}$.

Third mode (350 cps) is essentially second flexural with U and V out of phase.

It can be concluded that, with the shrouds locked (fixed tangentially), there exists a margin of 30 percent between a 2-diameter blade-disc mode and a 2/rev excitation at a design point speed of 3624 rpm. If the shroud were to break free (slip) below approximately 1500 rpm, then the first flexural mode of the blades could be excited during an acceleration. Thus, it has become a primary design criteria that the shrouds lock, and remain locked, at a speed less than 1500 rpm. A disc-blade mode would not be encountered, for it appears to have remained above the 2/rev excitation stimulus line.

The great uncertainty of this analysis resides in the tip shroud behavior and its effect on the vibration amplitude. Due to the radius ratio, some sort of 2/rev will unavoidably be encountered in the operating range. With sufficient stimulus and control over its application, the system can be made to migrate from a free- to a fixed-tip motion at a low enough speed to ensure a high-flex design.

From this coupled blade-disc analysis, it would appear that nowhere inside the operating envelope of the engine can a 3-diameter disc mode be excited. What has been said concerning the shroud locking with a diameter disc mode applies equally as well with a 3-diameter mode.

To determine the sensitivity of this analysis to the value imputed for rim stiffness, two cases were run differing only in torsional stiffness. For the 2-diameter first mode, a decrease of 23 cps or 13 percent was experienced between the hand calculated rim stiffness of 16.7 and the membrane analogy of 11.576. The lower limit (the latter stiffness) was used throughout this investigation.

5.1.1.1.5 Other Components

- Spinner

The spinner is comprised of two components, the spinner cover and the spinner cone. The former bolts onto the latter through shank nuts retained on the inner cone. This allows for the removal of the cover for inspection of instrumentation or the removal of the complete fan rotor.

The spinner cone forms not only the inner flowpath but also acts as a forward blade retainer. If after the removal of the cover the cone is unbolted from the forward disc flange, then individual blades can be removed.

Both components will be fabricated from 17-4PH steel. SNAP computer program runs have determined the surface effective stresses to be as shown in Figure 78.

- Air Seal

This component performs a three-fold purpose. First, it seals individual blades from recirculating leakage flows around the blade platforms; second, it acts as an aft blade retainer; lastly, it seals the aft rotor cavity from the high pressure fan discharge air.

The 17-PH alloy steel is being utilized in this component. Stress levels are nominal for this type of hardware.

5.1.1.2 Fan B Rotor

The Fan B rotor has 26 cantilevered blades with a radius ratio of 0.5. The blade aspect ratio is 1.90, 1.70, and 1.59 at the hub, midspan, and tip, respectively.

The blade dovetail is attached to the disc by a straight single-tang dovetail. The platform surface is integral with the disc. The blades are retained in an axial direction by forward and aft retainer rings which butt up against the ends of the dovetail. They are bolted to the disc at flanges on the forward and aft side of the disc. These bolt circles will also serve as balancing planes. The aft seal is integral with the aft retainer. The nose cone consists of two pieces forward and aft. The aft portion is integral with the forward blade retainer, while the forward piece is attached to the aft by a bolted flange.

The disc is integral with a spacer cone. The spacer cone connects to the forward shaft by a bolted flange.

There is a combination instrumentation duct and telemetry package which connects to the forward flange of the disc using the same bolts as the forward retainer.

5.1.1.2.1 Blade Design

● Material Selection

The three candidates for fan blade material were 7075-T73 aluminum, 6-4 titanium, and 410 stainless steel. These materials were evaluated based on material cost, fabrication cost, and performance. A summary of this evaluation is shown in Table XVII. Based on this comparison, aluminum was selected as the primary blade material.

The major drawback of aluminum as a blade material is its relatively low fatigue strength. However, on the test stand it is anticipated that the vibratory stress levels will be low enough to enable aluminum to be used. As a precaution, however, a decision was made to purchase a set of titanium blades as backup for the aluminum blades.

The 7075 aluminum forgings for the blades were purchased from Alcoa Company in the F (as forged) condition. Bar forgings, measuring 12 x 7 x 23 inches, were necessary to provide an adequate envelope for the blade. These forgings were heat treatable to the 7075-T73 condition and were qualified to Mil-A-22771B in the T73 condition. In addition to the testing specified in Mil-A-22771B, these forgings were 100 percent ultrasonically inspected. Also, microscopic and macroscopic examinations were conducted by Alcoa to assure uniformity of the forged material. With the exception of ultrasonic inspection, all testing was conducted on one forging out of each lot of approximately 14. The tensile properties shown in Table XVIII are the requirement of Mil-A-22771B.

Material properties for the aluminum are shown in Figures 86 and 87 and in Tables XIX and XX. Little data are available on the fatigue properties of the 7075-T73 aluminum under combined load. Therefore, fatigue tests are being conducted to establish a Goodman diagram. The anticipated Goodman diagram shown in Figure 86 is based on Alcoa's rotating beam fatigue data and tensile test data. The two lines represent the high and low endurance limits seen on all types of 7075-T73 (forgings, plate, rod, etc.). Also shown on this graph, and in Figure 87 and Table XX, are results of preliminary tests being conducted on a sample forging which was selected at random from the blade forgings purchased for the aluminum blade. The fatigue data represent the runout stress from the S/N curve in Figure 87. Both the preliminary endurance and tensile data were high, compared to the majority of data reported by the vendor. Additional tests are being conducted to de-

Table XVII. Fan B Blade Material Comparison

Material	Material Cost	Fabrication Cost	Performance				
			Weight	Stiffness/ Density	Fatigue Prop.	Disc and D/T Stresses	Over-all Toughness
Aluminum	(1)*	(1)	(1)	(2)	(3)	(1)	(3)
Steel	(2)	(3)	(3)	(1)	(1)	(3)	(1)
Titanium	(3)	(2)	(2)	(3)	(2)	(2)	(2)
* (1) (2) Indicates order of preference (3)							

Table XVIII. Tensile Properties for 7075-T73 Aluminum and 6Al-4V Titanium

<u>7075-T73 Aluminum</u>			
	<u>Tensile</u>	<u>Yield</u>	<u>Elongation</u>
Longitudinal	66,000 psi	56,000	7%
Long Transverse	64,000 psi	54,000	4%
Short Transverse	61,000 psi	52,000	3%
<u>6Al-4V Titanium</u>			
Tensile Strength	130,000 psi Min.		
Yield Strength	120,000 psi Min.		
% Elongation in 2 inches	10%		
Reduction of Area	25%		

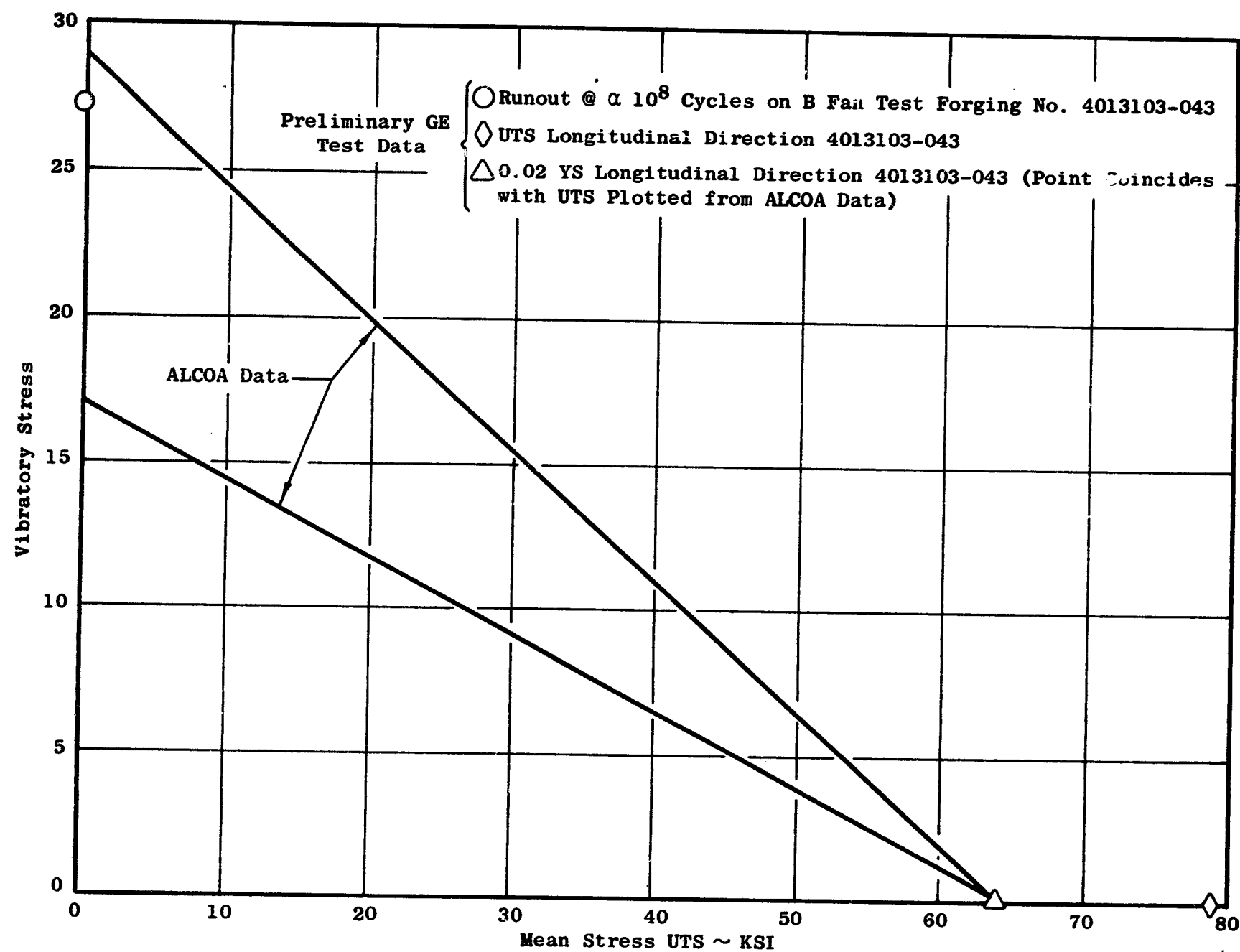


Figure 86. Goodman Diagram for 7075-T73 Aluminum, Estimated from Data in ALCOA Green Letter No. 206, August 1965)

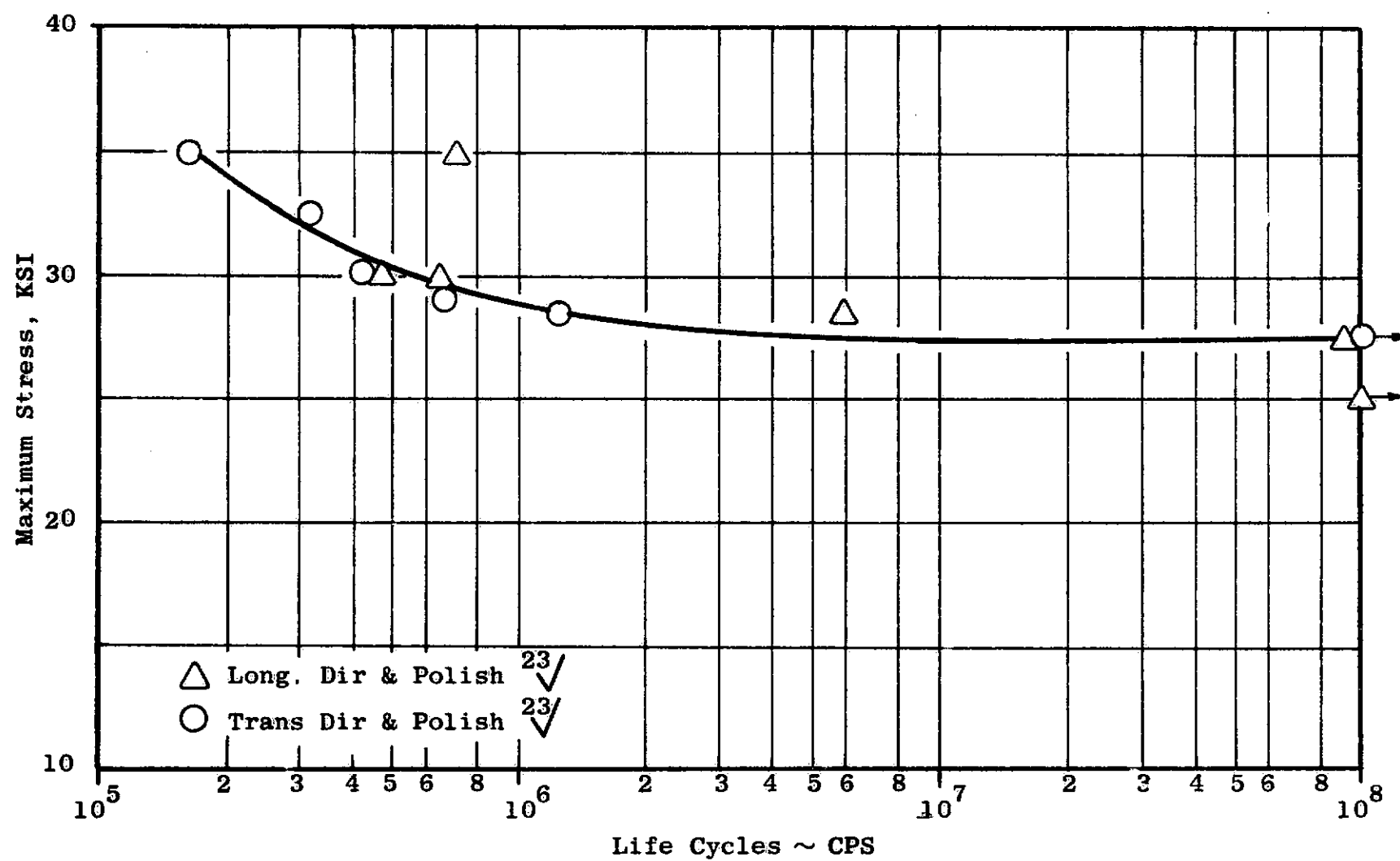


Figure 87. Quiet Engine Fan B Rotating Beam Fatigue Data for a 7075 Al Forging, Ambient Temperature (Fan Blade Test Forging No. PN 4013103-043)

Table XIX. Aluminum Material Properties from ALCOA Green Letter
No. 206, August 1965

7075-T73 Aluminum	
Allowable Stress at 10^8 Cycles	
17-27 ksi	
<u>Properties at RT</u> $E = 10.3 \times 10^6$ $G = 3.9 \times 10^6$ $\sigma_u = 66 \text{ ksi}$ $\sigma_y = 56 \text{ ksi}$	<u>Properties at 200°F</u> $E = 9.8 \times 10^6$ $G = 3.7 \times 10^6$ $\sigma_u = 57 \text{ ksi}$ $\sigma_y = 53 \text{ ksi}$
<u>Physical Properties</u> $\gamma = 0.101 \text{ Lb/In.}^3$	

Table XX. Tensile Properties of 7075 Aluminum Taken from Fan B Specimen
Blade Forging No. 4013103-043 at Room Temperature

Specimen No.	Direction	UTS KSI	0.2%YS KSI	0.2%YS KSI	Elong %	RA %
ST-1	Long Dir	82.5	74.6	66.7	9	24.5
ST-2	Long Dir	74.7	65.5	58.0	12	33.3
ST-3	Long Dir	80.7	72.2	66.3	11	29.3
Average		<u>79.3</u>	<u>70.8</u>	<u>63.7</u>	<u>10.7</u>	<u>29.0</u>
LT-4	Long Transverse	76.8	67.5	59.2	6.5	12.2
LT-5	Long Transverse	74.0	65.0	56.2	5	6.8
LT-6	Long Transverse	74.7	65.8	58.7	5.5	9.5
Average		<u>75.2</u>	<u>66.1</u>	<u>58.0</u>	<u>5.7</u>	<u>9.5</u>

termine the endurance limit of specimens with various degrees of shot peening. The method of shot peening which provides the most improvement in endurance strength will be used on the combined load specimens. This method will also be used on the blade.

The Goodman curve used to determine vibratory allowable stresses on the aluminum airfoil is the approximated version based on the vendor's (Alcoa) minimum data. These allowables are probably conservative. A more accurate Goodman line will be used when available.

The 6-4 titanium forgings for the titanium backup blades will be die forgings with a one-half-inch envelope on all surfaces. The forgings will be certified to the requirements of General Electric Specification Number C50TF22 CLB (6 Al-4V Titanium Base Alloy Compressor Blades and Vanes). Tensile properties required by this specification are also shown in Table XVIII. All forgings will be 100 percent ultrasonically inspected.

Additional material properties for the titanium are shown in Table XXI and Figure 88. Allowable vibratory stresses were originally set using the Goodman diagram in Figure 88.

- Blade Geometry

Major blade geometrical variables, as a function of airfoil height, are shown in Figures 89 through 92. All of these parameters have a major influence on the mechanical design. However, due to acoustic and aerodynamic considerations, only the thickness distribution was varied by mechanical design. In addition, the root t_m/c was restricted to a maximum of 0.09 due to choking problems. During the preliminary design, approximately thirty thickness distributions were investigated resulting in the curve shown in Figure 89, which provided the maximum obtainable first flexural frequency for both aluminum and titanium.

- Airfoil Analysis (Aluminum)

Failure is assumed to occur when the combination of steady and alternating stresses reaches the limiting line of the Goodman diagram. This line is a function of time and temperature, and may, therefore, be different for different flight conditions.

It may be further scaled down to account for scatter in material data, erosion, corrosion, and other factors which may affect fatigue strength. The usual design criterion for the blade dovetail is that its worst point should fall within the diagram line. Similarly, for the same loads, the worst point on the disc dovetail should be inside its diagram line (ideally, slightly farther inside than the blade dovetail).

Table XXI. Material Properties, Fan B Ti 6Al-4V Forging, Allowable Stress at 10^7 Cycles, 50-60 KSI

<u>Properties at R_T</u>	<u>Properties at 200°F</u>
$E = 16 \times 10^6 \text{ psi}$	$E = 15.3 \times 10^6 \text{ psi}$
$G = 5.9 \times 10^6 \text{ psi}$	$G = 5.6 \times 10^6 \text{ psi}$
$\sigma_u = 143 \text{ KSI}$	$\sigma_u = 130 \text{ KSI}$
$\sigma_{0.2Y} = 102.5 \text{ KSI} (-3 \text{ dev})$	$\sigma_{0.02Y} = 89.5 \text{ KSI} (-3 \text{ dev})$
<u>Physical Properties</u>	
$\gamma = 0.161 \text{ lb/in.}^3$	

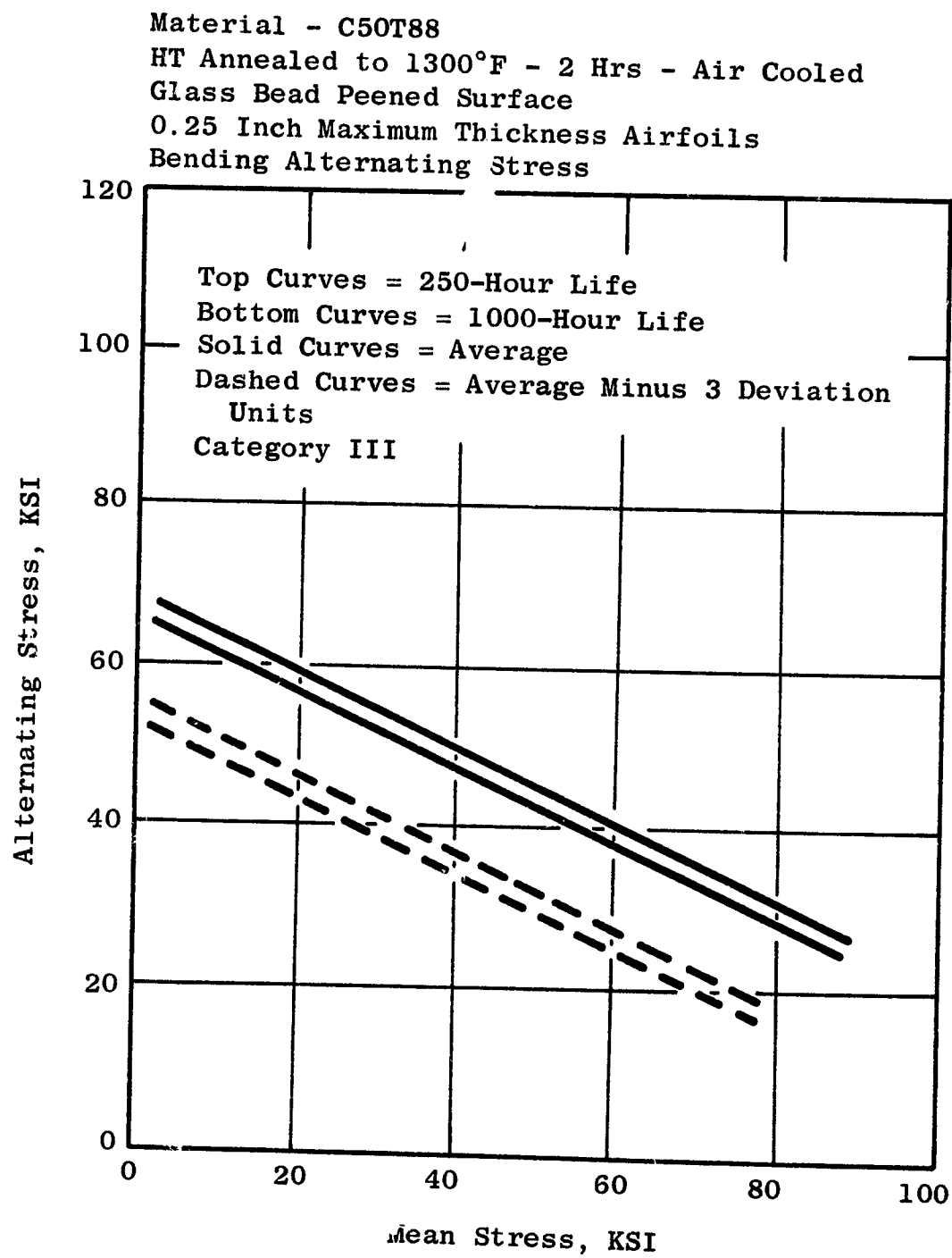


Figure 88. Stress Range Diagram for Fan B Ti 6Al-4V
 Blades at 400°F

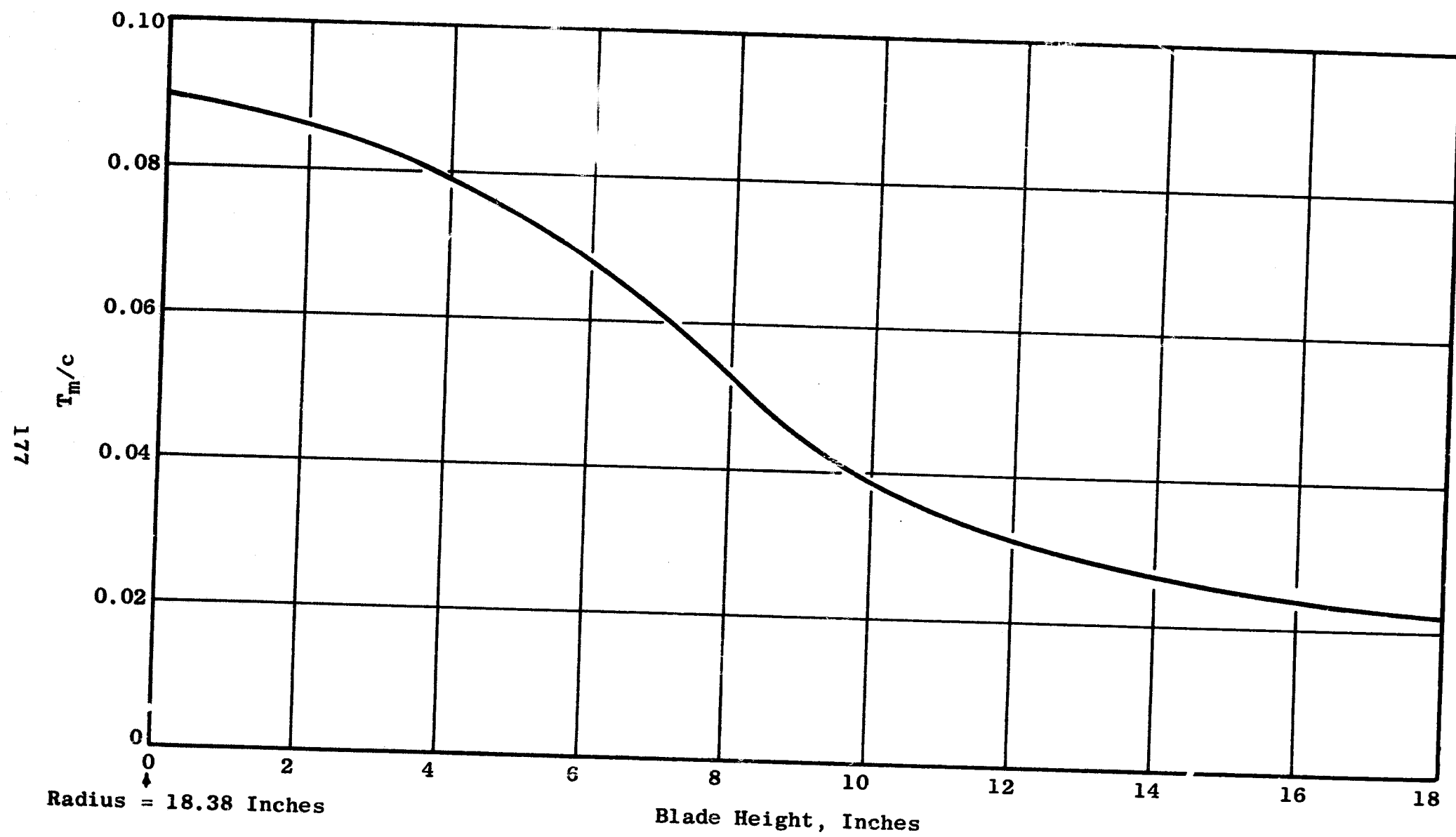


Figure 89. Quiet Engine Fan B Aluminum Airfoil T_m/c Vs Blade Height

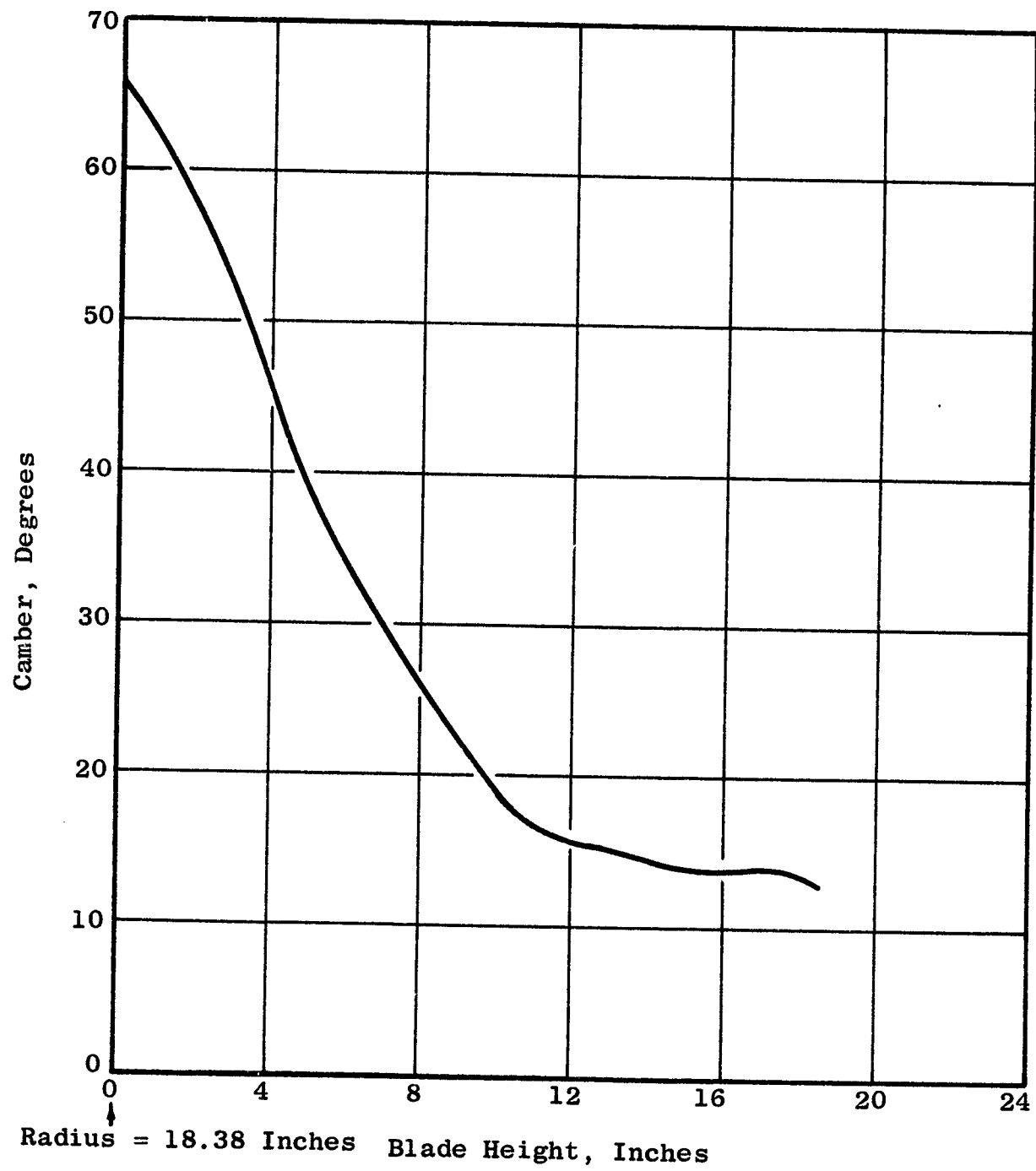


Figure 90. Quiet Engine Fan B Camber Vs Blade Height

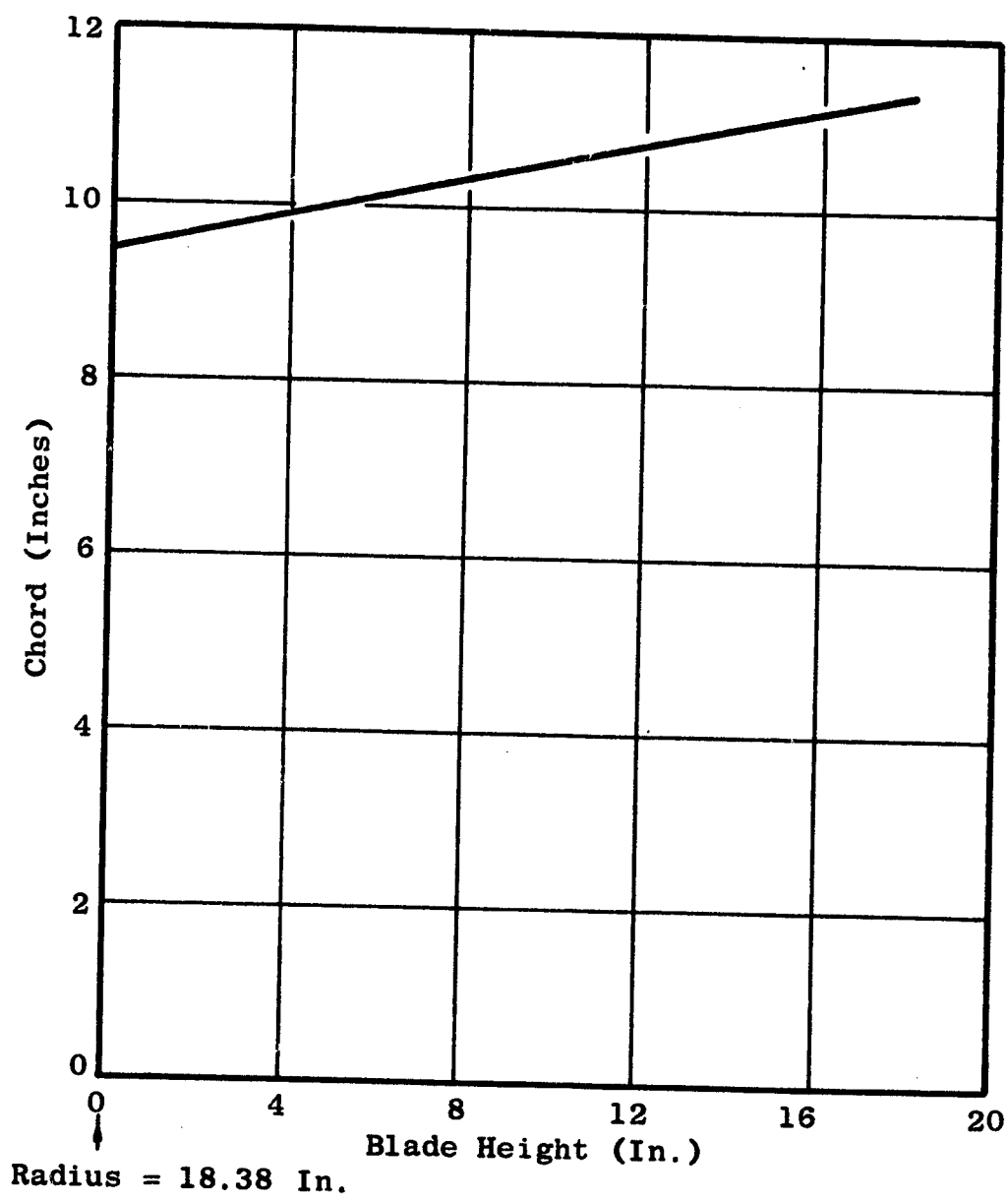
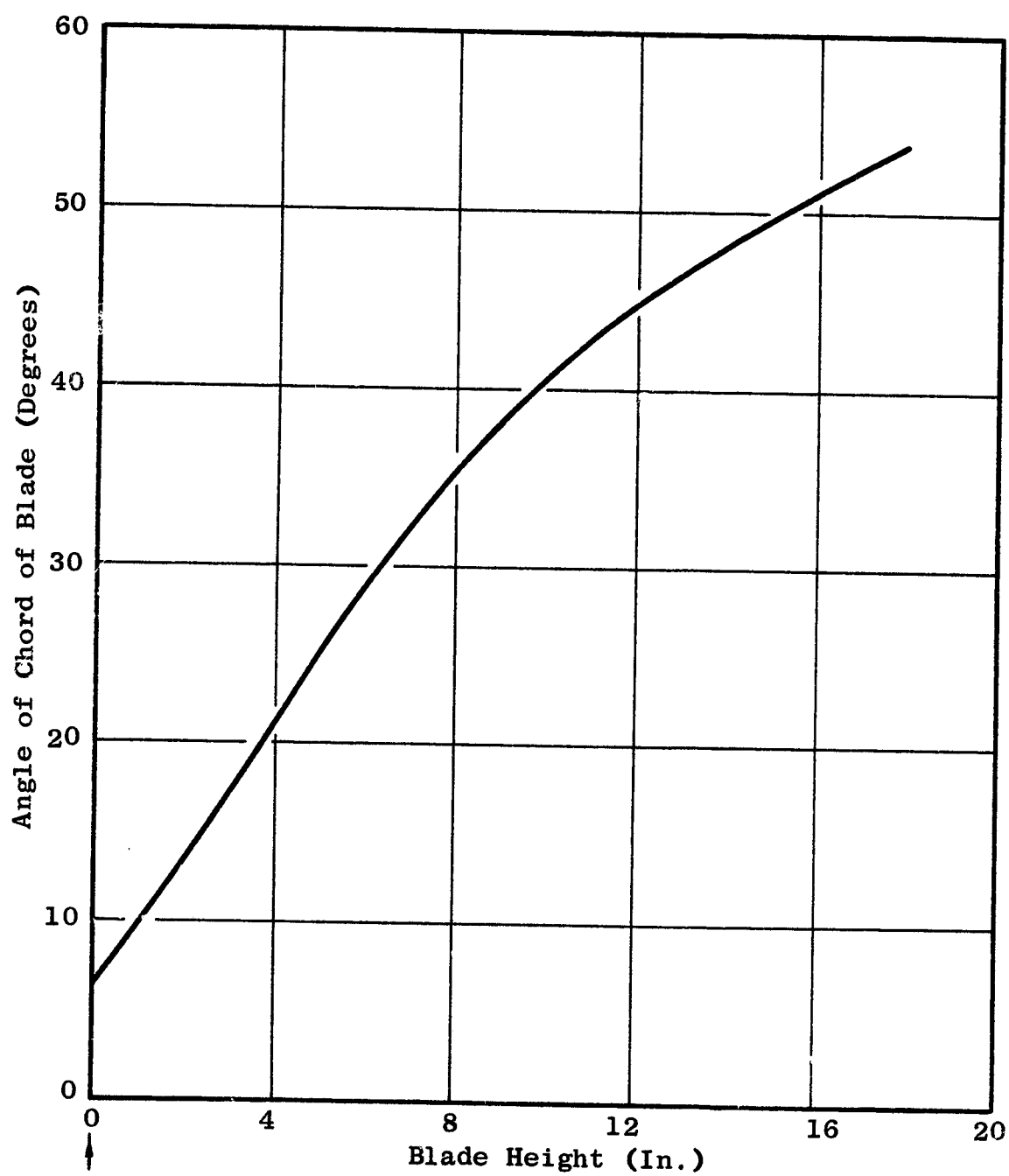


Figure 91. Quiet Engine Fan B Chord Vs Blade Height



Radius = 18.38 In.

Figure 92. Quiet Engine Fan B Angle of Chord of Blade Vs Blade Height

The Twisted Blade Computer Program was used to calculate airfoil resonant frequencies, airfoil stress, and airfoil deflections. It was also used to calculate required tilt and pretwist in the airfoil.

Airfoil stresses were determined for the blade operating at 3986 rpm. Tilt and pretwist were set for the blade at 3300 rpm.

Figure 93 is a Campbell diagram of the aluminum blade presenting first flexural, second flexural, and first torsional resonant frequencies from 0 to 3986 rpm. A coupled blade-disc analysis was conducted to establish the first flexural frequency of the blade on a semirigid platform. Calculations were made at 3624 and 3486 rpm. Coupled blade frequencies from these calculations were 1 to 2 cps lower than the first flexural frequencies of the blade on a rigid platform. A line was extrapolated from these points through the operating range of the engine. Percentage margins above the two per rev line were calculated. These are also shown in Figure 93. A minimum 15 percent margin is desirable over the operating range of the fan. The aluminum blade exceeds these requirements with 15.7 percent margin at 3624 rpm rotor speed.

Reduced velocity was calculated and plotted versus incidence angle in Figure 94. The reduced stiffness of the aluminum and titanium blades appears sufficient to keep the blade well out of the torsional instability region indicated on the graph. The area of this instability region has been established through test data from other engines, plus considerable aeromechanical test data and analysis.

The airfoil is tilted 0.03 radian about the least moment of inertia. Tilt was established by calculating stresses in the blade at various degrees of tilt and plotting these stresses on a Goodman diagram for comparison. Figure 95 is a Goodman diagram with the most critical stress areas on the blade plotted at various degrees of tilt. Maximum reduction in stress in the aluminum blade could be obtained with 0.05 radian tilt. However, 0.03 radian was selected as a better compromise between the aluminum and titanium blades.

Blade pretwist was established by calculating blade untwist at 3300 rpm and adding this to the existing blade twist. Figure 96 is a graph showing blade pretwist versus blade height.

Steady state stresses in the blade occur as a result of tension, twisting, and bending caused by centrifugal and gas loads. These stresses are accurately calculated by the Twisted Blade Computer Program in all areas of the airfoil except in those areas immediately adjacent to the airfoil root platform. Here, because of the angle of the root platform, these stresses must be corrected slightly from bench test results on the blade.

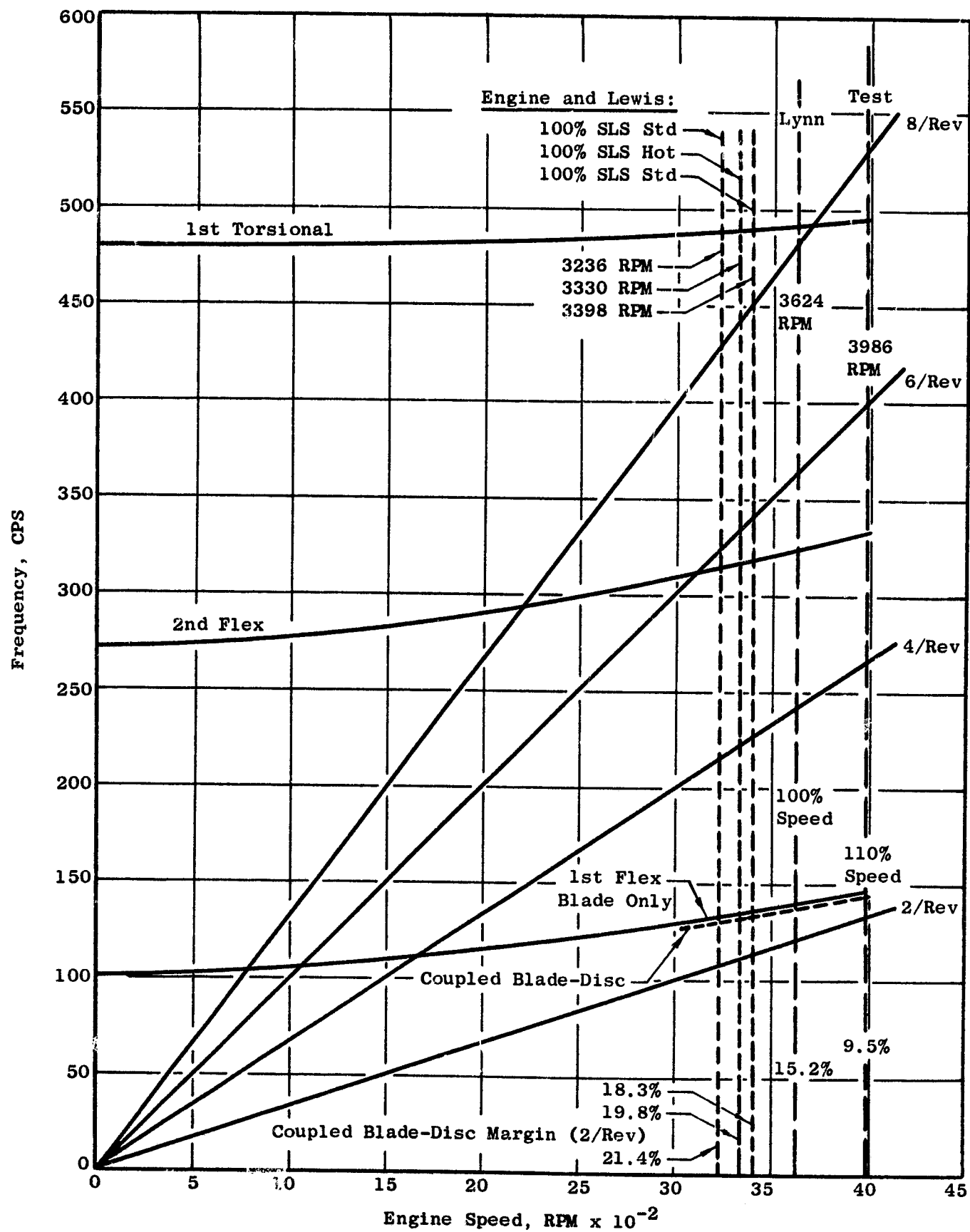


Figure 93. Campbell Diagram for the Fan B Aluminum Blade

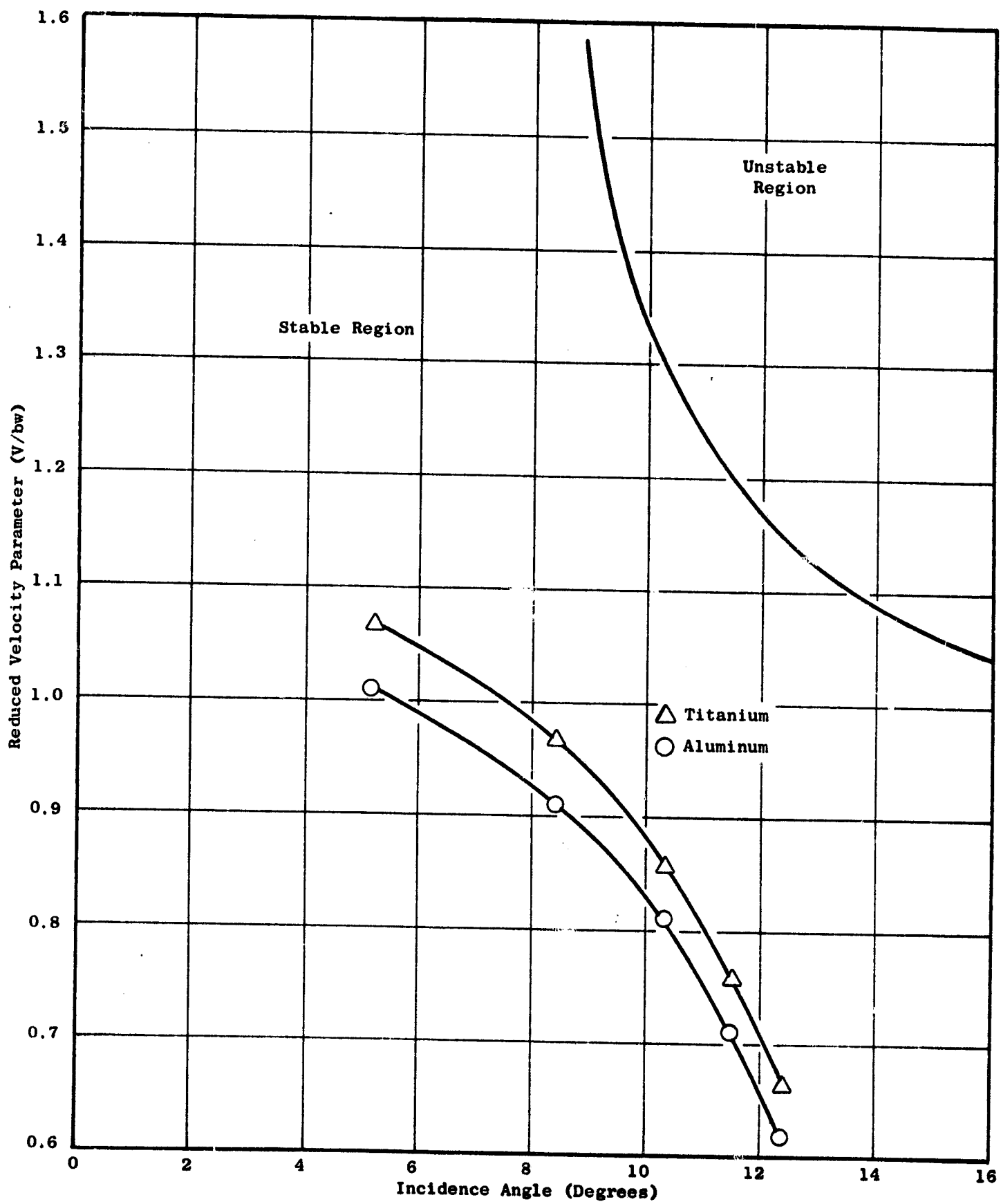


Figure 94. Fan B Blade Stability

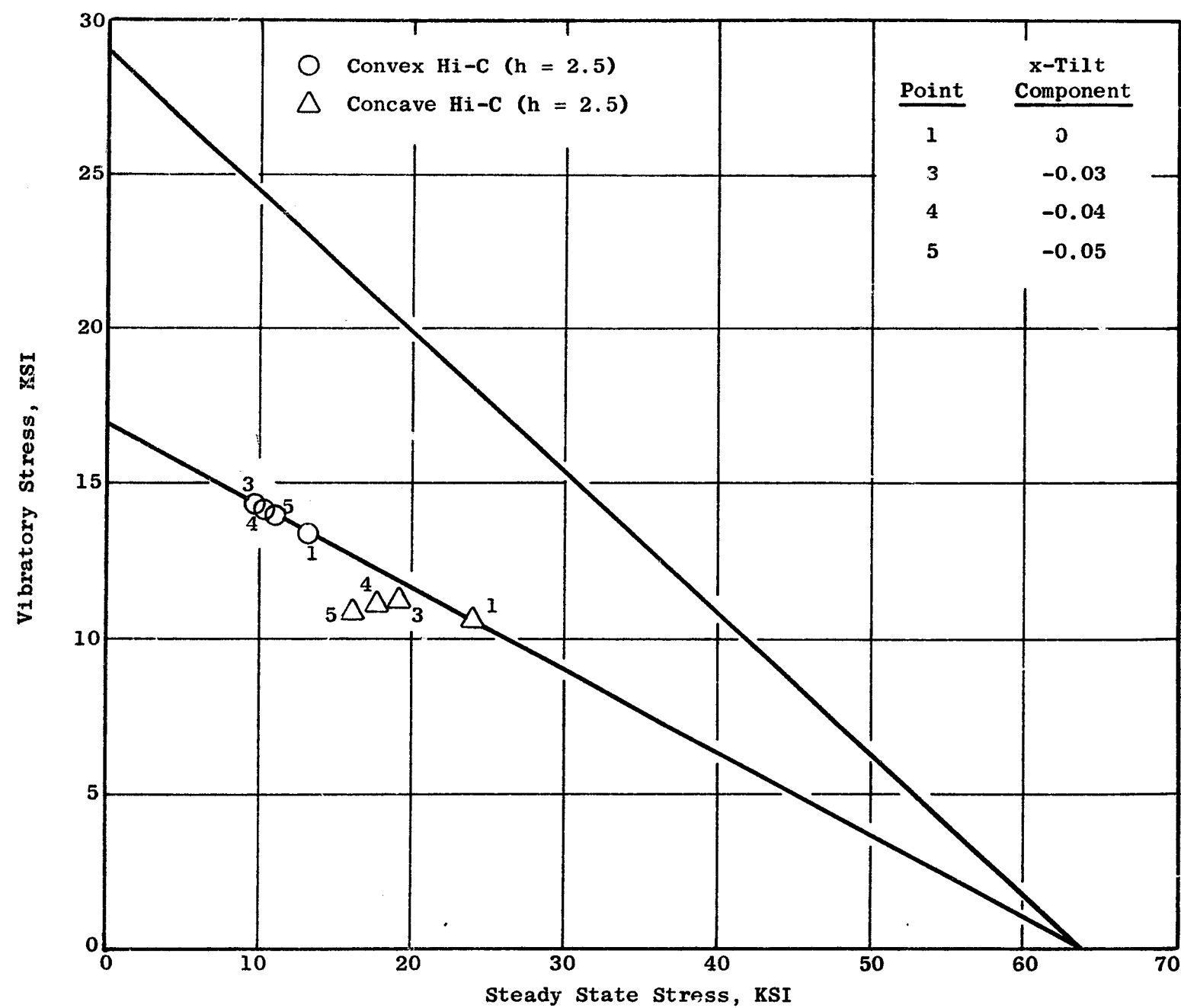


Figure 95. Goodman Diagram, Fan B Aluminum Blade

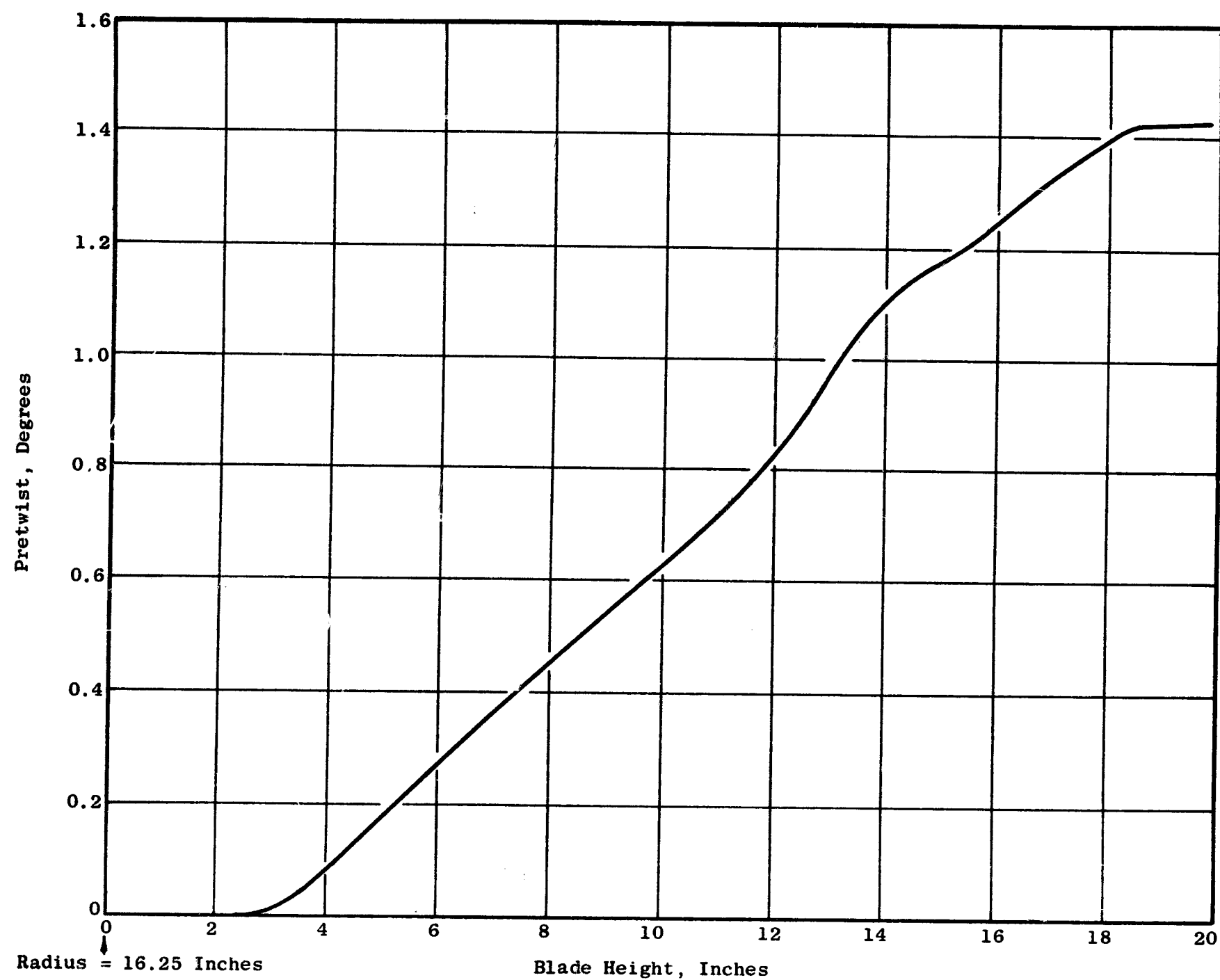


Figure 96. Fan B Blade Pretwist Distribution

Figure 97 is a plot of the radial and tangential air loads versus blade height at 3624 rpm. The loads at 3986 rpm are approximated by increasing these loads by a factor of 1.1 squared. This is based on the assumption that the air loads increase with the square of the increased rpm/ the existing rpm [i.e. $(3986/3624)^2 = 1.12$].

Figures 98 and 99 are the concave "Hi C", convex "Hi C", leading and trailing edge, steady state stresses plotted versus blade height. Maximum steady state stress is 26 ksi at the concave "Hi C", 2.95 inches above the midpoint of the dovetail flank surface.

The vibratory stress levels cannot be predicted because the vibratory loads are unknown. Vibratory stress distribution can be established, however, by imposing an arbitrary deflection on the blade and computing the resulting stresses. A normalized vibratory stress distribution is thus obtained. Figure 100 is the vibratory stress distribution at 3986 rpm in the first flexural mode. Relative stresses at the leading edge, trailing edge, concave and convex "Hi C" are plotted versus blade height. The maximum combined stress point was determined by comparing relative vibratory and steady state stress distributions. Figure 101 is a Goodman diagram with the three highest combined stress points for the aluminum blade at 3986 rpm in the first flexural mode. The maximum combined stress point is at 2.95 inches above the dovetail reference plane on the convex Hi C.

Tip deflections for the aluminum and titanium blades are reported in Table XXII.

Table XXII. Fan B Blade Tip Deflections for Blade Only at 3986 RPM

<u>Material</u>	<u>Tangential (In.)</u>	<u>Axial (In.)</u>	<u>Twist (Degrees)</u>
Aluminum 70750T73	-0.694	0.191	1.88
Titanium Ti-6Al-4V	-0.622	0.146	1.67

• Blade Dovetail (Aluminum)

The blade dovetails were analyzed using loads and moments taken from the Twisted Blade Analysis with the airfoil set at Goodman limits in first flexural mode. Figure 102 is a sketch showing the boundary loads for the

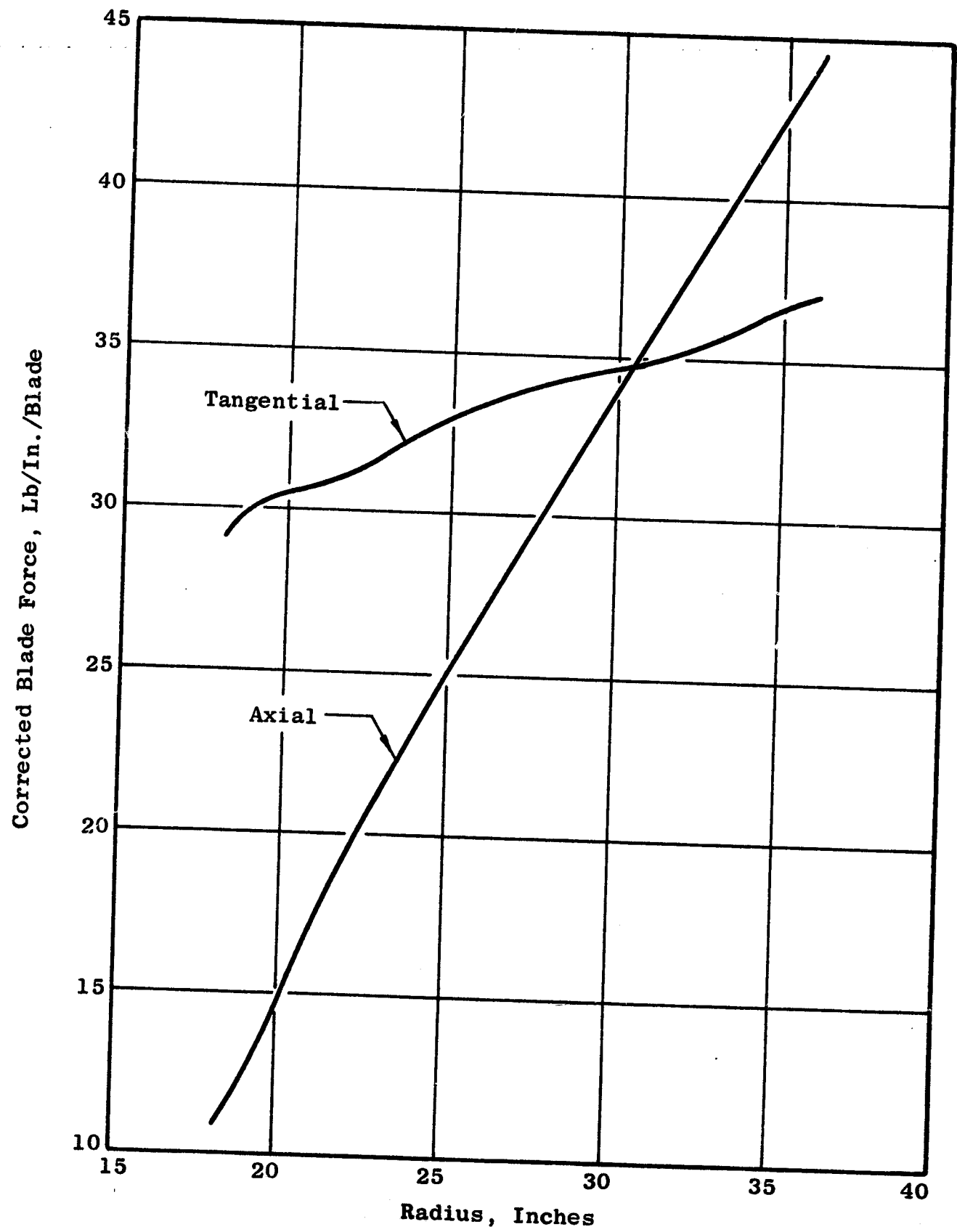


Figure 97. Quiet Engine Fan B Blade Loads at 3624 RPM

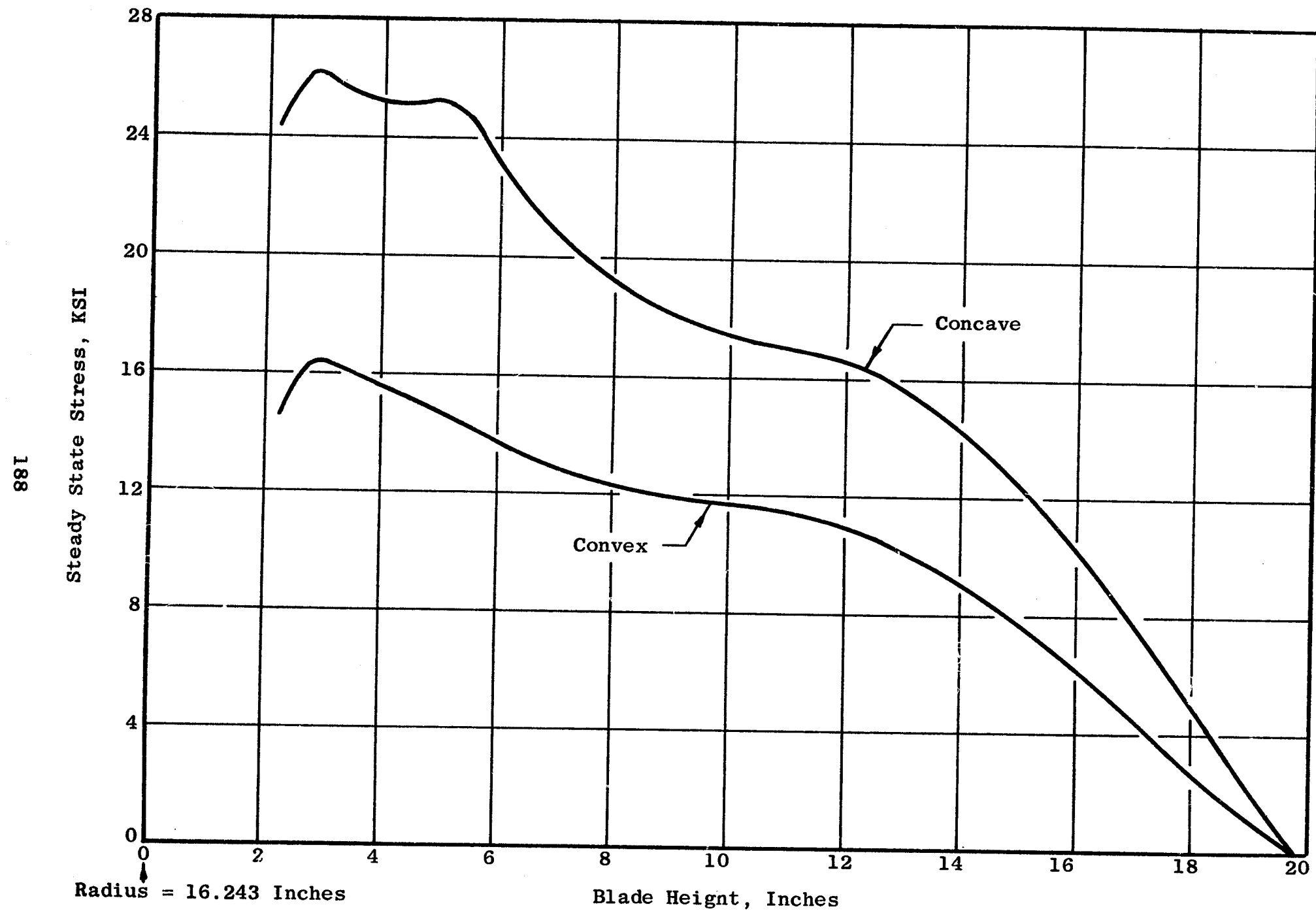


Figure 98. Quiet Engine Fan B Aluminum Blade Steady State Stress Vs Blade Height (N = 3986 RPM, Concave and Convex Sides)

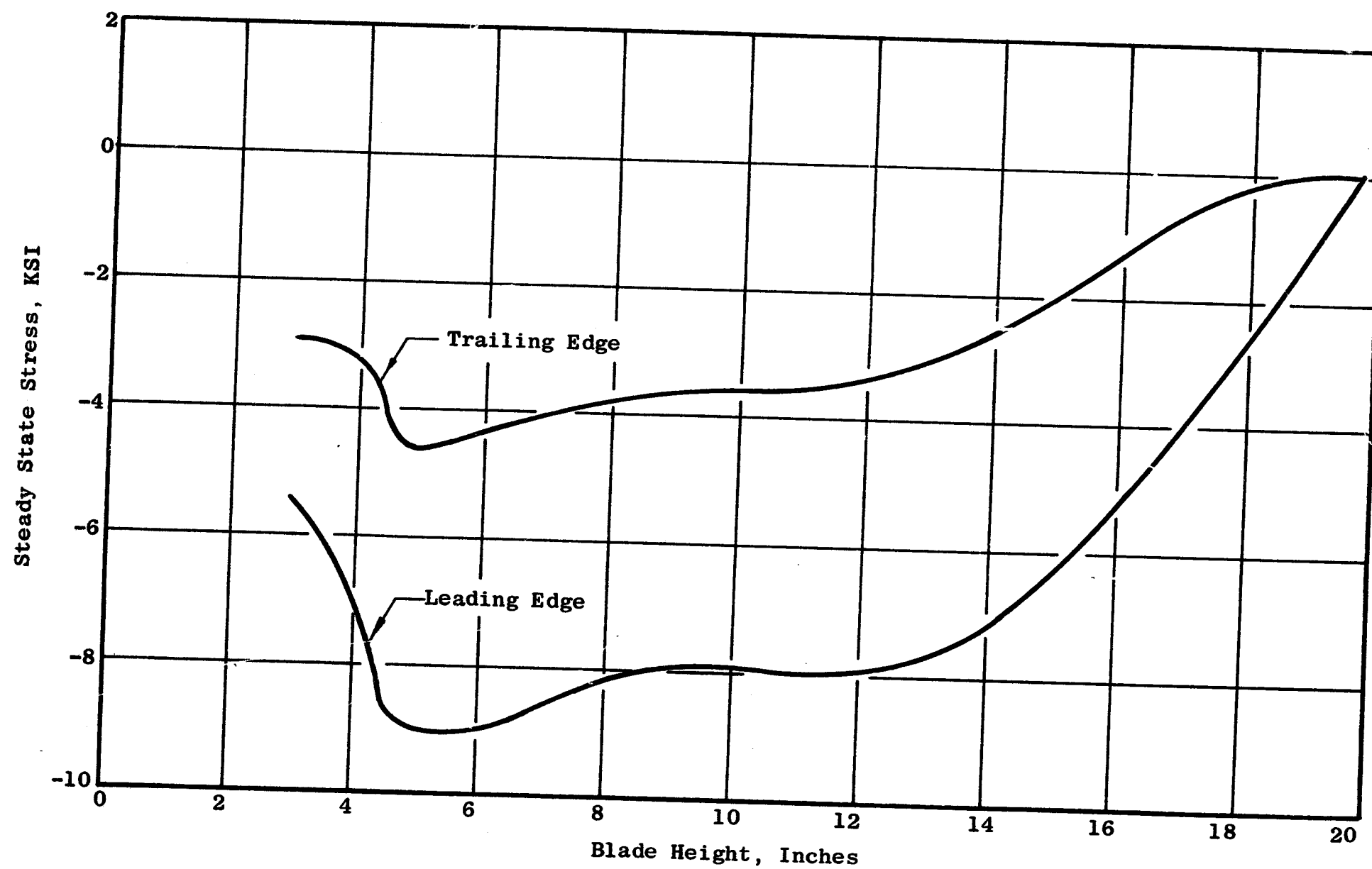


Figure 99. Quiet Engine Fan B Aluminum Blade Steady State Stress Vs Blade Height ($N = 3986$ RPM, Leading and Trailing Edges)

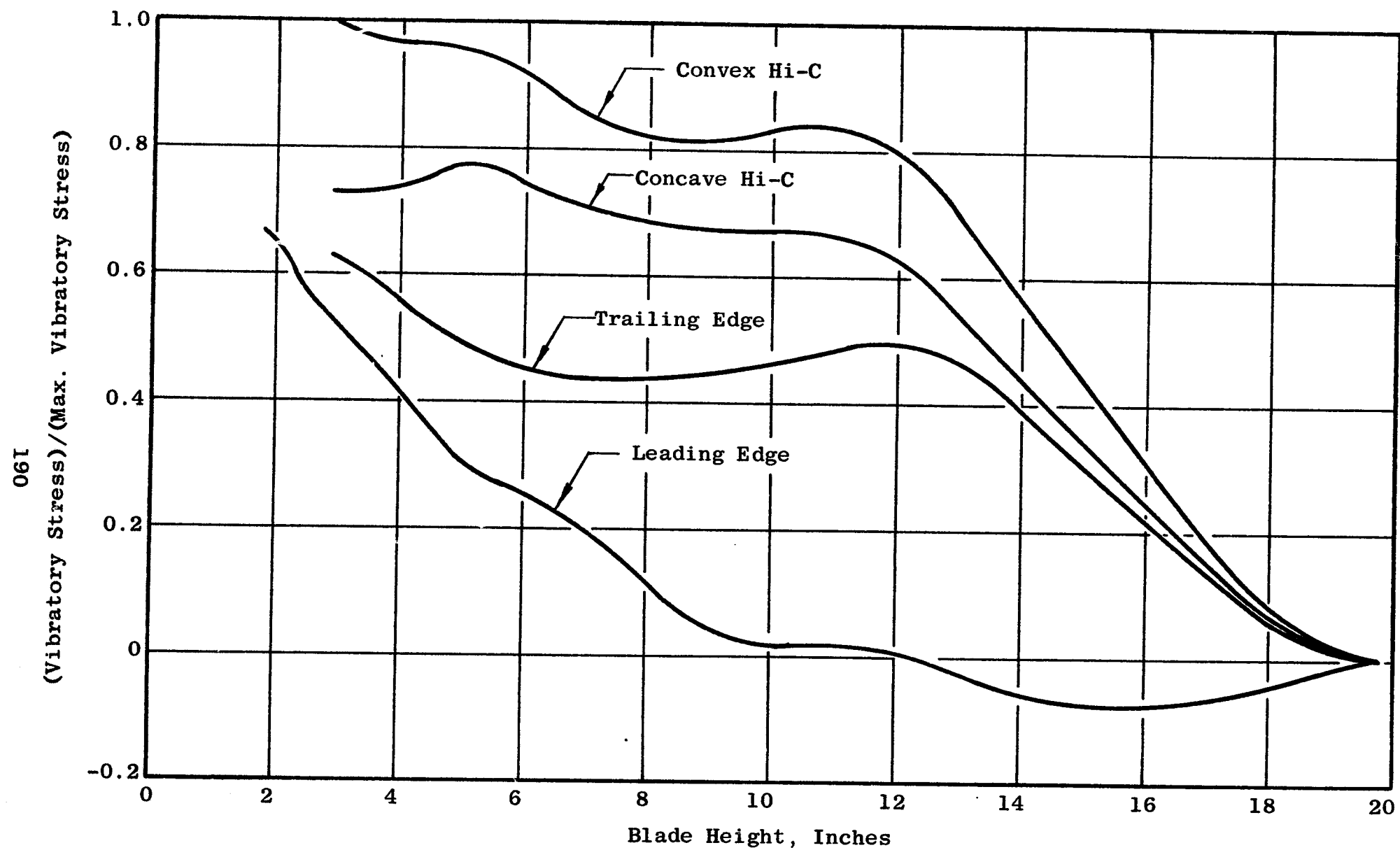


Figure 100. Quiet Engine Fan B Aluminum Blade Vibratory Stress Vs Blade Height in the 1st Flexural Mode (N = 3986 RPM)

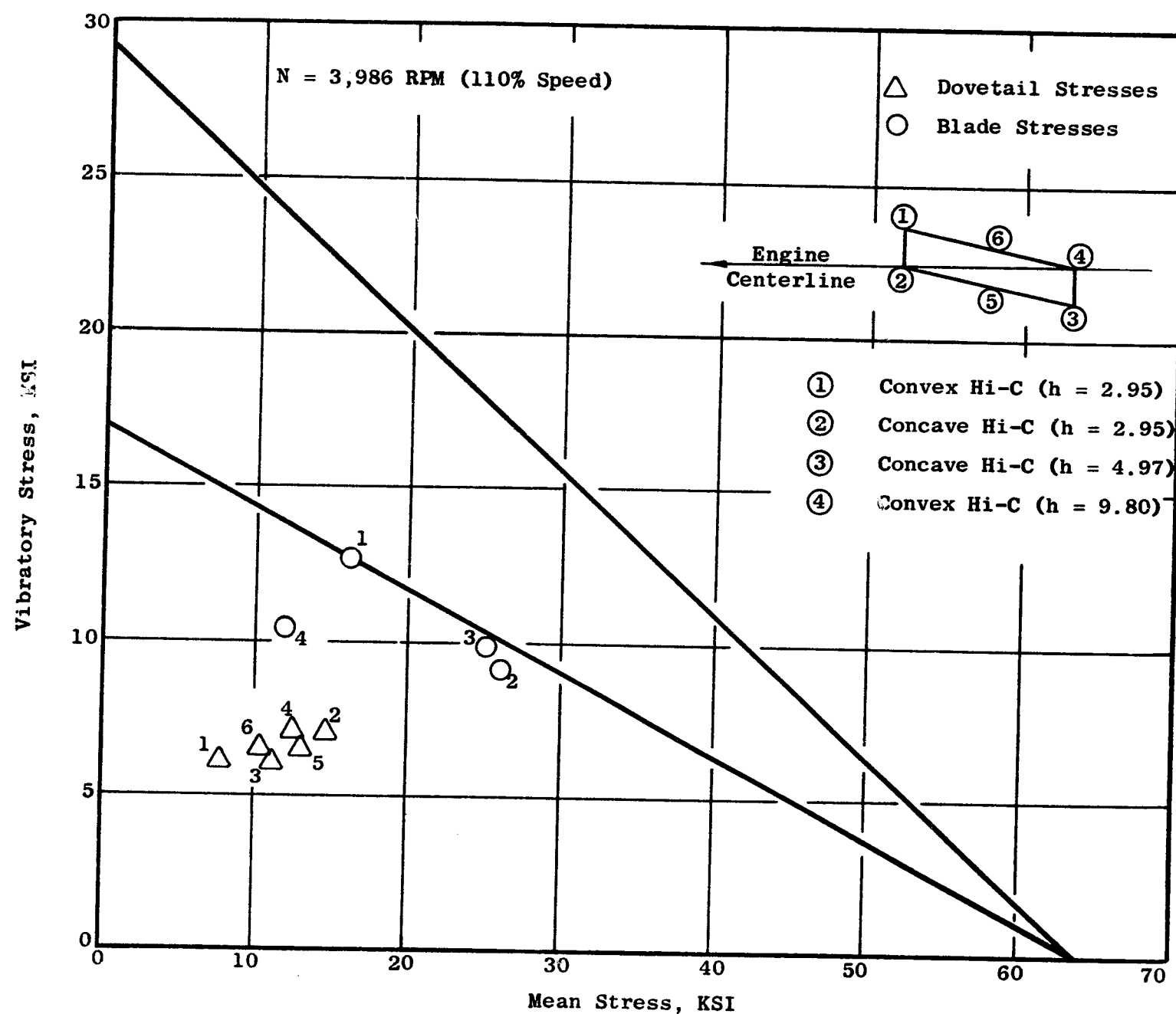
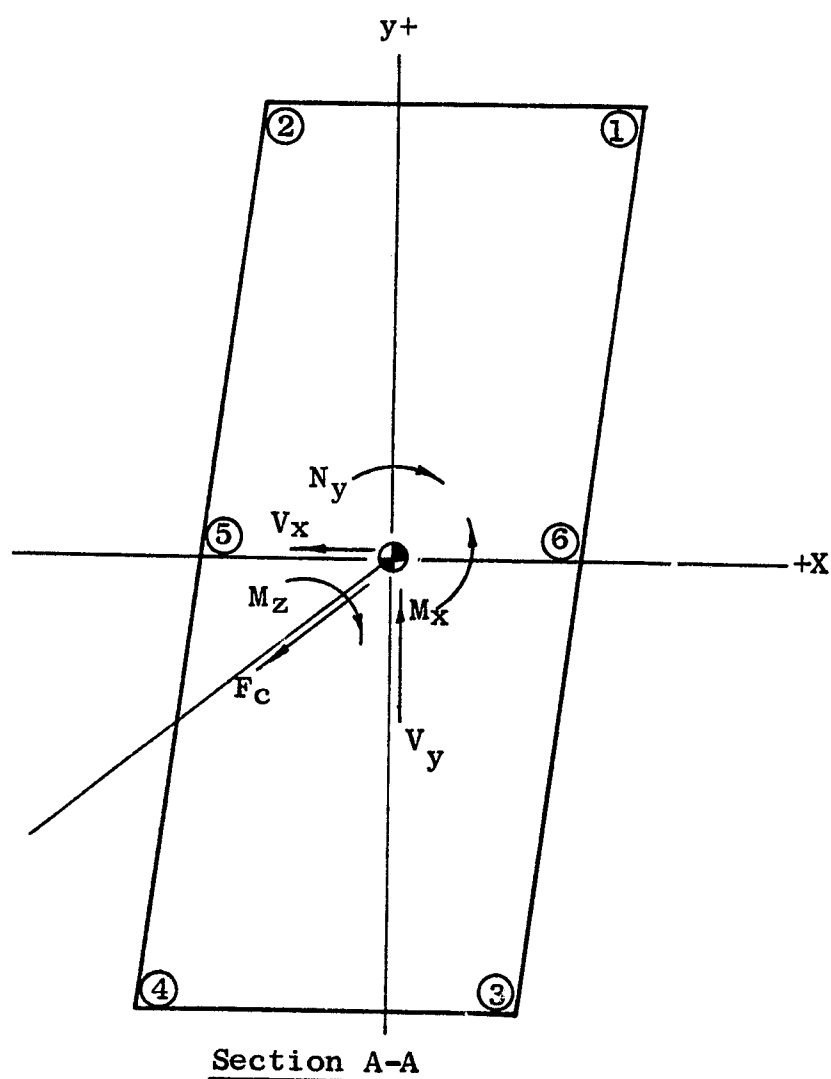
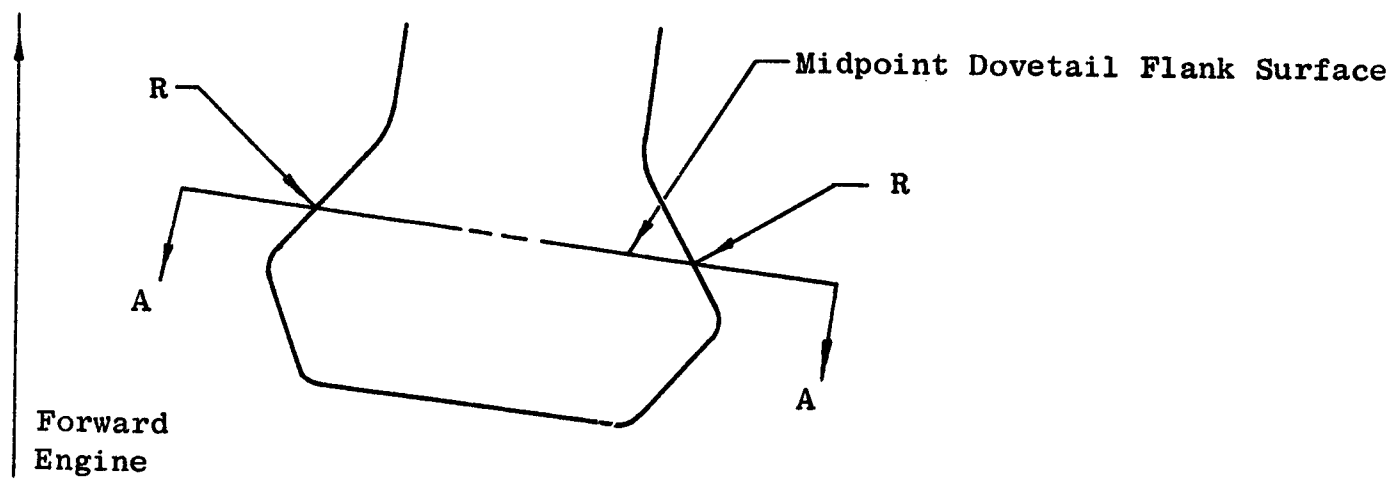


Figure 101. Quiet Engine Fan B Goodman Diagram Showing Location of Critical Stress Points for Aluminum Blades in the 1st Flexural Mode at 3986 RPM



Blade Loads at 3986 RPM

Load Component	Aluminum	Titanium
F_c (Lbs)	104,160	168,220
M_x (In.-Lbs)	-3,260	-1,473
M_y (In.-Lbs)	3,199	9,024
M_z (In.-Lbs)	-4,660	-9,118
V_x (Lbs)	-1,417	-1,774
V_y (Lbs)	610	610

Figure 102. Blade Dovetail Boundary Loads

dovetail and also a listing of the loads for both the aluminum and titanium dovetails at 3986 rpm. Loads used in consideration of dovetail stresses are taken through the CG of the dovetail (Section A-A, Figure 102). The reaction loads (R) from the disc are assumed to be point loads at approximately the midpoint of the dovetail flank surface. Load distributions along the length of the dovetail on each flank surface are calculated. The disc and blade dovetails are assumed to be rigid, thereby giving a linear load distribution.

Two stresses are considered: the stress in the neck and the stress in the tang. The formula for calculating stresses in the tang are empirical. They were derived from results of photoelasticity tests. These two stresses are combined to determine an effective stress in the root fillet. The formula for effective stress is also based on test data. Table XXIII is the calculated steady state and allowable vibratory loads and stresses. They are shown plotted on the Goodman diagram of Figure 101. The combined stresses are well below the Goodman line.

- Airfoil Analysis (Titanium)

The frequencies for the titanium blade are shown in the Campbell diagram in Figure 103. Margins of the coupled blade/disc frequencies over the 2/rev line are lower than the aluminum blade. This is due to the slightly lower modulus/mass ratio of the titanium.

Figures 104 to 108 are steady state and vibratory stress distributions of the titanium blade. Allowable combined stresses are plotted on the Goodman diagrams in Figures 109 through 111.

Tip deflections for the titanium blade were slightly less than the aluminum, due to the higher tensile and shear moduli of the titanium.

- Blade Dovetail (Titanium)

The dovetail stresses in the titanium were calculated by two methods. The first was the same used on the aluminum blade dovetail. Results of this analysis are shown in Table XXIV and plotted on the Goodman diagrams in Figures 109 through 111. These stresses are well below the Goodman line.

Dovetail stresses were also analyzed using a finite element displacement method. Load distribution was calculated based on the deflection of the disc dovetail in relation to the blade dovetail. Figure 112 is a sketch of the blade portion of the model with the calculated stresses at each element center of gravity. Maximum stresses are 60 and 64 ksi at the ends of the mating surface with the disc. This is somewhat higher than the stresses calculated with the outer method.

Table XXIII. Aluminum Blade Dovetail Stresses

<u>Location</u>	<u>Total Stress</u>	<u>Neck Stress</u>	<u>Tang Stress</u>	<u>Load S/V (*-Extreme)</u>
1 (S)	7946.62	4552.52	3921.5	5384.1
(V)	6145.57	5838.99	666.22	671.936
2 (S)	11103.1	10931.4	5003.83	6870.11
(V)	-7168.59	-6598.35	-1049.92	-1058.93
3 (S)	11354.4	7793.79	4404.	6046.56
(V)	-6145.57	-5838.99	-666.22	-671.936
4 (S)	12533.7	8495.96	4962.94	6813.98
(V)	7168.59	6598.35	1049.92	1058.93
5 (S)	13201.6	9362.59	4703.91	6458.34
(V)	6661.59	-6218.67	-858.069	-865.431
6 (S)	10395.5	6524.24	4442.22	6099.04
(V)	6661.59	6218.67	858.069	865.431

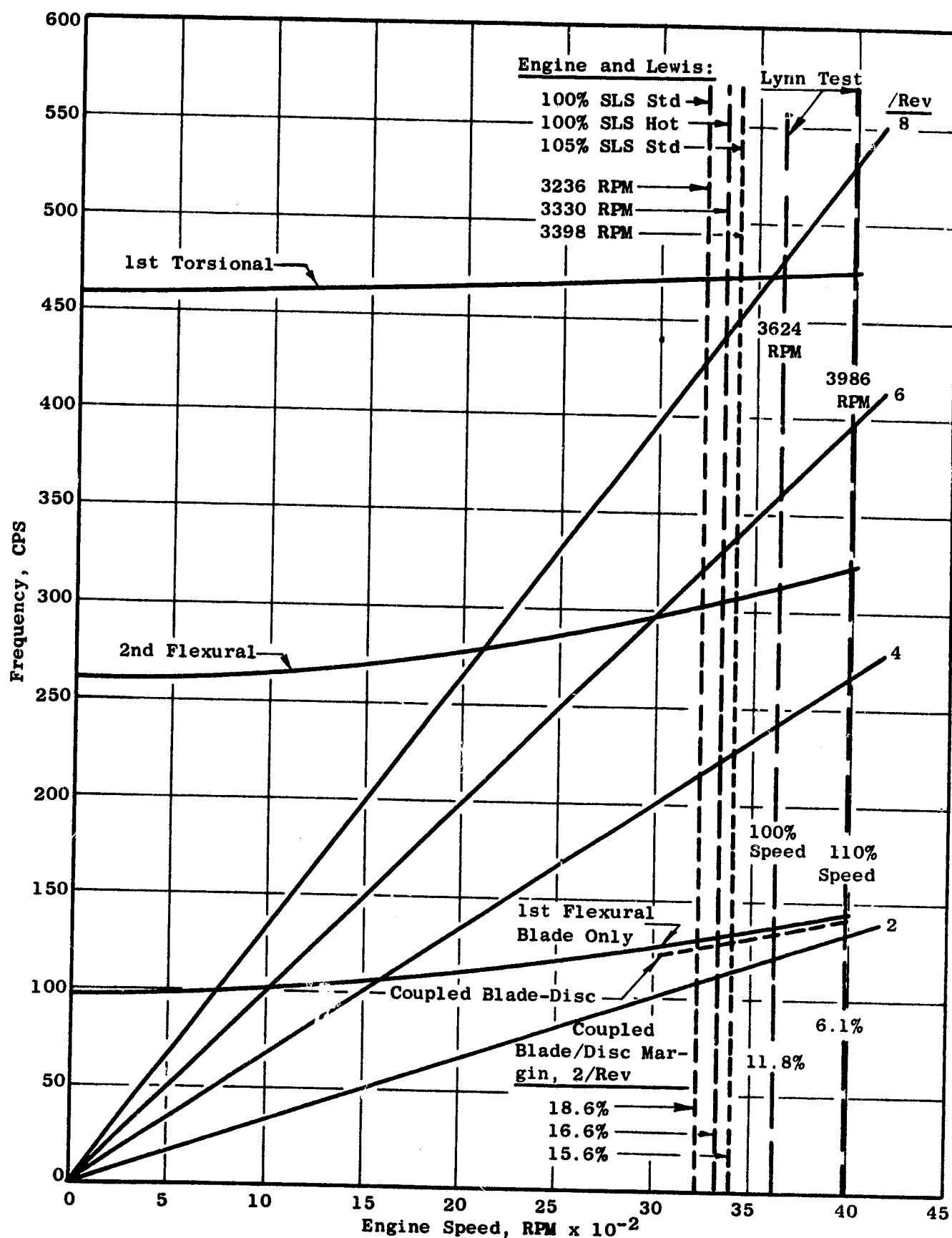


Figure 103. Campbell Diagram for the Fan B Titanium Blade

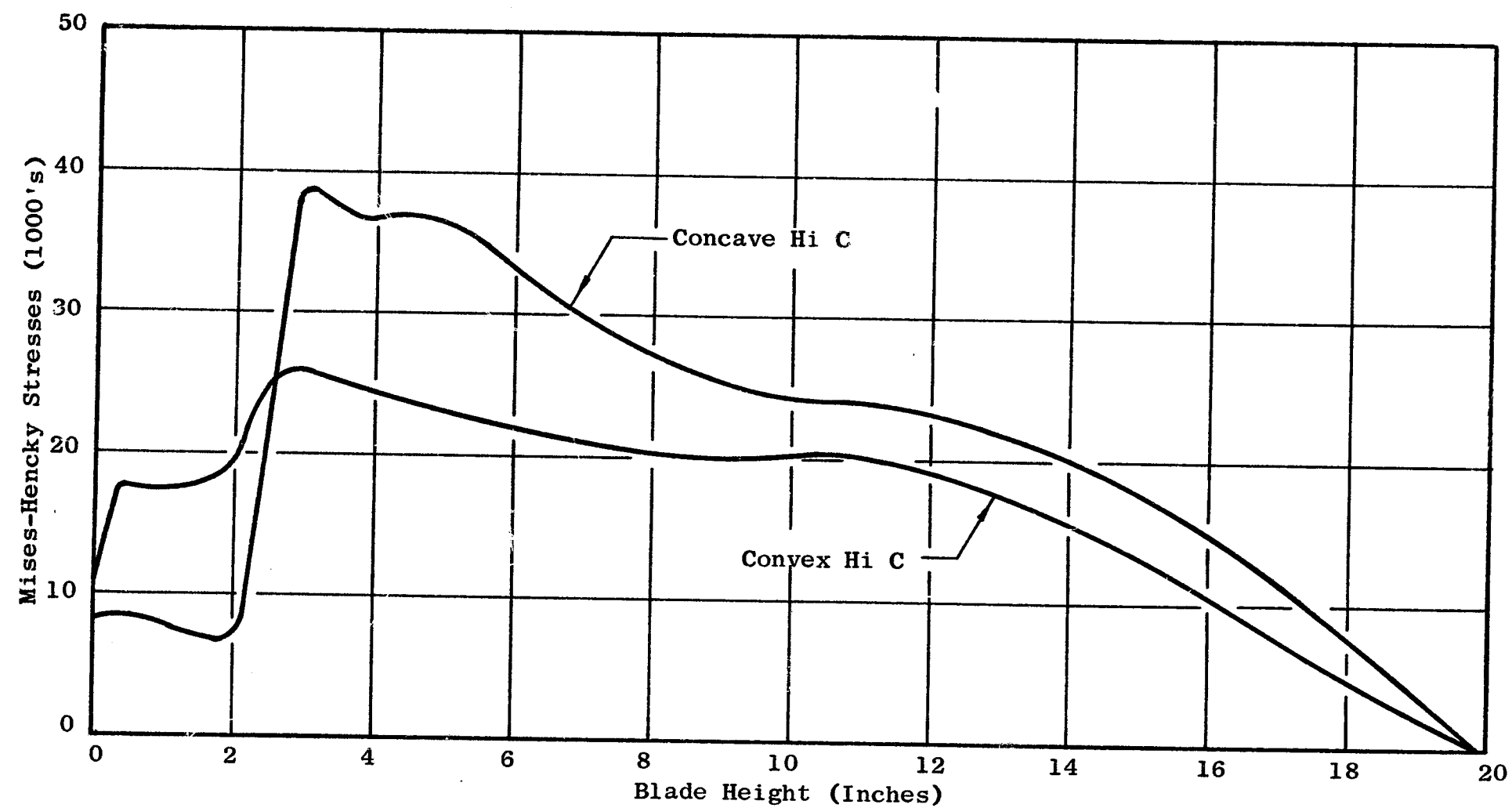


Figure 104. Titanium Blade Steady State Stress Vs Blade Height (N = 3986 RPM - 110% Speed)

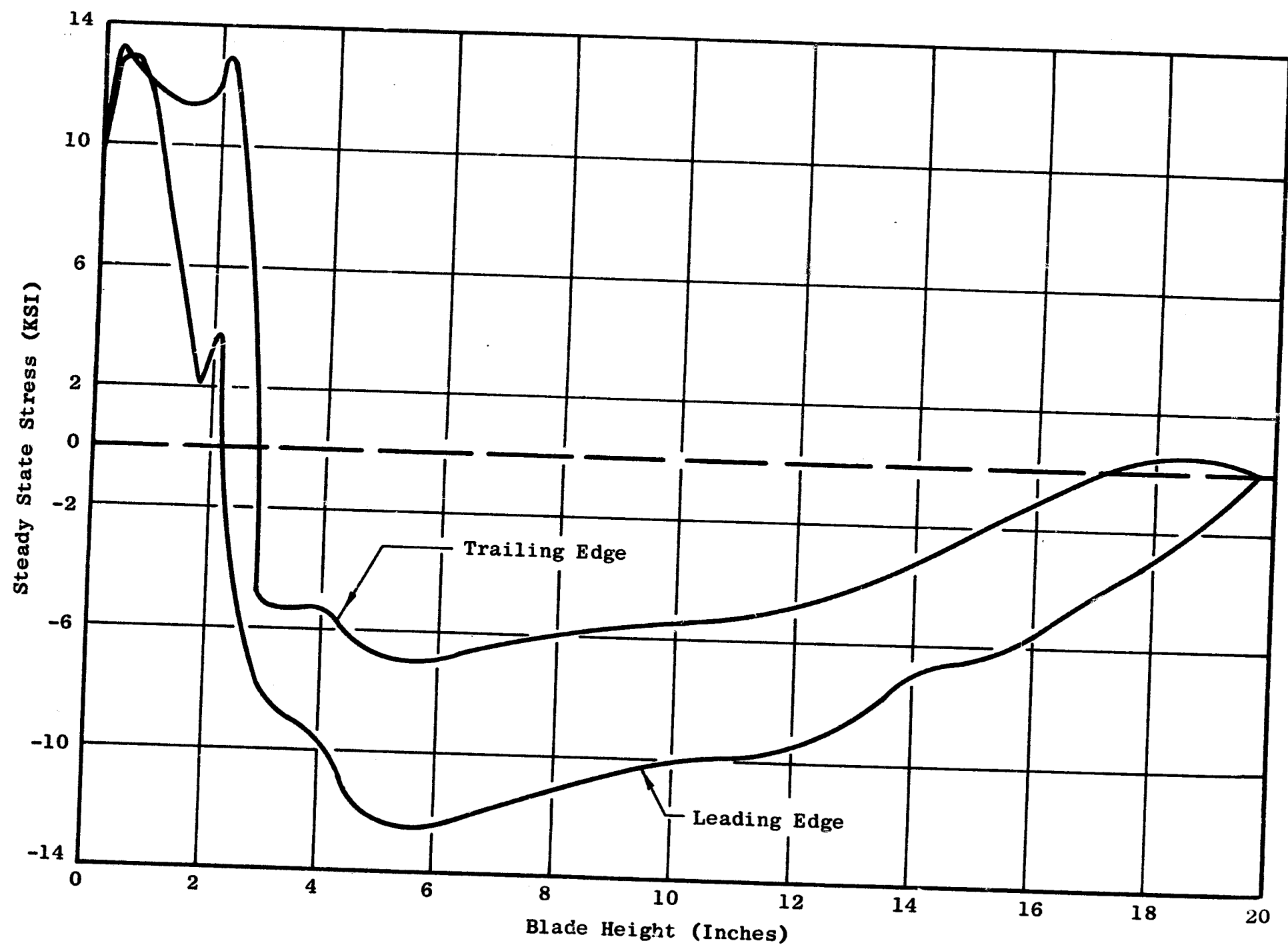


Figure 105. Titanium Blade Steady State Stress Vs Blade Height (N = 3986 RPM - 110% Speed)

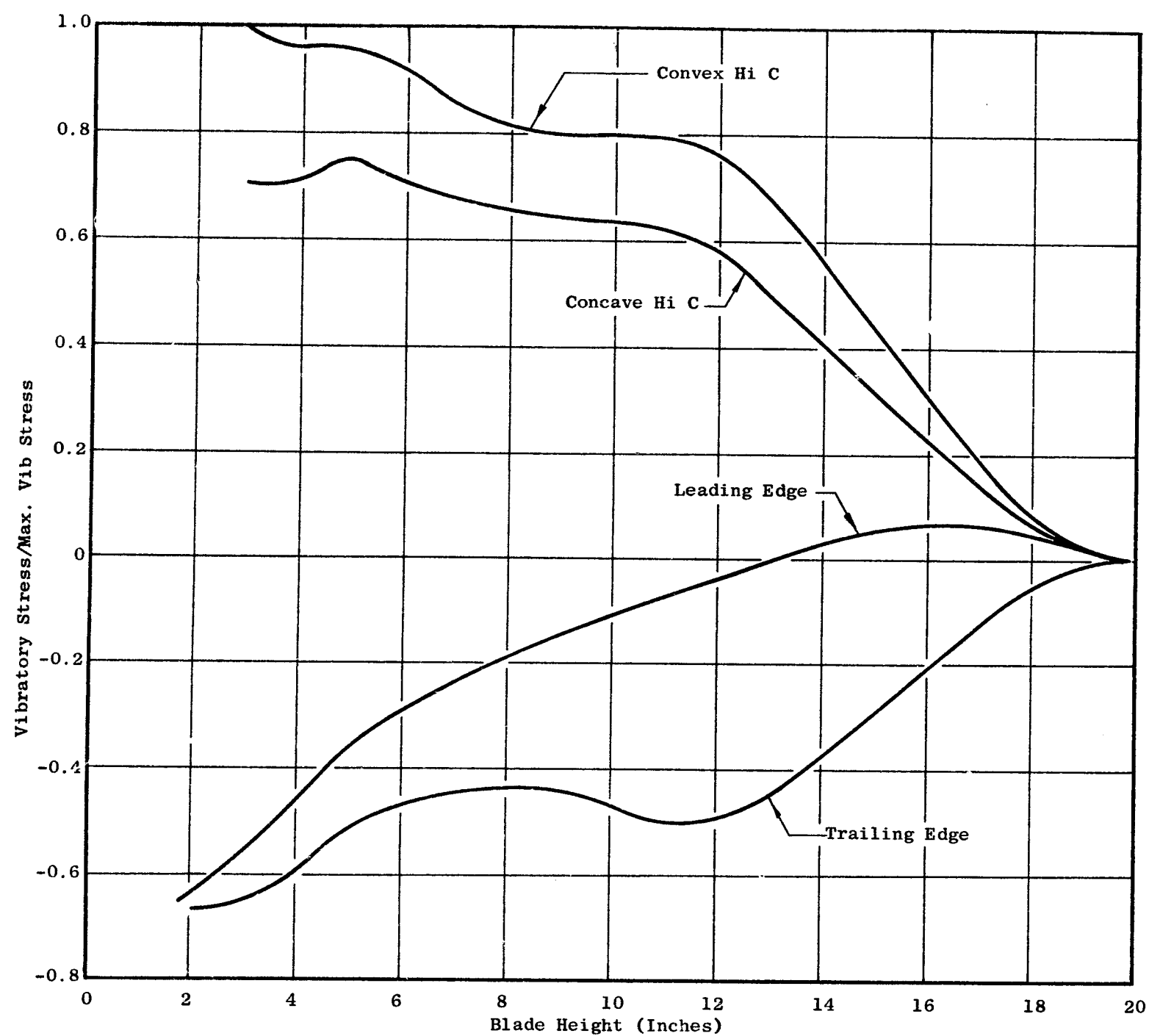


Figure 106. Titanium Blade Vibratory Stress Vs Blade Height for the 1st Flexural Mode (N = 3986 RPM)

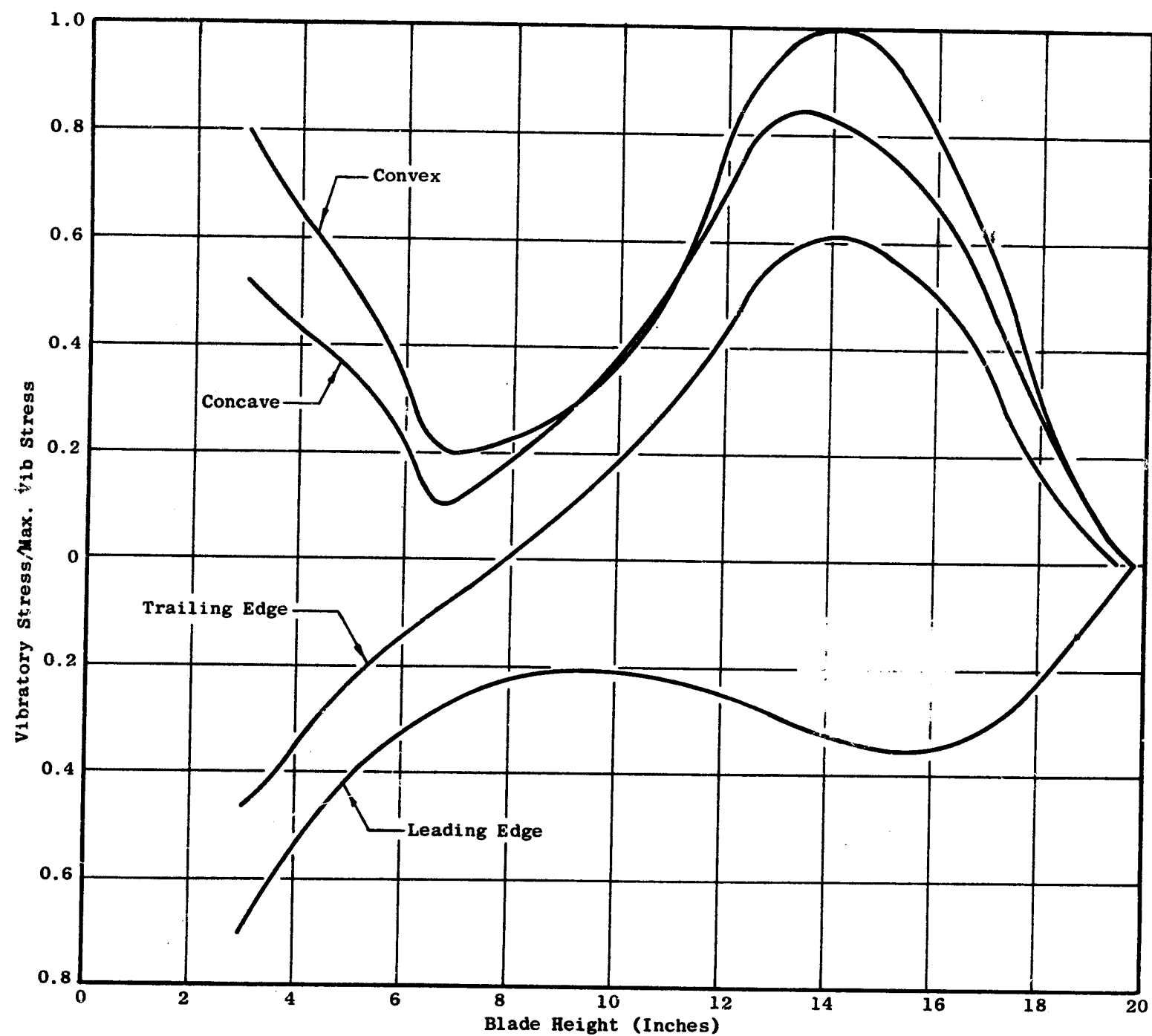


Figure 107. Titanium Blade Vibratory Stress Vs Blade Height for the 2nd Flexural Mode (N = 3986 RPM)

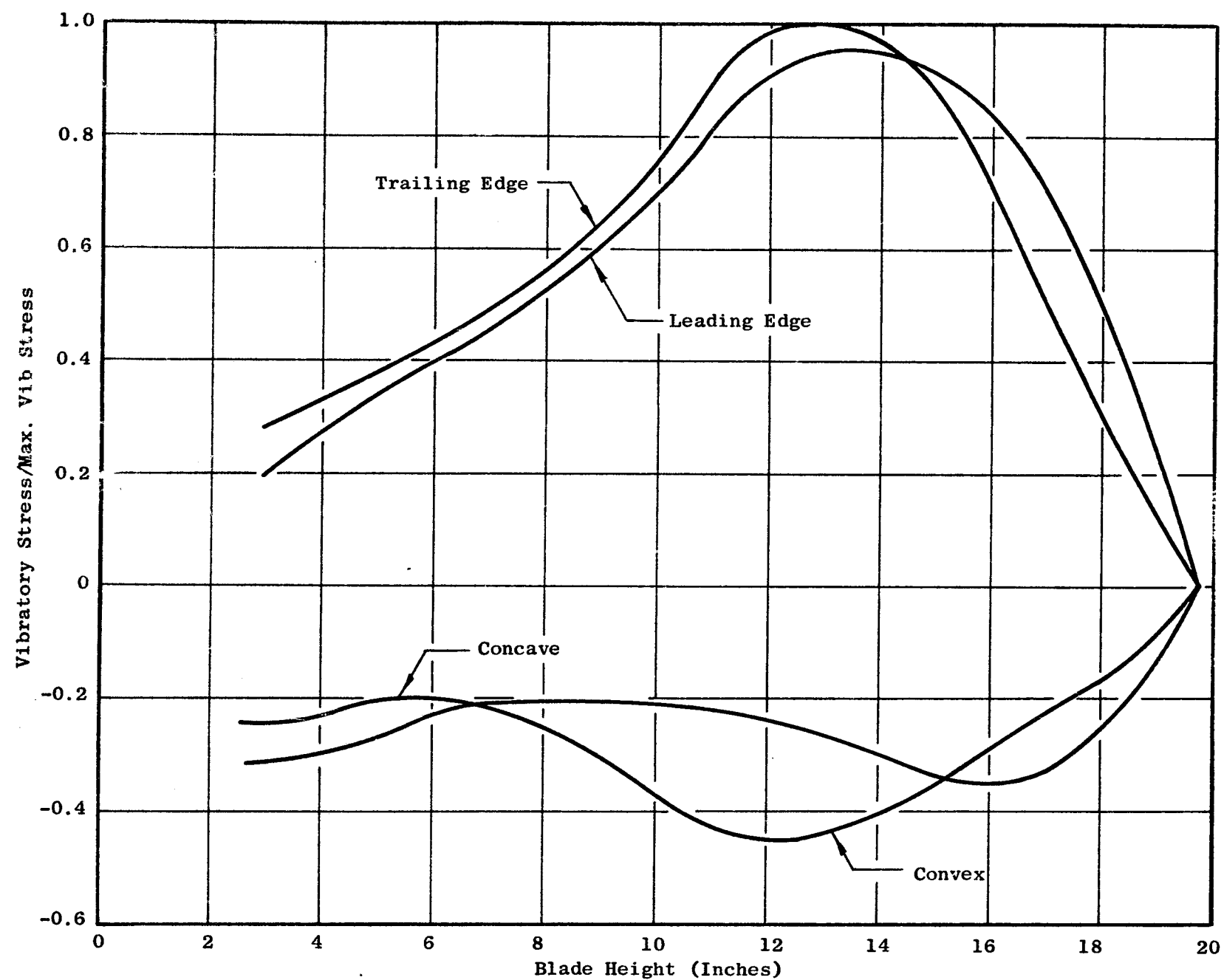


Figure 108. Titanium Blade Vibratory Stress Vs Blade Height for the 1st Torsional Mode (N = 3986 RPM)

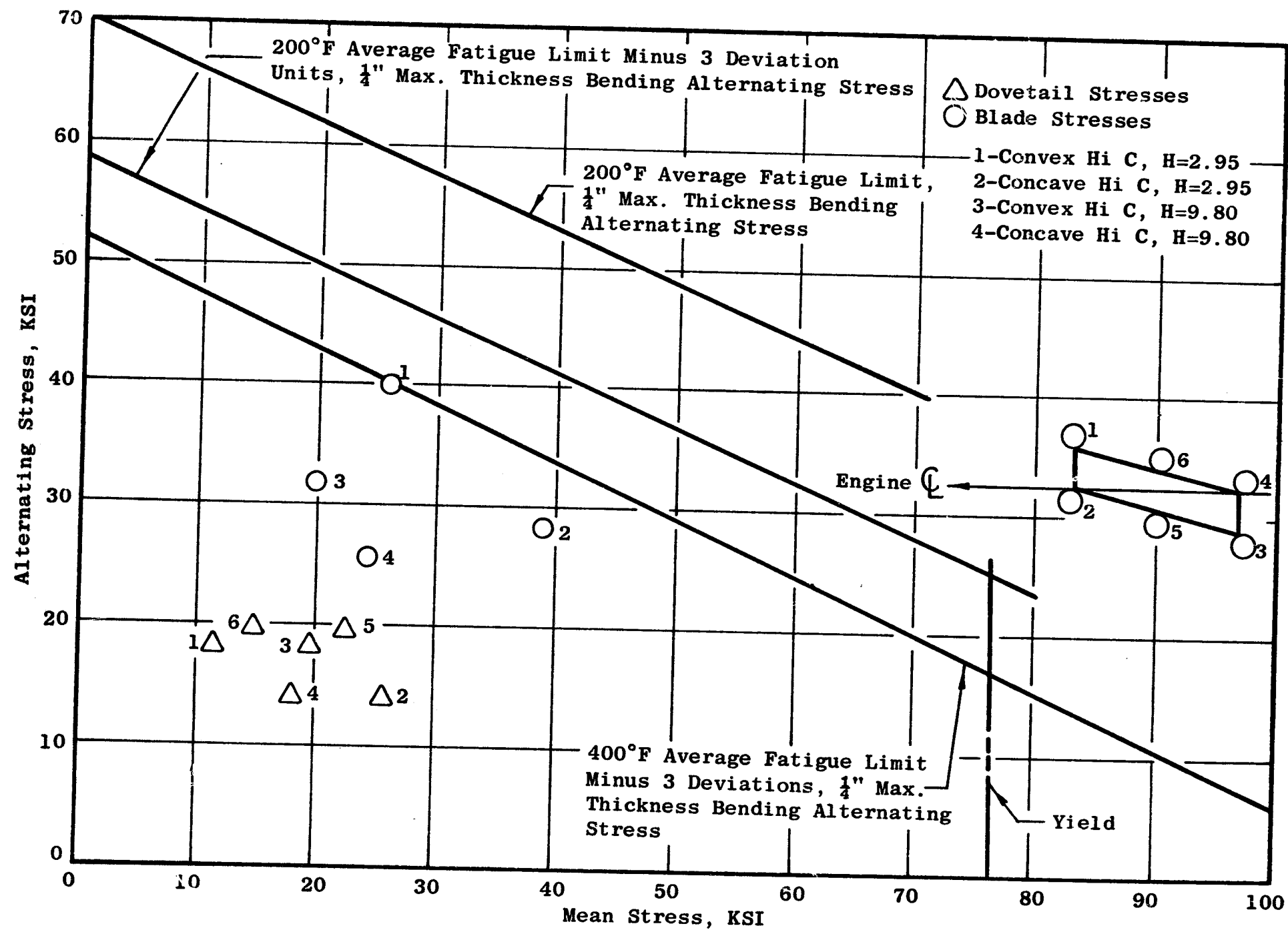


Figure 109. Goodman Diagram for Ti 6Al-4V Titanium Blades, Showing the Location of Critical Stress Points in the First Flexural Mode (N = 3986 RPM - 110% Speed)

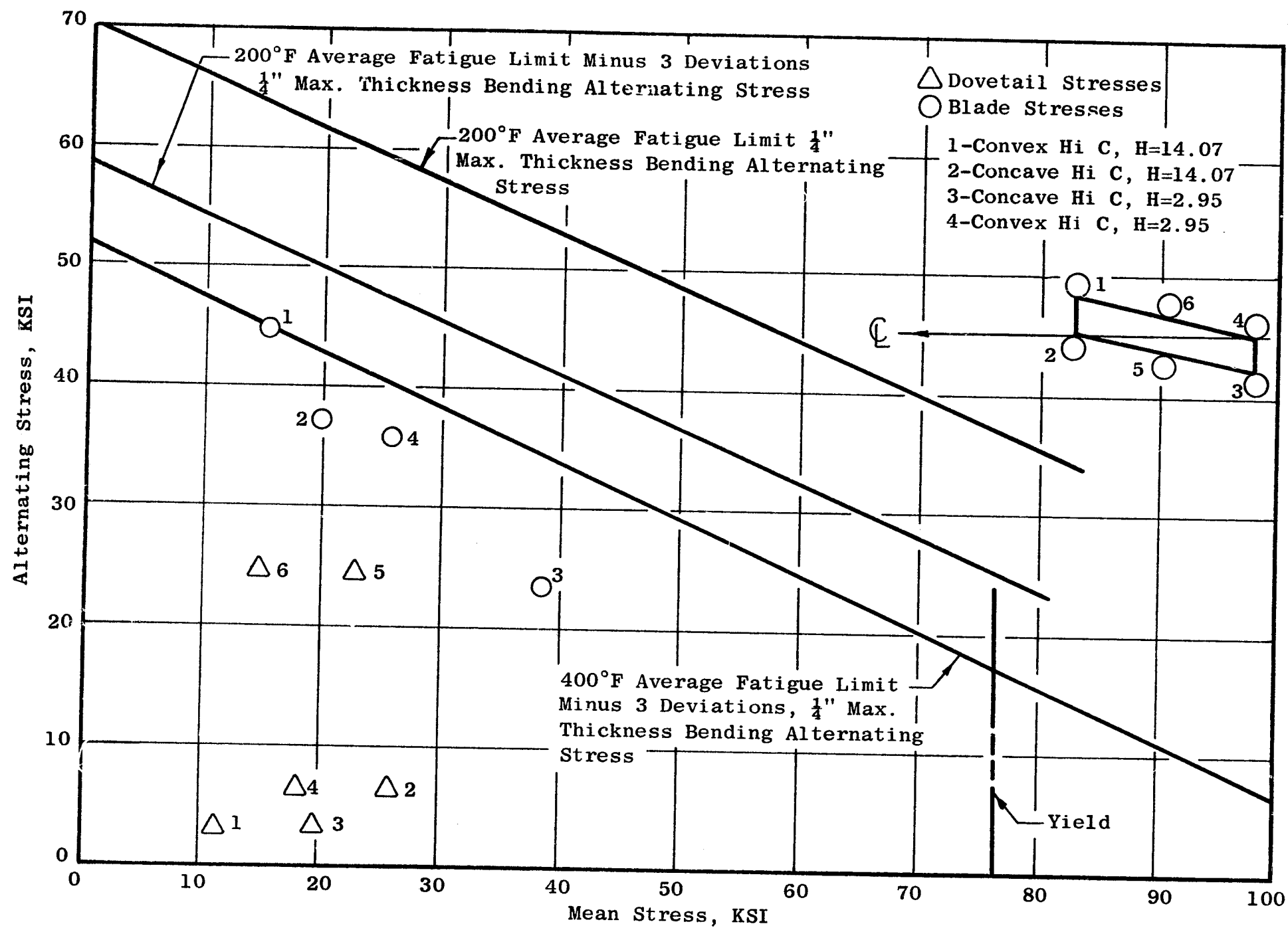


Figure 110. Goodman Diagram for Ti 6Al-4V Titanium Blades, Showing the Location of Critical Stress Points in the Second Flexural Mode (N = 3986 RPM - 110% Speed)

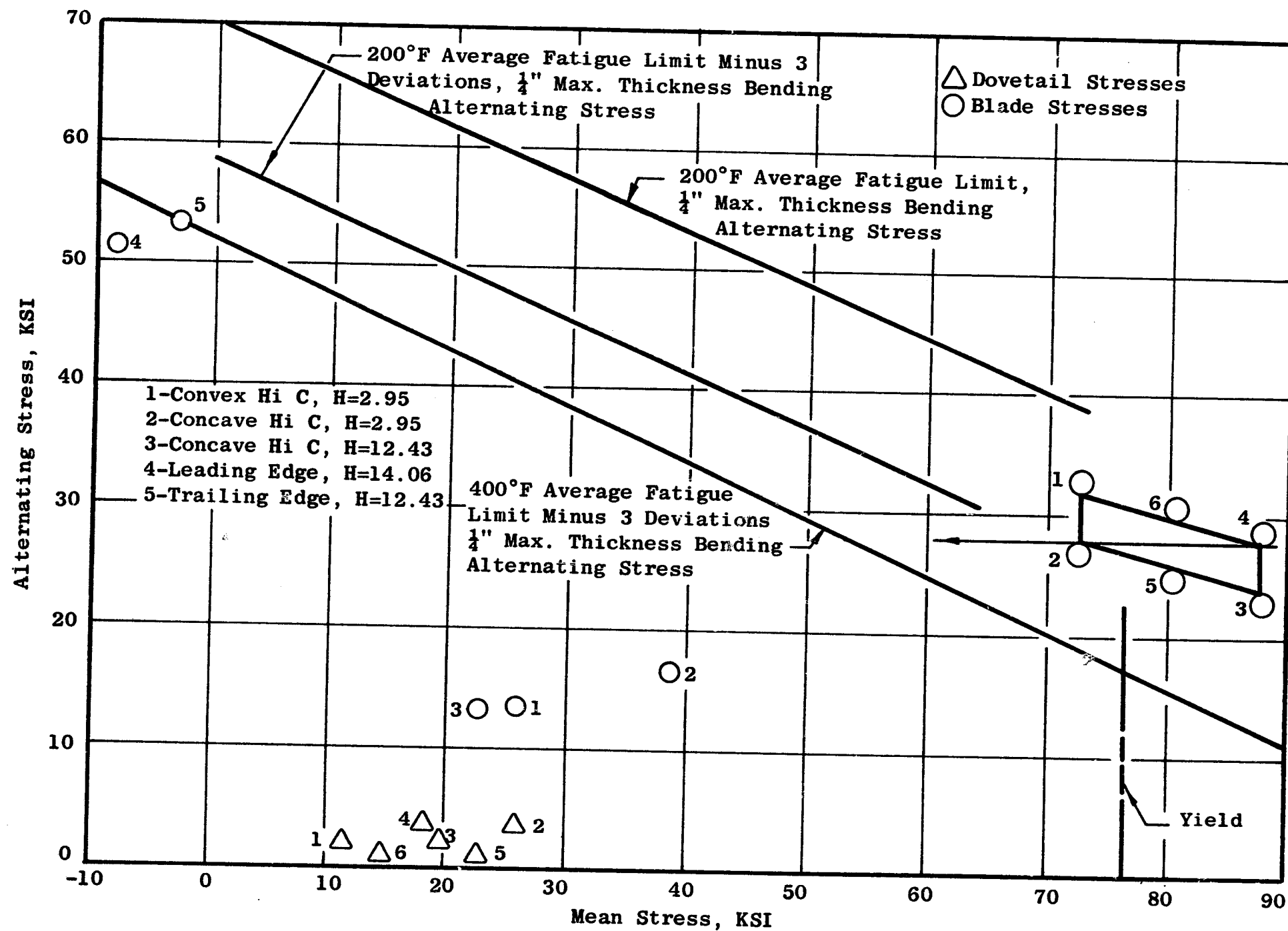


Figure 111. Goodman Diagram for Ti 6Al-4V Titanium Blades, Showing the Location of Critical Stress Points in the First Torsional Mode (N = 3986 RPM - 110% Speed)

Table XXIV. Fan B Titanium Blade Dovetail Stresses

<u>Location</u>	<u>Total Stress</u>	<u>Neck Stress</u>	<u>Tang Stress</u>	<u>Load S/V (*-Extreme)</u>
1 (S)	11520.5	5977.58	6252.28	8584.19
(V)	1832.04	1492.45	480.707	484.831
2 (S)	25921.7	19507.6	8406.34	11541.7
(V)	1418.98	803.751	708.628	714.708
3 (S)	19652.8	13953.1	7181.9	9860.54
(V)	-1832.04	-1492.45	-480.70	-484.831
4 (S)	18210.9	11849.1	7676.22	10539.2
(V)	-1418.98	-803.751	-708.628	-714.708
5 (S)	22798.5	16730.3	7794.12	10701.1
(V)	19679.8	-344.351	113.961	114.939
6 (S)	14879.9	8913.35	6964.25	9561.71
(V)	19679.8	344.351	-113.961	-114.939

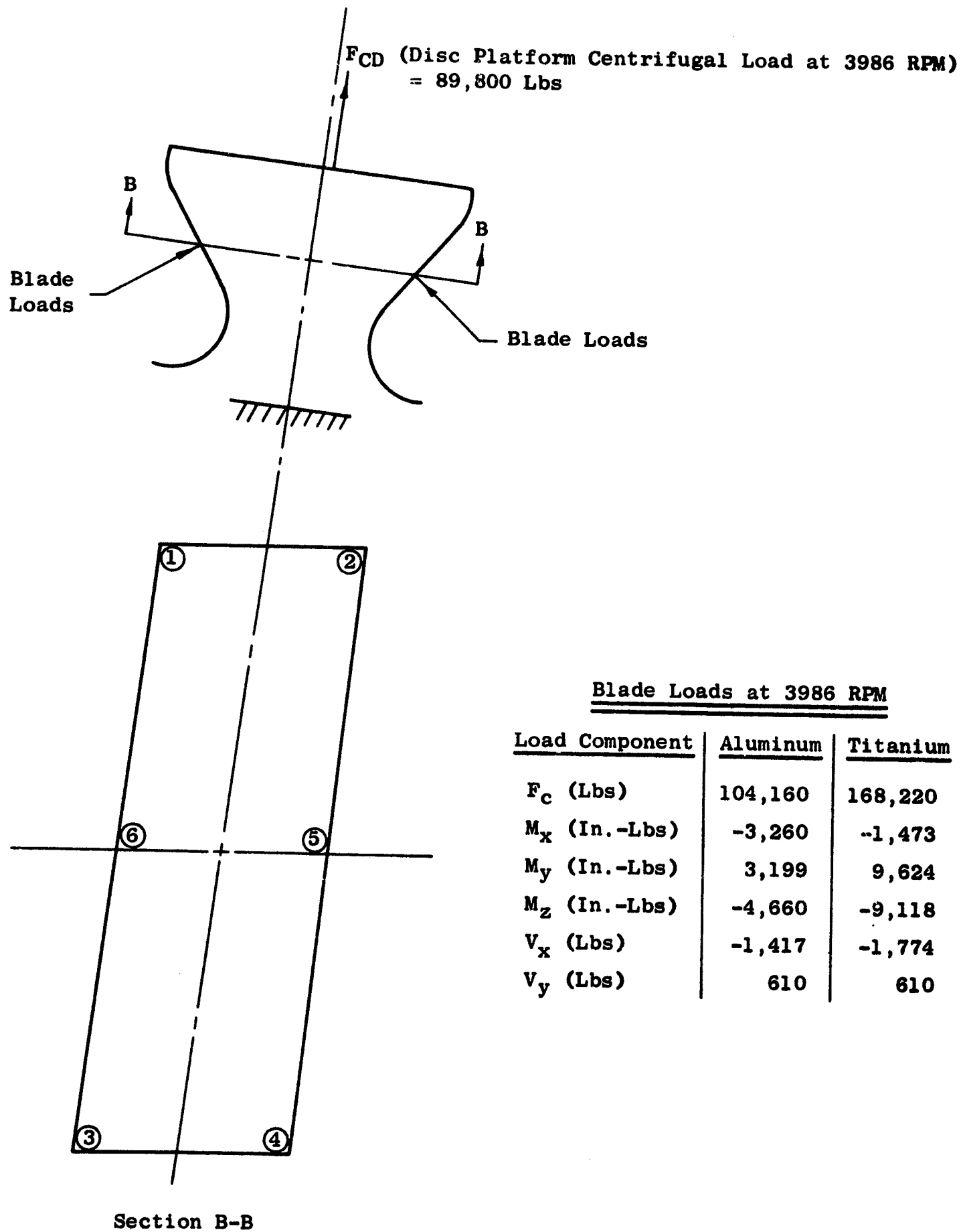


Figure 112. Disc Dovetail Boundary Loads

- Bench Tests

Prior to rig testing, the blades will be bench tested. The blade will be clamped in a set of dovetail jaws and vibrated with an electromagnet. Resonant frequencies will be obtained in this manner. Vibration stress distribution in the first few resonant nodes will be obtained by vibrating a blade instrumented with several hundred strain gages. Since the vibratory stress distribution will not vary appreciably with centrifugal load, data from this test can be used to place strain gages on the blade for read-out at operating speed.

Blade endurance strength will be established by a bench fatigue test of at least three blades. The test is conducted by clamping an instrumented blade at the dovetail and exciting it in its first flexural mode with a siren until failure occurs. Data from this test will be plotted on the Goodman diagram for comparison with the material test data.

Finally an end effects test will be conducted to correct stresses at the blade root calculated by the Twisted Blade Program. While the blade is clamped at the dovetail, stresses at the root will be measured under a known moment applied about the x, y, and z axis of the blade. These data will be applied to the moments calculated by the Twisted Blade Program to calculate blade stresses at the root.

5.1.1.2.2 Disc Design

- Material Selection

Criteria for selection of the disc material was that it be of high strength, low cost, readily available, and easily forged in large sections. An alloy steel was the natural choice and AMS 4340 was selected because it has good properties, is relatively inexpensive, and (more important) readily available (due to a nickel shortage, forgings of stainless alloys such as AM 355 or 17-4 PH require a long lead time). The disc will be machined from a pancake forging which is certified to AMS 6414A (vacuum remelt). The forging will be ultrasonically inspected prior to final machining.

Just prior to final machining, the disc will be heat treated to a 311-352 Brinell Hardness (33R - 38R). In this condition, the alloy is expected to have the minimum mechanical properties shown in Table XXV.

Table XXV. Material Properties of AISI 4340 at Room Temperature

E	30×10^6	σ ULT	145,000 PSI
G	11.7×10^6	σ .02Y	130,000 PSI

$$\gamma = 0.283 \text{ lb/in.}^3$$

- Loads and Temperatures

Table XXVI gives the rim loads used in the disc analysis. The stresses and deflection in the disc were calculated with the disc operating at 3986 rpm in the Lynn FSFT with titanium blades. Maximum operating temperature was assumed to be 200°F.

- Disc Dovetail

The method used for analyzing a disc dovetail is almost exactly the same as the method used to analyze the blade dovetail. The major difference is that the centrifugal load of the disc dead rim must be included in the analysis. Figure 112 is a sketch of the disc dovetail with the applied loads. The load distribution along the length of the disc dovetail is reported in Table XXVI along with the steady state and vibratory stresses. Figure 113 is a Goodman diagram for the 4340 material with the combined dovetail stresses plotted. These stresses are well below the allowable Goodman line.

Figure 114 is the model for the disc portion of the finite element blade-disc dovetail analysis. Again maximum stress occurs at the ends of the mating surfaces of the blade-disc dovetails.

- Disc Stresses

Figure 114 shows radial, tangential, and effective stress versus disc diameter for the disc rotating at 3986 rpm with titanium blades. Maximum effective stress is at the disc bore. Average tangential stress is 44 percent ultimate tensile stress of the 4340. This analysis was conducted with centrifugal loads only -- no moments or shear loads were included.

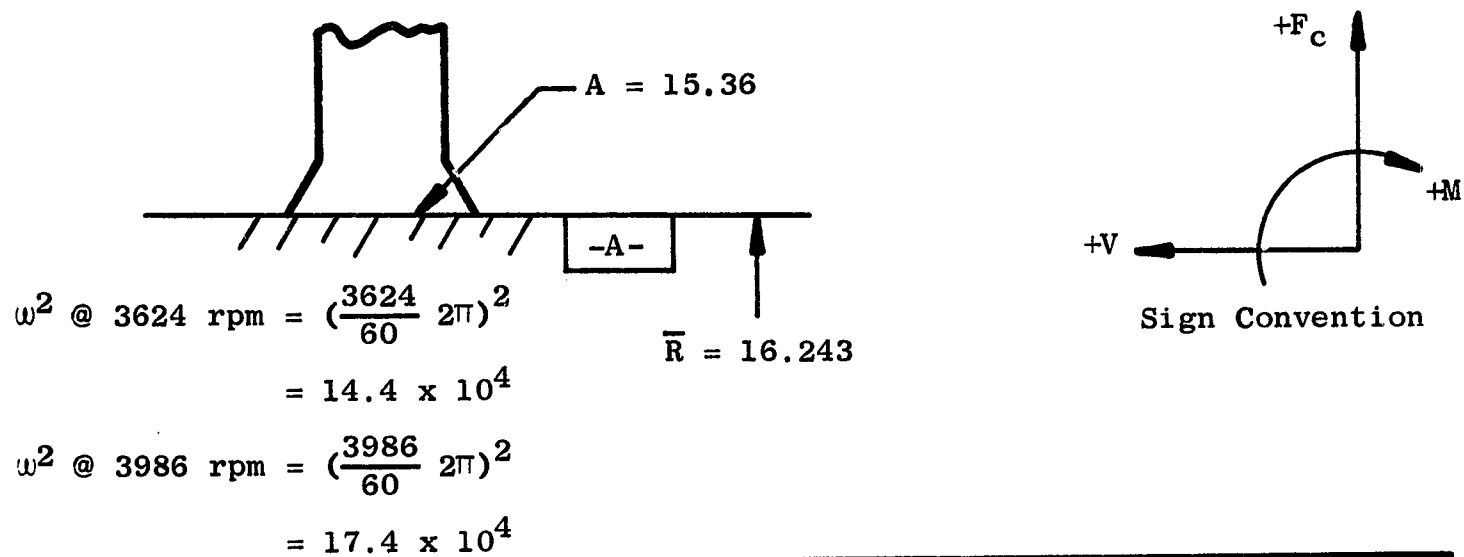
An analysis of the deflections and stresses of the entire rotor system at various speeds was conducted. Figures 115 through 117 give results of this analysis. Figure 115 gives the loads and boundary conditions used in the analysis. Figure 116 gives stresses calculated at the member joints. Maximum stress is at the disc bore. These stresses vary from those reported in Figure 114 because bending and shear loads are considered. Figure 117 gives axial, radial, and rotating deflections. Deflection at the disc rim was only 8.7×10^{-4} radians. This gives essentially negligible axial movement at the blade tip (0.017). All in all, the disc is extremely stable, stresses are nominal.

- Other Rotor Components

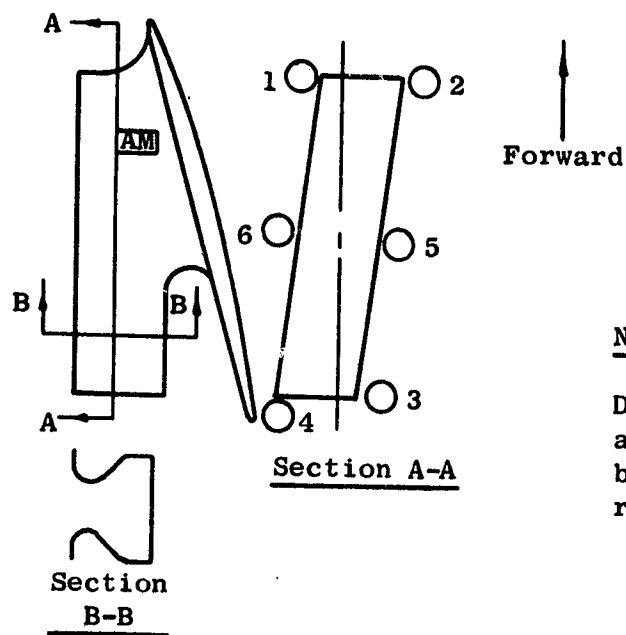
The spinner nose and cone are both fabricated from 6061T4 aluminum. Aluminum was selected because it is inexpensive and easy to process. Stresses in the spinner are nominal (Ref: Figures 116 and 117).

Table XXVI. Fan B Disc Rim Loads

Twisted blade loads at base are about midpoint dovetail pressure surface. This is shown as Plane -A- below:



Material	Comment	Load	3624 RPM		3986 RPM	
			Load/ Blade	Rim Load lb/in.	Load/ Blade	Rim Load lb/in.
Aluminum 7075-T73 = 0.098 lb/in. ³	Airfoil	F _c	74 700	---	90 500	---
	Airfoil	M _x	-2 847	-724	-3 259	-830
	Airfoil	V _y	508.5	129.5	610	155.1
	Platform & Lower DT	F _c	11 300	---	13 660	---
	Disc Dead Load	F _c	74 400	---	89 800	---
	Total F _c		160 400	40 800	193 960	49 300
Titanium 6-4 = 0.161 lb/in. ³	Airfoil	F _c	121 400	---	146 800	---
	Airfoil	M _x	-1 356	-346	-1 473	-375
	Airfoil	V _y	508.5	129.5	610	155.4
	Platform & Lower DT	F _c	18 600	---	22 420	---
	Disc Dead Load	F _c	74 400	---	89 800	---
	Total F _c		214 400	54 500	258 000	65 600
Steel 403 SS or 17-4PH	Airfoil	F _c	214 100	---	259 000	---
		M _x	1 331	348	1 734	441
		V _y	5 085	129.5	610	155.4
		F _c	32 600	---	39 000	---
		F _c	74 400	---	89 300	---
	Total F _c		321 100	81 900	367 800	93 000



Note:

Disc dovetail combined stresses are plotted. Stresses are based on Ti blades at 3986 rpm in 1st flexural mode.

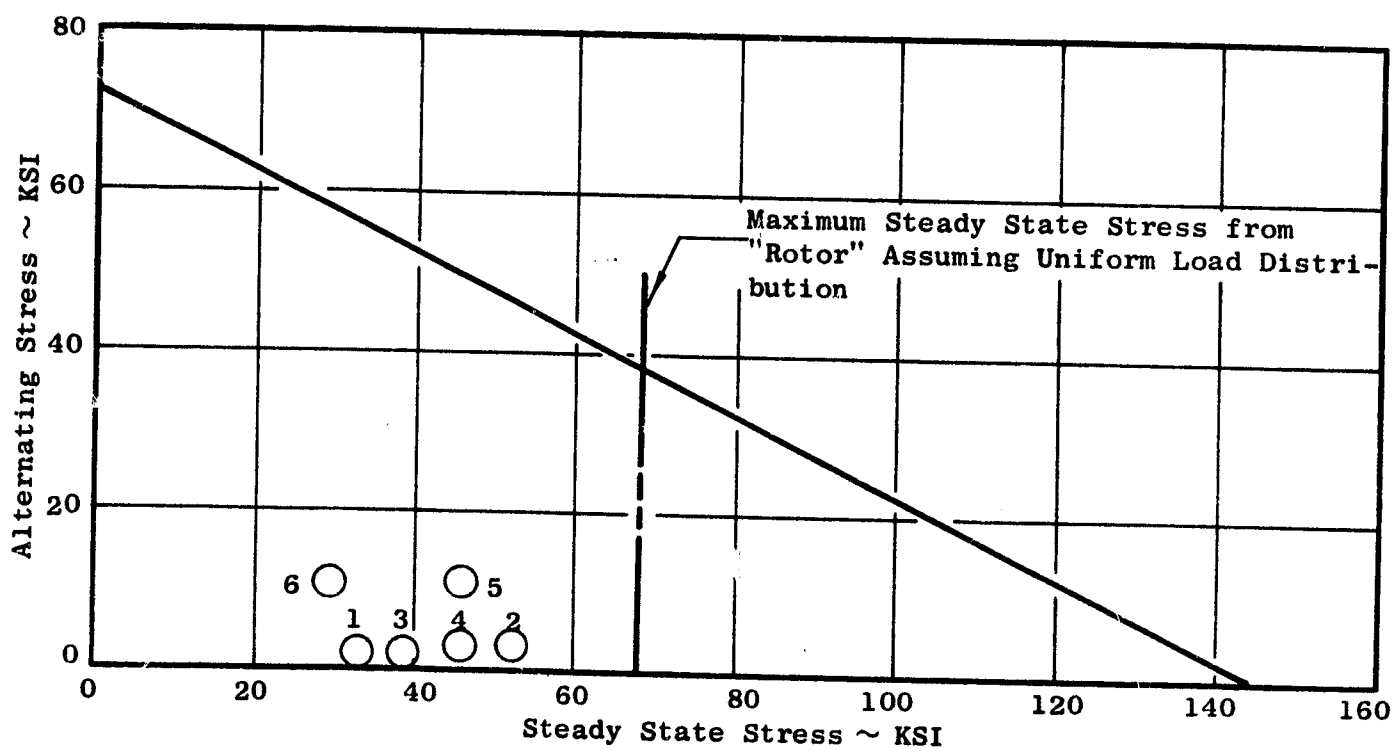


Figure 113. Fan B Goodman Diagram for a 4340 Steel Rotor Disc

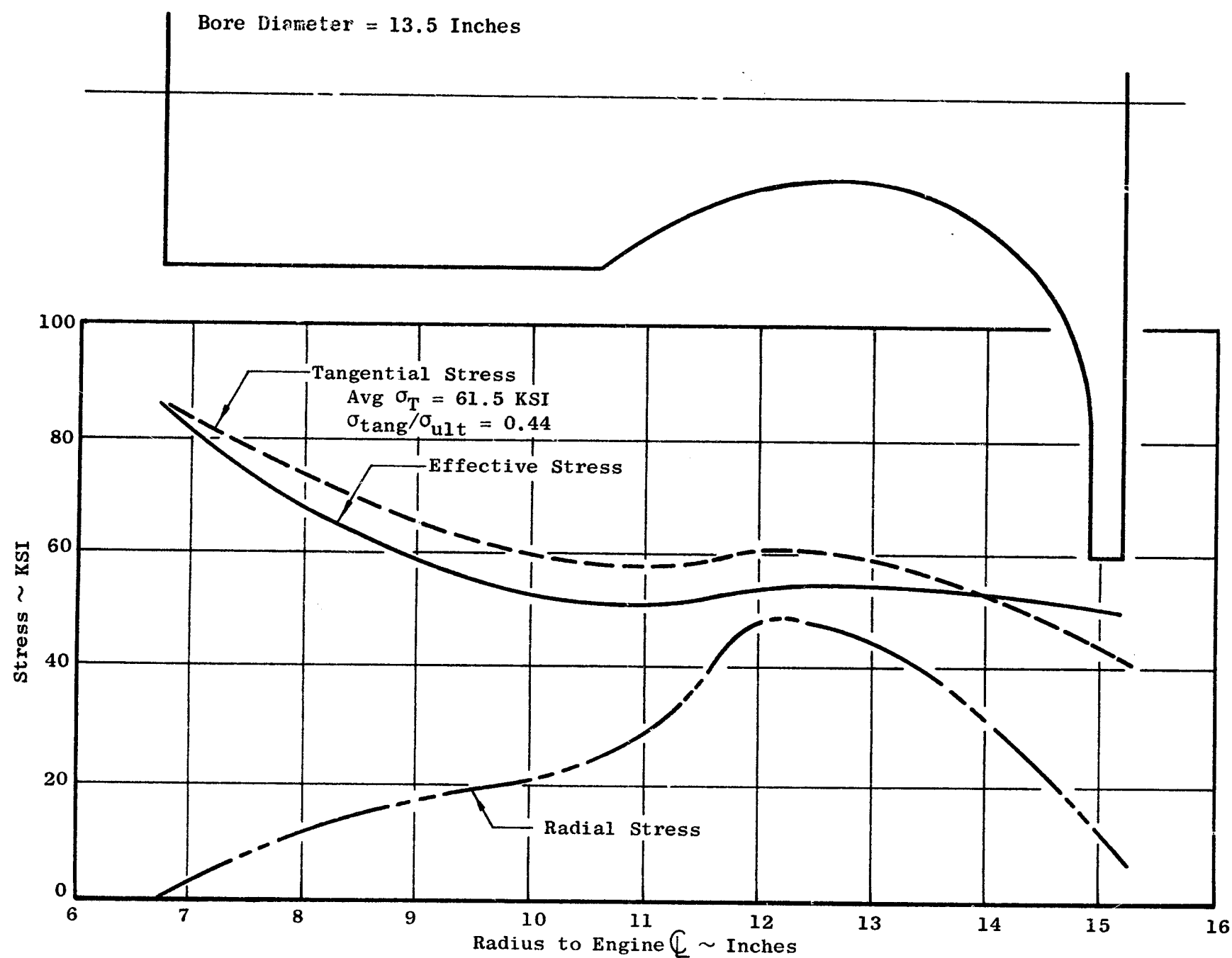


Figure 114. Fan B Rotor Disc Elastic Disc Stresses Vs Radius (Titanium Blade, $N = 3986$ RPM, $\Delta T = 130^\circ\text{F}$)

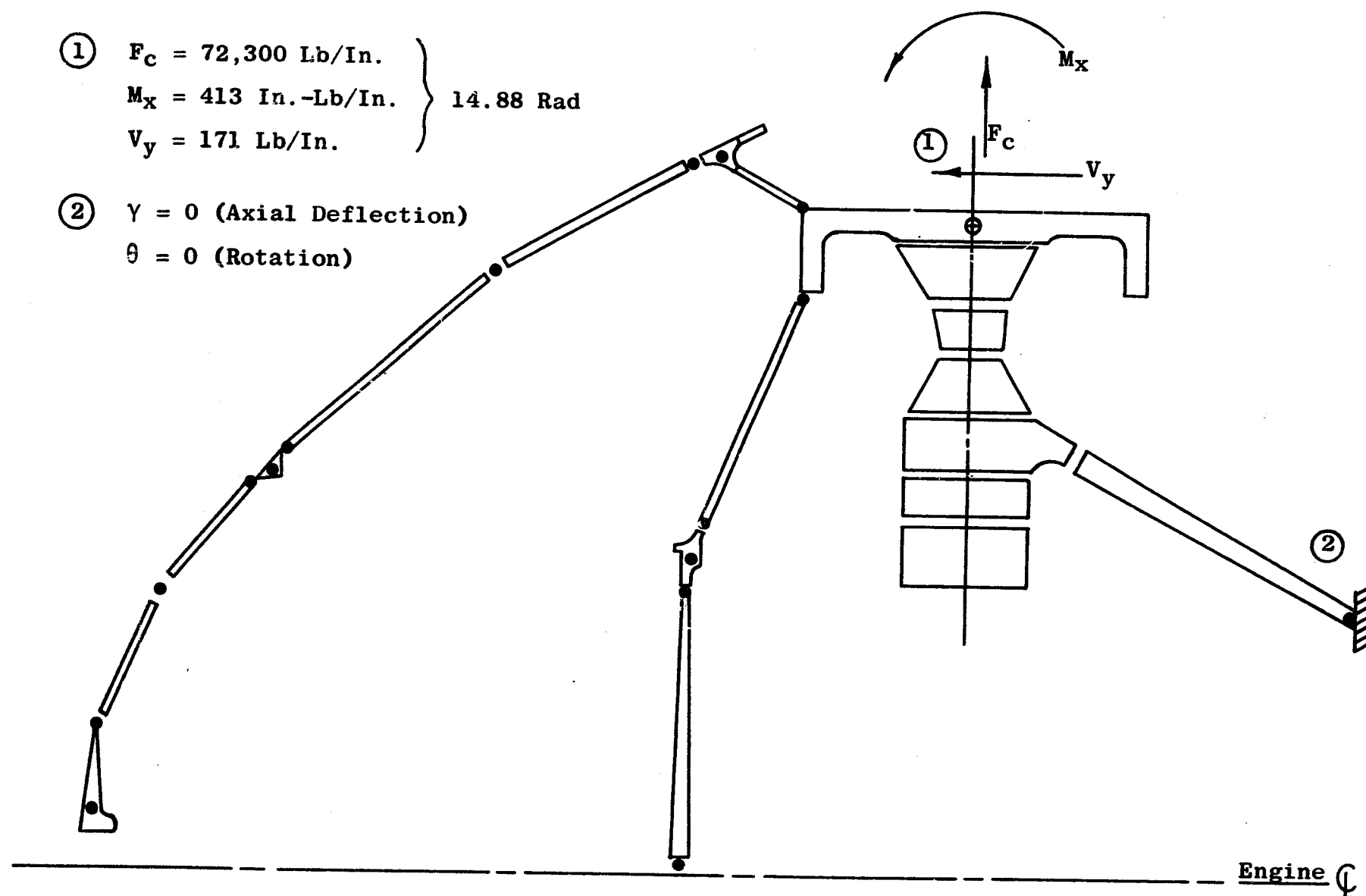


Figure 115. Model, Quiet Engine B Configuration Fan Rotor Boundary Loads (Titanium Blades, 3986 RPM)

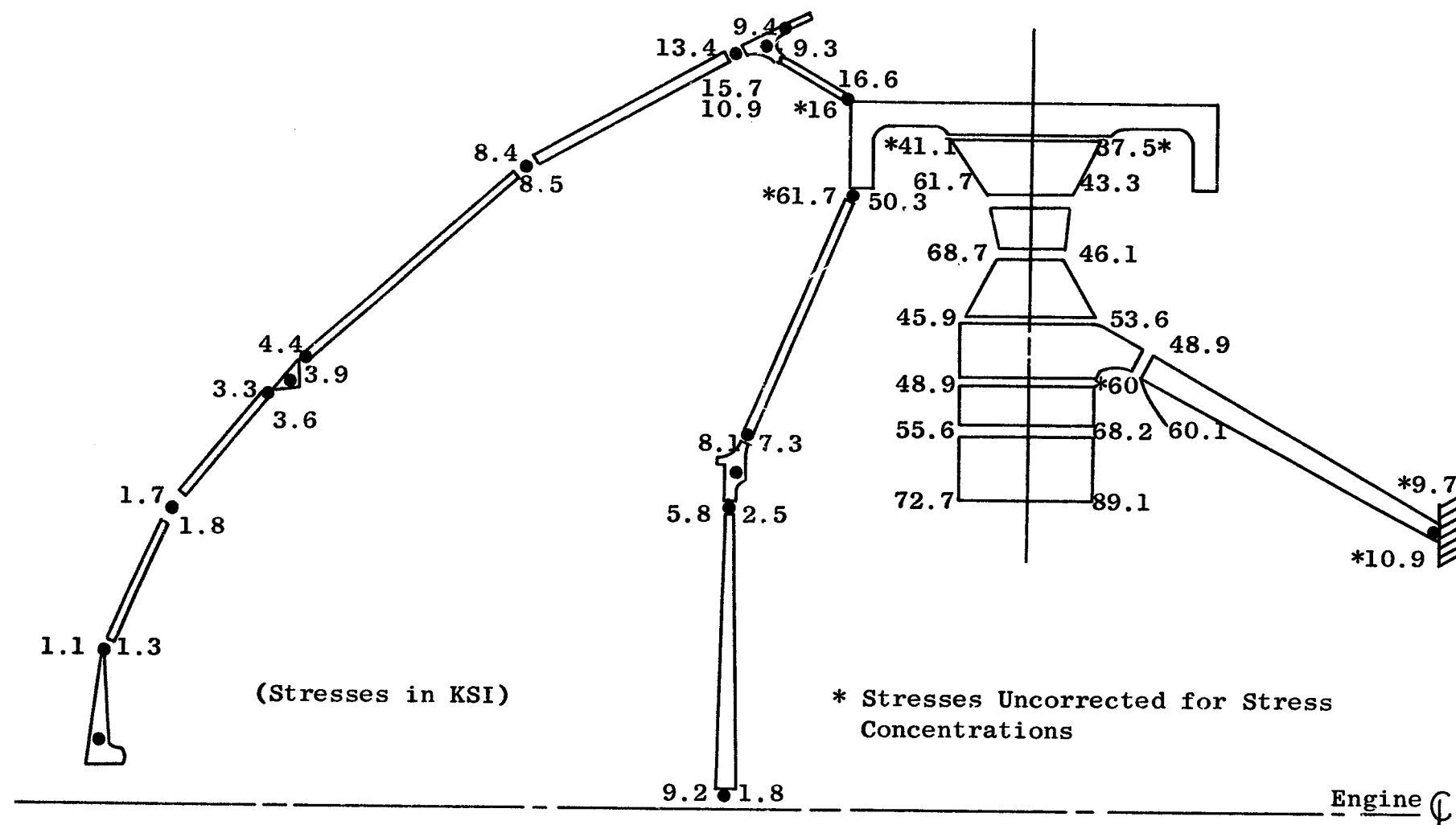


Figure 116. Model, Quiet Engine B Configuration Fan Rotor Stresses (Titanium Blades, 3986 RPM)

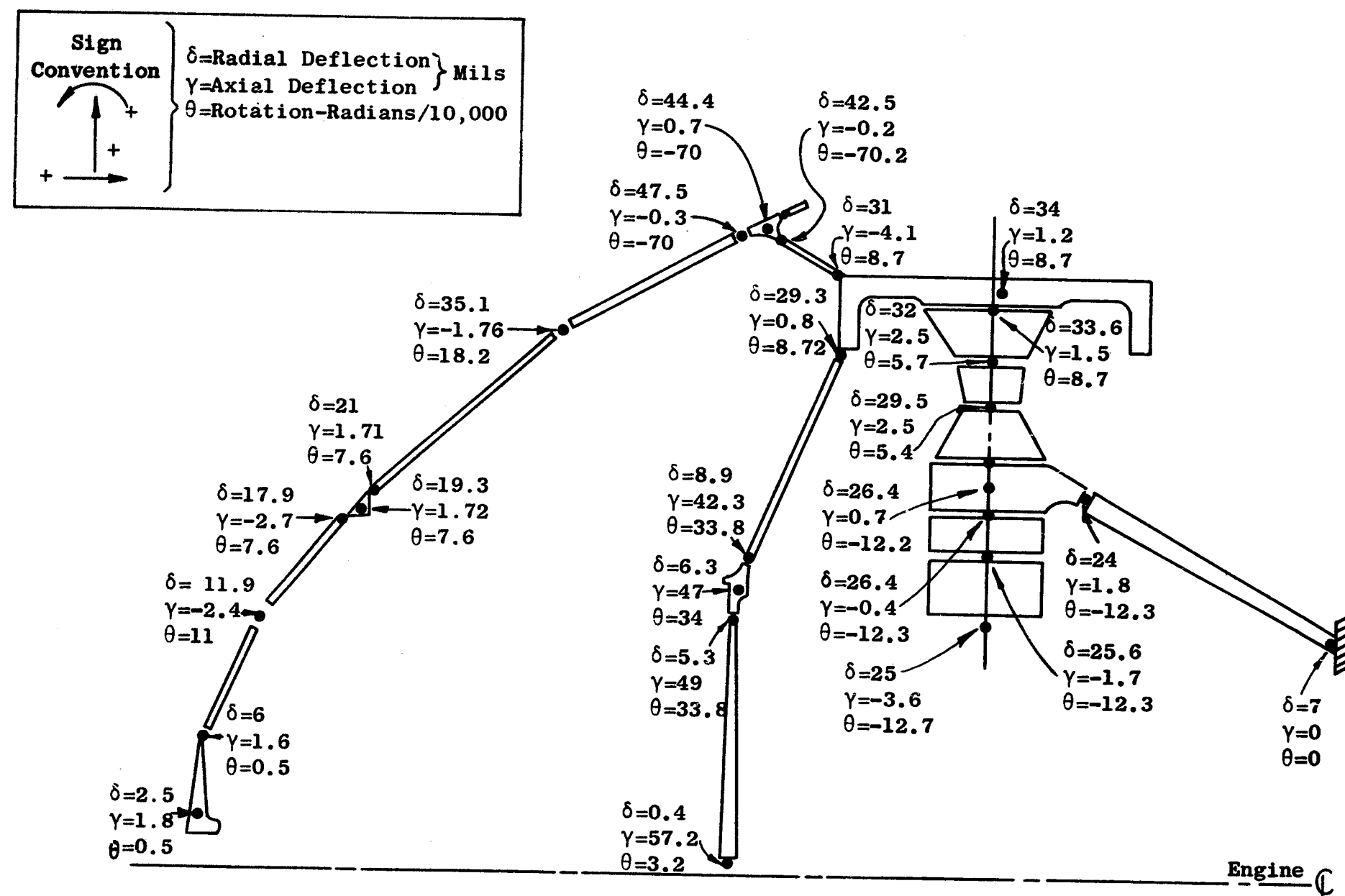


Figure 117. Model, Quiet Engine B Configuration Fan Rotor Deflections (Titanium Blades, 3986 RPM)

The telemetry adapter hardware was fabricated from 17-4PH stainless steel. Stresses and deflections for this hardware are also shown in Figures 116 and 117.

5.1.1.3 Fan C Rotor

The Fan C rotor is a high tip speed, low aerodynamic loaded fan with low noise capabilities. The fan has 26 blades, a design tip speed of 1550 feet per second, and a radius ratio of 0.36.

5.1.1.3.1 Blade Design

For the Fan C rotor, aspect ratio of 2.2 necessitates the use of a mid-span damper to high flex the rotor blades. Figures 118 through 122 define the blade geometry as a function of airfoil height. The combination of a low radius ratio and a high tip speed results in a fan blade with a large twist gradient, which ultimately results in high steady state stresses. The blade has modified platforms which butt against the disc and form the lower flowpath. A conventional single-tang dovetail is to be used, held in place with a thick spacer between the blade and disc, thereby, allowing individual assembly of the fan blades.

• Stresses

The blade stresses calculated from a Twisted Blade Computer Program are high as anticipated. The two principle factors contributing are:

- 1) High centrifugal loads due to speed
- 2) Large bending and twisting moments produced by high twist and damper fixity

The original geometry determined by Air Design was stress analyzed and found to be marginal in the area of the midspan damper. A new airfoil thickness was generated (with no significant aerodynamic loss) with the thickness beefed up around the shroud, resulting in satisfactory steady state stresses (Figures 123 through 126).

An advanced titanium alloy Ti-6Al-6V-2Sn was chosen for the high speed fan. Fatigue properties for a given steady state stress are far superior to those for any other titanium alloy. High stresses occur at three blade positions:

- 1) Damper location
- 2) Airfoil root
- 3) Dovetail tangs

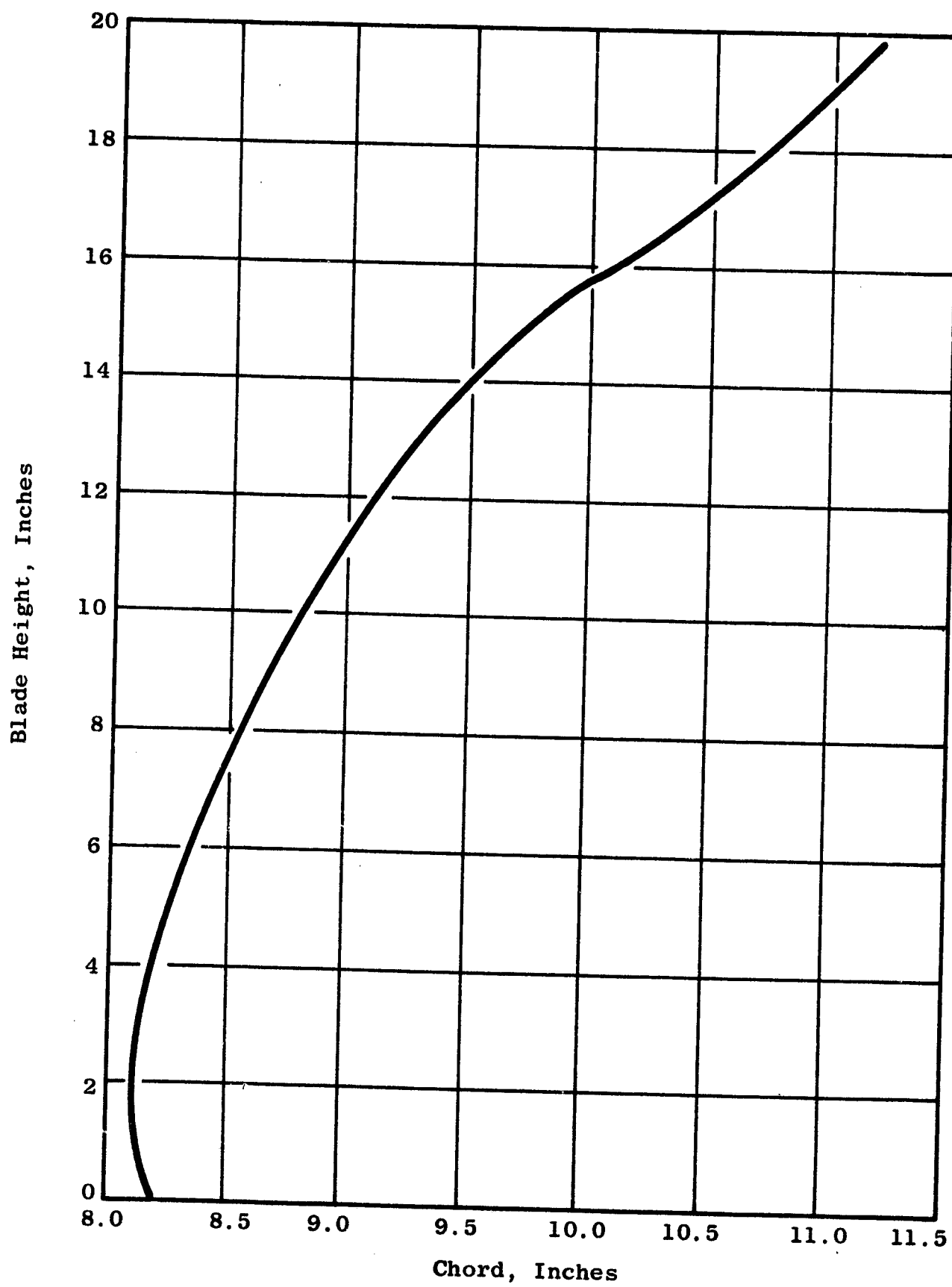


Figure 118. Fan C Airfoil Chord Distribution

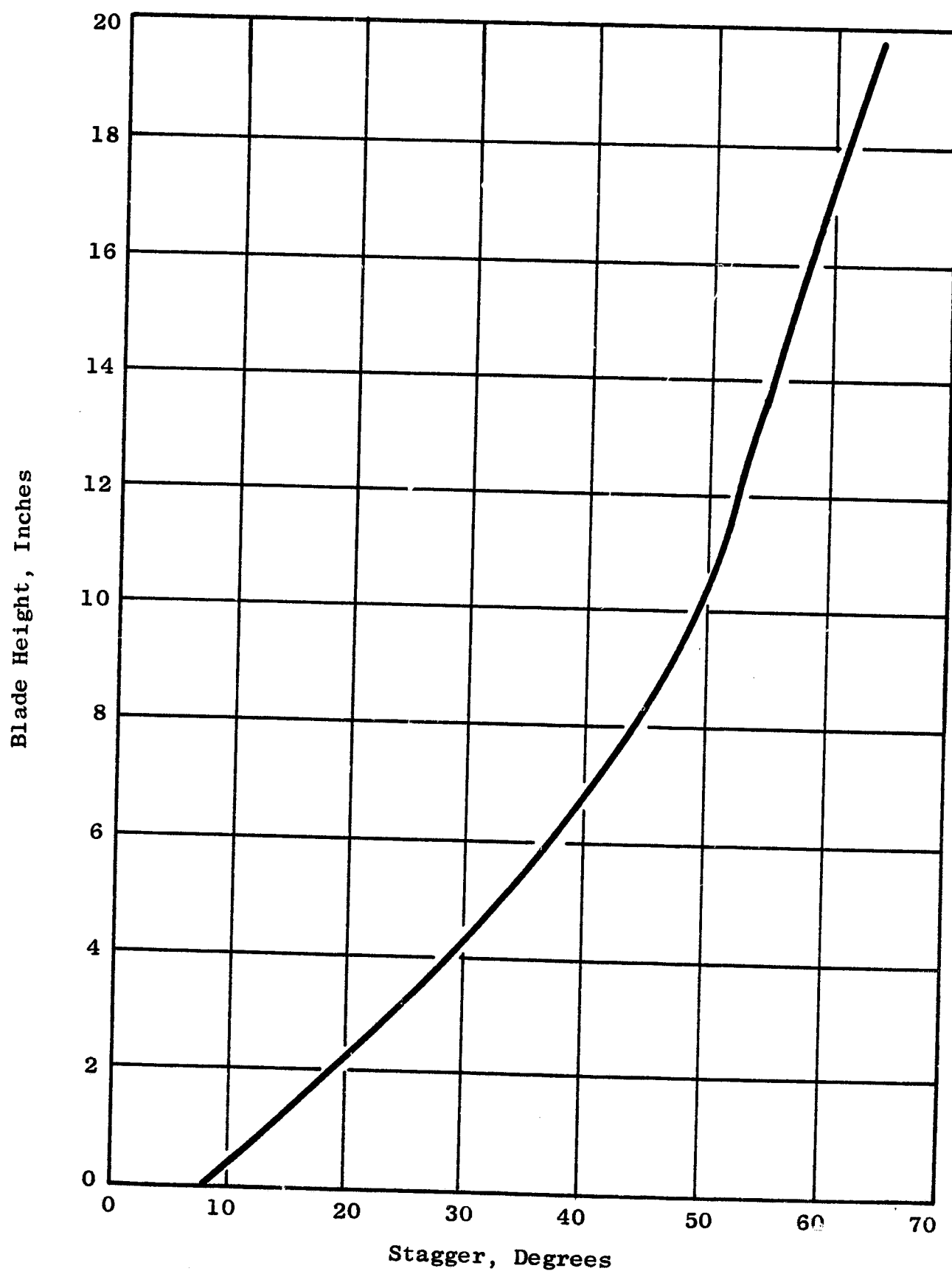


Figure 119. Fan C Airfoil Stagger Variation

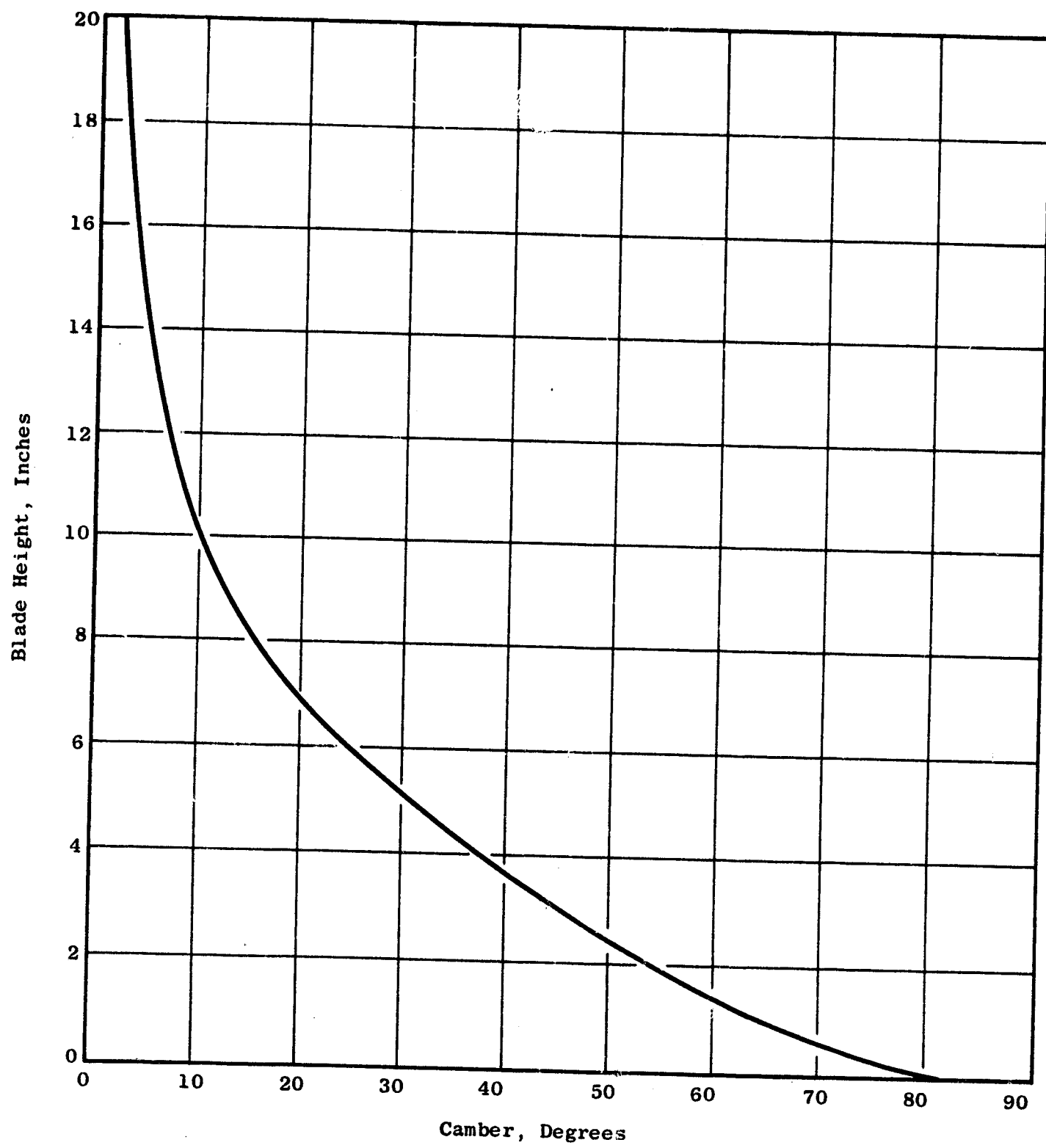


Figure 120. Fan C Airfoil Camber Variation

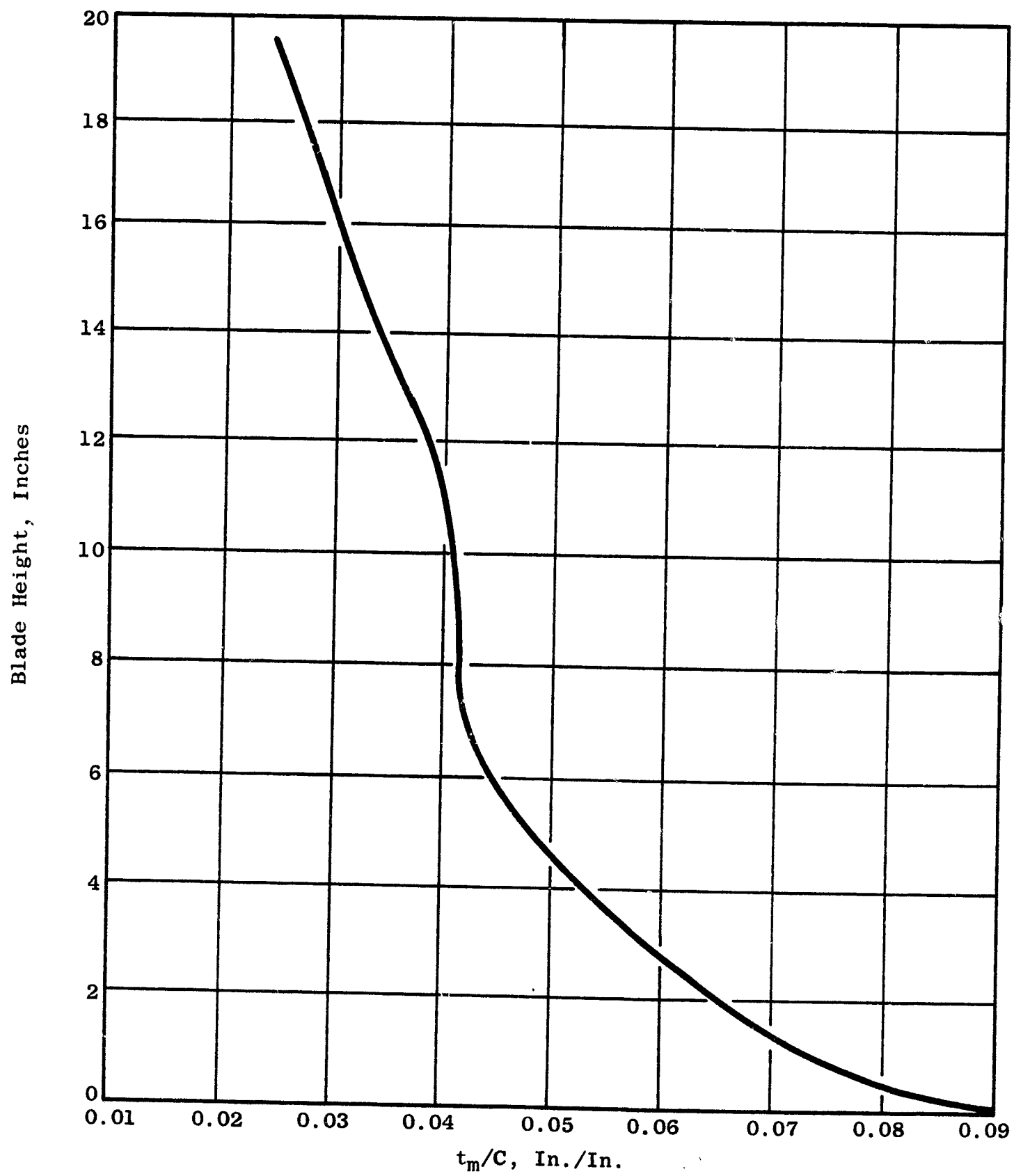


Figure 121. Fan C Airfoil Thickness Distribution

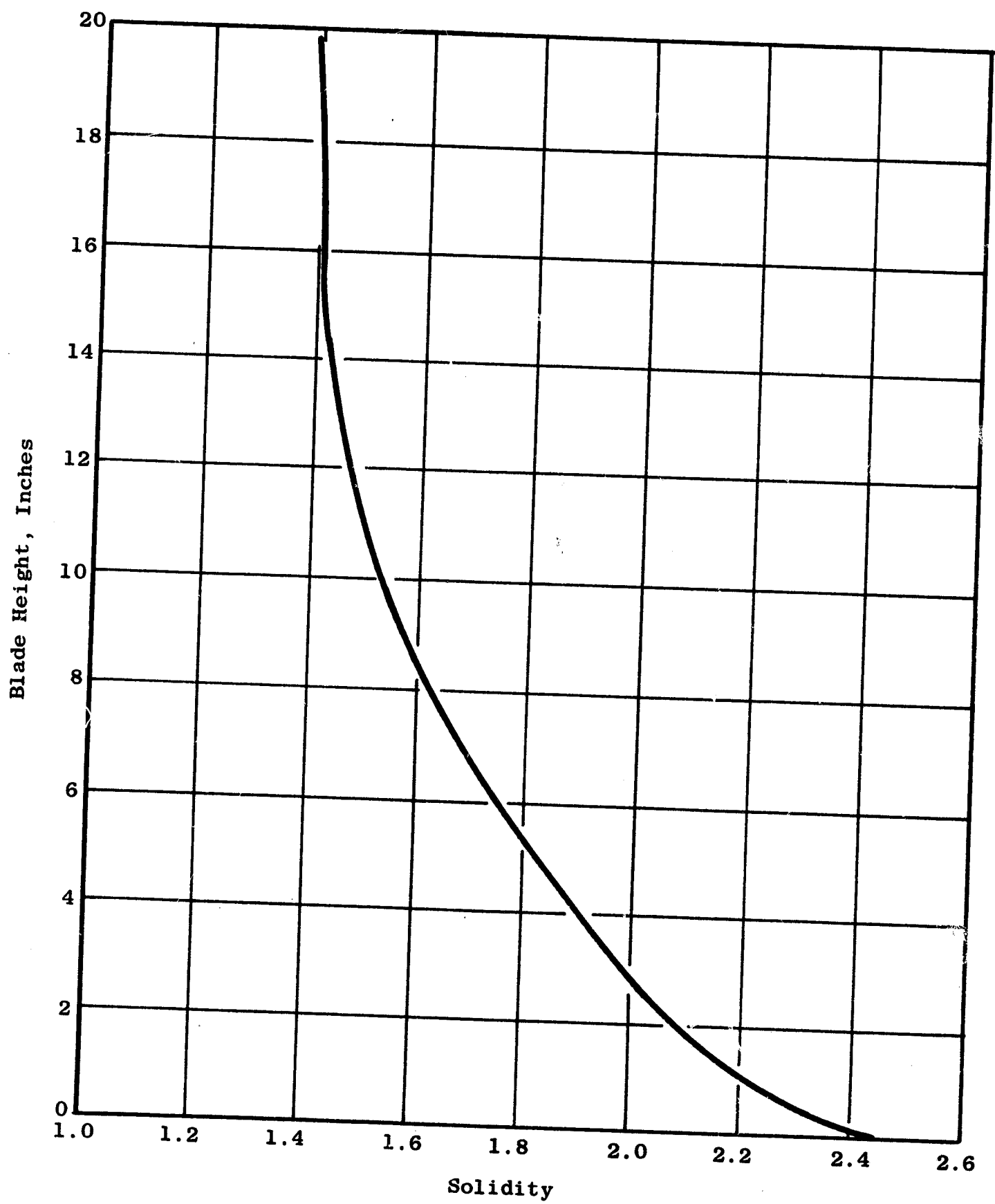


Figure 122. Fan C Airfoil Solidity Variation

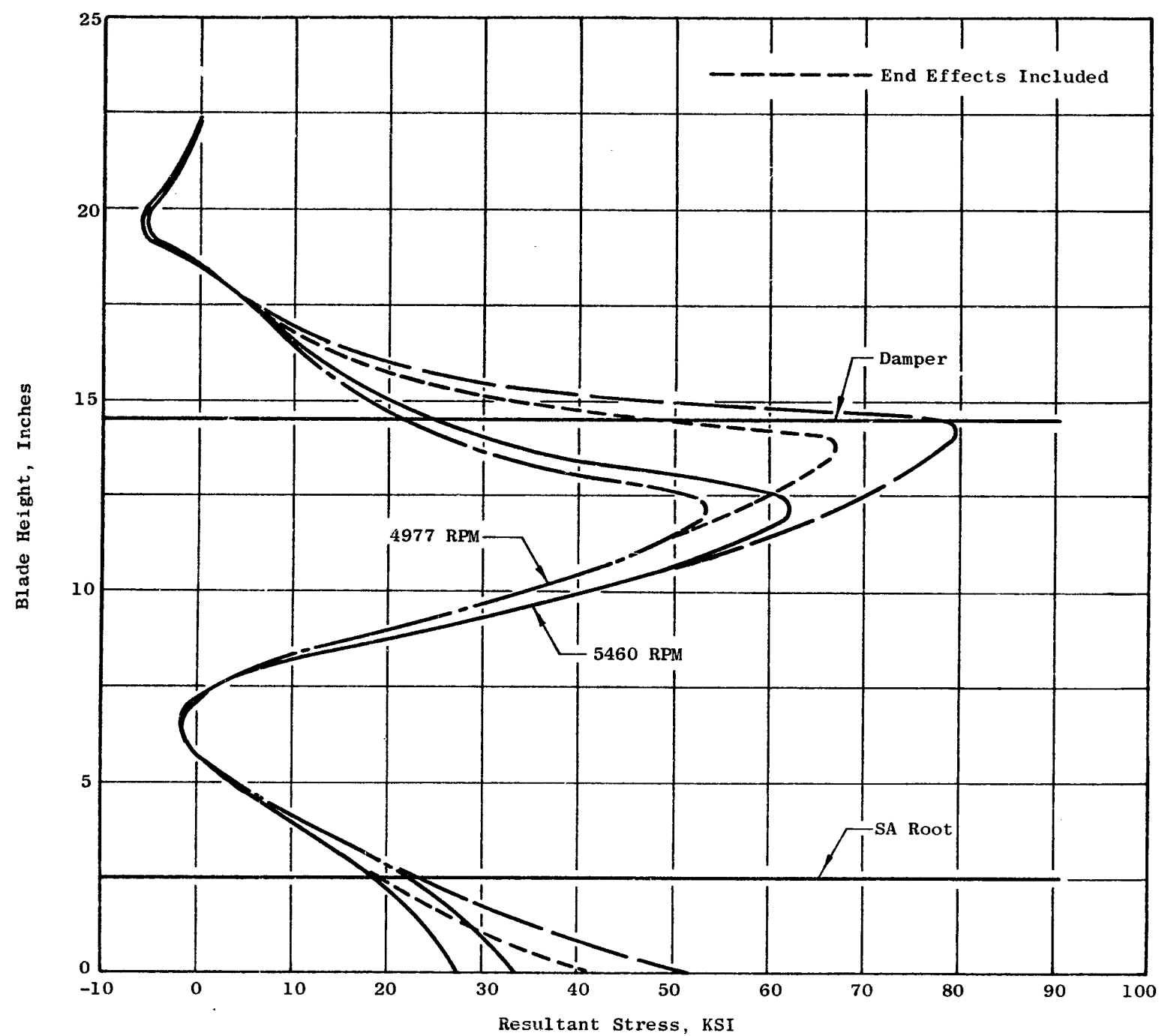


Figure 123. Fan C Leading Edge Steady State Blade Stress

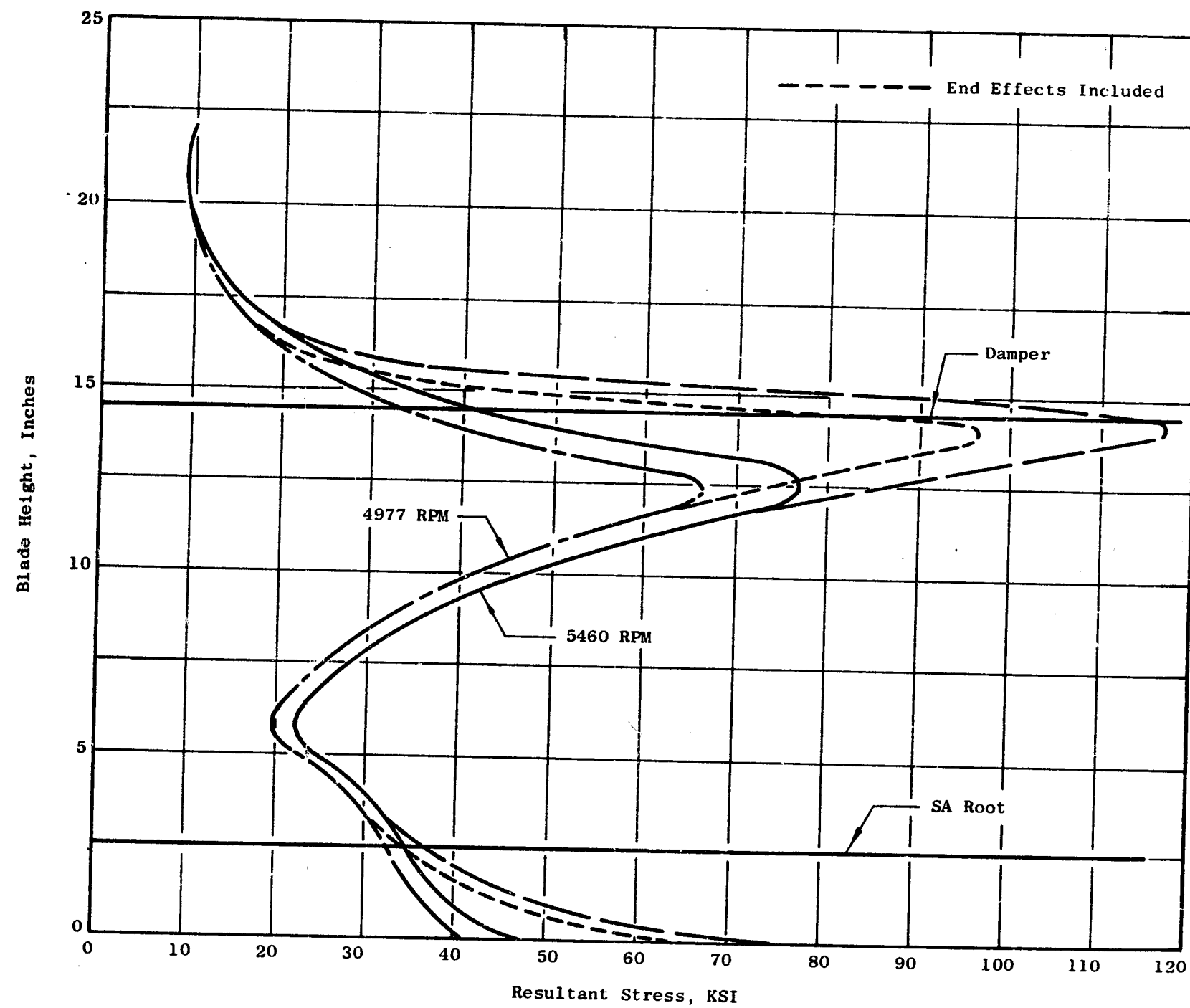


Figure 124. Fan C Trailing Edge Steady State Blade Stress

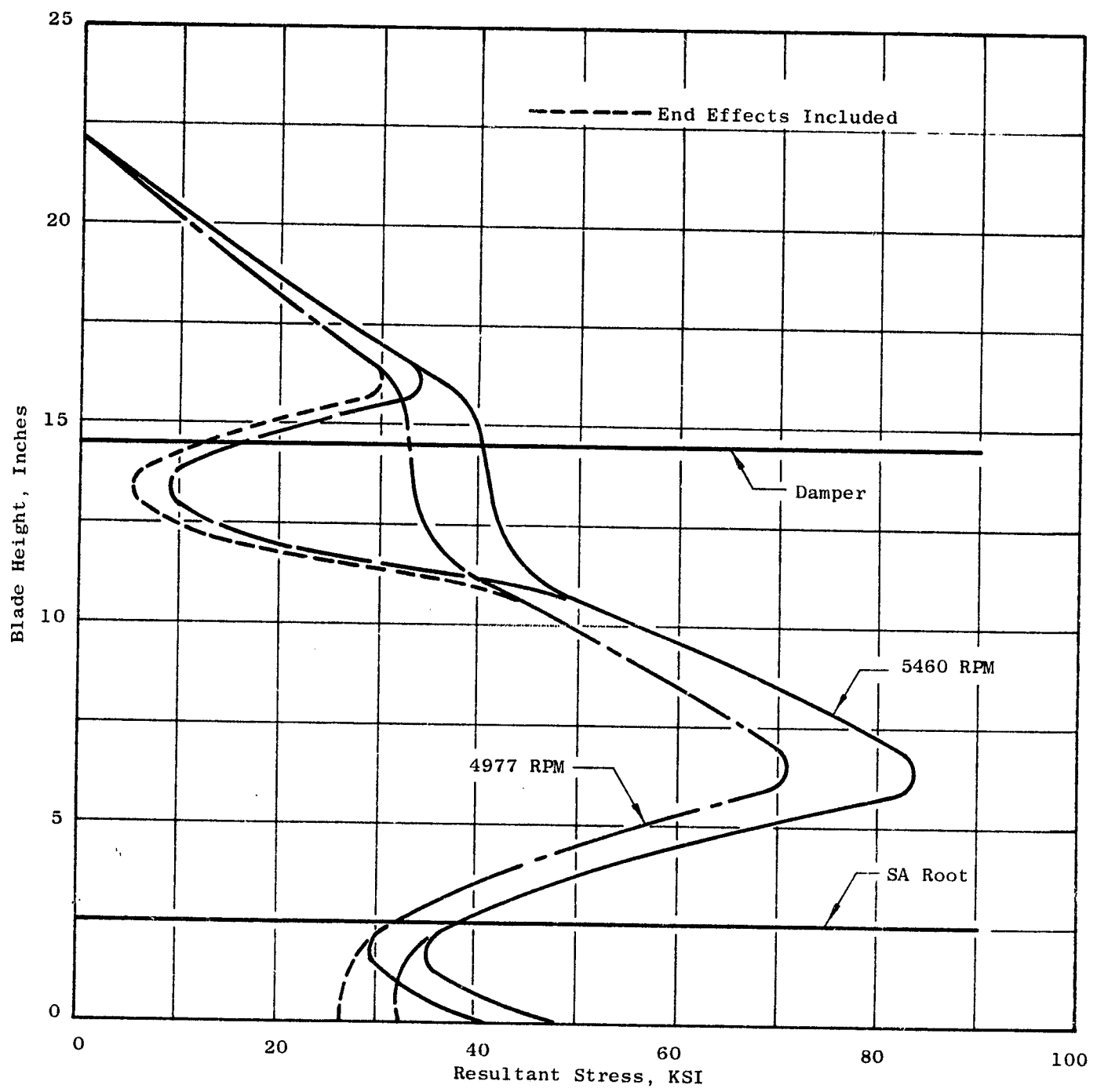


Figure 125. Concave Side Steady State Blade Stress

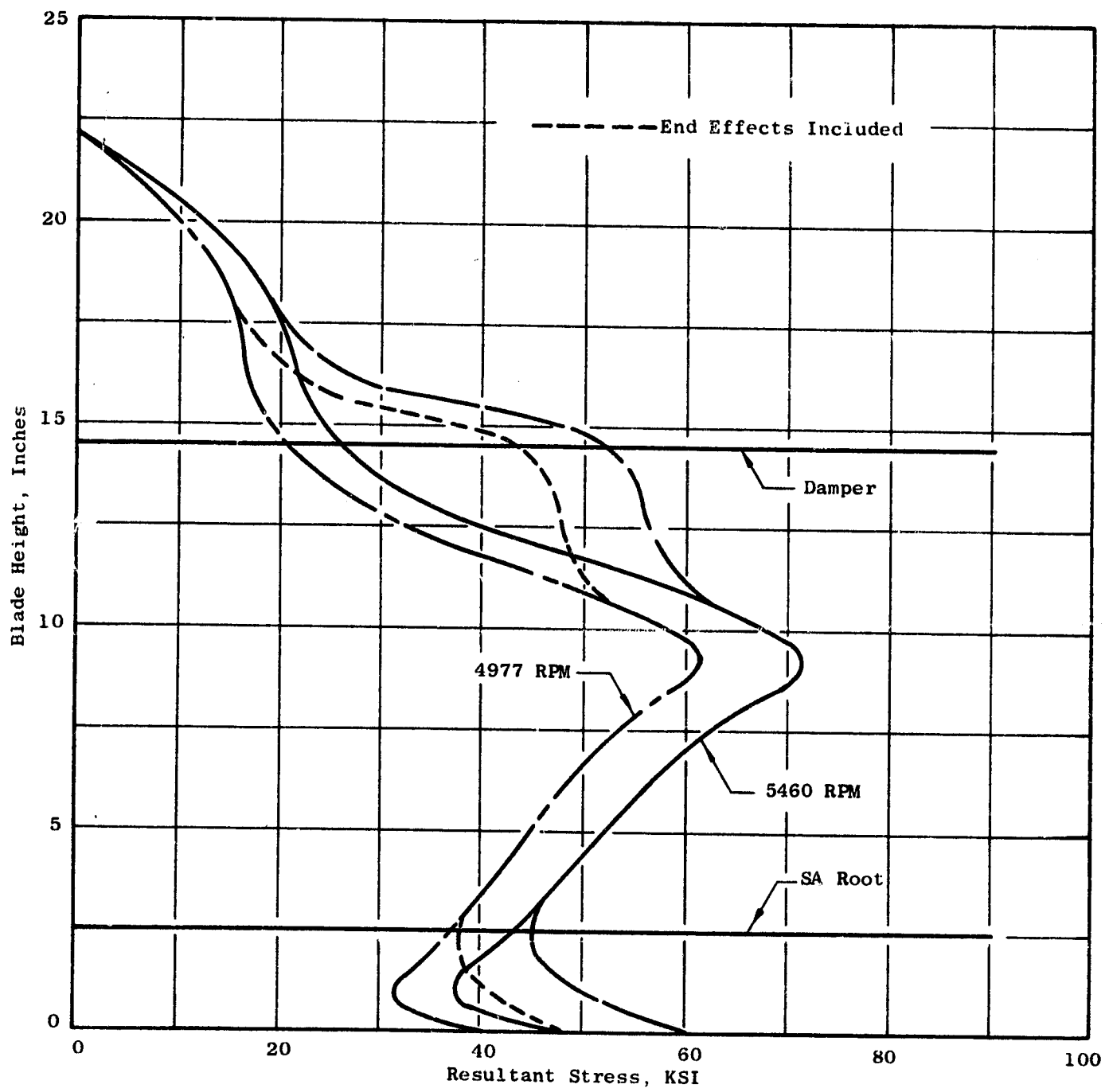


Figure 126. Convex Side Steady State Blade Stress

The highest airfoil steady state stress is present in the vicinity of the damper and in the dovetail area as shown in Figure 124. The allowable vibratory stress for the first (most excitable) mode is shown in Figure 127. The combined stress is plotted on the Goodman diagram, Figure 128. The design criteria for the blade was to not let the steady state stress exceed 105 kpsi. A former criterion to design the dovetail stronger than the airfoil was revised to have the maximum dovetail stress lay under the Goodman diagram (Figure 128).

- Frequencies

The design criteria for fan blades is as follows:

- 1) The first natural frequency will be 15 percent higher than the frequency associated with two excitations per revolution at a given speed condition.
- 2) The first natural torsional frequency will be of such a value as to assure that no flutter instability can be excited.

The resonant frequencies of the Fan C blade are shown as a function of speed (Campbell diagram) Figure 129. The first flexural blade frequency at 5460 rpm is 213 hz, 17 percent above the 2/rev line. The torsional frequency at the same condition is 499 hz, a value high enough to satisfy flutter criteria. Unknown at this time, is how those actual frequencies will be to predicted values, but bench frequency checks will be performed when hardware is finished.

5.1.1.3.2 Midspan Damper

The criteria for designing the airfoil damper was to position it as far inboard as possible and still high flex the blade. This would result in the thinnest possible shroud design, which is aerodynamically advantageous. This position was found to be 60 percent of airfoil height. A finite element analysis was performed on many shroud configurations until a final single-face shroud was determined to be the most feasible. The shroud faces will have a tolerance of zero to minus five thousandths, so that upon assembly the airfoils are locked up. The dampers are being machined so that at full fan speed the radial growth of the dampers will make the shroud centerline a circle. At zero speed on buildup, the adjacent shrouds will "droop" by fifty thousandths. Damper thickness is shown in Figure 130, and corresponding steady state stresses are illustrated in Figure 131.

Cross sections of the damper are elliptical to optimize flow losses past the shrouds. Glass masters are made of axial sections through the shroud, similar to those made for airfoil sections in order to obtain a close tolerance damper.

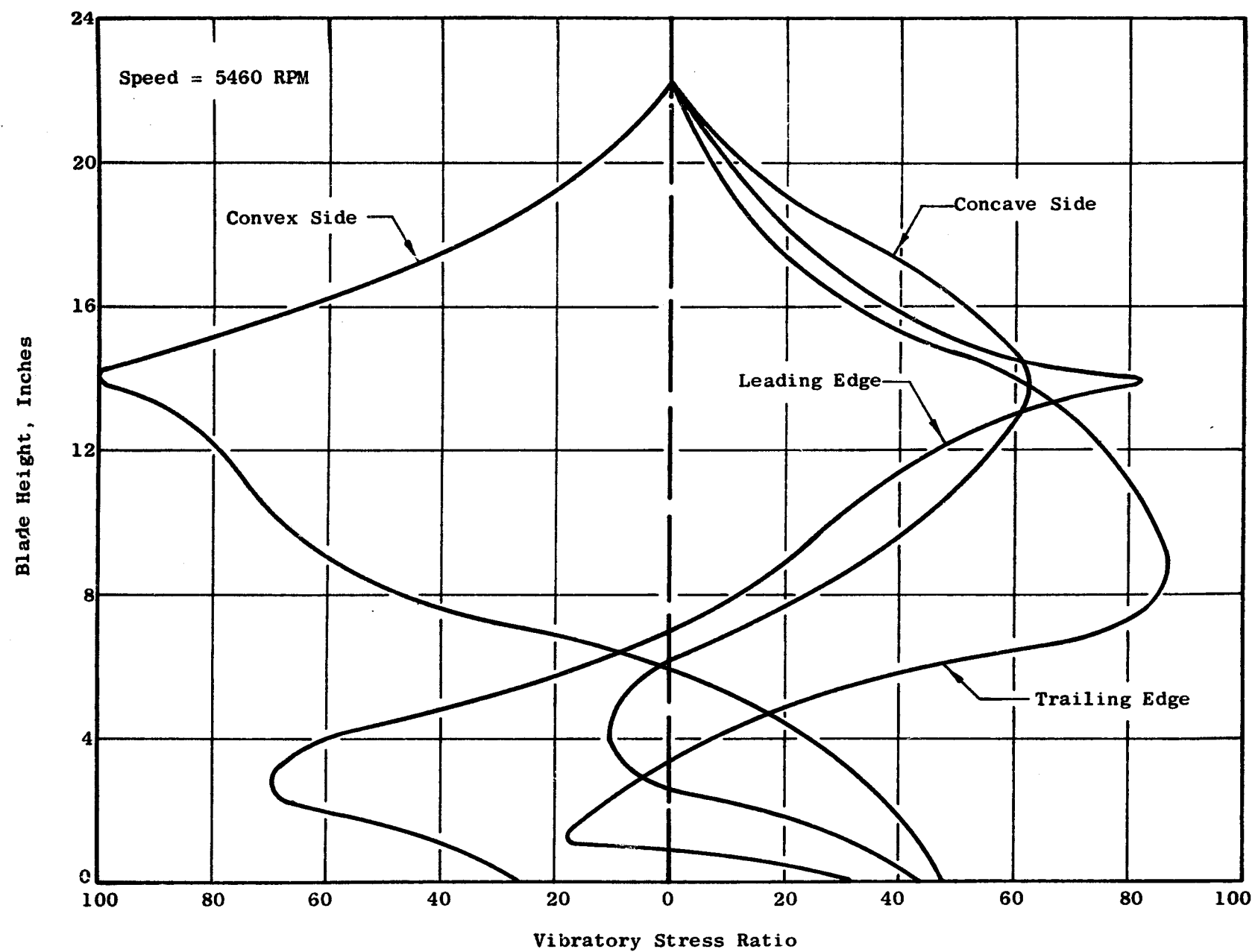


Figure 127. Fan C Allowable Vibratory Stress Ratio, First Flexural Mode

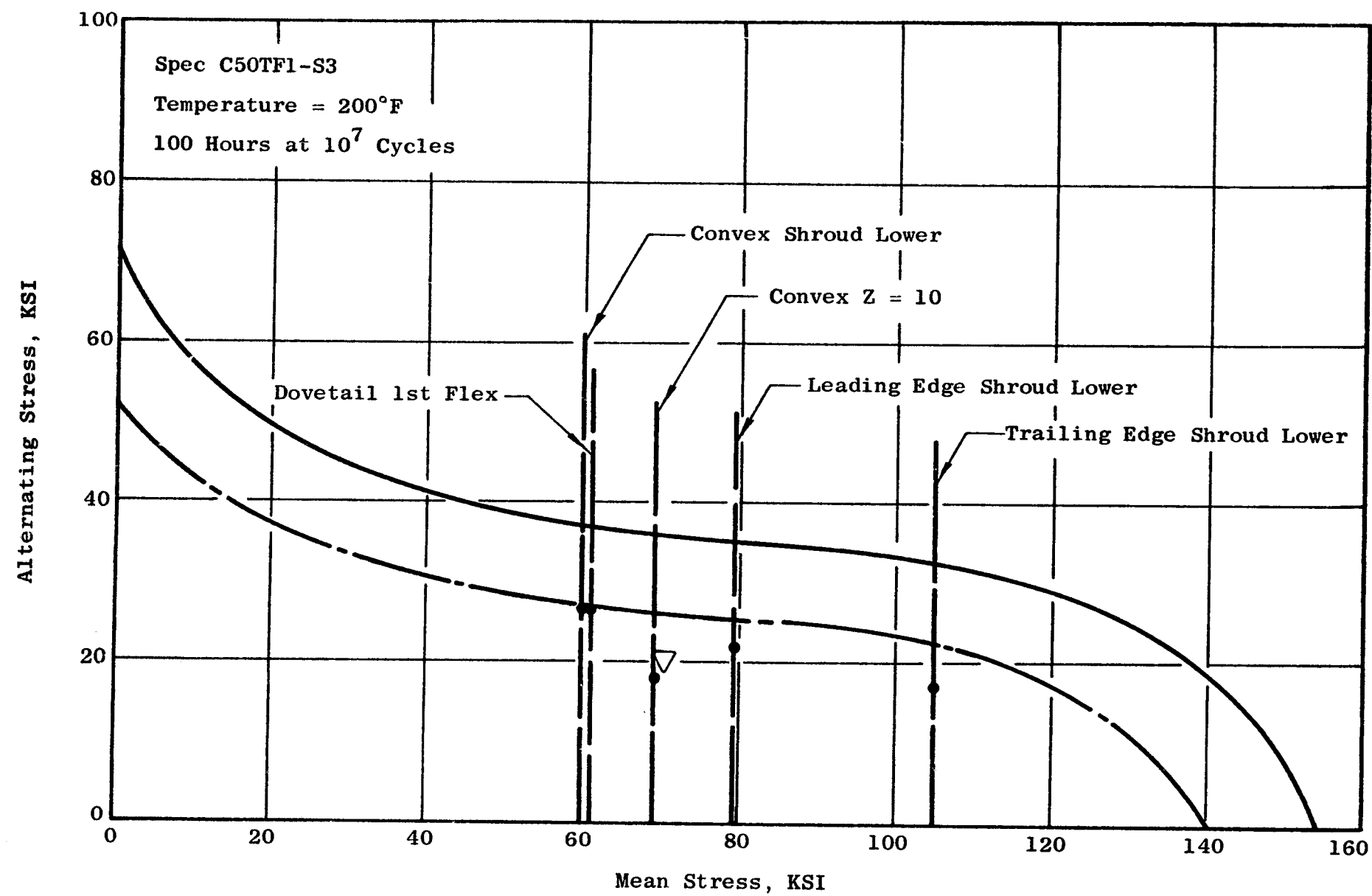


Figure 128. Fan C Blade Goodman Diagram

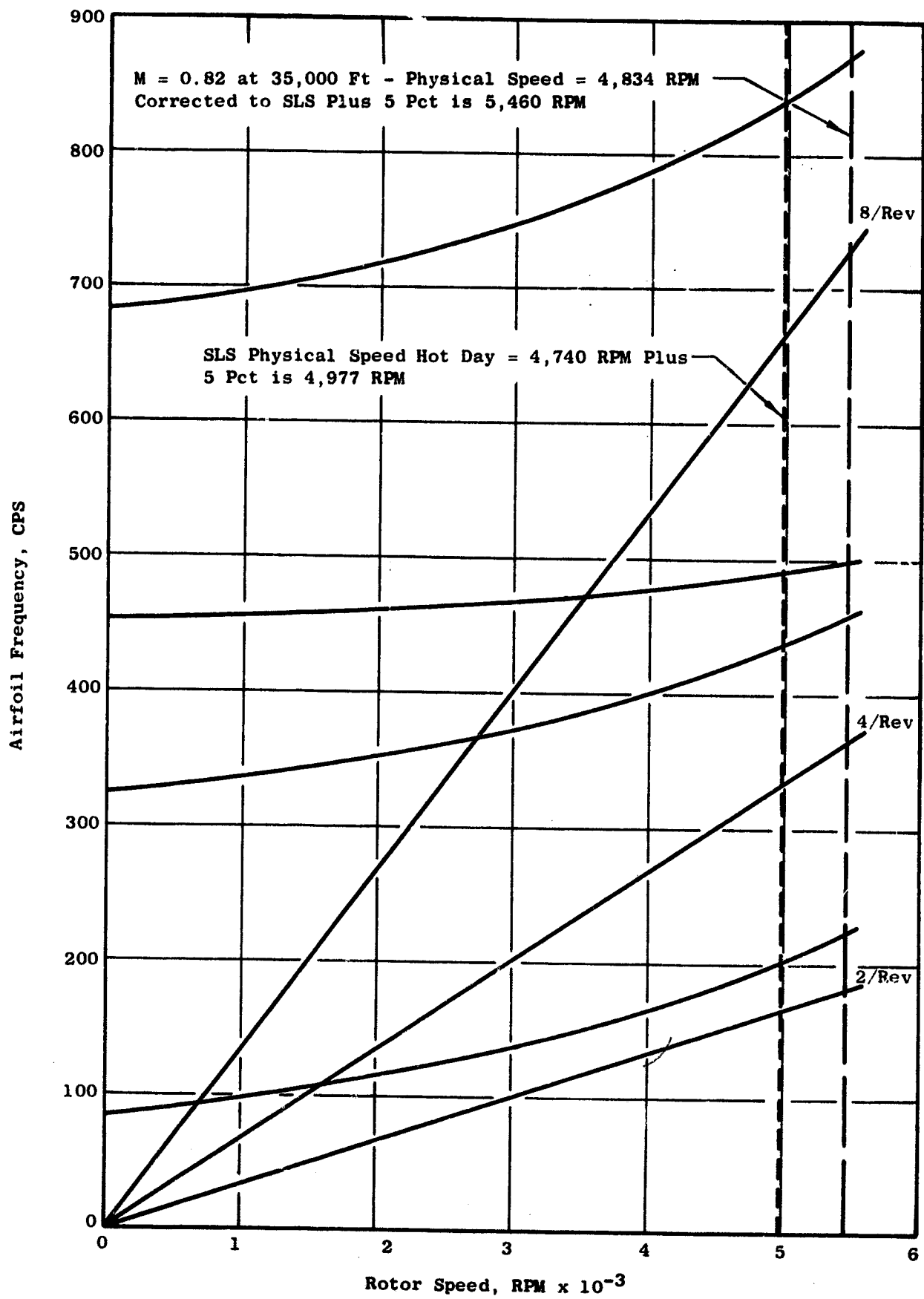


Figure 129. Fan C Blade Campbell Diagram

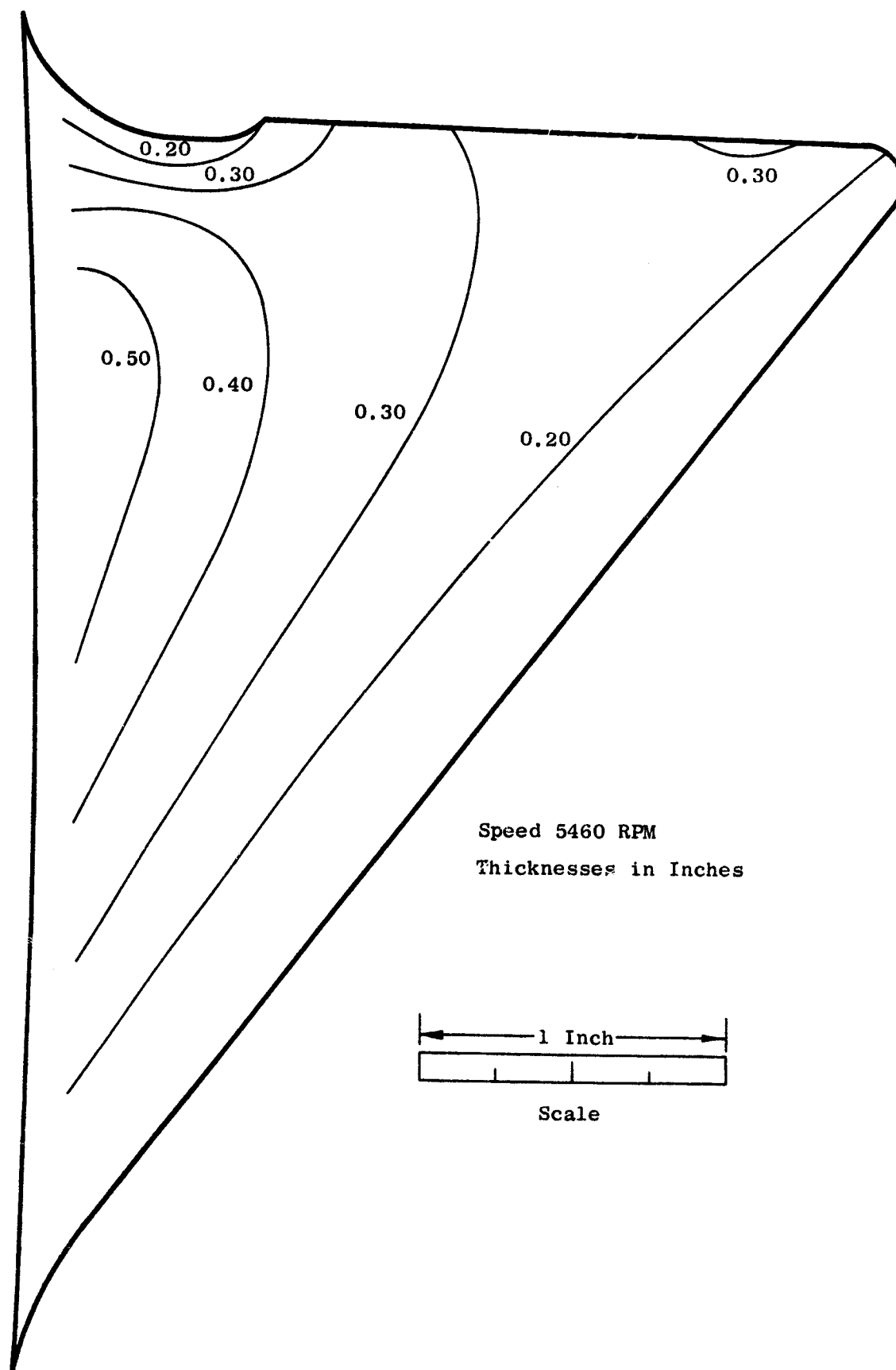


Figure 130. Fan C Blade Shroud Thickness Distribution

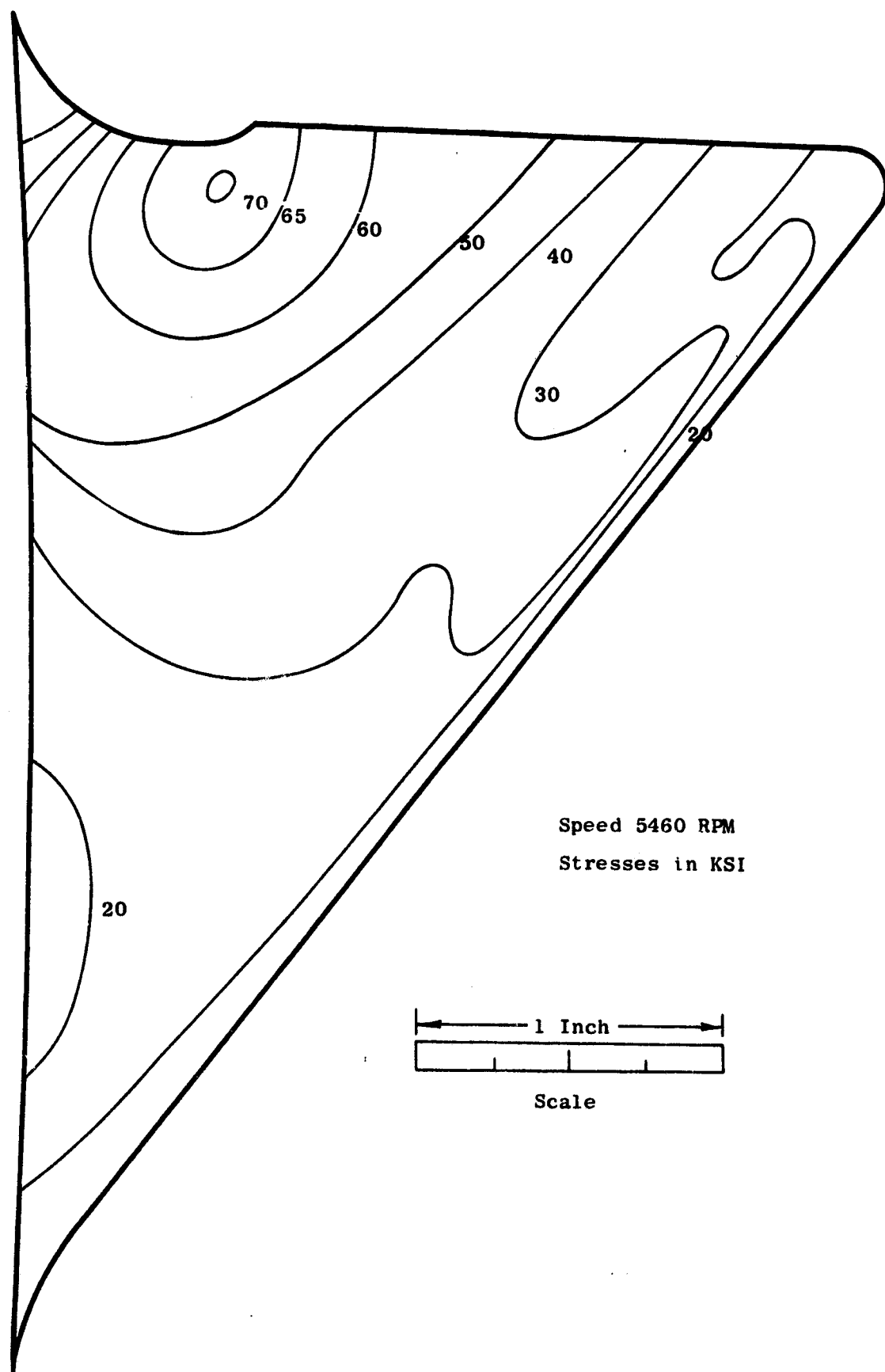


Figure 131. Fan C Blade Shroud Effective Steady State Stress Distribution

- Stresses

Maximum steady state stresses are found to be circa 70,000 psi. The boundary conditions were assumed to be that as a cantilever beam (fixed-free), but strain gage data obtained from another similar shrouded fan blade revealed that some fixity at the shroud tips exists. New boundary conditions are being run to determine stress distribution for these conditions. A deflection plot of the shroud is shown in Figure 132.

5.1.1.3.3 Disc

The high speed fan disc is a conventional disc with an integral torque cone which will connect to either the fan test facility or engine low pressure drive shaft. The forward and aft retainer will be connected to scalloped flanges on each side of the disc by 52 1/4-inch body-bound bolts. The top of the disc will form the lower flowpath, thus eliminating the need for separate spacers. Material selected was a high strength steel, D6AC, needed for the highly stressed dovetail region.

- Stresses

The dovetail stresses were computed by an empirical program which consists of equations verified by many actual dovetail tests. Blade and disc stresses are shown in Tables XXVII and XXVIII. No Goodman diagram exists for the chosen material at present, but vibratory runout data confirm that the material is acceptable at present stress levels.

The disc and cone stresses were computed by a finite element analysis program which predicts stresses shown in Figure 133 at 5460 rpm. Allowable stresses from design criteria are compared to computed values, Table XXIX.

Table XXIX. Fan C Disc Stress Summary

<u>Area</u>	<u>Computed Stresses</u>	<u>Allowable From Design Criteria</u>
Web	104	115 (0.02% Yield)
Bore	127	130 (0.20% Yield)
Aug. Tangential	92	98 (70% Ultimate)

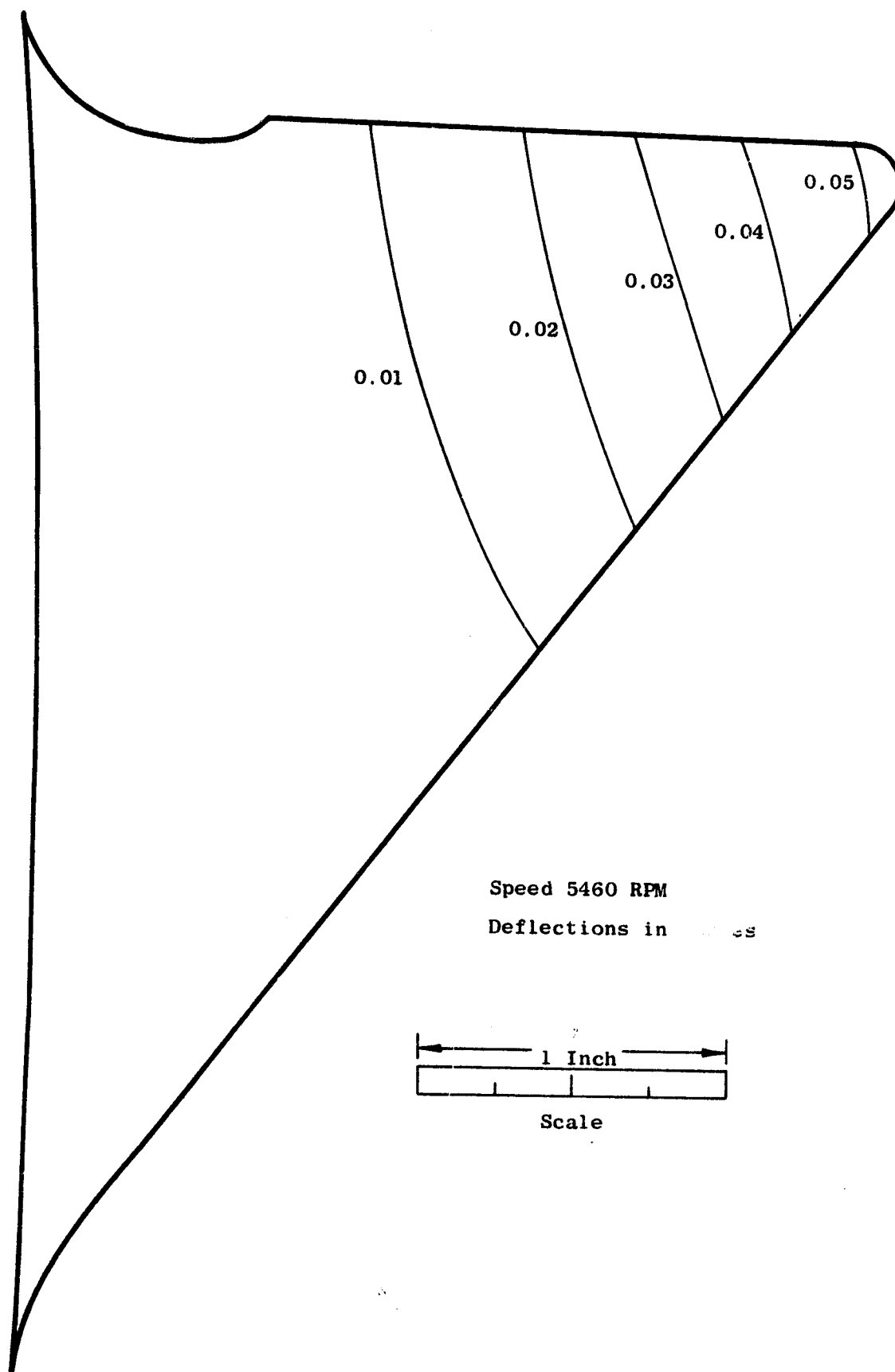


Figure 132. Fan C Blade Shroud Radial Deflection Distribution

Table XXVII. Dovetail Stresses for Fan C Blade

<u>Loc</u>	<u>Total</u>	<u>Neck</u>	<u>Tang</u>	<u>Tang-Fn</u>	<u>Shear</u>	<u>Load</u>
1 S	35630	12542	24659	2.205	14103	11184
1 V	-26943	-18062	-10858	2.205	-4206	-3335
2 S	72157	42414	34621	2.205	19800	15701
2 V	-4503	2675	-4503	2.205	-1744	-1383
3 S	61003	33138	31757	2.205	18162	14403
3 V	26943	18062	10858	2.205	4206	3335
4 S	54017	25619	31490	2.205	18009	14281
4 V	4503	-2675	4503	2.205	1744	1383
5 S	71003**	37776	33189	2.205	18981	15052
5 V	12654**	10369	3177	2.205	1231	976
6 S	51159**	19081	28075	2.205	16056	12732
6 V	12654**	-10369	-3177	2.205	-1231	-976

S = Steady
V = Vibratory

** Total stresses at locations 5 and 6 are effective stresses including torsional shear

Table XXVIII. Dovetail Stresses for Fan C Disc

<u>Loc</u>	<u>Total</u>	<u>Neck</u>	<u>Tang</u>	<u>Tang-Fn</u>	<u>Shear</u>	<u>Crush</u>
1 S	35455	26475	10185	0.911	10167	24842
1 V	-35468	-30135	-6592	0.911	-3032	-7409
2 S	75280	63653	14300	0.911	14274	34876
2 V	6745	6745	-2734	0.911	-1258	-3073
3 S	67881	57174	13117	0.911	13093	31992
3 V	35468	30135	6592	0.911	3032	7409
4 S	48555	37224	13007	0.911	12983	31722
4 V	-6745	-6745	2734	0.911	1258	3073
5 S	71583**	60414	13709	0.911	13684	33434
5 V	19774**	18440	1929	0.911	887	2168
6 S	42010**	31849	11596	0.911	11575	28282
6 V	19774**	-18440	-1929	0.911	-887	-2168

S = Steady

V = Vibratory

** Total stresses at locations 5 and 6 are effective stresses including torsional shear

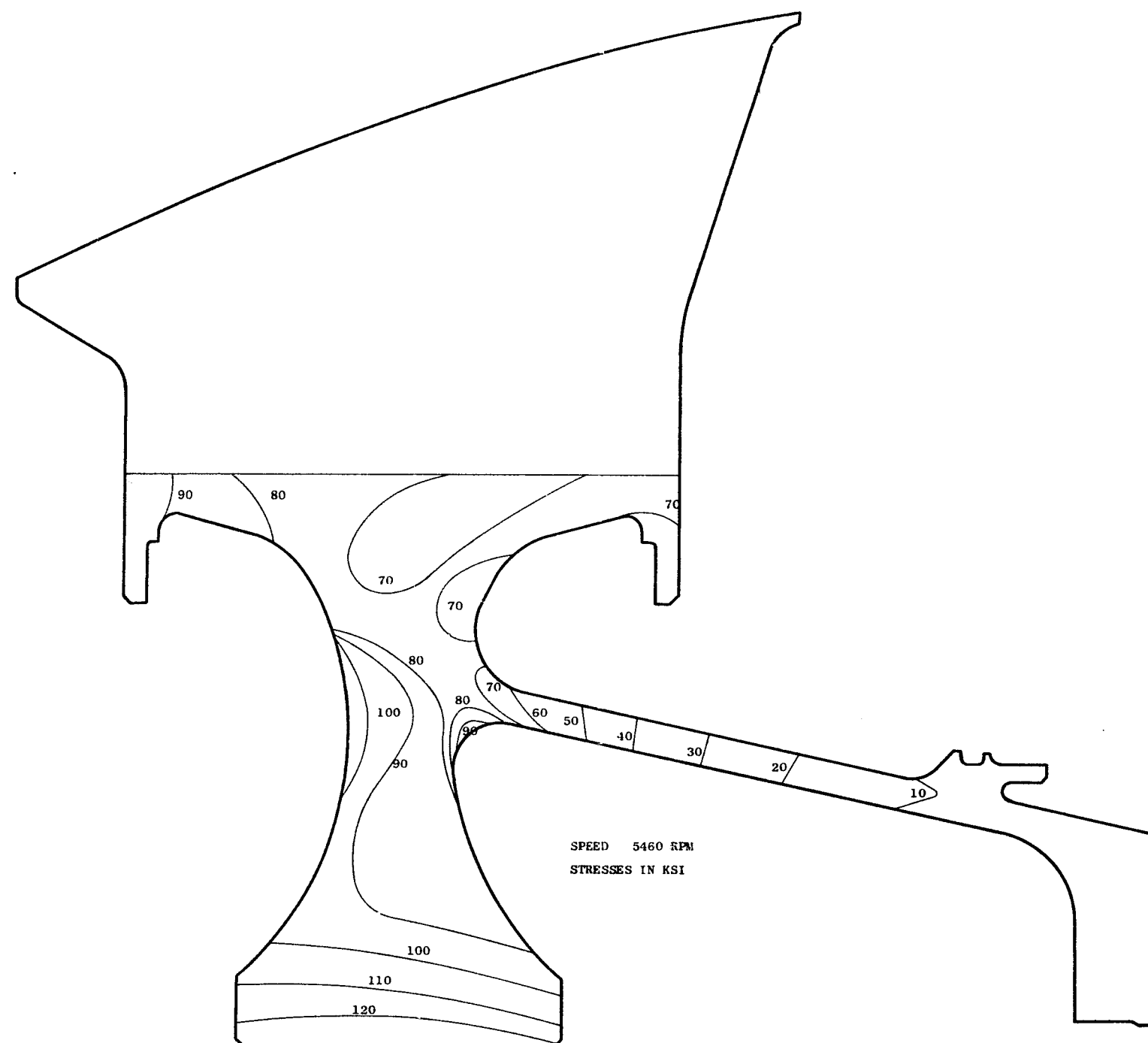


Figure 133. Fan C Steady State Disc Stress Distribution

- System Effects

Analysis is still in progress to determine vibratory characteristics of the blades, telemetry system, disc, and cone acting as a system. Spring constants have been determined for the cone and telemetry system which will define the boundary conditions for the rigidity of the blades and discs. Blade frequencies should not drop significantly, due to the massive geometry of the rotor components. If any undesirable frequency change may arise, disc geometry will be modified to yield satisfactory conditions.

5.1.1.3.4 Other Rotor Components

The aft retainer, forward retainer, and bulletnose are made from 17-4PH stainless steel. The bulletnose is attached to the forward spinner by 26 number ten horizontal bolts. The telemetry package is attached to the forward disc flange by an adapter. The package is positioned as far forward as possible to relieve stress in the adapter ring holding the package to the disc flange. The high speed fan hardware aft of the torque cone is identical to hardware employed by the low speed Fan B.

5.2 FAN STRUCTURES DESIGN

5.2.1 Summary

This section presents the methods and procedures used in the aeromechanical design of three light boilerplate stator and fan frame modules for full scale fan configurations A, B, and C. These modules were designed to be adaptable between the full scale fan test facility at General Electric - Lynn, the NASA-Lewis facility, and the full scale experimental engine.

The frames feature twelve equally-spaced radial struts which penetrate the core casings and connect all frame casings and rings. They also provide passages for lube lines, air lines, scavenge tubes, and the power take-off (PTO) shaft. The frames also feature replaceable preformed sound suppression panels bolted to the frame casings.

Features of the fan stators include continuously/hydraulically operable bypass cascades and adjustable core cascades, with the possibility of varying the flow incidence angles of each $\pm 10^\circ$ from the nominal. Both core and bypass cascades are comprised of individually-replaceable high-boss design vanes. Abradable seal rub surfaces are featured over the fan rotor. The stators also feature replaceable preformed sound suppression panels on all flowpath surfaces.

5.2.1.1 Fan A Structures

The Fan A Full Scale Fan Test (FSFT) vehicle (see Figure 134) is characterized by its relatively low tip speed and shrouded, short-chord high-aspect-ratio blades.

Fan A is somewhat shorter than the Fan B configuration due to the reduced axial spacing requirement between the rotor and stator airfoils. Also, the OGV configuration for Fan A is composed of only one stage of core OGV vanes.

The Fan A FSFT vehicle will utilize the same inlet, adapter, and facility components to be used on Fan B. This has been made possible by inlet and exhaust dimensions common to both vehicles. The fan frames of the two configurations will be interchangeable.

5.2.1.1.1 Fan A Frame

The frame assembly is similar to the TF39 and CF6 in design only. In place of using a cast and welded construction, the frame's flanges and shells are machined out of low carbon steel forgings. The struts in the core are machined from low carbon steel forgings, and service passages are EDM'd through for access lines into the fan sump. The struts in the bypass are hollow, fabricated from low carbon steel. The frame is not designed to be so overly massive that it presents handling problems. Unnecessary weight is removed from the structure wherever possible.

The backbone of the frame is the center weldment consisting of the two ringed-shell elements, which form part of the core inlet flowpath, joined by twelve radial struts. The system of twelve radial struts, two of which are flared at the trailing edge for transition into two pylons aft of the frame, connect the center weldment to the outer shell of the frame. Strut airfoil-shaped slots are EDM'd into the shell and ring elements through which the struts are inserted and joined to these elements by welding. The forward and aft fan roller bearings are supported by a system of cones which attach to the inner flanges of the center weldment. The two pylon struts, located in the 6- and 12-o'clock positions, house the PTO shaft and provide attachment for the forward engine mount, respectively. The thickness has been increased on the 6-o'clock strut in the core region to facilitate the PTO shaft. The PTO shaft damper bearing is located in the area between the center weldment and the bypass duct portion of the frame. A pylon strut in the bypass duct is provided for the PTO shaft housing, and a gearbox mount pad is provided on the outer perimeter of the frame, above the pylon strut. A shear plate, connecting the 11- and 12-o'clock struts in the region between the bypass and the core duct, distributes the forward mount side loads. Bosses are welded to the outer shell to provide attachment positions for frame handling.

The forward, single-point engine mount system is located at 12 o'clock, directly below the pylon strut, which, in this case, serves as a smooth aerodynamic transition for the engine-to-aircraft attaching pylon. Struts, 10-

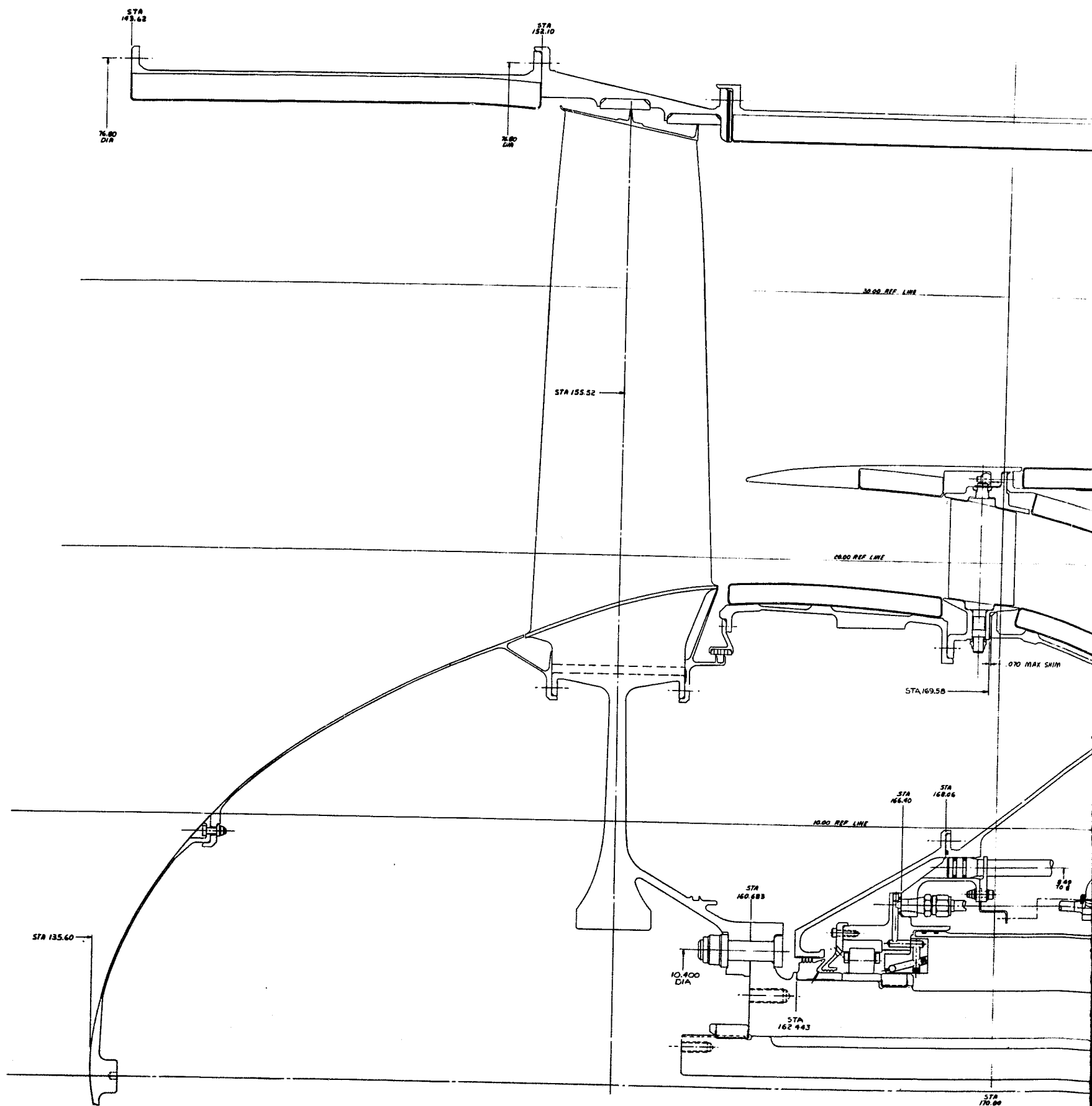


Figure 134. Fan A Full

FOLDOUT FRAME

cated directly adjacent to the pylon struts, are staggered five degrees away from the pylon to permit proper airflow distribution around the pylon.

The bypass duct struts, having a 10.0-inch chord, are butt-welded to the transition section of the 19.27-inch chord core strut. To minimize local stress concentrations, the transition section is designed to form smooth load transfer paths between the core and the duct sections of the frame. Passages in the struts are provided for lube scavenge lines, sump cavity pressurization air, drain and lube lines. Table XXX identifies specific uses of each strut.

- Sump and bearing support systems

The bearing support cone is designed to transmit the No. 1 bearing loads into the fan frame. The forward flange provides fittings for mounting the oil scavenge tubes and supports the "oil in" lines for the Nos. 1 and 2 bearings.

The static seal is supported from the bearing support cone. A nickel-graphite labyrinth seal at the forward face of the cone pressurizes the sump area and prevents oil from leaking from the sump scavenge cavity. The seal support cone flange is sealed by an "o"-ring. The No. 1 and No. 2 bearing housings contain the lube jets for the bearing lubrication system and retain the bearings. The sump shield forms the sump wall between the No. 1 bearing housing and sump shield retainer, by use of two "o"-rings at each end. The sump shield retainer provides the transition from the sump shield to the frame.

- Material Selection - Fan Frames, Sump, and Bearing Support Systems

The material selections for these fan structural components are shown in Table XXXI.

Table XXX. Fan A Fan Frame Strut Service Identification

<u>Strut Number</u>	<u>Purpose</u>
1	Engine mount and pylon
2	Supplies pressurization air to forward and aft sumps
3	Instrumentation leadout
4	Supplies pressurization air to forward and aft sumps
5	Supplies oil to forward and aft sump bearings
6	Instrumentation leadout
7	PTO housing acts as a scavenge for sump oil and pylon
8	Instrumentation leadout
9	Supplies oil to forward and aft sump bearings
10	Instrumentation leadout
11	Acts as a vent line for sump and instrumentation leadout
12	Takes outside thrust loads from the engine mount on Strut No. 1

Table XXXI. Material Selection for the Fan A Structural Components

<u>Component</u>	<u>Material</u>
Basic frame (struts, casings, and rings)	- AMS 5062 except 1018-1022 carbon range Low cost and adequate strength at the maximum operating temperature at 200°F
Frame 12-o'clock strut (thrust point)	- 1023 carbon steel (36 ksi min., 0.2% yield)
Instrumentation pads and shear plate	- AMS 5062
Bearing cones, housings, and supports	- AMS 5062
Sump shield and retainer	- AMS 5062
Seal rub surface	- Nickel-graphite flame spray

● Analysis of Fan Frame and Bearing Support System

The analysis was performed on the fan frame utilizing the "MASS" computer system for axial, radial, and overturning moment loads.

The frame was represented by a 105-jointed model consisting of 66 curved beams (rings), 14 straight beams (struts), and 21 all purpose connectors. Due to symmetry, the model was analyzed as a 180-degree structure.

The frame is manufactured from low carbon steel, and Young's Modulus, density, and thermal coefficient were selected based on this material.

Deflection coefficients for the different loading conditions are as follows for the Lynn Installation (see Table XXXII and Figure 135).

Load Type	Applied at	Reacted at
Axial	9	2
Radial	9	2
Overturning Moment	9	2
Radial	11	2
Overturning Moment	11	2

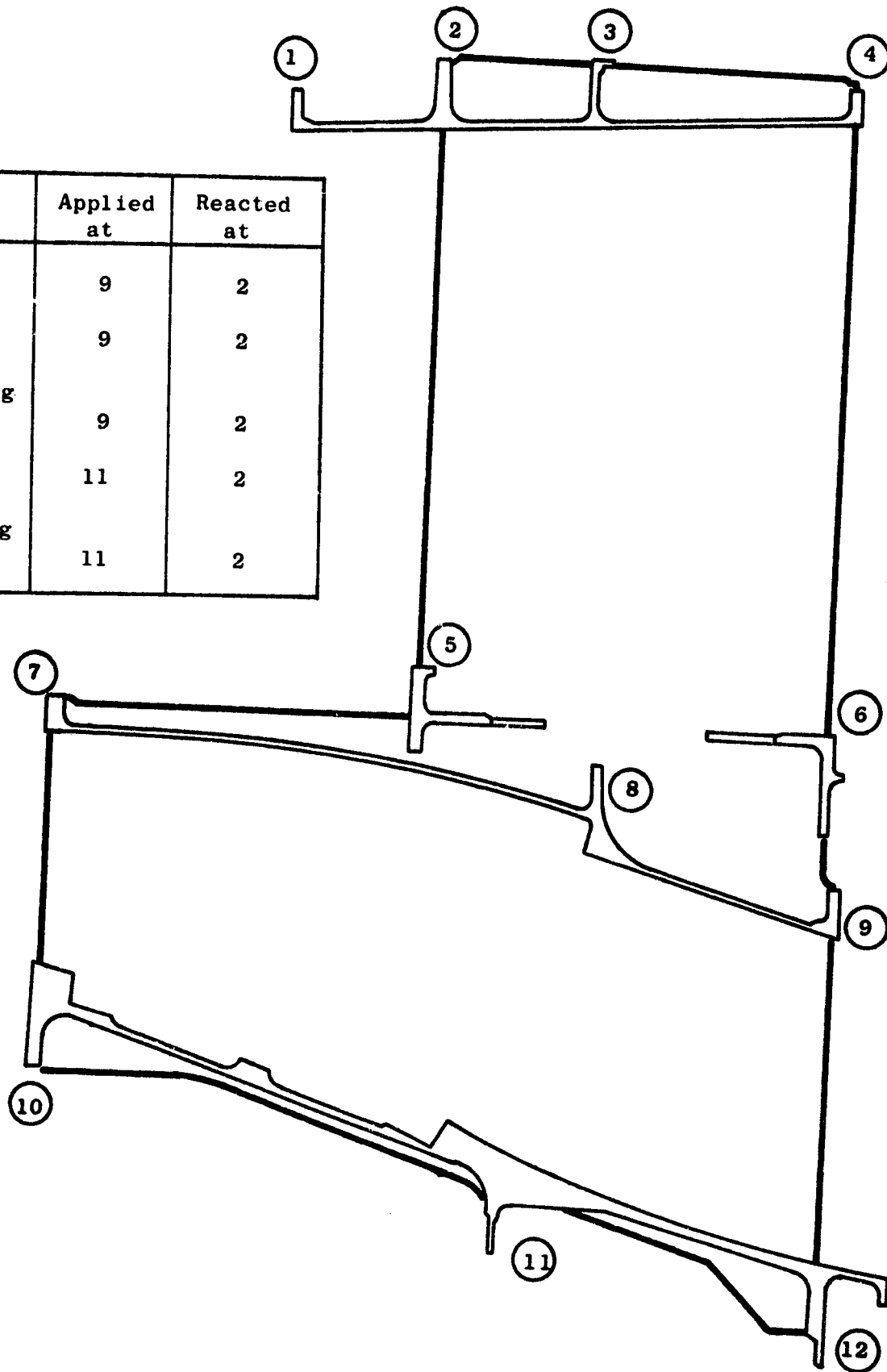


Figure 135. Fan A FSFT Fan Frame Loading

Table XXXII. Deflection Coefficients - Lynn Installation

Load Type	Applied At	Reacted At	Deflection Coefficient
*Axial	9	2	1.076×10^{-7} In./lbs
*Radial	9	2	1.852×10^{-6} In./lbs
*Overturning Moment	9	2	6.02×10^{-10} Rad/In.-lbs
+Radial	11	2	6.7244×10^{-8} In./lbs
+Overturning Moment	11	2	2.630×10^{-9} Rad/In.-lbs

*Applied at inner forward core; reacted at aft outer bypass
 +Applied at inner aft core; reacted at aft outer bypass

Figure 135 consists of a drawing of the fan frame at its 12-o'clock position and a chart outlining the five loading conditions used. The circled numbers on the drawing represent the rings of the structure.

Figure 136 represents the model as a three-dimensional plot and is included to give a general picture of what was actually analyzed. The heavy lines depict struts, while the thin straight lines indicate all purpose connectors. Curved lines indicate rings. Notice that the plates representing the casing in the other models are not present on the A and B, as shear lag was used for the same purpose.

Figure 137 depicts the three basic loading configurations used in the analysis.

Figure 138 consists of three side views of the frame which indicate the actual locations of maximum stresses that the outer struts will receive.

The stress in the 12-o'clock strut in the annular flow splitter area, due to the main thrust and vertical load uniball, has been analyzed by the "ROTOR" computer program which employs finite element techniques. Figure 139 illustrates a model of the system and a stress map of the results for a sinusoidal loading imposed by the uniball. The maximum steady state stress for test cell conditions was established at 17,000 psi. On the Goodman diagram for this frame strut material, illustrated in Figure 140, the allowable alternating stress is 28,700 psi. The maximum alternating stress for test cell conditions is 9620 psi. This represents a margin of 3. The engine system loads are completely examined in Section 5.2.1.4.

-Shear Plate

The shear plate located between the Number 11 and 12 strut on the A, B,

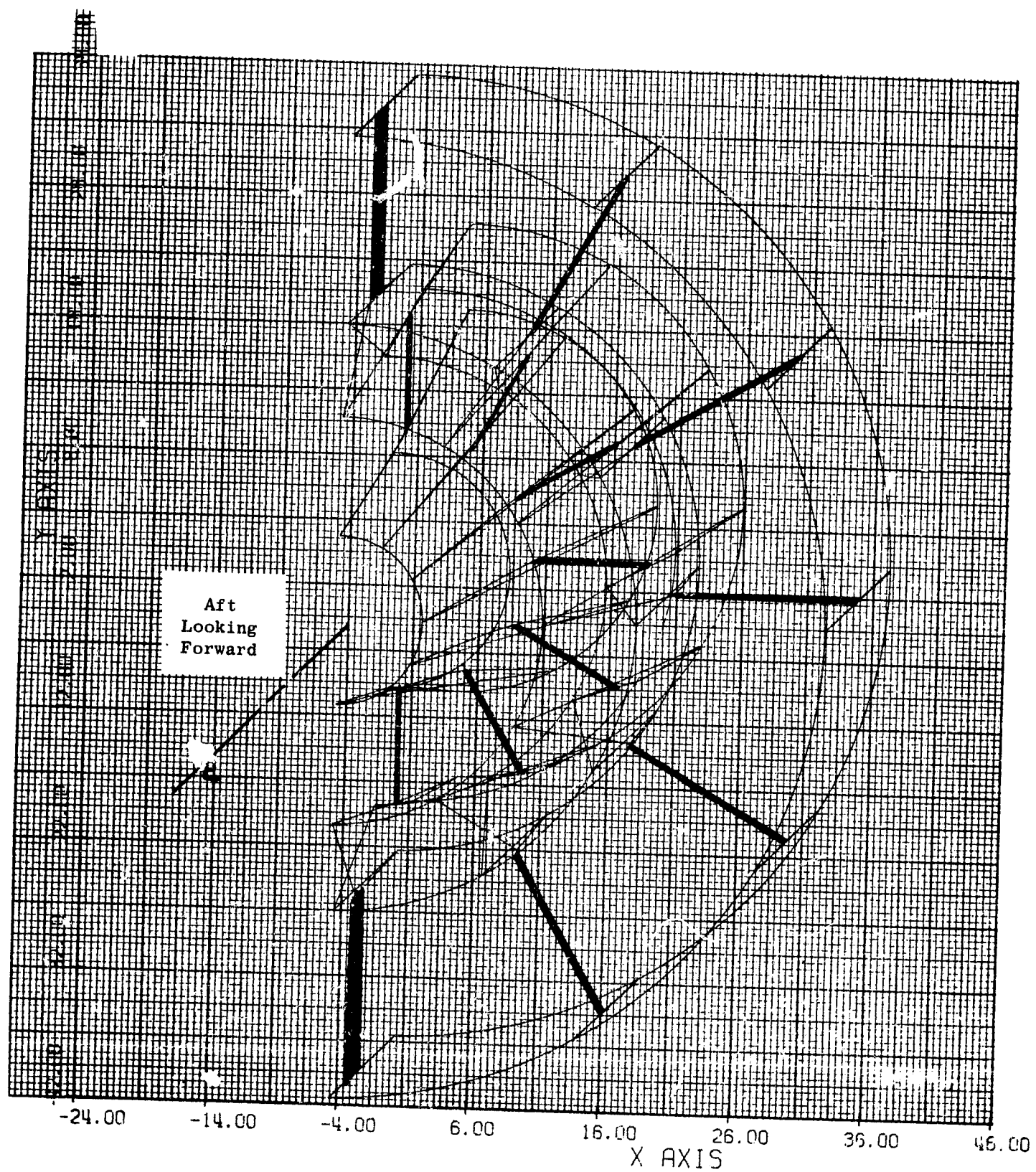
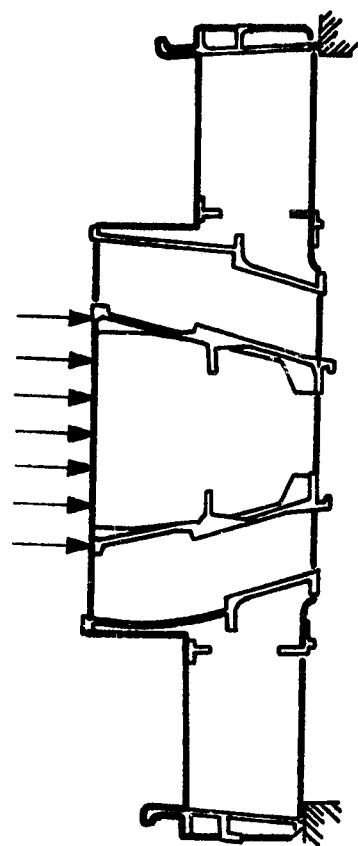
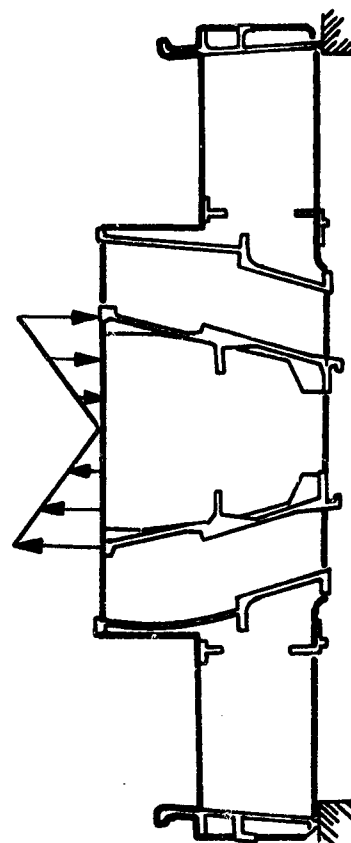


Figure 136. Fan A Fan Frame Analytical Model



Axial



Overturning Moment

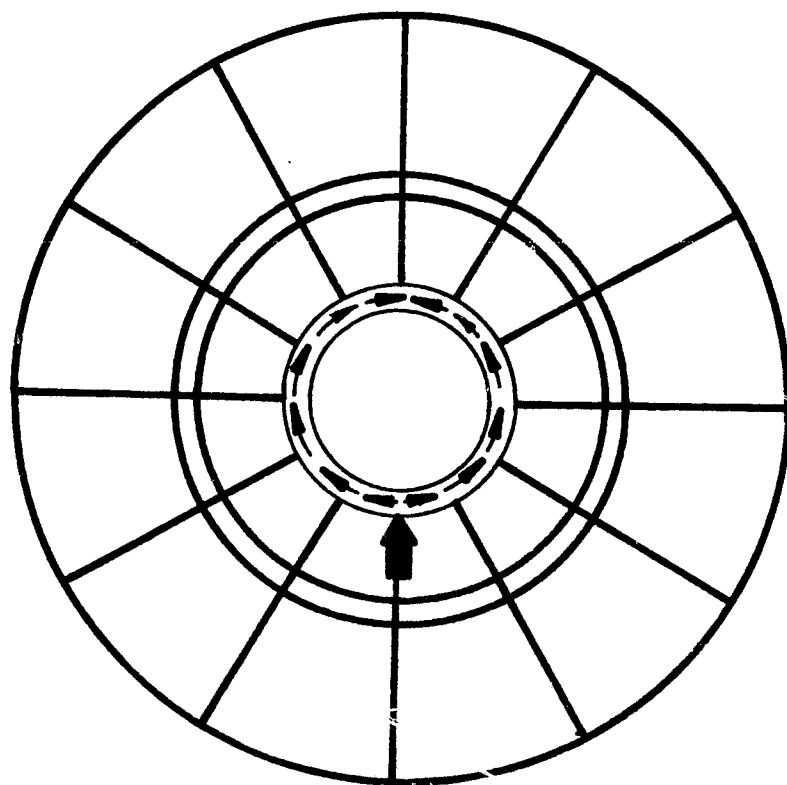


Figure 137. Fan A Frame Analytical Loading Configurations

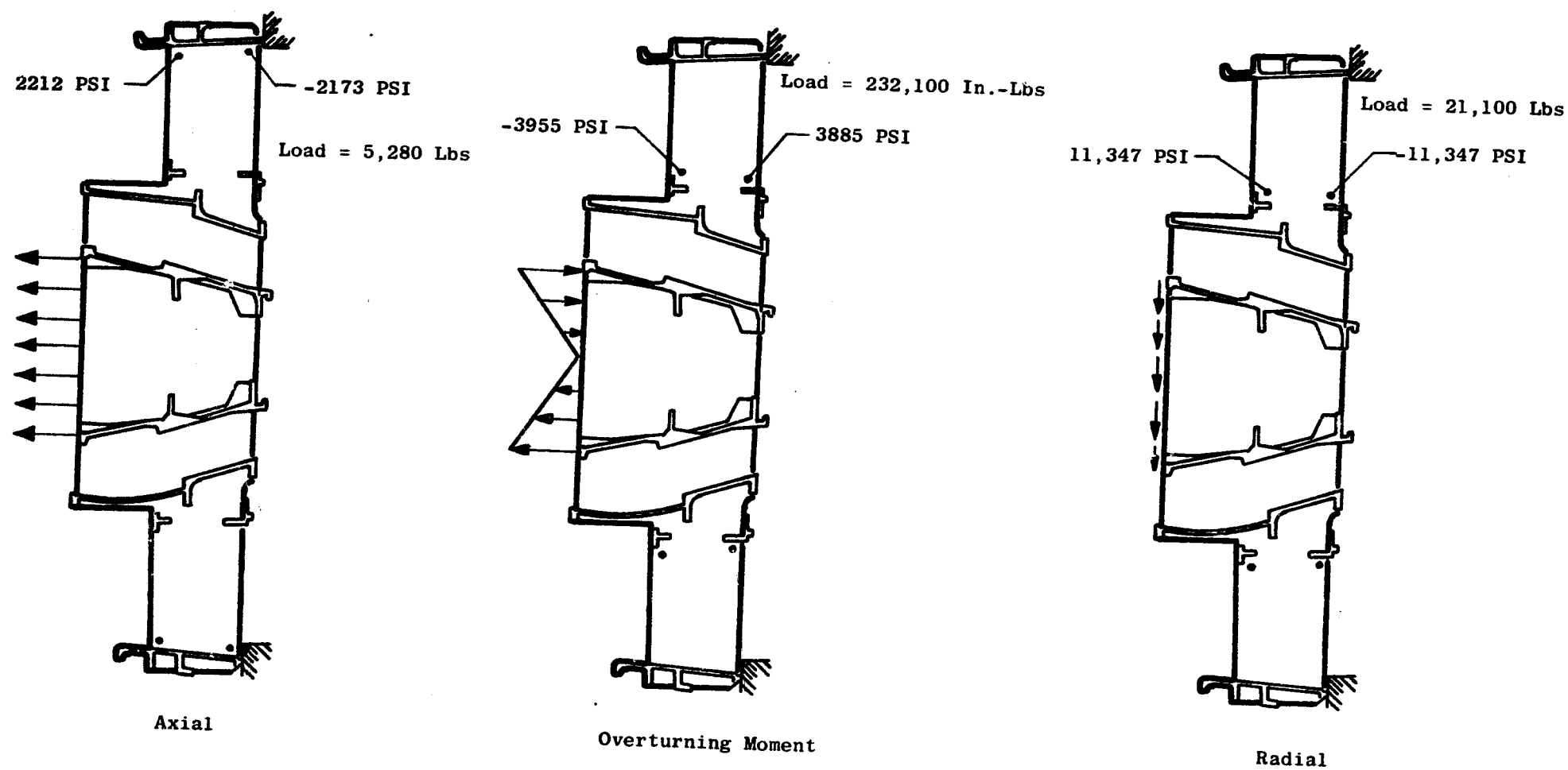
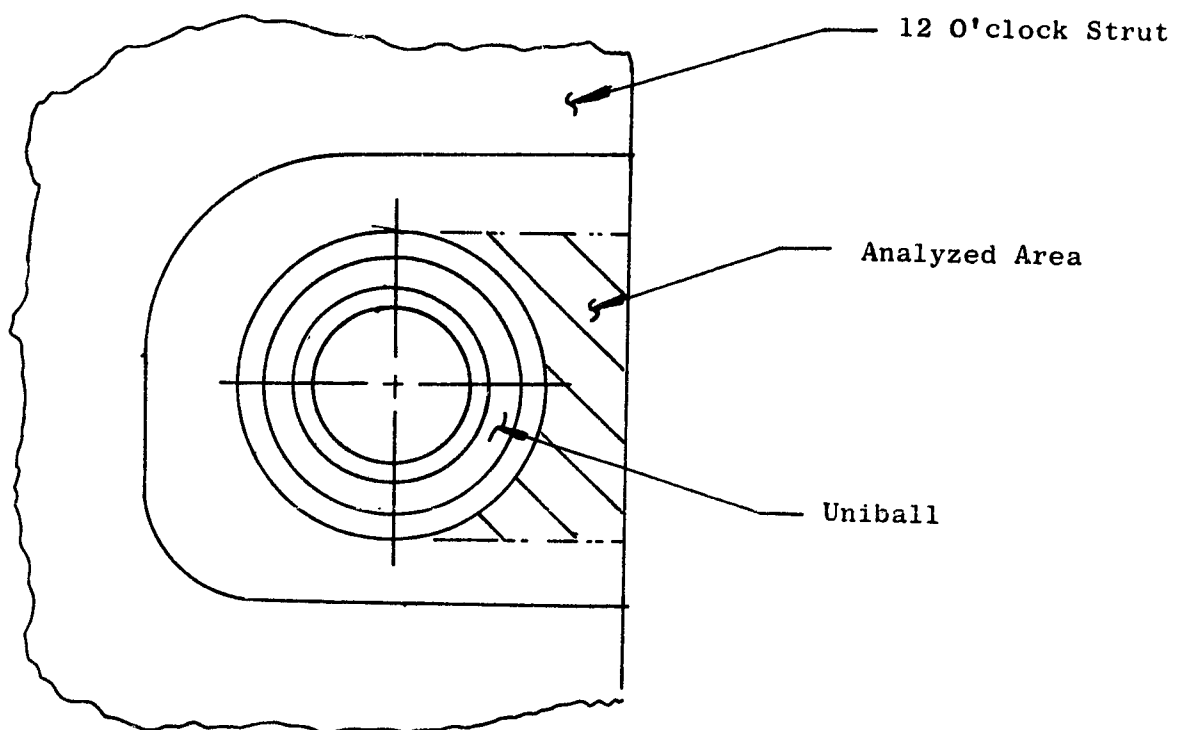
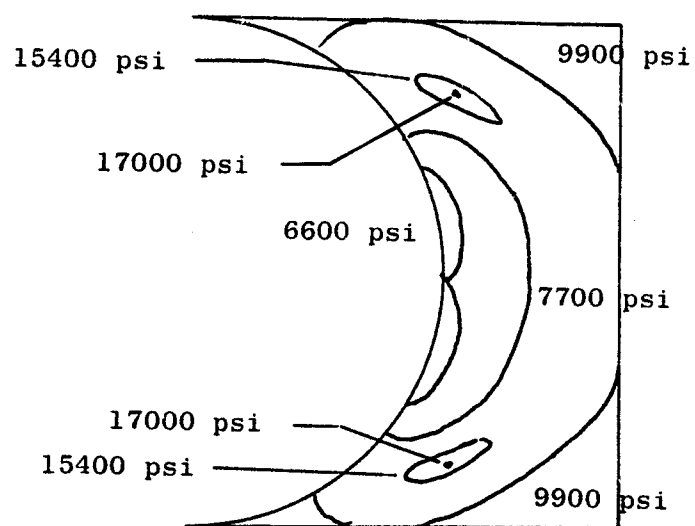
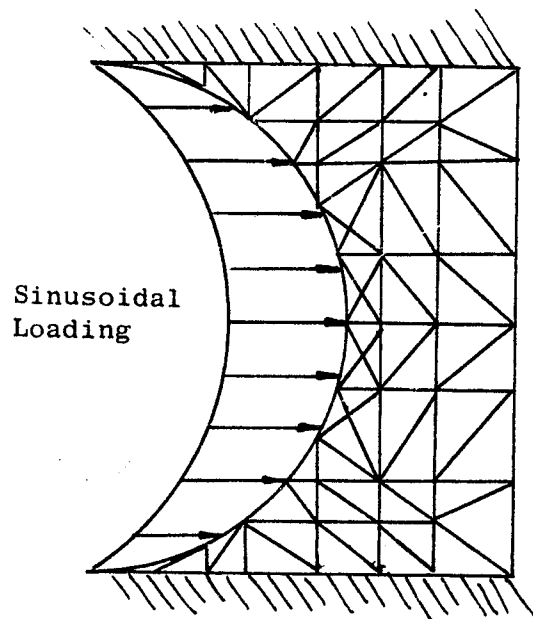


Figure 138. Fan A Frame Maximum Stresses



Top View - 12-O'clock Strut - Engine Mount System



Stress Map

Figure 139. Fan A Engine Mount Analytical Model and Results

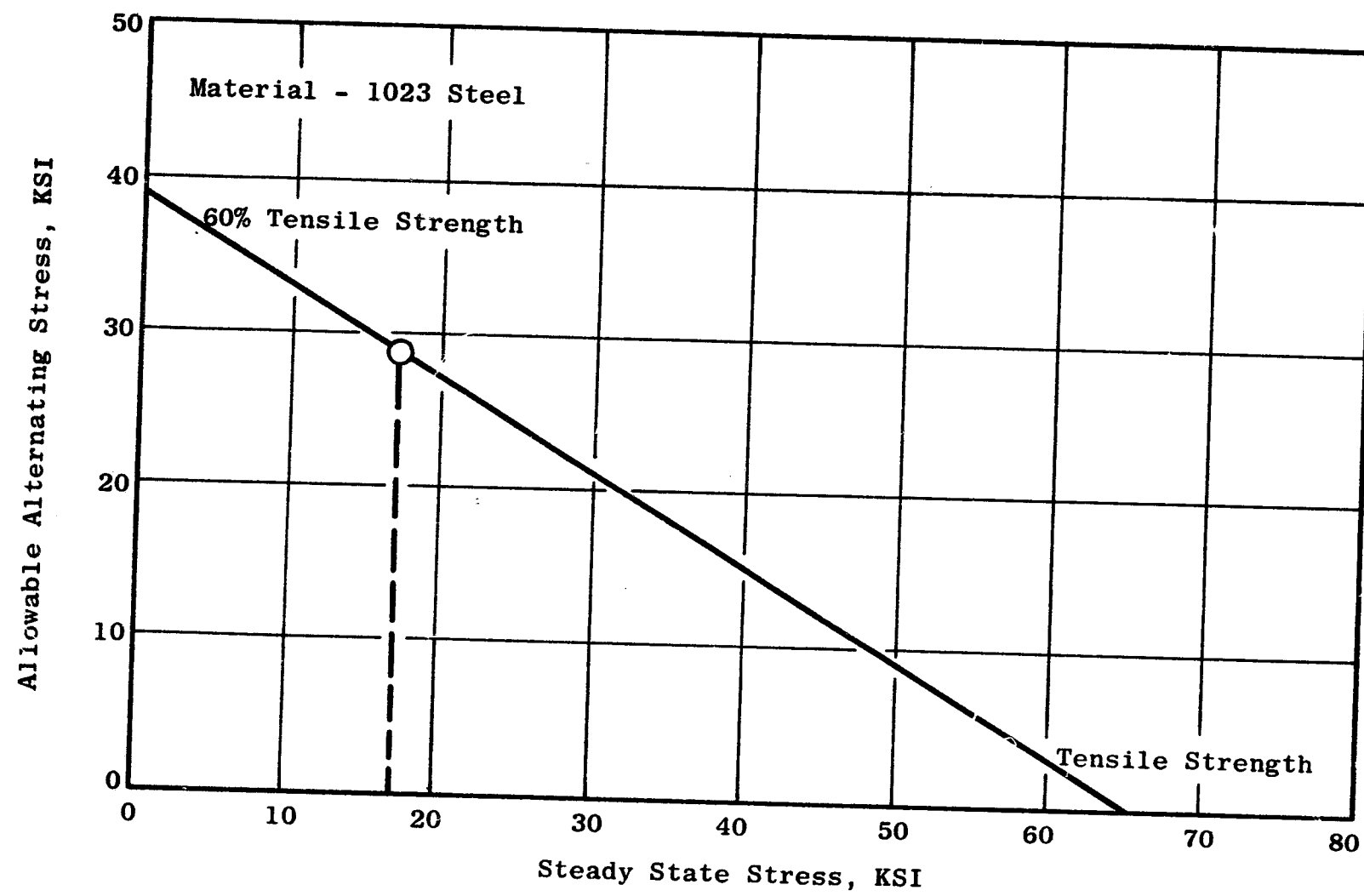


Figure 140. Fan A Engine Mount Allowable Alternating Stress

and C frames provided a smooth load flow from the side load link into the fan frame. The A/B fan has the highest stressed shear plate with a shear stress of 7,300 psi for the maximum steady state flight side load.

-Bearing Support System

The bearing support cone, sump shield, and static seal were analyzed using time-sharing computer programs to determine the resonant frequencies (see Figure 141). The static seal was analyzed to determine W/R. It was found to be substantially below the classic seal stability criteria of 0.2×10^{-3} inches per inch.

● Instrumentation Provisions

Instrumentation has been provided in both the core and bypass ducts to determine the flow characteristics in these regions. Static pressure taps are located at various axial and angular locations in the core duct. Static pressure taps are also provided in the bypass duct around the circumference at one axial position. Radial rakes, to measure total temperature and pressure, are located at various angular locations in the bypass duct.

Access has been provided in the outer core casing, aft of the acoustic material, for sonic probes.

5.2.1.1.2 Fan A Stator

The fan stator assembly is a nonflight-weight structure with variable bypass stream outlet guide vanes and adjustable outlet guide vanes in the core stream. The outlet guide vanes direct and diffuse the air leaving the fan rotor providing optimum inlet incidence and exit swirl angles in the aerodynamic flowpaths between the fan rotor and fan frame. The flow surfaces of the bypass duct and core duct are lined with sound suppression panels to reduce noise generated by the fan and core components.

The bypass stream cascade is composed of 90 individually machined variable stator vanes rigidly attached to the outer duct casing and supported by shrouds at the duct inner flowpath. The principle of the classical high-boss design (Figure 142) of the outer attachment is to translate the vane gas bending moments into couple loads on the circumferential casing ring. The inner end of the vane is located with a pinned connection to prevent translation; however, the configuration will not resist a moment. The intersection of the vane airfoil and trunnion introduces stress concentrations,

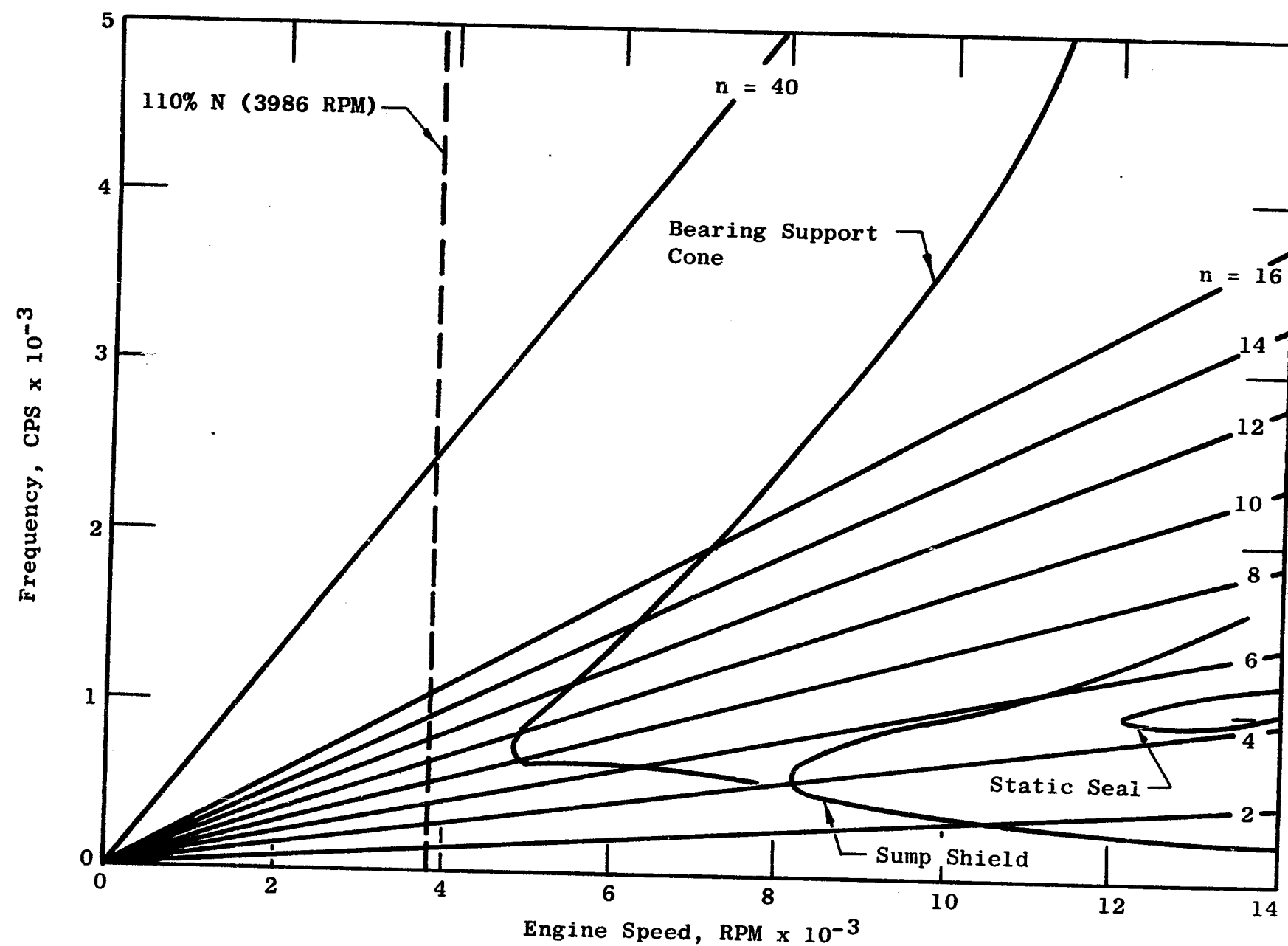


Figure 141. Campbell Diagram Fan A Bearing Support System

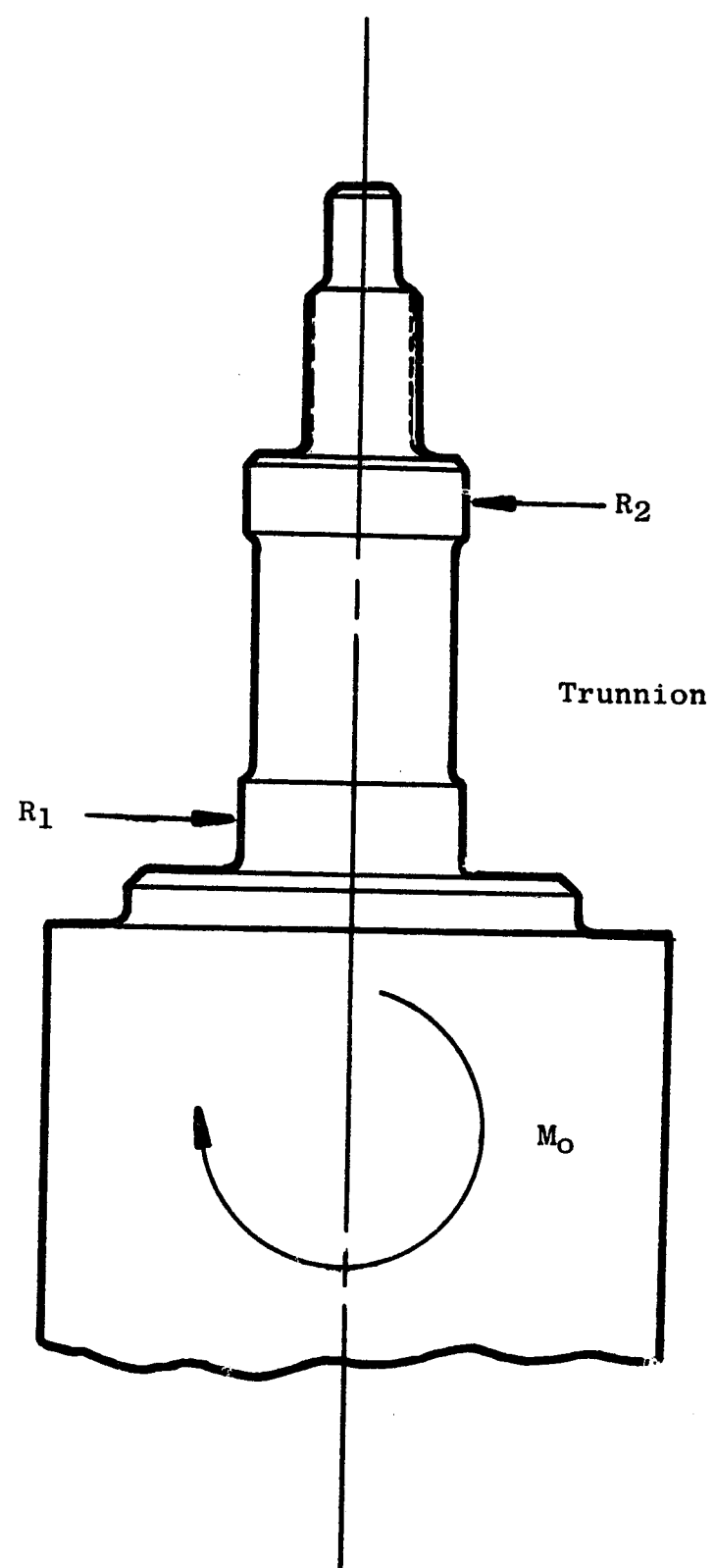


Figure 142. High Boss Vane

as a result of the reduction in available load carrying area, which indicate the vane structural limits. This intersection has been provided with a generous button diameter which minimizes these concentrations. The advantage of the structurally-stiff vane supports is in the significantly increased level of the first flexural and torsional frequencies. This frequency level provides the ability to avoid rotor blade passing resonance in the unstable one and two per rev excitation range.

Airfoil parameters for the Fan A cascades are presented in Table XXXIII.

Table XXXIII. Fan A Airfoil Pitchline Data

<u>Parameter</u>	<u>Bypass</u>	<u>Core</u>
Number of Vanes	90	90
Chord	3.05	2.6
Camber	43.2	47.4
Stagger	13.3	15.8
Aspect Ratio	3.88	1.42
T_m/c	0.054	0.059
Type	Series 65	Series 65

The vanes are radially secured in the outer duct casing by locknuts. The vanes are coated with Dow Corning 3400 bonded lubricant to minimize rotational friction, reducing actuation loading and providing corrosion resistant protection for the airfoils.

Lever arms, rigidly attached to the vane stems by drive pins, are used to position and vary the vane stagger angles. Actuation of the bypass stream vane cascade is accomplished through a circumferentially-driven actuation ring. The ring contains radial pins which pass through spherical bearings located in the lever arm ends. These spherical bearings are employed to minimize wear between the radial pin and lever arm and to eliminate torsional load on the arm during rotation.

Relative positioning between the vanes and lever arms is maintained through a broached hole in the lever arms which mates to the double-slabbbed vane stems. The torque transmission from the actuation ring to the vanes

occurs through this mating joint, providing the capability to rotate the vane cascade. The lever arms are a basic J79 design that has been lengthened to provide an increased moment arm. The lever arms are machined from AMS 5736 bar stock. The actuation ring is machined from a ring forging or a rolled and welded bar.

The outlet guide vane cascade in the core duct consists of a single row of vanes. The vane angular positions are established by the use of slatted outer vane stems and broached rectangular locating plates. Adjustment of the vane stagger angle is accomplished through use of alternate sets of locating plates having the orientation of the broached holes varied. This vane cascade, like the bypass cascade, is capable of varying ± 10 degrees from the nominal vane position in two-degree increments.

The inner shrouds of the core cascade and the duct cascade are circumferentially split at the vane stem hole centerline to allow component assembly. The forward segment of the duct inner shroud and the aft segment of the core inner shroud are also split axially for assembly purposes. These shrouds, mounted through casings from the fan frame, provide support for the respective vane cascades.

The aerodynamic flowpath between the core and duct passages is defined by the flow splitter immediately aft of the fan rotor. This 360-degree shell is mounted through the core inlet outer casing to the fan frame. The flange joint at this intersection also contains the core vane outer shroud and provides a rigid structural ring near the vane-mounting plane. A sound suppression panel, located immediately aft of the splitter nose, defines the core outer flowpath into the core cascade.

The bypass vane cascade and core vane cascade are each supported by a 360-degree casing at their respective outer mounting points. These casings are machined from low carbon steel forgings and attached to shells mounted on the fan frame.

The core inlet inner casing, and the two core casings located aft of the core cascade, are 360-degree shells machined from aluminum forgings. Sound suppression panels are attached to these casings forming the remainder of the aerodynamic flowpath into the fan frame.

● Material Selection for Fan Stator Components

The material selection for fan stator components is given in Table XXXIV.

Table XXXIV. Material Selection, Fan Stator Components

Component	Fan A	Fan B	Fan C
Case - Inlet	6061-T652	6061-T652	6061-T652
Case - Rotor (1)	6061-T652	6061-T652	6061-T652
Case - Duct	6061-T4	6061-T4	6061-T4
Case - OGV Outer	AMS 5062	AMS 5062	AMS 5062
Actuation Ring	AMS 5062	AMS 5062	AMS 5062
Lever Arm	A-286	A-286	A-286
Spherical Bearing	440C SS	440C SS	440C SS
Splitter	6061-T652	6061-T652	6061-T652
Mount Ring - Forward	AMS 5062	AMS 5062	AMS 5062
Mount Ring - Aft	N/A	AMS 5062	AMS 5062
Case - Core Outer	6061-T652	6061 T652	AMS 5062
Shroud - Duct	AMS 5062	AMS 5062	AMS 5062
Case - OGV Inner	6061-T652	6061-T652	AMS 5062
Case - Core Inlet	6061-T652	6061-T652	6061-T652
Shroud - Core Forward	AMS 5062	AMS 5062	AMS 5062
Shroud - Core Aft	N/A	AMS 5062	AMS 5062
Case - Core Inner	6061-T652	6061-T652	6061-T652
<p>(1) Abradable material - Nomex honeycomb filled with epoxy-resin phenolic microballoons. Wear characteristics are described in "Nomex and P6TF1 Abradable Seal Material", written by John Daunt, dated June 25, 1968, Report No. TM68-427.</p>			

- Analysis, Fan Stator Components

-Vanes

The steady state stress (from the Twisted Blade Analysis) versus airfoil radial height for the bypass and core vanes is shown in Figures 143 and 144, respectively.

The maximum vane stress concentration factor which occurs at the intersection of airfoil and outer boss fillet radius on the core vane is 1.48.

The Goodman diagram showing the allowable alternating stress versus steady state stress for the selected vane material is shown in Figure 145.

The Campbell diagrams showing the vane Twisted Blade Program resonance frequencies versus engine operating speeds are shown on Figures 146 and 147.

The reduced velocity parameters, calculated at the maximum point of rotation as determined by the Twisted Blade Program, are shown for the bypass and core vanes on Figure 148.

The vane clearances for the nominal and fully-actuated positions are listed in Table XXXV. These values are determined using the root mean squared tolerance stackup method.

Table XXXV. Fan A Vane Clearances

Location	Bypass OGV		Core OGV	
	Maximum Travel	Nominal Position	Maximum Travel	Nominal Position
LE Outer, Inch	0.003	0.013	0.003	0.013
LE Inner, Inch	0.005	0.014	0.002	0.021
TE Outer, Inch	0.003	0.011	0.003	0.011
TE Inner, Inch	0.005	0.011	0.002	0.010

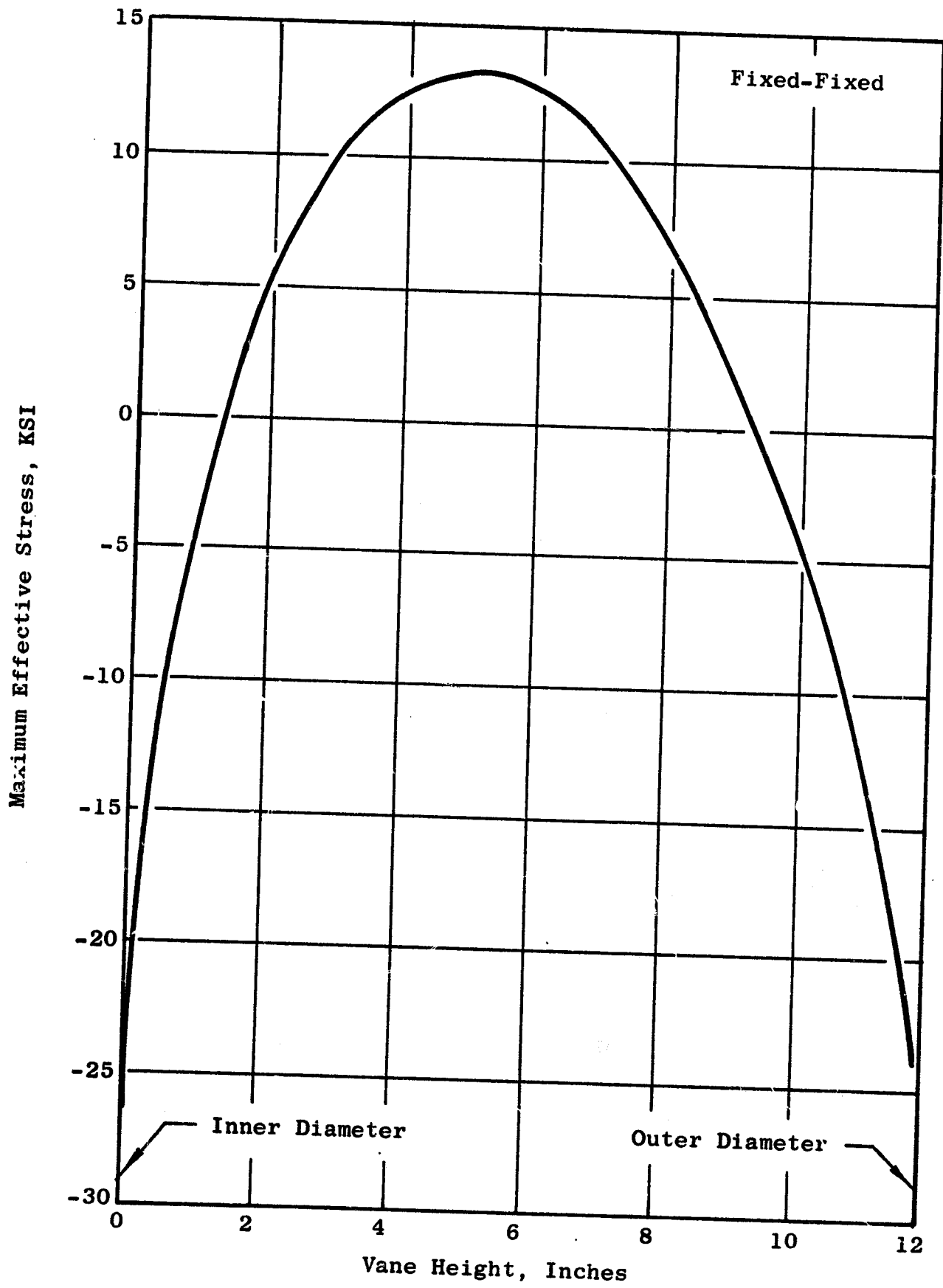


Figure 143. Fan A Bypass OGV Stress Distribution, Hi C Point, Convex Side

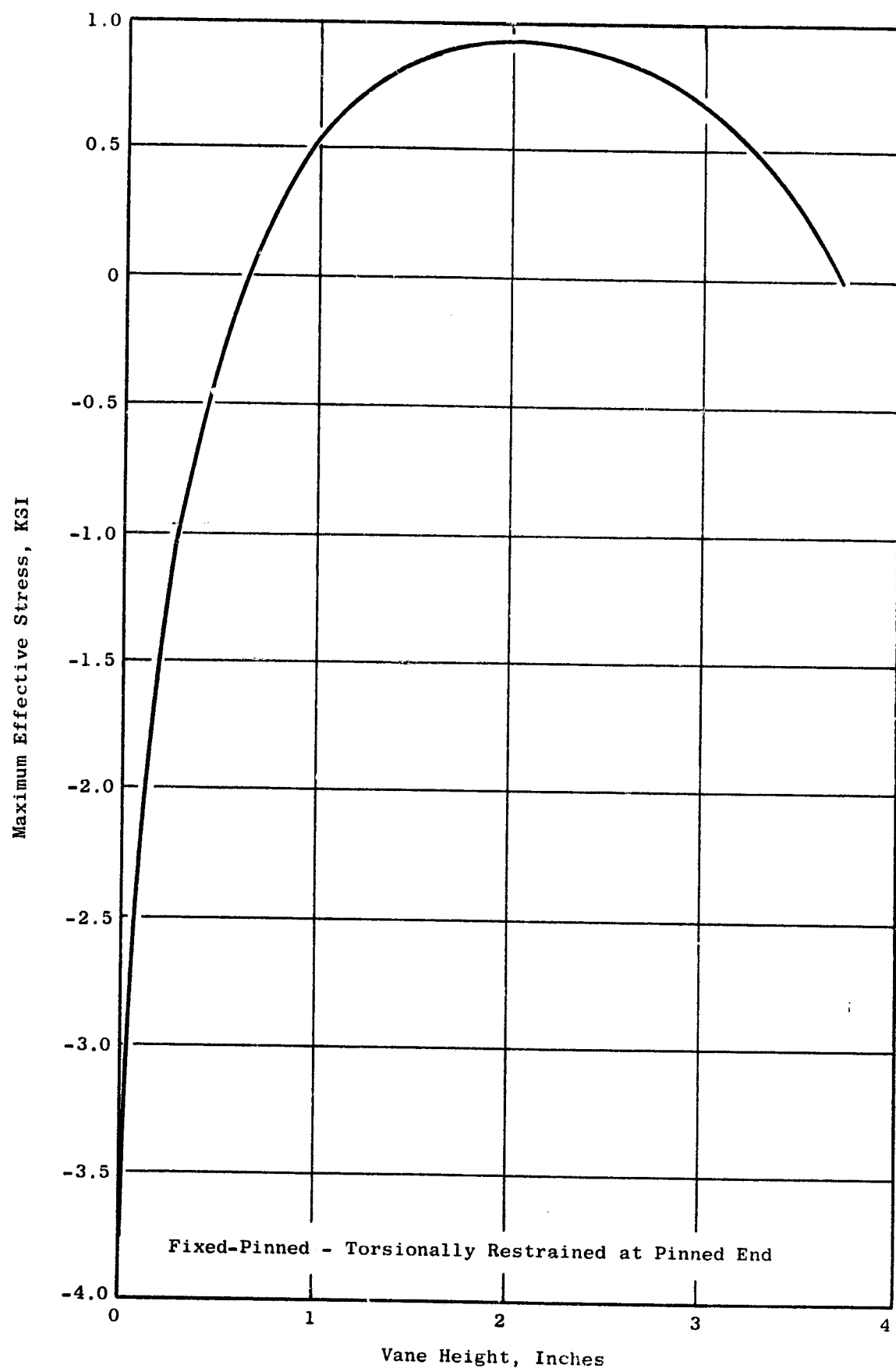


Figure 144. Fan A Core OGV Stress Distribution, Hi C Point, Convex Side

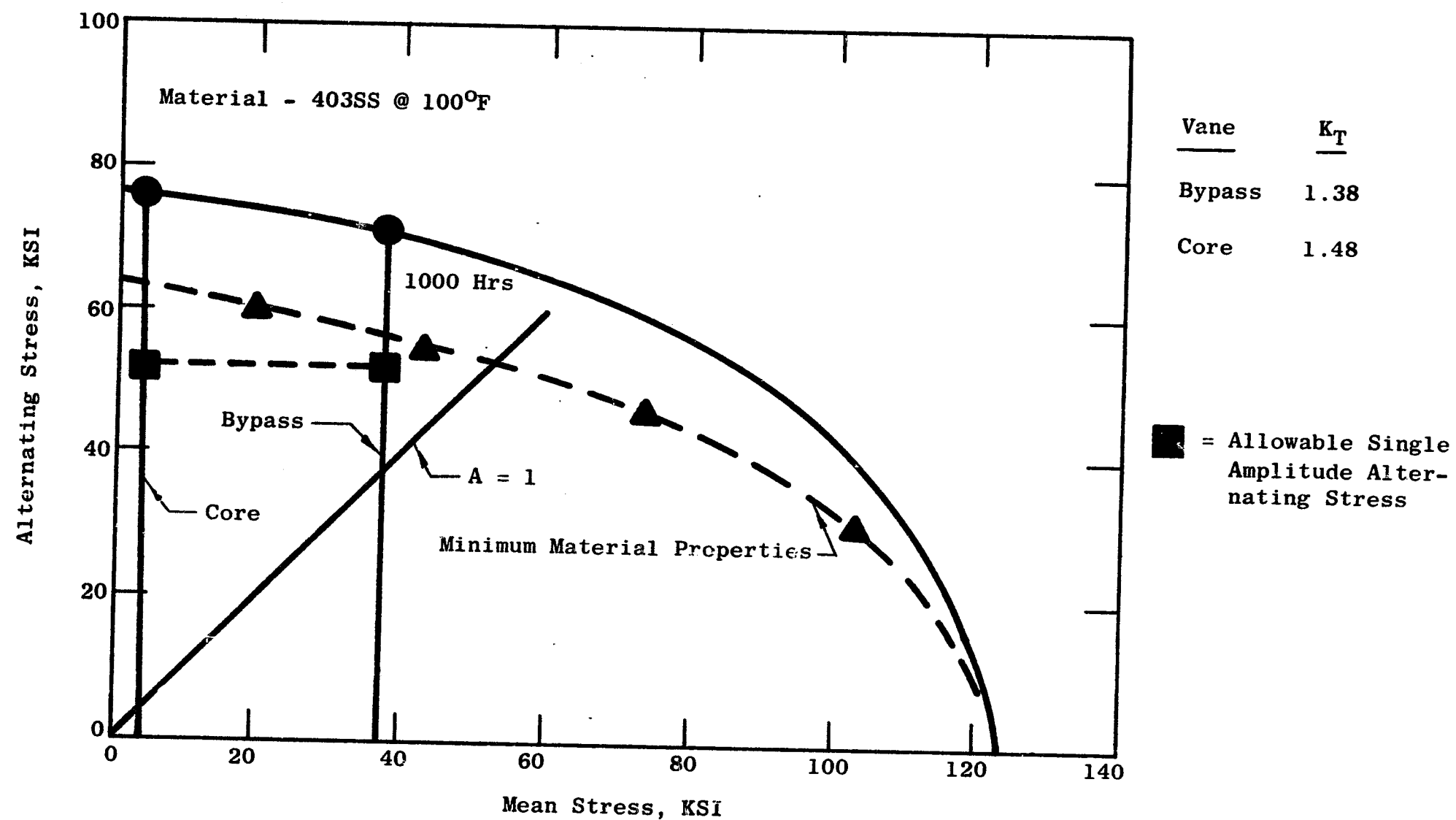


Figure 145. Fan A Vane Goodman Diagram

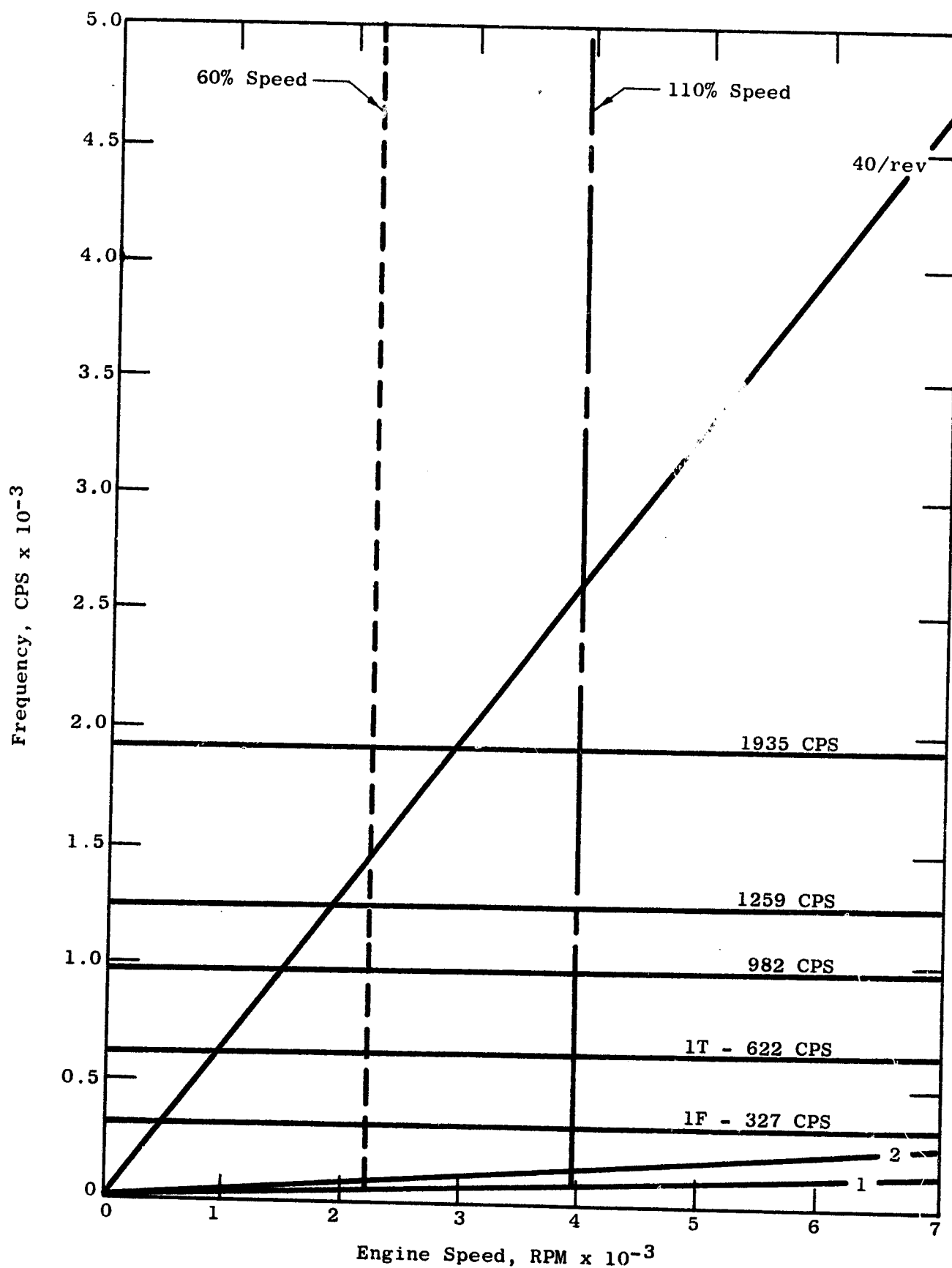


Figure 146. Campbell Diagram, Fan A Bypass OGV

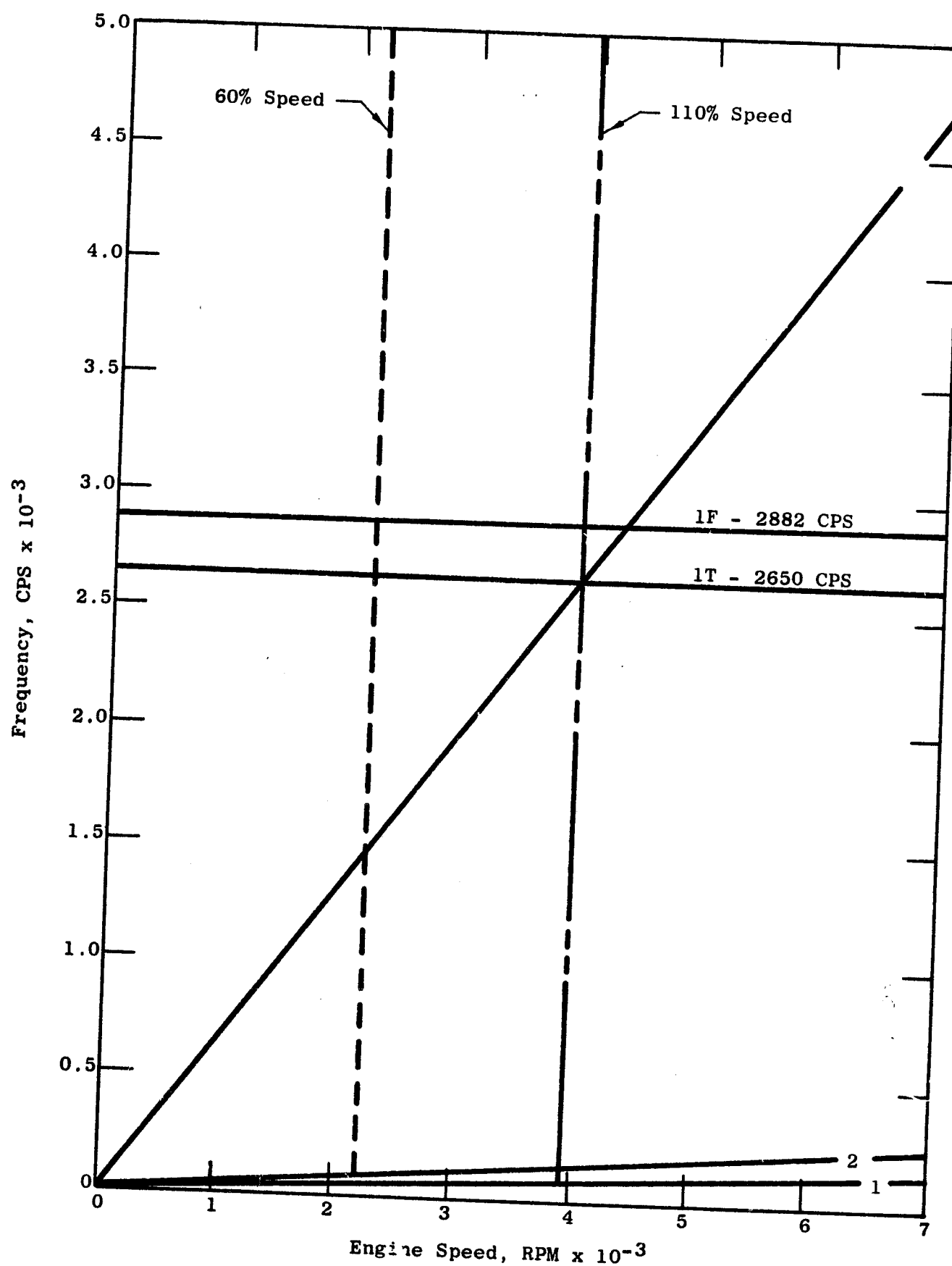


Figure 147. Campbell Diagram, Fan A Core OGV

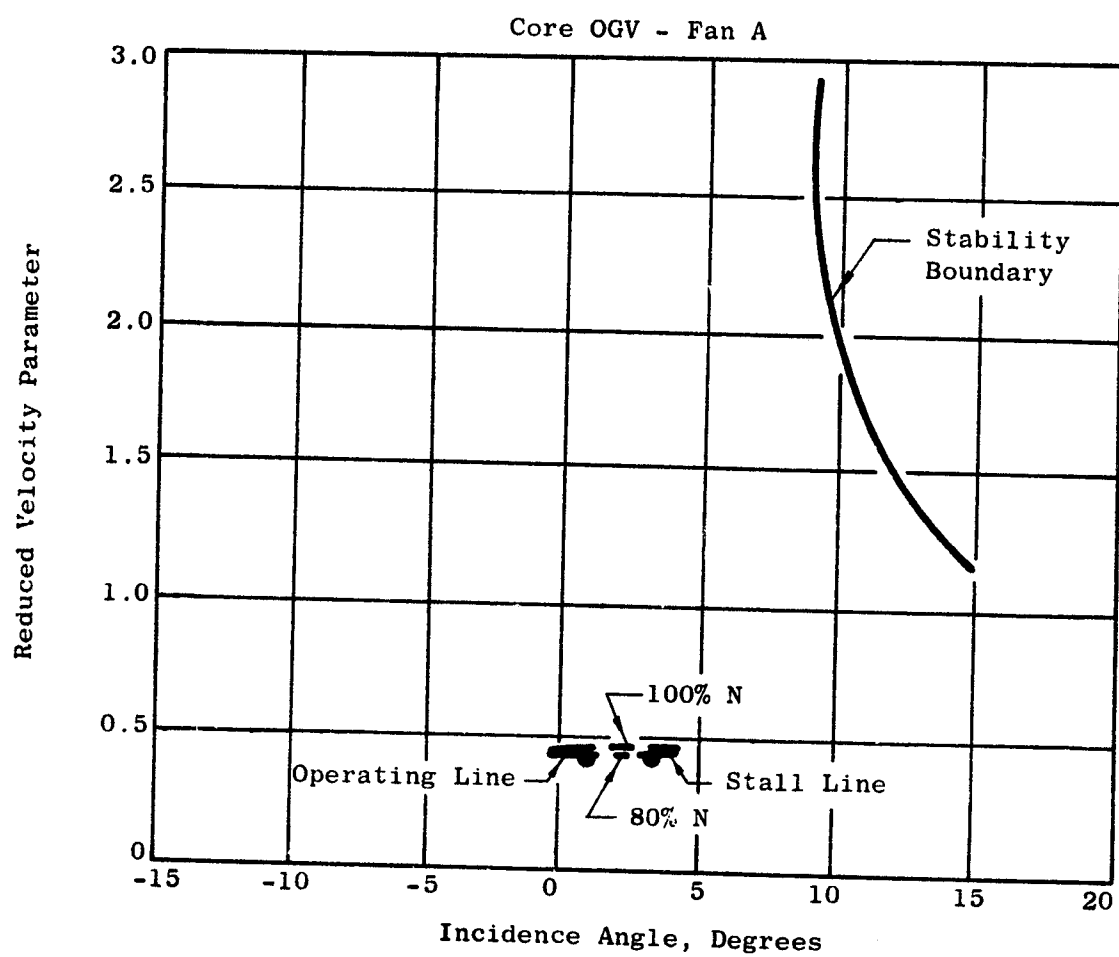
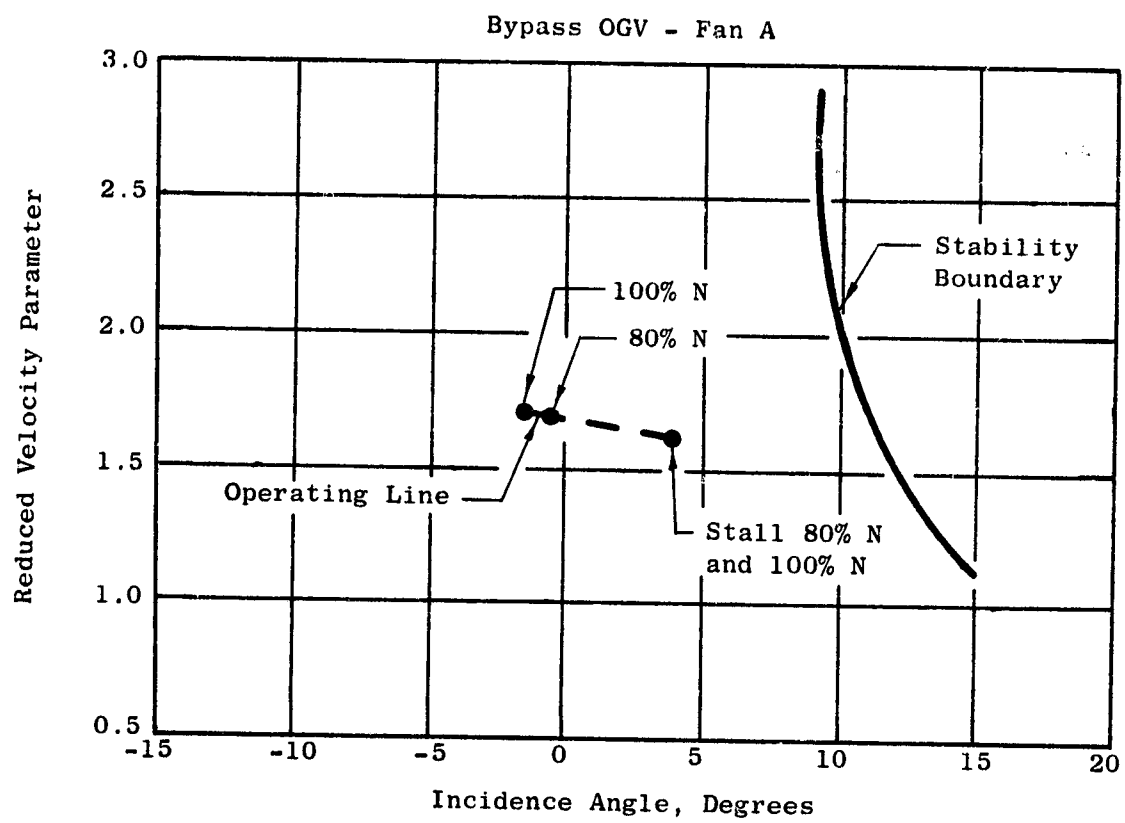


Figure 148. Fan A Vane Stability Plots

-Casings

The Campbell diagrams for the various casings are shown in Figure 149. These figures show the casings are designed to be free of resonant response in the engine operating range.

The duct casing which mounts the accessory gearbox for engine operation has been analyzed by the MASS computer program for a 10g gearbox load for the more critical Fan B casing.

The deflections and stresses for the Fan A casing will be similar to, but lower than, the values calculated for the less rigid Fan B casing. The maximum deflection calculated was 7 mils with accompanying low stresses.

-Actuation System

The vane actuation systems for Fans A, B, and C are essentially the same. The analysis of the actuation systems was confined to the B Fan, since it has the highest vane loading.

- Stator Vanes - Instrumentation and Scope Limits

Prior to their installation in the fan test vehicles, stator vanes will undergo substantial vibration testing. Bench testing will include determination of the following items:

- Natural frequencies
- Nodal patterns
- Strain distribution

Figure 150 depicts a typical gage pattern employed to define stress distribution. Data will be generated for excitation frequencies up through the passing frequencies of the fan rotor blades.

Engine gage locations will be selected on the basis of the strain distributions. Past history indicates that one to three individual gage locations will provide sufficient response at each of the critical frequencies to provide limits of sufficient magnitude for scope observation. Vanes will be instrumented and constantly monitored on oscilloscopes during each of the fan testing periods. The vibratory stress data provide assurance that the vanes are operating below their maximum allowable stress levels, indicate maintenance of mechanical integrity by way of identical data at repeated operating points, and identify the approach of/or operation in stall.

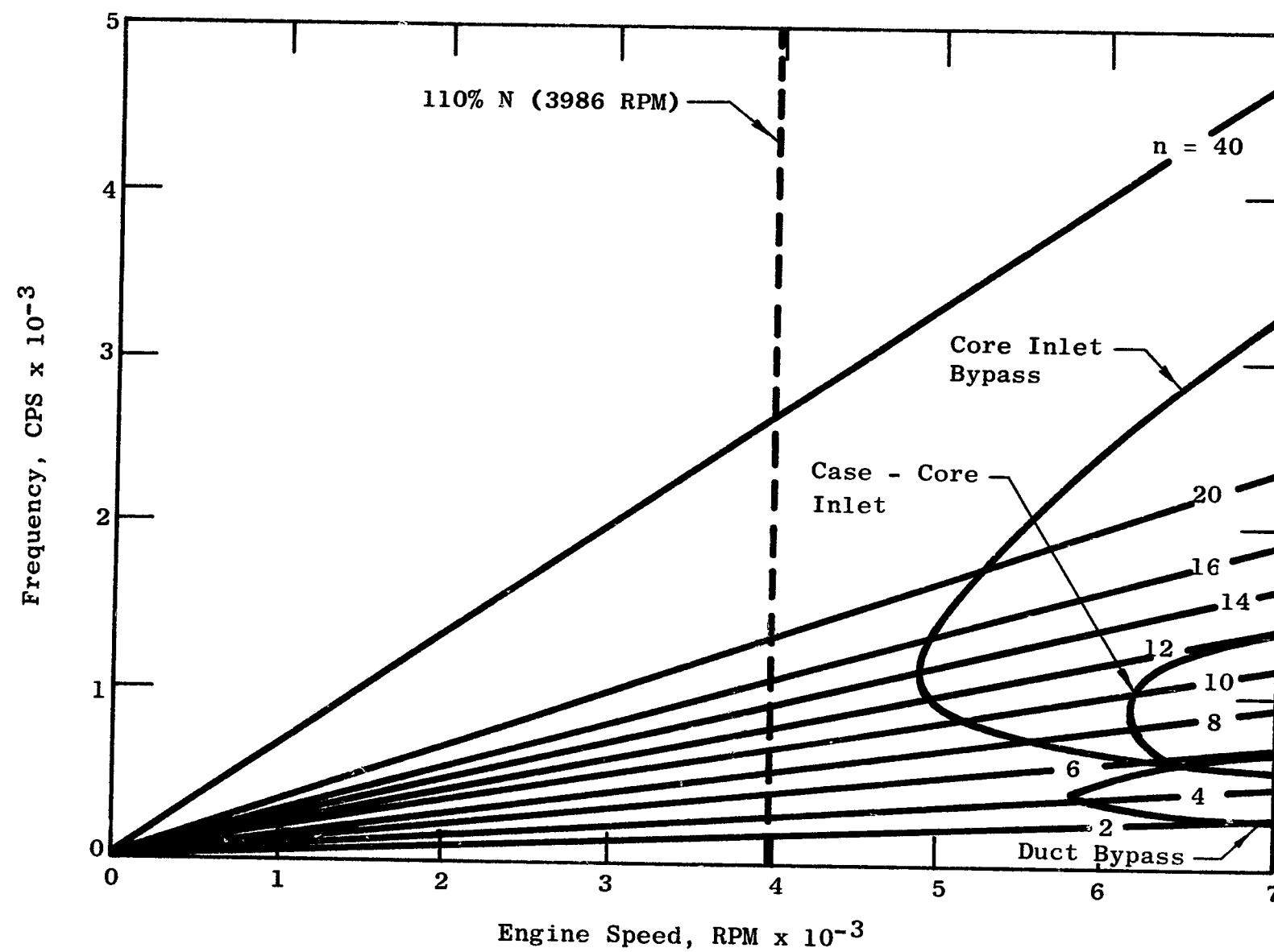


Figure 149. Campbell Diagram, Fan A Casings

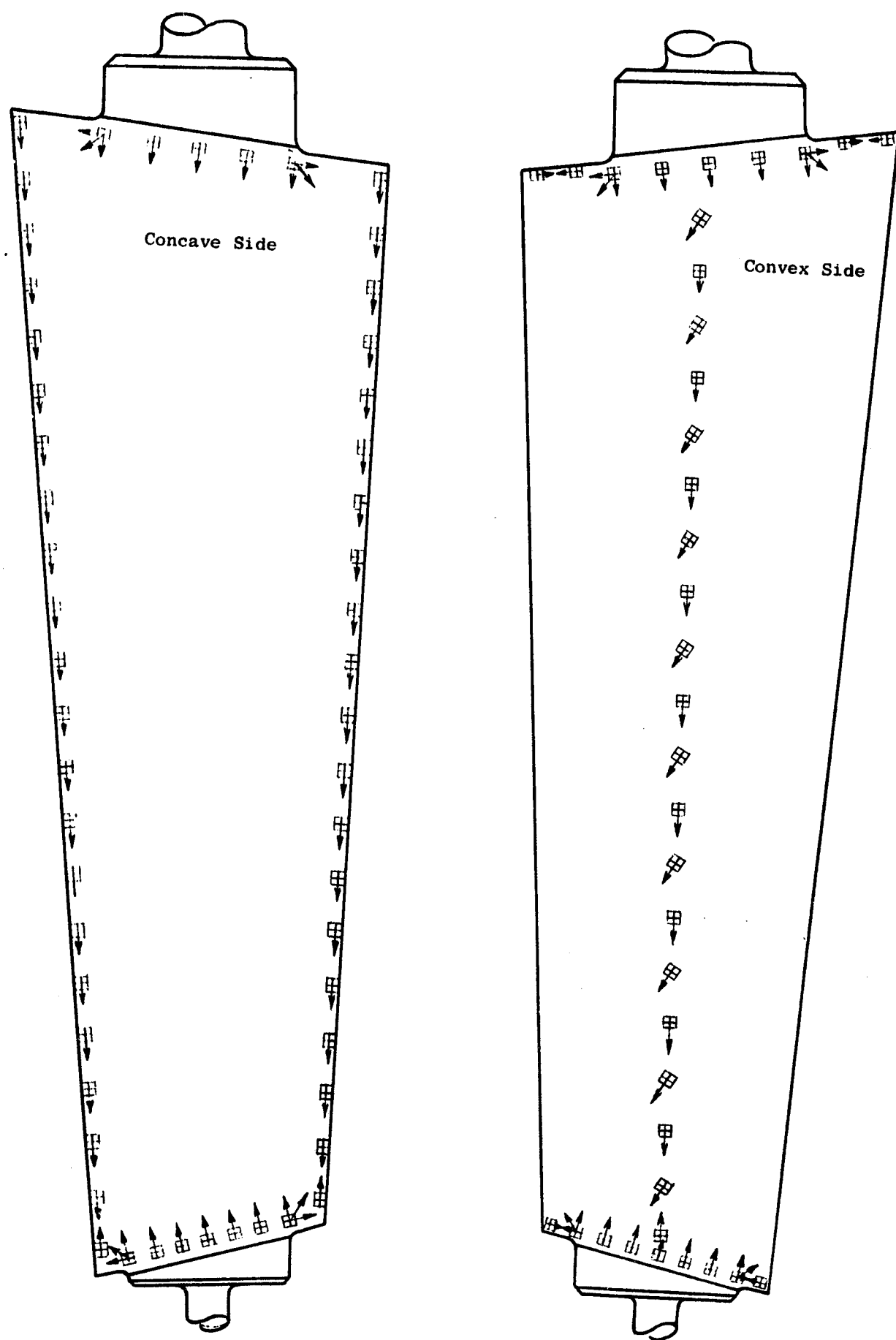


Figure 150. Typical Strain Gage Map, Bench Test

Scope limits will be established for each of the selected gage locations at each critical frequency. The basis for determination of the scope limits is the Twisted Blade steady state stress distribution and the vibratory strain distribution. The Goodman diagram for the pertinent vane material provides the required link between the two values. The procedure is to determine, for each critical frequency, that point on the vane at which there is the minimum allowable vibratory stress. Stress concentrations are applied to the allowable vibratory limits in those areas where the airfoil intersects the platform. In most cases, the point of application of the engine strain gages is not the point of minimum allowable vibratory stress. The vibratory stress of the engine gage location must be suitably ratioed to indicate the stress level present at the point of minimum allowable vibratory stress. Safety factors are applied to account for vane-to-vane variations (only three vanes of the cascade will be instrumented), electrical circuit tolerance, and gage mislocation (small variations may exist between the selected gage location determined by the bench test data and the actual location of the engine gages being read on the oscilloscopes).

- Instrumentation Provisions, Core and Bypass Ducts

Instrumentation has been provided in both the core and bypass ducts to determine the flow characteristics in these regions. A great many static pressure taps are located in these regions. Static pressure taps are clustered around the circumference of all shrouds at both the leading and trailing edge of the OGV's. Static pressure taps are located around the circumference at many axial locations in the core duct, the bypass duct, and the splitter. Traversing rakes are provided to measure total temperature and pressure. These rakes are located around the circumference of both the core and bypass ducts between the rotor and the OGV's.

5.2.1.1.3 Acoustic Panels

The sound suppression panels are positioned around the outer and inner periphery of the core and duct flowpaths. These panels are split into angular segments to facilitate manufacturing and to minimize assembly problems.

The sound suppression panels are an adhesively-bonded construction of aluminum sheet and fiberglass. The core material is a two-ply E293/181 glass fabric corrugation bonded with FM-123 supported film adhesive. This construction forms a slotted double-diamond design for maximum noise attenuation and formability during processing.

The porous aluminum faceplate is fabricated from 5052 aluminum, contour stretch-formed and bonded to the core material by FM-123 adhesive. Removable panels have a three-ply E293/181 glass fabric backing sheet bonded to the opposite face of the core material. The permanently-installed panels bond the open face directly to a recess in the casing.

The end closure in the axial direction is EPON-934 epoxy resin adhesive. In the circumferential direction, the core is joined to the side using FM-37 epoxy adhesive foam.

Where static pressure readings are required, a one-inch diameter 5052 aluminum plug with a 0.040-inch diameter hole is inserted into the panel, as shown in Figure 151. It is bonded to the backing sheet and faceplate by EPON-901/B-3 adhesive.

To accomplish the bolting connection, a drilled phenolic-glass laminated rod (NEMA grade G-12) is pinned in place to the glass fabric backing sheet. The core material is then bonded to the backing sheet as above, and the rod is bonded to the core with EPON901/B-3. The edge and ends are filled as above, and the porous aluminum faceplate is bonded to the assembly. Holes are drilled through the faceplate, and the assembled male and female portions of the insert are placed in the holes. The female portion is bonded to the glass rod with EPON934 and is held in place by screws through the backing sheet into the male portion of the insert.

5.2.1.2 Fan B Structures

The first Engine fan configuration to be designed and tested will be Configuration B (see Figure 152), which is characterized by wide-chord/low-aspect-ratio fan blades and a relatively low tip speed. It will also incorporate sound suppression techniques common to all fans in this program, such as selection of airfoil quantities, rotor-stator spacing, and duct wall treatment. The major fan components (such as the fan rotor, the fan stator, and the fan frame) will be designed for interchangeability between the full-scale fan test (FSFT) facility at General Electric-Lynn, the NASA-Lewis facility, and the full-scale experimental engine.

The FSFT vehicle for Fan B, and all other configurations, will consist of the aforementioned fan components adapted to an existing double-annulus fan discharge control assembly installed in the Lynn fan and compressor test facility.

The discharge control assembly includes an integral drive shaft, bearing and lubrication system, concentric annulus flowpath elements, and independently variable valving systems in both the core and the fan discharge passages. Provisions will be made in both the facility and the fan components for the incorporation of instrumentation to measure aerodynamic and acoustical performance of the fan.

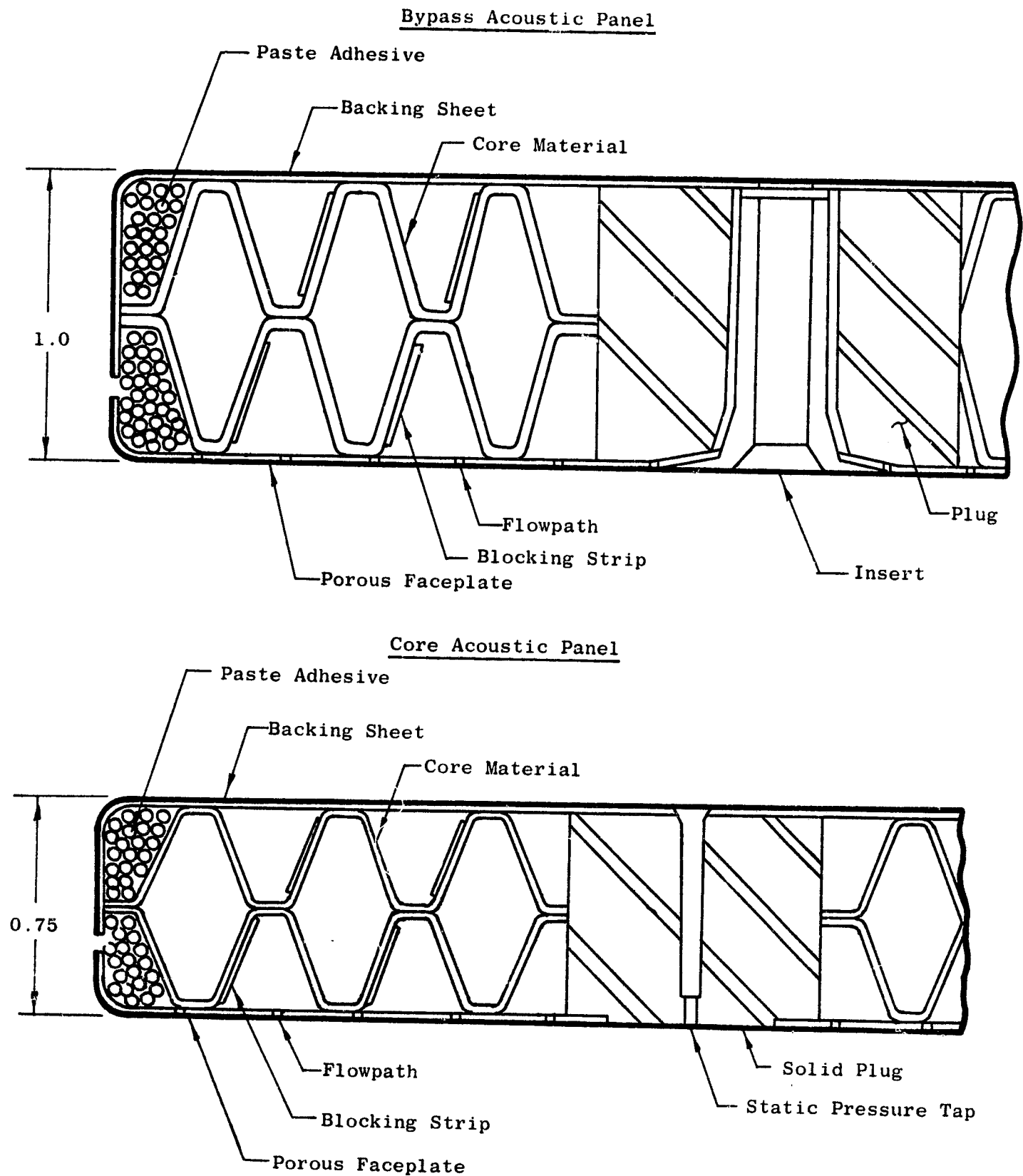


Figure 151. Bypass and Core Acoustic Panel Construction

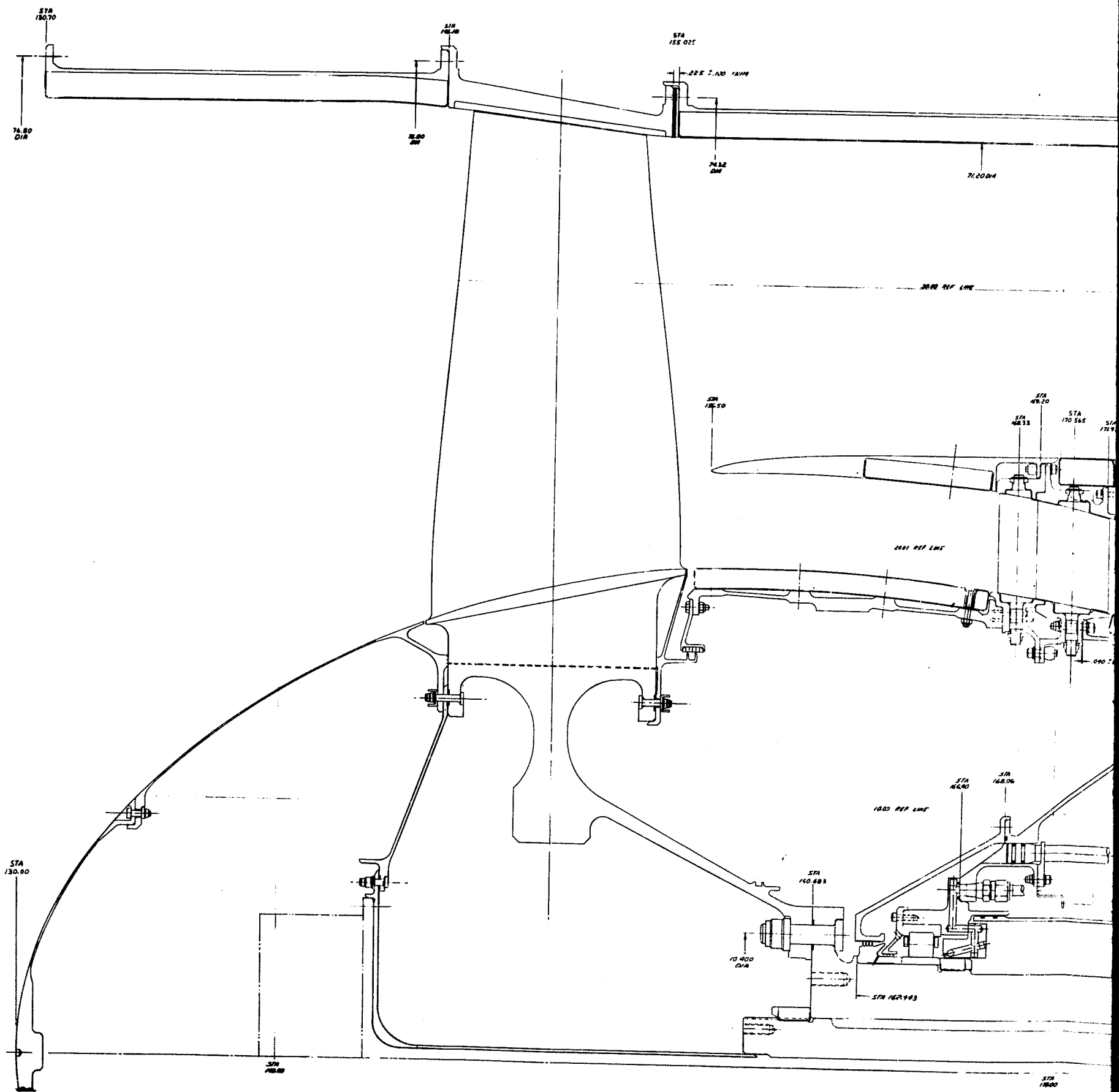


Figure 152. Fan B FSFT S

0

FOLDOUT FRAME



5.2.1.2.1 Fan B Frame

The Fan B frame is identical to the Fan A frame except for the magnitude of the loads shown in Figure 153.

5.2.1.2.2 Fan B Stator

Fan B is a low-tip-speed, low-aspect-ratio fan rotor vehicle. The 60 bypass stream outlet guide vanes were designed using the same techniques used on the Fan A design and meet the same design criteria.

The core stream outlet guide vane assembly is composed of a low camber forward vane and a moderate camber aft vane. There are 60 forward and 60 aft vanes. The vane stagger angle is set by a broached locating plate and the use of double-slabbed outer vane stems. Adjustment of the vane stagger angles is accomplished by replacing the locating plates with plates which have the broached hole at a different angle. This allows the stagger angle to be increased or decreased in 2° increments to a total variation from nominal of ± 10 degrees (see Figure 154).

The axial gap between the trailing edge of the forward vane and the leading edge of the aft guide vane is maintained by rotating the forward mount ring and shroud circumferentially. Six equally spaced rabbets allow the mount ring and shroud to rotate with respect to the adjoining casings. Airfoil data are presented in Table XXXVI.

Table XXXVI. Fan B Airfoil Pitchline Data

Parameter	Core		
	Bypass	Fwd.	Aft
Number of Vanes	60	60	60
Chord	4.589	2.0	3.0
Camber	44.2	11.6	43.1
Stagger	13.5	41.8	12.1
Aspect Ratio	2.582	1.91	1.23
T_m/c	0.057	0.05	0.05
Type	Series 65	Arbitrary	Series 65

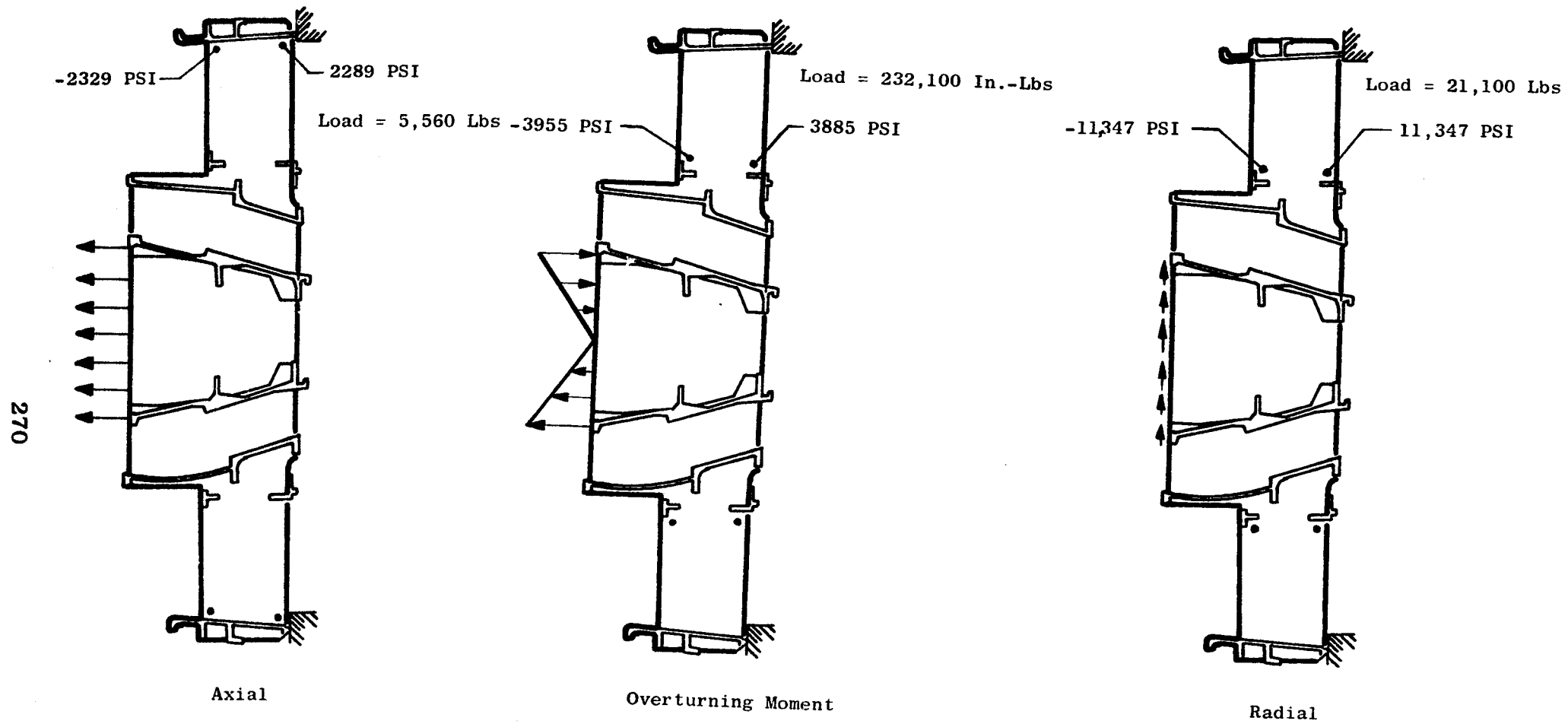


Figure 153. Fan B Frame Maximum Stresses

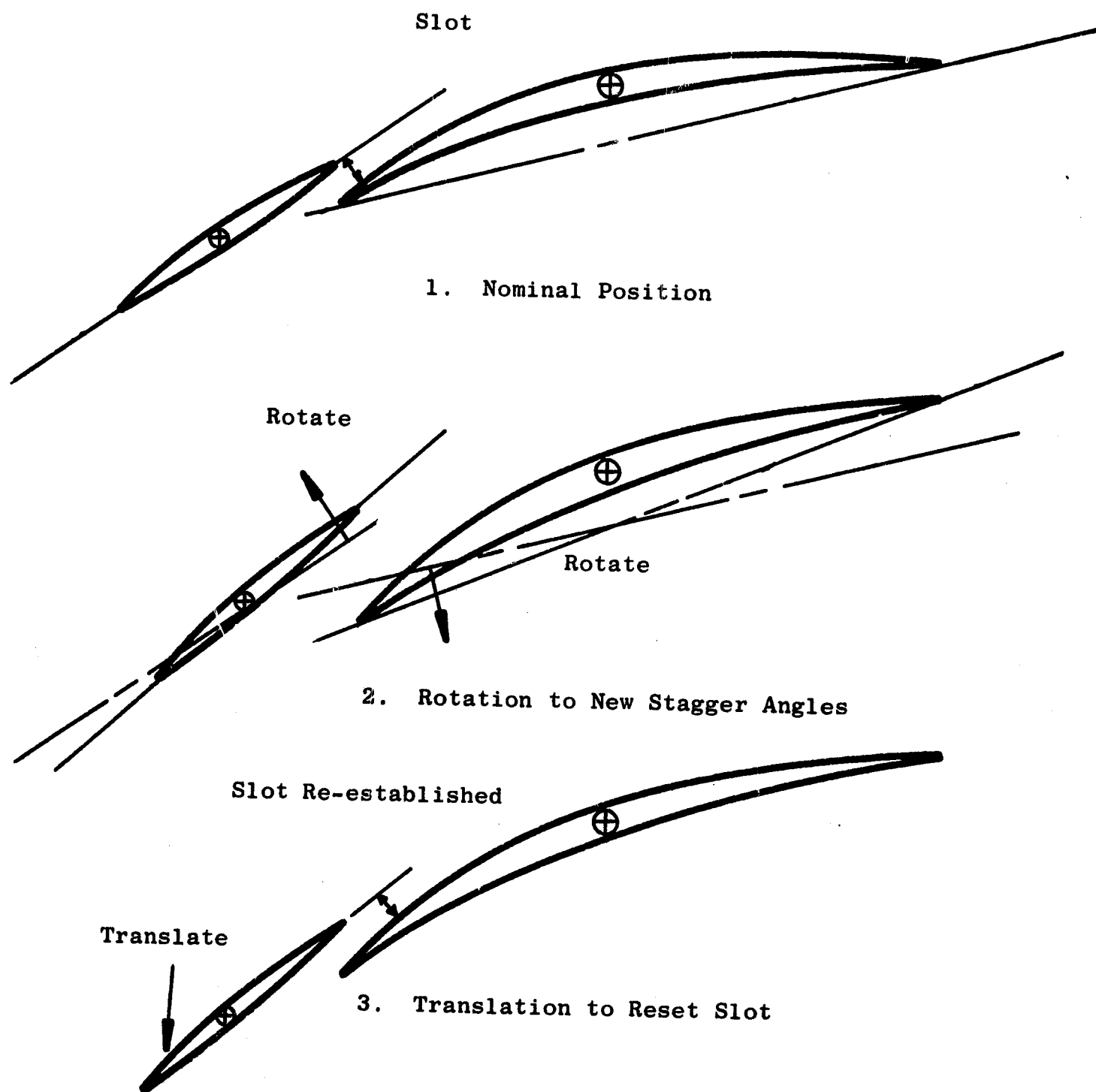


Figure 154. Fans B and C Core Stream OGV Mechanics

- Analysis, Fan Stator Components

-Vanes

The steady state stress (from the Twisted Blade Analysis) versus airfoil radial height for the bypass and core vanes is shown in Figures 155, 156, and 157, respectively.

The maximum vane stress concentration factor, which occurs at the intersection of airfoil and outer boss fillet radius on the bypass vane, is 1.38.

The Goodman diagram, showing the allowable alternating stress versus steady state stress for the selected vane material, is shown in Figure 158.

The Campbell diagrams showing the vane Twisted Blade Program resonance frequencies versus engine operating speeds are shown on Figures 159, 160, and 161.

The reduced velocity parameters, calculated at the maximum point of rotation as determined by the Twisted Blade Program, are shown for the bypass and core vanes on Figures 162 and 163, respectively.

The vane clearances for the nominal and fully-actuated positions are listed in Table XXXVII.

Table XXXVII. Fan B Vane Clearances

Location	Bypass OGV	Core OGV	
	Nominal Position	Fwd Nominal Position	Aft Nominal Position
LE Outer*	0.019	0.017	0.026
LE Inner	0.014	0.010	0.013
TE Outer	0.014	0.015	0.011
TE Inner	0.012	0.013	0.011
* Minimum clearance at maximum vane travel for all cases = 0.010			

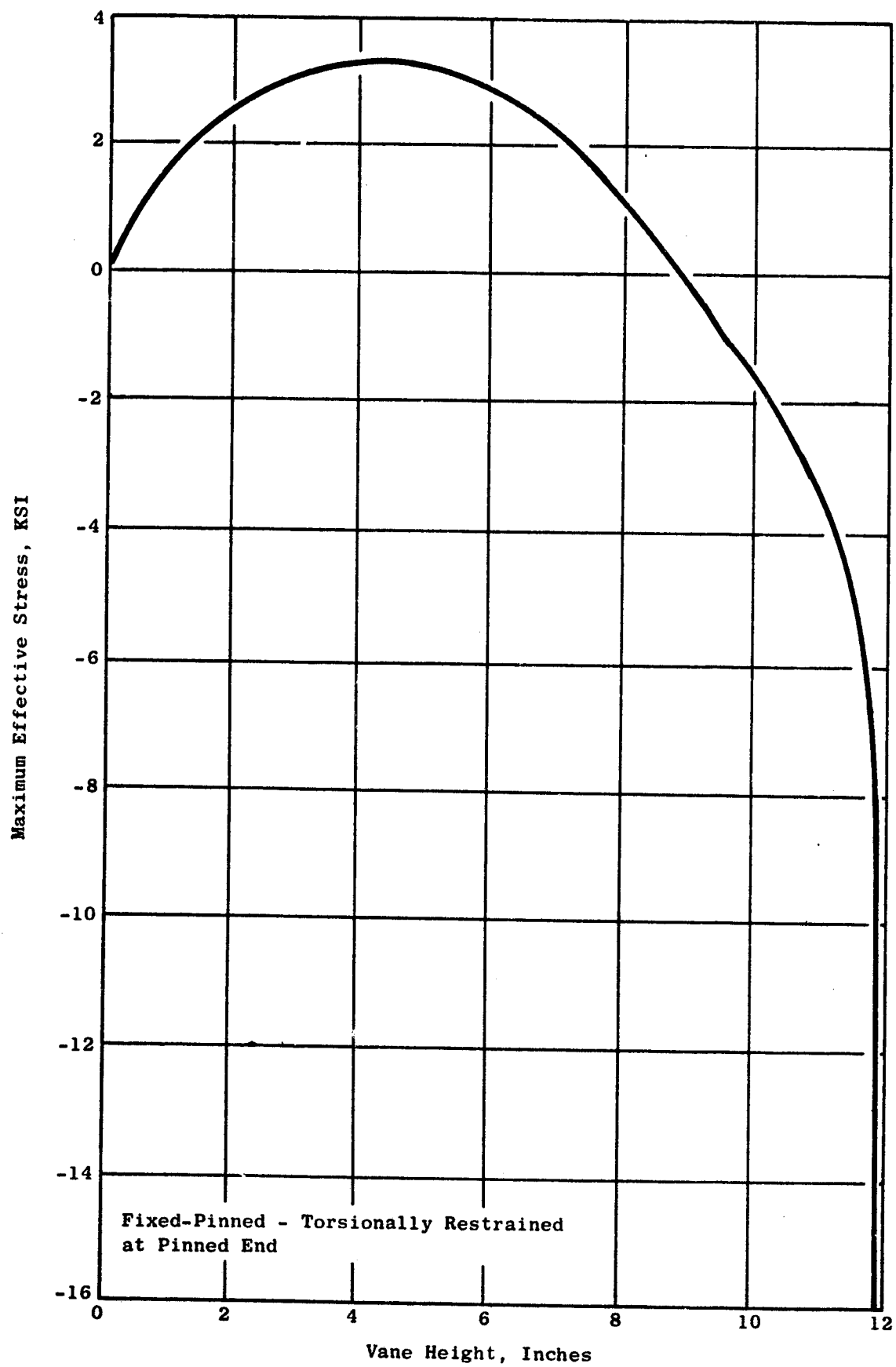


Figure 155. Fan B Bypass OGV Stress Distribution, Hi C Point, Convex Side

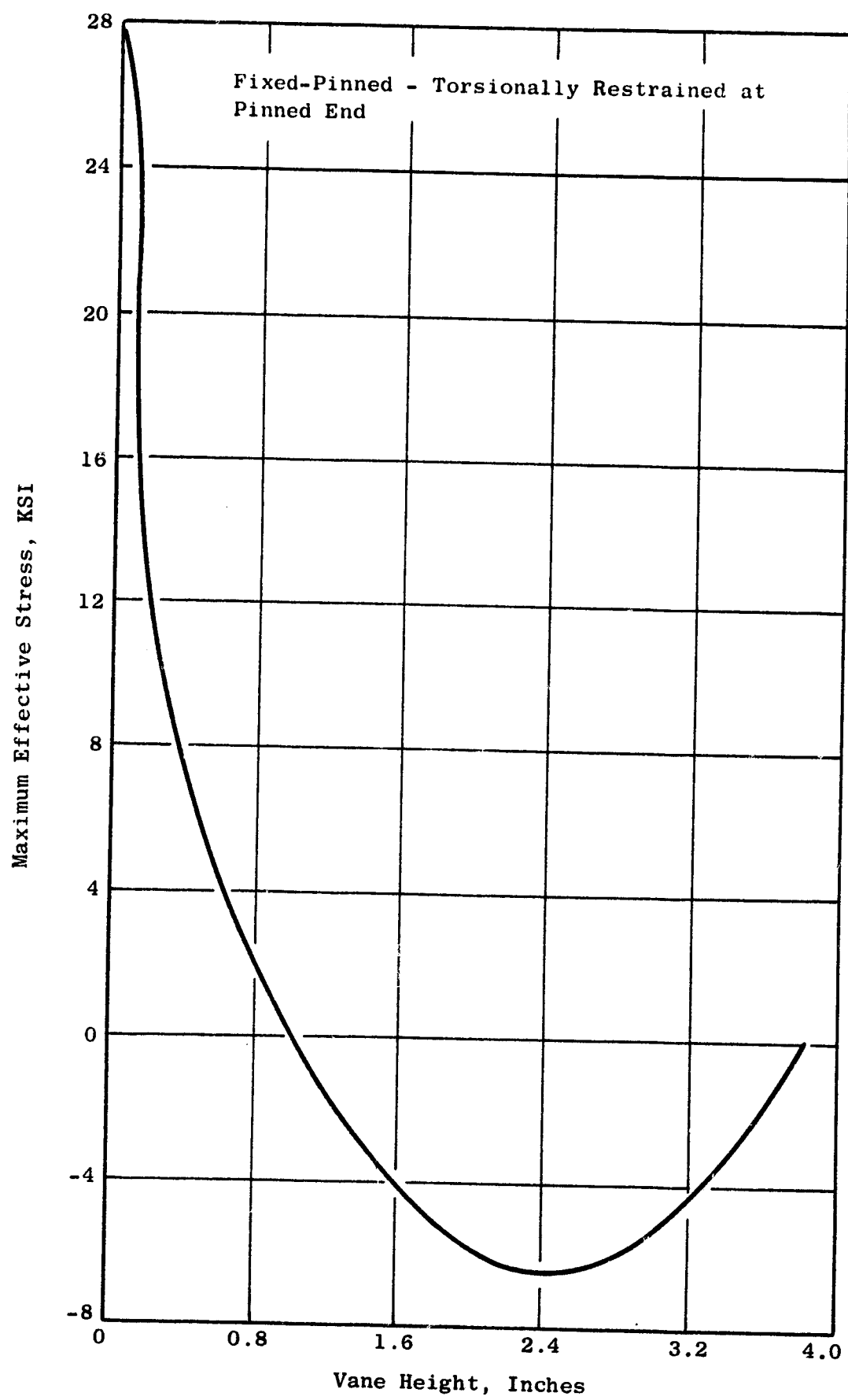


Figure 156. Fan B Forward Core OGV Stress Distribution, Leading Edge

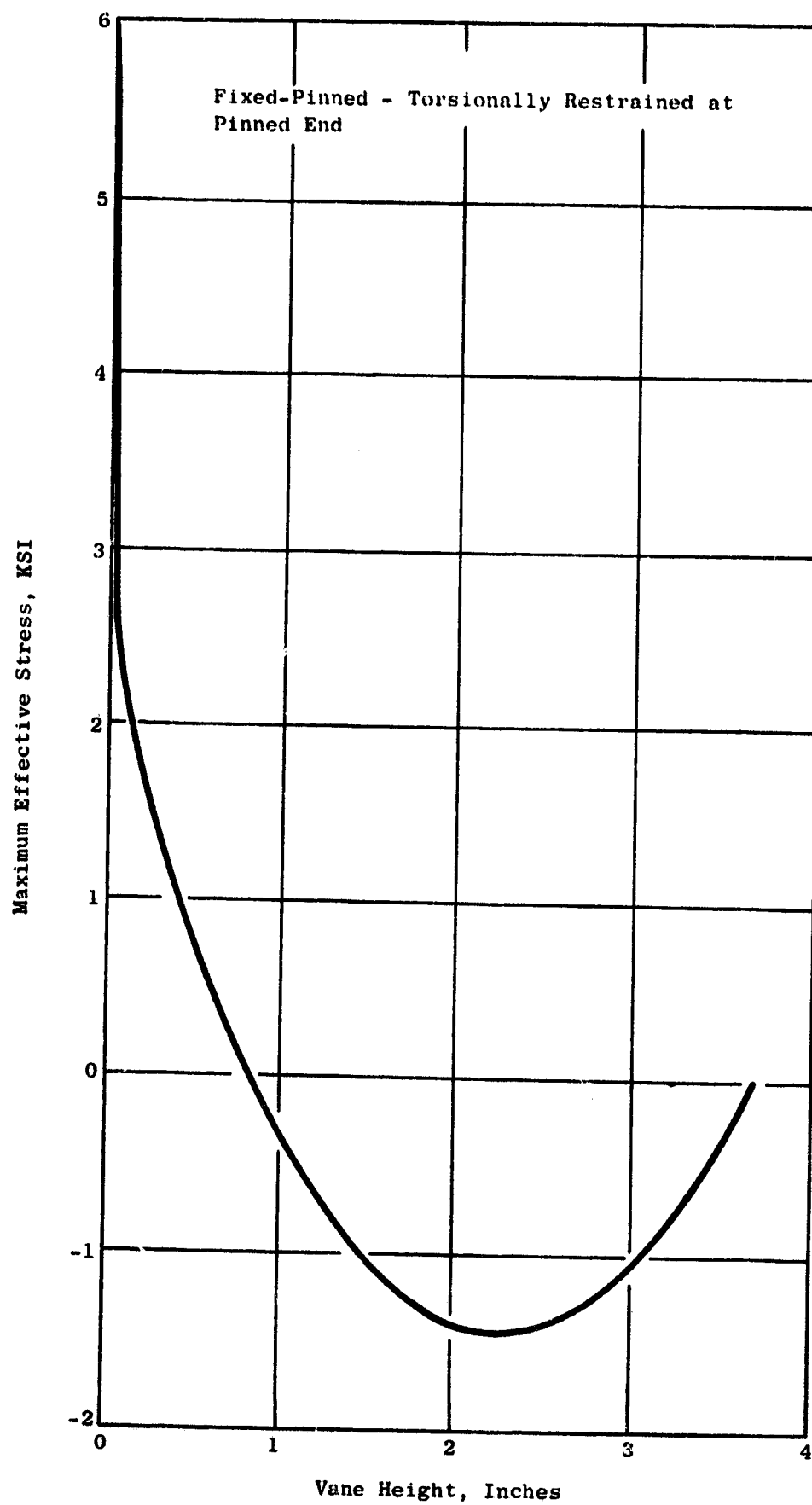


Figure 157. Fan B Aft Core OGV Stress Distribution, Trailing Edge

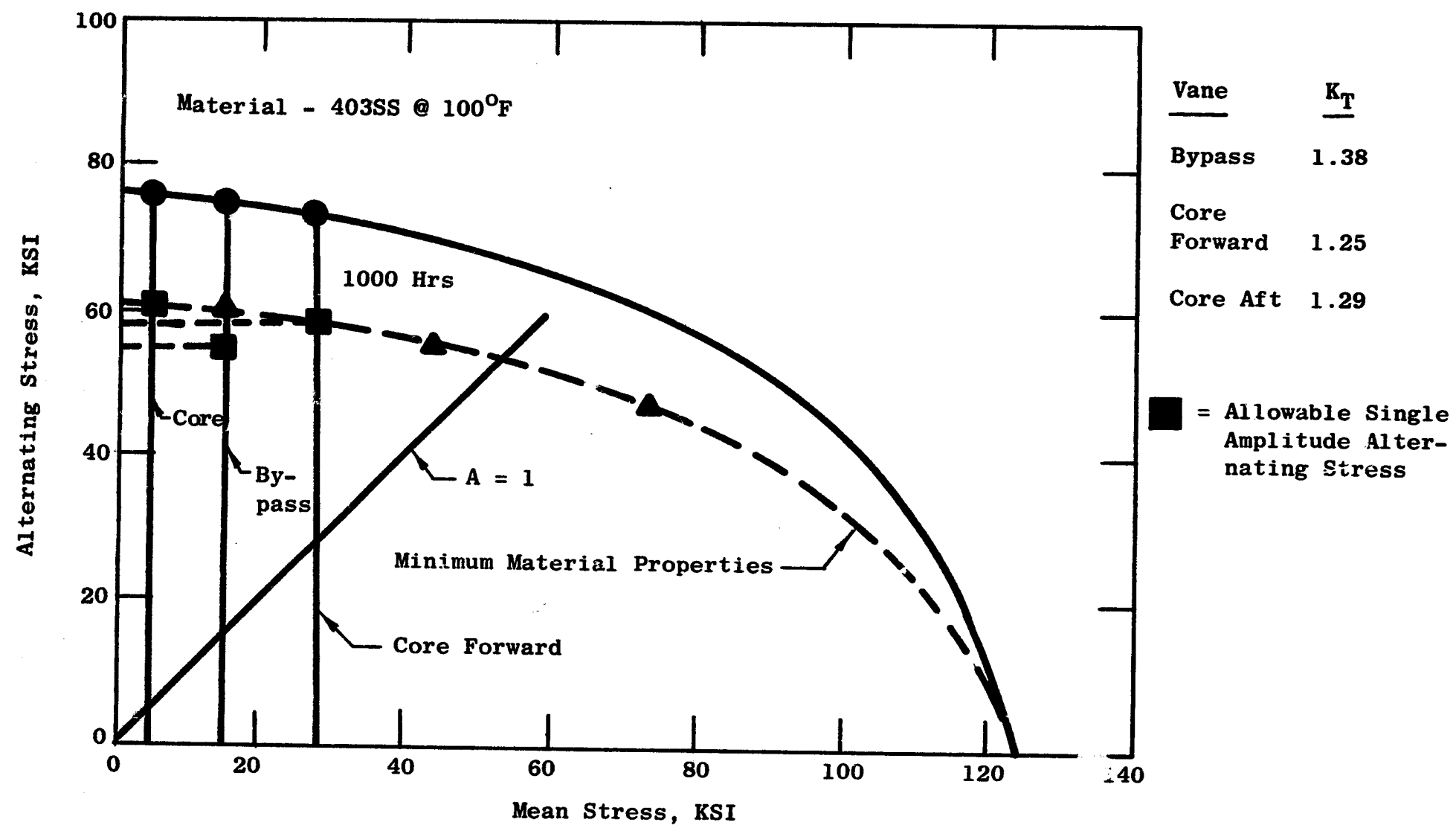


Figure 158. Goodman Diagram, Fan B Vane

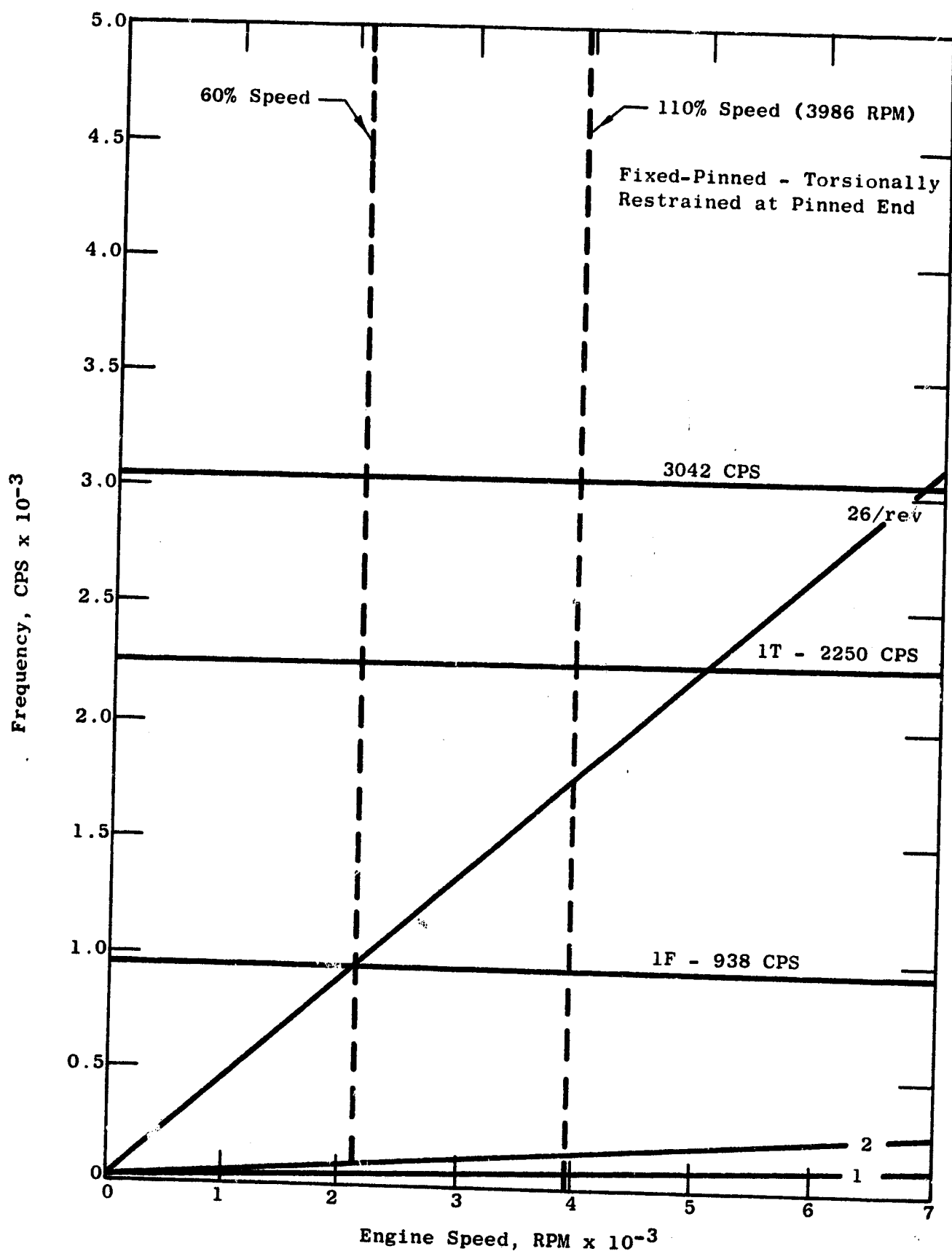


Figure 159. Campbell Diagram for the Fan B Forward Core OGV

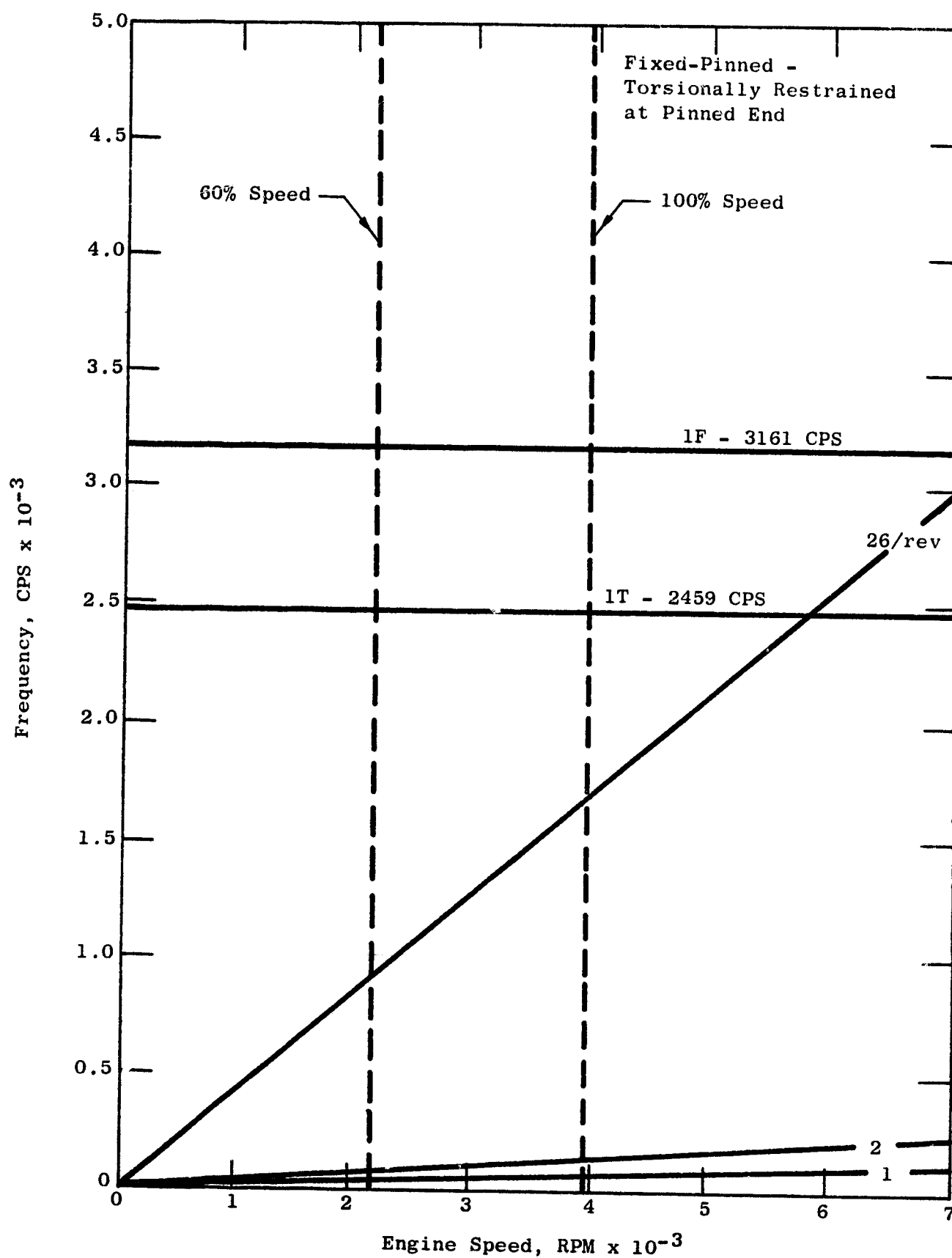


Figure 160. Campbell Diagram for the Fan B Aft Core OGV

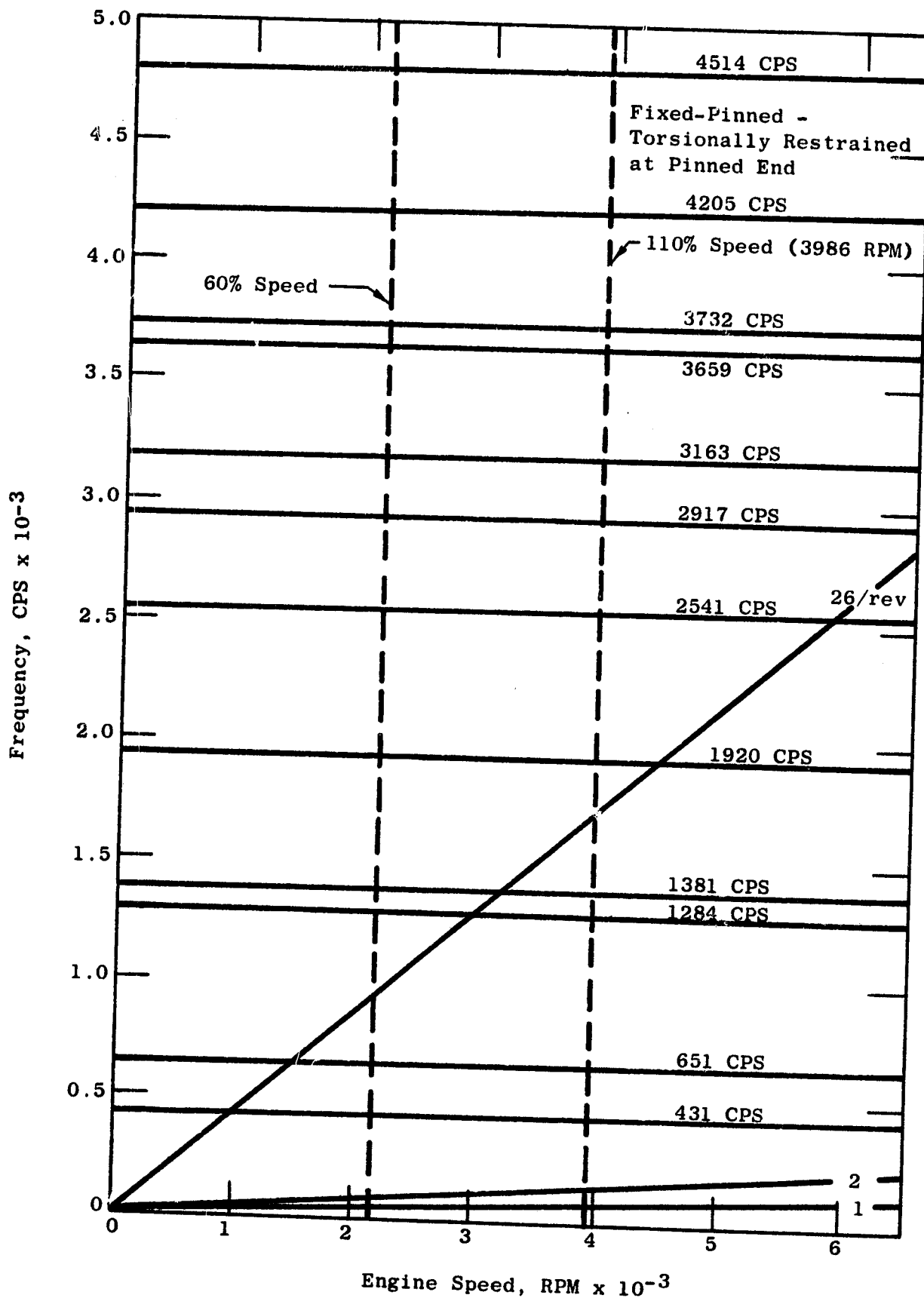


Figure 161. Campbell Diagram for the Fan B Bypass OGV

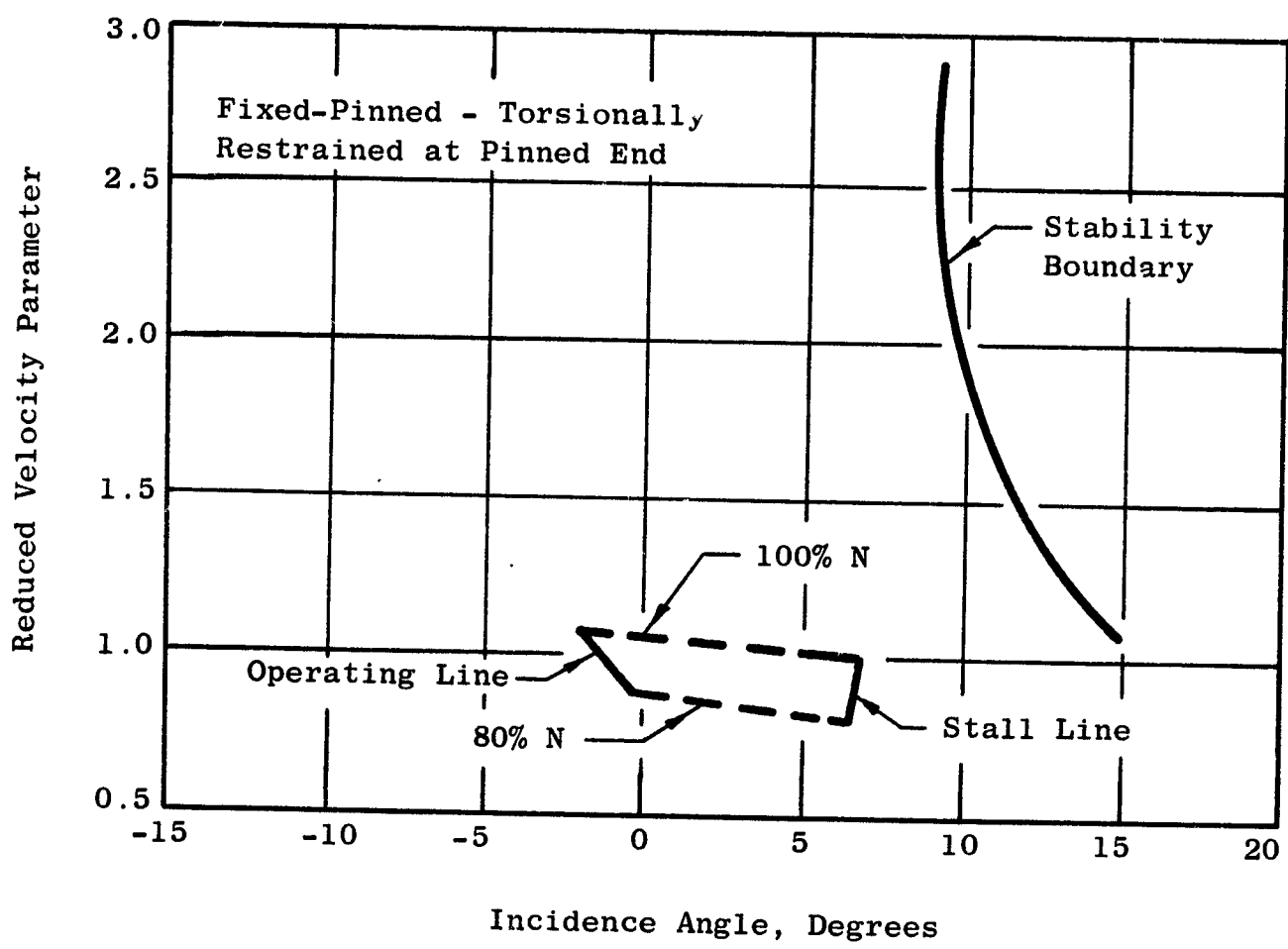


Figure 162. Vane Stability Plot for the Fan B Bypass OGV

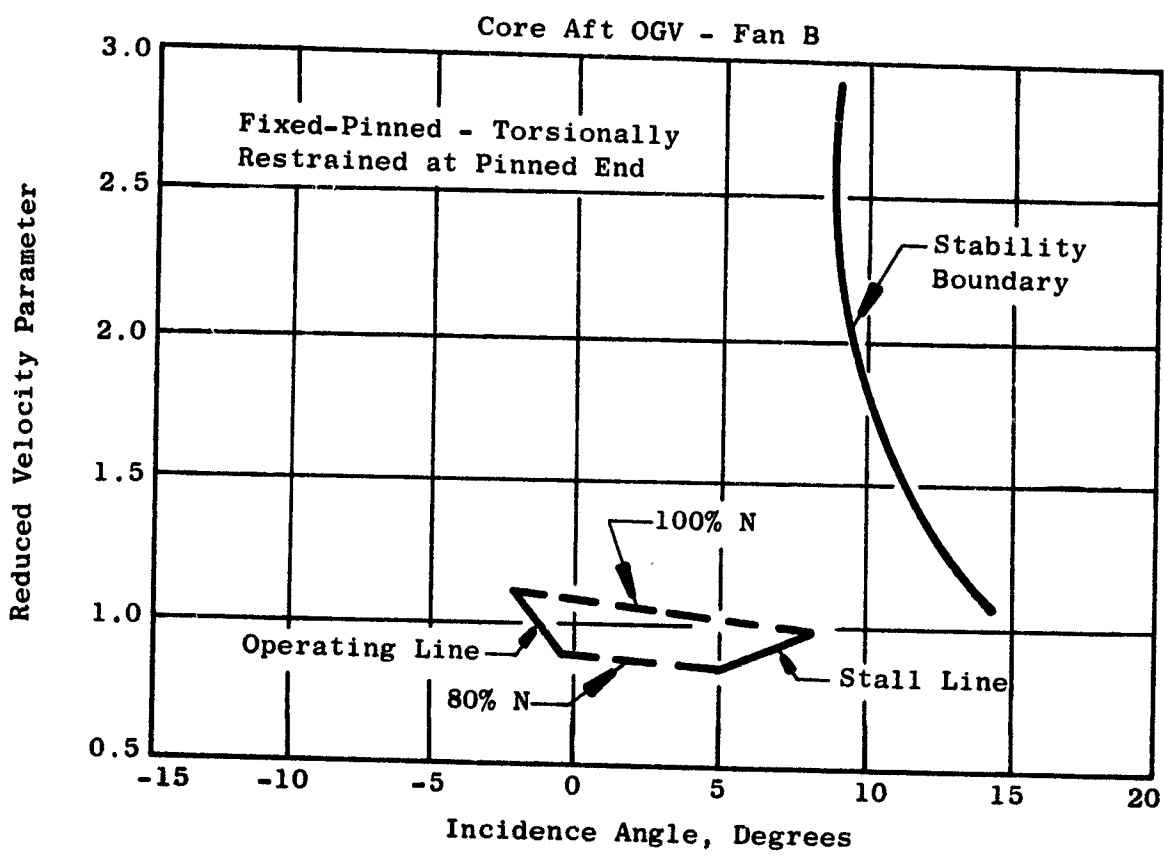
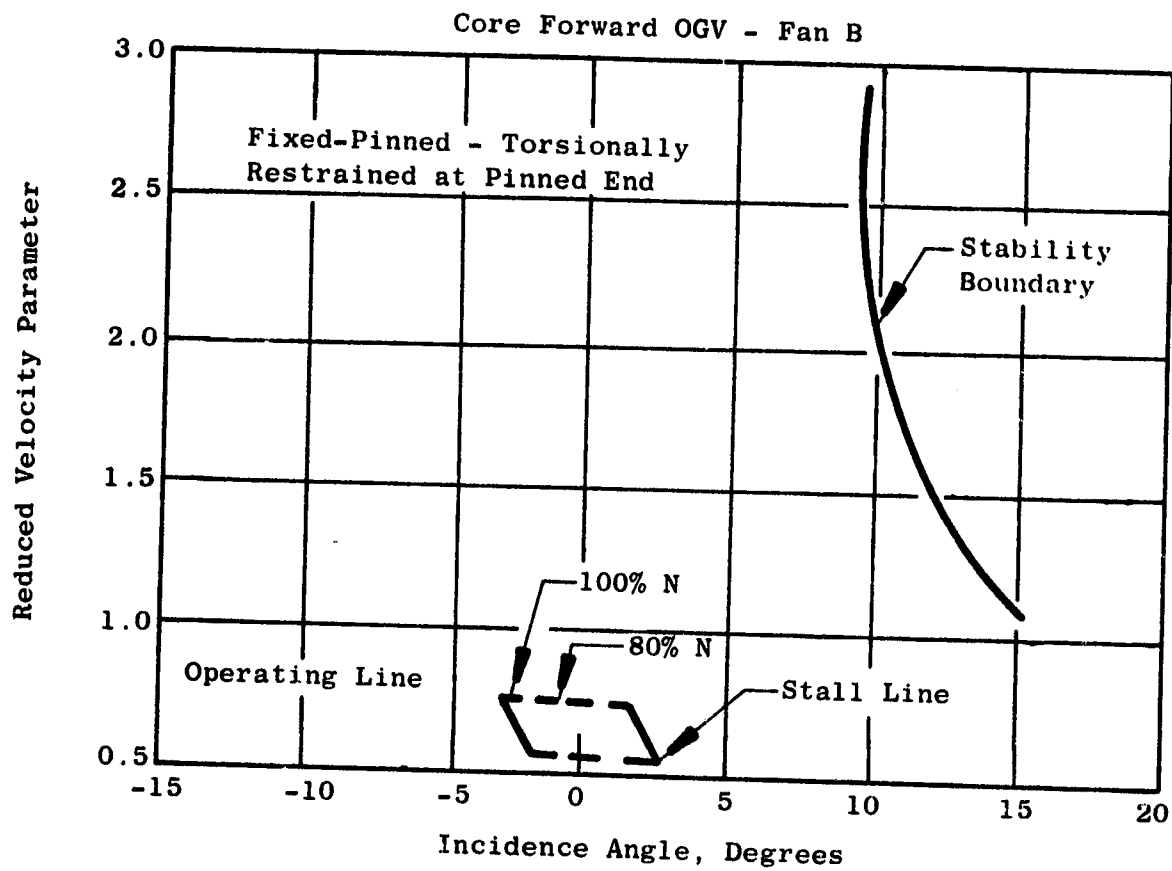


Figure 163. Vane Stability Plots for the Fan B Core OGV's

-Casings

The Campbell diagrams for the various vehicle casings are shown in Figure 164. This figure shows that the casings are designed to be free of resonant response in the engine operating range.

The duct casing which mounts the accessory gearbox for engine operation has been analyzed by the MASS computer program for a 10g gearbox load. The Fan B casing was analyzed because its rigidity is more critical than for Fans A and C. This is due to the longer distance between the forward flange and the gearbox mount. The maximum deflection calculated was 7 mils with accompanying low stresses.

-Actuation System

The vane actuation system is designed to vary the vane incident angles $\pm 10^\circ$ from nominal. It was determined that 7,461 pounds of force at 100 percent speed and 3,200 pounds of force at 50 percent speed would be needed to actuate the duct OGV's. Because of this magnitude of force, longer lever arms of the basic J79 design were machined from AMS 5736 barstock. This longer lever arm reduces the required actuation force input to 3,857 pounds at 100 percent speed and 1,654 pounds at 50 percent speed. Thus, the ring deformation was reduced. The total required actuation force input consisted of aerodynamic frictional loadings. Friction forces result from vane trunnion reactions and the 12 shoes which maintain the roundness of the actuation ring. Aerodynamic loadings resulted in a moment about the stacking axis of the vane. Both the aerodynamic loading and the friction loading must be overcome to actuate the ring.

The critical buckling load of the lever arm for the outer OGV was calculated and exceeds the actual load by a factor of 4. The bending stress of the pin linking the lever arm and actuation ring is well below the yield point, indicating that no problem is to be expected with the actuation ring assembly.

5.2.1.3 Fan C Structures

Fan C features a relatively lower aerodynamically-loaded fan than either Fan A or Fan B. Fan pressure ratio is slightly higher, permitting a lower bypass ratio and reduced tip diameter, compared to the low-tip-speed configurations. Design philosophy for this fan is otherwise the same as that described previously for Fans A and B.

The Fan C FSFT vehicle (see Figure 165) will use the same discharge control assembly and test facility as the low-tip-speed fans. The inlet system and

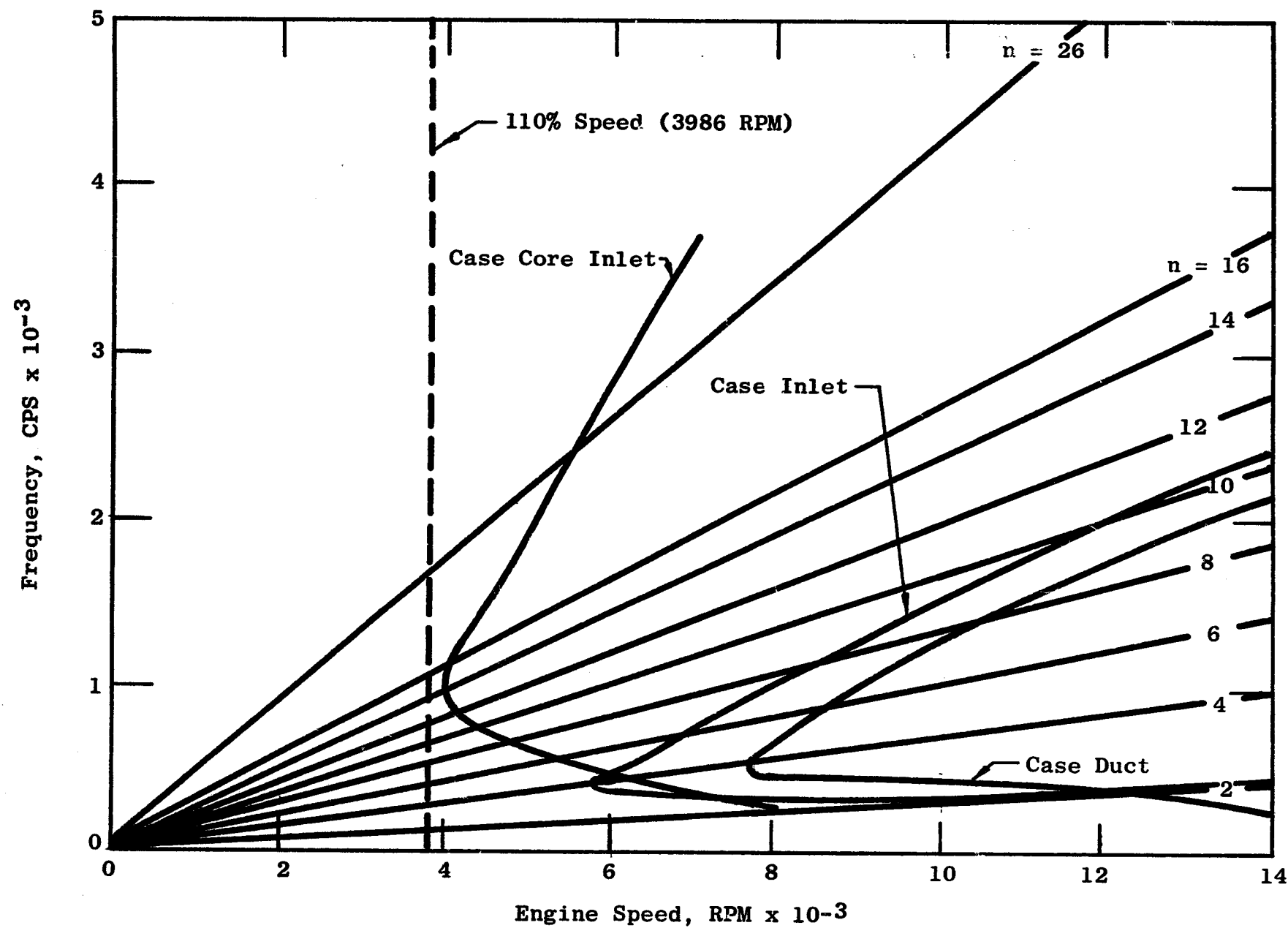


Figure 164. Campbell Diagram for the Fan B Casings

exhaust adapters, however, will be new components because of the reduction in diameter for this configuration.

5.2.1.3.1 Fan C Frame

The Fan C frame employs the same design philosophy and performs the same functions as the Fans A and B frame. The basic difference between the frame configurations is the flowpath contours, characterizing the reduced tip diameter requirement for Fan C.

Fans A and B require sump seal pressurization from eighth-stage air (reduced in pressure and temperature), while Fan C uses fan discharge air for sump seal pressurization. This Fan C sump pressurization air is drawn off in a strut leading edge, similar to methods employed on the CF6 engine.

Fan C struts 2, 4, 10, and 12, in addition to the strut service described in Table XXX, are modified to have a 0.985 recovery diffuser EDM'd into the leading edge to provide the sump pressurization air.

The materials used in the Fan C frame are identical to those materials used for Fans A and B frame.

• Analysis of Fan Frame

The analysis was performed on the fan frame utilizing the MASS computer system for axial, radial, and overturning moment loads. Analysis consisted of two different sets of boundary conditions (one dealing with the structure as if it was fixed to a wall and the other considering the frame as being mounted in the engine).

The model consisted of 203 joints comprising a system of 132 curved beams, 28 straight beams, 28 all-purpose connectors, and 36 plates. Due to symmetry, the frame was analyzed as a 180° structure utilizing a mirror image concept with the boundary conditions.

Deflection coefficients for the over-all frame are as follows, and were obtained for the Lynn installation:

<u>Load Type</u>	<u>Deflection Coefficient</u>
* Axial	1.863 x 10 ⁻⁷ in.-lbs
* Radial	1.438 x 10 ⁻⁷ in.-lbs
* Overturning Moment	5.325 x 10 ⁻¹⁰ Rad/In.-lbs
+ Radial	6.91 x 10 ⁻⁸ in.-lbs
+ Overturning Moment	2.235 x 10 ⁻⁹ Rad/In.-lbs

*Loads were applied at forward inner core and fixed at aft outer bypass.
+Applied at aft inner core; reacted at aft outer bypass.

Deflection coefficients required for the engine vibration analysis are listed in Tables XXXVIII through XLI. The information provided accurately describes the deflection modes created by the engine configuration.

Data required for the vibration analysis of the frame only are listed in Tables XLII and XLIII. The data were obtained by assuming that the Facility Test Vehicle used for the Lynn installation is rigid relative to the frame.

Figure 166 represents the MASS model as a three-dimensional plot and is included to give the reader a general picture of what was actually analyzed. The heavy lines depict struts, while the thin straight lines indicate all-purpose connectors. Curved lines indicate rings. Plates can be recognized by the rhombuses, and are a means of inputting the thin shells which represent the casings between rings.

Figure 167 depicts the three basic loading configurations used in the analysis.

Figure 168 consists of a drawing of the fan frame at its 12-o'clock position and a chart outlining the thirteen loading conditions used. The circled numbers on the drawing represent the rings of the structure.

Figure 169 consists of three side views of the frame which indicate the actual locations of maximum stresses that the outer struts will receive.

5.2.1.3.2 Fan C Stator

The basic design philosophy of the fan stator is identical to Fan A except for the core outlet guide vanes. The single row of vanes is replaced by two overlapping rows of vane cascades each containing 60 vanes. Angular positions of both rows are maintained by the use of slabbed outer vane trunnions and broached rectangular plates. Adjustment of vane stagger angles is accomplished through the use of a new set of broached plates. There will be individual sets of plates to achieve a $\pm 10^\circ$ variability in 2° increments. The inner shroud contains two splits normal to the vehicle centerline (passing through the vane trunnion centerline) to facilitate assembly and teardown.

After the tandem vanes are adjusted, a circumferential translation of the forward vane mount ring and shroud resets the original gap between the trailing edge of the forward vane and the leading edge of the aft vane.

Airfoil data are presented in Table XLIV.

Table XXXVIII. Fan C Frame Deflection Coefficients, Overturning Moment Data

Ring	Radial+ Def in./in.-lbs	Axial* Def in./in.-lbs	Ring Radius, inches	Theta (θ), rad/in.-lbs
3	1.9639×10^{-6}	1.635×10^{-5}	34.75	4.705×10^{-7}
8	1.6595×10^{-6}	1.245×10^{-6}	17.04	7.306×10^{-8}
9	0	0	15.63	0
10	-8.5158×10^{-7}	-1.28×10^{-5}	12.44	-1.029×10^{-6}
11	-2.8539×10^{-6}	-1.449×10^{-5}	8.88	-1.632×10^{-6}
12	-4.3234×10^{-6}	-1.55×10^{-5}	6.89	-2.25×10^{-6}
3'	0	0	34.75	0
8'	0	-1.9×10^{-4}	17.04	-1.115×10^{-5}
9'	-5.2643×10^{-4}	-1.825×10^{-4}	15.63	-1.168×10^{-5}
10'	0	-1.62×10^{-4}	12.44	-1.302×10^{-5}
11'	6.9761×10^{-4}	-1.375×10^{-4}	8.88	-1.548×10^{-5}
12'	0	-1.22×10^{-4}	6.89	-1.771×10^{-5}

† Tangential Deflection of ring at horizontal centerline for horizontal couple

* Deflection from graph used to calculate Theta (θ).

θ = Tan θ for small angles.

Rings 3, 8, 9, 10, 11, 12 load applied on Ring 10 and reacted aft outer core.

Rings 3', 8', 9', 10', 11', 12' load applied on Ring 10 and reacted at Ring 3.

Table XXXIX. Fan C Frame Deflection Coefficients, Overturning Moment Data

Ring	Radial ⁺ Def in./in.-lbs	Axial* Def in./in.-lbs	Ring Radius, inches	Theta (θ), rad/in.-lbs
3	2.2854×10^{-6}	6.41×10^{-5}	34.75	1.847×10^{-6}
8	-2.5951×10^{-7}	5.89×10^{-6}	17.04	3.457×10^{-7}
9	0	---	15.63	0
10	-8.5024×10^{-6}	-2.0×10^{-5}	12.44	-1.608×10^{-6}
11	-6.9074×10^{-6}	-3.58×10^{-5}	8.88	-4.032×10^{-6}
12	-5.8656×10^{-6}	-3.98×10^{-5}	6.89	-5.791×10^{-6}
3'	3.1326×10^{-6}	1.122×10^{-4}	34.75	3.229×10^{-6}
8'	-8.838×10^{-7}	8.4×10^{-7}	17.04	4.929×10^{-7}
9'	0	0	15.63	0
10'	-2.8374×10^{-5}	-2.87×10^{-5}	12.44	-2.307×10^{-6}
11'	-8.2124×10^{-6}	-4.8×10^{-5}	8.88	-5.405×10^{-6}
12'	5.3588×10^{-6}	-5.9×10^{-5}	6.89	-8.563×10^{-6}

⁺ Tangential deflection of ring at horizontal centerline for horizontal couple.

* Deflection from graph used to calculate Theta (θ)

θ = Tan α for small angles

Rings 3, 8, 9, 10, 11, 12 load applied on Ring 10 and reacted aft outer core.

Rings 3', 8', 10', 11', 12' load applied on Ring 10 and reacted at Ring 3

Table XL. Fan C Frame Deflection Coefficients, Radial Shear Loads

Ring	Radial ⁺ Def in./in.-lbs	Axial* Def in./in.-lbs	Ring Radius, inches	Theta (θ), rad/in.-lbs
3	4.0333×10^{-4}	4.51×10^{-4}	34.75	1.298×10^{-5}
8	-1.6381×10^{-5}	3.12×10^{-5}	17.04	1.831×10^{-6}
9	0	0	15.63	0
10	-9.1427×10^{-4}	---	12.44	---
11	-5.8495×10^{-4}	-7.9×10^{-5}	8.88	-8.896×10^{-6}
12	-3.4965×10^{-4}	-1.225×10^{-4}	6.89	-1.778×10^{-5}
3'	0	0	34.75	0
8'	-4.4184×10^{-3}	1.275×10^{-3}	17.04	7.482×10^{-5}
9'	-3.9972×10^{-3}	1.26×10^{-3}	15.63	8.061×10^{-5}
10'	-5.8192×10^{-3}	1.01×10^{-3}	12.44	8.119×10^{-5}
11'	-4.6981×10^{-3}	7.3×10^{-4}	8.88	8.221×10^{-5}
12'	-3.9339×10^{-3}	5.98×10^{-4}	6.89	8.679×10^{-5}

⁺ Tangential deflection of ring at horizontal centerline for vertical load application.

* Deflection from graph used to calculate Theta (θ)

θ = Tan φ for small angles

Rings 3, 8, 9, 10, 11, 12 load applied on Ring 10 and reacted aft outer core.

Rings 3', 8', 10', 11', 12' load applied on Ring 10 and reacted at Ring 3

Table XLI. Fan C Frame Deflection Coefficients, Radial Shear Loads

Ring	Radial ⁺ Def in./in.-lbs	Axial* Def in./in.-lbs	Ring Radius, inches	Theta (θ), rad/in.-lbs
3	-4.1737×10^{-4}	2.11×10^{-4}	34.75	6.072×10^{-6}
8	-1.4381×10^{-5}	1.43×10^{-5}	17.04	8.392×10^{-7}
9	0	0	15.63	0
10	-5.7394×10^{-4}	-1.25×10^{-5}	12.44	-1.005×10^{-6}
11	-5.6594×10^{-4}	-3.11×10^{-5}	8.88	-3.502×10^{-6}
12	-5.5024×10^{-4}	-4.42×10^{-5}	6.89	-6.415×10^{-6}
3'	-4.1226×10^{-4}	---	34.75	---
8'	-1.2535×10^{-5}	0	17.04	0
9'	0	0	15.63	0
10'	-3.5883×10^{-4}	-1.91×10^{-5}	12.44	-1.535×10^{-6}
11'	-5.3744×10^{-4}	---	8.88	-1.535×10^{-6}
12'	-6.5124×10^{-4}	---	6.89	---

⁺ Tangential deflection of ring at horizontal centerline for vertical load application.

* Deflection from graph used to calculate Theta (θ).

θ = Tan θ for small Theta

Rings 3, 8, 9, 10, 11, 12 load applied on Ring 11 and reacted aft outer core.

Rings 3', 8', 10', 11', 12' load applied on Ring 12 and reacted aft outer core.

Table XLII. Fan C Frame Deflection Coefficients, Overturning Moment Data

Ring or Loc.	Radial ⁺ Def in./in.-lbs	Axial* Def in./in.-lbs	Ring Radius, inches	Theta (θ), rad/in.-lbs
3	0	0	34.75	0
A	2.0595×10^{-6}	-1.537×10^{-4}	19.78	-7.77×10^{-6}
10	1.0269×10^{-4}	-1.325×10^{-4}	12.44	-1.065×10^{-5}
12	-5.8133×10^{-5}	-1.01×10^{-4}	6.89	-1.466×10^{-5}
3'	0	0	34.75	0
A'	1.0118×10^{-6}	-1.74×10^{-4}	19.78	-8.797×10^{-6}
10'	9.9312×10^{-5}	-1.75×10^{-4}	12.44	-1.407×10^{-5}
12'	-5.8777×10^{-5}	-1.54×10^{-4}	6.89	-2.235×10^{-5}

⁺ Tangential deflection of ring at horizontal centerline for horizontal couple.

* Deflection from graph used to calculate Theta (θ).

θ = Tan θ for small Theta.

Rings 3, A, 10, 12 load applied on Ring 10 and reacted on 4.

Rings 3', A', 10', 12' load applied on Ring 12 and reacted on 4.

Table XLIII. Fan C Frame Deflection Coefficients, Radial Shear Loads

Ring or Loc.	Radial ⁺ Def in./in.-lbs	Axial* Def in./in.-lbs	Ring Radius, inches	Theta (θ), rad/in.-lbs
3	0	0	34.75	0
A	-3.6897×10^{-4}	-3.82×10^{-4}	19.78	-1.931×10^{-5}
10	-1.4383×10^{-3}	-3.1×10^{-4}	12.44	-2.492×10^{-5}
12	-2.9952×10^{-5}	-1.95×10^{-4}	6.89	-2.83×10^{-5}
3'	0	0	34.75	0
A'	-3.331×10^{-4}	9.3×10^{-4}	19.78	4.702×10^{-5}
10'	-4.5546×10^{-5}	6.6×10^{-4}	12.44	5.305×10^{-5}
12'	-6.9085×10^{-4}	3.58×10^{-4}	6.89	5.196×10^{-5}

⁺ Tangential deflection of ring at horizontal centerline for vertical load application.

* Deflection from graph used to calculate Theta (θ).

θ = Tan θ for small Theta.

Rings 3, A, 10, 12 load applied on Ring 10, reacted on 4.

Rings 3', A', 10', 12' load applied on Ring 12, reacted on 4.

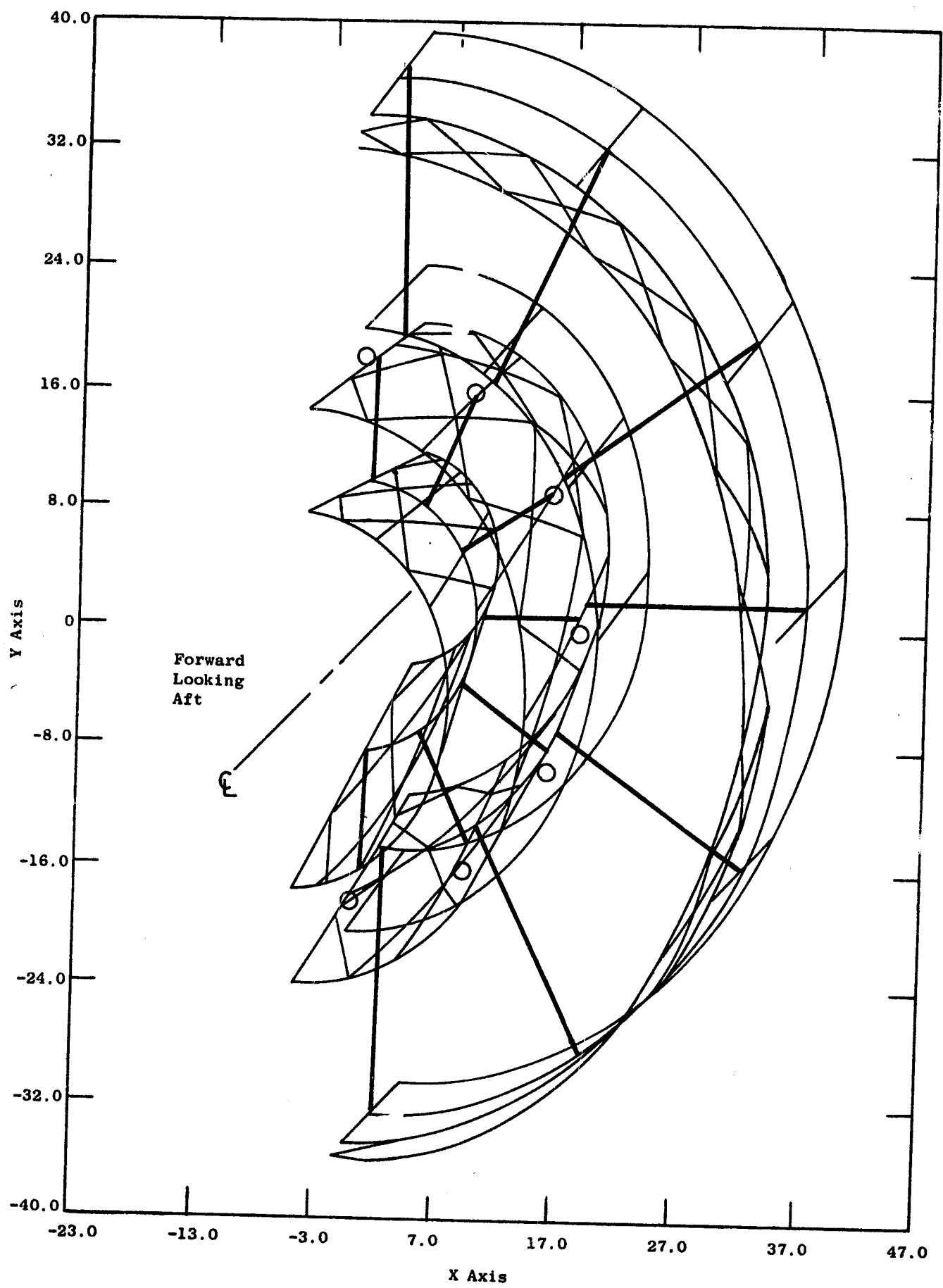
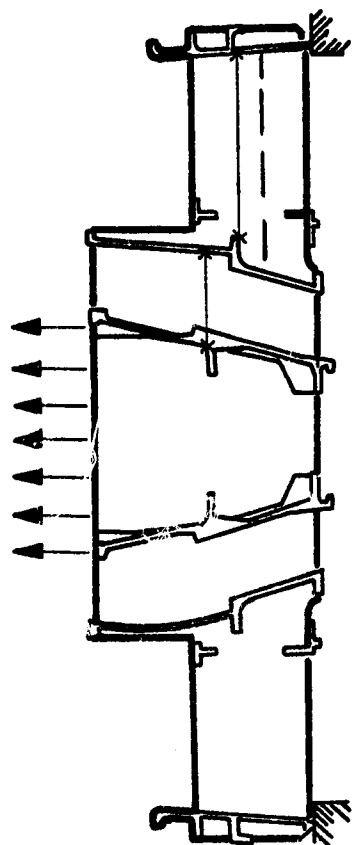
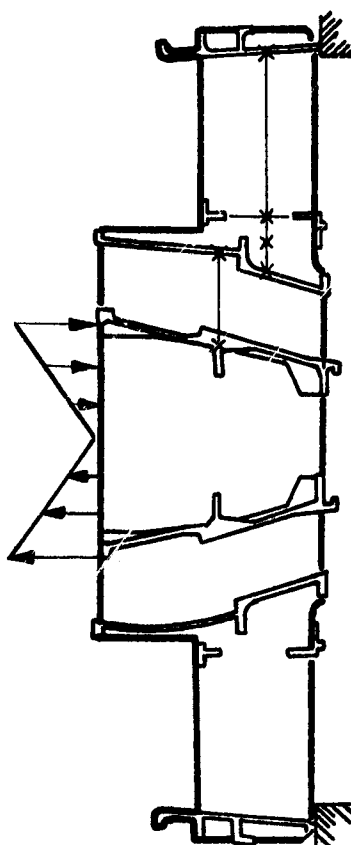


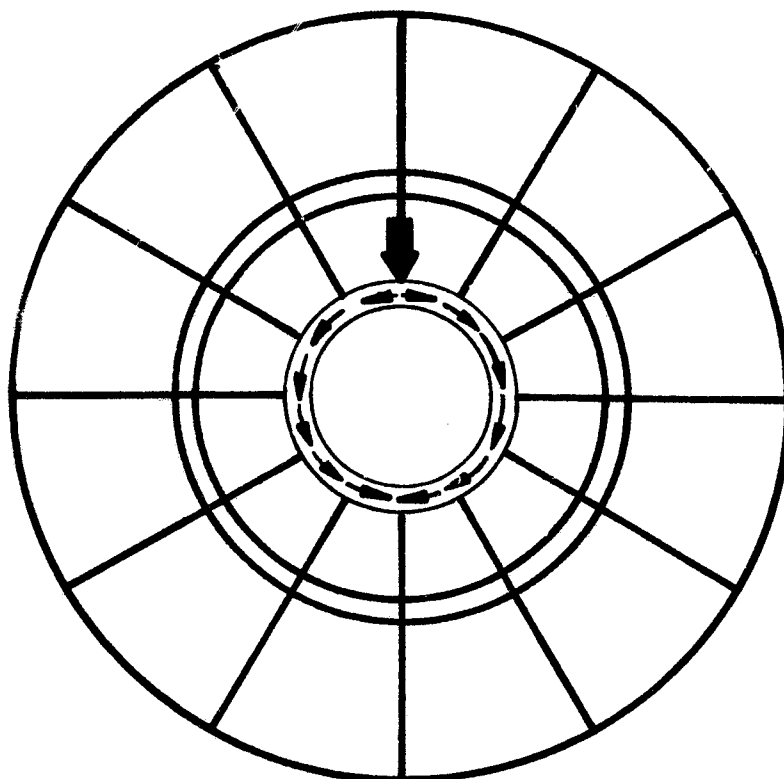
Figure 166. Fan C Frame Analytical Model



Axial



Overturning Moment



Radial Shear

Figure 167. Fan C Frame Analytical Loading Configurations

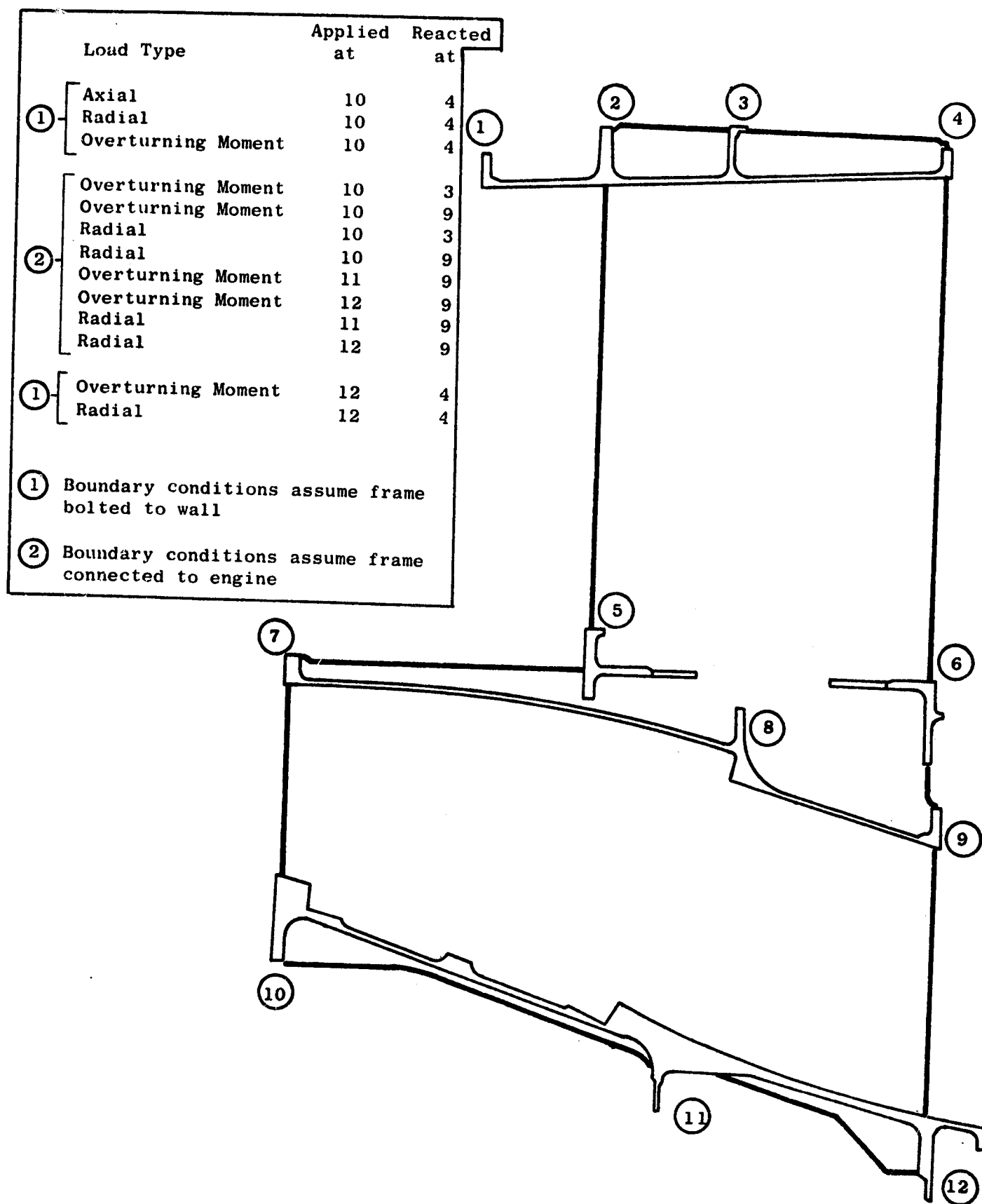


Figure 168. Fan C Frame Loading Cases, 12-O'clock Side View

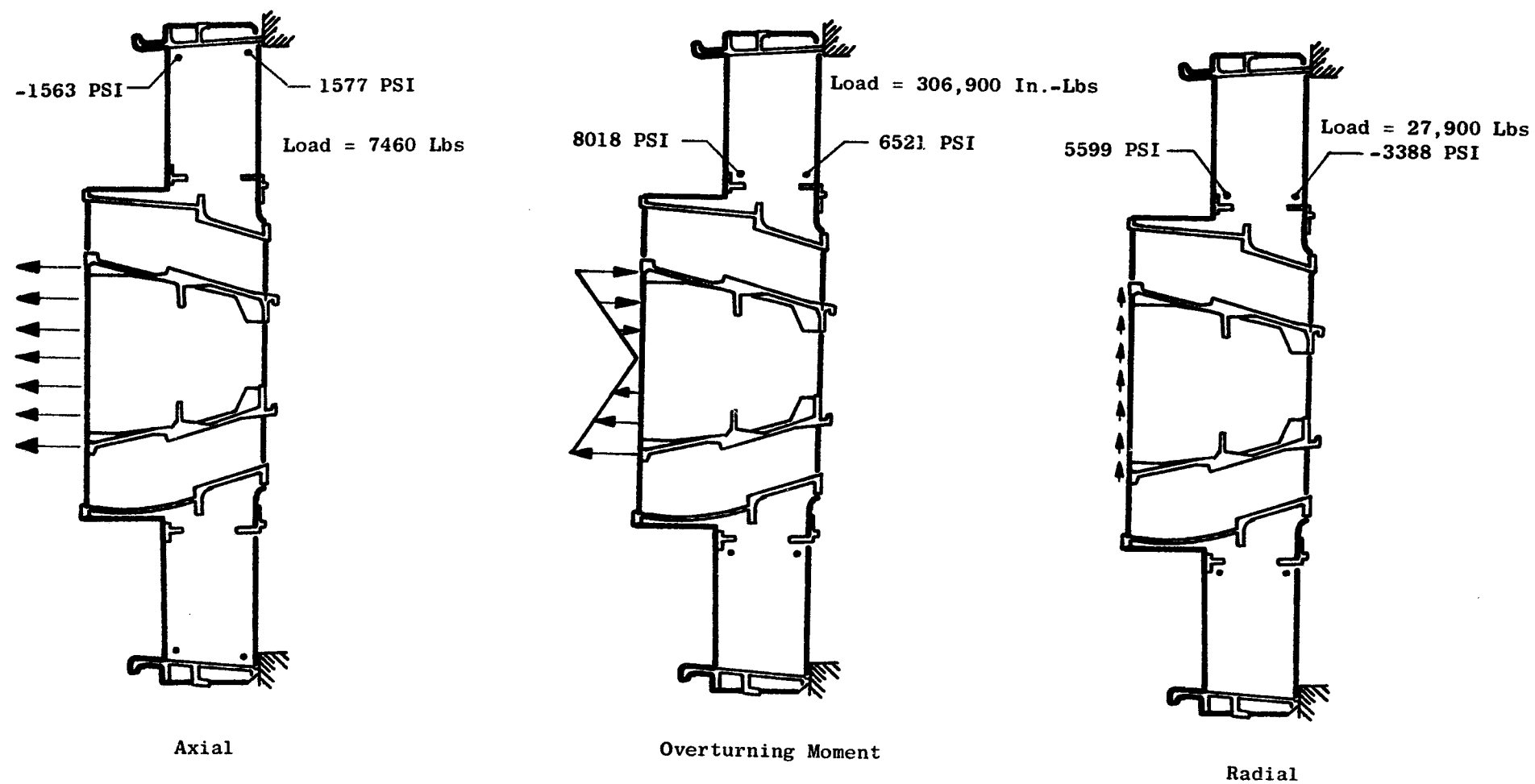


Figure 169. Fan C Frame Maximum Stresses

Table XLIV. Fan C Airfoil Pitchline Data

Parameter	Core		
	Bypass	Fwd.	Aft
Number of Vanes	60	60	60
Chord	3.92	1.6	2.4
Camber	42.7	11.3	37.2
Stagger	13.0	36.4	10.1
Aspect Ratio	3.04	2.65	1.81
T_m/c	0.057	0.071	0.04
Type	Series 65	Arbitrary	Arbitrary

• Analysis, Fan Stator Components

-Vanes

The steady state stress (from the Twisted Blade Analysis) versus airfoil radial height for the bypass and core vanes is shown in Figures 170, 171, and 172, respectively.

The maximum vane stress concentration factor, which occurs at the intersection of airfoil and outer boss fillet radius on the bypass vane, is 1.46.

The Goodman diagram showing the allowable alternating stress versus steady state stress for the selected vane material is shown in Figure 173.

The Campbell diagrams showing the vane Twisted Blade Program resonance frequencies versus engine operating speeds are shown in Figures 174, 175, and 176. Figure 176 indicates that the aft core OGV has a first flexural response for a 26/rev excitation at about 70 percent operating speed. This condition is tolerable due to the lack of variation of the aft cascade incidence angle. However, the aft core OGV has been redesigned. The value of t_{max}/c has been reduced from 5 to 4. This change will have a beneficial effect on fan performance, in addition to decreasing the vane's critical frequency response out of the engine operating range.

The reduced velocity parameters, calculated at the maximum point of rotation as determined by the Twisted Blade Program, are shown for the bypass and core vanes on Figures 177 and 178, respectively.

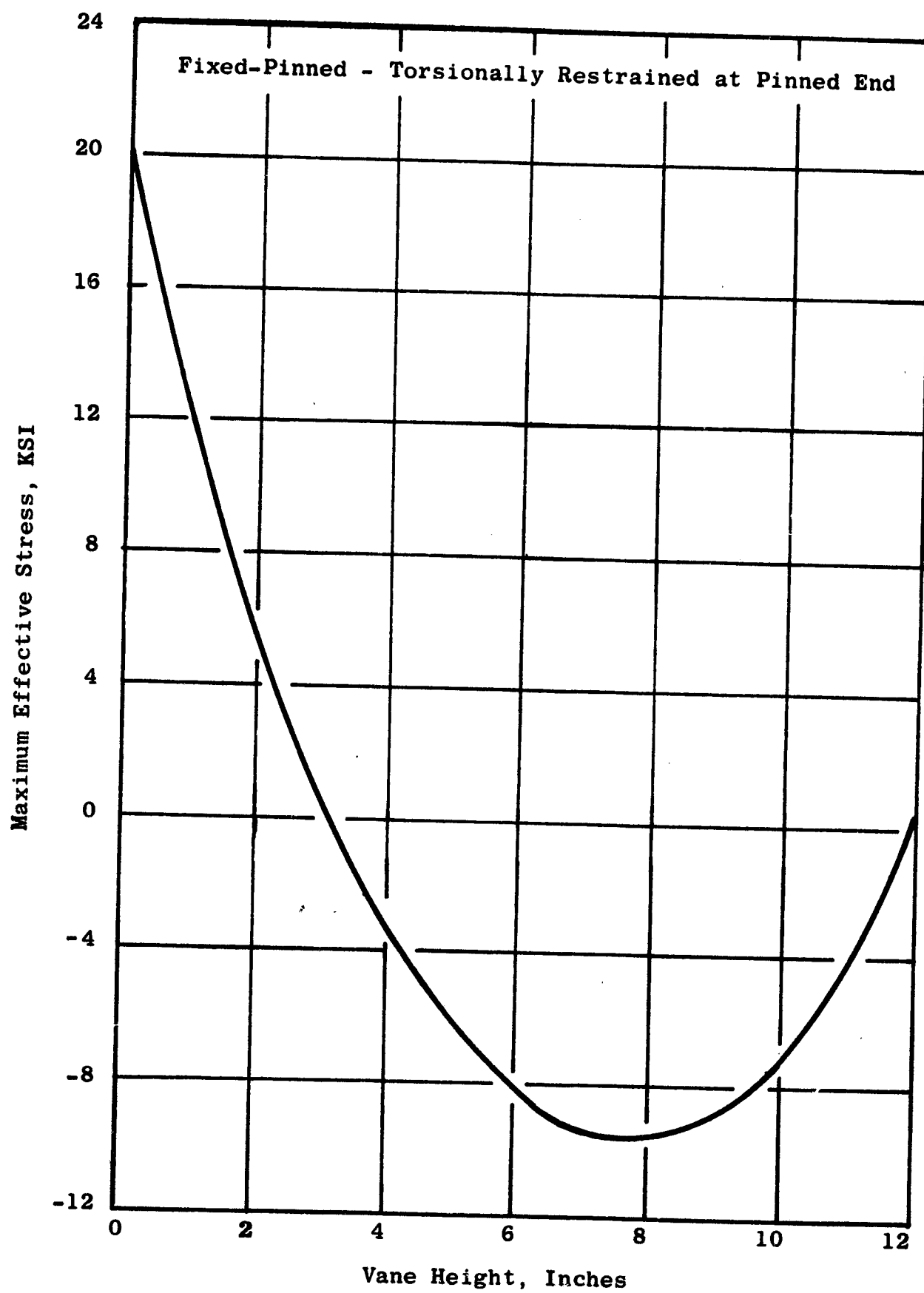


Figure 170. Fan C Bypass OGV Stress Distribution, Trailing Edge

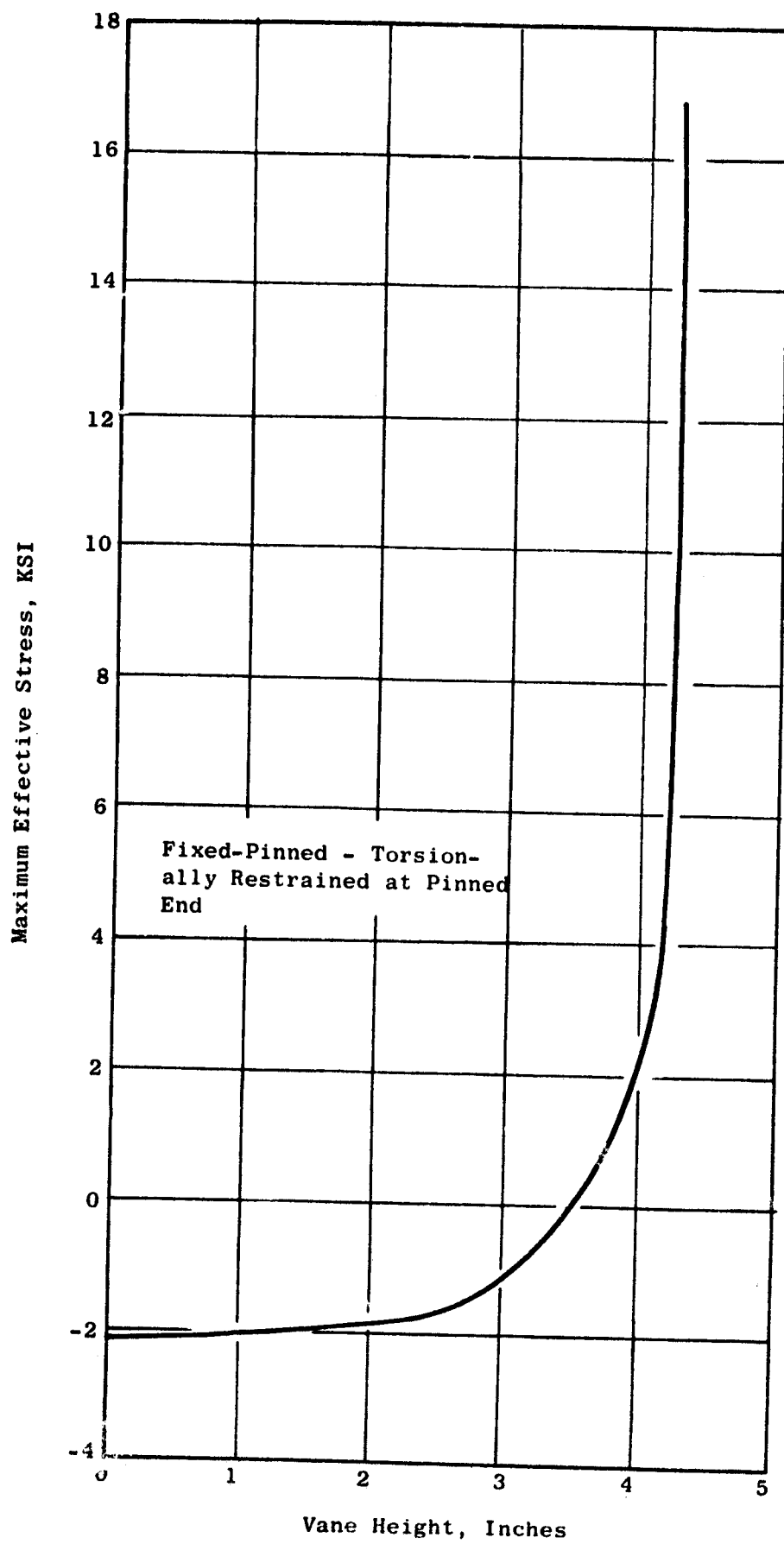


Figure 171. Fan C Forward Core OGV Stress Distribution, Trailing Edge

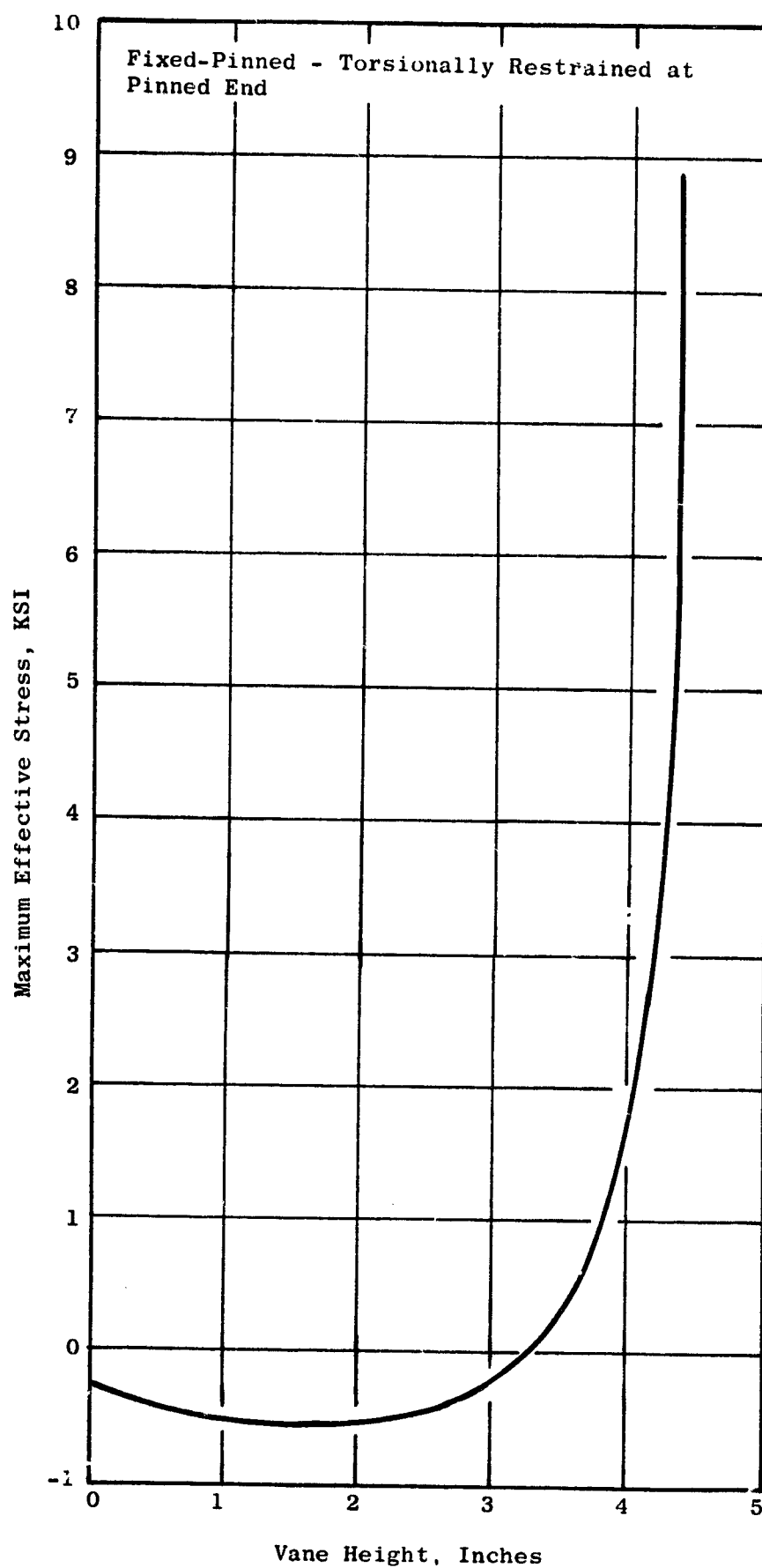


Figure 172. Fan C Aft Core OGV Stress Distribution, Leading Edge

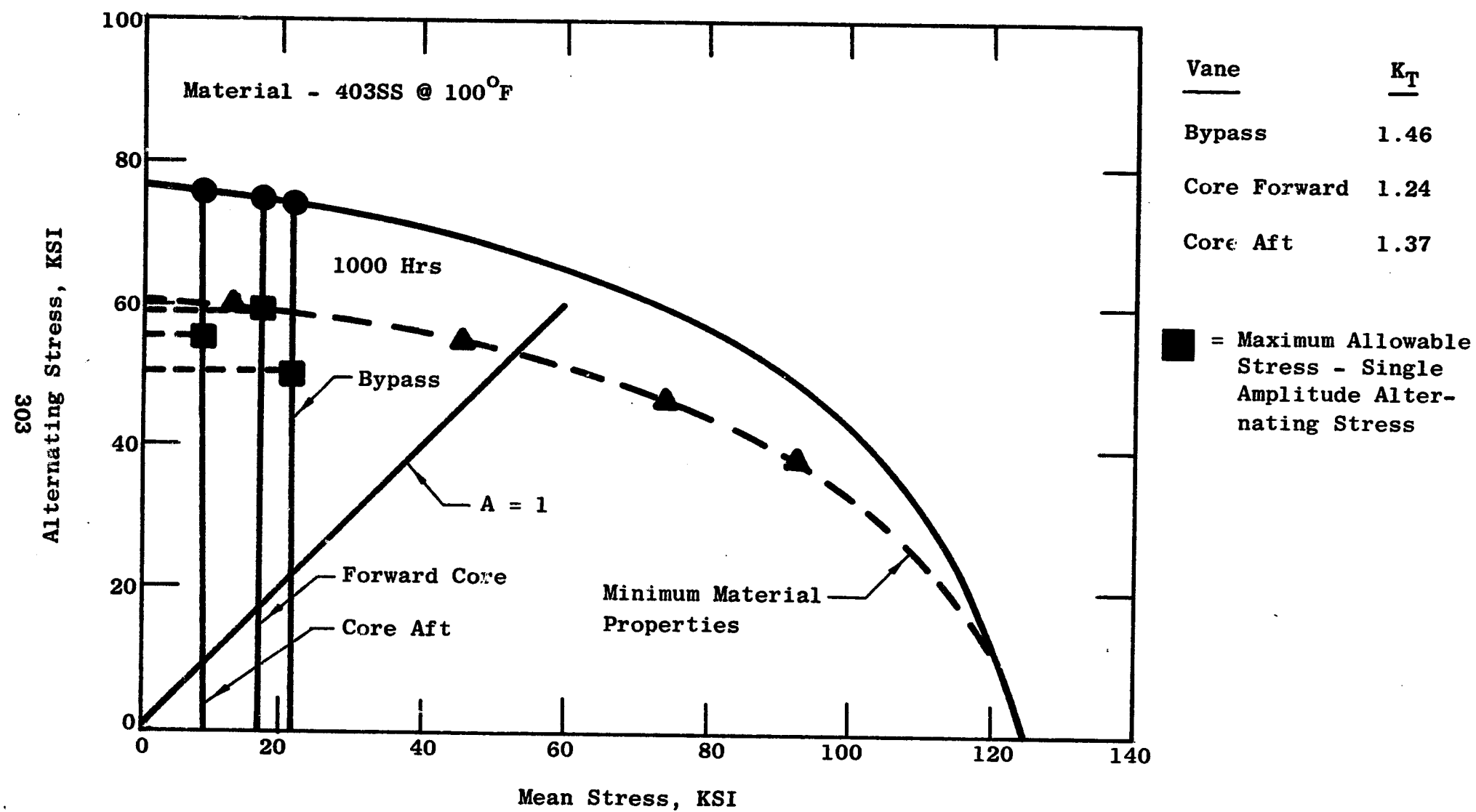


Figure 173. Goodman Diagram, Fan C Vane

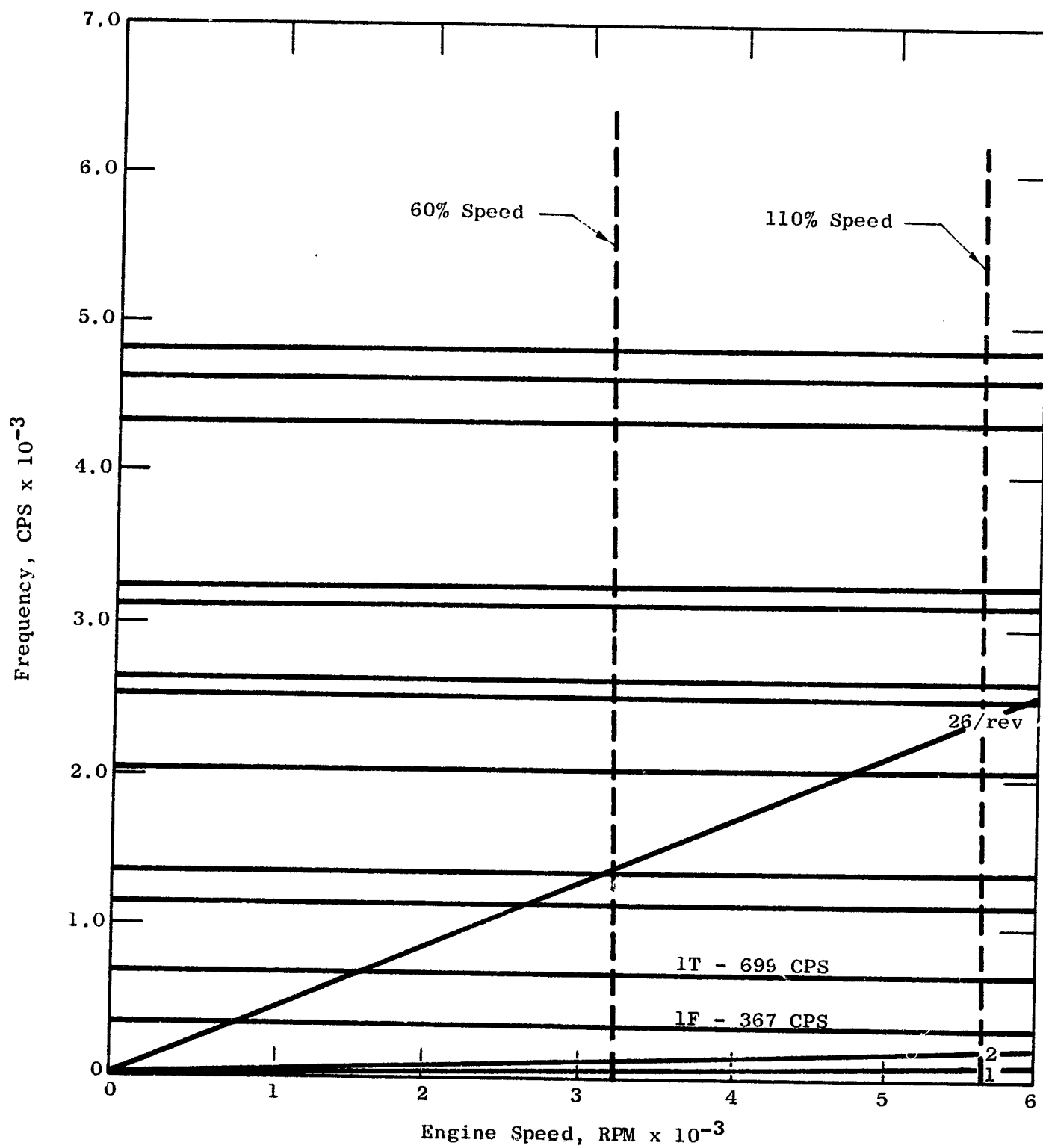


Figure 174. Campbell Diagram, Fan C Bypass OGV

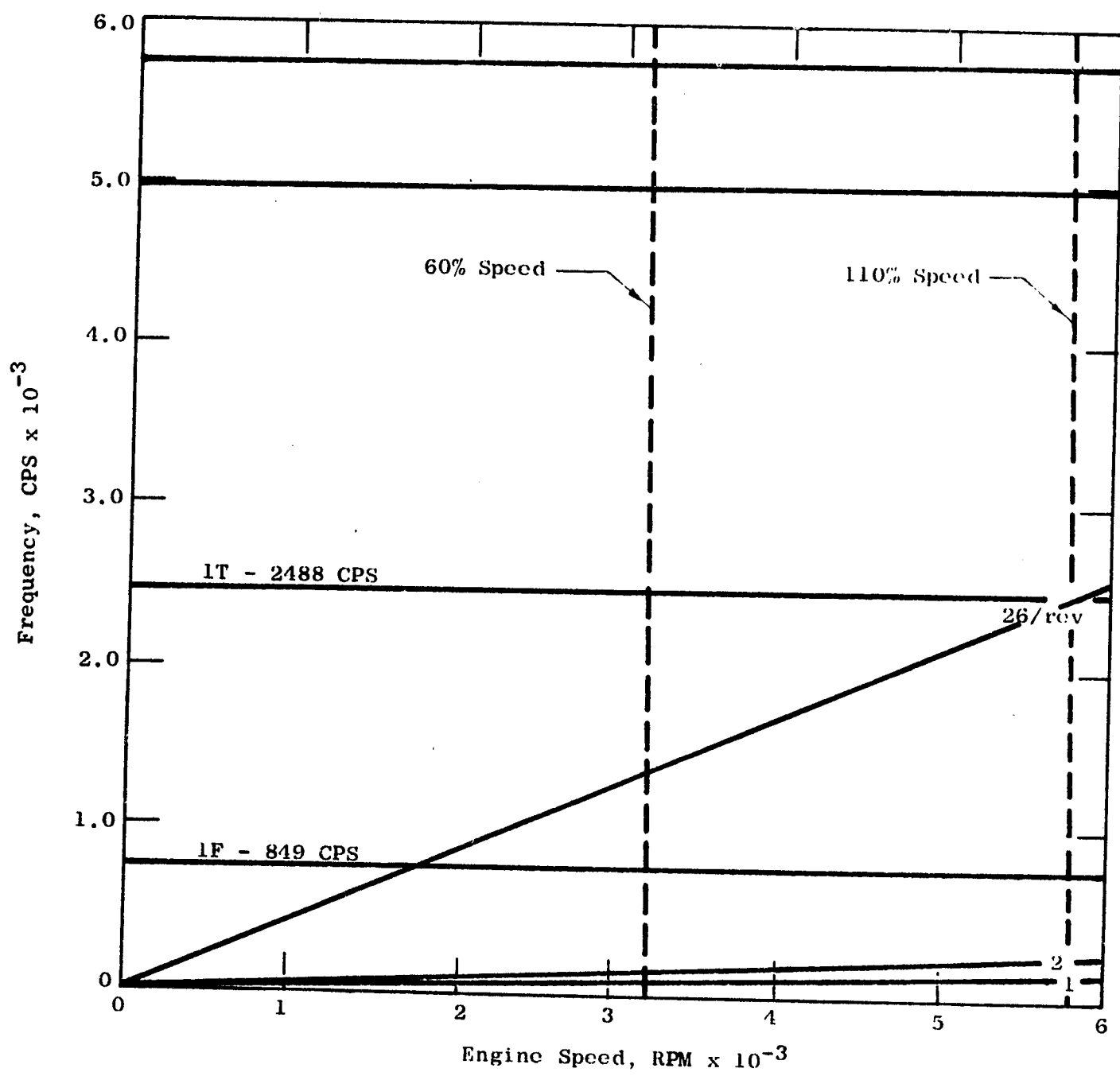


Figure 175. Campbell Diagram, Fan C Forward Core OGV

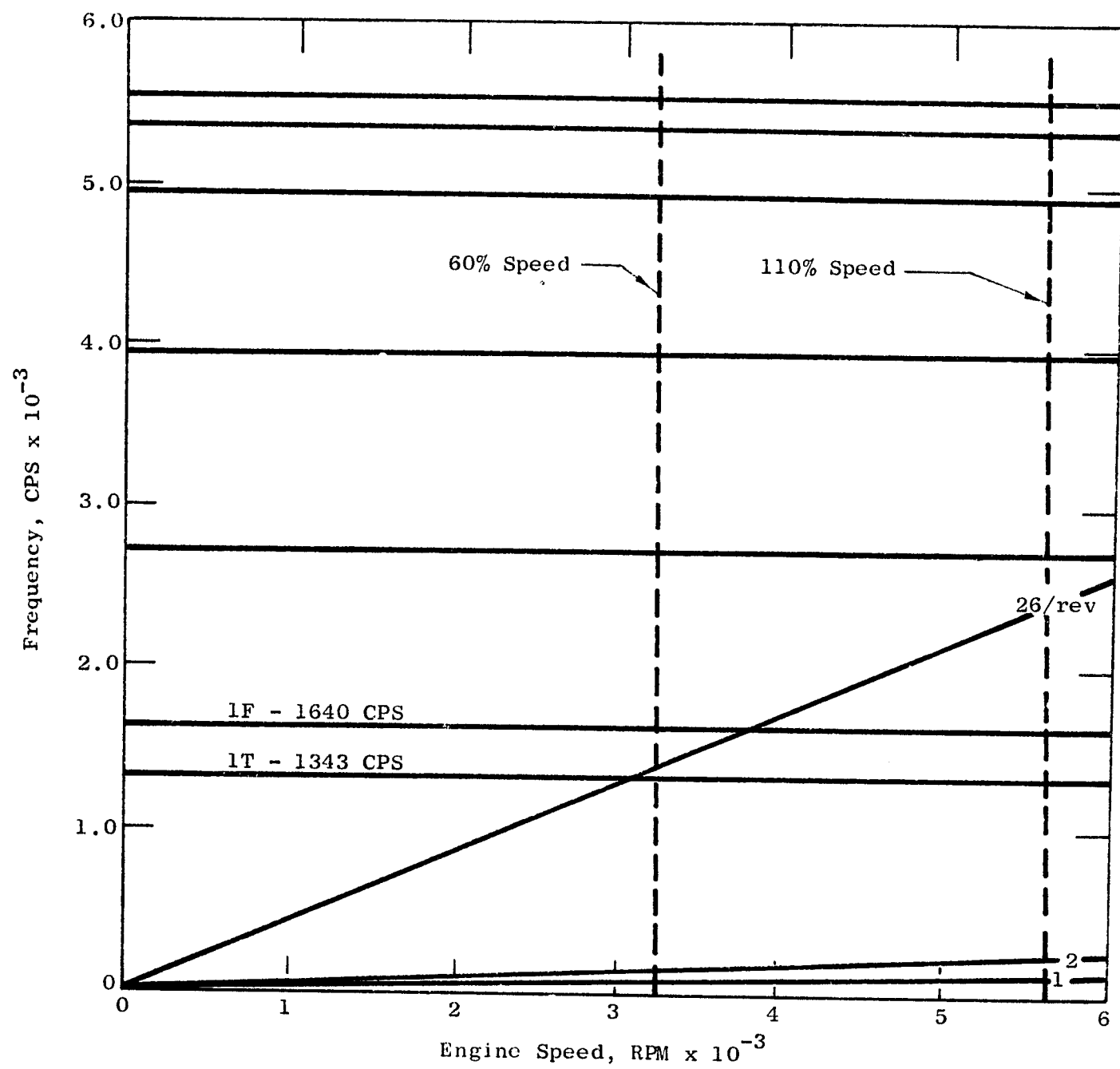


Figure 176. Campbell Diagram, Fan C Aft Core OGV

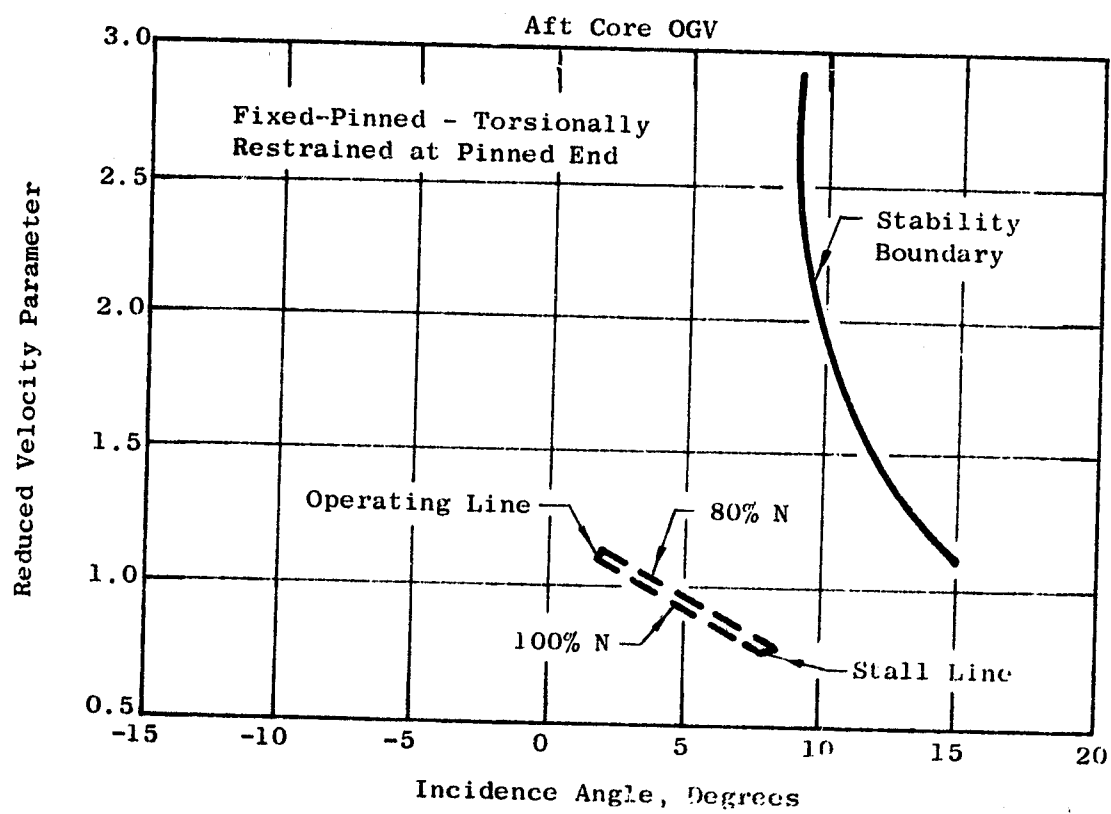
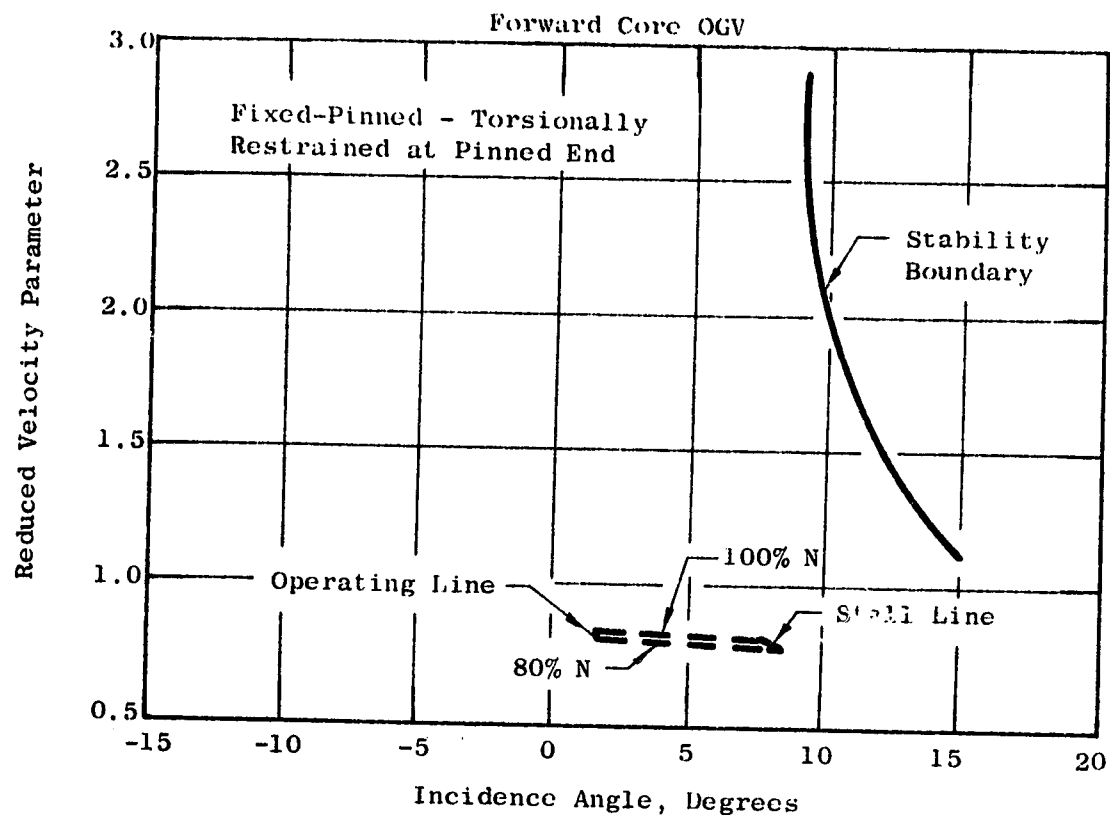


Figure 177. Vane Stability Plots for the Fan C Core OGV's

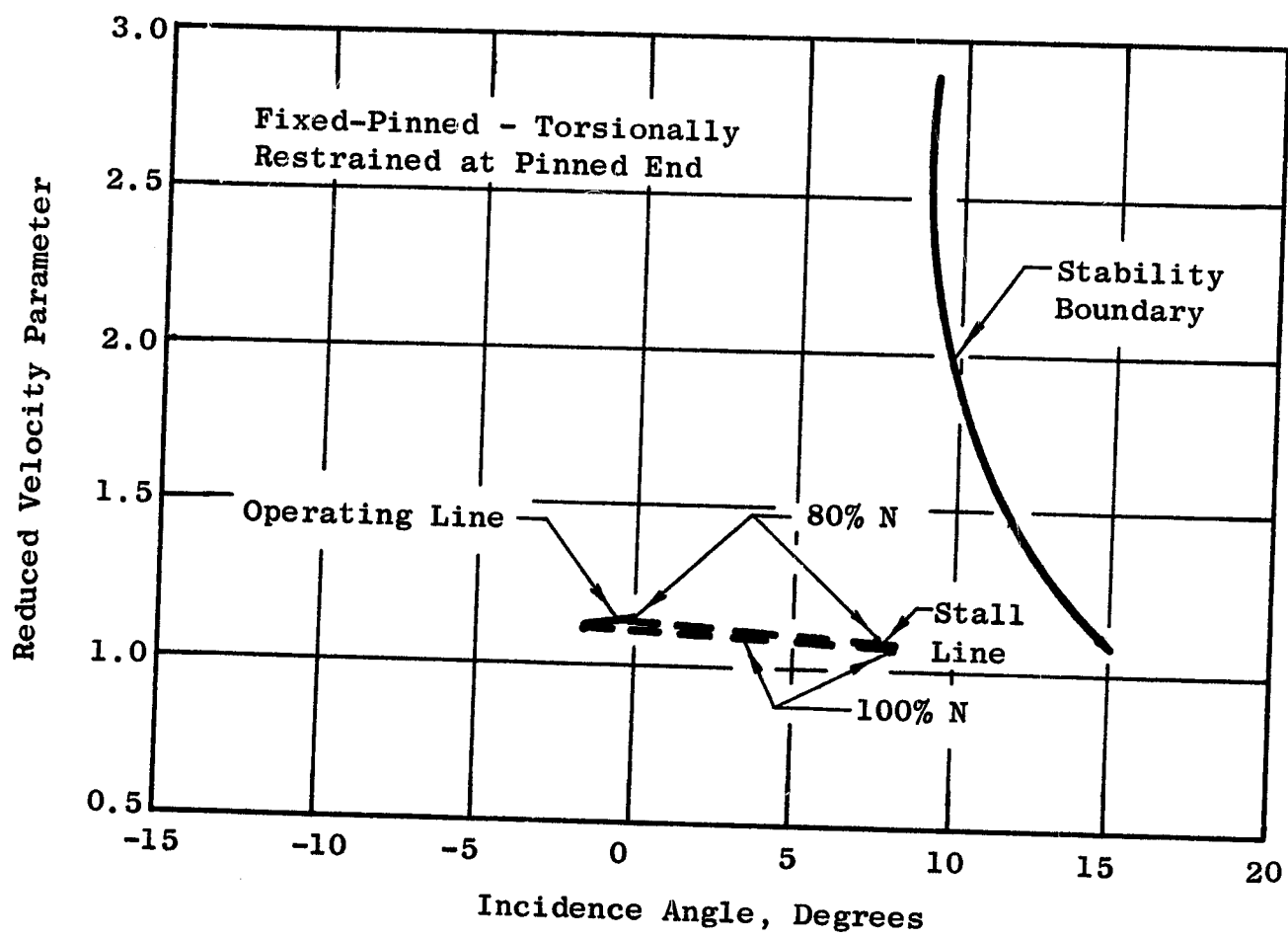


Figure 178. Vane Stability Plot for the Fan C Bypass OGV's

The vane clearances for the nominal and full actuated positions are listed in Table XLV.

Table XLV. Fan C Vane Clearances

Location	Bypass OGV	Core OGV	
	Nominal Position	Fwd Nominal Position	Aft Nominal Position
LE Outer	0.017	0.018	0.025
LE Inner	0.022	0.011	0.014
TE Outer	0.012	0.018	0.011
TE Inner	0.011	0.013	0.011
Minimum clearance at maximum vane travel for all cases = 0.010			

-Casings

The Campbell diagrams for the various vehicle casings are shown in Figure 179. This figure shows that the casings are designed to be free of resonant response in the engine operating range.

The duct casing, which mounts the accessory gearbox for engine operation, has been analyzed by the MASS computer program for a 10g gearbox load for the more critical Fan B casing.

The deflections and stresses for the Fan C casing will be similar to, but lower than, the values calculated for the less rigid Fan B casing. The maximum deflection calculated was 7 mils with accompanying low stresses.

5.2.1.4 Engine Design

5.2.1.4.1 Fan Module

The fan modules, and specifically the fan frames, have been designed such that the module can be used for engine testing with a minimum of modi-

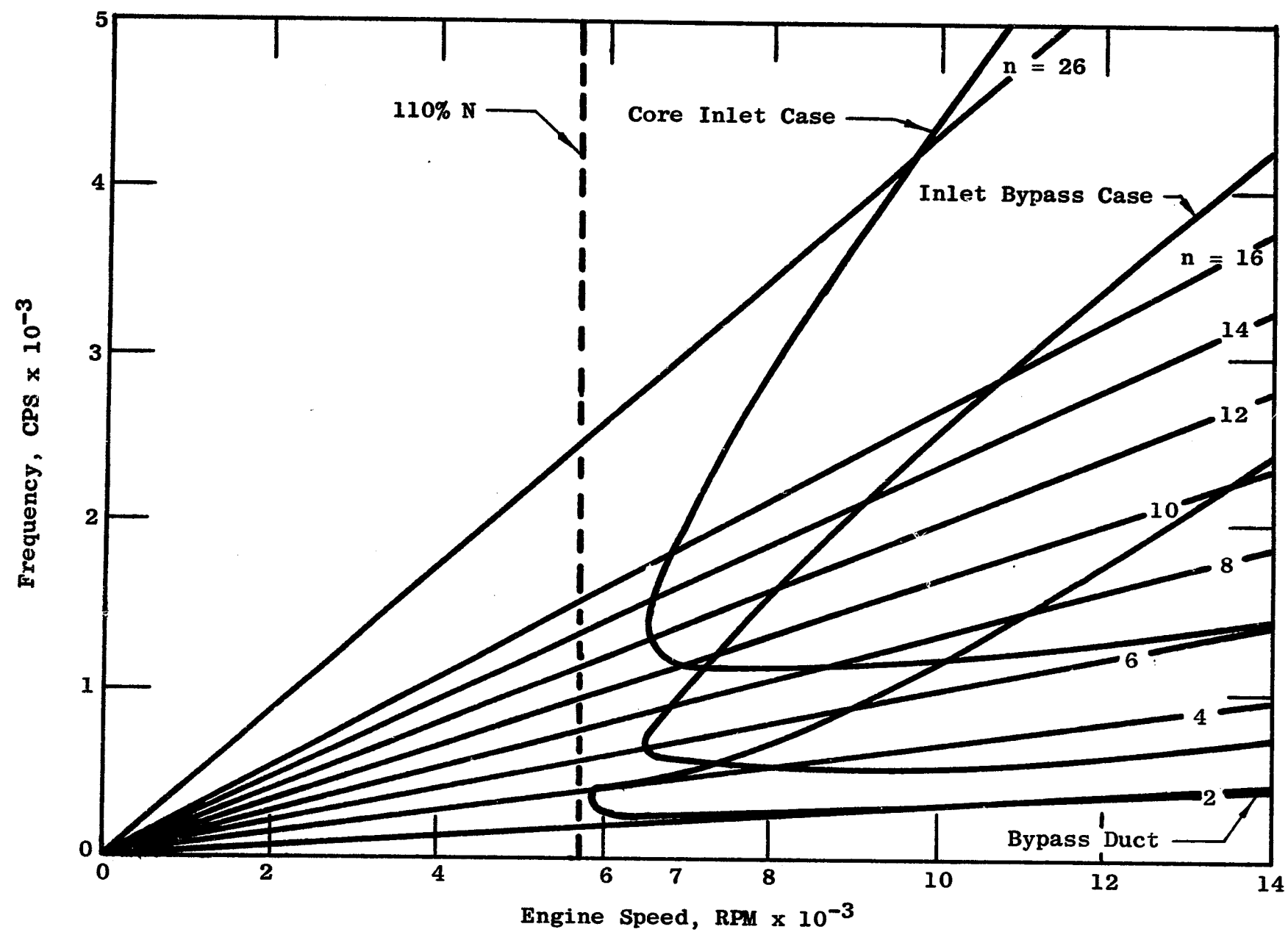


Figure 179. Campbell Diagram for the Fan C Casings

figuration (see Figure 180). Attachment of the core compressor to the frame is accomplished without alteration of either part. Due to the difference in fan bypass ratios, the engine ducting and fan nozzles are new hardware. Mounting the CF6 gearbox required only redesigned brackets, otherwise that system is identical to the CF6. The fan modules, as modified for engine operation, are shown in Figures 181, 182, and 183.

- Bearing Support Cones

The core inlet flowpath for the three fan designs is radially smaller than the CF6, requiring the bearing support cone to be modified. This is accomplished by maintaining the configuration of the forward portion of the cone as is, and altering the cone angle between the two rear flanges to suit the new requirements.

- Fan Frame

Design of the frames has considered engine requirements such as required stiffnesses, engine mounting, and service-line access. These features have been described in previous sections.

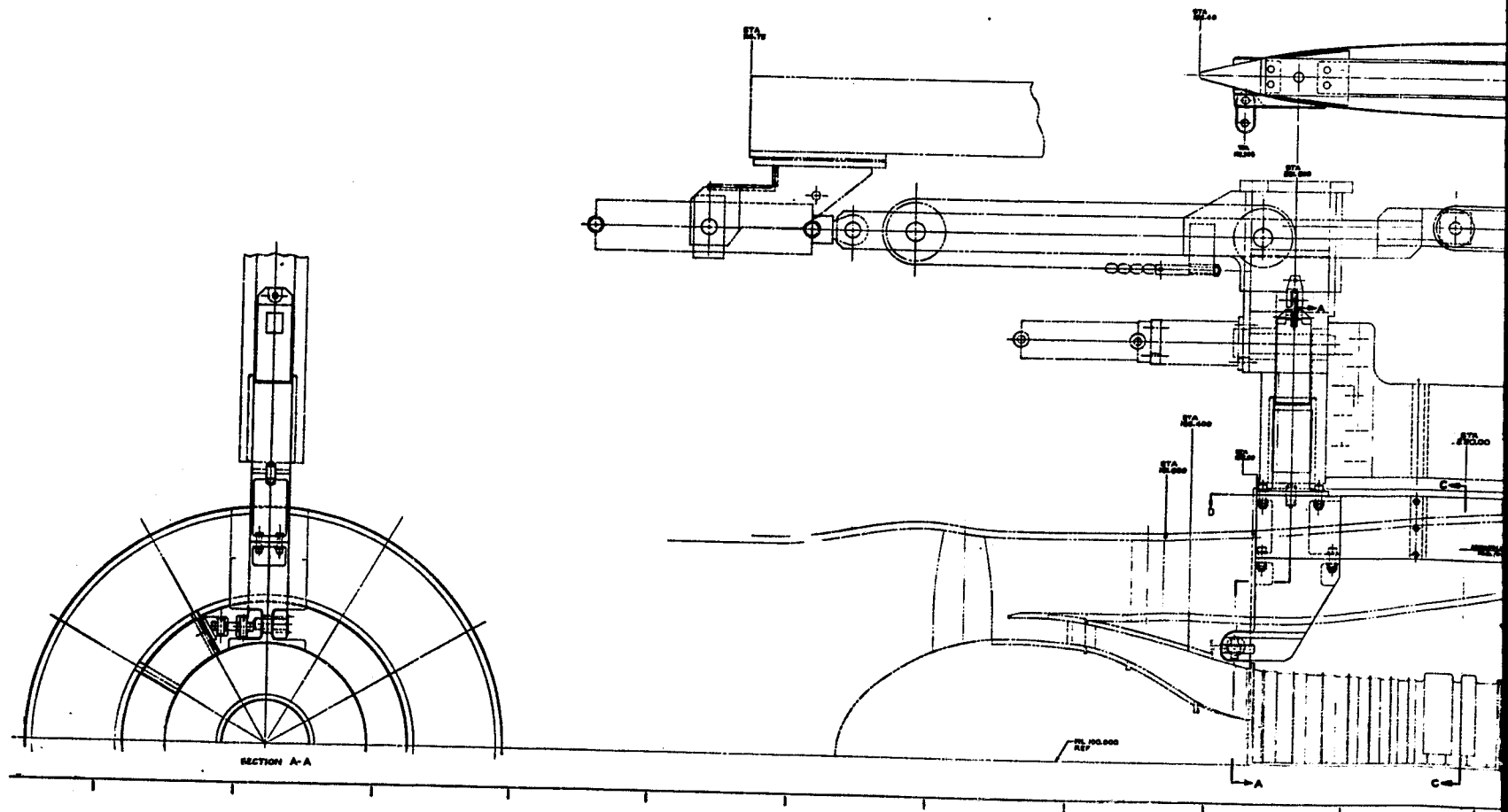
5.2.1.4.2 Engine Mount System

The mounting system for the demonstrator engines (Figure 184) is a two-plane system similar in principle to the CF6 configuration. It is a non-redundant system allowing accurate determination of all resultant loads. The use of spherical bearings at each end of the individual mount links restricts resultant loads to the axis of the link. Mount links are arranged so that the engine is stable when subjected to axial, vertical, and side loads and roll, pitch, and yaw moments. The mount system is designed to support the engine for both steady state and vibratory load conditions.

The forward mount is attached to the 12-o'clock fan frame strut in the annular flow splitter area. Axial, side, and vertical loads are transmitted through the forward mount and its accompanying side linkage.

The aft mount plane is located at the turbine midframe. The three links of the aft mount plane transmit vertical, side, and torque loads from the engine to the engine support structure.

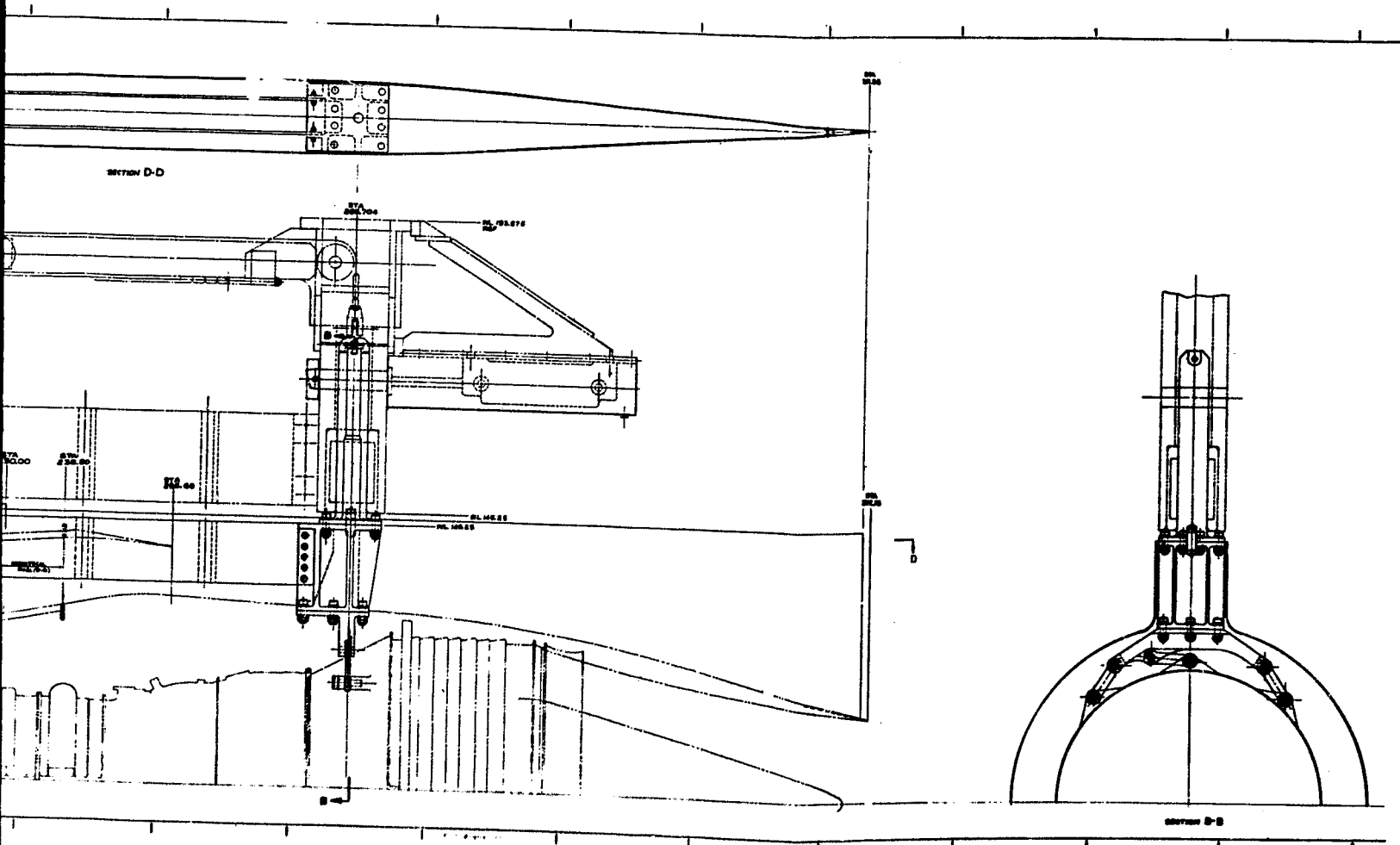
Two mounting systems have been designed for the demonstrator engines -- one for the "A" and "B" engines and one for the "C" engine. Although the



PRECEDING PAGE BLANK NOT FILMED

Figure 180. Fan B Eng

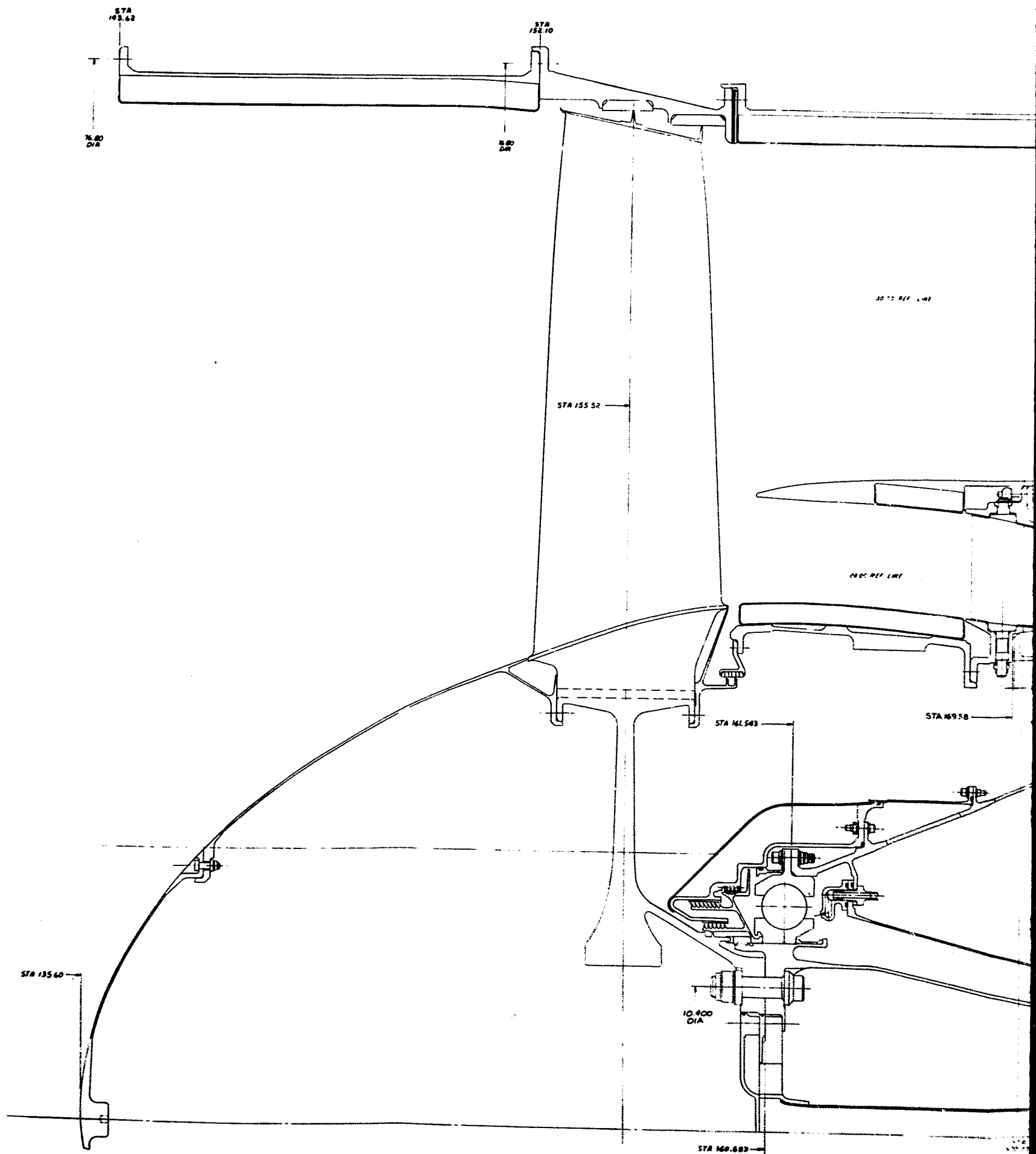
FOLDOUT FRAME

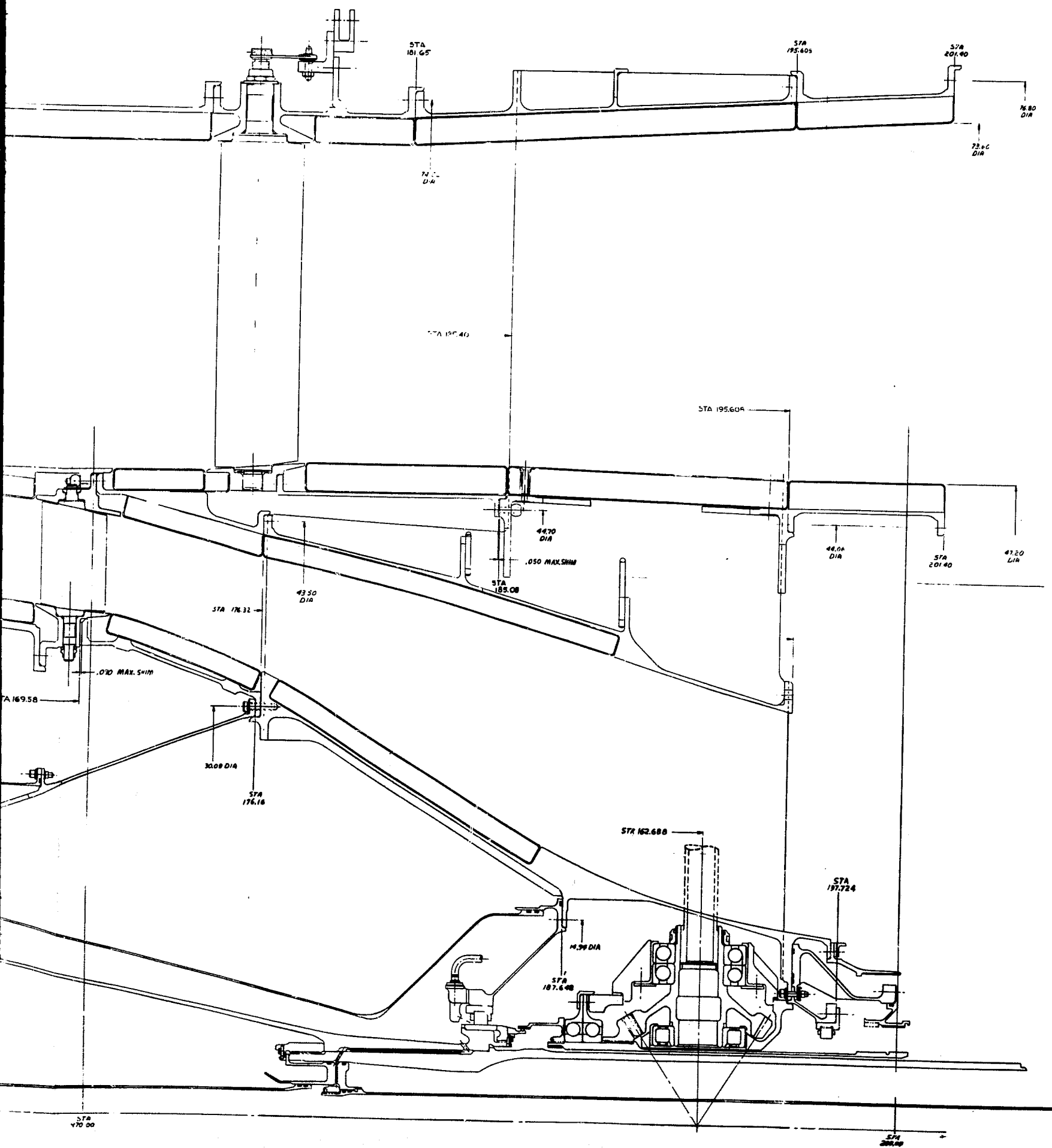


Engine Installation

FOLDOUT FRAME

2





Fan A Engine Configuration

FOLDOUT FRAME
2

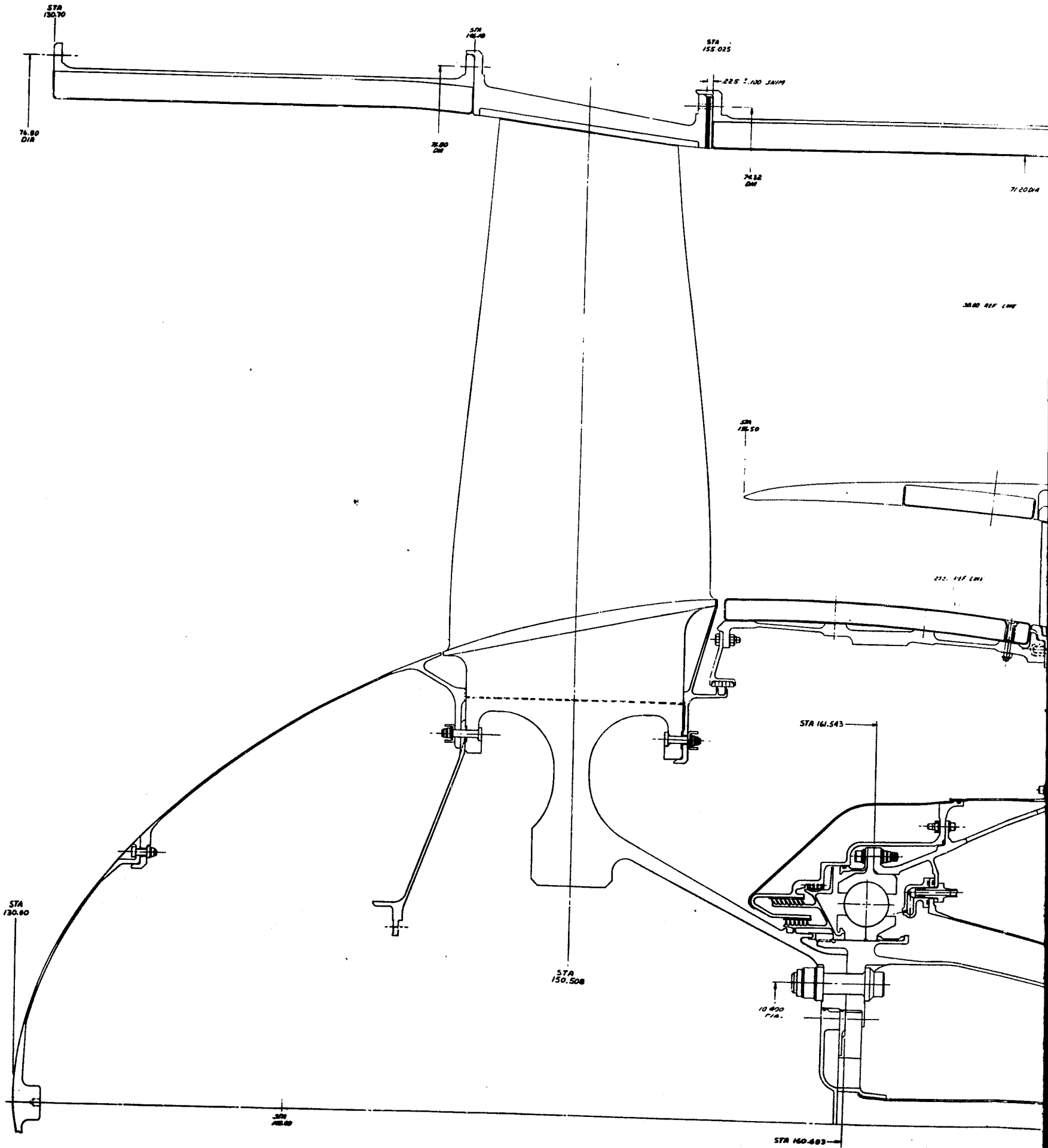


Figure 182. Fan B End

FOLDOUT FRAME



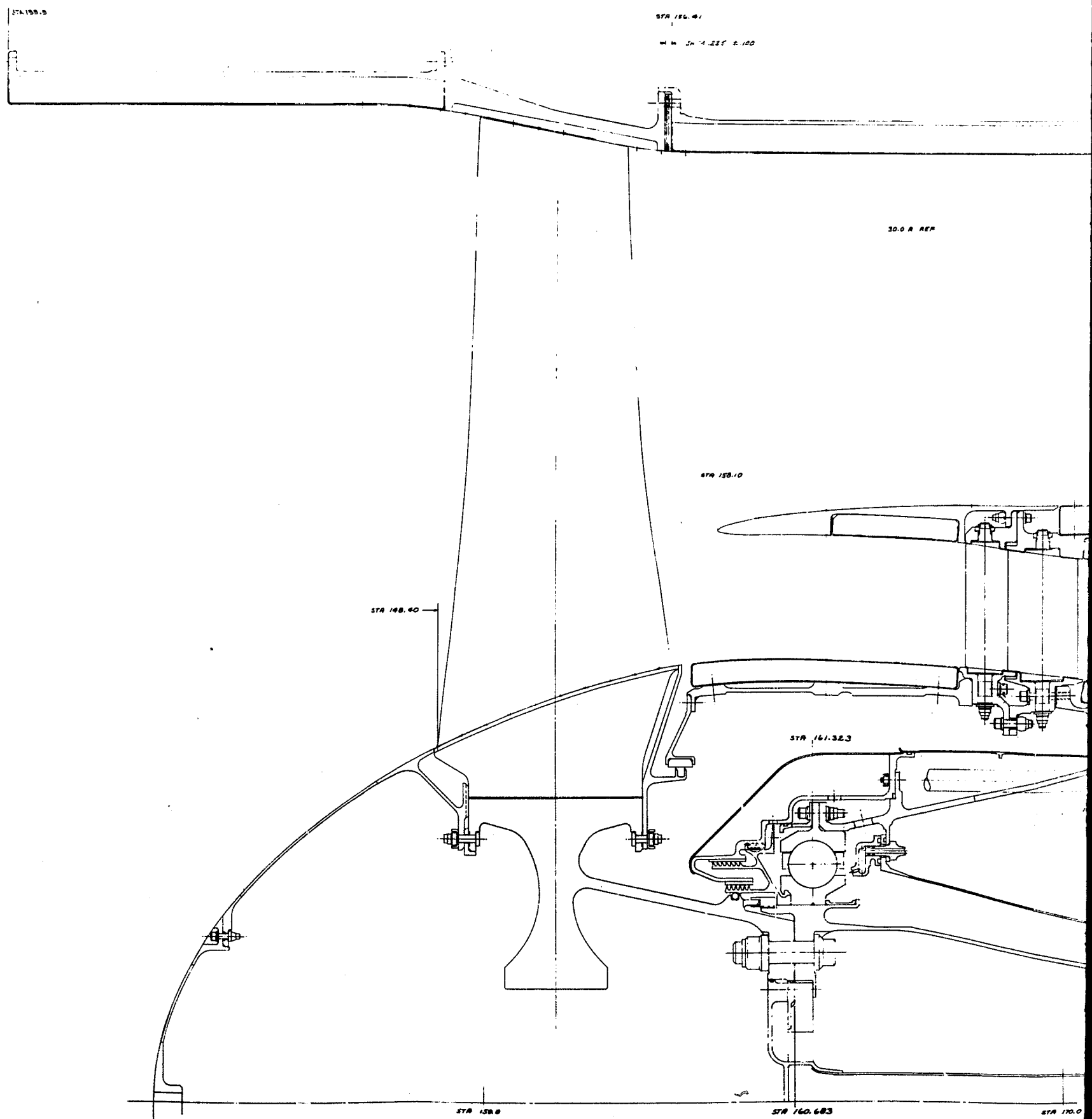
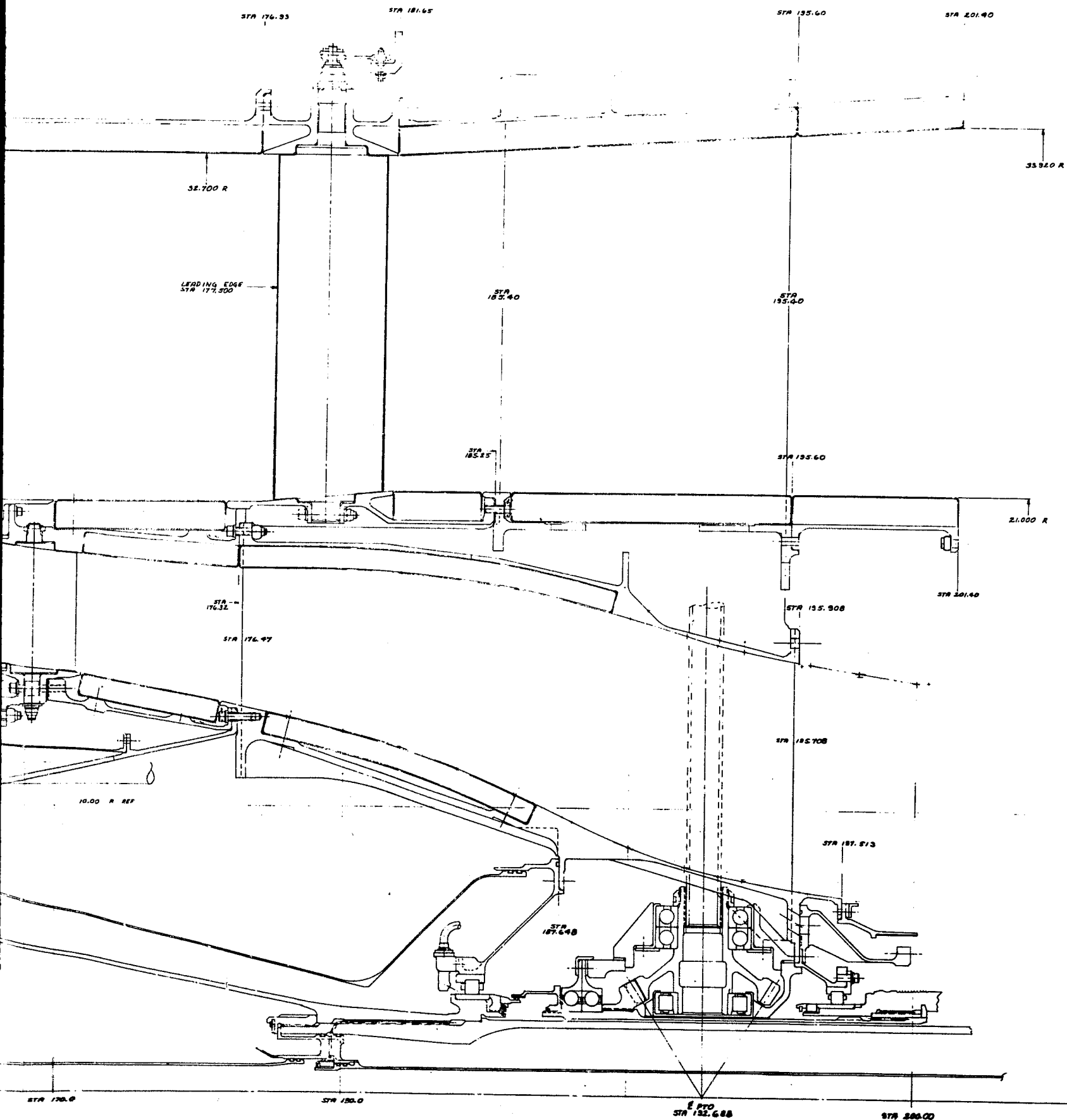


Figure 183. Fan C Eng



C Engine Configuration

FOLDOUT FRAME

2

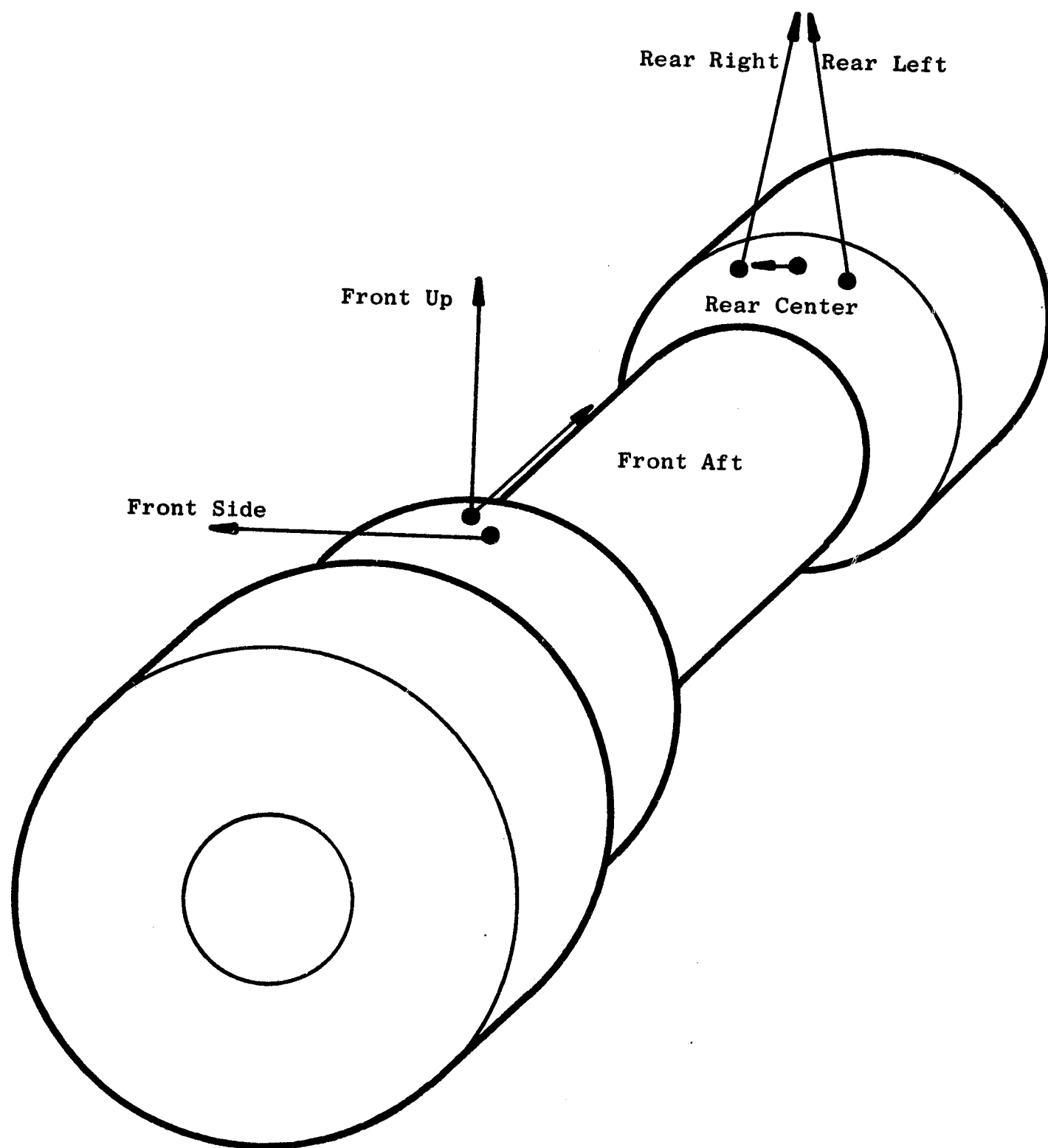


Figure 184. Engine Mounting System, Location of Load Components

basic configuration for the two systems is identical, the C engine's reduced bypass area requires dimensional changes to the mounting system.

- Design Requirements

Like the CF6 engine, the mounting system for the demonstrator engines is designed so that all forces in the links and main front mount structure are statically determinant. This condition is met by assuring the following requirements:

- a) All reaction points on the engine must have spherical bearings, free to rotate about all axes passing through the point of load application.
- b) The thrust force must be reacted at only one point on the engine, whereas side and vertical loads are reacted in two planes.
- c) Moments about the engine longitudinal axis must be reacted in only one transverse mounting plane.
- d) There are only two transverse mounting planes in which all mounting loads are reacted.
- e) The mounting system must not restrain the engine thermal expansion in any direction.

- Loading

The mounting system has been designed to support the engine under test cell loading (Table XLVI) and flight loading (Table XLVII), as determined from the flight maneuver envelope illustrated in Figure 185 and the derived Table XLVIII. Figure 184 illustrates the locations of the six load components. A factor of safety of 2.0 has been applied to all loadings for determination of link stresses. Vibratory loads were applied to both test cell and flight operation. Allowable vibratory loads were determined by calculating "G" loading corresponding to deflection limits established for the CF6 engine: 0.004 inch radial and 0.002 inch axial deflection for the low pressure system, 0.001 inch radial and 0.0005 inch axial deflection for the high pressure system. The resulting vibratory "G" loads for the "A/B" engines were 1.948 "G's" radial and 0.934 "G's" axial, acting at the engine centers of gravity (buttline 100, centerline 100, station 219.3). The C engine vibratory loads were 2.753 "G's" radial and 1.377 "G's" axial acting at the engine center of gravity. The larger vibrational loadings for the C engine result from the increased rpm of both the low and high pressure systems.

Table XLVI. Maximum Test Cell Loads, Engine Mounts

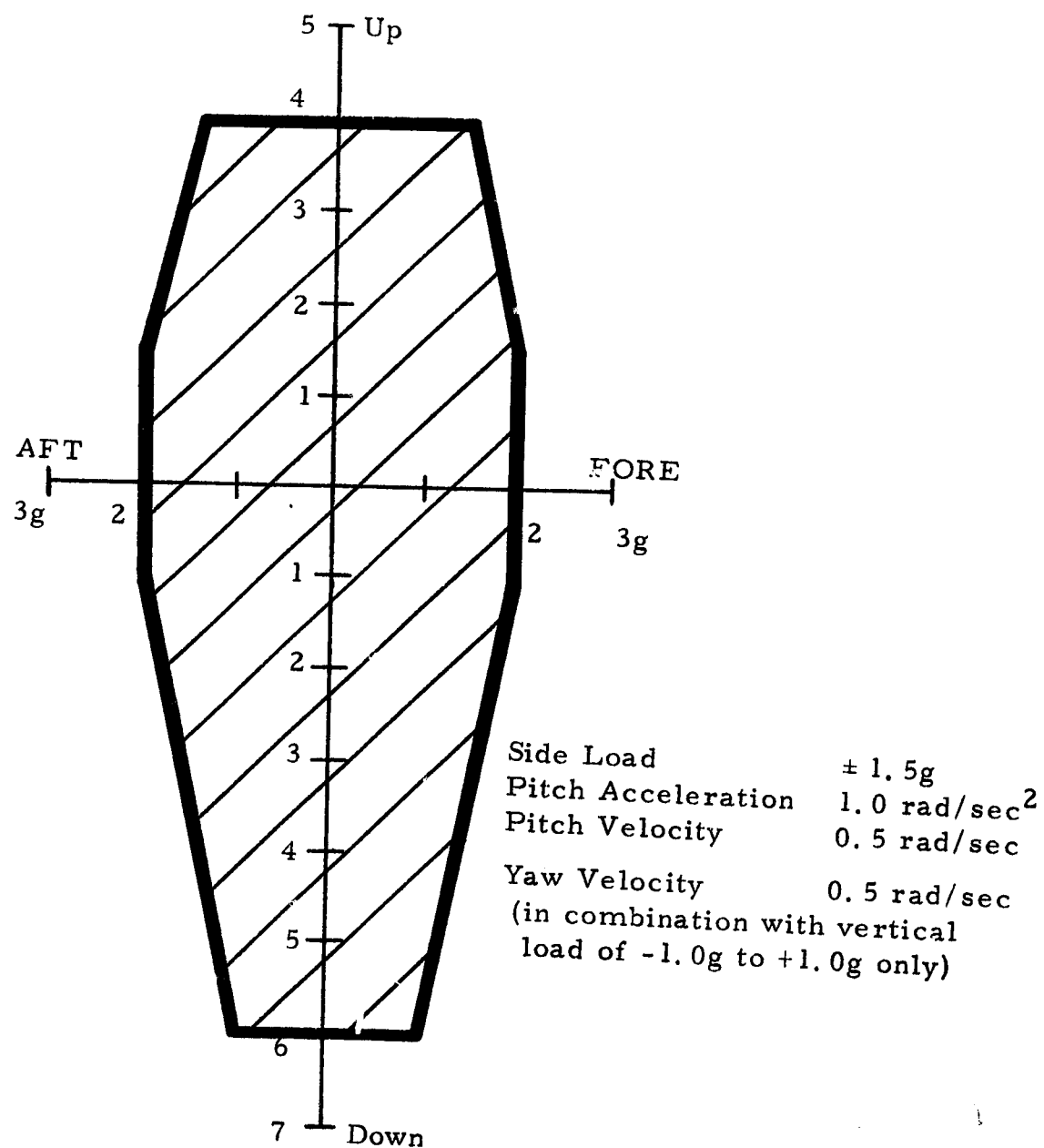
Location	A and B Engines		C Engine	
	Steady State	Vibratory	Steady State	Vibratory
Front Vertical	9 547	21 148	8 800	27 400
Front Side	0	18 501	0	24 300
Front Aft	22 000	12 434	22 000	17 200
Rear Left Link	5 054	30 095	4 500	35 900
Rear Right Link	5 054	22 195	4 500	23 400
Rear Center Link	0	37 495	0	34 200

Table XLVII. Maximum Flight Loads, Engine Mounts

Location	A and B Engines		C Engine	
	Steady State	Vibratory	Steady State	Vibratory
Front Vertical	93 252	17 970	86 232	23 444
Front Side	38 258	15 721	37 318	20 393
Front Aft	44 624	10 566	43 028	14 478
Rear Left Link	52 336	25 574	73 127	30 200
Rear Right Link	47 607	18 860	60 377	19 695
Rear Outer Link	64 177	31 862	66 777	28 755

Table XLVIII. Flight Conditions for Maximum Flight Loads

Maximum Load	Front Vert.	Front Side	Front Aft	Rear Left	Rear Right	Rear Center
G's Up	-6	0	0	-6	-6	0
G's Side	-1.5	1.5	-1.5	1.5	-1.5	-1.5
G's Forward	-1	2	2	1	1	2
Pitch Accel	1	1	1	1	1	5
Pitch Velocity	0.5	0.5	0.5	0.5	0.5	0.5
Yaw Accel	0	0	0	0	0	2
Yaw Velocity	0	0.5	0.5	0	0	0
Thrust Forward	22 000	22 000	22 000	22 000	22 000	22 000



NOTES:

1. Load factors and angular accelerations and velocities are taken about the center of gravity of the engine.
2. Side loads and gyroscopic loads do not act simultaneously.
3. All loading conditions occur over the range from zero to maximum engine thrust.
4. At landing, angular accelerations increase to a limit of 5 rad/sec^2 in pitch and 2 rad/sec^2 in yaw.

Figure 185. Flight Maneuver Loading Diagram

Materials of the mounting system components have been selected to limit component stresses at the design temperature to whichever is lower:

- a) 100% of minimum 0.2% offset yield strength
- b) 80% of minimum ultimate tensile strength

The vibratory stress of the link components is smaller than the allowable vibratory stress for the component's material as specified by its Goodman diagram.

- Mount System Material Selection

Table XLIX presents a summary of the mount system components, their vendor and/or material designation, and their maximum strength capabilities.

- Mount System Analysis

The MOUNT time-sharing computer program was used to determine mount loads. The MASS computer analysis was used to calculate mount system deflections and stresses.

The maximum test cell deflection for the B engine configuration at the center of the main thrust uniball is 0.009 inch aft and negligible to the side.

The maximum link stress for test cell operation is 88000 psi (based upon a safety factor of two, applied to the operational loads).

- Facility Mount Adapter

The facility mount adapter ties the engine mounting systems to the CF6 test cell support structure. It is designed to fall within the upper pylon coordinates of the A, B, and C engines. A single adapter, Figure 186, accommodates both the A/B and C engine configurations. Figures 180 and 187 illustrate the adapter as it will be assembled in the test cell buildup of the A/B and C engines, respectively. The primary difference between the support structure of the two configurations is the location of the aft mount. The aft mount of the C engine is 3.92 inches farther forward than its A/B counterpart.

The adapter is a welded-and-bolted 17-4PH structure. The large vertical pins of the adapter are designed to fit into the existing CF6 support and hoist structure. Due to a reduced pylon width, the large beam component of the adapter assembly connecting the forward and aft mounting planes must

Table XLIX. Mount System Material Summary

<u>Component</u>	<u>Vendor/Material</u>	<u>Strengths</u>
Main Thrust and Vertical Load Uniball	Network Electronic No. HU26-101 Ball and Race - Plated Alloy Steel	Ultimate Static Load 850000 lbs radial
Main Thrust and Vertical Load Pins	AMS 5643 (17-4PH)	125000 psi 0.2% yield strength at 150°F
Front Mount Structure	AMS 5643 (17-4PH)	125000 psi 0.2% yield strength at 150°F
Front Side Link	AMS 5643 (17-4PH)	125000 psi 0.2% yield strength at 150°F
Front Side Link Uniballs	Southwest Products Co. No. SWRR-16 Ball and Race - Plated Alloy Steel	Ultimate Static Load 480000 lbs radial
Aft Mount Yoke	AMS 5643	(Same as above)
Aft Mount, Double-Rod End (B Engine - CF-6 Part)	Southwest Products Co. No. LC1136 Ball and Link - Alloy Steel	Ultimate Static Load 480000 lbs radial
Aft Mount Links (C Engine)	AMS 5643 (17-4PH)	Ultimate Static Load 480000 lbs radial
Aft Mount Link Uniballs (C Engine)	Southwest Products Co. No. SUDN 16 Ball and Race - Plated Alloy Steel	Ultimate Static Load 310000 lbs radial

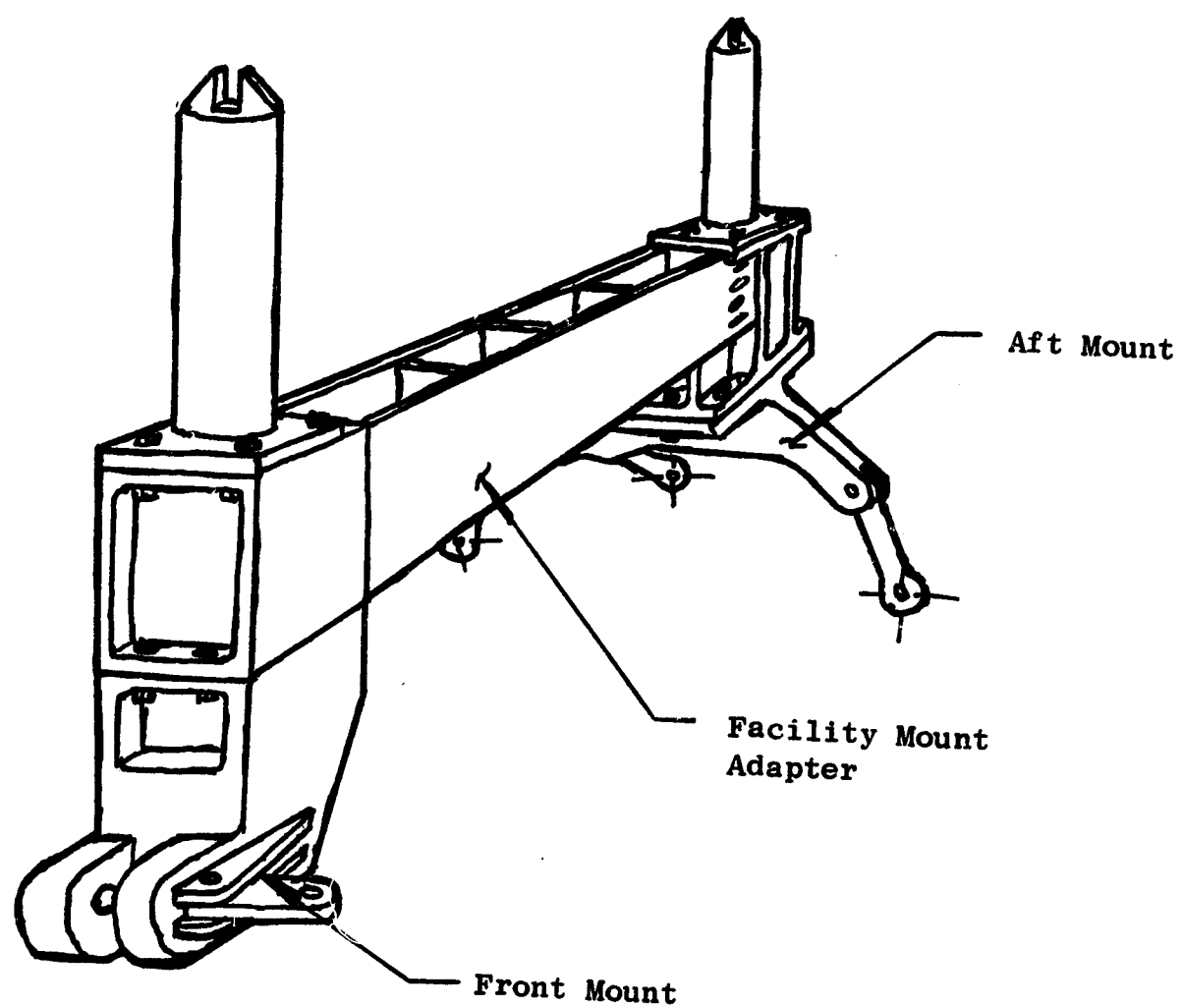


Figure 186. Engine Mount System and Facility Mount Adapter

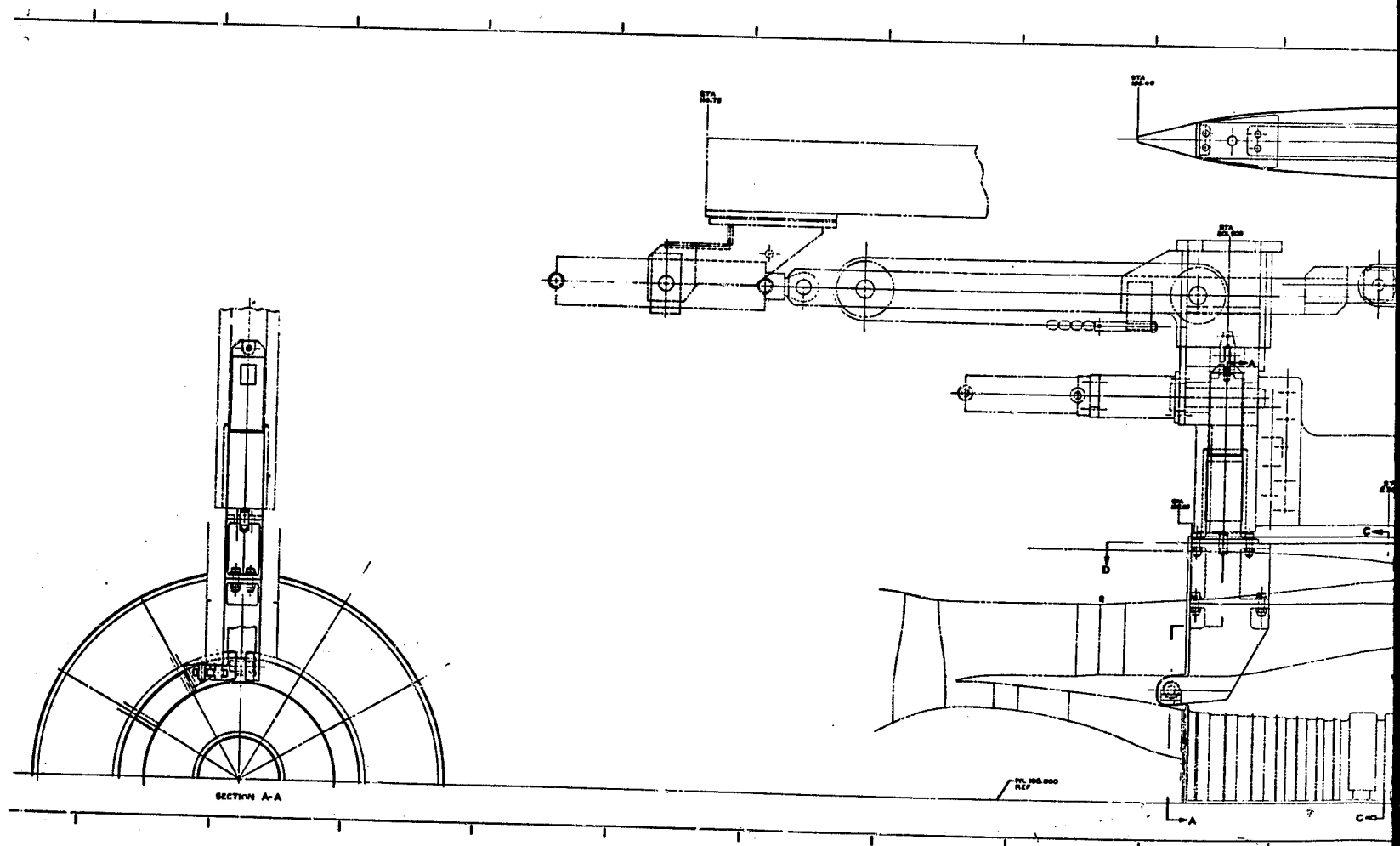


Figure 187. Fan C -

FOLDOUT FRAME

0

1

be somewhat narrower than the corresponding component of the CF6 configuration (6 inches compared to 11 inches). The resulting loss in stiffness is compensated by an increase in beam depth.

The length between mounts compensates for the thermal growth of the engine such that the links of the aft mount become aligned vertically during engine operation.

5.2.1.4.3 Bypass Ducting, Pylons, and Fan Nozzle

The bypass ducting and fan nozzle of the demonstrator engines are split aluminum casings. Ducting between the fan frame and fan nozzle is designed to accommodate attachment of sound suppression panels. The bolted in, removable panels will be similar in configuration to those used in the fan modules. The combination of split casings and removable panels provides ready access to the core engine. The outer ducting maintains its shell integrity through its bolted attachment to the large beam of the facility mount adapter.

The upper and lower pylons will be nonstructural, aluminum fabrications. The upper pylon, which extends from the fan frame to the turbine nozzle, is bolted to the inner bypass duct and cowl and the facility mount adapter. The lower pylon, which extends from the fan frame to the end of the fan nozzle, is bolted to the inner and outer bypass ducts. Figure 187 illustrates the upper pylon configuration.

PRECEDING PAGE BLANK NOT FILMED

6.0 LOW PRESSURE TURBINE AERODYNAMIC DESIGN

6.1 SUMMARY

This section presents the aerodynamic design of the experimental quiet engine low pressure turbines. Two different low pressure turbine designs are required for the experimental quiet engine configurations because of the fan requirements of two different low pressure rotor rpm's. The low pressure rotor rpm for Fans A and B is approximately 3300, while that for Fan C is approximately 4700.

The rotor speed (3300 rpm) for Fans A and B is essentially the same as for the CF6 low pressure rotor, resulting in a good match with the CF6 turbine. Therefore, a turbine consisting of the first four stages of the five-stage CF6 was selected to drive Fans A and B. The first four stages only are required, as the lower bypass ratio of 5.3 (compared to 6.2 of the CF6) results in a lower work output requirement. The average stage loading is lower than for the CF6, the exit Mach number is lower, and the exit swirl is nearly zero; hence, the turbine efficiency should be high. It was necessary to reduce the flow function of the turbine by about 3.5 percent, and this was accomplished by a small change in the first stage vane.

The turbine requirements for driving Fan C, due to the increased rpm, are such that the basic CF6 design could not be used. A new high-loading design, matching the high pressure turbine diameter (and with a consequently simplified turbine midframe and duct) was selected for Fan C. With the high rpm and wheel speed available, a two-stage turbine will satisfy the requirements. The turbine has essentially zero exit swirl, and the exit Mach number is consistent with that for the CF6 five-stage turbine.

The turbines for all fans are operating at even more conservative conditions of temperature and pressure level, compared to the original CF6 design conditions. The inlet temperature is lower, the inlet pressure is less, and, for Fans A and B, the rpm is about 3 percent less. The rpm for Fan C is higher, but the diameter is smaller, and, in general, it is a conservative design for stresses.

The turbine exit Mach numbers are low and the exit swirl is small, which should contribute to low noise operation. For Fans A and B, the exit Mach number is 0.285, and the exit swirl is 4 degrees. For Fan C, the exit Mach number is 0.40 and the exit swirl is 1 degree.

6.2 FANS A, B, AND C LOW PRESSURE TURBINE DESIGN REQUIREMENTS

The important parameters established by the cycle operating conditions are listed as follows with data given for sea level static — standard day, and also for the design point at altitude cruise conditions of 35K, M 0.820, standard day.

Parameter	Fan A		Fan B		Fan C	
	SLS	Cruise	SLS	Cruise	SLS	Cruise
Inlet Temperature, °R	1691	1567	1670	1545	1661	1532
Inlet Pressure, psia	51.8	21.8	52.8	22.3	54.3	22.8
Exit Pressure, psia	20.16	7.25	20.15	7.27	18.81	6.22
Pressure Ratio	2.57	3.01	2.62	3.06	2.88	3.67
Flow, lb/sec	131.2	57.6	134.4	59.4	141.6	61.7
Inlet Flow Function	104.1	104.7	104.0	104.7	106.3	105.7
Turbine Speed, rpm	3271	3373	3317	3375	4706	4834
Turbine Corrected Speed	79.54	85.20	81.17	85.86	115.5	123.5
Shaft Work, BTU/lb	89.4	93.8	89.8	93.8	95.6	104.0
Turbine Energy Function	0.0529	0.0599	0.0538	0.0607	0.0576	0.0679
Reynolds Number Index	0.817	0.373	0.844	0.388	0.872	0.401
Turbine Efficiency	0.918	0.910	0.917	0.910	0.903	0.895

6.3 FANS A AND B LOW PRESSURE TURBINE

The low pressure turbine for driving Fans A and B is the first four stages of the CF6 five-stage turbine. The only modification required to the CF6 turbine was a reduction of about 3.5 percent in flow function, which was accomplished by a reduction in the first-stage vane throat area. The inlet pressure and temperature were lower and, due to the lower bypass ratio of the Quiet Engine, the required work output per pound of flow was less. This resulted in a reduction in over-all turbine pressure ratio to 2.63 on the Quiet Engine, for the four-stage group. This unloaded the latter stages of the turbine somewhat and resulted in about four degrees of forward running swirl at the SLS point. The average turbine loading was reduced to 0.764 on the Quiet Engine four-stage. The effect on incidence angles on the vanes and blades was in the direction of a few degrees more negative angle of attack. The turbine efficiency should be somewhat improved by the reduction of the low pressure turbine design parameters. The fourth-stage exit annulus area resulted in an exit Mach number of 0.285, which is quite conservative and should be favorable for low turbine exit noise.

Low pressure turbine maps for Fans A and B are shown in Figures 188 and 189. The operating points for SLS and altitude cruise are indicated on the maps. Low pressure turbine design data for Fans A and B at the maximum-power operating conditions are presented in Table L.

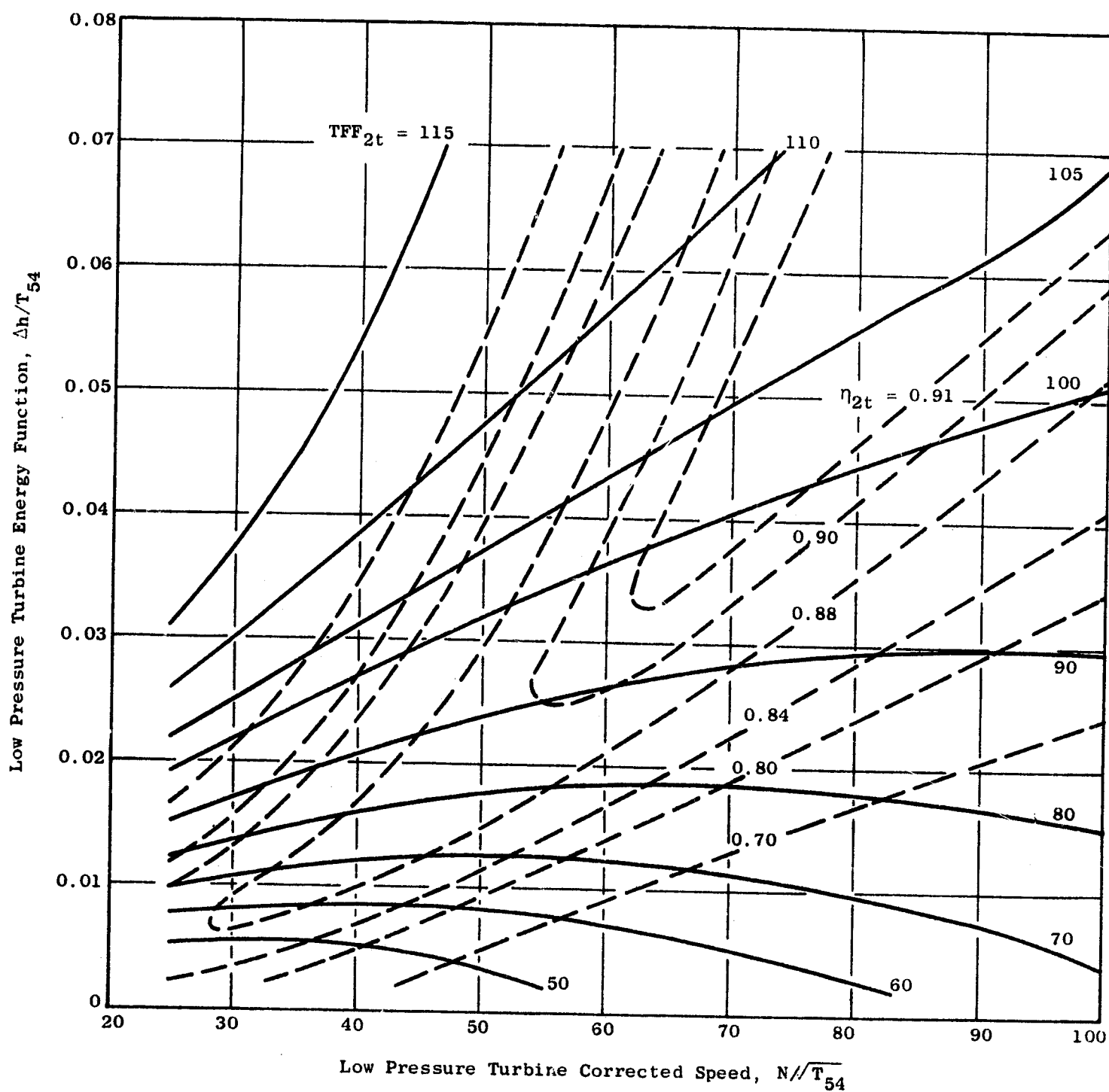


Figure 188. Engine Configuration A, Low Pressure Turbine Map

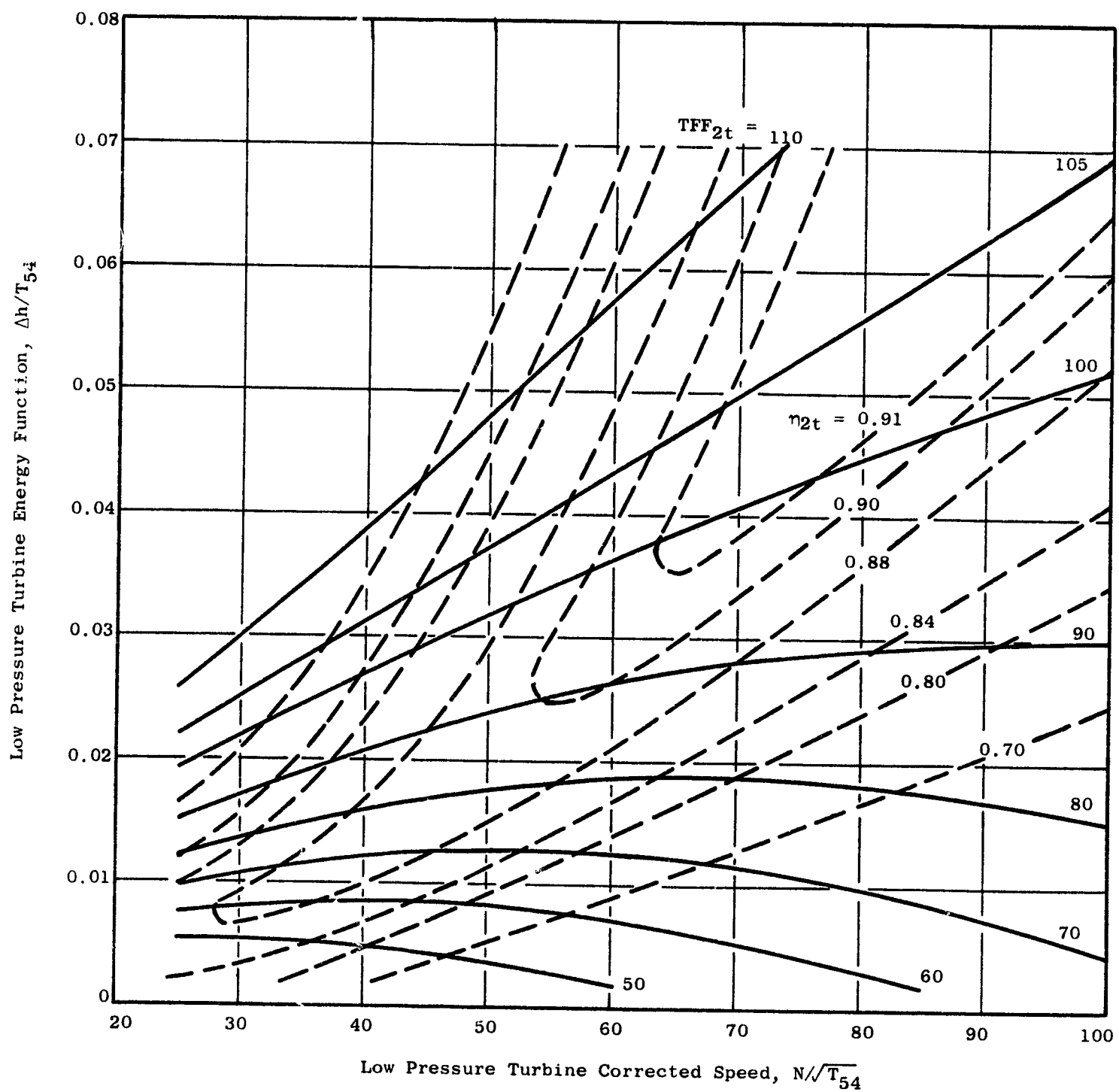


Figure 189. Engine Configuration B, Low Pressure Turbine Map

Table L. Design Data, Fans A and B, Maximum-Power Operating Conditions

Stage	1		2		3		4		Turbine Total	
Diameter	ID	OD	ID	OD	ID	OD	ID	OD		
Vanes:										
Exit diameter, inches	40.40	48.27	38.72	48.23	36.15	48.20	33.51	48.16		
Number	84		84		96		108			
Inlet angle	0	0	20.06	16.63	13.20	10.24	4.67	3.33		
Exit angle	66.15	62.16	62.69	57.25	60.14	52.57	56.71	46.65		
Inlet pressure, psia	51.80		38.10		29.05		23.32			
Inlet temperature, °R	1691		1577		1480		1407			
Blades:										
Exit diameter, inches	39.80	48.26	37.65	48.22	34.90	48.18	32.23	48.15		
Number	166		142		126		112			
Inlet angle	50.05	30.25	44.21	16.57	38.57	0	32.36	-15.86		
Exit angle	55.04	57.97	50.93	55.72	46.14	54.18	39.12	52.23		
Exit Mach no.	0.287		0.288		0.285		0.285			
Exit Swirl angle	18.2		11.5		3.9		-4.3			
Stage:										
Shaft work, BTU/lb	30.60		26.35		19.45		14.00		89.40	
Blade velocity, pitch, U_p	629		613		593		574			
Loading, $gJ\Delta h/2U_p^2$	0.966		0.837		0.685		0.526		0.764	
Turbine efficiency	0.911		0.913		0.912		0.897		0.9177	
Note - All angles measured from axial direction in degrees.										

6.4 FAN C LOW PRESSURE TURBINE

A new turbine design was required to drive Fan C, because of the large increase in rpm with the high-tip-speed fan. Because of the higher rotative speed, fewer stages were required, and a highly-loaded two-stage design was selected of approximately the same diameter as the high pressure turbine. This resulted in a pitch loading on the first stage of 1.47 and an over-all average turbine loading of 1.035. The exit Mach number is set at 0.406, which is consistent with present design practice, and the exit swirl angle is about one degree.

The low pressure turbine map for Fan C is shown in Figure 190; the operating points for SLS and altitude cruise are also indicated.

The low pressure turbine design data for Fan C at the SLS maximum-power operating condition are shown in Table LI.

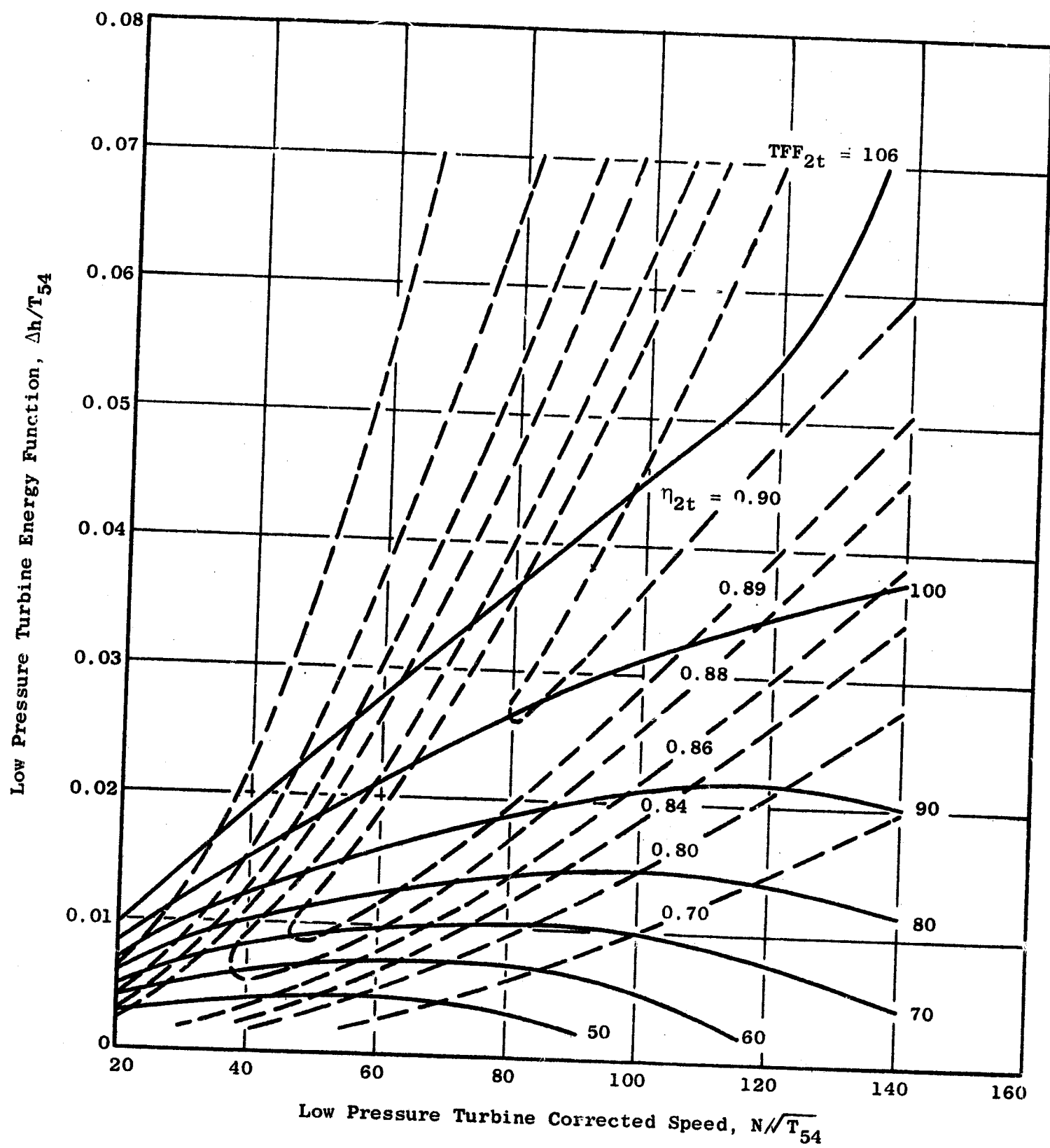


Figure 190. Engine Configuration C, Low Pressure Turbine Map

Table LI. Design Data, Fan C, Maximum-Power Operating Condition

Stage	1		2		Total Turbine	
Diameter	ID	OD	ID	OD		
<u>Vanes</u>						
Exit diameter, inches	29.78	40.88	31.00	43.91		
Number	60		120			
Inlet angle	0	0	52.29	42.84		
Exit angle	73.28	67.60	62.24	53.30		
Inlet pressure, psia	54.3		27.3			
Inlet temperature, °R	1661		1425			
<u>Blades</u>						
Exit diameter, inches	30.35	42.26	31.50	45.00		
Number	118		130			
Inlet angle	67.57	45.33	44.67	0		
Exit angle	65.37	65.38	43.12	52.81		
Exit Mach no.	0.542		0.406			
Exit swirl angle	47.2		1.3			
<u>Stage</u>						
Shaft work, BTU/lb	64.4		31.2		95.6	
Blade velocity, pitch, Up	745		785			
Loading, $gJ\Delta h/2U_p^2$	1.470		0.641		1.035	
Turbine efficiency	0.892		0.904		0.903	
Note: All angles measured from axial direction, in degrees.						